UNIVERSIDAD COMPLUTENSE DE MADRID
FACULTAD DE CIENCIAS QUÍMICAS
DEPARTAMENTO DE QUÍMICA INORGÁNICA I

TESIS DOCTORAL

Metal-cation arrangement control in secondary building units of metal-organic frameworks and their translation to oxides

Control de la disposición de cationes metálicos en unidades de construcción secundarias de estructuras metal-orgánicas y su transferencia a óxidos

MEMORIA PARA OPTAR AL GRADO DE DOCTORA

PRESENTADA POR

Celia Castillo Blas

DIRECTORES

María de los Ángeles Monge Bravo
Felipe Gándara Barragán

Madrid
Ed. electrónica 2019

UNIVERSIDAD COMPLUTENSE DE MADRID

FACULTAD DE CIENCIAS QUÍMICAS

DEPARTAMENTO DE QUÍMICA INORGÁNICA I

TESIS DOCTORAL

Control de la disposición de cationes metálicos en unidades de construcción secundarias de estructuras metal-orgánicas y su transferencia a óxidos

Metal-cation arrangement control in secondary building units of metal-organic frameworks and their translation to oxides

MEMORIA PAR OPTAR AL GRADO DE DOCTOR

PRESENTADA POR

Celia Castillo Blas

DIRECTORES

María de los Ángeles Monge Bravo

Felipe Gándara Barragán

Madrid, 2019

Universidad Complutense de Madrid

Facultad de Ciencias Químicas

Departamento de Química Inorgánica I

Control de la disposición de cationes metálicos en unidades de construcción secundarias de estructuras metal-orgánicas y su transferencia a óxidos.

Memoria para optar al grado de Doctor presentada por

Celia Castillo Blas

Bajo la dirección de

Prof. María de los Ángeles Monge Bravo

Dr. Felipe Gándara Barragán

Tutor Académico

Prof. Regino Sáez Puche

Madrid, 2019

Metal-cation arrangement control in secondary building units of metal-organic frameworks and their translation to oxides

PhD Thesis

Celia Castillo Blas

Supervisors

Prof. María de los Ángeles Monge Bravo

Dr. Felipe Gándara Barragán

Tutor Académico

Prof. Regino Sáez Puche

Multifunctional and Supramolecular Materials Group

Instituto de Ciencia de Materiales de Madrid – Consejo Superior de Investigaciones Científicas

Madrid, 2019

A mi madre

“El genio se compone del 2% de talento y del 98% de perseverante aplicación”

L. Van Beethoven

Contents

Resumen

Los *metal-organic frameworks* (MOFs) son materiales cristalinos porosos compuestos por una parte orgánica, denominada linker (ligando orgánico que une los centros metálicos) y una parte inorgánica, que puede ser un catión metálico o un clúster de estos, conocida en química reticular como unidades de construcción secundarias (*secondary building units*) o SBUs. La combinación de diferentes SBUs y linkers da lugar a estructuras periódicas con porosidad permanente, diferentes topologías y utilidad en numerosas aplicaciones.

La selección del catión metálico es crucial en la determinación tanto de las características estructurales del MOF resultante, como en las propiedades físicas y químicas del mismo. Recientemente se ha dado un paso adelante con la introducción de mezclas de diferentes iones metálicos en una misma SBU con el fin de modular las propiedades de estos materiales, así por ejemplo la introducción de diferentes tierras raras para la obtención de termómetros con centros luminiscentes, o la utilización de diferentes cationes de la serie *p* para modular la actividad catalítica, en reacciones multi-componentes entre otras.

Existen diferentes estrategias de síntesis para lograrlo: empleo de metaloligandos, modificación post-sintética, y síntesis en un paso, que consiste en combinar los diferentes precursores durante el procedimiento sintético. En este último caso, la incorporación de los metales a los sitios cristalográficos es generalmente al azar, generan materiales dopados, o soluciones sólidas de MOFs.

La novedad del trabajo presentado en esta tesis reside en el desarrollo de la capacidad para incorporar múltiples cationes metálicos de una manera ordenada y dirigida, lo que resulta en la programación por primera vez de secuencias ordenadas de cationes dentro de las SBUs que forman el MOF, y la posterior transferencia de estas SBUs secuenciadas a otro tipo de compuestos. El trabajo presentado en esta tesis se centra por tanto en aumentar el nivel de complejidad en el campo de la química reticular, consiguiendo controlar el orden y la distribución de metales de diferente naturaleza dentro de las SBUs.

Para conseguirlo, en primer lugar, se han estudiado los factores que controlan la incorporación de un segundo metal en una fase conocida, como es la TMPF-88. Esta fase contiene zinc y dos linkers diferentes: el 1,2,4-triazol y el ácido 4, 4'-(hexafluoroisopropiliden)bis(benzoico) (H_2hfipbb). Tras la adición de diferentes cantidades del segundo metal, cobalto en este caso, aparecen nuevas fases competitivas. La realización de un estudio cinético, junto con la realización de cálculos de energía de formación DFT, demuestran que en las fases cinéticamente controladas se incorpora una mayor cantidad del segundo metal. En cambio, en las que son de control termodinámico, el segundo metal se incorpora tan sólo en cantidades traza y aparecen otras fases competitivas.

En base a esto, se eligió como plataforma para la incorporación de metales de diferente naturaleza (cobalto, manganeso y calcio) y sus combinaciones un MOF, conocido como ZnPF-1, y cuya síntesis se controla cinéticamente. Este MOF se compone del ligando H_2hfipbb y una SBU en forma de hélice de tetraedros de zinc. Se han estudiado las diferentes relaciones molares iniciales de los metales Zn:Mn:Co:Ca, denominadas *códigos molares*. El empleo de diferentes códigos molares que incluyen manganeso, calcio y cobalto en algunas proporciones, no varía la topología de la red, aunque en algunos casos al ordenarse estos metales dentro de la SBU la celda unidad del MOF se dobla con respecto a la estructura inicial de ZnPF-1. Todos los compuestos obtenidos (treinta y ocho) se han caracterizado empleando diferentes técnicas: generales (ATG, AE, ICP), microscópicas (SEM-EDS) y difractométricas (difracción de rayos-X de monocristal y de polvo). Dada la proximidad de los cationes utilizados en cuanto a su número de electrones, es imposible distinguir por rayos-X las posiciones de los átomos de zinc, cobalto y manganeso dentro de la SBU. Por ello se recurrió a experimentos de difracción de neutrones de polvo que, en combinación con el resto de técnicas permiten deducir la secuencia de los cationes metálicos dentro de la SBU, generando control a escala atómica. Además, en algunos casos, gracias a los refinamientos Rietveld multi-fase de los experimentos obtenidos en difracción de neutrones y a la presencia de gradientes de composición dentro de un mismo cristal, se demuestra que, dentro de un mismo cristal, puede haber diferentes fases: una con la celda doblada, y otra sin doblar. De esta forma, se observa que el orden de las secuencias de hasta cuatro cationes metálicos a la vez dentro de las SBUs puede controlarse, tanto a la escala atómica, como a escala mesoscópica. Para evaluar la influencia de la presencia

de varias secuencias atómicas, y su distribución mesoscópica dentro de estos materiales, se realizan estudios de propiedades magnéticas, obteniendo diferentes comportamientos según las secuencias de las SBUs.

Finalmente, se ha tratado de obtener óxidos multimetálicos de composición programada para su uso como catalizadores en la reacción de reducción de oxígeno (ORR). Así, diecisiete de los MOFs con SBUs secuenciadas obtenidos, se han transformado mediante un tratamiento térmico a óxidos con estructuras tipo espinela, los cuales conservan la composición de las secuencias del MOF precursor. Estos óxidos multi-metálicos se han evaluado como catalizadores de la reacción de reducción de oxígeno (ORR), fundamental en el desarrollo de celdas de combustible. De su comportamiento se deduce que pequeñas modificaciones en las proporciones de los metales producen variaciones importantes en la actividad electrocatalítica en las reacciones, tanto en términos de densidad de corriente como en número de electrones transferidos, obteniéndose en algunos de ellos valores comparables al del catalizador comercial Pt/C (20% peso), a la vez que presentan estabilidad y tolerancia al metanol.

Summary

Metal-organic frameworks (MOFs) are crystalline, porous materials composed of an organic part, denoted linker, and an inorganic part, which can be a metal cation or cluster, known in reticular chemistry as secondary building unit (SBU). The combination of different SBUs and linkers results in periodic structures with permanent porosity and different topologies, which are useful in many applications.

The choice of metal cation is key in determining the resulting MOF structural features, as well as in their resulting physical and chemical properties. Recent advances have appeared regarding the incorporation of mixtures of different metal cations within a given SBU, with the aim of modulating the properties of these materials. For instance, it has been demonstrated the introduction of multiple rare-earth elements for the obtaining of luminescent materials for thermometry, or the combination of various *p* elements for the tuning of the catalytic activity of MOFs in multicomponent reactions.

There are different synthetic strategies to accomplish this: use of metaloligands, post-synthetic metal exchange, and one pot synthesis combining different metal precursors during the synthetic procedure. In this case, the incorporation of the various metal elements in the crystallographic sites generally takes place randomly, resulting in doped materials, or solid solution MOFs.

The novelty of this thesis lies on the development of the ability to incorporate multiple metal cations in an ordered and addressable manner, which results for the first-time in programming metal-cation sequenced SBUs to form MOFs, and their translation to other types of materials. Thus, the work presented in this thesis is focused in increasing the level of complexity in reticular chemistry, being able to control the order and arrangement of different metal cations within the SBUs.

To accomplish this, the factors that govern the incorporation of a second metal cation in a known MOF, denoted TMPF-88, has been studied, in the first place. This MOF is made of zinc and two different linkers, 1,2,4-triazole, and 4, 4'-(hexafluoroisopropyliden)bis(benzoic)

acid (H_2hfipbb). Upon addition of different amounts of a second cation, cobalt, new competing phases appear. The results of a kinetic study along with DFT based formation energy calculations demonstrate that kinetically controlled phases allow the incorporation of larger amount of the secon metal. On the other hand, thermodinamically controlled phases only allows the incorporation of the second metal element in traze amounts, and with presence of other competing phases.

Based on these results, the MOF known as ZnPF-1 was selected as platform for the incorporation of different combinations of multiple metal elements (cobalt, manganese, and calcium) because this MOF synthesis is kinetically controlled. ZnPF-1 is composed of H_2hfipbb as organic linker, and a helix-shaped SBU made of tetrahedral zinc atoms. Different Zn:Mn:Co:Ca initial metal molar ratios, denoted molar codes, have been investigated. The use of different molar codes does not result in topology changes. However, in some cases the MOF unit cell has a double volume compared to that of the ZnPF-1 initial structure, because some of the metal cations are now ordered in the SBU. All the thirty-eight obtained compounds have been fully characterized by general (TGA, EA, ICP), microscopy (SEM-EDS), and diffraction (single crystal and powder X-ray) techniques. Due to the similar atomic number of zinc, cobalt, and manganese, it is not possible to determine their position with just the use of X-ray. Therefore, neutron powder diffraction experiments have been carried out to elucidate the metal atom sequences, in combination with the rest of techniques. As result, atomic level control on the metal cation arrangements has been accomplished. Moreover, through multiphase Rietveld refinements and determination of compositional gradients in some crystals, the presence of multiple crystalline phases with single, and double unit cell has been demonstrated. Consequently, it has been possible to exert atomic and mesoscopic level control on SBUs composed of up to four different metal elements. The influence of the various atomic sequences, and their distribution within the crystals has been evaluated with the evaluation of the magnetic properties. Different magnetic behaviors have been observed accordingly.

Finally, multimetal oxides with programmable composition have been prepared for their use as electrocatalysts in the oxygen reduction reaction (ORR). In particular, seventeen MOFs with sequenced SBUs have been transformed to spinel type oxides through a thermal treatment, whereas the resulting oxides maintain the parent MOF metal ratios. These multi-

metal oxides have been tested as catalyst for ORR, which is an important reaction for the development of fuel cells. From the obtained results, tt can be deduced that small modifications in the metal ratios produce large variations in the solids activity, both in terms of current density as in the number of transferred electrons. In some cases, values that are comparable to those of commercial Pt/C (20 wt%) have been obtained, with high stability and methanol tolerance.

CHAPTER 1:

INTRODUCTION

1.1. Introduction to Metal-Organic Frameworks

According to IUPAC (International Union of Pure and Applied Chemistry) metal-organic frameworks are defined as '*a coordination polymer (or coordination network) with an open framework containing potential voids'*. On the other hand, '*a coordination polymer is a coordination compound continuously extending in 1, 2, or 3 dimensions through coordination bonds*'. Thus, a coordination network is defined as '*a coordination compound extending, through coordination bonds, in 1 dimension, but with cross-links between two or more individual chains, loops or spiro-links, or a coordination compound extending through coordination bonds in 2 or 3 dimensions'*.[1]

Consistent with these definitions, metal-organic frameworks or MOFs can be described as crystalline porous materials composed of an inorganic part, which can be an inorganic cluster or cation, also called secondary building unit (SBU), and an organic part, denoted as linker, which is an organic ligand.[2] The combination between different linkers and different SBUs results in different metal-organic frameworks with different topology, porosity and dimensionality (figure 1.1).

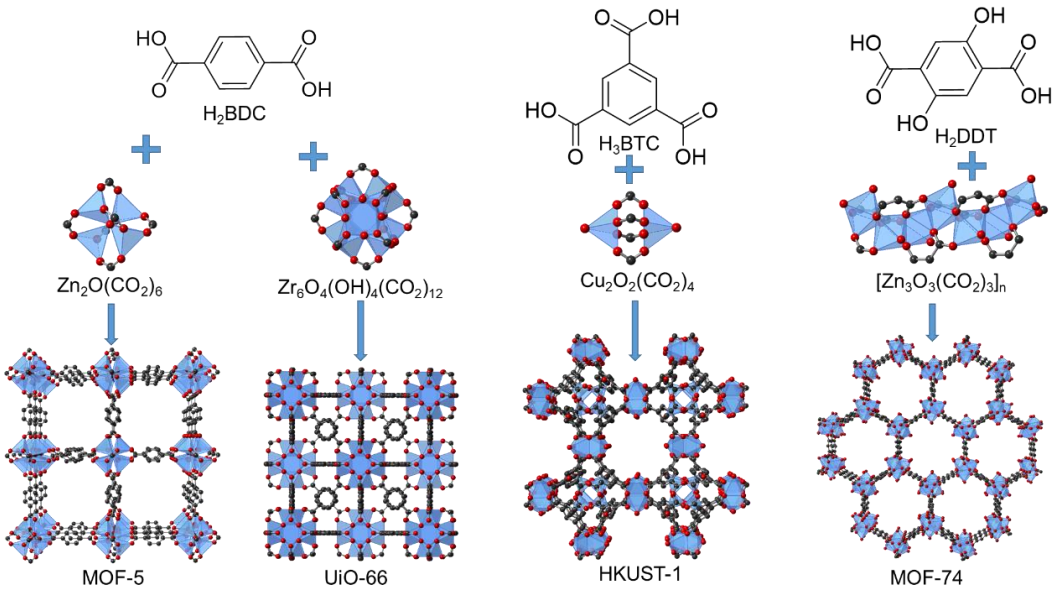

Figure 1. 1. Some representative examples of MOFs. The combination of different organic linkers and inorganic secondary building units results in MOFs with different porosity and topology.

Secondary building units (SBUs) is a term described for the first time by Yaghi *et al*. in 1995 as the moiety that included the metal cluster and the coordination sites of the linker.[3] SBUs play a key factor in the MOFs design, because they confer mechanical stability and versatility depending on the nature of the metal and the organic linker. (figure 1.2. A).

From a historical point of view, it is important to appreciate the relevance of the SBU approach on the development of MOFs. In 1960s materials consisting of single-metal nodes, such as Cu^{2+} bonding to neutral organic donor linkers, commonly based on nitriles were reported.[4-5] Later, pyridine-based linkers were also used to form this type of materials.[5] However, these structures were found to be frail and without architecture stability, because of the weak non-directional bonds linking their constituents and flexibility around the single-metal nodes. In addition, these coordination polymers did not possess porosity and their structures collapsed when the guest molecules were removed. In the 1990's decade it was discovered by Li, *et al.* the first example of a material, which could guest pyridine molecules in its channels, and was thermally stable up to 350 °C. This new material was composed of an organic rigid tritopic carboxylic acid binding with metal ions.[6] Two years later, Kitagawa and co-workers reported another similar material, which could adsorb gases in a reversible way in a pressure range of 1-36 atm without deformation of the crystal framework.[7] Only one year later, the first material which exhibit gas adsorption at low pressures was published by Yaghi *et al*.[8] This material, called MOF-2, was composed of a zinc polynuclear cluster node. Its architectural stability is attributed to the fact that the framework is entirely composed of strong bonds, and the bonds are directional, locking down the position of the metal centers in the SBUs.[9]

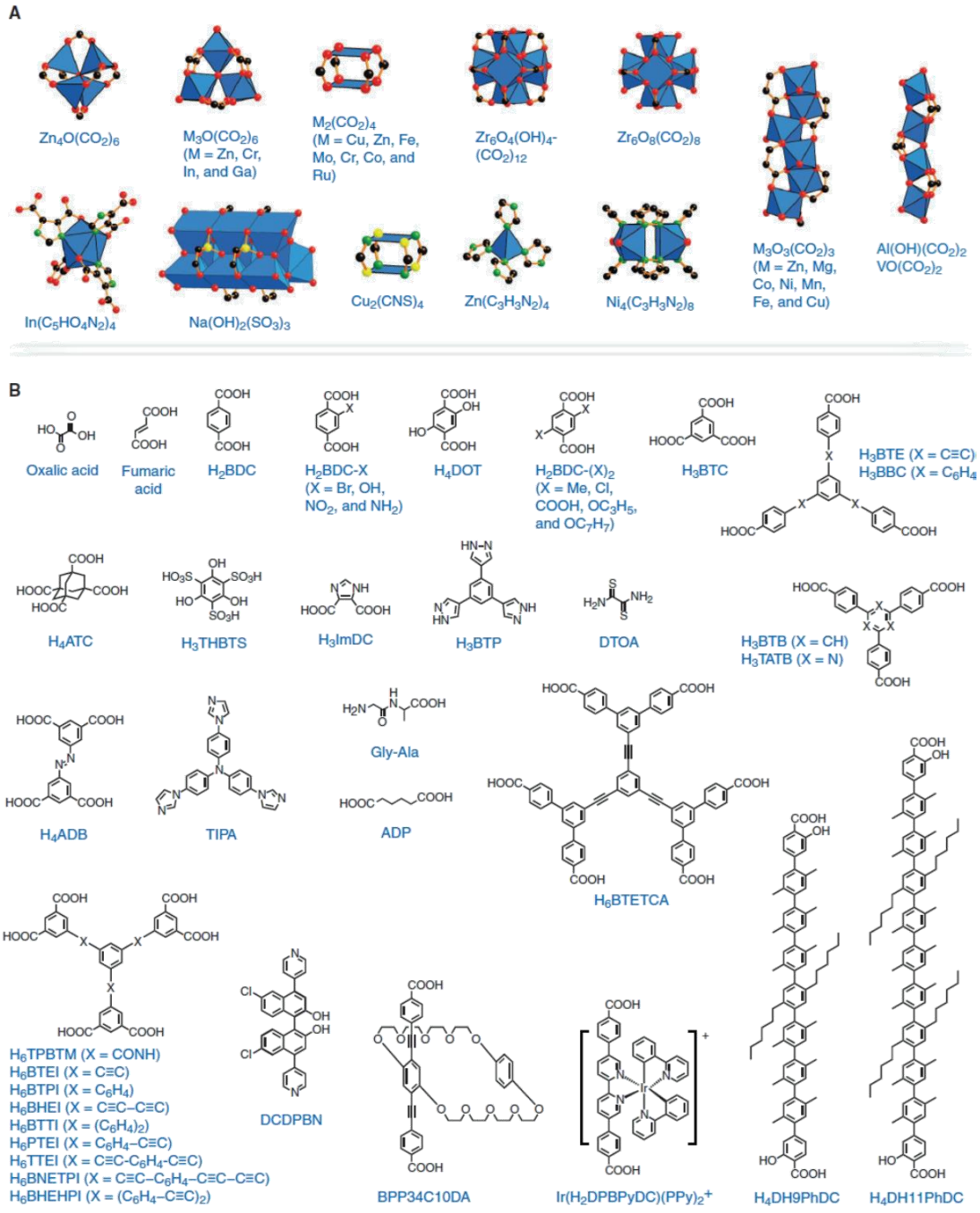

Figure 1. 2. Inorganic secondary SBU (A) and organic linkers (B). Color code: black (C), red (O), green (N), yellow (S), purple (P), light green (Cl), blue polyhedral (metal ions). Hydrogen atoms are omitted for clarity.[2] *Copyright 2013 of Science.*

Nevertheless, the definitive revolution in the field of porous coordination materials appeared in 1999 with two reports by Williams *et al*. and Yaghi *et al*. Williams presented a material called HKUST-1 composed of 1,3,5-benenetricarboxylic acid and copper, which possessed permanent porosity and could adsorb N_2 in a reversible way with a Brunauer-Emmett-Teller [10] surface area value of 692.2 m^2g^{-1}.[11] Yaghi reported a material with permanent porosity and a very high N_2 uptake, largely exceeding the values shown by other microporous materials known until that moment. This material, denoted MOF-5, was composed of an inorganic Zn-cluster and 1,4-benzenedicarboxylic acid as linker. It exhibited a BET specific surface area value of 2320 m^2g^{-1}.[12]

Another important outcome in MOF chemistry arising from the SBU approach is the definition of the isoreticularity. This property allows the modification of MOFs while maintaining the same topology of a structure, for example by employing linkers of increasing length while maintaining the same geometry. MOF topology is denoted with a three-letter code, and it exclusively depends on the connectivity of the inorganic SBUs and the organic linkers (figure 1.3). Thus, isoreticular expansion has been used to prepare ultrahighly porous MOFs through the use of a given SBUs combined with linkers of increasing size, while maintain the same geometry than the parent MOF. The subsequent MOFs in an isoreticular series are often named IRMOF to denote that they were designed using the isoreticular expansion of the original parent structure. The first example of an isoreticular MOF series was based on MOF-5, with a **pcu** topology (figure 1.4).[13] Other successful examples of using this strategy are the series of **fcu** based Zr-MOFs,[14-15] or the MOF-74 series.[16]

On the other hand, organic linkers can possess different chemical nature, rigidity, and points of extension (figure 1.2.B). The chemical nature of organic ligands is variable (carboxylic, nitrogenated, sulfonates), being the most employed carboxylic acid-based linkers. Typically, linkers employed in the formation of porous MOFs are rigid, composed of one or multiple phenyl rings, but other flexible linkers have also been employed in MOFs synthesis, such as (4,4'-hexafluoroisopropylidene)bis(benzoic) acid (H_2hfipbb). The points of extension depend on the nature and the number of functional groups present in the organic linker, which can be heterotopic (two or more different functional groups) or homotopic (two or more equal

functional groups), and they might have two (ditopic), three (tritopic) four (tetratopic), six (hexatopic) points of extension, among others.[2]

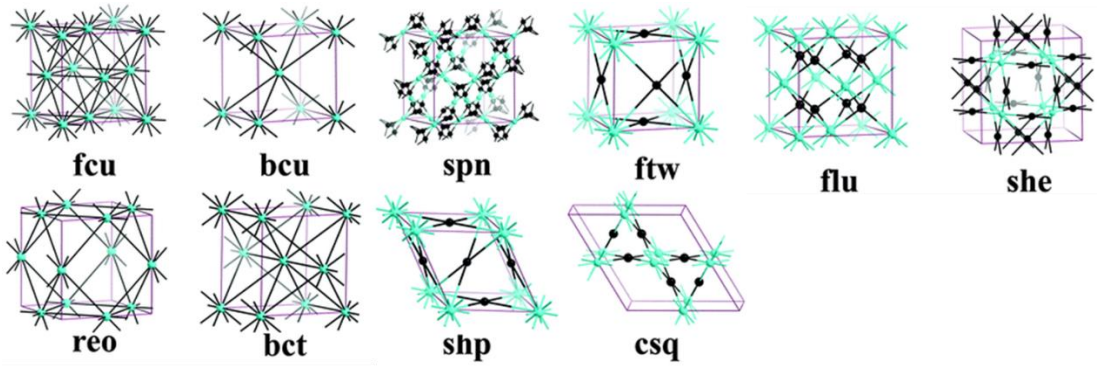

Figure 1. 3. Representative network topologies in many reported MOFs. The topological symbols have been summarized in previous reviews. For example, ***fcu*** *indicates a face-centered cubic net;* ***scu*** *and* ***ftw*** *refer to (4,8)- and (4,12)-connected network;* ***reo****originated from the packing of* ReO_3 *lattice.*[17] *Reprinted with permission. Copyright©2016 Royal Society of Chemistry.*

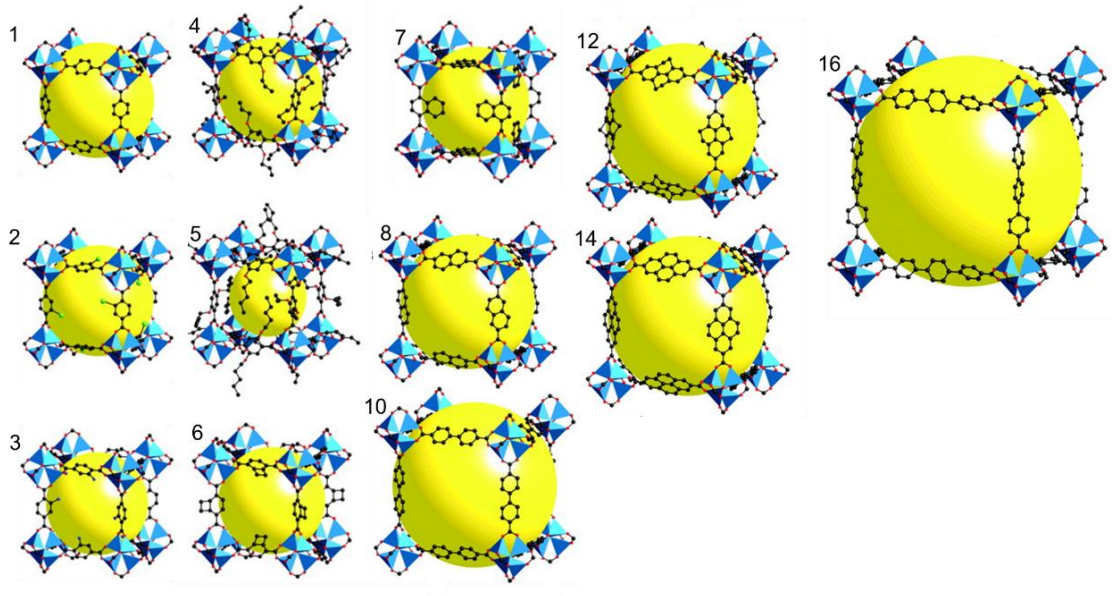

Figure 1. 4. Single crystal x-ray structures of IRMOF-n (n = 1 through 7, 8, 10, 12, 14, and 16), labeled respectively. The doubly interpenetrated IRMOFs (9, 11, 13, and 15) are not shown [see text and (23)]. Color scheme is as follows: Zn (blue polyhedra), O (red spheres), C (black spheres), Br (green spheres in ***2****), amino-groups (blue spheres in* ***3****). The large yellow spheres represent the largest van der Waals spheres that would fit in the cavities without touching the frameworks. All hydrogen atoms have been omitted, and only one orientation of disordered atoms is shown for clarity.*[13] *Reprinted with permission. Copyright 2002 of Science.*

Based on the above described features, MOFs have marked a new era in the field of material science, with more than 80,000 reported structures in the last twenty years thanks to versatility and tunability of these materials.[18] The versatility of MOFs results from the huge number of possible combinations between the different nature linkers and the SBU with different positions and number of the extension points, resulting in different topologies (figure 1.4).[2, 17]

Thus, MOFs are promising materials to be employed in many applications, such as separation and storage of gases,[19-21] luminescence applications,[22] bio-imaging,[23] drug delivery[24] and heterogeneous catalysts,[25] among other applications in energy and life technologies.[26]

1.2. Multication Metal-Organic Frameworks Synthesis

The versatility of MOFs arguably emerges from their modular nature based on the assembly of metal-based inorganic secondary building units (SBUs) and organic linkers; and the structural and topological features of MOFs arise from the geometry and points of extension of both building components.[27] Thus, the selection of metal element governs the type of SBU to be formed, which in turns dictates the framework topology. Importantly, it also influences most of the properties of the resulting MOF, from chemical stability to sorption selectivity or catalytic activity. Thus, while typically MOFs have been formed with the use of only one metal element, the introduction of multiple metal atoms within a given framework expands the range of properties that can be displayed by a desired MOF family.

Consequently, a number of different approaches have been developed in order to incorporate multiple metal elements within a certain MOF. Three are the main approaches to achieve MOFs with structures bearing more than one metal cation: use of organic ligands with additional metal binding sites (metalloligands), post-synthetic metal exchange, or the one-pot synthesis of multi-metal MOFs (figure 1.5).

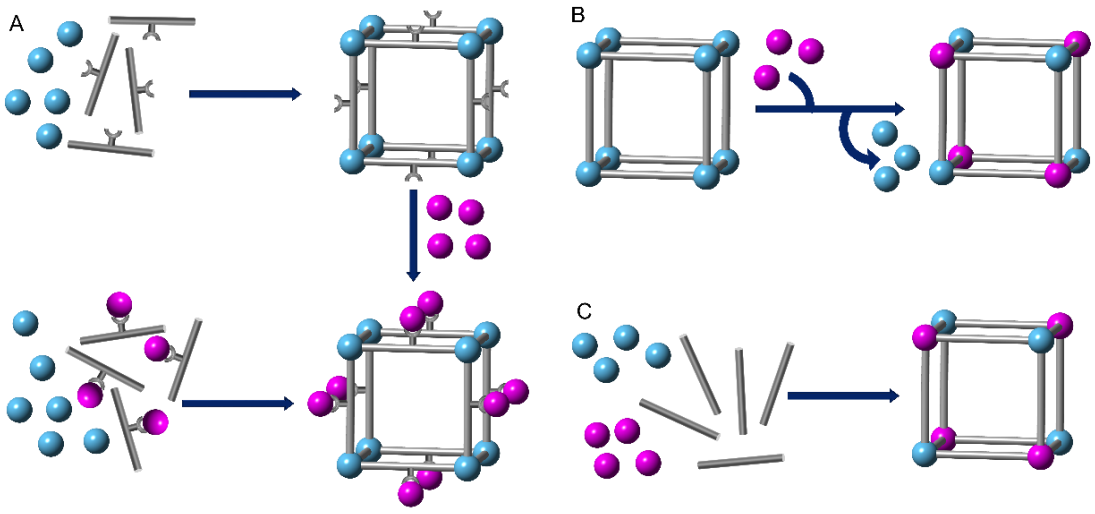

Figure 1. 5. Illustration of possible pathways for the incorporation of various metal elements in MOFs. (A) MOFs formation with linkers containing additional metal binding sites; (B) Post-synthetic cation exchange; (C) One-pot synthesis with multiple metal elements. Metal elements are represented as colored spheres, and organic linkers as grey cylinders.

The degree of control on the incorporation of the additional metal sites into the MOFs, as well as the number of elements that can be introduced strongly depend on the selected methodology. In this introduction, some of these approaches are discussed, highlighting selected relevant examples from the literature and with special focus on the one-pot synthesis of multi-metal MOFs.

1.2.1. MOFs with linkers containing metal-binding sites.

Metal-cations form inorganic clusters through the formation of coordination bonds with the linkers to build up the MOF extended structures. As a way of incorporating additional metal cations different to those forming the inorganic SBUs, it is possible to use organic linkers that possess additional metal binding sites. These additional metal binding sites are not playing any structural role in the construction of the MOF, but they are incorporated as additional chemical decoration of the framework, to provide the MOF with extra functionalities. Organic linkers bearing additional metal binding sites can be referred to as metalloligands. The metalloligand approach offers as main advantage the control over the position of the additional metal-cation, as result of the pre-defined location of the metal binding site in the MOF organic linker. As such, it allows the tuning of the MOF pore environment. Several types of metallo-ligands have been reported in the construction of multi-metal MOFs, including β-diketones,[28] acetylacetonates,[29] Schiff bases,[30] oxamates,[31] pyridines,[32] dipyrrinates, and most notably, metallo-porphyrin based linkers, among others.

The first reported examples of heterometallic MOFs were made with the use of dipyrrinates metalloligands.[33] The frameworks [Co(4-pyrdpm)$_3$] and [Fe(4-pyrdpm)$_3$] ((4-pyrdpm) = 5-(4-pyridyl)-4,6-dipyrrinato)) were employed as metalloligands in combination with a solution of Ag(I), resulting in two isostructural bimetallic MOFs, MOF-Co/Ag-1 and MOF-Fe/Ag-1. Later, the influence of the Ag counterion employed in the synthesis was studied on the resulting topology,[34] and continued with the study of new examples of heterobimetallic MOFs by combination of [M(4-pyrdpm)$_3$] (M = Ga or In) and different Ag-salts.[35]

On the other hand, bipirydin based ligands have been extensively employed for the incorporation of additional metal sites in MOFs, thanks to its ability to easily chelate metal cations. MOF-253 [Al(OH)(bpydc)] (H_2bpydc = 2,2′-bipyridine-5,5′-dicarboxylic acid) has a

highly porous structure and surface area exciding 2100 $m^2 \cdot g^{-1}$, and it allows the incorporation of metal cations into the bipyridine sites of the organic linkers.[36] Thus, palladium or copper complexes were formed in nearly quantitative yield following a post-synthetic metalation process, resulting in an enhancement of the gas sorption selectivity properties of the MOFs (figure 1.6). There are many other examples of other MOFs where metal complexes have been incorporated by using bipyridine based organic linkers. Among them, several members of the zirconium-MOF family have been prepared with the use of these linkers,[37] exploiting the high chemical stability of zirconium MOFs and adding new properties arising from the introduction of active complexes in the linkers, such as incorporation of iridium complexes for water oxidation,[38] or rhenium complexes for carbon dioxide reduction.[39]

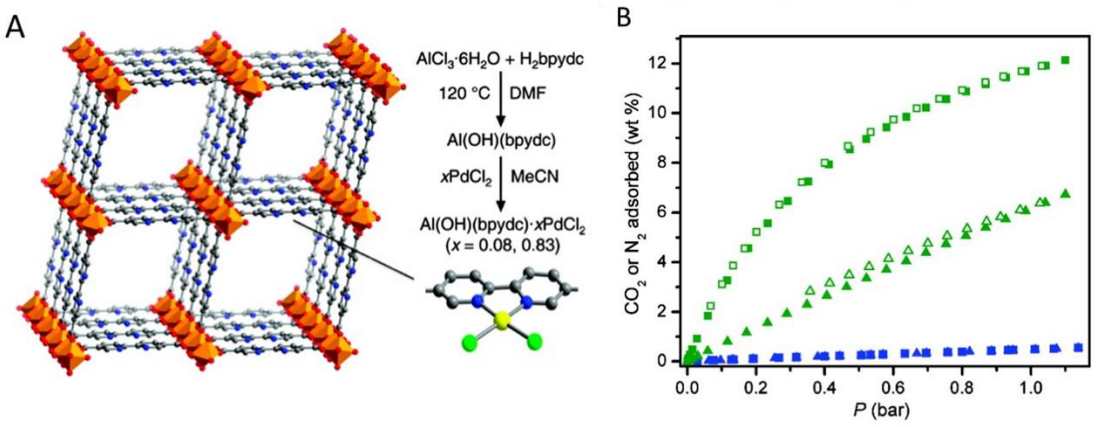

Figure 1. 6. (A) The structure of MOF-253 includes metal binding sites in the bipyridine based linkers, which can be used to create palladium complexes. (B) The 298 K carbon dioxide isotherm of MOF-253 (green triangles) and MOF-253·0.97Cu(BF4)2, (green squares) evidence the differences in gas sorption properties.[36] Reprinted with permission. Copyright 2010 American Chemical Society.

Metalloporphyrins are the family of metalloligands most extensively employed as MOF linkers. Due to their electronic properties, the use of porphyrins as linkers in MOFs is of interest, for example to introduce active redox sites. Thus, metalloporphyrins-based MOFs are excellent candidates for the preparation of heterogeneous catalyst for oxidation reactions.[40-42] In addition, the geometry of the porphyrin molecules might be advantageous in the design of MOFs with particular topologies. New zirconium MOFs have been prepared with the use of porphyrin linkers, as well as the corresponding multimetallic materials with the use of the metalated analogues or with a post-synthetic metalation.[43] Thus, MOF-525 and MOF-545 were

the first examples of MOFs prepared with the combination of zirconium SBUs and the porphyrin based linker TCCP (tetrakis(4-carboxyphenyl)porphyrin), resulting in materials with **ftw** and **csq** topologies (figure 1.7). MOF-525 and -545 were metalated with iron(III) and Cu(II) without losing their high surface area (above 2000 $m^2 \cdot g^{-1}$). Several metalated versions of MOF-545 were shortly after reported by Zhou's group, who proved that they exhibit highly effective biomimetic oxidation activity with different substrates in aqueous media.[44] Other examples of zirconium MOFs have been subsequently reported with the use of related porphyrin based linkers, such as M-TPPCOOMe (M = Ni, Co or Fe; TPPCOOMe = 5,10,15,20-Tetrakis(4-methoxycarbonylphenyl)porphyrin).[45]

In addition to zirconium, metalloporphyrins have also been employed to construct MOFs based on other metal elements. For example, zwiterionic MOF composed of a cationic Fe(III) or Mn(III)-porphyrin with a $[In(CO_2)_4]^-$ cluster, which was tested in electrocyclization reactions,[46] or a MOF prepared using a hexatopic porphyrin linker denoted HCPP (5,15-bis(4´-carbomethoxyphenyl)-10,20-bis(3,5-biscarboethoxyphenyl)porphyrin) in combination with SBUs formed by 3d (Mn or Co), 4f (Pr, Gd or Yb), or 4d (Pb or In) metal elements.[47] In this line, there are other examples with the Zr6 cluster and other metalloligands such as $[Cu_4I_4(Ina)_4]^{4-}$ (Ina = isonicotinate) employed as catalyst in the styrene oxide ring-opening reaction with mono alcohols.[48]

The combination of transition and rare earth metals has a great interest for obtaining heterometallic MOFs with luminescent properties. Different structural types of Ln-Ni(id_a) (id_a = iminodiacetic acid) have been studied, obtaining new heterometallic MOFs with formula $\{[Ln_4(ox)_3(Ni(id\_a)_2)_3(H_2O)_6]\}_n \cdot xH_2O$ (ox = oxalate; Ln = Dy, La, Nd, Eu, Gd or Pr) where the Ln-oxalate tetramers (type I), dimers (type II) or one dimensional polymer (type III) are bridged by the metalloligand$[Ni(id_a)_2]^{2-}$.[49] Ln-Cu(metalloligands) with magnetic properties have also been reported, such as the $\{[Dy_2Cu_3(id\_a)_6] \cdot 1.5H_2O\}_n$ material, which presents a weak ferromagnetic interaction between the metal ions.[50] $[Ln(H_2O)_zCu_3(Hmesox)_3DMSO] \cdot xH_2O \cdot yDMSO$ materials (Ln(III) = La, Ce, Pr, Nd and Eu; H_4mesox = dihydroxymalonic acid; and DMSO = dimethylsulfoxide) have been prepared by crystal growth in agarose gel in a mixed solvent (DMSO/water) medium.

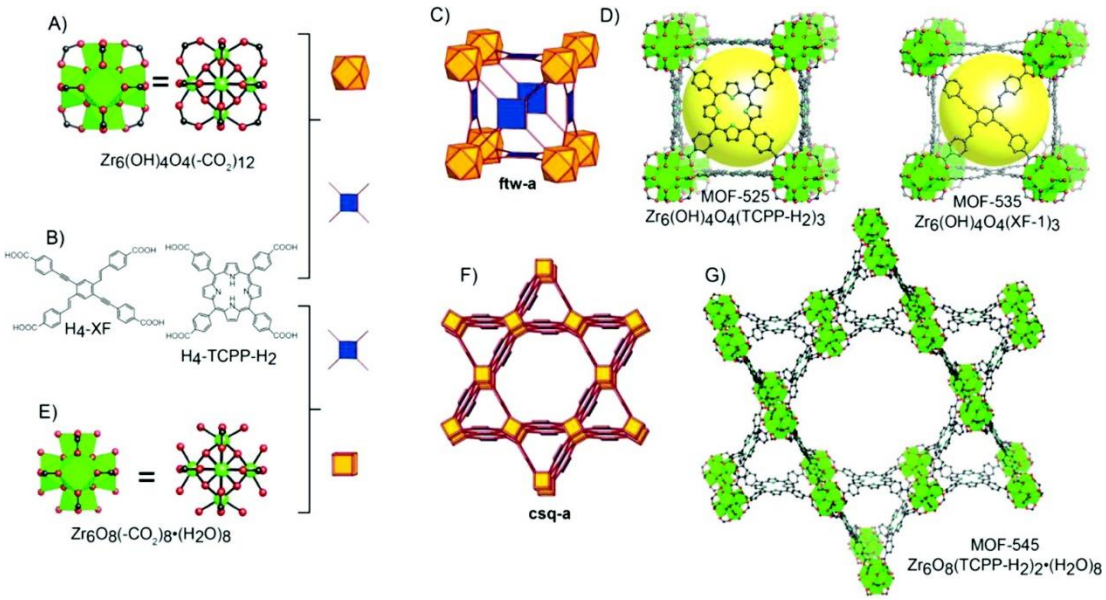

*Figure 1. 7. MOF-525 and -545 were prepared by combining Zr_6 SBUs and the porphyrin linker TCCP. In MOF-525, the zirconium SBU has 12 points extension, and the framework belongs to the **ftw** topology, whereas in MOF-525 the SBU has a cubic shape, and the framework is of the **csq** type. In both cases, additional metal cations can be introduced in the porphyrin linkers.[43]Reprinted with permission. Copyright 2012 American Chemical Society.*

The magnetic susceptibility study performed for $LaCu_3$ revealed the occurrence of antiferromagnetically coupled Cu(II) equilateral triangles whose apical positions can also be occupied by water molecules.[51] In addition, five new crystalline lanthanoid-metalloporphyrin porous frameworks composed of the octatopic Zn-OCPP linker (tetrakis-(3,5-dicarboxyphenyl)porphyrin = OCPP) and a rod-shaped SBU with formula $\{NaGd(H_2O)_2(COO^-)_4\}_n$ have been recently reported.[52]

1.2.2. Post-synthetic metal exchange.

Transmetalation, cation exchange process, or ion methatesis, is a post-synthetic method used to substitute the metal cations employed in the MOF SBU formation by other metal elements, while maintaining the original MOF structure. The synthetic method typically consists of immersing the selected MOF into a solution saturated with the metal cations to be introduced

in the structure.[53] With some exceptions where the transmetalation process is quantitative, typically the cation exchange is only partly completed, so that the resulting MOF contains a mixture of metal elements. Nonetheless, this method has been proven to be effective is cases where a desired MOF SBU is only obtained with certain cations, and the formation of isoreticular materials with other metal elements is sought. This is, for instance, the case of metal substitution in MOF-5, where the introduction of metal cations with redox activity in the prototypical zinc acetate SBU was accomplished following this methodology (figure 1.8).[54]

Figure 1. 8. Transmetalation process in MOF-5 with different metals by the inorganic SBU reduction or oxidation. Zinc (yellow), iron (orange), titanium (maroon), chlorine (green), nitrogen (blue), oxygen (red) and carbon (white).[54] Reprinted with permission. Copyright 2013 American Chemical Society.

The metal exchange process has also been proved to be effective in order to increase the gas sorption capacity of MOFs by means of introducing elements with higher affinity towards the selected gas. Thus, Dinca and Long demonstrated the increase in the H_2 storage capacity of MOFs derived from the exchange of Mn^{2+} centers in the family of $\{Mn_3[(Mn_4Cl)_3(btt)_8(CH_3OH)_{10}]_2\}$ (btt = 1,3,5-benzenetristetrazolate) materials, by other metal elements.[55]

The formation of titanium MOFs through partial cation exchange of parent zirconium MOFs is a topic of interest.[56-57] However, despite the incorporation of titanium into the materials has been accomplished, there is controversy regarding the actual location of the titanium cations. Thus, recent studies indicate that the addition of titanium cations takes place through a grafting process into the SBU[58] or in the form of nanoscale surface deposited titanium oxide,[58-59] rather than an actual cation exchange in the SBU. This is in line with computational studies that correlates the energetic stability of bimetallic MOFs, showing that the titanium/zirconium metal exchange is not energetically favourable.[60]

A recently reported MOF, based on zinc and a pyrazole carboxylic acid linker, has demonstrated that an exquisite control in the cation exchange is possible. In this case, formation of metal cation vacancies is initially produced by an acid treatment, which removes a quarter of the metal ions and half of the linkers. Subsequently, new metal cations are further incorporated into the MOF structure at the vacancy positions. The characterization of vacancies formation and metal replacement was followed using single crystal X-ray diffraction (figure 1.9).[61]

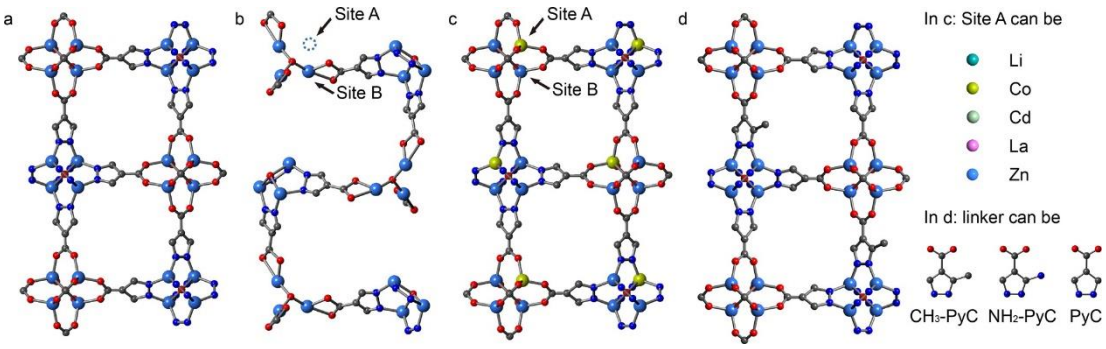

Figure 1. 9. Ordered vacancies and cation exchange in MOF single-crystals: a) Parent MOF without vacancies; b) with vacancies and c) and d) with metal cations in the vacancies: cobalt replaced and 4-CH_3 substitution in the linker in c) and d), respectively. Zinc (light blue), nitrogen (dark blue), oxygen (red) and carbon (gray).[61] Reprinted with permission. Copyright (2014) American Chemical Society.

In some occasions, transmetalation occurs in a specific and easily detectable way and it can be used for sensing metal cations. For instance this is the case of the detection of Fe^{3+} in aqueous solution by fluorescence changes in metal exchanged MIL-53(Al).[62] The cation exchange between Fe^{3+} and Al^{3+} in MIL-53(Al) metallic centers generates the quenching of the emission of MIL-53(Al) due to the transformation of strong-fluorescent MIL-53(Al) to weak-fluorescent MIL-53(Fe), allowing highly selective and sensitive detection of Fe^{3+} ions in a 3-200 µM concentration range (figure 1.10).

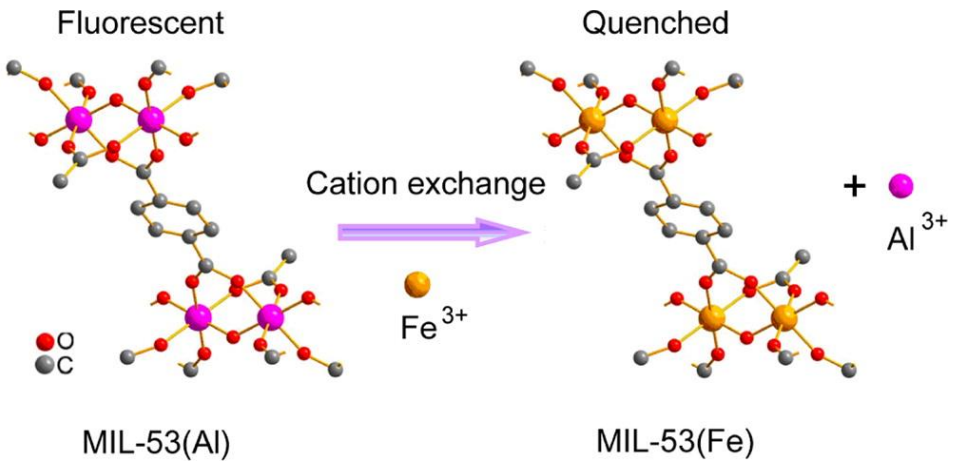

Figure 1. 10. The transmetalation of Fe^{3+} cation in the fluorescent MIL-53(Al) resulting in a MIL-53(Fe) which is quenched.[62] Reprinted with permission. Copyright (2013) American Chemical Society.

In addition, various examples of a variant of post-synthetic metal exchange have been reported. This method consists of the incorporation of a second metal cation in defective MOFs by exchange of extraframework cations. This is the case of $[Ni_8(OH)_4(H_2O)_2(BDP\_X)_6]$ (H_2BDP_X=1,4-bis(pyrazol-4-yl)benzene-4-X with X=H (1), OH (2), NH_2 (3)) systems where defects are generated by immersing the MOF in KOH ethanolic solutions[63] and extraframework Ba^{2+} ions are introduced into the porous structure (figure 1.11).[64]

Second metal cations can be located into the pores with this synthetic approach. For instance, new luminescent properties were induced with the bio-MOF-1 doped with rare earth cations thanks to the exchange between dimethylammonium ion sited in the pore with the metal-cations.[65-66]

1.2.3. One-pot synthesis of multi-metal MOFs.

The most direct approach for the incorporation of multiple metal elements into a MOF is the combination of different metal precursors during the MOF synthesis. As opposed to the previously discussed approaches where the resulting materials are generally bimetallic, following this strategy it is possible to incorporate a larger number of different metal cations in the same SBU.

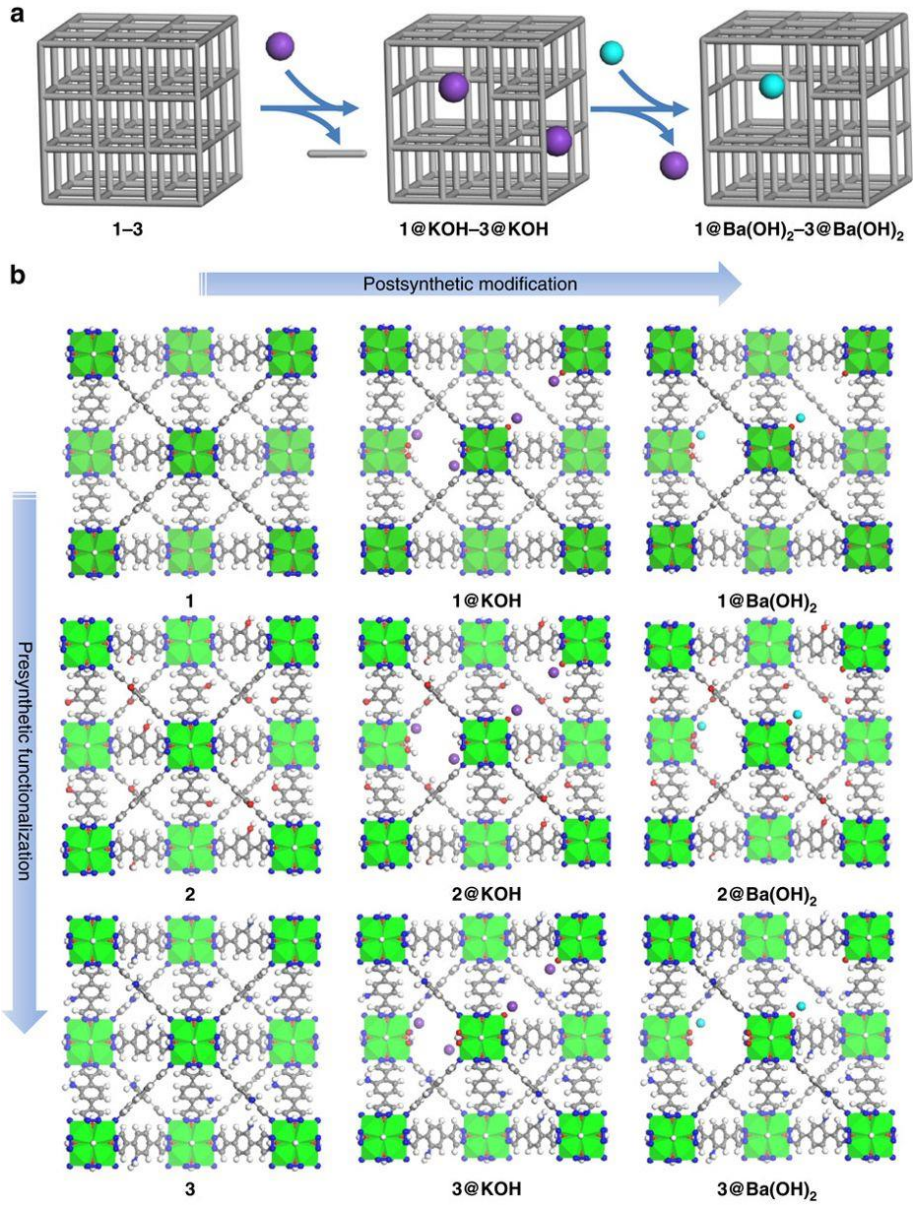

Figure 1. 11. Schematic representation of the successive PSMs, from pristine nickel pyrazolate [$Ni_8(OH)_4(H_2O)_2(BDP\_X)_6$] ($H_2BDP\_X$=1,4-bis(pyrazol-4-yl)benzene-4-X with X=H (1), OH (2), NH_2 (3)) frameworks to yield the missing linker defective K[$Ni_8(OH)_3(EtO)_3(BDP\_X)_{5.5}$] (1@KOH, 3@KOH) and $K_3[Ni_8(OH)_3(EtO)(BDP\_O)_5]$ (2@KOH) and subsequently, the ion exchanged $Ba_{0.5}[Ni_8(OH)_3(EtO)_3(BDP\_X)_{5.5}]$ (1@Ba(OH)$_2$, X=H; 3@Ba(OH)$_2$, X=NH_2), and $Ba_{1.5}[Ni_8(OH)_3(EtO)(BDP\_O)_5]$ (2@Ba(OH)$_2$) materials. Organic linker (grey bar), potassium (purple), barium (cyan). (b) Overview of the structures of the studied materials used for the selective capture of SO_2. The presynthetic functionalization of the organic spacers with -OH and -NH_2 polar tags are shown top to bottom. The successive PSMs are shown left to right. Ni (green octahedra); K (purple); Ba (cyan); C (grey); N (blue); O (red); H (white).[64] *Reprinted with permission. Copyright (2017) Nature.*

Lanthanide based MOFs are a particularly favourable case for the preparation of multi-metal MOFs, as rare-earth elements are easily found forming solid solutions. The controlled introduction of multiple lanthanide cations within a MOF structure allows the modification of the luminescence properties of the solids. A series of multi-metallic lanthanide based MOFs was prepared, with emission properties that could be finely tuned through the control of the initial metal ratios (figure 1.12).[67] Similarly, through the combination of lanthanide cations with the 3,5-disulfobenzoic acid linker, a series of MOFs was prepared with an heptanuclear SBU, where the emission of the triplet state of the linker in the gadolinium material is highly efficient, and the external efficiency is dramatically enhanced with the incorporation of small amounts of europium and/or terbium in the multi-metal analogues. This series of MOFs were evaluated as materials for lighting and thermometry.[68]

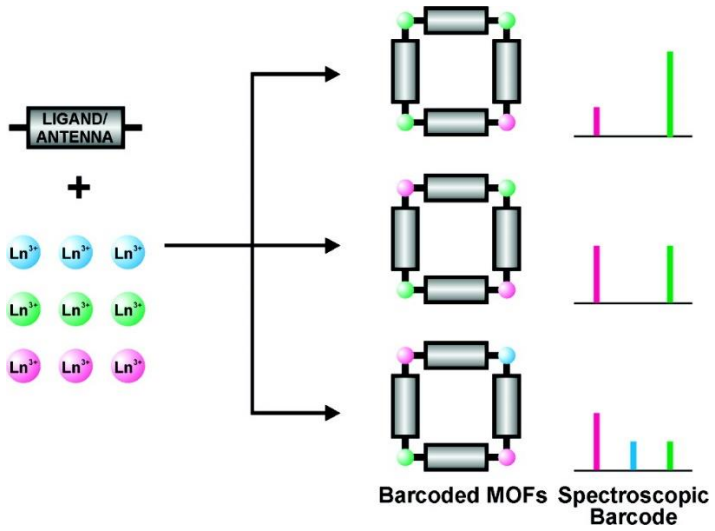

Figure 1. 12. Controlled Preparation of Barcoded MOFs.[67] Reprinted with permission. Copyright (2009) American Chemical Society.

The ability to combine multiple metal cations allows the modification of the catalytic properties of a certain MOF type. Thus, the catalytic activity of a series of solid solution MIL-100 (Sc, M, with M = Al, Cr, Fe) materials in Lewis acid catalysed Friedel-Craft reactions was found to be related to the amount of scandium.[10] In another example of multi-metal MOFs based on the same trimeric SBU, a series of porphyrin based materials prepared with a single metal element (Mg, Mn, Co, Ni, and Fe) as well as the corresponding multimetal materials

(Mn_xFe_{3-x}, Ni_xFe_{3-x}, Co_xNi_{3-x}, Mn_xCo_{3-x}, Mn_xMg_{3-x}, and Mn_xNi_{3-x}) were reported (figure 1.13).[69] Spectroscopic analyses of this family of materials showed that the multi-metal MOFs might appear forming domains of cations, as well as in the form of well-mixed systems, with different performance in the photo-oxidation of 1,5-dihydroxynaphthalene. Recently, a study that shows how the incorporation of iron cations within the MIL-53(Al) MOF endows this material with catalytic activity in the conversion of methane to methanol was reported.[70] The enzyme-like catalytic activity of this material arises from the ability to isolate oxo-bridged iron units within the multi-metal MOF SBU. Also, the modification of the electronic structure of a new titanium MOF by adding a second metal cation has been reported, resulting in a tuning of the material band-gap, and consequently in its photocatalytic activity.[71]

Moreover, the catalytic activity of solid-solution MOFs can actually be tuned by virtue of the combination of multiple metal cations, so that solid-solution MOFs exhibit different activity than their single metal counterparts. Thus, in 2015 my group synthesized a series of solid solution MOFs based on the combination of group 13 elements, and general formula $[In_xGa_{1-x}(O_2C_2H_4)_{0.5}(hfipbb)]$ [$H_2hfipbb$ = 4,4′-(hexafluoroisopropylidene)bis(benzoic acid)].[72] These MOFs are isostructural with their single metal analogues, synthesized with Al, Ga, or In. The catalytic activity of this series of MOFs in the one-pot multicomponent Strecker reaction was evaluated, and differences in the behaviour of the materials were correlated with their metal ratios. Thus, by using the Ga or In MOF as catalyst, only reaction intermediates or by-products were yielded. However, the combination of both elements in the form of solid solution MOFs resulted in the obtaining of the desired α-aminonitrile Strecker product (figure 1.14). The differences in activity are rationalized based on the ability of the solid solution material to address the different stages involved in the reaction mechanism by virtue of the presence of multiple metal cations.

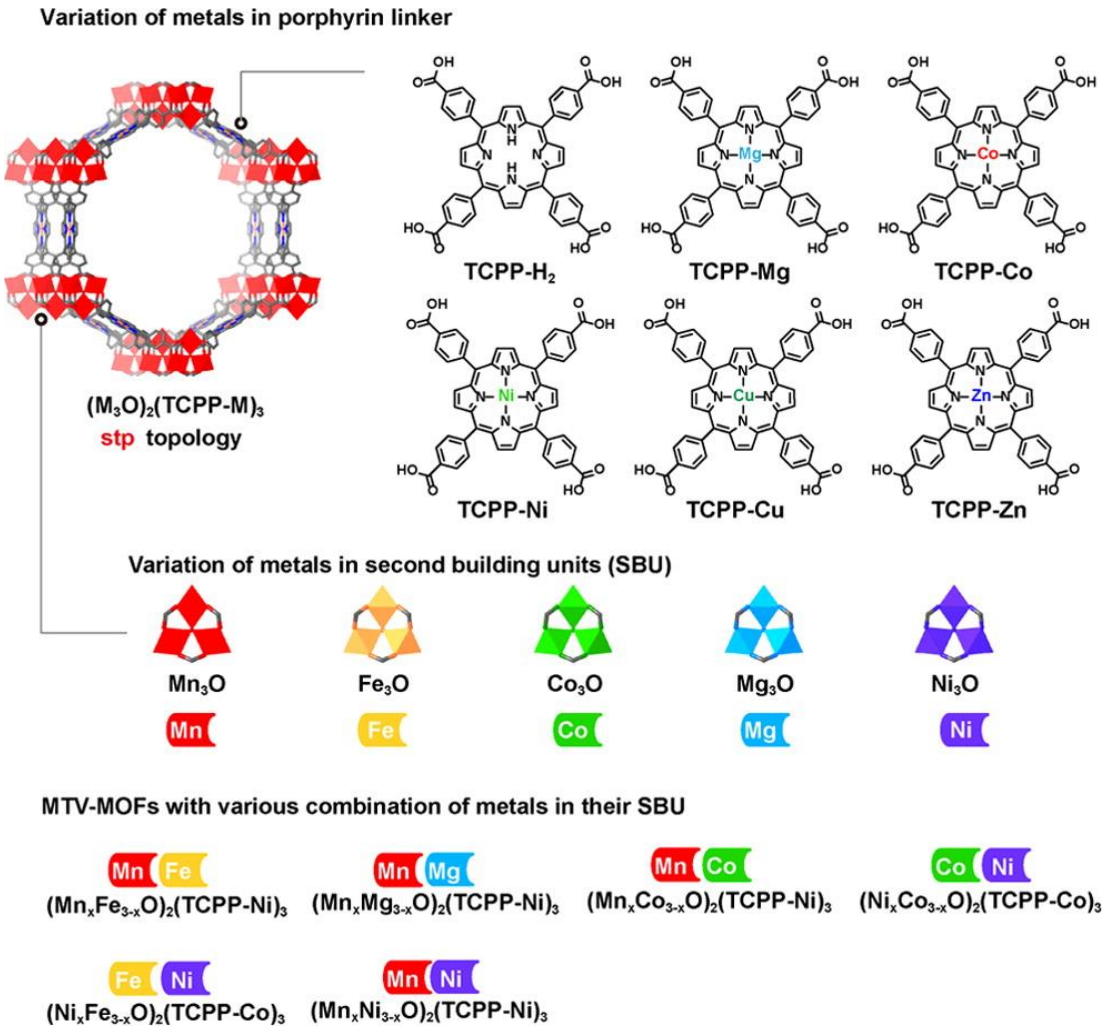

Figure 1. 13. Single component MOF series, $(M_3O)_2(TCPP\text{-}M)_3$, constructed by five different SBUs and six different porphyrin linkers, and corresponding MTV-MOFs with mixed-metal SBUs.[69] *Reprinted with permission. Copyright (2017) American Chemical Society.*

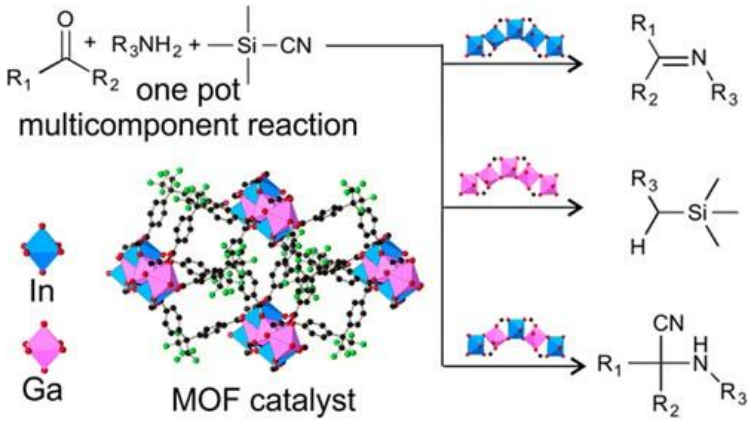

Figure 1. 14. Solid solution $[In_xGa_{1-x}(O_2C_2H_4)_{0.5}(hfipbb)]$ MOF as heterogeneous catalyst. The MOF composition has a direct influence in the obtained product of the multi-component Strecker reaction. Indium (light blue), gallium (pink), carbon(black), fluorine (green).[72] Reprinted with permission. Copyright (2015) American Chemical Society.

Regarding transition metal solid-solution MOFs, it is worth pointing out the case of MOF-74. This MOF was first reported by Yaghi et al. in 2005[73] with the use of zinc as metal cation, followed by other reports where the same MOF structure type was obtained with the use of Co,[74] Mg,[75] Ni,[76] Mn,[77] Cu,[78] and Fe.[79] In all cases, the metal cations appear in octahedral coordination environment in the rod-shaped SBU used to build up this structure. Influence of the selected metal element on the sorption properties of this MOF type have been extensively evaluated, including the case of mixed metal Zn/Co MOF-74.[80] In addition to the elements that have been previously used to produce single metal MOF-74 a combination of 2, 4, 6, 8, and 10 different metal elements in MOF-74 was also demonstrated.[81] It was demonstrated the feasibility of the one pot synthesis to incorporate other cations that would not afford this MOF type if used alone, such as barium, strontium, or calcium. The incorporation of the employed metal elements was demonstrated with ICP and EDS mapping analysis of the samples (figure 1.15). The results of the analyses showed that while all the metal elements were effectively incorporated into MOF-74 crystals, different metal distributions were found for individual crystals. Recently, an approach to obtain bimetallic MOF-74, based on the use of a one-dimensional coordination polymer as starting material to produce Zn/M-MOF-74 (M = Ni, Mg) with 1:1 metal ratios has been reported (figure 1.16).[82]

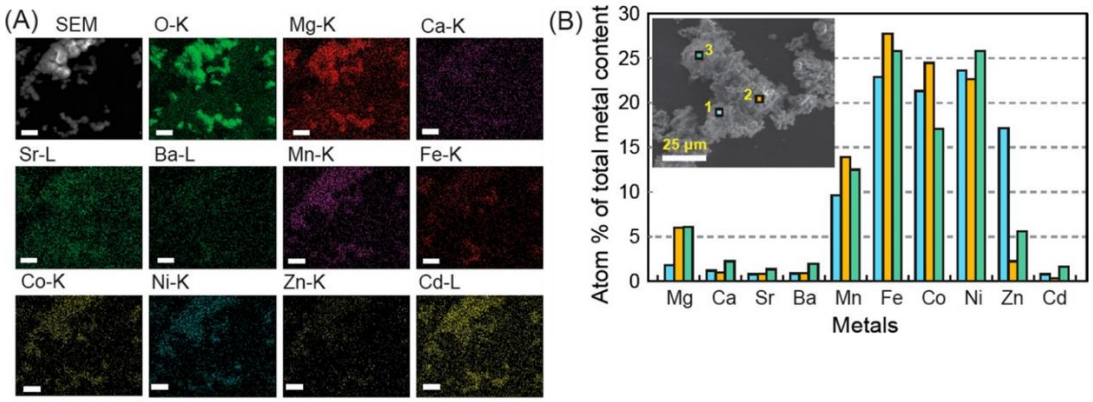

Figure 1. 15. EDS analysis of M10M-MOF-74. (A) SEM image and EDS mapping of the same sample area, demonstrating the presence of oxygen and each of the 10 metals. Scale bar, 10 µm. (B) Ratio of metals found in three distinct regions of a different M10M-MOF-74 sample (indicated by different colors: blue, orange, and green). Inset: SEM image indicating the specific region in which EDS was collected to quantify the ratio of metals present.[81] *Reprinted with permission. Copyright (2014) American Chemical Society.*

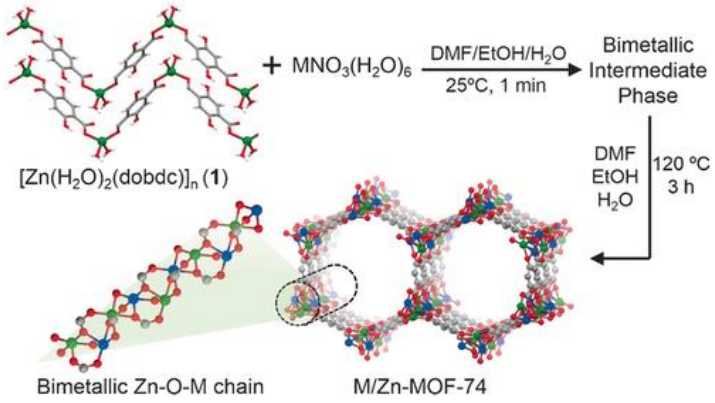

Figure 1. 16. Synthetic strategy for the heterogeneous phase preparation of bimetallic MOF-74 structures via template-directed approach, in which 1D metal-organic polymer with well-defined binding pockets used as a structural template for preparation of well-ordered bimetallic MOF-74s. M=secondary metal (Mg or Ni=blue), Zn=green, C=gray, O=red. Hydrogen atoms are omitted for clarity.[82] *Reprinted with permission. Copyright (2014) Wiley.*

1.3. Compounds and Composites Derived from MOFs

Recently, the use of the MOFs-derived advanced nanomaterials has received a great interest because of their applications such as electrochemical energy storage. MOFs-derived materials have proved to be particularly suitable for electrochemical applications because MOFs have tunable chemical composition that can be designed at molecular level.[83-91] Therefore, MOFs have been employed as sacrificial template to produce high surface area and ordered nanostructured materials including carbon,[92] metal oxides,[93] metal oxides-carbon composites (M/MO@C)[94] and metallic nanoparticles-carbon composites[95] for electrochemical applications. The MOF derived materials possess the unique advantages translated from their parent MOF of controlled porosity and high specific surface areas. Moreover, MOFs can be converted to the desired product using a one-step calcination process, which enhances their practical application at the pilot and industrial scale (figure 1.17).[96-97]

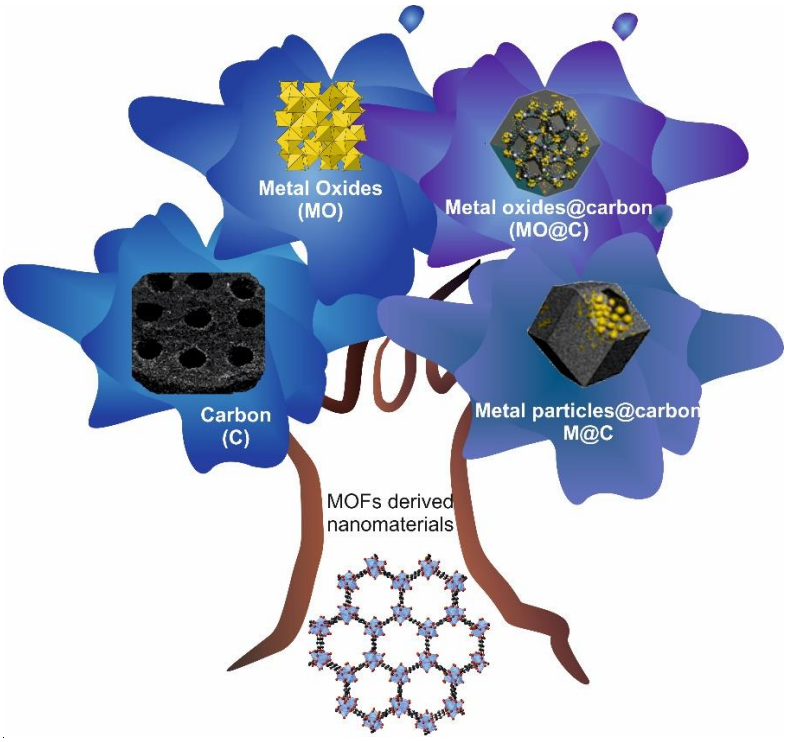

Figure 1. 17. Schematic illustration showing the different MOF-derived nanocomposites, such as carbons, metal oxides, metal oxides@carbon composites or metal particles@carbon, among others.

1.3.1. Carbons derived from MOFs

Nanoporous carbon has attracted wide attention of the scientific community because of the abundant resources and excellent thermal and chemical stability. Furthermore, high surface area carbons have also been widely used to fabricate other highly efficient redox active nanostructures for energy storage, which further demonstrate its importance. Nevertheless, the developing of novel techniques and methods that could help in tailoring the porosity and morphology of the carbonaceous nanostructures is very important. Different materials have been introduced to develop highly ordered nanoporous carbon. Because of their high surface area, MOFs are excellent candidates for derivation of carbonaceous materials with desired inherent properties, such as high specific surface area, or high chemical and thermal stability, among others. Since MOFs are constructed from a combination of inorganic SBUs with organic linkers, their decomposition at higher temperatures under different conditions could generate a large variety of products from porous carbon to metal oxides, metal sulfides, metal carbides, metal, or metal oxides decorated carbon composites.[98-102]

Carbon can be derived from MOFs by carbonization in several ways with or without post-treatment. MOF carbonization without any secondary precursors commonly results in low surface area carbon, and this has been addressed by post-treatment of the carbonized product. Heating a mixture of carbonized product with potassium hydroxide at high temperatures followed by acid washing to remove impurities typically results in high surface area carbons (>2000 m^2g^{-1}).[103] It was assumed that the heating rate, carbonization time and MOF ligands play a critical role in the resulting carbonaceous materials.

Since MOFs inherently consist of metallic species, which are an integral part of the whole structure, it is essential to remove these metallic species to get high surface area carbon. In this sense, an efficient approach was introduced by using Zn-MOFs to derive carbon materials.[104] Firstly, a MOF precursor is decomposed by a thermal treatment in inert atmosphere, where Zn was converted to zinc oxide.[105] This oxide is reduced into Zn at 900 °C and, later evaporated at this temperature leaving behind highly porous carbon.

In another similar example, a two-step carbonization process at 550 °C and 900 °C of isoreticular MOFs (IRMOFs) was monitored with the use of X-ray diffraction and optical

spectra of the products (figure 1.18). The MOFs were converted into a MO-carbon composite at lower temperature (<750 °C) upon degradation of the main MOF structure and an increase in temperature led to the formation of pure carbonaceous material at 900 °C. Zn species were reduced from ZnO into Zn and subsequent vaporization of Zn led to the formation of a pure carbonaceous product with a high surface area of 3447 m^2g^{-1}.[106]

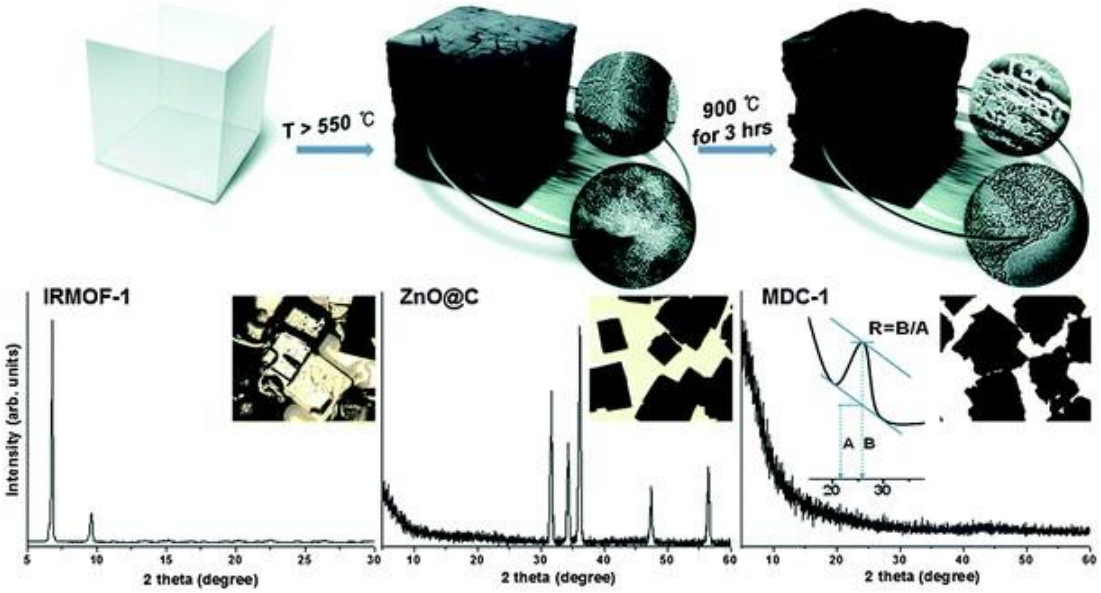

Figure 1. 18. Structural changes of IRMOF-1 with heat treatment to yield MDC-1: schematic view (top) and powder X-ray diffraction (PXRD) patterns with corresponding optical micrographs (bottom).[106] Reproduced with permission of the American Chemical Society.

On the other hand, at lower carbonization temperatures or for MOFs consisting of other higher-boiling-point metals, such as iron, cobalt, copper or nickel, carbonized samples can retain the metallic species. These MOFs generate extremely porous carbon products after a post-acid wash treatment.[107]

In addition, the dimensionality can be kept from the MOF precursor to carbon products ranging from zero-dimensional (0D) to 3D. The 0D carbon material can be prepared from ZIF-8 nanoparticles. These particles are heated at 500 °C, which give carbon nanodots with an average particle size of 2.2 nm (Figure 1.19.a).[108] Carbon nanotubes, a typical one-dimensional (1D) material, can be prepared from MOFs with metal species such as Fe, Co, and Ni. During the high temperature treatment process, metallic Fe, Co or Ni nanoparticles were first formed

and then they catalyzed the carbon nanotube formation on their surface. Thus, a Ni-MOF, $Ni_3(BTC)_2 \cdot 12H_2O$ (BTC = benzene-1,3,5-tricarboxylate), was pyrolyzed in a conventional tube furnace under 500 °C for 20 h, which resulted in multi-walled carbon nanotubes (MWCNT) without any additional catalyst or carrier gas (Figure 1.19.b).[109] Two-dimensional carbon materials can also be prepared from MOFs.[110] Graphene-like carbon nanosheets are obtained from ZIF-7-glucose composite carbonized under an argon (Ar) atmosphere at 950 °C for 5 hours (Figure 1.19.c). It was found that the addition of glucose as the carbon source was important for the formation of graphene-like structures, which was attributed to the pre-melting and polymerization of glucose before complete ZIF-7 carbonization. The morphology of MOF-derived materials was also extended to a 3D nanostructure.[111] Al-BTC metal-organic aerogels were constructed from simply mixing aluminum nitrate and BTC, followed by a supercritical CO_2 drying process. The aerogel was then converted into 3D carbon after carbonization and purification (Figure 1.19.d).

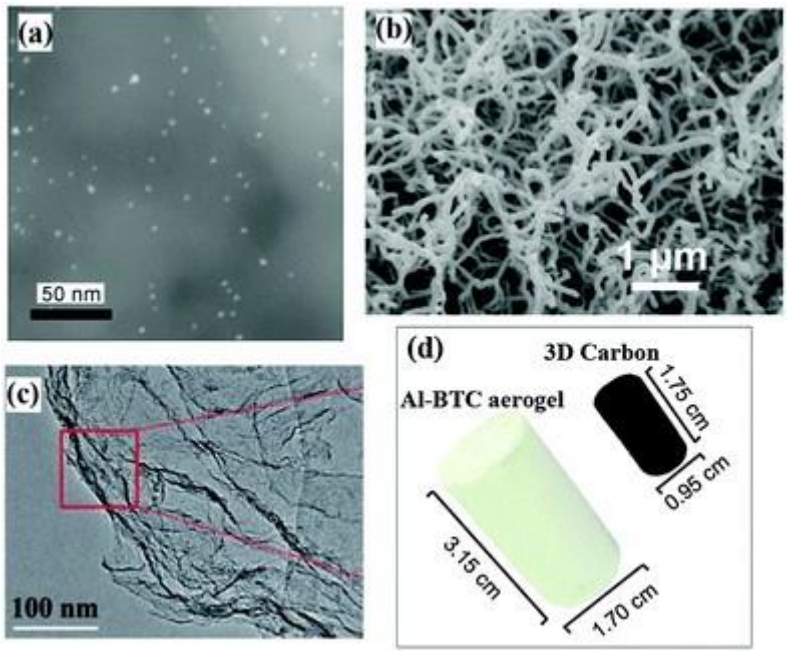

Figure 1. 19. MOF-derived 0D to 3D carbon materials. (a) High angle dark field-scanning transmission electron microscopy (HAADF-STEM) image of ZIF-8 derived quantum sized carbon nanodots.[108] (b) Scanning electron microscopy (SEM) image of Ni-MOF derived MWCNT.[109] Reproduced with permission from the Royal Society of Chemistry. (c) High-resolution transmission electron microscopy (HRTEM) image of ZIF-7 derived graphene-like carbon nanosheets.[110] Reproduced with permission from the Royal Society of Chemistry. (d) Photograph of an integrated Al-BTC aerogel and its derived 3D carbon.[111] Reproduced with permission from the Royal Society of Chemistry

The samples obtained showed a hierarchically porous structure and a high surface area (1820 m^2g^{-1}). These examples demonstrate the structural versatility of MOF-derived carbon products.

1.3.2. Metal oxides derived from MOFs

Among the plethora of methods available to prepare metal oxides, the thermal treatment.of MOFs has emerged as an alternative and promising route to obtain metal oxides with tailored nanostructures and compositions.[112] The resulting nanoporous oxide materials typically retain the shape and porosity features of the parent MOFs, which are favorable for obtaining large surface area. To date, various porous metal oxide nanomaterials have been derived from MOF precursors, including cupric oxide (CuO),[113-114] cobalt oxide (Co_3O_4),[115-116] iron oxide (Fe_2O_3),[110, 117] magnesium oxide (MgO),[118] manganese oxide (Mn_2O_3),[118-120] nickel oxide (NiO),[112, 121] titanium dioxide (TiO_2),[122] and zinc oxide (ZnO).[105, 123-124] Recently, this has been expanded to mixed transition metal oxides, such as ferrites ($CoFe_2O_4$ and $Mn_{1.8}Fe_{1.2}O_4$)[125] and cobaltites ($ZnCo_2O_4$, $Zn_xCo_{3-x}O_4$,Tian,[126] and $ZnMn_2O_4$[127]).

During the synthesis of metal-oxides, it is important to control a number of parameters, such as surface area, composition, particle size and shape, and oxidation state. Recently, composition control through MOF-derived oxides was demonstrated. Nanoplates assemblies of $ZnMn_2O_4$ were prepared from bimetallic-MOFs through heat treatment (Figure 1.20). The temperature control was determinant for obtaining the desired spinel oxide.[127] The obtaining of mixed valence metal oxides hollow structures (CuO/CuO_2) has been accomplished by thermolysis at 350 °C from $[Cu_3(BTC)_2]_n$, as shown in figure 1.21.[128]

In 2010, Co_3O_4 particles were obtained from a Co-MOF, with a size of about 25 nm, but a low surface area of 5.3 m^2g^{-1}.[129] A selective conversion of MIL-88B (Materiaux de l'Institut Lavoisier/Materials from the Lavoisier Institute) to generate either Fe_2O_3 or Fe_3O_4 rods was demonstrated. The calcination in air could only provide hematite (Fe_2O_3 *via* direct thermal conversion of MIL-88B) but that a two-step method (calcination followed by heating in inert atmosphere) provided the magnetite (Fe_3O_4), as shown in figure 1.22.[130]

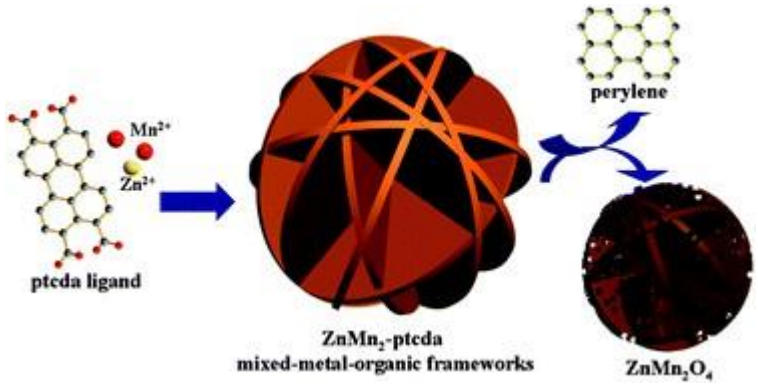

Figure 1. 20. Illustration of the two step process for the preparation of spinel $ZnMn_2O_4$ using zinc manganese-3,4,9,10-perylene tetracarboxylic dianhydride as a precursor for an 'escape-by-crafty scheme' strategy.[127] Reproduced with the permission of the Royal Society of Chemistry.

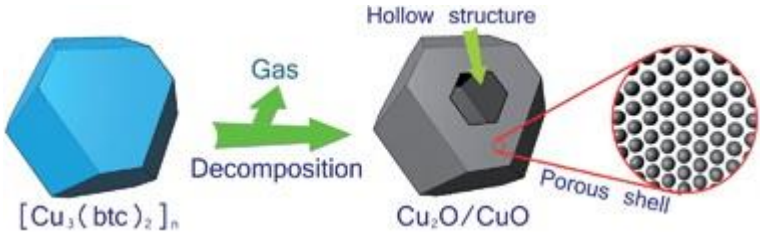

Figure 1. 21. Depiction of the schematic formation of CuO/CuO_2 hollow polyhedrons with a porous shell.[128] Reproduced with the permission of the Royal Society of Chemistry.

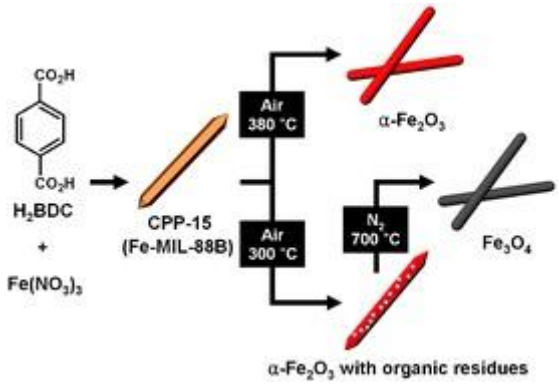

Figure 1. 22. The selective preparation of hematite (α-Fe_2O_3) and magnetite (Fe_3O_4) nanorods from coordination polymer particle nanorods (CCP). H_2BDC = 1,4-benzenedicarboxylic acid.[130] Reproduced with permission from Royal Society of Chemistry.

Using MIL-88(Fe) MOF as the sacrificial template, spindle like mesoporous structures of Fe_2O_3 with a surface area of 75 m^2g^{-1} were obtained.[110] In this case, two-step thermolysis

method was used, which includes the pyrolization in N_2 environment, followed by a calcination in air.

The structure of the resulting oxide depends, mainly on the initial composition of the MOF, the temperature and the time of thermal treatment. Calcination process of MOF precursors, which contain cobalt, manganese, and iron usually results in spinel oxides.

Several MOFs with core-shell structures have been developed for various applications, but deriving core-shell metal oxide nanostructures from MOFs has been challenging. As an example, a two-step method to prepare Co_3O_4@$NiCo_2O_4$ double-shelled nanocages with different shell compositions using MOF particles as precursors has been reported.[131] In this work, ZIF-67 particles are dispersed in $Ni(NO_3)_2$ solution to produce ZIF@Ni-Co yolk-shelled structures. Afterward, annealing treatment is applied to further convert the ZIF-67 cores and Ni-Co shells into Co_3O_4 (inner core) and $NiCo_2O_4$ (external shell), respectively (figure 1.23).

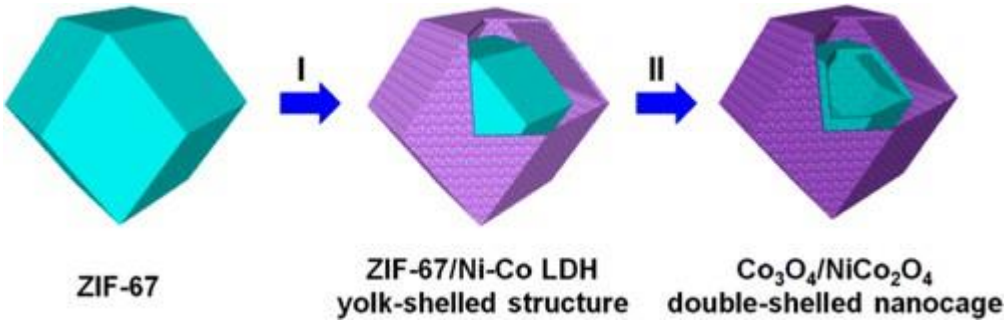

Figure 1. 23. Schematic illustration of the formation process of Co_3O_4@$NiCo_2O_4$ double-shelled nanocages. Reproduced with permission.[131] Copyright 2015, American Chemical Society.

Very recently, the thermal conversion of $Co_3[Fe(CN)_6]_2$@$Ni_3[Co(CN)_6]_2$ nanotubes to porous Fe_2O_3@$NiCo_2O_4$ nanocages was demonstrated. It can be seen clearly in figure 1.24 that the nanocages are hollow, where Fe, Co and Ni are well distributed on the edges.[132]

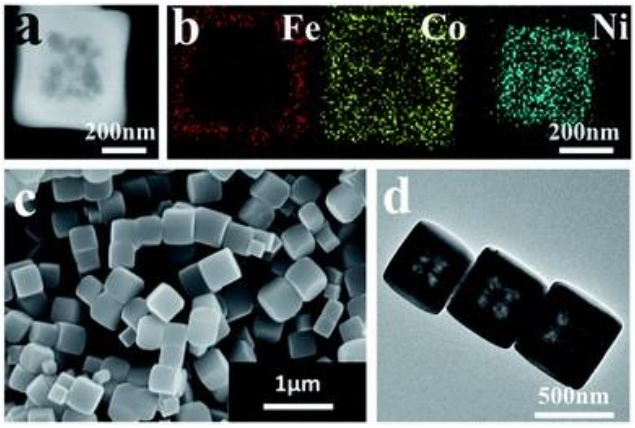

Figure 1. 24. a) HAADF-STEM image, b) elemental mapping, c) SEM image and d) TEM image of Fe_2O_3@$NiCo_2O_4$ nanocages.[132] Reproduced with permission from Royal Society of Chemistry.

1.3.3. Metal-oxides carbon composites derived from MOFs

Metal oxides are employed in many electrochemical energy storage and conversion applications, for which a high specific surface area is desirable. Thus, researchers are studying new synthetic methods to obtain metal oxide-carbon (MO@C) composites.[133-134] Synthesizing MO@C composites by traditional chemical synthesis methods leads to poor control over the metal oxide particles sizes because of the agglomeration that could affect the performance of the electrode materials. Since MOFs can generate high surface area carbon upon heating, thermolysis can be optimized to obtain highly porous composites: MO@C and M@C.

An example where exceptionally well dispersed iron nano-particles in a porous carbon matrix, prepared from a MOF, has been reported by Gascon et al.[135] The strategy consists of an impregnation of the Fe-MOF precursor (Basolite F-300) with a carbon source followed by a pyrolysis (figure 1.25).

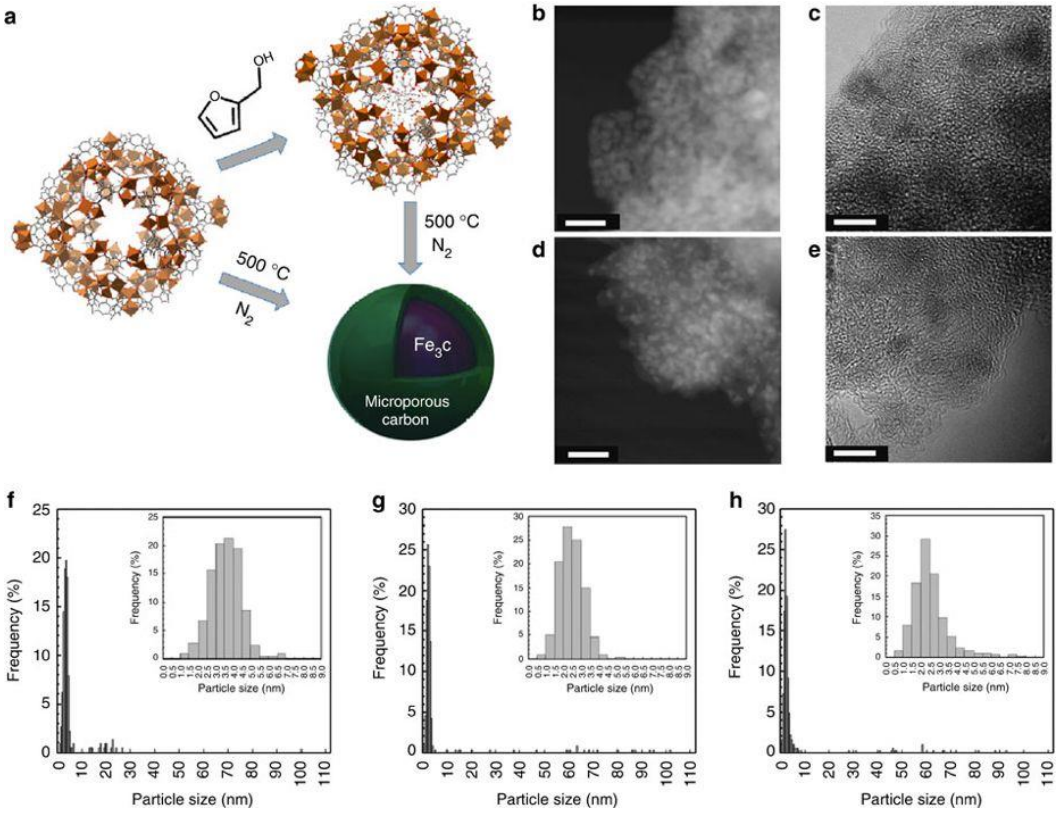

Figure 1. 25. MOF-mediated synthesis (MOFMS) strategy and electron microscopy characterization. a) MOFMS strategy: for the Basolite F-300. b) High-angle annular dark-field scanning electron (HAADF STEM) micrograph of 38-Fe@C (scale bar, 20 nm). c) High-resolution (HRTEM) micrograph of 38-Fe@C (scale bar, 5 nm). d) HAADF STEM of 25-Fe@C (scale bar, 20 nm). (e) HRTEM of 25-Fe@C (scale bar, 5 nm). f) Particle size histograms obtained from TEM analysis using at least 900 nanoparticles for 38-Fe@C. (g) Particle size histograms obtained from TEM analysis using at least 900 nanoparticles for 31-Fe@C. (h) Particle size histograms obtained from TEM analysis using at least 900 nanoparticles for 27-Fe@C. Inserts in the histograms (f,g,h) depict the particle size distribution of nanoparticles smaller than 9 nm (representing in every case more than 95% of the nanoparticles counted in the samples).[135] *Reproduced with the permission of Nature.*

In one curious example, a hybrid Co_3O_4-carbon porous nanowire arrays was synthesized from a Co-naphthalenedicarboxylate MOF with a layered crystalline structure, as the precursor (Figure 1.26). The hybrid was directly grown on Cu foil through a low-temperature (80 °C) hydrothermal process. Next, the inorganic and organic components in the MOF were converted respectively into Co_3O_4 and carbon *via* carbonization under a N_2 atmosphere, which resulted in the formation of hybrid nanowires with simultaneously generated pores inside. The resulting material possesses a high surface area of 251 m^2g^{-1} and a large carbon content of 52.1 wt %.[136]

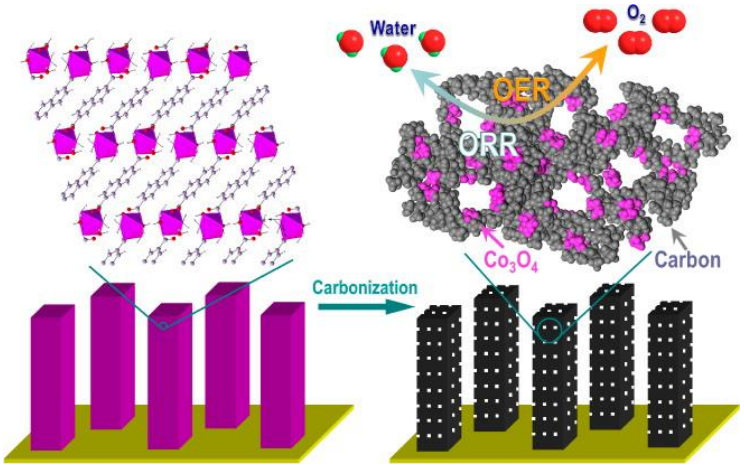

Figure 1. 26. Schematic illustration for the fabrication of Co_3O_4-C nanowire arrays.[136] Reproduced with permission of American Chemical Society.

An important study about the limits to obtain metal, metal oxides and mixed metal-metal oxides particles concludes that the reduction potential plays a critical role in determining the resultant product. If the reduction potential of the coordination metal is −0.27 or higher, the carbonization process produces metallic species upon thermolysis. However, if the reduction potential is lower than −0.27, thermolysis leads the formation of metal oxide in the resulting product (figure 1.27).[137]

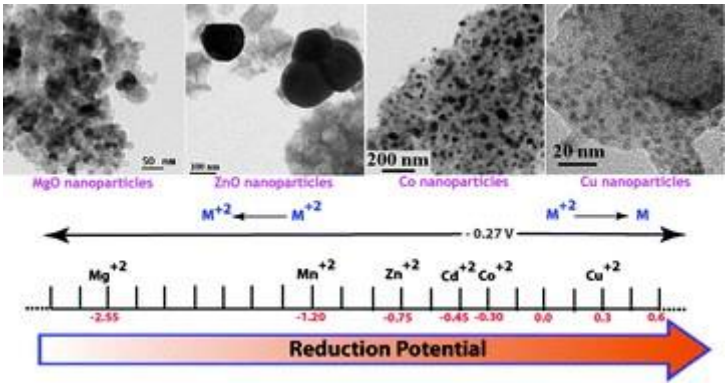

Figure 1. 27. The effect of reduction potential of metal atoms presents in the MOFs on the formation of the metal-metal oxide nanoparticles. Metals having a reduction potential above −0.27 V undergo thermolysis in an N_2 atmosphere to give pure metal nanoparticles, whereas metals with a reduction potential less than −0.27 V, even in an N_2 atmosphere, produce only metal oxides.[137] Reproduced with permission from the Royal Society of Chemistry.

The study was performed with several MOFS, such as: MOF-4, HKUST-1, Zn-ADA-1, MnHFMOF-D, MOF-CJ4, Cd-MOF-1, etc.

1.3.4. Metal nanoparticles@MOFs

Different methods have been reported to obtain M@MOF composites including: solid grinding, microwave assisted chemical vapor deposition, encapsulation, and wetness impregnation.[138] The successful incorporation of nanoparticles into MOF structures by taking into account the reactivity of organic-inorganic moieties during MOF synthesis has been reported in different reviews.[95, 139]

The solid grinding method is also an effective and facile route to fabricate M-NPs into porous materials.[140-141] During grinding, the volatile precursor is sublimated and its vapor diffuses rapidly through the cavities of the MOF, which results in well-distributed deposition of the precursor. The metal precursor embedded in the porous MOF is treated with H_2 gas at high temperature, which produces very small M-NPs. Haruta and Xu *et al*. reported several heterogeneous catalysts prepared by simple grinding of [Au(acac)$(CH_3)_2$] (acac = acetylacetonate) and porous MOFs such as MOF-5, HKUST-1, ZIF-8, and MIL-53(Al)(figure 1.28).[142] The nanocomposites of small Au nanoparticles and ZIF-8 show catalytic activity toward CO oxidation reaction to produce CO_2.

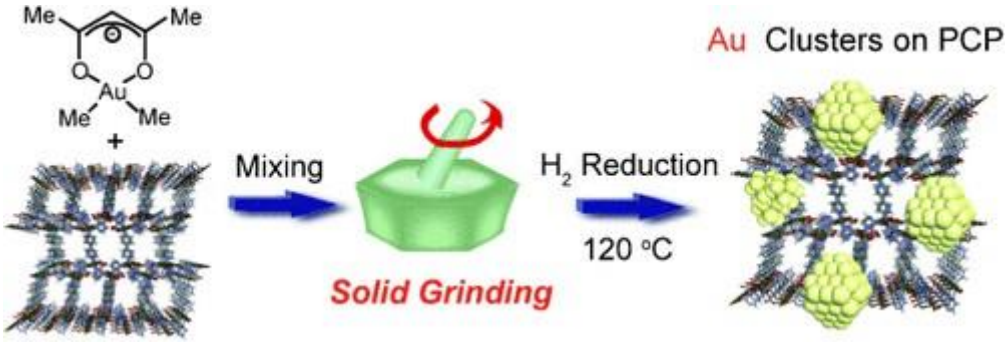

Figure 1. 28. Schematic illustration of the formation process of (PCP) porous coordination polymers@Au. Reproduced with permission.[142] Copyright 2008, Wiley-VCH.

Microwave irradiation has been used as a synthetic method to introduce different Pd, Cu and Pd-Cu nanoparticles of 2-3 nm size inside the pores of MIL-101, and 4-6 nm nanoparticles on the external crystals surface. First, by using the microwave-irradiation heating method, the activation of the pores of MIL-101 and the rapid chemical reduction of metal precursors were simultaneously performed in the presence of a reducing agent (figure 1.29).[143]

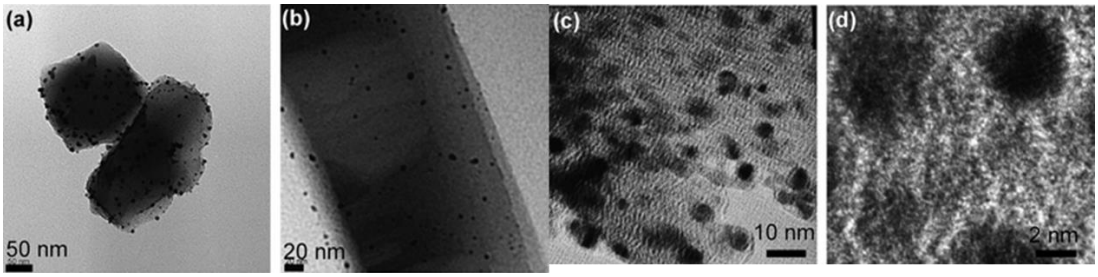

Figure 1. 29. TEM images of Pd nanoparticles-doped MIL-101. Nanoparticles on the surface are larger than those located inside the MOF.[143] Reproduced with permission from the Royal Society of Chemistry.

The chemical vapor deposition (CVD) can be performed by two different ways: volatilization of organometallic precursors followed by hydrogenolysis, or by a thermal treatment.[144] In this technique, a dried MOF and a volatile metal precursor are placed in two separate glass vials in a Schlenk tube. The tube is evacuated, sealed and kept at proper temperature depending on the vapor pressure of the metal precursor under vacuum. Upon infiltration of the metal precursor into the MOF, the MOF crystal color could be changed. When hydrogenolysis of the composite material is carried out to reduce the metal precursor, metal nanoparticles incorporated in the MOF are generated (figure 1.30).[145-147]

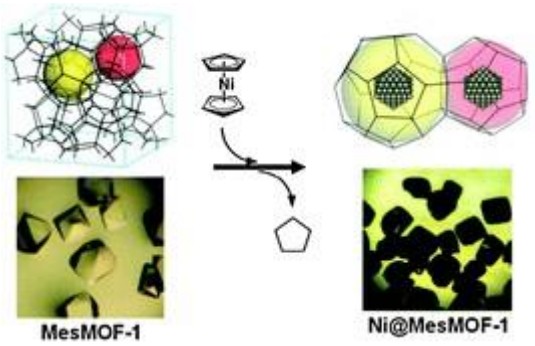

Figure 1. 30. Preparation of Ni@MesMOF-1by CVD using hydrogenolysis.[146] Reproduced with permission from the Royal Society of Chemistry.

This CVD method was also employed for the preparation of bimetallic nanoparticles such as FePt, PdPt, and RuPt in a MOF by loading MOF-5 with a combination of two different metal-organic CVD precursors. After hydrogen treatment, the composite material of MOF-5 incorporating a bimetallic nanoalloy was obtained. In this reaction, the selection of proper temperature for hydrogenolysis is important, because if mild conditions are applied to avoid decomposition of the host framework MOF-5, both precursors could not be reduced to

bimetallic alloy nanoparticles. When harsh conditions were applied to achieve quantitative co-hydrogenolysis of the precursors, the hydrogenation of benzenedicarboxylic acid linkers in MOF-5 occurred to yield *cis*/*trans*-1,4-cyclohexane dicarboxylic acid.[147]

Most common metal precursors for this method are organometallic complexes, which have adequate sizes to enter into the cavities of the MOFs, such as phosphines derivatives, 1,5-cyclooctadiene, cyclopentadiene-derivatives, etc.[138, 147-148]

On the other hand, the encapsulation method has been generalized for decorating MOF pores with different types of nanoparticles, which have been used to impart specific functionalities. Pre-synthesized metal nanoparticles that are capped by stabilizing agents can be encapsulated in MOFs by introducing NPs into a synthetic solution containing molecular building blocks for MOFs. When individually capped nanoparticles are encapsulated in MOFs, the size of nanoparticles can be easily controlled, and agglomeration of nanoparticles can be restricted in the host framework. In a work reported by Hupp and co-workers the encapsulation in ZIF-8 of the (PVP) polyvinylpyrrolidone-capped nanomaterials with various sizes, shapes and compositions has been reported. By mixing PVP-capped Au NPs with a methanolic solution of zinc nitrate and 2-methylimidazole, Au@ZIF-8 was isolated by centrifugation. After isolation, the supernatant did not contain Au NPs, implying that almost all NPs were encapsulated in ZIF-8. This strategy was successfully extended to other nanomaterials such as Pt, CdTe, Fe_3O_4 and lanthanide-doped $NaYF_4$ nanoparticles, and Ag cubes, polystyrene spheres, or β-FeOOH rods, whose surfaces were modified by PVP (figure 1.31).[139]

Other employed approach is the immersion of MOFs in metal salts solutions followed by a reduction. The metal precursors most extensively used are metal nitrate and chloride, which are completely dissolved in an organic solvent or water. When the dried MOF is soaked in the metal ion solution, the metal ions are infiltrated into the empty pores. After removal of the guest solvent molecules, the metal ions impregnated in the solid support are reduced by H_2 gas, to obtain metal nanoparticles embedded in the MOF. This method has been employed to prepare Pd nanoparticles embedded in MIL-100(Al).[149]

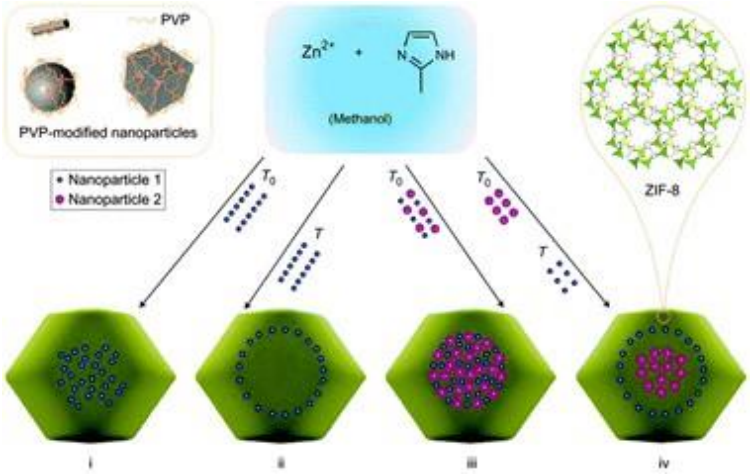

Figure 1. 31. Scheme of the controlled encapsulation of nanoparticles in ZIF-8 crystals. Through surface modification with surfactant PVP, nanoparticles of various sizes, shapes and compositions can be encapsulated in a well-dispersed fashion in ZIF-8 crystals, which formed by the assembly of zinc ions and imidazolate ligands.[139] Reproduced with permission from the Royal Society of Chemistry.

Moreover, Maspoch *et al.* have reported a multi-layered zeolitic imidazole framework composite, prepared from a sequential deconstruction-reconstruction process. The incorporation of Au or Cu/Pd nanoparticles onto the deconstructed ZIF-8 or ZIF-67 crystal surface does not disrupt the reconstruction of the ZIF particle. This allows to obtain ZIF-on-NPs-on-ZIF composites particles with more than one class of inorganic particles, such as depicted in the figure 1.32.[150]

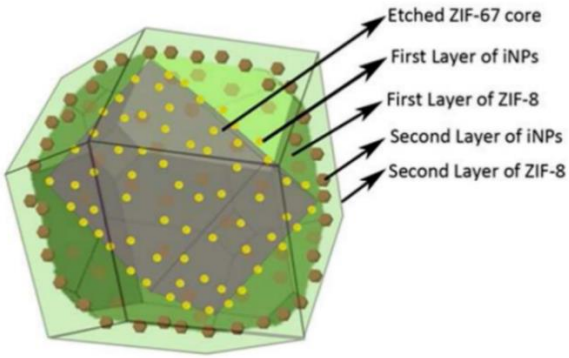

Figure 1. 31. Schematic depiction of the ZIF-based composites formed to two different layers of inorganic nanoparticles (iNPs).[150] Reproduced with permission from the American Chemical Society.

1.4. References

1. Batten, S. R.; Champness, N. R.; Chen, X.-M.; Garcia-Martinez, J.; Kitagawa, S.; Öhrström, L.; O'Keeffe, M.; Suh, M. P.; Reedijk, J., Coordination polymers, metal–organic frameworks and the need for terminology guidelines. *CrystEngComm* **2012,** *14* (9), 3001-3004.

2. Furukawa, H.; Cordova, K. E.; O'Keeffe, M.; Yaghi, O. M., The Chemistry and Applications of Metal-Organic Frameworks. *Science* **2013,** *341* (6149).

3. Yaghi, O. M.; Li, H., Hydrothermal Synthesis of a Metal-Organic Framework Containing Large Rectangular Channels. *Journal of the American Chemical Society* **1995,** *117* (41), 10401-10402.

4. Kinoshita, Y.; Matsubara, I.; Higuchi, T.; Saito, Y., The Crystal Structure of Bis(adiponitrilo)copper(I) Nitrate. *Bulletin of the Chemical Society of Japan* **1959,** *32* (11), 1221-1226.

5. Hoskins, B. F.; Robson, R., Design and construction of a new class of scaffolding-like materials comprising infinite polymeric frameworks of 3D-linked molecular rods. A reappraisal of the zinc cyanide and cadmium cyanide structures and the synthesis and structure of the diamond-related frameworks $[N(CH_3)_4][Cu^{I}Zn^{II}(CN)_4]$ and CuI[4,4',4",4"'-tetracyanotetraphenylmethane] $BF_4.xC_6H_5NO_2$. *Journal of the American Chemical Society* **1990,** *112* (4), 1546-1554.

6. Yaghi, O. M.; Li, G.; Li, H., Selective binding and removal of guests in a microporous metal–organic framework. *Nature* **1995,** *378* (6558), 703-706.

7. Kondo, M.; Yoshitomi, T.; Matsuzaka, H.; Kitagawa, S.; Seki, K., Three-Dimensional Framework with Channeling Cavities for Small Molecules: $\{[M_2(4, 4'\text{-bpy})_3(NO_3)_4]\cdot xH_2O\}n$ (M = Co, Ni, Zn). *Angewandte Chemie International Edition in English* **1997,** *36* (16), 1725-1727.

8. Li, H.; Eddaoudi, M.; Groy, T. L.; Yaghi, O. M., Establishing Microporosity in Open Metal−Organic Frameworks: Gas Sorption Isotherms for Zn(BDC) (BDC = 1,4-Benzenedicarboxylate). *Journal of the American Chemical Society* **1998,** *120* (33), 8571-8572.

9. Jiang, J.; Zhao, Y.; Yaghi, O. M., Covalent Chemistry beyond Molecules. *Journal of the American Chemical Society* **2016,** *138* (10), 3255-3265.

10. Wright, P. A.; Mitchell, L.; Clarke, M.; Seymour, V. R.; Ashbrook, S. E. M.; Williamson, P.; Ehrlichova, B.; Anderson, A. E.; Acerbi, N.; Daniels, L.; Walton, R., Mixed-metal MIL-100(Sc,M) (M=Al, Cr, Fe) for Lewis acid catalysis and tandem C -C bond formation and alcohol oxidation. *Chemistry - A European Journal* **2014,** *20* (51), 17185-17197.

11. Chui, S. S. Y.; Lo, S. M. F.; Charmant, J. P. H.; Orpen, A. G.; Williams, I. D., A Chemically Functionalizable Nanoporous Material $[Cu_3(TMA)_2(H_2O)_3]_n$. *Science* **1999,** *283* (5405), 1148.

12. Li, H.; Eddaoudi, M.; O'Keeffe, M.; Yaghi, O. M., Design and synthesis of an exceptionally stable and highly porous metal-organic framework. *Nature* **1999,** *402*, 276.

13. Eddaoudi, M.; Kim, J.; Rosi, N.; Vodak, D.; Wachter, J.; Keeffe, M.; Yaghi, O. M., Systematic Design of Pore Size and Functionality in Isoreticular MOFs and Their Application in Methane Storage. *Science* **2002,** *295* (5554), 469.

14. Wang, T. C.; Bury, W.; Gómez-Gualdrón, D. A.; Vermeulen, N. A.; Mondloch, J. E.; Deria, P.; Zhang, K.; Moghadam, P. Z.; Sarjeant, A. A.; Snurr, R. Q.; Stoddart, J. F.; Hupp, J. T.; Farha, O. K., Ultrahigh Surface Area Zirconium MOFs and Insights into the Applicability of the BET Theory. *Journal of the American Chemical Society* **2015,** *137* (10), 3585-3591.

15. Gutov, O. V.; Bury, W.; Gomez-Gualdron, D. A.; Krungleviciute, V.; Fairen-Jimenez, D.; Mondloch, J. E.; Sarjeant, A. A.; Al-Juaid, S. S.; Snurr, R. Q.; Hupp, J. T.; Yildirim, T.; Farha, O. K., Water-Stable Zirconium-Based Metal–Organic Framework Material with High-Surface Area and Gas-Storage Capacities. *Chemistry – A European Journal* **2014,** *20* (39), 12389-12393.

16. Deng, H.; Grunder, S.; Cordova, K. E.; Valente, C.; Furukawa, H.; Hmadeh, M.; Gándara, F.; Whalley, A. C.; Liu, Z.; Asahina, S.; Kazumori, H.; O'Keeffe, M.; Terasaki, O.; Stoddart, J. F.; Yaghi, O. M., Large-Pore Apertures in a Series of Metal-Organic Frameworks. *Science* **2012,** *336* (6084), 1018.

17. Bai, Y.; Dou, Y.; Xie, L.-H.; Rutledge, W.; Li, J.-R.; Zhou, H.-C., Zr-based metal–organic frameworks: design, synthesis, structure, and applications. *Chemical Society Reviews* **2016,** *45* (8), 2327-2367.

18. Kalmutzki, M. J.; Hanikel, N.; Yaghi, O. M., Secondary building units as the turning point in the development of the reticular chemistry of MOFs. *Science Advances* **2018,** *4* (10), eaat9180.

19. Millward, A. R.; Yaghi, O. M., Metal−Organic Frameworks with Exceptionally High Capacity for Storage of Carbon Dioxide at Room Temperature. *Journal of the American Chemical Society* **2005,** *127* (51), 17998-17999.

20. Furukawa, H.; Ko, N.; Go, Y. B.; Aratani, N.; Choi, S. B.; Choi, E.; Yazaydin, A. Ö.; Snurr, R. Q.; O'Keeffe, M.; Kim, J.; Yaghi, O. M., Ultrahigh Porosity in Metal-Organic Frameworks. *Science* **2010,** *329* (5990), 424.

21. Li, J.-R.; Kuppler, R. J.; Zhou, H.-C., Selective gas adsorption and separation in metal-organic frameworks. *Chemical Society Reviews* **2009,** *38* (5), 1477-1504.

22. Cui, Y.; Yue, Y.; Qian, G.; Chen, B., Luminescent Functional Metal–Organic Frameworks. *Chemical Reviews* **2012,** *112* (2), 1126-1162.

23. Della Rocca, J.; Liu, D.; Lin, W., Nanoscale Metal–Organic Frameworks for Biomedical Imaging and Drug Delivery. *Accounts of Chemical Research* **2011,** *44* (10), 957-968.

24. Horcajada, P.; Gref, R.; Baati, T.; Allan, P. K.; Maurin, G.; Couvreur, P.; Férey, G.; Morris, R. E.; Serre, C., Metal–Organic Frameworks in Biomedicine. *Chemical Reviews* **2012,** *112* (2), 1232-1268.

25. Corma, A.; García, H.; Llabrés i Xamena, F. X., Engineering Metal Organic Frameworks for Heterogeneous Catalysis. *Chemical Reviews* **2010,** *110* (8), 4606-4655.

26. Li, S.-L.; Xu, Q., Metal-organic frameworks as platforms for clean energy. *Energy & Environmental Science* **2013,** *6* (6), 1656-1683.

27. O'Keeffe, M.; Yaghi, O. M., Deconstructing the Crystal Structures of Metal–Organic Frameworks and Related Materials into Their Underlying Nets. *Chemical Reviews* **2012,** *112* (2), 675-702.

28. Carlucci, L.; Ciani, G.; Maggini, S.; Proserpio Davide, M.; Visconti, M., Heterometallic Modular Metal–Organic 3D Frameworks Assembled via New Tris-β-Diketonate Metalloligands: Nanoporous Materials for Anion Exchange and Scaffolding of Selected Anionic Guests. *Chemistry – A European Journal* **2010,** *16* (41), 12328-12341.

29. Chen, B.; Fronczek, F. R.; Maverick, A. W., Porous Cu−Cd Mixed-Metal−Organic Frameworks Constructed from $Cu(Pyac)_2$ {Bis[3-(4-pyridyl)pentane-2,4-dionato]copper(II)}. *Inorganic Chemistry* **2004,** *43* (26), 8209-8211.

30. Cho, S.-H.; Ma, B.; Nguyen, S. T.; Hupp, J. T.; Albrecht-Schmitt, T. E., A metal-organic framework material that functions as an enantioselective catalyst for olefin epoxidation. *Chemical Communications* **2006,** (24), 2563-2565.

31. Cangussu, D.; Pardo, E.; Dul, M.-C.; Lescouëzec, R.; Herson, P.; Journaux, Y.; Pedroso, E. F.; Pereira, C. L. M.; Stumpf, H. O.; Carmen Muñoz, M.; Ruiz-García, R.; Cano, J.; Julve, M.; Lloret, F., Rational design of a new class of heterobimetallic molecule-based magnets: Synthesis, crystal structures, and magnetic properties of oxamato-bridged $M_3'M_2$ ($M'=Li^{I}$ and Mn^{II}; $M=Ni^{II}$ and Co^{II}) open-frameworks with a three-dimensional honeycomb architecture. *Inorganica Chimica Acta* **2008,** *361* (12), 3394-3402.

32. Noro, S.-i.; Kitagawa, S.; Yamashita, M.; Wada, T., Novel 2-dimensional coordination polymer constructed from a multi-functional metalloligand. *CrystEngComm* **2002,** *4* (29), 162-164.

33. Halper, S. R.; Cohen, S. M., Heterometallic Metal−Organic Frameworks Based on Tris(dipyrrinato) Coordination Complexes. *Inorganic Chemistry* **2005,** *44* (3), 486-488.

34. Halper, S. R.; Do, L.; Stork, J. R.; Cohen, S. M., Topological Control in Heterometallic Metal−Organic Frameworks by Anion Templating and Metalloligand Design. *Journal of the American Chemical Society* **2006,** *128* (47), 15255-15268.

35. Stork, J. R.; Thoi, V. S.; Cohen, S. M., Rare Examples of Transition-Metal−Main-Group Metal Heterometallic Metal−Organic Frameworks from Gallium and Indium Dipyrrinato Complexes and Silver Salts: Synthesis and Framework Variability. *Inorganic Chemistry* **2007,** *46* (26), 11213-11223.

36. Bloch, E. D.; Britt, D.; Lee, C.; Doonan, C. J.; Uribe-Romo, F. J.; Furukawa, H.; Long, J. R.; Yaghi, O. M., Metal Insertion in a Microporous Metal−Organic Framework Lined with 2,2′-Bipyridine. *Journal of the American Chemical Society* **2010,** *132* (41), 14382-14384.

37. Tu, T. N.; Nguyen, M. V.; Nguyen, H. L.; Yuliarto, B.; Cordova, K. E.; Demir, S., Designing bipyridine-functionalized zirconium metal–organic frameworks as a platform for clean energy and other emerging applications. *Coordination Chemistry Reviews* **2018,** *364*, 33-50.

38. Wang, C.; Wang, J.-L.; Lin, W., Elucidating Molecular Iridium Water Oxidation Catalysts Using Metal–Organic Frameworks: A Comprehensive Structural, Catalytic, Spectroscopic, and Kinetic Study. *Journal of the American Chemical Society* **2012,** *134* (48), 19895-19908.

39. Choi, K. M.; Kim, D.; Rungtaweevoranit, B.; Trickett, C. A.; Barmanbek, J. T. D.; Alshammari, A. S.; Yang, P.; Yaghi, O. M., Plasmon-Enhanced Photocatalytic CO2 Conversion within Metal–Organic Frameworks under Visible Light. *Journal of the American Chemical Society* **2017,** *139* (1), 356-362.

40. Zhao, M.; Ou, S.; Wu, C.-D., Porous Metal–Organic Frameworks for Heterogeneous Biomimetic Catalysis. *Accounts of Chemical Research* **2014,** *47* (4), 1199-1207.

41. Farha, O. K.; Shultz, A. M.; Sarjeant, A. A.; Nguyen, S. T.; Hupp, J. T., Active-Site-Accessible, Porphyrinic Metal−Organic Framework Materials. *Journal of the American Chemical Society* **2011,** *133* (15), 5652-5655.

42. Wang, K.; Feng, D.; Liu, T.-F.; Su, J.; Yuan, S.; Chen, Y.-P.; Bosch, M.; Zou, X.; Zhou, H.-C., A Series of Highly Stable Mesoporous Metalloporphyrin Fe-MOFs. *Journal of the American Chemical Society* **2014,** *136* (40), 13983-13986.

43. Morris, W.; Volosskiy, B.; Demir, S.; Gándara, F.; McGrier, P. L.; Furukawa, H.; Cascio, D.; Stoddart, J. F.; Yaghi, O. M., Synthesis, Structure, and Metalation of Two New Highly Porous Zirconium Metal–Organic Frameworks. *Inorganic Chemistry* **2012,** *51* (12), 6443-6445.

44. Feng, D.; Gu, Z.-Y.; Li, J.-R.; Jiang, H.-L.; Wei, Z.; Zhou, H.-C., Zirconium-Metalloporphyrin PCN-222: Mesoporous Metal–Organic Frameworks with Ultrahigh Stability as Biomimetic Catalysts. *Angewandte Chemie International Edition* **2012,** *51* (41), 10307-10310.

45. Feng, D.; Chung, W.-C.; Wei, Z.; Gu, Z.-Y.; Jiang, H.-L.; Chen, Y.-P.; Darensbourg, D. J.; Zhou, H.-C., Construction of Ultrastable Porphyrin Zr Metal–Organic Frameworks through Linker Elimination. *Journal of the American Chemical Society* **2013,** *135* (45), 17105-17110.

46. Johnson, J. A.; Petersen, B. M.; Kormos, A.; Echeverría, E.; Chen, Y.-S.; Zhang, J., A New Approach to Non-Coordinating Anions: Lewis Acid Enhancement of Porphyrin Metal Centers in a Zwitterionic Metal–Organic Framework. *Journal of the American Chemical Society* **2016,** *138* (32), 10293-10298.

47. Tripuramallu, B. K.; Goswami, S.; Goldberg, I., Open MOFs with Unique Hexatopic Zinc-5,15-bis(4′-carboxyphenyl)-10,20-bis(3′,5′-dicarboxyphenyl)porphyrin Linker. *Crystal Growth & Design* **2018,** *18* (1), 230-241.

48. Tan, Y.-X.; Yang, X.; Li, B.-B.; Yuan, D., Rational design of a flu-type heterometallic cluster-based Zr-MOF. *Chemical Communications* **2016,** *52* (94), 13671-13674.

49. Kong, X.-J.; Ren, Y.-P.; Long, L.-S.; Huang, R.-B.; Zheng, L.-S.; Kurmoo, M., Influence of reaction conditions on the channel shape of 3d-4f heterometallic metal-organic framework. *CrystEngComm* **2008,** *10* (10), 1309-1314.

50. Ma, J.-x.; Huang, X.-f.; Song, X.-q.; Zhou, L.-q.; Liu, W.-s., Syntheses and characterization of 3D heterometallic (3d–4f) metal–organic frameworks: Reversible de- and rehydration performance and magnetic properties. *Inorganica Chimica Acta* **2009,** *362* (9), 3274-3278.

51. Gil-Hernández, B.; Gili, P.; Quirós, M.; Sanchiz, J., Mesoxalate as Cu(ii)–Ln(iii) linker in the construction of MOFs in DMSO/water medium. *CrystEngComm* **2015,** *17* (34), 6555-6565.

52. Tripuramallu, B. K.; Titi, H. M.; Roy, S.; Verma, R.; Goldberg, I., Ameliorated synthetic methodology for crystalline lanthanoid-metalloporphyrin open frameworks based on a multitopic octacarboxy-porphyrin scaffold: structural, gas sorption and photophysical properties. *CrystEngComm* **2016,** *18* (4), 515-520.

53. Brozek, C. K.; Dincă, M., Cation exchange at the secondary building units of metal–organic frameworks. *Chemical Society Reviews* **2014,** *43* (16), 5456-5467.

54. Brozek, C. K.; Dincă, M., Ti^{3+}-, $V^{2+/3+}$-, $Cr^{2+/3+}$-, Mn^{2+}-, and Fe^{2+}-Substituted MOF-5 and Redox Reactivity in Cr- and Fe-MOF-5. *Journal of the American Chemical Society* **2013,** *135* (34), 12886-12891.

55. Dincă, M.; Long, J. R., High-Enthalpy Hydrogen Adsorption in Cation-Exchanged Variants of the Microporous Metal−Organic Framework $Mn_3[(Mn_4Cl)_3(BTT)_8(CH_3OH)_{10}]_2$. *Journal of the American Chemical Society* **2007,** *129* (36), 11172-11176.

56. Wang, A.; Zhou, Y.; Wang, Z.; Chen, M.; Sun, L.; Liu, X., Titanium incorporated with UiO-66(Zr)-type Metal–Organic Framework (MOF) for photocatalytic application. *RSC Advances* **2016,** *6* (5), 3671-3679.

57. Sun, D.; Li, Z., Robust Ti- and Zr-Based Metal-Organic Frameworks for Photocatalysis. *Chinese Journal of Chemistry* **2017,** *35* (2), 135-147.

58. Santaclara, J. G.; Olivos-Suarez, A. I.; Gonzalez-Nelson, A.; Osadchii, D.; Nasalevich, M. A.; van der Veen, M. A.; Kapteijn, F.; Sheveleva, A. M.; Veber, S. L.; Fedin, M. V.; Murray, A. T.; Hendon, C. H.; Walsh, A.; Gascon, J., Revisiting the Incorporation of Ti(IV) in UiO-type Metal–Organic Frameworks: Metal Exchange versus Grafting and Their Implications on Photocatalysis. *Chemistry of Materials* **2017,** *29* (21), 8963-8967.

59. Denny, M. S.; Parent, L. R.; Patterson, J. P.; Meena, S. K.; Pham, H.; Abellan, P.; Ramasse, Q. M.; Paesani, F.; Gianneschi, N. C.; Cohen, S. M., Transmission Electron Microscopy Reveals Deposition of Metal Oxide Coatings onto Metal–Organic Frameworks. *Journal of the American Chemical Society* **2018,** *140* (4), 1348-1357.

60. Trousselet, F.; Archereau, A.; Boutin, A.; Coudert, F.-X., Heterometallic Metal–Organic Frameworks of MOF-5 and UiO-66 Families: Insight from Computational Chemistry. *The Journal of Physical Chemistry C* **2016,** *120* (43), 24885-24894.

61. Tu, B.; Pang, Q.; Wu, D.; Song, Y.; Weng, L.; Li, Q., Ordered Vacancies and Their Chemistry in Metal–Organic Frameworks. *Journal of the American Chemical Society* **2014,** *136* (41), 14465-14471.

62. Yang, C.-X.; Ren, H.-B.; Yan, X.-P., Fluorescent Metal–Organic Framework MIL-53(Al) for Highly Selective and Sensitive Detection of Fe^{3+} in Aqueous Solution. *Analytical Chemistry* **2013,** *85* (15), 7441-7446.

63. Colombo, V.; Montoro, C.; Maspero, A.; Palmisano, G.; Masciocchi, N.; Galli, S.; Barea, E.; Navarro, J. A. R., Tuning the Adsorption Properties of Isoreticular Pyrazolate-Based Metal–Organic Frameworks through Ligand Modification. *Journal of the American Chemical Society* **2012,** *134* (30), 12830-12843.

64. Rodríguez-Albelo, L. M.; López-Maya, E.; Hamad, S.; Ruiz-Salvador, A. R.; Calero, S.; Navarro, J. A. R., Selective sulfur dioxide adsorption on crystal defect sites on an isoreticular metal organic framework series. *Nature Communications* **2017,** *8*, 14457.

65. An, J.; Shade, C. M.; Chengelis-Czegan, D. A.; Petoud, S.; Rosi, N. L., Zinc-Adeninate Metal−Organic Framework for Aqueous Encapsulation and Sensitization of Near-infrared and Visible Emitting Lanthanide Cations. *Journal of the American Chemical Society* **2011,** *133* (5), 1220-1223.

66. Shen, X.; Yan, B., Photofunctional hybrids of lanthanide functionalized bio-MOF-1 for fluorescence tuning and sensing. *Journal of Colloid and Interface Science* **2015,** *451*, 63-68.

67. White, K. A.; Chengelis, D. A.; Gogick, K. A.; Stehman, J.; Rosi, N. L.; Petoud, S., Near-Infrared Luminescent Lanthanide MOF Barcodes. *Journal of the American Chemical Society* **2009,** *131* (50), 18069-18071.

68. D'Vries, R. F.; de la Peña-O'Shea, V. A.; Snejko, N.; Iglesias, M.; Gutiérrez-Puebla, E.; Monge, M. A., H_3O_2 Bridging Ligand in a Metal–Organic Framework. Insight into the Aqua-Hydroxo↔Hydroxyl Equilibrium: A Combined Experimental and Theoretical Study. *Journal of the American Chemical Society* **2013,** *135* (15), 5782-5792.

69. Liu, Q.; Cong, H.; Deng, H., Deciphering the Spatial Arrangement of Metals and Correlation to Reactivity in Multivariate Metal–Organic Frameworks. *Journal of the American Chemical Society* **2016,** *138* (42), 13822-13825.

70. Osadchii, D. Y.; Olivos-Suarez, A. I.; Szécsényi, Á.; Li, G.; Nasalevich, M. A.; Dugulan, I. A.; Crespo, P. S.; Hensen, E. J. M.; Veber, S. L.; Fedin, M. V.; Sankar, G.; Pidko, E. A.; Gascon, J., Isolated Fe Sites in Metal Organic Frameworks Catalyze the Direct Conversion of Methane to Methanol. *ACS Catalysis* **2018,** *8* (6), 5542-5548.

71. Castells-Gil, J.; Padial, N. M.; Almora-Barrios, N.; Albero, J.; Ruiz-Salvador, A. R.; González-Platas, J.; García, H.; Martí-Gastaldo, C., Chemical Engineering of Photoactivity in Heterometallic Titanium–Organic Frameworks by Metal Doping. *Angewandte Chemie International Edition* **2018,** *57* (28), 8453-8457.

72. Aguirre-Díaz, L. M.; Gándara, F.; Iglesias, M.; Snejko, N.; Gutiérrez-Puebla, E.; Monge, M. Á., Tunable Catalytic Activity of Solid Solution Metal–Organic Frameworks in One-Pot Multicomponent Reactions. *Journal of the American Chemical Society* **2015,** *137* (19), 6132-6135.

73. Rosi, N. L.; Kim, J.; Eddaoudi, M.; Chen, B.; O'Keeffe, M.; Yaghi, O. M., Rod Packings and Metal−Organic Frameworks Constructed from Rod-Shaped Secondary Building Units. *Journal of the American Chemical Society* **2005,** *127* (5), 1504-1518.

74. Dietzel, P. D. C.; Morita, Y.; Blom, R.; Fjellvåg, H., An In Situ High-Temperature Single-Crystal Investigation of a Dehydrated Metal–Organic Framework Compound and Field-Induced Magnetization of One-Dimensional Metal–Oxygen Chains. *Angewandte Chemie International Edition* **2005,** *44* (39), 6354-6358.

75. Dietzel, P. D. C.; Blom, R.; Fjellvåg, H., Base-Induced Formation of Two Magnesium Metal-Organic Framework Compounds with a Bifunctional Tetratopic Ligand. *European Journal of Inorganic Chemistry* **2008,** *2008* (23), 3624-3632.

76. Dietzel, P. D. C.; Panella, B.; Hirscher, M.; Blom, R.; Fjellvåg, H., Hydrogen adsorption in a nickel based coordination polymer with open metal sites in the cylindrical cavities of the desolvated framework. *Chemical Communications* **2006,** (9), 959-961.

77. Zhou, W.; Wu, H.; Yildirim, T., Enhanced H_2 Adsorption in Isostructural Metal−Organic Frameworks with Open Metal Sites: Strong Dependence of the Binding Strength on Metal Ions. *Journal of the American Chemical Society* **2008,** *130* (46), 15268-15269.

78. Sanz, R.; Martínez, F.; Orcajo, G.; Wojtas, L.; Briones, D., Synthesis of a honeycomb-like Cu-based metal–organic framework and its carbon dioxide adsorption behaviour. *Dalton Transactions* **2013,** *42* (7), 2392-2398.

79. Bhattacharjee, S.; Choi, J.-S.; Yang, S.-T.; Choi, S. B.; Kim, J.; Ahn, W.-S., Solvothermal Synthesis of Fe-MOF-74 and Its Catalytic Properties in Phenol Hydroxylation. *Journal of Nanoscience and Nanotechnology* **2010,** *10* (1), 135-141.

80. Botas, J. A.; Calleja, G.; Sánchez-Sánchez, M.; Orcajo, M. G., Effect of Zn/Co ratio in MOF-74 type materials containing exposed metal sites on their hydrogen adsorption behaviour and on their band gap energy. *International Journal of Hydrogen Energy* **2011,** *36* (17), 10834-10844.

81. Wang, L. J.; Deng, H.; Furukawa, H.; Gándara, F.; Cordova, K. E.; Peri, D.; Yaghi, O. M., Synthesis and Characterization of Metal–Organic Framework-74 Containing 2, 4, 6, 8, and 10 Different Metals. *Inorganic Chemistry* **2014,** *53* (12), 5881-5883.

82. Kim, D.; Coskun, A., Template-Directed Approach Towards the Realization of Ordered Heterogeneity in Bimetallic Metal–Organic Frameworks. *Angewandte Chemie International Edition* **2017,** *56* (18), 5071-5076.

83. Wagner, T.; Haffer, S.; Weinberger, C.; Klaus, D.; Tiemann, M., Mesoporous materials as gas sensors. *Chemical Society Reviews* **2013,** *42* (9), 4036-4053.

84. Walcarius, A., Mesoporous materials and electrochemistry. *Chemical Society Reviews* **2013,** *42* (9), 4098-4140.

85. Linares, N.; Silvestre-Albero, A. M.; Serrano, E.; Silvestre-Albero, J.; García-Martínez, J., Mesoporous materials for clean energy technologies. *Chemical Society Reviews* **2014,** *43* (22), 7681-7717.

86. Perego, C.; Millini, R., Porous materials in catalysis: challenges for mesoporous materials. *Chemical Society Reviews* **2013,** *42* (9), 3956-3976.

87. Lou, X. W.; Archer, L. A.; Yang, Z., Hollow Micro-/Nanostructures: Synthesis and Applications. *Advanced Materials* **2008,** *20* (21), 3987-4019.

88. Yu, L.; Hu, H.; Wu, H. B.; Lou, X. W., Complex Hollow Nanostructures: Synthesis and Energy-Related Applications. *Advanced Materials* **2017,** *29* (15), 1604563.

89. Yu, L.; Wu, H. B.; Lou, X. W. D., Self-Templated Formation of Hollow Structures for Electrochemical Energy Applications. *Accounts of Chemical Research* **2017,** *50* (2), 293-301.

90. Li, Y.; Shi, J., Hollow-Structured Mesoporous Materials: Chemical Synthesis, Functionalization and Applications. *Advanced Materials* **2014,** *26* (20), 3176-3205.

91. Zhao, Y.; Jiang, L., Hollow Micro/Nanomaterials with Multilevel Interior Structures. *Advanced Materials* **2009,** *21* (36), 3621-3638.

92. Hu, M.; Reboul, J.; Furukawa, S.; Radhakrishnan, L.; Zhang, Y.; Srinivasu, P.; Iwai, H.; Wang, H.; Nemoto, Y.; Suzuki, N.; Kitagawa, S.; Yamauchi, Y., Direct synthesis of nanoporous carbon nitride fibers using Al-based porous coordination polymers (Al-PCPs). *Chemical Communications* **2011,** *47* (28), 8124-8126.

93. Cho, W.; Lee, Y. H.; Lee, H. J.; Oh, M., Systematic transformation of coordination polymer particles to hollow and non-hollow In_2O_3 with pre-defined morphology. *Chemical Communications* **2009,** (31), 4756-4758.

94. Xia, W.; Zou, R.; An, L.; Xia, D.; Guo, S., A metal–organic framework route to in situ encapsulation of Co@Co_3O_4@C core@bishell nanoparticles into a highly ordered porous carbon matrix for oxygen reduction. *Energy & Environmental Science* **2015,** *8* (2), 568-576.

95. Moon, H. R.; Lim, D.-W.; Suh, M. P., Fabrication of metal nanoparticles in metal–organic frameworks. *Chemical Society Reviews* **2013,** *42* (4), 1807-1824.

96. Amali, A. J.; Sun, J.-K.; Xu, Q., From assembled metal–organic framework nanoparticles to hierarchically porous carbon for electrochemical energy storage. *Chemical Communications* **2014,** *50* (13), 1519-1522.

97. Banerjee, A.; Upadhyay, K. K.; Puthusseri, D.; Aravindan, V.; Madhavi, S.; Ogale, S., MOF-derived crumpled-sheet-assembled perforated carbon cuboids as highly effective cathode active materials for ultra-high energy density Li-ion hybrid electrochemical capacitors (Li-HECs). *Nanoscale* **2014,** *6* (8), 4387-4394.

98. Wang, X.-F.; Song, X.-Z.; Sun, K.-M.; Cheng, L.; Ma, W., MOFs-derived porous nanomaterials for gas sensing. *Polyhedron* **2018,** *152*, 155-163.

99. Zhang, L.; Wu, H. B.; Lou, X. W., Metal–Organic-Frameworks-Derived General Formation of Hollow Structures with High Complexity. *Journal of the American Chemical Society* **2013,** *135* (29), 10664-10672.

100. Xie, X.-C.; Huang, K.-J.; Wu, X., Metal–organic framework derived hollow materials for electrochemical energy storage. *Journal of Materials Chemistry A* **2018,** *6* (16), 6754-6771.

101. Kang, M. S.; Lee, D.-H.; Lee, K.-J.; Kim, H. S.; Ahn, J.; Sung, Y.-E.; Yoo, W. C., Porosity- and content-controlled metal/metal oxide/metal carbide@carbon (M/MO/MC@C) composites derived from MOFs: mechanism study and application for lithium-ion batteries. *New Journal of Chemistry* **2018,** *42* (23), 18678-18689.

102. You, B.; Jiang, N.; Sheng, M.; Drisdell, W. S.; Yano, J.; Sun, Y., Bimetal–Organic Framework Self-Adjusted Synthesis of Support-Free Nonprecious Electrocatalysts for Efficient Oxygen Reduction. *ACS Catalysis* **2015,** *5* (12), 7068-7076.

103. Wang, Q.; Xia, W.; Guo, W.; An, L.; Xia, D.; Zou, R., Functional Zeolitic-Imidazolate-Framework-Templated Porous Carbon Materials for CO_2 Capture and Enhanced Capacitors. *Chemistry – An Asian Journal* **2013,** *8* (8), 1879-1885.

104. Liu, B.; Shioyama, H.; Akita, T.; Xu, Q., Metal-Organic Framework as a Template for Porous Carbon Synthesis. *Journal of the American Chemical Society* **2008,** *130* (16), 5390-5391.
105. Leznoff, D. B.; Xue, B.-Y.; Batchelor, R. J.; Einstein, F. W. B.; Patrick, B. O., Gold−Gold Interactions as Crystal Engineering Design Elements in Heterobimetallic Coordination Polymers. *Inorganic Chemistry* **2001,** *40* (23), 6026-6034.

106. Yang, S. J.; Kim, T.; Im, J. H.; Kim, Y. S.; Lee, K.; Jung, H.; Park, C. R., MOF-Derived Hierarchically Porous Carbon with Exceptional Porosity and Hydrogen Storage Capacity. *Chemistry of Materials* **2012,** *24* (3), 464-470.

107. Hu, M.; Reboul, J.; Furukawa, S.; Torad, N. L.; Ji, Q.; Srinivasu, P.; Ariga, K.; Kitagawa, S.; Yamauchi, Y., Direct Carbonization of Al-Based Porous Coordination Polymer for Synthesis of Nanoporous Carbon. *Journal of the American Chemical Society* **2012,** *134* (6), 2864-2867.

108. Amali, A. J.; Hoshino, H.; Wu, C.; Ando, M.; Xu, Q., From Metal–Organic Framework to Intrinsically Fluorescent Carbon Nanodots. *Chemistry – A European Journal* **2014,** *20* (27), 8279-8282.

109. Chen, L.; Bai, J.; Wang, C.; Pan, Y.; Scheer, M.; You, X., One-step solid-state thermolysis of a metal–organic framework: a simple and facile route to large-scale of multiwalled carbon nanotubes. *Chemical Communications* **2008,** (13), 1581-1583.

110. Xu, X.; Cao, R.; Jeong, S.; Cho, J., Spindle-like Mesoporous α-Fe_2O_3 Anode Material Prepared from MOF Template for High-Rate Lithium Batteries. *Nano Letters* **2012,** *12* (9), 4988-4991.

111. Xia, W.; Qiu, B.; Xia, D.; Zou, R., Facile preparation of hierarchically porous carbons from metal-organic gels and their application in energy storage. *Scientific Reports* **2013,** *3*, 1935.

112. Salunkhe, R. R.; Kaneti, Y. V.; Yamauchi, Y., Metal–Organic Framework-Derived Nanoporous Metal Oxides toward Supercapacitor Applications: Progress and Prospects. *ACS Nano* **2017,** *11* (6), 5293-5308.

113. Li, T.-T.; Qian, J.; Zheng, Y.-Q., Facile synthesis of porous CuO polyhedron from Cu-based metal organic framework (MOF-199) for electrocatalytic water oxidation. *RSC Advances* **2016,** *6* (81), 77358-77365.

114. Banerjee, A.; Singh, U.; Aravindan, V.; Srinivasan, M.; Ogale, S., Synthesis of CuO nanostructures from Cu-based metal organic framework (MOF-199) for application as anode for Li-ion batteries. *Nano Energy* **2013,** *2* (6), 1158-1163.

115. Salunkhe, R. R.; Tang, J.; Kamachi, Y.; Nakato, T.; Kim, J. H.; Yamauchi, Y., Asymmetric Supercapacitors Using 3D Nanoporous Carbon and Cobalt Oxide Electrodes Synthesized from a Single Metal–Organic Framework. *ACS Nano* **2015,** *9* (6), 6288-6296.

116. Li, C.; Chen, T.; Xu, W.; Lou, X.; Pan, L.; Chen, Q.; Hu, B., Mesoporous nanostructured Co_3O_4 derived from MOF template: a high-performance anode material for lithium-ion batteries. *Journal of Materials Chemistry A* **2015,** *3* (10), 5585-5591.

117. Zhang, L.; Wu, H. B.; Madhavi, S.; Hng, H. H.; Lou, X. W., Formation of Fe_2O_3 Microboxes with Hierarchical Shell Structures from Metal–Organic Frameworks and Their Lithium Storage Properties. *Journal of the American Chemical Society* **2012,** *134* (42), 17388-17391.

118. Kim, T. K.; Lee, K. J.; Cheon, J. Y.; Lee, J. H.; Joo, S. H.; Moon, H. R., Nanoporous Metal Oxides with Tunable and Nanocrystalline Frameworks via Conversion of Metal–Organic Frameworks. *Journal of the American Chemical Society* **2013,** *135* (24), 8940-8946.

119. Maiti, S.; Pramanik, A.; Mahanty, S., Electrochemical energy storage in Mn_2O_3 porous nanobars derived from morphology-conserved transformation of benzenetricarboxylate-bridged metal–organic framework. *CrystEngComm* **2016,** *18* (3), 450-461.

120. Zheng, F.; Xu, S.; Yin, Z.; Zhang, Y.; Lu, L., Facile synthesis of MOF-derived Mn_2O_3 hollow microspheres as anode materials for lithium-ion batteries. *RSC Advances* **2016,** *6* (96), 93532-93538.

121. Kong, S.; Dai, R.; Li, H.; Sun, W.; Wang, Y., Microwave Hydrothermal Synthesis of Ni-based Metal–Organic Frameworks and Their Derived Yolk–Shell NiO for Li-Ion Storage and Supported Ammonia Borane for Hydrogen Desorption. *ACS Sustainable Chemistry & Engineering* **2015,** *3* (8), 1830-1838.

122. Xiu, Z.; Alfaruqi, M. H.; Gim, J.; Song, J.; Kim, S.; Thi, T. V.; Duong, P. T.; Baboo, J. P.; Mathew, V.; Kim, J., Hierarchical porous anatase TiO_2 derived from a titanium metal–organic framework as a superior anode material for lithium ion batteries. *Chemical Communications* **2015,** *51* (61), 12274-12277.

123. Kimitsuka, Y.; Hosono, E.; Ueno, S.; Zhou, H.; Fujihara, S., Fabrication of Porous Cubic Architecture of ZnO Using Zn-terephthalate MOFs with Characteristic Microstructures. *Inorganic Chemistry* **2013,** *52* (24), 14028-14033.

124. Yang, X.; Qiu, L.; Luo, X., ZIF-8 derived Ag-doped ZnO photocatalyst with enhanced photocatalytic activity. *RSC Advances* **2018,** *8* (9), 4890-4894.

125. Zheng, F.; Zhu, D.; Shi, X.; Chen, Q., Metal–organic framework-derived porous Mn1.8Fe1.2O4 nanocubes with an interconnected channel structure as high-performance anodes for lithium ion batteries. *Journal of Materials Chemistry A* **2015,** *3* (6), 2815-2824.

126. Tian, D.; Zhou, X.-L.; Zhang, Y.-H.; Zhou, Z.; Bu, X.-H., MOF-Derived Porous Co_3O_4 Hollow Tetrahedra with Excellent Performance as Anode Materials for Lithium-Ion Batteries. *Inorganic Chemistry* **2015,** *54* (17), 8159-8161.

127. Zhao, J.; Wang, F.; Su, P.; Li, M.; Chen, J.; Yang, Q.; Li, C., Spinel $ZnMn_2O_4$ nanoplate assemblies fabricated via “escape-by-crafty-scheme” strategy. *Journal of Materials Chemistry* **2012,** *22* (26), 13328-13333.

128. Hu, L.; Huang, Y.; Zhang, F.; Chen, Q., CuO/Cu_2O composite hollow polyhedrons fabricated from metal–organic framework templates for lithium-ion battery anodes with a long cycling life. *Nanoscale* **2013,** *5* (10), 4186-4190.

129. Liu, B.; Zhang, X.; Shioyama, H.; Mukai, T.; Sakai, T.; Xu, Q., Converting cobalt oxide subunits in cobalt metal-organic framework into agglomerated Co_3O_4 nanoparticles as an electrode material for lithium ion battery. *Journal of Power Sources* **2010,** *195* (3), 857-861.

130. Cho, W.; Park, S.; Oh, M., Coordination polymer nanorods of Fe-MIL-88B and their utilization for selective preparation of hematite and magnetite nanorods. *Chemical Communications* **2011,** *47* (14), 4138-4140.

131. Hu, H.; Guan, B.; Xia, B.; Lou, X. W., Designed Formation of Co_3O_4/$NiCo_2O_4$ Double-Shelled Nanocages with Enhanced Pseudocapacitive and Electrocatalytic Properties. *Journal of the American Chemical Society* **2015,** *137* (16), 5590-5595.

132. Huang, G.; Zhang, L.; Zhang, F.; Wang, L., Metal–organic framework derived Fe_2O_3@$NiCo_2O_4$ porous nanocages as anode materials for Li-ion batteries. *Nanoscale* **2014,** *6* (10), 5509-5515.

133. Xia, W.; Mahmood, A.; Zou, R.; Xu, Q., Metal–organic frameworks and their derived nanostructures for electrochemical energy storage and conversion. *Energy & Environmental Science* **2015,** *8* (7), 1837-1866.

134. Shen, K.; Chen, X.; Chen, J.; Li, Y., Development of MOF-Derived Carbon-Based Nanomaterials for Efficient Catalysis. *ACS Catalysis* **2016,** *6* (9), 5887-5903.

135. Santos, V. P.; Wezendonk, T. A.; Jaén, J. J. D.; Dugulan, A. I.; Nasalevich, M. A.; Islam, H.-U.; Chojecki, A.; Sartipi, S.; Sun, X.; Hakeem, A. A.; Koeken, A. C. J.; Ruitenbeek, M.; Davidian, T.; Meima, G. R.; Sankar, G.; Kapteijn, F.; Makkee, M.; Gascon, J., Metal organic framework-mediated synthesis of highly active and stable Fischer-Tropsch catalysts. *Nature Communications* **2015,** *6*, 6451.

136. Ma, T. Y.; Dai, S.; Jaroniec, M.; Qiao, S. Z., Metal–Organic Framework Derived Hybrid Co_3O_4-Carbon Porous Nanowire Arrays as Reversible Oxygen Evolution Electrodes. *Journal of the American Chemical Society* **2014,** *136* (39), 13925-13931.

137. Das, R.; Pachfule, P.; Banerjee, R.; Poddar, P., Metal and metal oxide nanoparticle synthesis from metal organic frameworks (MOFs): finding the border of metal and metal oxides. *Nanoscale* **2012,** *4* (2), 591-599.

138. Esken, D.; Turner, S.; Lebedev, O. I.; Van Tendeloo, G.; Fischer, R. A., Au@ZIFs: Stabilization and Encapsulation of Cavity-Size Matching Gold Clusters inside Functionalized Zeolite Imidazolate Frameworks, ZIFs. *Chemistry of Materials* **2010,** *22* (23), 6393-6401.

139. Lu, G.; Li, S.; Guo, Z.; Farha, O. K.; Hauser, B. G.; Qi, X.; Wang, Y.; Wang, X.; Han, S.; Liu, X.; DuChene, J. S.; Zhang, H.; Zhang, Q.; Chen, X.; Ma, J.; Loo, S. C. J.; Wei, W. D.; Yang, Y.; Hupp, J. T.; Huo, F., Imparting functionality to a metal–organic framework material by controlled nanoparticle encapsulation. *Nature Chemistry* **2012,** *4*, 310.

140. Jiang, H.-L.; Liu, B.; Akita, T.; Haruta, M.; Sakurai, H.; Xu, Q., Au@ZIF-8: CO Oxidation over Gold Nanoparticles Deposited to Metal−Organic Framework. *Journal of the American Chemical Society* **2009,** *131* (32), 11302-11303.

141. Jiang, H.-L.; Lin, Q.-P.; Akita, T.; Liu, B.; Ohashi, H.; Oji, H.; Honma, T.; Takei, T.; Haruta, M.; Xu, Q., Ultrafine Gold Clusters Incorporated into a Metal–Organic Framework. *Chemistry – A European Journal* **2011,** *17* (1), 78-81.

142. Ishida, T.; Nagaoka, M.; Akita, T.; Haruta, M., Deposition of Gold Clusters on Porous Coordination Polymers by Solid Grinding and Their Catalytic Activity in Aerobic Oxidation of Alcohols. *Chemistry – A European Journal* **2008,** *14* (28), 8456-8460.

143. El-Shall, M. S.; Abdelsayed, V.; Khder, A. E. R. S.; Hassan, H. M. A.; El-Kaderi, H. M.; Reich, T. E., Metallic and bimetallic nanocatalysts incorporated into highly porous coordination polymer MIL-101. *Journal of Materials Chemistry* **2009,** *19* (41), 7625-7631.

144. Lim, D.-W.; Yoon, J. W.; Ryu, K. Y.; Suh, M. P., Magnesium Nanocrystals Embedded in a Metal–Organic Framework: Hybrid Hydrogen Storage with Synergistic Effect on Physi- and Chemisorption. *Angewandte Chemie International Edition* **2012,** *51* (39), 9814-9817.

145. Hermes, S.; Schröter, M.-K.; Schmid, R.; Khodeir, L.; Muhler, M.; Tissler, A.; Fischer, R. W.; Fischer, R. A., Metal@MOF: Loading of Highly Porous Coordination Polymers Host Lattices by Metal Organic Chemical Vapor Deposition. *Angewandte Chemie International Edition* **2005,** *44* (38), 6237-6241.

146. Park, Y. K.; Choi, S. B.; Nam, H. J.; Jung, D.-Y.; Ahn, H. C.; Choi, K.; Furukawa, H.; Kim, J., Catalytic nickel nanoparticles embedded in a mesoporous metal–organic framework. *Chemical Communications* **2010,** *46* (18), 3086-3088.

147. Schröder, F.; Henke, S.; Zhang, X.; Fischer, R. A., Simultaneous Gas-Phase Loading of MOF-5 with Two Metal Precursors: towards Bimetallics@MOF. *European Journal of Inorganic Chemistry* **2009,** *2009* (21), 3131-3140.

148. Schröder, F.; Esken, D.; Cokoja, M.; van den Berg, M. W. E.; Lebedev, O. I.; Van Tendeloo, G.; Walaszek, B.; Buntkowsky, G.; Limbach, H.-H.; Chaudret, B.; Fischer, R. A., Ruthenium Nanoparticles inside Porous $[Zn_4O(bdc)_3]$ by Hydrogenolysis of Adsorbed [Ru(cod)(cot)]: A Solid-State Reference System for Surfactant-Stabilized Ruthenium Colloids. *Journal of the American Chemical Society* **2008,** *130* (19), 6119-6130.

149. Zlotea, C.; Campesi, R.; Cuevas, F.; Leroy, E.; Dibandjo, P.; Volkringer, C.; Loiseau, T.; Férey, G.; Latroche, M., Pd Nanoparticles Embedded into a Metal-Organic Framework: Synthesis, Structural Characteristics, and Hydrogen Sorption Properties. *Journal of the American Chemical Society* **2010,** *132* (9), 2991-2997.

150. Avci, C.; Yazdi, A.; Tarrés, M.; Bernoud, E.; Bastús, N. G.; Puntes, V.; Imaz, I.; Ribas, X.; Maspoch, D., Sequential Deconstruction–Reconstruction of Metal–Organic Frameworks: An Alternative Strategy for Synthesizing (Multi)-Layered ZIF Composites. *ACS Applied Materials & Interfaces* **2018,** *10* (28), 23952-23960.

CHAPTER 2:

OBJECTIVES

Objectives

The main objectives of the present thesis are enumerated as follows:

1- To study the crystal phase competition by addition of a second metal cation in a complex system with two ligands and two metals. In particular, we have explored the system composed by zinc, cobalt, 1,2,4-triazole and 4,4'-(hexafluoroisopropylidene)bis(benzoic) acid (H_2hfipbb).
   a. Synthetic studies: reaction media, solvents, reagents concentration, temperature, and time. Crystals obtaining.
   b. Phase identification, purification and structure determinations.
   c. Energy formation calculations with density functional theory (DFT).
   d. Evaluation of the kinetic or thermodynamic control that governs each reaction.

2- Combination of multiple metal elements at specific positions in a controllable way at atomic and mesoscopic scales.
   a. Selection of the MOF parent structure with rod-shaped inorganic secondary building unit (SBU), and kinetic control of the reaction.
   b. Selection of metal elements at judiciously selected molar ratios combination (up to four different cations).
   c. Synthesis: influence of different metal ratios, control of the crystallization with the multiple metal cations.
   d. Complete characterization of the obtained materials: inductively coupled plasma optical emission spectrometry (ICP-OES), thermalgravimetric analyses (TGA), powder X-ray diffraction (PXRD), and scanning electron microscopy with energy dispersive X-ray spectroscopy (SEM-EDS).
   e. Study of the possible phase transitions by single crystal X-ray diffraction and powder neutron diffraction.
   f. Neutron diffraction refinements to determine the metal atoms occupations.

g. Relationship composition-mesoscopic arrangement, in the obtained multi-metal MOFs
h. Tuning MOF properties by varying the cation arrangement in multi-metal SBUs. Study of their magnetic properties as a proof of concept.

3- To study the possibility of translating the encoded metal-cation arrangements from the metal-organic frameworks to multimetal oxides. The main goal is to program the composition of electrocatalytically active multimetal oxides.
   a. Thermal treatment of the multi-cation MOFs with controlled metal arrangements.
   b. Total characterization of each product after calcinations, structural type identification.
   c. Study of correlation between MOF precursor and obtained oxides.
   d. Evaluation of multimetal oxides as oxygen reduction reaction (ORR) electrocatalysts.
   e. Analysis and evaluation of the results.

CHAPTER 3:

EXPERIMENTAL SECTION

3.1. General Techniques

3.1.1. Elemental Analysis (EA)

The carbon, nitrogen, and hydrogen content for all synthesized materials was determined by elemental analysis. The dried pure samples were sent to the Servicio Interdepartamental de Investigación (SIdI) services at the Universidad Autónoma de Madrid, where they were weighted employing a micro-scale Metteler-Toledo XP6. Later, they were put into an ECO CHNS-932 analyzer where the carbon, nitrogen, and hydrogen content of each sample is obtained.

3.1.2. Thermogravimetric Analysis (TGA)

The thermal stability for all pure samples was determined using a TGA/ATD simultaneous model STD Q600 from TA Instruments equipment in a temperature range between 40 °C and 800 °C in air (100 mL/min flow) atmosphere and heating rate of 10 °C/min. The measurements were performed by the service of *análisis térmico* at Instituto de Ciencia de Materiales Madrid.

3.1.3. Inductively coupled plasma – optical emission spectroscopy (ICP-OES)

ICP-OES was used to quantify the metal content all the samples in this thesis. The measurements were performed by the service of *análisis químico* at ICMM.

ICP analyses were performed with a Plasma Emission Spectrometer ICP PERKIN ELMER model OPTIMA 2100 DV. Samples were calcined at 800 °C in a furnace for an overnight period prior to digestion. Typically 10 mg of calcined sample were digested in 5 mL of a 1:3 HNO_3 (Sigma Aldrich 67.7%):HCl (Sigma Aldrich 30%) mixture (v:v) and 0.5 mL of H_2SO_4 (Sigma Aldrich 98%), and taken to a 15 mL volume with distilled water. Calcination was found to be required due to the low solubility of the organic linker in the acid aqueous media required for the ICP analysis. The measurements were performed by the service of *análisis químico* at Instituto de Ciencia de Materiales Madrid.

3.2. Diffraction Techniques

3.2.1. Single crystal X-ray diffraction experimental details

Crystals were selected with a polarized optical microscope for a single crystal X-ray diffraction experiment. Single crystal X-ray data were collected in Bruker four circle kappa-diffractometers equipped with a Cu INCOATED microsource, operated at 30W power (45kV, 0.60mA) to generate Cu Kα radiation (λ = 1.54178 Å), and a Bruker VANTEC 500 area detector (microgap technology) or a Bruker PHOTON II area detector (CPAD Technology). Diffraction data were collected exploring over the reciprocal space in a combination of φ and ω scans to reach a resolution of 0.85 Å, with a completeness > 95%, and redundancy >3. For this, either a generic hemisphere collection strategy or a specific one determined using Bruker APEX3[1] software suite was used. The exposure time was adjusted based on the size and diffracting quality of the specimens, each exposure covering 1º in ω or φ. Unit cell dimensions were determined for least-squares fit of reflections with I>4σ. The structures were solved by direct methods implemented in SHELX package. The hydrogen atoms were fixed at their calculated positions using distances and angle constraints. All calculations were performed using APEX3 software for data collection and OLEX2-1.2[2] and SHELXTL[3] to resolve and refine the structure. All non-hydrogen atoms were anisotropically refined.

It should be noted that the chemical composition deduced from the X-ray diffraction data do not necessarily correspond with that of the bulk analytically determined, due to the close atomic number of the employed elements.

Some of collected compounds of chapter 5, especially those collected at low temperatures might have a large electron density hole due the coincidence of lattice parameters of both crystal phases, resulting in that the collected diffraction spots will inevitably have contribution from both phases. Since single crystal X-ray diffraction only provides average information, the resulting R factors and Flack parameters are higher here than in other cases. In addition, the two enantiomorphic space groups are typically observed in the samples presented at chapter 5. The space groups *P6$_5$22* and *P6$_1$22*, and *P6$_4$22* and *P6$_2$22* appear in the case of the double cell and simple cell phase, respectively.

3.2.2. Powder X-ray diffraction (PXRD) experimental details

PXRD patterns were measured with a Bruker D8 diffractometer with a copper source operated at 1600 W, with step size = 0.02° and exposure time = 0.5 s/step. PXRD measurements were used to check the purity of the obtained microcrystalline products by comparison of the experimental results with the calculated patterns obtained from single-crystal X-ray diffraction data.

3.2.3. Neutron powder diffraction. Instruments and experimental details

Neutron powder diffraction experiments were performed on the high-resolution multidetector and on the high-intensity powder diffractometers D2B and D1B (figure 3.2), respectively, at the Institut Laue-Langevin (ILL) in Grenoble (France), and HRPT at the Paul Scherrer Institut (PSI) in Villigen (Swizterland).

-D1B (ILL)

The samples were contained in a 6 mm cylindrical vanadium can and placed on a vanadium-tailed 69ILHV25 cryostat. The data sets were collected with neutrons of calibrated wavelength 2.526038 Å. Silicon and $Na_2Ca_3Al_2F_{14}$ were used as calibrants, and used to refine the instrumental function parameters, which are summarized in table 3.1.

The data reduction (including the application of some basic operations as those related with the addition of several patterns or detector efficiency corrections) was done with the LAMP software[4]. Rietveld refinements were performed using the Reflex module of Materials Studio 8.0[5]. Initial atomic coordinates were taken from the single crystal determined structures.

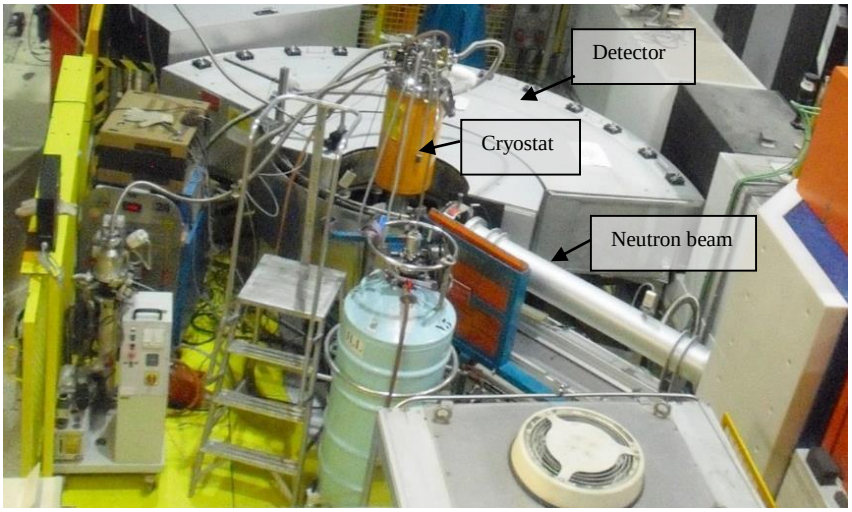

Figure 3. 1 Picture of D1B instrument with the cryostat as environment.

Function	Pseudo-Voight	
	U	2.022529
	V	-0.678846
	W	0.182300
	X	0.0000
	Y	0.0000
	Z	0.0000
Zero point	0.7900	
	S_L	0.0000
	D_L	0.0000

Table 3. 1. Refined instrumental values for D1B instrument.

-D2B (ILL)

The diffractometer D2B (figure 3.2) is a high-flux diffractometer characterized by the very high take-off angle (135°) for the monochromator, which has a relatively large mosaic spread of 20' to compensate for the corresponding intensity (Δl/l) loss. It is 300 mm high, focusing vertically onto about 50 mm; this large incident vertical divergence is matched by 200 mm high detectors and collimators. A complete diffraction pattern is obtained after about 25 steps of 0.05° in 2θ, since the 128 detectors are spaced at 1.25° intervals. Such scans take typically 30 minutes; they are repeated to improve statistics.

The samples were contained in a 6 mm cylindrical vanadium can and placed on a vanadium-tailed orange cryostat. The data sets were collected with calibrated neutrons of wavelength 1.5923 Å.

The high-resolution neutron diffraction profiles were collected at 300 K for $Zn_{0.59}Co_{0.41}$(hfipbb), $Zn_{0.21}Co_{0.79}$(hfipbb) and $Zn_{0.50}Mn_{0.50}$(hfipbb), at 50 K for $Zn_{0.59}Co_{0.41}$(hfipbb), and at 10 K for $Zn_{0.21}Co_{0.79}$(hfipbb) in this diffractometer, covering a 2θ range of 0.2 to 150, every 0.05 degrees.

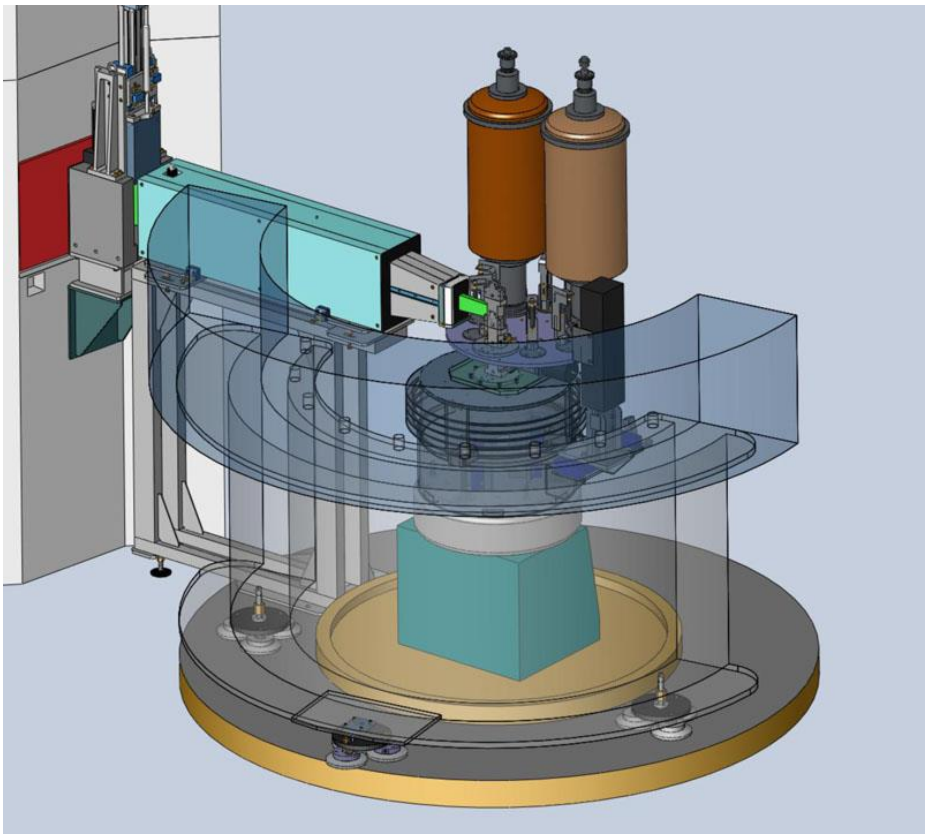

Figure 3. 2. Schematic depiction of D2B instrument with the orange cryostat as environment.

The data reduction (including the application of some basic operations as those related with the addition of several patterns or detector efficiency corrections) was done with the LAMP software.[4] From silicon and $Na_2Ca_3Al_2F_{14}$ as calibrants, the function parameters summarized in table 3.2 were calculated and refined. Rietveld refinements were performed using the Reflex

module of Materials Studio 8.0.[5] Initial atomic coordinates were taken from the single crystal determined structures.

Function	Pseudo-Voight	
	U	0.650743
	V	-0.647521
	W	0.41578
	X	0.041650
	Y	0.065832
	Z	0.00000
Zero	0.15470	
	S_L	0.04000
	D_L	0.02000

Table 3. 2. Resolution values for D2B instrument.

-HRPT (PSI)

The multidetector instrument HRPT[6] is a high-flux diffractometer (Figure 3.3). This instrument is also equipped with the computer controlled sample changer for eight samples for room temperature, sample changer for four and for five samples with sample rotation for the temperature range 1.5 - 315 K. A wide range of neutron wavelengths λ = 1.04-2.96 Å is available. Due to the use of a large position sensitive (PSD) ^{3}He detector, simultaneous measurements are possible within a scattering angle range of 160 degrees with angular step 0.1°. The detector can be positioned on air cushions also at intermediate positions and the angular step can be e.g. 0.05° or less.

High resolution neutron powder diffraction experiments were collected at 300 K and in covering a 2 theta (θ) range of 3.5 to 165 degrees, using a refined wavelength value 1.493869 Å. From silicon and $Na_2Ca_3Al_2F_{14}$ as calibrants, the function parameters summarized in table 3.3 were calculated and refined.

Rietveld refinements were performed using the Reflex module of Materials Studio 8.0.[5] Initial atomic coordinates were taken from the single crystal determined structures.

Figure 3. 3. Picture of HRPT instrument with the cryostat as environment.

Function	Pseudo-Voight	
	U	0.050683
	V	-0.125911
	W	0.169504
	X	0.00000
	Y	0.048467
	Z	0.00000
Zero	0.30166	
	S_L	0.04000
	D_L	0.02000

Table 3. 3. Refined resolution values for HRPT instrument.

3.3. Microscopy Techniques

3.3.1. Scanning Electron Microscopy (SEM) and energy dispersive X-ray spectroscopy (EDS)

Scanning electron microscopy images and energy dispersive X-ray spectra were collected with an S-3000N microscope, equipped with an ESED and an INCAx-sight of Oxford Instruments, respectively. All samples were prepared for SEM and EDS by dispersing the material onto a double sided adhesive conductive carbon tape that was attached to a flat aluminum sample holder and were metallized with a gold layer of 15 nm with a Quórum Q150T-S sputter. The measurements were performed in the *Servicio Interdepartamental de Investigación* at Universidad Auntónoma Madrid.

3.3.2. Field-Emission Scanning Electron Microscopy (FE-SEM)

Field emission scanning electron microscopy (FE-SEM) were collected with a Philips XL 30 S-FEG microscope. All samples were prepared for FESEM by dispersing the material onto a double sided adhesive conductive carbon tape that was attached to a flat aluminum sample holder and were metallized with a chromium layer of 12 nm with a Quórum Q150T-S sputter. The measurements were performed in the *Servicio Interdepartamental de Investigación* at Universidad Auntónoma Madrid.

3.3.3. Transmission Electron Microscopy (TEM)

Selected area electron diffraction (SAED) and transmission electron microscopy (TEM) images were achieved with a JEOL JEM 2100 transmission electron microscope operated at an accelerating voltage of 200 kV. Energy dispersive X-ray spectra were collected with an ESED and an INCAx-sight of Oxford Instruments. All samples were prepared for TEM and EDS by dispersing the material onto a copper grid, using ethanol as solvent. The measurements were performed in the *Centro Nacional de Microscopía Electrónica*.

3.4. Oxygen Reduction Reaction Methodology

The oxygen reduction reaction (ORR) activity was investigated using an Autolab PGSTAT302N with a three-electrode setup (figure 3.4). A platinum mesh and an Ag/AgCl/KCl (0.1 M) were used as counter and reference electrodes, respectively. The active material was prepared mixing 3.5 mg of super P carbon black and 1.5 mg of the corresponding catalytic oxide with 47.5 µL of Nafion 177 and 117 µL of absolute ethanol. The mixture was sonicated for 15 minutes. The glassy carbon rotating-disk-working electrode (RDE, 4 mm in diameter) was polished and coated twice, by drop casting, with 3.5 µL of slurry. All electrochemical measurements, including cyclic voltammograms (CV), linear sweep voltammograms (LSV) on a RDE at a rotation rate of up to 2000 rpm, and chronoamperometry were performed at room temperature in 0.1 M KOH solutions, previously purged with high purity either nitrogen or oxygen for at least 1 hour. Both CV and LSV were recorded at 10 mVs^{-1} scan rate and the potential window ranged from 0.0 to -0.8 V. The stability and tolerance of the materials to methanol (CH_3OH) crossover was studied by chronoamperometry measurements, which were performed at 1600 rpm over 5000s and upon the addition of CH_3OH (0.3 M final concentration) to the O_2-saturated 0.1 M KOH electrolyte.

Figure 3. 4. Equipment used in ORR measurements. Left: Autolab PGSTAT302N, right: rotation disk electrode, cell.

3.5. References

1. Inc, B. A. *APEX3, SAINT and SADABS*, v 2016.9-0; Bruker AXS In, Madison, Wisconsin, USA, 2015.

2. Dolomanov, O. V.; Bourhis, L. J.; Gildea, R. J.; Howard, J. A. K.; Puschmann, H., OLEX2: a complete structure solution, refinement and analysis program. *Journal of Applied Crystallography* **2009,** *42* (2), 339-341.

3. Sheldrick, G. M., A short history of SHELX. *Acta Crystallographica Section A* **2008,** *64* (1), 112-122.

4. Richard, D.; Ferrand, M.; Kearley, G.J., Analysis and Visualisation of Neutron-Scattering Data. *Journal of Neutron Research* **1996**, *4*, 33-39.

5. Biovia, Materials Studio 8.0. **2016**.

6. Fischer, P.; Frey, G.; Koch, M.; Könnecke, M.; Pomjakushin, V.; Schefer, J.; Thut, R.; Schlumpf, N.; Bürge, R.; Greuter, U.; Bondt, S.; Berruyer, E., High-resolution powder diffractometer HRPT for thermal neutrons at SINQ. *Physica B: Condensed Matter* **2000,** *276-278*, 146-147.

CHAPTER 4

CRYSTAL PHASE COMPETITION BY ADDITION OF A SECOND METAL CATION IN A COMPLEX SYSTEM WITH TWO LIGANDS AND TWO METALS

4.1. Introduction

In this chapter a synthetic study that involves the combination of zinc and cobalt with two different linkers is presented. The aim of this chapter is to understand how the synthesis conditions led to the formation of a desired crystal phase with a mixture of metal elements distributed in the inorganic SBUs.

Nowadays the incorporation of a second metal element in MOFs is a *hot topic*, as it was discussed in the chapter 1. However, it is still unclear which are the most important parameters that influence the introduction of a second metal cation in a system. In many reported examples, this introduction drives to phase segregation and thus, the impossibility to prepare a solid solution MOF of a given structure. Here, the introduction of a second metal cation in a phase, denoted as Zn-TMPF-88, previously obtained in my research group is studied (TMPF = transition metal polymeric framework).

Originally, this phase MOF is composed of zinc as metal cation and two different linkers: dicarboxylic 4,4'-hexaflouroisopropylidene-bis-benzoic acid (H_2hfipbb) and 1,2,4-triazole. H_2hfipbb is a V-shaped fluorinated ligand described in chapter 1, which has been previously studied employed in by my research group.[1-3] and other groups in the preparation of MOFs. On the other hand, 1,2,4-triazole is here used as a coligand. Formerly, in the research group, the combination of H_2hfipbb with different N containing coligands, such phenantroline or bipyridin, among others, had been also studied, resulting in a large structural variability of the obtained MOFs.[4-5]

Moreover, as mentioned in chapter 1, the synthesis of multimetal cation MOFs prepared with only H_2hfipbb linker and group 13 elements had been previously studied in my group.[6] However, transition multication MOFs with this ligand, have not been obtained before. Cobalt is introduced in the system as a second metal cation to study its influence in the reaction media.

Therefore, the studied system was composed of the combination of H_2hfipbb and 1,2,4-triazole, as linkers along with zinc and cobalt, two metal cations that typically exhibit similar coordination environment. As result of the synthetic study four new MOFs, denoted TMPF-88, TMPF-90, TMPF-91, and TMPF-95 have been obtained (figure 4.1). The introduction of

two kinds of linkers results in a complex system with multiple possible combinations of reactants. Thus, this study demonstrates that the introduction of a second metal cation in the synthesis media significantly modifies the reaction system, resulting in the appearance of competing crystalline phases, which might even undergo phase transformation. The results presented here illustrate the importance of the synthesis variables such as pH and solvents in the formation of the desired solid solution MOFs, where a mixture of metal cations can be disorderly incorporated into the SBUs. Furthermore, the value of the metal cation ratio added in the synthesis drastically influences the appearance of new phases, and that under certain conditions the incorporation of a second metal cation can only be achieved at a trace level.

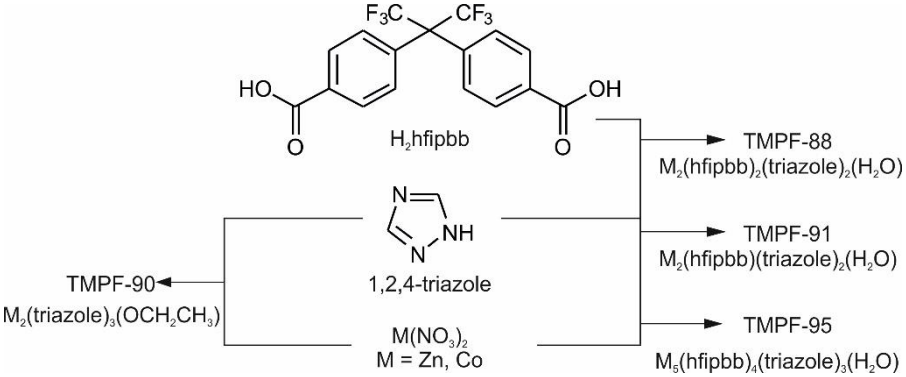

Figure 4. 1. Combination of dicarboxylic 4,4'-hexaflouroisopropylidene-bis-benzoic acid (H_2hfipbb), 1,2,4-triazole and zinc and cobalt precursor salts results in the formation of four new MOFs. In the MOF formulae, M might stand for Zn, or a mixture of Zn and Co in various ratio, as explained in the text.

4.2. Optimized Synthetic Conditions

4.2.1. Synthesis of TMPF-88, $M_3(hfipbb)_2(triazole)_2(H_2O)$. A mixture of H_2hfipbb (130 mg, 0.33 mmol), 1,2,4-triazole (75 mg 1.09 mmol), $Zn(NO_3)_2 \cdot 6H_2O$ (100 mg, 0.34 mmol) in 5 ml of distilled water and 5 ml of absolute ethanol was stirred at room temperature for 5 minutes. The resulting mixture was placed in a Teflon-lined steel autoclave and heated at 170°C for 18 hours. After cooling to room temperature, colorless crystals were filtered off and washed with distilled water, ethanol and acetone. TMPF-88 was also obtained as a pure phase with a mixture of Zn and Co, for synthesis carried out with the amounts shown in Table 4.1, entries 3-6.

4.2.2. Synthesis of TMPF-90, $M_2(triazole)_3(OCH_2CH_3)$. A mixture of 1,2,4-triazole (69 mg, 1 mmol), $Zn(NO_3)_2 \cdot 6H_2O$ (24 mg, 0.08 mmol), $Co(NO_3)_2 \cdot 6H_2O$ (6 mg, 0.02 mmol) and a mixture of water:ethanol (3 ml:3 ml) was stirred at room temperature for 10 minutes. The resulting mixture was heated at 90°C for 18 hours. After cooling to room temperature, a yellow powder was filtered off and washed with distilled water, ethanol and acetone. TMPF-90 was also obtained as a pure phase for synthesis reactions carried out with the amounts shown in Table 4.1, entries 7-10.

4.2.3. Synthesis of TMPF-91, $M_2(hfipbb)(triazole)_2(H_2O)$. A mixture of H_2hfipbb (130mg, 0.33 mmol), 1,2,4-triazole (75 mg, 1.09 mmol), $Zn(NO_3)_2 \cdot 6H_2O$ (91 mg, 0.31 mmol), $Co(NO_3)_2 \cdot 6H_2O$ (9 mg, 0.03 mmol) and a mixture of water:ethanol (5 ml:5 ml) was stirred at room temperature for 10 minutes. To the resulting mixture 300 µL of an aqueous 1M solution of HNO_3 was added to adjust the pH to ~2.5 and the reaction mixture was placed in a Teflon-lined steel autoclave and heated at 170 °C 18 hours. After cooling to room temperature colorless crystals were filtered off and washed with distilled water, ethanol and acetone. TMPF-91 was also obtained as pure phase for synthesis reactions carried out with the amounts shown in Table 4.1, entries 1 and 2.

Table 4. 1. Optimized synthetic conditions for obtaining pure samples. Temperature = 170°C, and reaction time = 18 hours.

Entry	Initial amounts					Experimental	
	H_2hfipbb mg, mmol	1,2,4-triazole mg, mmol	$Zn(NO_3)_2$ mg, mmol	$Co(NO_3)_2$ mg, mmol	H_2O:EtOH	Phase TMPF	Formula[a]
1	130, 0.33	75, 1.09	100, 0.34	-	5ml:5ml	91	Zn_2(hfipbb)(triazole)$_2$
2	130, 0.33	75, 1.09	91, 0.31	9, 0.03	5ml:5ml	91	$Zn_{1.90}Co_{0.10}$(hfipbb)(triazole)$_2$
3	130, 0.33	75, 1.09	100, 0.34	-	5ml:5ml	88	Zn_3(hfipbb)$_2$(triazole)$_2$($H_2$0)
4	130, 0.33	60, 0.87	91, 0.31	9, 0.03	10ml:0ml	88	$Zn_{2.98}Co_{0.02}$(hfipbb)$_2$(triazole)$_2$(H_2O)
5	130, 0.33	60, 0.87	80, 0.27	19, 0.07	10ml:0ml	88	$Zn_{2.96}Co_{0.04}$(hfipbb)$_2$(triazole)$_2$(H_2O)
6	130, 0.33	60, 0.87	67, 0.23	33, 0.11	10ml:0ml	88	$Zn_{2.96}Co_{0.04}$(hfipbb)$_2$(triazole)$_2$(H_2O)
7	-	69, 1.00	6, 0.02	24, 0.08	3ml:3ml	90	$Zn_{0.86}Co_{1.14}$(triazole)$_3$(CH_3CH_2O)
8	-	69, 1.00	17, 0.05	17, 0.05	3ml:3ml	90	$Zn_{1.10}Co_{0.90}$(triazole)$_3$(CH_3CH_2O)
9	-	69, 1.00	24, 0.08	6, 0.02	3ml:3ml	90	$Zn_{1.21}Co_{0.79}$(triazole)$_3$(CH_3CH_2O)
10	-	69, 1.00	-	34, 0.10	3ml:3ml	90	Co_2(triazole)$_3$(CH_3CH_2O)
11[b]	130, 0.33	60, 0.87	33, 0.11	65, 0.22	10ml:0ml	95	$Zn_{1.84}Co_{3.16}$(hfipbb)$_4$(triazole)$_2$(H_2O)

[a]Formula determined by elemental and ICP analyses. [b]Reaction time = 3 days

4.2.4. Synthesis of TMPF-95, M_5(hfipbb)$_4$(triazole)$_3$(H_2O). A mixture of H_2hfipbb (130mg, 0.33 mmol), 1,2,4-triazole (60 mg, 0.87 mmol), $Zn(NO_3)_2 \cdot 6H_2O$ (33 mg, 0.11 mmol), $Co(NO_3)_2 \cdot 6H_2O$ (65 mg, 0.22 mmol) and 10ml of distilled water was stirred at room temperature for 5 minutes. The resulting mixture was placed in a Teflon-lined steel autoclave and heated at 170°C for 72 hours. After cooling to room temperature purple crystals were filtered off and washed with distilled water, ethanol and acetone. Yield 61% (102 mg).

4.3. Structural Description

4.3.1. TMPF-88, $M_3(hfipbb)_2(triazole)_2(H_2O)$. The compound crystallizes in the monoclinic crystal system (*C2/c* space group) The cell parameters determined for this structure are: a = 36.4551(9) Å, b = 18.1156(4) Å, c = 14.1588(4) Å, β = 93.1865(13)° and V = 9329.8(4) $Å^3$. The main crystallographic and refinement data for this compound are shown in Table 4.2 and the ORTEP representation of TMPF-88 asymmetric unit is shown in Figure 4.2. This asymmetric unit has three crystallographically independent zinc atoms in a tetrahedral coordination environment. The Zn atoms are coordinated to six carboxylate groups from the $hfipbb^{2-}$ linkers and three triazolate anions. A water ligand completes the coordination sphere of Zn2. In addition, another water ligand with partial occupancy was located at 2.67 Å from Zn3. The position of Zn3 could actually be split into two positions, so that this atom is partially found in a tetrahedral environment and in a trigonal bypiramidal environment when there is the presence of this additional water ligand. The occupancy for the two positions of Zn3 was refined to a 51 (tetrahedral) :49 (bypiramidal) ratio.

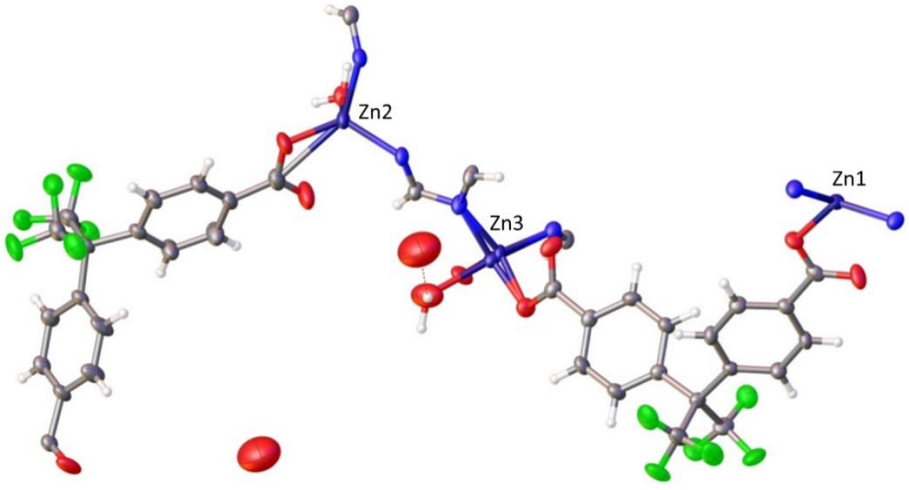

Figure 4. 2. Representation of the asymmetric unit for TMPF-88 material. Atoms: Zn in purple; C in gray; O in red; N in blue; F in green and protons in white. Ellipsoids are displayed at the 50% probability level.

*Table 4. 2. Crystallographic and refinement data for **TMPF-88**.*

Compound	**TMPF-88**	
Formula	$C_{38}H_{23}F_{12}N_6O_{10.7}Zn_3$	
Molecular Weight	1158.95 g·mol^{-1}	
Temperature	296 (2) K	
Wavelenght	1.54178 Å	
Crystal system	Monoclinic	
Space group	*C2/c*	
Unit cell dimensions	a = 36.4551(9) Å	α = 90°
	b = 18.1156(4) Å	β = 93.1865(13)°
	c = 14.1588(4) Å	γ = 90°
Volume	9329.8(4) Å^3	
Z	8	
Density (calculated)	1.645 g·cm^{-3}	
Absorption coefficient (μ)	2.793 mm^{-1}	
F(000)	4613.0	
Crystal size	0.2 × 0.12 × 0.02	
2Θ range for data collection	4.858° to 130.598°	
Index ranges	-41 ≤ h ≤ 42, -21 ≤ k ≤ 21, -16 ≤ l ≤ 16	
Reflections collected	38120	
Independent reflections	7787 [R_{int} = 0.0598, R_{sigma} = 0.0418]	
Data / restraints / parameters	7787/0/650	
Goodness of fit on F^2	1.064	
Final R indexes [I> 2σ(I)]	R_1 = 0.0406	wR_2 = 0.1283
R indexes (all data)	R_1 = 0.0517	wR_2 = 0.1593
Largest diff. peak hole	0.66 e·Å^{-3}	-0.69 e·Å^{-3}

The inorganic SBUs consist of three metal cations with tetrahedral environment (figure 4.3.A). They have a linear shape and are disposed along the *c* axis. These SBU chains are linked through triazolate anions with other linear shaped SBUs along the *a* axis and through hfipbb linkers along the *c* axis. Triazolate and hfipbb linkers connect the SBUs to form a three dimensional framework, with channels running along the *c* axis (figure 4.3.B). The channels are of 8.8 by 8.4 Å dimensions.

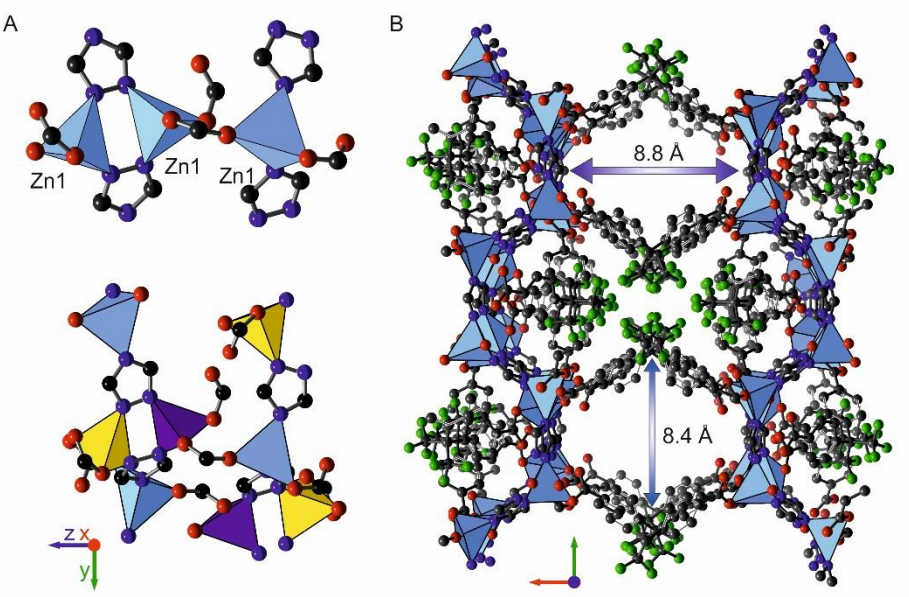

Figure 4. 3. A) The inorganic SBU in TMPF-88 is composed of three linearly disposed tetrahedral metal cations (up). Interaction between SBUs chains of different tetrahedral metal centers: Zn1(purple), Zn2 (blue) and Zn3 (yellow) along the a axis (down); B) Depiction of TMPF-88 3D structure, viewed along the c axis. Carbon is black, oxygen is red, fluorine is green and nitrogen is cyan. Blue polyhedra represent metal (Zn, Co) cations. Hydrogen atoms are omitted for clarity.

4.3.2. TMPF-90, M_2(triazole)$_3$(OCH_2CH_3). Zn_2(triazole)$_3$(CH_3CH_2OH) only appears as microcrystalline powder under optimized synthetic conditions. Thus, it was necessary to growth the crystals employing different synthetic conditions. A small single crystal was obtained in a synthesis carried out with a mixture of Zn(acetate)$_2$, 1,2,4-triazole and H_2hfipbb in a 1:3:1 molar ratio, heated at 150 °C overnight. However, the small size of the crystal and its poor diffracting quality made impossible completing a full diffraction data collection. Nevertheless, with data collected up to 1.1 Å and 49.3% completeness, it was possible to obtain

the unit cell parameters and an initial set of atomic coordinates. The experimental PXRD patterns in a silicon sample holder and the one calculated with this data set are in good agreement, and a Rietveld refinement was then carried out to confirm the crystal structure, with final refinement indicators being Rwp = 3.71%, Rp = 2.55% (Figure 4.4).

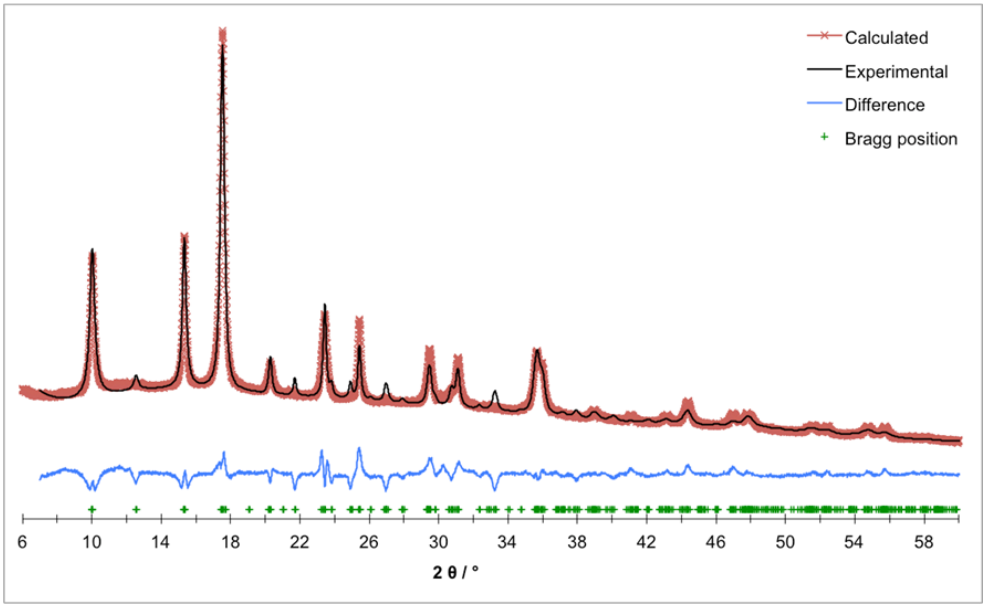

Figure 4. 4. Rietveld X-ray powder refinement plot for TMPF-90, showing calculated (red), refined (black) and difference (blue) patterns. Bragg positions are marked as green crosses.

The main crystallographic and refinement data for this compound are shown in Table 4.3. This compound crystallizes in the orthorhombic crystal system (*Pnma* space group). The asymmetric unit is composed of two crystallographically independent metal atoms, one in tetrahedral and the other in octahedral coordination environment, two triazole linkers and one coordinated ethanol molecule. The tetrahedral metal centers are coordinated to three N atoms from the triazole linkers, and the fourth coordination position is occupied by an O atom from the ethanol solvent ligand, which should be deprotonated to account for the charge balance. Conversely, the octahedral centers are coordinated exclusively by N atoms from triazole. The metal centers are linked through the 1,2,4-triazolate anions, such as the nitrogen atoms in positions 1 and 2 coordinate to the octahedral cations. Each tetrahedral cation is thus linked to six octahedral cations, which are disposed forming rods along the *a* axis (figure 4.5).

*Table 4. 3. Crystal data and structure refinement values for **TMPF-90**.*

Compound	**TMPF-90**	
Formula	$C_8H_6N_9OZn_3$	
Molecular Weight	374.97 g·mol^{-1}	
Temperature	296 (2) K	
Wavelenght	1.54178 Å	
Crystal system	Orthorhombic	
Space group	*Pnma*	
Unit cell dimensions	a = 7.598(7) Å	α = 90°
	b = 10.016(6) Å	β = 90°
	c = 17.457(8) Å	γ = 90°
Volume	1328.7(5) Å^3	
Z	4	
Density (calculated)	1.809 g·cm^{-3}	
Final R indexes [$I > 2\sigma(I)$]	R_p = 2.34%	R_{wp} = 3.43%

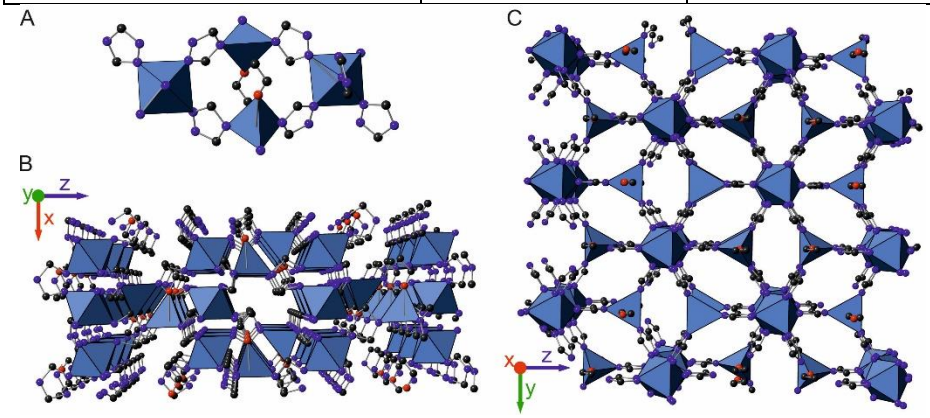

Figure 4. 5. A) The inorganic SBU of TMPF-90 is composed of tetrahedral and octahedral metal centers; they are linked by triazole linkers. B) 3D structural representation of TMPF-90 along b axis. Structural representation of TMPF-90 viewed along a axis. Blue polyhedra represent metal (Zn,Co) cations. Carbon is grey, oxygen is red and nitrogen is dark blue. Hydrogen atoms are omitted for clarity.

4.3.3. TMPF-91, M_2(hfipbb)(triazole)$_2$(H_2O). The main crystallographic and refinement data for this compound are shown in Table 4.4, and the ORTEP representation of TMPF-91 asymmetric unit is shown in Figure 4.6. This compound crystallizes in the monoclinic crystal system (*Cc* space group). There are two crystallographically independent Zn atoms in the asymmetric unit. One of them is in a tetrahedral coordination environment, coordinated to two nitrogen atoms from the triazolate anions, and to two oxygen atoms, one from a carboxylic group of hfipbb and the other one is a water ligand. The second Zn atom is pentacoordinated, with a square pyramidal environment. The coordination sphere is made of four nitrogen atoms from triazolate anions, and one oxygen atom from a carboxylic group from the hfipbb linker. The atoms are connected along the *a* and *c* axes by triazolate anions (figure 4.7.A), while the hfipbb linker connect the metal cations along the *b* axis. The resulting three-dimensional structure is densely packed, with no accessible open space (figure 4.7.B).

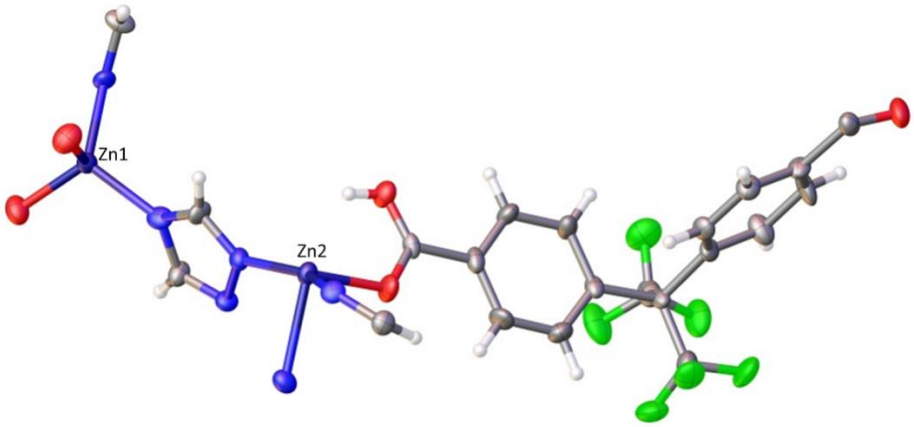

Figure 4. 6. Representation of the asymmetric unit for TMPF-91 material. Atoms: Zn in purple; C in gray; O in red; N in blue; F in green and protons in white. Ellipsoids are displayed at the 50% probability level.

*Table 4. 4. Crystallographic and refinement data for **TMPF-91**.*

Compound	**TMPF-91**	
Formula	$C_{21}H_{14}F_6N_6O_5Zn_5$	
Molecular Weight	675.12 g·mol^{-1}	
Temperature	296 (2) K	
Wavelenght	1.54178 Å	
Crystal system	Monoclinic	
Space group	*Cc*	
Unit cell dimensions	a = 10.0888(4) Å	α = 90°
	b = 33.8241(11) Å	β = 96.002(2)°
	c = 7.0903(2) Å	γ = 90°
Volume	9329.8(4) Å^3	
Z	4	
Density (calculated)	1.864 g·cm^{-3}	
Absorption coefficient (μ)	3.328 mm^{-1}	
F(000)	1344.0	
Crystal size	0.08 × 0.06 × 0.02	
2Θ range for data collection	5.226° to 130.358°	
Index ranges	-11 ≤ h ≤ 11, -39 ≤ k ≤ 39, -8 ≤ l ≤ 8	
Reflections collected	6938	
Independent reflections	3504 [R_{int} = 0.0449, R_{sigma} = 0.0674]	
Data / restraints / parameters	3504/2/361	
Goodness of fit on F^2	1.182	
Final R indexes [I> 2σ(I)]	R_1 = 0.0406	wR_2 = 0.1120
R indexes (all data)	R_1 = 0.0514	wR_2 = 0.1438
Largest diff. peak hole	0.75e·Å^{-3}	-0.68 e·Å^{-3}
Flack parameter	0.02(3)	

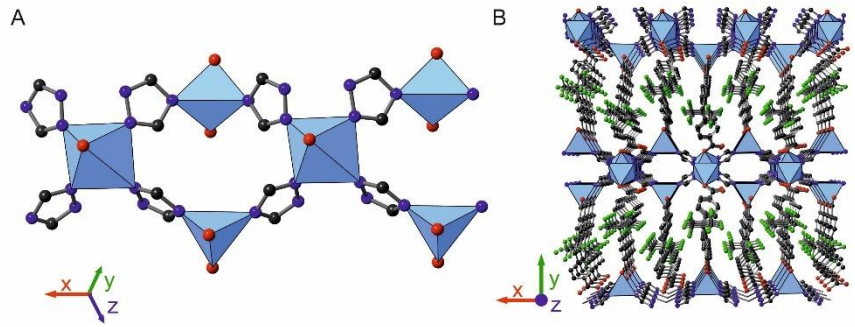

*Figure 4. 7. A) The inorganic SBU in TMPF-91 can be understood as rods of metal cations, which are linked by triazolate anions. B) Representation of the three dimensional structure of the **TMPF-91** viewed along c. Carbon is grey, oxygen is red, fluorine is green and nitrogen is dark blue. Blue polyhedral represent metal (Zn, Co) cations. Hydrogen atoms are omitted for clarity.*

4.3.4. TMPF-95, M_5(hfipbb)$_4$(triazole)$_3$(H_2O). The main crystallographic and refinement data for this compound are shown in Table 4.5, and the ORTEP representation of TMPF-95 asymmetric unit is shown in Figure 4.8. The compound crystallizes in the monoclinic crystal system (*$P2_1/n$* space group), in the form of prismatic pink crystals. The asymmetric unit is formed by five crystallographically independent metal atoms, three of them in a tetrahedral coordination environment, and the other two ones in an octahedral environment. Thus, the inorganic SBUs are U-shaped, consisting of five metal cations, which are coordinated to eight carboxylic groups and to four triazolates, with a total SBU coordination number of twelve (figure 4.9.A). The metal cations were assigned as cobalt during the crystal structure refinement, although elemental analysis indicates the presence of zinc. The positions of these two elements were indistinguishable in the structure, indicating that they must be disorderly occupying the five metal positions of the framework. The coordination of the SBUs through the linkers results in a three dimensional structure with a calculated 10.5 % of accessible void space (figure 4.9.B).

*Table 4. 5. Crystallographic and refinement data for **TMPF-95**.*

Compound	**TMPF-95**	
Formula	$C_{72}H_{38}F_{24}N_6O_{17.48}Co_5$	
Molecular Weight	2017.37 g·mol^{-1}	
Temperature	296 (2) K	
Wavelenght	1.54178 Å	
Crystal system	Monoclinic	
Space group	$P2_1/n$	
Unit cell dimensions	a = 14.8692(5) Å	α = 90°
	b = 24.8713(8) Å	β = 91.621(2)°
	c = 22.1361(7) Å	γ = 90°
Volume	8183.0(5) Å^3	
Z	4	
Density (calculated)	1.638 g·cm^{-3}	
Absorption coefficient (μ)	8.887 mm^{-1}	
F(000)	4011.0	
Crystal size	0.18 × 0.10 × 0.04	
2Θ range for data collection	5.346° to 131.76°	
Index ranges	-17 ≤ h ≤ 17, -29 ≤ k ≤ 27, -26 ≤ l ≤ 23	
Reflections collected	62029	
Independent reflections	13811 [R_{int} = 0.1282, R_{sigma} = 0.1092]	
Data / restraints / parameters	13811/12/1202	
Goodness of fit on F^2	1.013	
Final R indexes [I> 2σ(I)]	R_1 = 0.0776	wR_2 = 0.1994
R indexes (all data)	R_1 = 0.1298	wR_2 = 0.2400
Largest diff. peak hole	0.87 e·Å^{-3}	-0.73 e·Å^{-3}

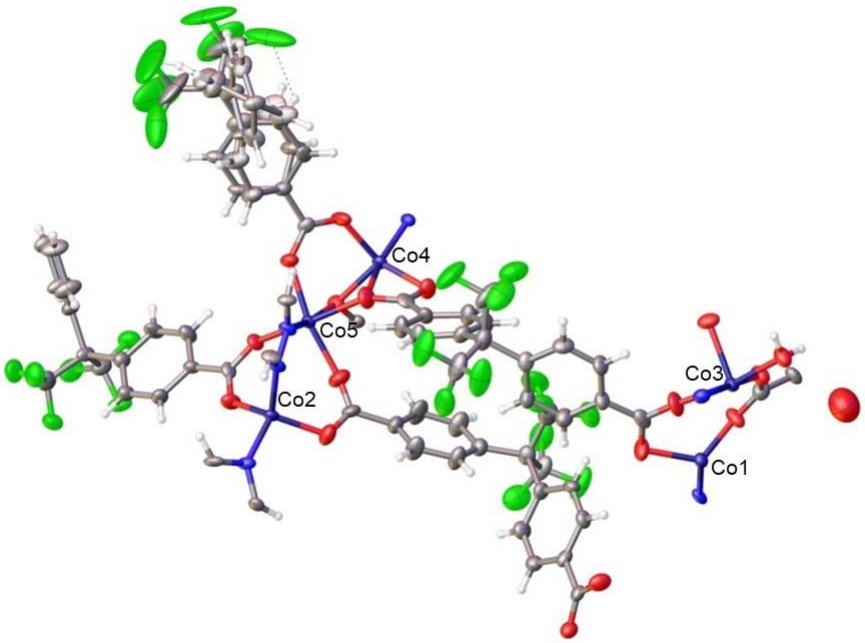

Figure 4. 8. Representation of the asymmetric unit for TMPF-91 material. Atoms: Zn in purple; C in gray; O in red; N in blue; F in green and protons in white. Ellipsoids are displayed at the 50% probability level.

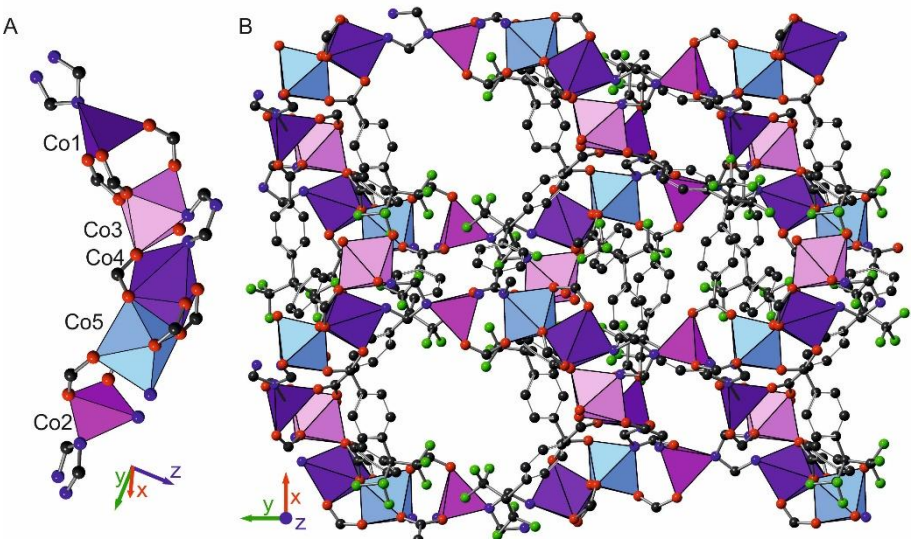

Figure 4. 9. A) The inorganic SBUs in TMPF-95 are composed of five U-shaped disposed polyhedral metal cations. B) Representation of the three dimensional structure of TMPF-95. Carbon is grey, oxygen is red, fluorine is green and nitrogen is dark blue. Polyhedra represent metal (Zn, Co) cations. Hydrogen atoms are omitted for clarity.

4.4. Characterization (EA, TGA, XRPD, N_2 isotherm)

All the pure samples described in table 4.1 were characterized by different methods, including elemental analysis, inductively coupled plasma optical emission spectroscopy (ICP-OES), thermogravimetric analyses, X-ray powder diffraction and in the case of TMPF-88 the specific surface area was calculated by an experiment of N_2 adsorption.

Thermogravimetric analyses (TGA) show that TMPF materials are thermally stable up to 350-390 °C (figure 4.10.). Elemental analyses show check the purity of compounds (Table 4.6.). The final residue for all MOFs is a mixture of ZnO (*P6₃mc*) and Co_3O_4 (*Fd-3m*), depending on the MOF composition.

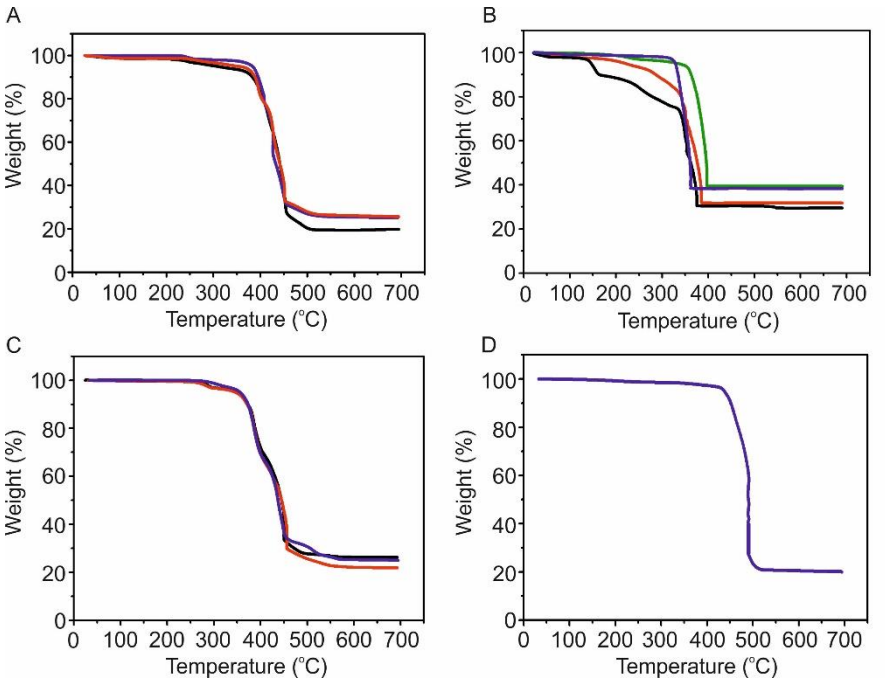

Figure 4. 10. Thermogravimetric analyses plots from: A) TMPF-88 phase TGAs with formulae: $Zn_3(hfipbb)_2(triazole)_2(H_2O)$ (black), $Zn_3(hfipbb)_2(triazole)_2(H_2O)$ (blue) and $Zn_3(hfipbb)_2(triazole)_2(H_2O)$ (red); B) TMPF-90 phase TGAs with formulae: $Zn_{0.86}Co_{1.14}(triazole)_3(CH_3CH_2O)$ (blue), $Zn_{1.10}Co_{0.90}(triazole)_3(CH_3CH_2O)$ (black), $Zn_{1.21}Co_{0.79}(triazole)_3(CH_3CH_2O)$ (red) and $Co_2(triazole)_3(CH_3CH_2O)$ (green); C) TMPF-91 phase TGAs with formulae: $Zn_2(hfipbb)(triazole)_2$ (black) and $Zn_{1.90}Co_{0.10}(hfipbb)(triazole)_2$ (blue); D) TMPF-95 phase TGAs with formula: $Zn_{1.84}Co_{3.16}(hfipbb)_4(triazole)_2(H_2O)$.

The organic content of the pure samples was determined by elemental (CHN) analyses. Experimental values of %C and %H are slightly higher than the calculated for the empty

framework, probably due to molecules of solvent water or ethanol are physisorbed in the crystal surfaces. The exact amount of metals introduced in the sample was determined by ICP-OES and in all cases is in agreement with the energy dispersive spectroscopy (EDS) analyses (discussed in the part 4.6).

Entry	Phase	Formula	CHN Analyses found (calculated)			ICP Analyses	
			%C	%H	%N	%Zn	%Co
1	91	$Zn_2(hfipbb)(triazole)_2$	38.11 (37.42)	2.37 (1.94)	12.25 (12.47)	17.62	-
2	91	$Zn_{1.90}Co_{0.10}(hfipbb)(triazole)_2$	36.75 (37.42)	2.15 (1.94)	13.90 (12.47)	16.75	0.87
3	88	$Zn_3(hfipbb)_2(triazole)_2(H_2O)$	39.19 (39.51)	1.89 (2.01)	7.24 (7.27)	16.70	-
4	88	$Zn_{2.98}Co_{0.02}(hfipbb)_2(triazole)_2(H_2O)$	40.95 (39.51)	2.20 (2.01)	6.78 (7.27)	16.86	0.10
5	88	$Zn_{2.96}Co_{0.04}(hfipbb)_2(triazole)_2(H_2O)$	41.11 (39.51)	2.11 (2.01)	6.80 (7.27)	16.76	0.20
6	88	$Zn_{2.96}Co_{0.04}(hfipbb)_2(triazole)_2(H_2O)$	41.20 (39.51)	2.18 (2.01)	6.82 (7.27)	16.75	0.20
7	90	$Zn_{0.86}Co_{1.14}(triazole)_3(CH_3CH_2O)$	24.12 (23.29)	1.76 (1.67)	36.05 (38.80)	15.19	17.84
8	90	$Zn_{1.10}Co_{0.90}(triazole)_3(CH_3CH_2O)$	24.09 (23.29)	1.81 (1.67)	35.91 (38.80)	19.07	14.06
9	90	$Zn_{1.21}Co_{0.79}(triazole)_3(CH_3CH_2O)$	23.91 (23.29)	1.79 (1.67)	35.95 (38.80)	21.37	12.57
10	90	$Co_2(triazole)_3(CH_3CH_2O)$	23.80 (23.29)	1.88 (1.67)	37.64 (38.80)	-	-
11	95	$Zn_{1.84}Co_{3.16}(hfipbb)_4(triazole)_2(H_2O)$	42.87 (42.87)	1.94 (1.90)	4.51 (4.17)	5.94	9.20

Table 4. 6. CHN analyses, ICP analyses and EDS analyses of all pure phases obtained in Table 4.1.

The PXRD patterns of the solid solution MOFs indicate that the all compounds maintain the parent structure. The results shown in figure 4.11. demonstrate the purity of all the compounds.

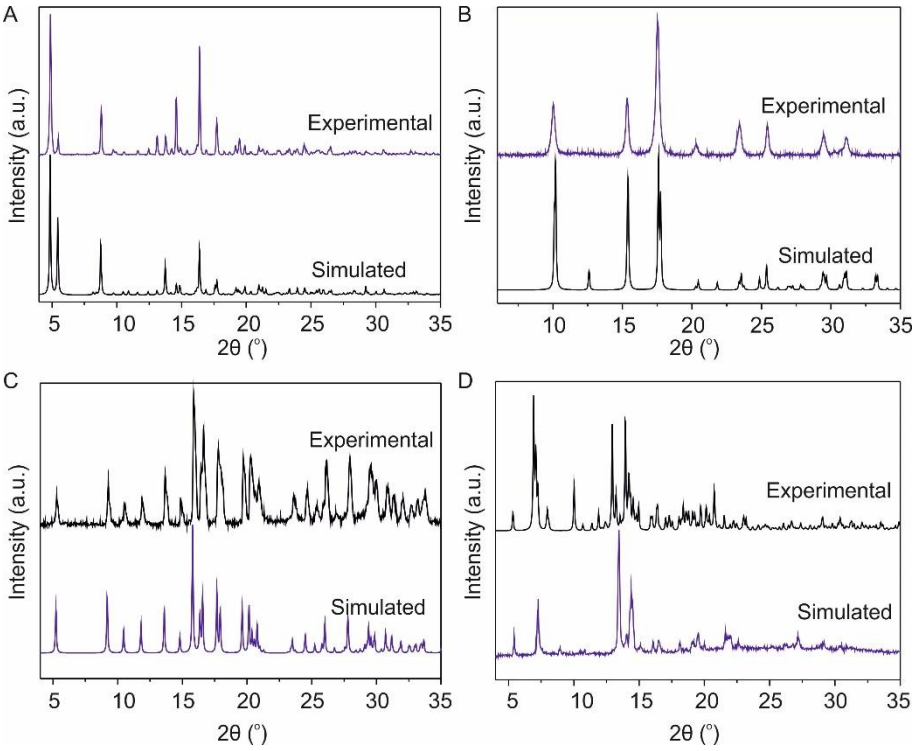

Figure 4. 11. Comparison of X-ray powder diffraction patterns of A) TMPF-88 experimental PXRD pattern (blue) and simulated from X-ray single crystal refinement data (black), B) TMPF-90 experimental PXRD pattern (blue) and simulated from X-ray single crystal refinement data (black), C) TMPF-91 experimental PXRD pattern (black) and simulated from X-ray single crystal refinement data (blue) and D) TMPF-95 experimental PXRD pattern (black) and simulated from X-ray single crystal refinement data (blue).

N_2 sorption isotherm shows that TMPF-88 is permanently porous, with a BET surface area of 121 m^2g^{-1} (190 m^2g^{-1} Langmuir). The gas sorption isotherm appears in figure 4.12.

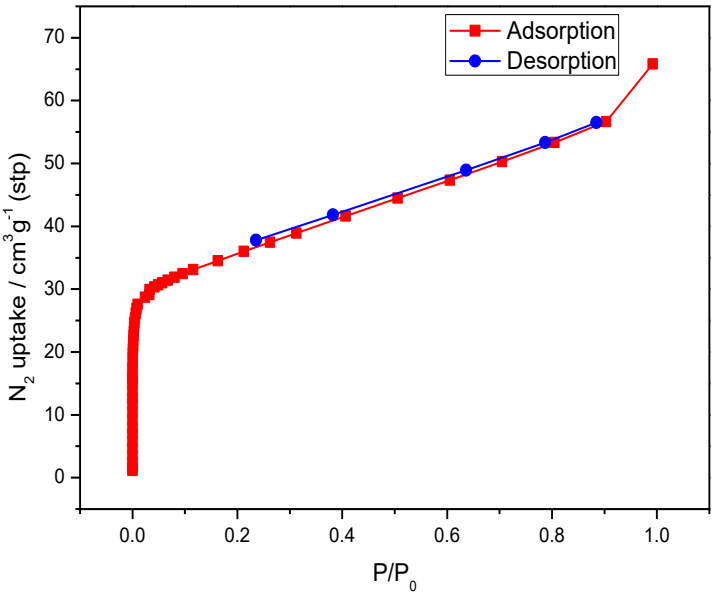

Figure 4. 12. Gas sorption isotherm for TMPF-88 showing adsorption (red) and desorption isotherm (blue) curves.

4.5. Discussion of the Synthetic Study

The combination of zinc nitrate with 1,2,4-triazole and H_2hfipbb in a 1:3:1 ratio resulted in obtaining Zn-TMPF-88 compound. Initially, we carried out the synthesis using water as the only solvent. Zn-TPMF-88 was isolated as a pure phase as shown by PXRD, although in a low yield, a fact the we attributed to the low solubility of H_2hfipbb in water, since a large amount of unreacted linkers remained in the reaction media. The use of a water:ethanol solvent mixture in a 1:1 ratio greatly improved the yield. With these optimized conditions, we then attempted to introduce cobalt in the structure by adding cobalt nitrate in the reaction media at the various Zn:Co ratios of 10:1, 8:1, 4:1, 2:1, 1:1, 1:2 and 0:1 (figure 4.13.). The measured pH of the synthesis initial mixtures was fixed with 1 M NaOH to a value of 3.5. This is the same pH value measured in the reaction carried out exclusively with zinc nitrate as the only metal salt. The phase diagram for the obtained products under these conditions for obtaining pure phases were further optimized and are listed in Table 4.1.

Surprisingly, the addition of cobalt even at the lowest 10:1 and 8:1 Zn:Co ratios precludes the formation of TMPF-88, resulting in the appearance of a different phase, TMPF-91. Pale pink microcrystalline powder was obtained in both cases, whose PXRD patterns are in agreement with the calculated ones (figure 4.11.).

When we increase the amount of cobalt in the reaction to 4:1, 2:1 and 1:1, TMPF-88 is obtained in the form of large pale pink crystals (500µm). However, the MOF now appears mixed with a yellow microcrystalline powder, which is actually formed by needle-like microcrystals (5µm) figure 4.14. This powder was identified as TMPF-90, according to the PXRD pattern. Since TMPF-90 only contains 1,2,4-triazole as the organic linker, we attempted to obtain TMPF-88 as a pure phase by decreasing the amount of triazole in the reaction media, which otherwise is added in excess (1.09 mmol). However, in all reactions with an amount of 1,2,4-triazole between 1.09 and 0.80 mmol, TMPF-90 is always present. Furthermore, if the amount of 1,2,4-triazole is lower than 0.80 mmol, TMPF-88 is no longer formed.

TMPF-90 phase could be obtained with various Zn:Co ratios (4:1, 1:1, 1:4 and 0:1) as a pure phase when H_2hfipbb is not added during the synthesis: The synthetic conditions are different and the reaction heating is carried out at 90°C. When the Zn/Co ratio lies below 1 and the

cobalt amount is larger than zinc amount, TMPF-88 is no longer formed. For syntheses with Zn:Co ratios 1:2, 1:4, 1:10 and 0:1, crystals corresponding to a previously reported MOF[7] with formula Co(hfipbb)(H_2hfipbb)$_{0.5}$.are obtained, along with another yellowish microcrystalline phase, which could not be identified.

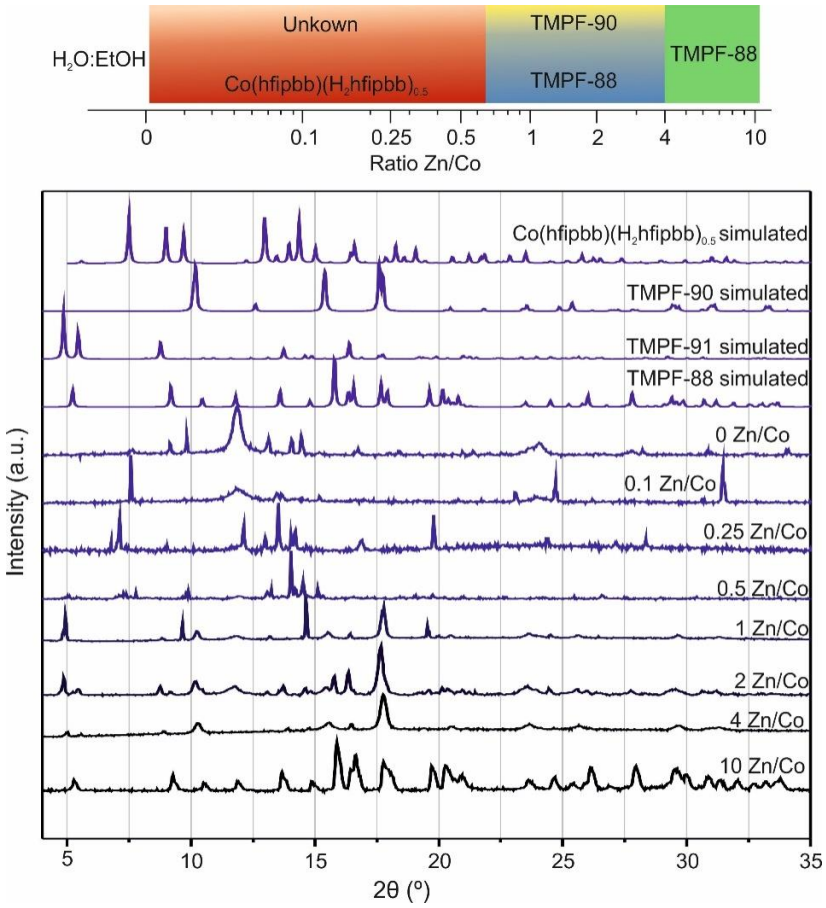

Figure 4. 13. The phase diagram for the obtained products with varying Zn/Co ratios with water and ethanol as solvents (up). For all experiments, temperature was 170 °C, and heating time 18h. The Zn/Co ratio is shown in the logarithmic scale, indicating the values that were investigated. PXRD patterns of the different simulated phases and the different obtained solids with Zn/Co ratios carried out in the explained conditions (down).

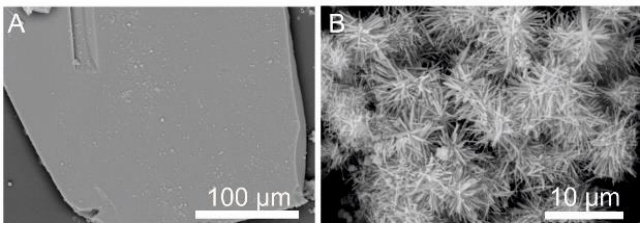

Figure 4. 14. SEM-pictures from A) Zn-Co-TMPF-88 and B) Zn-Co-TMPF-90.

According to the initial synthesis experiments, Zn-TMPF-88 could be obtained with the use of water as the only solvent, although in a low yield. Thus, another synthetic study with the mixture of zinc and cobalt in absence of ethanol was performed. Syntheses carried out with water as unique solvent result in a different phase diagram (figure 4.15.). Thus, in the absence of ethanol, TMPF-91 is no longer observed for any of the Zn:Co explored ratios. TMPF-88 can be obtained as pure phase, according to PXRD analyses, for various Zn:Co ratios of 10:1, 4:1 and 2:1. However, ICP analyses of the samples indicate that cobalt in present only in trace amount (0.10% Co, 16.86% Zn for 168 ratio Zn/Co; 0.18% Co, 16.81 %Zn with 93 ratio Zn/Co and 0.20 %Co, 16.76 %Zn with 84 ratio Zn/Co). Therefore, these values are not even detected by the EDS analyses due to its detection limit. With equimolar amounts of zinc and cobalt, TMPF-90 is again observed in the PXRD pattern, mixed with TMPF-88. A further increase in the amount of cobalt (Zn:Co 1:2) results in the appearance of a new phase, TMPF-95. However, TMPF-90 phase is still present according to the PXRD patterns, although as a minor phase. The Zn:Co ratio for TMPF-95 crystals according to EDS analysis is 1:2, which is coincident with initial ratio of the reactants.

With a further increase in the amount of cobalt in the synthesis mixture, and for Zn:Co ratios of 1:4, 1:10 and 0:1, crystals of the Co(hfipbb)(H_2hfipbb)$_{0.5}$ phase are ~~a~~ again formed along with a yellowish powder, similar to what we observed in the water:ethanol system. In addition, the unknown phase also appears in these ratios.

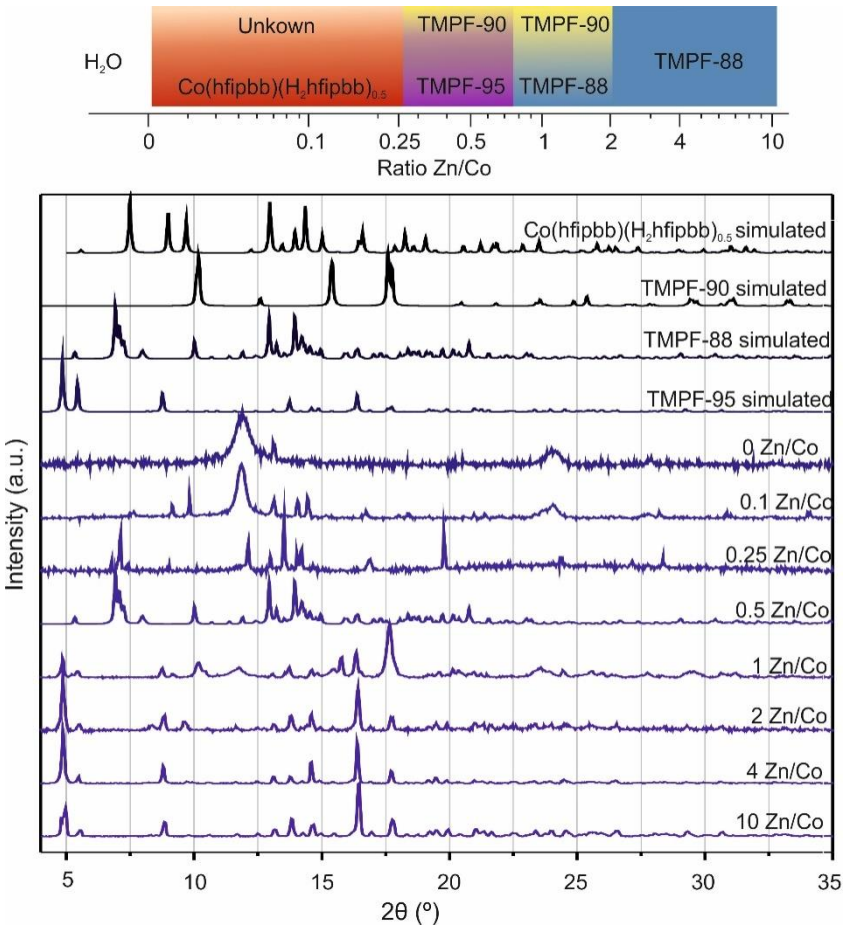

Figure 4. 15. The phase diagram for the obtained products with varying Zn/Co ratios with water as solvent. For all experiments, temperature was 170 °C, and the heating time 18h. The Zn/Co ratio is shown in the logarithmic scale, indicating the values that were investigated. PXRD patterns of the different simulated phases and the different obtained solids with Zn/Co ratios carried out in the explained conditions (down).

4.6. SEM-EDS Analyses

EDS analyses of the samples were carried out to evaluate the presence of both metals (Zn and Co) inside the crystals and to observe the homogeneity of the metals distribution along a crystal. However, this technique only offers qualitative information and the analyses must be compared with quantitative techniques such as ICP-OES. In addition, the detection limit for EDS is higher than other techniques, so this technique is not suitable for evaluating elements in trace amount.

4.6.1. TMPF-88. SEM images show plate crystals (500 µm) mixed with a microcrystalline powder formed by needle microcrystals (5µm), as observed in the SEM images in prepared samples with an initial 1:10 and 1:8 Zn:Co ratio with water and ethanol as solvents (figure 4.14). This powder was identified as TMPF-90, according to the PXRD pattern (figure 4.11). EDS analysis performed for the TMPF-88 crystals prepared with an initial 2:1 Zn:Co ratio demonstrates that cobalt is included in the MOF. However, the cobalt amount incorporated is substantially lower compared with the initial amount added (figure 4.16). In addition, the distribution of cobalt also varies along the same crystal, as shown by the measurements performed in different areas of the same crystal. Zn/Co ratios are in the range between 24 and 15, measured in three areas from three different crystals.

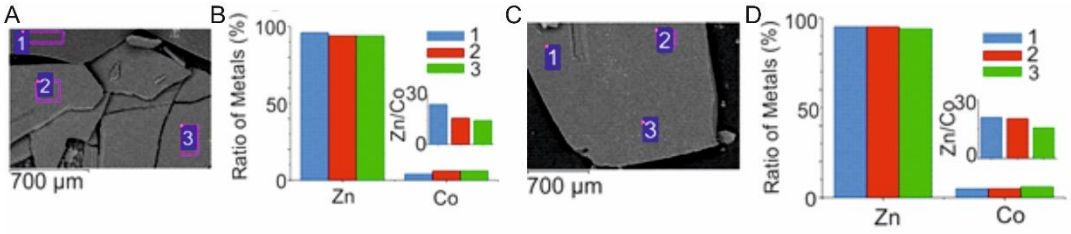

Figure 4. 16. A) SEM image showing TMPF-88 crystals corresponding to a sample prepared with an initial Zn:Co ratio 2:1 , indicating the points where the EDS analyses were performed. B) Plot of the ratio of metals (%) and the Zn/Co ratio determined by EDS analysis, where each column corresponds to the area indicated by a number in panel A. C) Sample preapred with an initial Zn:Co ratio 2:1 and shows the points in a same crystal. D) Plot of the ratio of metals (%) and the Zn/Co ratio determined by EDS analysis, where each column corresponds to the area indicated by a number in panel C.

4.6.2. TMPF-90. EDS analyses indicate that in this phase Zn:Co ratio is homogeneous along the sample. For the sample prepared with a 1:1 ratio, the Zn/Co ratio obtained in three different areas of a sample is 0.55:0.45 (figure 4.17.A). In the case of the sample prepared with a 4:1

ratio, a similar Zn/Co ratio is found in three areas of the sample (0.6:0.4) (figure 4.17.B), suggesting a preference for the introduction of cobalt over the zinc in this structure.

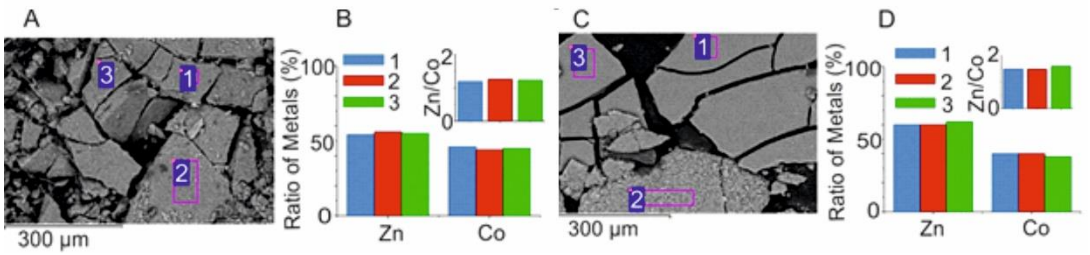

Figure 4. 17. A) SEM image showing TMPF-90 crystals corresponding to a sample prepared with an initial Zn:Co ratio 1:1 , indicating the points where the EDS analyses were performed. B) Plot of the ratio of metals (%) and the Zn/Co ratio determined by EDS analysis, where each column corresponds to the area indicated by a number in panel A. C) Sample preapred with an initial Zn:Co ratio 4:1 and shows the points in a same crystal. D) Plot of the ratio of metals (%) and the Zn/Co ratio determined by EDS analysis, where each column corresponds to the area indicated by a number in panel C.

4.6.3. TMPF-91. SEM images show plate like crystals as a major phase, although the presence of a small amount of smaller particles without well-defined shape is also observed. EDS analyses were performed on different areas of the crystals to determine whether cobalt was actually incorporated into the structure. The results indicate that cobalt is indeed present in the structure, although the quantified amount of cobalt is much lower than the one initially added, similar to TMPF-88. Furthermore, the Zn:Co ratio is not constant along the crystals. For the samples prepared with an initial 10:1 ratio, the Zn/Co ratios observed in the three areas of the same crystal are 34.0, 26.7 and 26.6 (figure 4.18). In the case of the sample prepared with an initial 8:1 Zn:Co ratio the differences are even larger, with the observed Zn/Co ratios of 21.9, 20.9 and 45.7.Although the experimental error associated with the variation in beam penetration in a tilted sample cannot be completely ruled out, these results seem to indicate that the incorporation of cobalt into the structure is not homogeneous, and therefore the MOF composition varies along the crystals. This is also in agreement with the differences in the composition previously reported for other multi-metal MOFs, such as MOF-74.[8]

4.6.4. TMPF-95. The Zn:Co ratio for TMPF-95 crystals according to EDS analyses is 1:2, which is coincident with the initial ratio of reactants (figure 4.19).

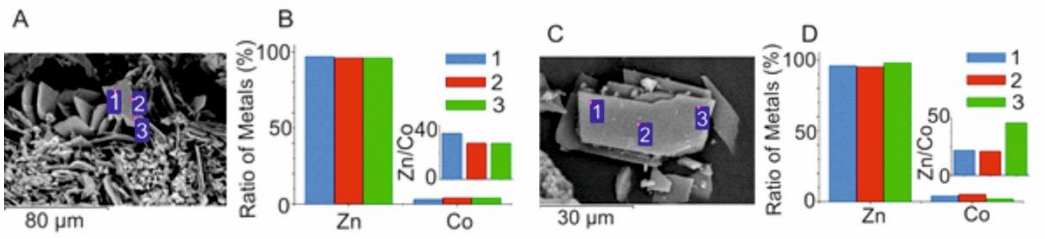

Figure 4. 18. A) SEM image showing TMPF-91 crystals corresponding to a sample prepared with an initial Zn:Co ratio 10:1 , indicating the points where the EDS analyses were performed. B) Plot of the ratio of metals (%) and the Zn/Co ratio determined by EDS analysis, where each column corresponds to the area indicated by a number in panel A. C) Sample preapred with an initial Zn:Co ratio 8:1 and shows the points in a same crystal. D) Plot of the ratio of metals (%) and the Zn/Co ratio determined by EDS analysis, where each column corresponds to the area indicated by a number in panel C.

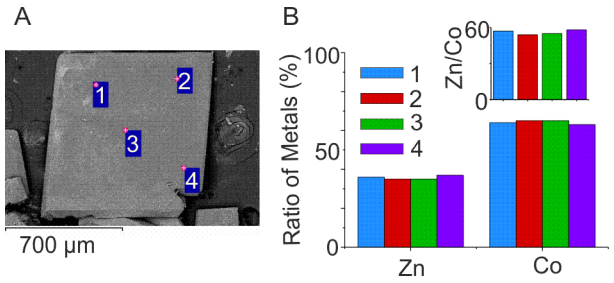

Figure 4. 19. SEM images corresponding to TMPF-95 crystals, indicating the areas where the EDS analyses were performed. A) Sample prepared with an initial Zn:Co ratio 1:2. B) Plot of the ratio of metals (5) and Zn/Co determined by EDS analysis, where each column corresponds to the area indicated by a number in panel A.

4.7. Kinetic Study

In an effort to understand this complex system and isolate TMPF-88 and TMPF-90 phases we then studied the kinetics of this reaction system, by collecting the PXRD patterns of the products obtained after reaction times of 1h, 2h, 3h, 4h, 6h, 8h and 18h (figure 4.20). After 1 hour of heating, only the unreacted H_2hfipbb linker appeared in the PXRD pattern. Interestingly, after 2 hours the PXRD pattern indicates the formation of an additional crystalline phase, which was identified as a MOF with a composition Zn(hfipbb), which was previously reported by us, and here on we denote as ZnPF-1.[9] TMPF-90 appears after 3 hours of heating, mixed with ZnPF-1. It seems reasonable to think that the formation of ZnPF-1 results in a higher relative concentration of triazole in the reaction solution, therefore favoring the formation of TMPF-90. After 4 hours of heating, the presence of TMPF-88 is already identified in the PXRD pattern, although still mixed with TMPF-90 and ZnPF-1. After 8 hours of heating, the intensities of the diffraction peaks corresponding to both ZnPF-1 and TMPF-90 drastically decrease. Visual inspection of the product under an optical microscope still shows the presence of a yellowish microcrystalline powder typical of TMPF-90, along with large plate-like crystals of TMPF-88, suggesting that is only partially re-dissolved. At this point, ZnPF-1 seems to be completely re-dissolved, as it is no longer observed in the PXRD pattern or visually under microscope. Interestingly, after a longer reaction times (18 h), the intensities corresponding to a TMPF-90 peaks increase again, being the final product a mixture of TMPF-88 and TMPF-90.

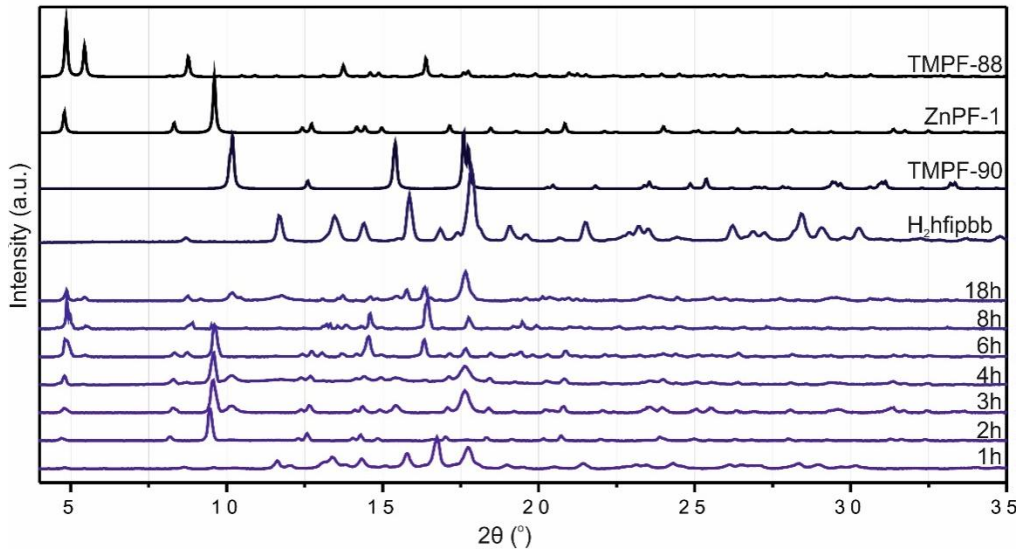

Figure 4. 20. Plot of the PXRD patterns corresponding to the samples obtained at different reaction times. The composition of the initial synthesis mixture is 130 mg, 0.33 mmol of H_2hfipbb; 75 mg, 1.09 mmol of triazole; 67 mg, 0.23 mmol of $Zn(NO_3)_2$ and 33 mg, 0.11 mmol of $Co(NO_3)_2$ in all cases. The simulated PXRD patterns of the phases involved in the kinetic study are shown in the top of the figure, for comparison.

4.8. DFT Calculations

To gain more insight on the formation of the different phases involved in the reaction, we estimated the structural stability of crystal phases and their synthesis mechanism during the MOF crystallization by means of theoretical calculations.[2, 4, 10-11]

In this work, formation energies were calculated (ΔE_{Form}) using the VASP package. The geometry optimization was determined using the experimental structures obtained by X-ray diffraction and always converged to a stable structure even though no symmetry constrains were imposed. The results of these calculations show that TMPF-90 and ZnPF-1 have very similar formation energies, much lower than that of TMPF-88, which is energetically more stable (figure 4.21).

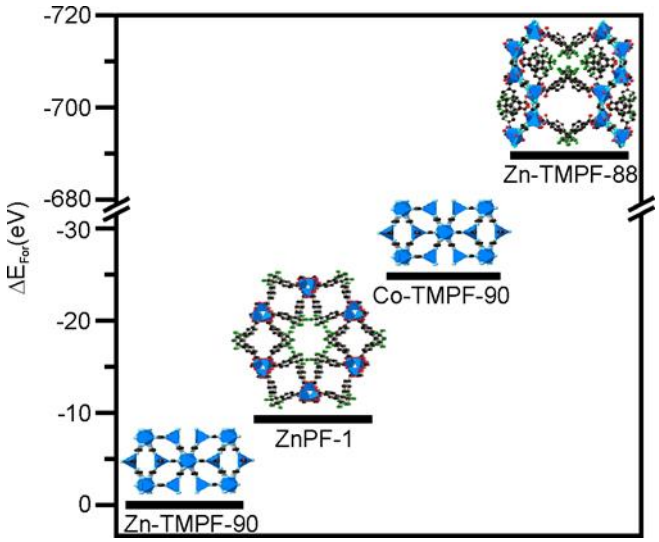

Figure 4. 21. Relative formation energies for the phases involved in the kinetic study. ΔE_{Form} values have been normalized to the most stable phase.

In the case of ZnPF-1 and TMPF-90, the calculations were performed assuming that zinc is the only metal present. However, taking into account that TMPF-90 can be obtained independently with both zinc and cobalt, we performed two calculations for this phase, one considering zinc as the only metal element (Zn-TMPF-90), and the other one with cobalt as the only metal element (Co-TMPF-90). This study shows that Co-based structure presents a higher stability than the Zn one. These results suggest that the inclusion of Co in the bimetallic

TMPF compounds might lead to a stabilization of their structures. Thus, small differences were observed in the case of TMPF-90 depending on the metal element included, although it is likely that the actual product is composed of both zinc and cobalt, being the formation energy order Zn-TMPF-90>ZnPF-1>Co-TMPF-90. Nevertheless, these calculations support the experimental observations of the kinetic study, demonstrating that in the mixed-metal system with multiple kinds of linkers, kinetically favored phases are readily formed, and consequently the composition and concentration of the synthesis media is not homogeneous.

4.9. Conclusions

First, from the obtained results we can deduce that the addition of a second metal element, even at a very low amount, drastically modifies the reaction media, inducing the formation of new phases, as shown by the formation of TMPF-91 with a 10:1 Zn:Co initial ratio using as solvent a mixture of water and ethanol.

Furthermore, in the mixed-metal, mixed-ligand system studied here, there is a competition in the MOF formation, where kinetically favored structures (ZnPF-1 and TMPF-90) appear at short reaction times, precluding the formation as a pure phase of other energetically more favorable solid-solution phases (TMPF-88).

In addition, another MOF was isolated (TMPF-95), which could be prepared only with a very specific Zn:Co ratio (1:2). Despite the restricted amount required for preparing this phase, the single crystal X-ray diffraction analysis indicates that the two metal cations are disorderly disposed occupying different crystallographic sites.

The cobalt amount introduced into the framework is substantially lower than the one initially added to the reaction in the cases of TMPF-91 and TMPF-88, according to EDS and ICP analyses, while in the case of TMPF-90 and TMPF-95, the two elements can be incorporated in comparable amounts. This is related with the kinetic study, where we observed the formation of TMPF-90 as kinetically favored product, which include larger amount of cobalt. This point will be key in the development of the work that will be discussed in the chapters 5 and 6.

This results have been reported in Dalton Transactions in 2016, 45, 4327, with the title '*Crystal phase competition by addition of a second metal cation in solid solution metal–organic frameworks'.*

4.10. References

1. Bernini, M. C.; de Paz, J. R.; Snejko, N.; Sáez-Puche, R.; Gutierrez-Puebla, E.; Monge, M. Á., Unusual Magnetic Behaviors and Electronic Configurations Driven by Diverse Co(II) or Mn(II) MOF Architectures. *Inorganic Chemistry* **2014,** *53* (24), 12885-12895.

2. Gándara, F.; de la Peña-O'Shea, V. A.; Illas, F.; Snejko, N.; Proserpio, D. M.; Gutiérrez-Puebla, E.; Monge, M. A., Three Lanthanum MOF Polymorphs: Insights into Kinetically and Thermodynamically Controlled Phases. *Inorganic Chemistry* **2009,** *48* (11), 4707-4713.

3. Bernini, M. C.; Platero-Prats, A. E.; Snejko, N.; Gutiérrez-Puebla, E.; Labrador, A.; Sáez-Puche, R.; Romero de Paz, J.; Monge, M. A., Tuning the magnetic properties of transition metal MOFs by metal-oxygen condensation control: the relation between synthesis temperature, SBU nuclearity and carboxylate geometry. *CrystEngComm* **2012,** *14* (17), 5493-5504.

4. Platero-Prats, A. E.; de la Peña-O'Shea, V. A.; Proserpio, D. M.; Snejko, N.; Gutiérrez-Puebla, E.; Monge, Á., Insight into the SBU Condensation in Mg Coordination and Supramolecular Frameworks: A Combined Experimental and Theoretical Study. *Journal of the American Chemical Society* **2012,** *134* (10), 4762-4771.

5. Aguirre-Díaz, L. M.; Iglesias, M.; Snejko, N.; Gutiérrez-Puebla, E.; Monge, M. Á., Toward understanding the structure-catalyst activity relationship of new indium MOFs as catalysts for solvent-free ketone cyanosilylation. *RSC Advances* **2015,** *5* (10), 7058-7065.

6. Aguirre-Díaz, L. M.; Gándara, F.; Iglesias, M.; Snejko, N.; Gutiérrez-Puebla, E.; Monge, M. Á., Tunable Catalytic Activity of Solid Solution Metal-Organic Frameworks in One-Pot Multicomponent Reactions. *Journal of the American Chemical Society* **2015,** *137* (19), 6132-6135.

7. Jiang, H.-L.; Xu, Q., Counterion-induced controllable assembly of 2D and 3D metal-organic frameworks: effect of coordination modes of dinuclear Cu(ii) paddle-wheel motifs. *CrystEngComm* **2010,** *12* (11), 3815-3819.

8. Wang, L. J.; Deng, H.; Furukawa, H.; Gándara, F.; Cordova, K. E.; Peri, D.; Yaghi, O. M., Synthesis and Characterization of Metal-Organic Framework-74 Containing 2, 4, 6, 8, and 10 Different Metals. *Inorganic Chemistry* **2014,** *53* (12), 5881-5883.

9. Monge, A.; Snejko, N.; Gutierrez-Puebla, E.; Medina, M.; Cascales, C.; Ruiz-Valero, C.; Iglesias, M.; Gomez-Lor, B., One Teflon ®-like channelled nanoporous polymer with a chiral and new uninodal 4-connected net: sorption and catalytic properties. *Chemical Communications* **2005,** (10), 1291-1293.

10. Bernini, M. C.; Snejko, N.; Gutierrez-Puebla, E.; Brusau, E. V.; Narda, G. E.; Monge, M. Á., Structure-Directing and Template Roles of Aromatic Molecules in the Self-Assembly Formation Process of 3D Holmium-Succinate MOFs. *Inorganic Chemistry* **2011,** *50* (13), 5958-5968.

11. D'Vries, R. F.; de la Peña-O'Shea, V. A.; Snejko, N.; Iglesias, M.; Gutiérrez-Puebla, E.; Monge, M. A., H_3O_2 Bridging Ligand in a Metal-Organic Framework. Insight into the Aqua-Hydroxo↔Hydroxyl Equilibrium: A Combined Experimental and Theoretical Study. *Journal of the American Chemical Society* **2013,** *135* (15), 5782-5792.

CHAPTER 5:

ADDRESSED REALIZATION OF MULTI-CATION COMPLEX ARRANGEMENTS IN METAL-ORGANIC FRAMEWORKS

5.1. Introduction

In chapter 4, we concluded that MOF phases that are formed through a kinetically controlled crystallization allows the incorporation of multiple metal cations, as opposed to thermodynamically controlled MOFs phases. This chapter describes the preparation and the characterization of materials with structures composed of multiple metal cations that are occupying specific crystallographic sites. Nowadays, the preparation of materials with controllable distribution of multiple elements remains a challenge due to the difficulty of simultaneously addressing the incorporation of different elements at desired, precise positions.

The starting point in this chapter is the kinetically favorable phase called ZnPF-1, first reported by our group in 2005.[1] This MOF is prepared with the use of 4,4'-(hexafluoroisopropylidene)bis(benzoic acid) (H_2hfipbb) as organic linker and zinc as metal element. It crystallizes in the hexagonal *P6$_4$22* space group (a = 21.22(1) Å, c = 7.710(5) Å). It possesses a helical, rod-shaped inorganic SBU formed by tetrahedral zinc atoms, and the three dimensional structure exhibits square and hexagonal channels running parallel to the *c* axis (figure 5.1). Despite this organic linker has been extensively employed to prepare different MOFs with various metal elements, thus far this MOF topology has only been reported with the use of zinc.

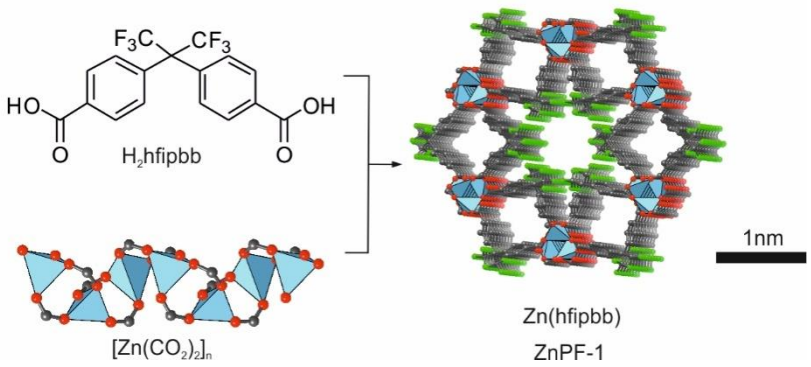

Figure 5. 1. ZnPF-1is formed by the combination of H_2fipbb with helical inorganic SBU where the zinc atoms are tetrahedrally coordinated. O, C and F atoms are depicted as red, gray, and green balls respectively, and pale blue tetrahedral represent zinc cations. Hydrogen atoms are omitted for clarity.

During the completion of the synthetic study described in chapter 4, we found that this phase, in addition to being kinetically favored, is re-dissolved in the reaction media with ethanol and

water as solvents.[2] Therefore, the reaction conditions of temperature and mixture of solvents must be similar to favor the re-dissolution of the ZnPF-1 and facilitate the incorporation of a second metal cation in the structure.

In this chapter, the metal elements used as additional metal cation in ZnPF-1 were cobalt, manganese and calcium. According to the findings described in chapter 4, cobalt was shown to be incorporated in phases with kinetically controlled crystallization, such as TMPF-90, occupying the same crystallographic sites than zinc. We then chose to expand the study regarding the preparation of a kinetically controlled MOF from mixtures containing both zinc and cobalt. In addition, the incorporation of cobalt is expected to result in modified properties, Cobalt has been employed in the chapter 4 and it can be incorporated in the kinetic controlled phases, such as TMPF-90. In TMPF-90 cobalt is occupying the same crystallographic sites than zinc, such as magnetism or redox behavior as heterogeneous catalyst.[5-8]. On the other hand, manganese was chosen because typically it presents an octahedral environment in coordination compounds, so its incorporation in this SBU composed by tetrahedral centers will be very interesting.[9-10] In addition, manganese incorporation can also induce new magnetic and redox properties.[8, 11-12] Finally, the addition of calcium, which possess different nature, coordination environment and radii is investigated

Through the combination of these four different metal elements at judiciously selected molar ratios, twenty-five MOFs of different composition and same topology have been prepared and characterized. The use of different diffraction and microscopic techniques, supported by DFT calculations, has been the key to determine the atomic and mesoscopic arrangements of the metal cations within the SBUs. These findings reported here offer a new general strategy to produce complex materials with required compositions and controllable arrangements of the metal cations for desired applications.

5.2. Synthesis of the Multi-Cation MOFs

All reagents and solvents employed were commercially available and used as received without further purification: 4,4′-hexafluoroisopropylidene-bis-(benzoic acid), H_2hfipbb (98% ABCR GmbH & Co); zinc nitrate, $Zn(NO_3)_2 \cdot 6H_2O$ (≥99% Scharlab); calcium nitrate, $Ca(NO_3)_2 \cdot 4H_2O$ (≥99% Sigma Aldrich); manganese chloride, $MnCl_2 \cdot 4H_2O$ (≥98% Sigma Aldrich) and cobalt nitrate, $Co(NO_3)_2 \cdot 6H_2O$ (≥99% Sigma Aldrich).

General synthetic procedure for all the MOFs involve the dissolution of the selected metal salts and the organic linker in a water:ethanol:nitric acid solvent mixture, followed by heating at 170°C for an overnight period. An illustrative example of the synthesis procedure is given here for the $Zn_{0.59}Co_{0.41}$(hfipbb) compound: H_2hfipbb (78 mg, 0.2 mmol), $Zn(NO_3)_2 \cdot 6H_2O$ (33 mg, 0.11 mmol) and $Co(NO_3)_2 \cdot 6H_2O$ (66 mg, 0.22mmol) were dissolved in 5 mL of distilled water and 5 mL of absolute ethanol and 300 μL of a 1M HNO_3 solution. The mixture was stirred at room temperature for 5 minutes, placed in a Teflon-lined steel autoclave, and heated at 170°C overnight. After cooling to room temperature, blue needle shaped crystals were filtered off, washed with water and acetone, and dry under vacuum (61 mg of solid recovered).

By maintaining a constant metal to linker molar ratio of 1.65 in all the cases, the rest of the materials were similarly prepared using the amounts of metal salt specified in tables 5.1. A and 5.1.B and keeping the same amounts of linker and solvents. In addition, the term “molar code” is coined to indicate the selected molar ratio between metal elements. The formulae were calculated according to ICP analyses results.

Compound*	Molar code				$Zn(NO_3)_2$	$MnCl_2$	$Co(NO_3)_2$	$Ca(NO_3)_2$	Yield
	Zn	Mn	Co	Ca	(mg,mmol)	(mg,mmol)	(mg,mmol)	(mg,mmol)	mg
$Zn_{0.89}Co_{0.11}$(hfipbb)	1	0	1	0	47, 0.16		46, 0.16		55
$Zn_{0.59}Co_{0.41}$(hfipbb)	1	0	2	0	33, 0.11		67, 0.23		61
$Zn_{0.55}Co_{0.45}$(hfipbb)	1	0	4	0	20, 0.07		75, 0.26		36
$Zn_{0.21}Co_{0.79}$(hfipbb)	1	0	10	0	9, 0.03		89, 0.030		19
$Zn_{0.72}Co_{0.17}Ca_{0.11}$(hfipbb)	1	0	1	1	33, 0.11		33, 0.11	30, 0.12	36
$Zn_{0.33}Co_{0.37}Ca_{0.30}$(hfipbb)	1	0	4	4	11, 0.04		40, 0.14	38, 0.16	15
$Zn_{0.37}Co_{0.14}Ca_{0.49}$(hfipbb)	1	0	1	8	11, 0.04		11, 0.04	75, 0.32	19
$Zn_{0.50}Mn_{0.50}$(hfipbb)	1	1	0	0	47, 0.16	34, 0.17			49
$Zn_{0.96}Ca_{0.04}$(hfipbb)	1	0	0	1	47, 0.16			42, 0.18	51
$Zn_{0.94}Ca_{0.06}$(hfipbb)	1	0	0	2	33, 0.11			57, 0.24	46
$Zn_{0.64}Ca_{0.36}$(hfipbb)	1	0	0	4	20, 0.07			64, 0.27	19
$Zn_{0.52}Ca_{0.48}$(hfipbb)	1	0	0	10	9, 0.03			71, 0.30	12
$Zn_{0.44}Mn_{0.44}Co_{0.12}$(hfipbb)	1	1	1	0	33, 0.11	22, 0.11	32, 0.11		41
$Zn_{0.54}Mn_{0.37}Co_{0.09}$(hfipbb)	2	1	1	0	50, 0.17	18, 0.09	26, 0.09		54
$Zn_{0.37}Mn_{0.50}Co_{0.13}$(hfipbb)	1	2	1	0	28, 0.09	36, 0.18	26, 0.09		22
$Zn_{0.32}Mn_{0.39}Co_{0.28}$(hfipbb)	1	1	2	0	28, 0.09	18, 0.09	50, 0.17		19
$Zn_{0.22}Mn_{0.32}Co_{0.46}$(hfipbb)	1	1	8	0	10, 0.03	8, 0.04	80, 0.27		26
$Zn_{0.12}Mn_{0.32}Co_{0.46}$(hfipbb)	1	3	9	0	6, 0.02	12, 0.06	54, 0.18		10
$Zn_{0.23}Mn_{0.44}Co_{0.33}$(hfipbb)	1	4	4	0	11,0.037	29, 0.147	43, 0.147		32
$Zn_{0.17}Mn_{0.41}Co_{0.42}$(hfipbb)	1	4	6	0	9, 0.030	24, 0.120	52, 0.180		30
$Zn_{0.12}Mn_{0.39}Co_{0.49}$(hfipbb)	1	6	12	0	5, 0.017	21, 0.104	61, 0.208		20
$Zn_{0.10}Mn_{0.40}Co_{0.50}$(hfipbb)	1	10	20	0	3, 0.011	21, 0.106	62, 0.212		12
$Zn_{0.17}Mn_{0.45}Co_{0.38}$(hfipbb)	1	12	6	0	5, 0.017	41, 0.208	30, 0.104		10
$Zn_{0.48}Mn_{0.42}Ca_{0.10}$(hfipbb)	1	1	0	1	33, 0.11	22, 0.11		24, 0.10	22
$Zn_{0.52}Mn_{0.30}Ca_{0.18}$(hfipbb)	1	1	0	8	11, 0.03	7, 0.03		64, 0.27	10

*Table 5. 1. A. Chemical formula and corresponding molar codes and amount of metal salts used for MOFs preparation. * Calculated from ICP analysis.*

Compound*	Molar code				$Zn(NO_3)_2$	$MnCl_2$	$Co(NO_3)_2$	$Ca(NO_3)_2$	Yield
	Zn	Mn	Co	Ca	(mg,mmol)	(mg,mmol)	(mg,mmol)	(mg,mmol)	mg
$Zn_{0.42}Mn_{0.42}Co_{0.11}Ca_{0.06}$(hfipbb)	1	1	1	1	25, 0.082	16, 0.082	24, 0.082	19, 0.082	53
$Zn_{0.13}Mn_{0.27}Co_{0.52}Ca_{0.03}$(hfipbb)	1	1	7	1	10, 0.033	7, 0.033	67, 0.231	8, 0.033	31
$Zn_{0.37}Mn_{0.28}Co_{0.13}Ca_{0.22}$(hfipbb)	1	1	1	7	10, 0.033	7, 0.033	10, 0.033	55, 0.231	26
$Zn_{0.16}Mn_{0.47}Co_{0.33}Ca_{0.03}$(hfipbb)	1	4	4	1	10, 0.033	26, 0.132	38, 0.132	8, 0.033	26
$Zn_{0.18}Mn_{0.24}Co_{0.41}Ca_{0.16}$(hfipbb)	1	1	4	4	10, 0.033	7, 0.033	38, 0.132	31, 0.132	23
$Zn_{0.24}Mn_{0.37}Co_{0.31}Ca_{0.08}$(hfipbb)	1	4	4	4	8, 0.025	20, 0.102	30, 0.102	24, 0.102	31
$Zn_{0.32}Mn_{0.40}Co_{0.15}Ca_{0.12}$(hfipbb)	1	4	1	4	10, 0.033	26, 0.132	10, 0.033	31, 0.132	22
$Zn_{0.46}Mn_{0.21}Co_{0.17}Ca_{0.15}$(hfipbb)	2	1	2	2	28, 0.094	9, 0.074	27, 0.094	22, 0.094	38
$Zn_{0.27}Mn_{0.34}Co_{0.26}Ca_{0.12}$(hfipbb)	1	2	2	4	11, 0.073	15, 0.073	21, 0.073	35, 0.147	20
$Zn_{0.21}Mn_{0.27}Co_{0.30}Ca_{0.22}$(hfipbb)	1	4	4	8	6, 0.019	15, 0.0.73	23, 0.078	37, 0.155	17
$Zn_{0.26}Mn_{0.16}Co_{0.37}Ca_{0.21}$(hfipbb)	1	1	4	8	7, 0.024	5, 0.024	27, 0.094	45, 0.189	21
$Mn_{0.41}Co_{0.59}$(hfipbb)	0	1	1	0		33, 0.165	48, 0.105		7
$Mn_{0.23}Co_{0.50}Ca_{0.27}$(hfipbb)	0	1	2	2		13, 0.066	38, 0.132	31, 0.132	11

*Table 5. 1. B. Chemical formula and corresponding molar codes and amount of metal salts used for MOFs preparation. * Calculated from ICP analysis.*

5.3. General Characterization of the Synthesized Compounds

The purity of all the compounds enumerated in tables 5.2.A and 5.2.B was checked by different techniques: elemental analyses, ICP-OES, TGA and X-ray powder diffraction.

The elemental and ICP-OES analyses are shown in tables 5.2.A and 5.2.B. Small differences observed between experimental and calculated %C and %H are attributed to the presence of solvent molecules inside the MOF channels. ICP analyses were carried out with samples prepared according the procedure described in chapter 3.

The presence of solvent molecules is corroborated also by TGA analyses, which show a weight loss around a 5% in the temperature range of 30-100 ºC (figure 5.2 and appendices). The thermal decomposition occurs in all cases around 450 ºC in one unique step.

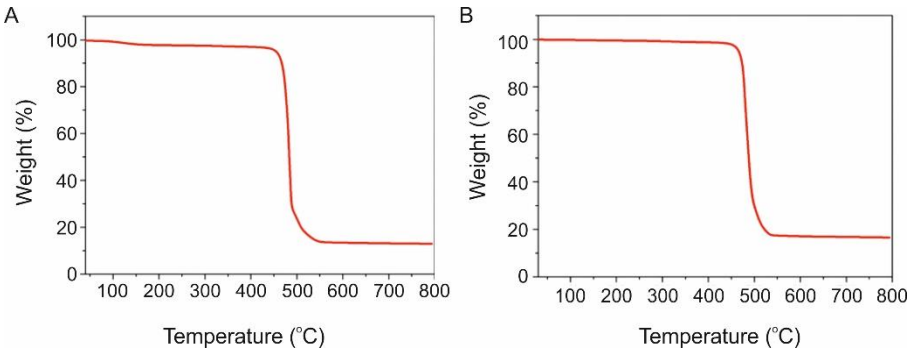

Figure 5. 2. Thermal gravimetric analyses of: A) $Zn_{0.64}Ca_{0.36}$(hfipbb) (Zn:Ca 1:4 molar code) and B) $Zn_{0.72}Co_{0.17}Ca_{0.11}$(hfipbb) (Zn:Co:Ca 1:1:1 molar code).

Compound	CHN Calculated			CHN Experimental			%Weight			
	%C	%H	%N	%C	%H	%N	Zn ppm	Mn ppm	Co ppm	Ca ppm
$Zn_{0.89}Co_{0.11}$(hfipbb)	44.89	1.77	0.00	42.17	2.10	0.17	12.79		1.43	
$Zn_{0.59}Co_{0.41}$(hfipbb)	45.08	1.78	0.00	44.99	1.86	0.27	8.52		5.33	
$Zn_{0.55}Co_{0.45}$(hfipbb)	45.10	1.78	0.00	44.96	2.00	0.17	7.94		5.86	
$Zn_{0.21}Co_{0.79}$(hfipbb)	45.32	1.79	0.00	45.62	1.89	0.12	3.05		10.33	
$Zn_{0.72}Co_{0.17}Ca_{0.11}$(hfipbb)	45.20	1.79	0.00	44.82	1.89	0.11	10.42		2.22	0.98
$Zn_{0.33}Co_{0.37}Ca_{0.30}$(hfipbb)	45.89	1.81	0.00	46.11	1.86	0.25	4.84		4.89	2.70
$Zn_{0.37}Co_{0.14}Ca_{0.49}$(hfipbb)	46.16	1.82	0.00	45.99	1.81	0.17	5.47		1.87	4.44
$Zn_{0.50}Mn_{0.50}$(hfipbb)	45.33	1.79	0.00	45.45	1.84	0.35	7.26	6.10		
$Zn_{0.96}Ca_{0.04}$(hfipbb)	44.92	1.77	0.00	44.82	1.89	0.11	13.81			0.35
$Zn_{0.94}Ca_{0.06}$(hfipbb)	44.97	1.78	0.00	45.84	2.33	0.08	13.53			0.53
$Zn_{0.64}Ca_{0.36}$(hfipbb)	45.73	1.81	0.00	45.92	1.84	0.15	9.37			3.23
$Zn_{0.51}Ca_{0.49}$(hfipbb)	46.15	1.82	0.00	46.00	1.90	0.11	7.67			4.34
$Zn_{0.44}Mn_{0.44}Co_{0.12}$(hfipbb)	45.35	1.79	0.00	46.03	2.35	0.15	6.39	5.37	1.57	
$Zn_{0.54}Mn_{0.37}Co_{0.09}$(hfipbb)	45.15	1.78	0.00	46.08	2.38	0.15	7.83	4.51	1.18	
$Zn_{0.37}Mn_{0.50}Co_{0.13}$(hfipbb)	45.41	1.79	0.00	45.89	2.37	0.11	5.38	6.11	1.70	
$Zn_{0.32}Mn_{0.39}Co_{0.28}$(hfipbb)	45.47	1.80	0.00	45.68	2.34	0.15	4.66	4.77	3.67	
$Zn_{0.22}Mn_{0.32}Co_{0.46}$(hfipbb)	45.44	1.79	0.00	46.17	2.40	0.17	3.20	3.91	6.03	
$Zn_{0.12}Mn_{0.32}Co_{0.46}$(hfipbb)	45.55	1.80	0.00	46.38	2.36	0.12	1.75	5.15	6.05	
$Zn_{0.23}Mn_{0.44}Co_{0.33}$(hfipbb)	45.49	1.80	0.00	46.03	2.36	0.21	3.35	5.38	4.33	
$Zn_{0.17}Mn_{0.41}Co_{0.42}$(hfipbb)	45.51	1.80	0.00	46.27	2.36	0.22	2.48	5.02	5.52	
$Zn_{0.12}Mn_{0.39}Co_{0.49}$(hfipbb)	45.54	1.80	0.00	46.01	2.51	0.25	1.75	4.78	6.44	
$Zn_{0.10}Mn_{0.40}Co_{0.50}$(hfipbb)	45.56	1.80	0.00	38.27	2.14	0.19	1.46	4.90	6.57	
$Zn_{0.17}Mn_{0.45}Co_{0.38}$(hfipbb)	45.53	1.80	0.00	46.26	2.38	0.35	2.48	5.51	4.99	
$Zn_{0.48}Mn_{0.42}Ca_{0.10}$(hfipbb)	45.51	1.80	0.00	46.19	2.36	0.12	6.99	5.14		0.89
$Zn_{0.52}Mn_{0.30}Ca_{0.18}$(hfipbb)	45.58	1.80	0.00	45.60	2.20	0.16	7.59	3.68		1.61

Table 5. 2. A. Tabulated results of CHN analyses and ICP analyses in % for all MOFs.

Compound	CHN Calculated			CHN Experimental			%Weight			
	%C	%H	%N	%C	%H	%N	Zn ppm	Mn ppm	Co ppm	Ca ppm
$Zn_{0.42}Mn_{0.42}Co_{0.11}Ca_{0.06}$(hfipbb)	45.41	1.79	0.00	46.07	2.48	0.03	6.15	5.13	1.44	0.53
$Zn_{0.13}Mn_{0.27}Co_{0.52}Ca_{0.03}$(hfipbb)	45.84	1.81	0.00	46.08	2.39	0.07	1.91	3.33	6.88	0.27
$Zn_{0.37}Mn_{0.28}Co_{0.13}Ca_{0.22}$(hfipbb)	45.52	1.80	0.00	46.02	2.00	0.10	5.83	5.02	1.45	0.71
$Zn_{0.16}Mn_{0.47}Co_{0.33}Ca_{0.03}$(hfipbb)	45.66	1.80	0.00	45.79	2.21	0.14	2.34	5.77	4.35	0.27
$Zn_{0.18}Mn_{0.24}Co_{0.41}Ca_{0.16}$(hfipbb)	45.81	1.81	0.00	46.01	2.04	0.21	2.61	4.51	4.06	2.14
$Zn_{0.24}Mn_{0.37}Co_{0.31}Ca_{0.08}$(hfipbb)	45.60	1.80	0.00	46.09	2.22	0.20	3.50	4.54	4.08	0.72
$Zn_{0.32}Mn_{0.40}Co_{0.15}Ca_{0.12}$(hfipbb)	45.76	1.80	0.00	45.88	2.21	0.22	4.68	4.92	1.98	1.08
$Zn_{0.46}Mn_{0.21}Co_{0.17}Ca_{0.15}$(hfipbb)	45.59	1.80	0.00	46.14	2.32	0.14	6.17	2.58	2.24	1.34
$Zn_{0.27}Mn_{0.34}Co_{0.26}Ca_{0.12}$(hfipbb)	45.71	1.81	0.00	46.09	2.17	0.31	3.95	4.18	3.43	1.08
$Zn_{0.21}Mn_{0.27}Co_{0.30}Ca_{0.22}$(hfipbb)	45.85	1.81	0.00	46.30	2.10	0.22	3.08	3.33	3.97	1.98
$Zn_{0.26}Mn_{0.16}Co_{0.37}Ca_{0.21}$(hfipbb)	45.15	1.78	0.00	45.86	1.91	0.29	3.76	3.28	4.82	1.86
$Mn_{0.41}Co_{0.59}$(hfipbb)	45.63	1.80	0.00	46.96	2.05	0.30		5.03	7.77	
$Mn_{0.23}Co_{0.50}Ca_{0.27}$(hfipbb)	46.08	1.82	0.00	45.95	2.14	0.37		2.85	6.65	2.44

Table 5. 2. B. Tabulated results of CHN analyses and ICP analyses in % for all MOFs.

Experimental PXRD patterns were compared with their corresponding simulated patterns calculated from single crystal X-ray diffraction refinement data to check the phase purity (figures 5.3 and 5.4 and appendices).

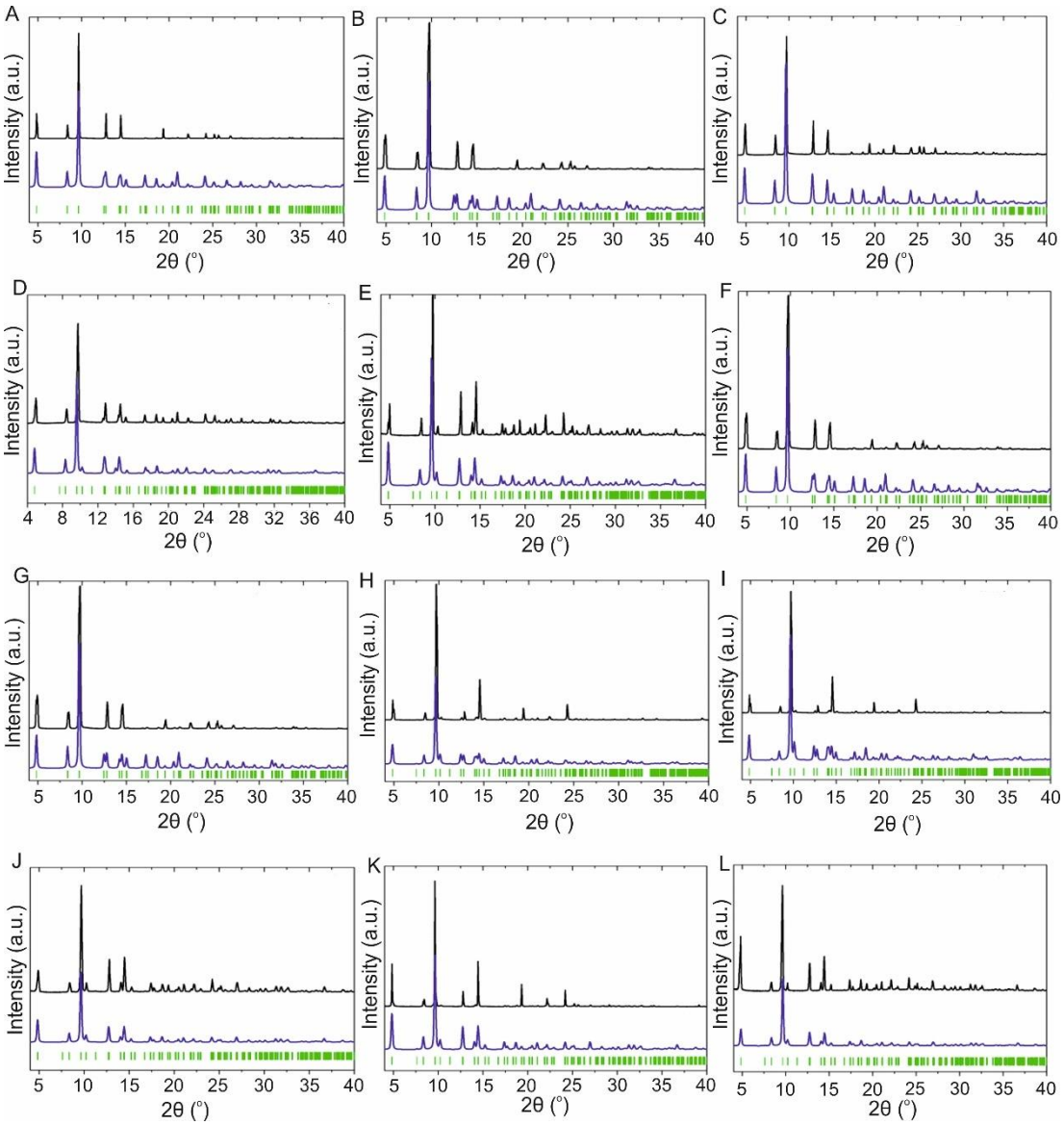

Figure 5. 3. Normalized powder XRD patterns of: A) $Zn_{0.89}Co_{0.11}$(hfipbb) (Zn:Co 1:1 molar code), B) $Zn_{0.59}Co_{0.41}$(hfipbb) (Zn:Co 1:2 molar code), C) $Zn_{0.55}Co_{0.45}$(hfipbb) (Zn:Co 1:4 molar code), D) $Zn_{0.21}Co_{0.79}$(hfipbb) (Zn:Co 1:10 molar code), E) $Zn_{0.50}Mn_{0.50}$(hfipbb) (Zn:Mn 1:1 molar code), F) $Zn_{0.96}Ca_{0.04}$(hfipbb) (Zn:Ca 1:1 molar code), G) $Zn_{0.94}Ca_{0.06}$(hfipbb) (Zn:Ca 1:2 molar code), H) $Zn_{0.64}Ca_{0.36}$(hfipbb) (Zn:Ca 1:4 molar code), I) $Zn_{0.52}Ca_{0.48}$(hfipbb) (Zn:Ca 1:10 molar code), J) $Zn_{0.44}Mn_{0.44}Co_{0.12}$(hfipbb) (Zn:Mn:Co 1:1:1 molar code), K) $Zn_{0.54}Mn_{0.37}Co_{0.09}$(hfipbb) (Zn:Mn:Co 2:1:1 molar code) and L) $Zn_{0.37}Mn_{0.50}Co_{0.13}$(hfipbb) (Zn:Mn:Co 1:2:1 molar code). Experimental (black), simulated from their correspondent single crystal X-ray diffraction data (blue), Bragg positions (green).

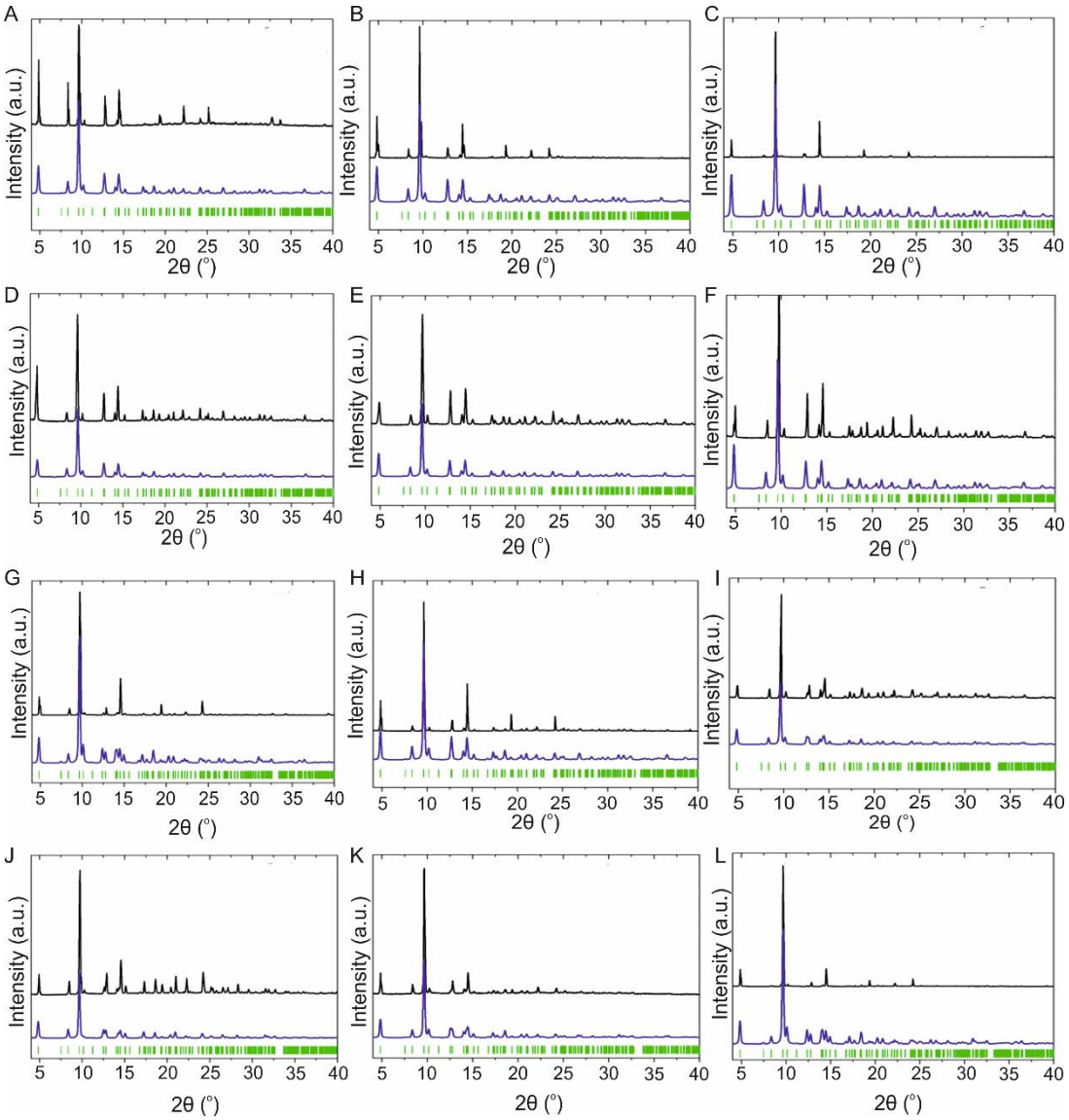

Figure 5. 4. Normalized powder XRD patterns of: A) $Zn_{0.32}Mn_{0.40}Co_{0.28}$(hfipbb) (Zn:Mn:Co 1:1:2 molar code), B) $Zn_{0.22}Mn_{0.32}Co_{0.46}$(hfipbb) (Zn:Mn:Co 1:1:8 molar code), C) $Zn_{0.12}Mn_{0.42}Co_{0.46}$(hfipbb) (Zn:Mn:Co 1:3:9 molar code), D) $Zn_{0.23}Mn_{0.44}Co_{0.33}$(hfipbb) (Zn:Mn:Co 1:4:4 molar code), E) $Zn_{0.17}Mn_{0.41}Co_{0.42}$(hfipbb) (Zn:Mn:Co 1:4:6 molar code), F) $Zn_{0.12}Mn_{0.39}Co_{0.49}$(hfipbb) (Zn:Mn:Co 1:6:12 molar code), G) $Zn_{0.17}Mn_{0.45}Co_{0.38}$(hfipbb) (Zn:Mn:Co 1:12:6 molar code), H) $Zn_{0.48}Mn_{0.42}Ca_{0.10}$(hfipbb) (Zn:Mn:Ca 1:1:1 molar code), I) $Zn_{0.52}Mn_{0.30}Ca_{0.18}$(hfipbb) (Zn:Mn:Ca 1:1:8 molar code), J) $Zn_{0.72}Co_{0.17}Co_{0.11}$(hfipbb) (Zn:Co:Ca 1:1:1 molar code), K) $Zn_{0.37}Co_{0.33}Ca_{0.30}$(hfipbb) (Zn:Co:Ca 1:4:4 molar code) and L) $Zn_{0.37}Co_{0.14}Ca_{0.49}$(hfipbb) (Zn:Mn:Co 2:1:1 molar code). Experimental (black), simulated from their correspondent single crystal X-ray diffraction data (blue), Bragg positions (green).

5.4. Zn:Co System: MOFs From an Adaptable SBU

The addition of cobalt nitrate in the initial mixture results in the formation of needle-like crystals with intense blue color. Initially, Zn:Co molar codes of 1:1, 1:2, 1:4 and 1:10 were selected to prepare the corresponding MOFs of variable composition.

The chemical composition of the bulk samples was determined by ICP and EA. A room temperature X-ray diffraction study of a single crystal prepared from a Zn:Co 1:2 molar code proved that this sample was isostructural to the original ZnPF-1. According to the structural refinement, there is only one crystallographic site corresponding to the metal atoms, which is occupied by both zinc and cobalt. Using SEM-EDS analyses it was observed that the amount of cobalt was larger in external areas of the crystals (figure 5.5). Moreover, the crystals were found to be hollow with a central hole running along the longest crystal axis. This hollow morphology and the concentration gradient were consistent with an Ostwald ripening process.[13] In this process, zinc-rich crystals are initially formed followed by partial re-dissolution of the internal faces and crystal growing of the external faces through the incorporation of cobalt in larger proportion (figure 5.6).

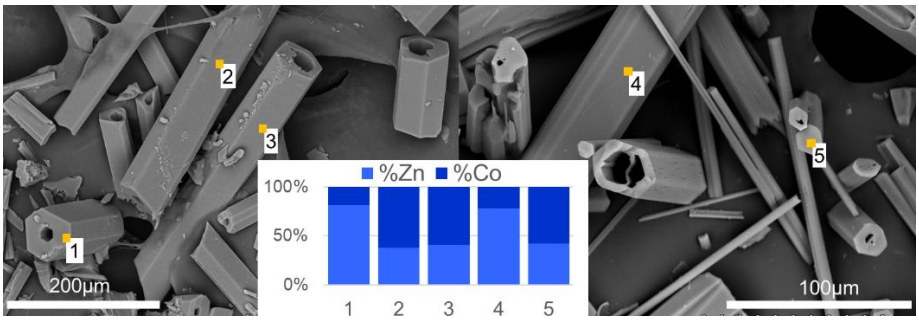

Figure 5. 5. SEM-EDS analyses corresponding to $Zn_{0.59}Co_{0.41}$(hfipbb) crystals (molar code: Zn:Co 1:2). Orange spots indicate the areas where EDS were performed. Plot (middle) shows the metal ratios by EDS analyses, where each column corresponds to the area indicated by a number in the SEM pictures.

These results are similar to the ones obtained for the samples prepared with molar codes Zn:Co 1:1 and 1:4. A kinetic study performed for the MOF prepared from a Zn:Co 1:2 molar code further validated this point as evidenced by the increase in cobalt incorporation with longer heating times up to 20 hours (figures 5.7).

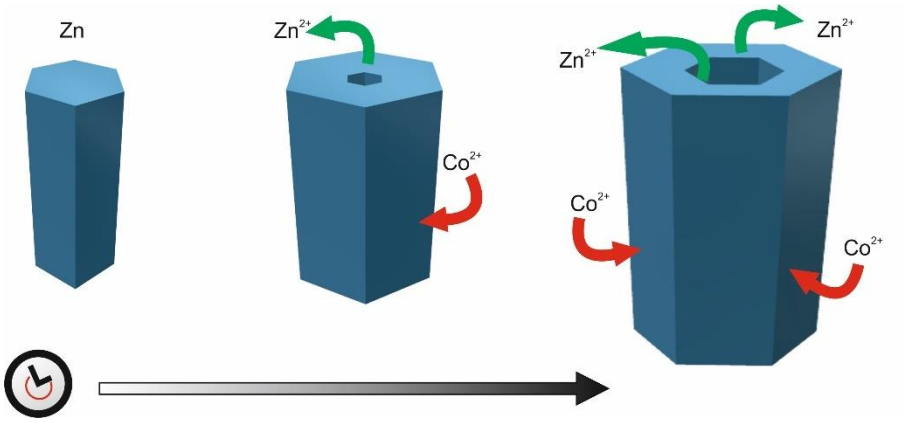

Figure 5. 6. Depiction of Ostwald ripening process over time.

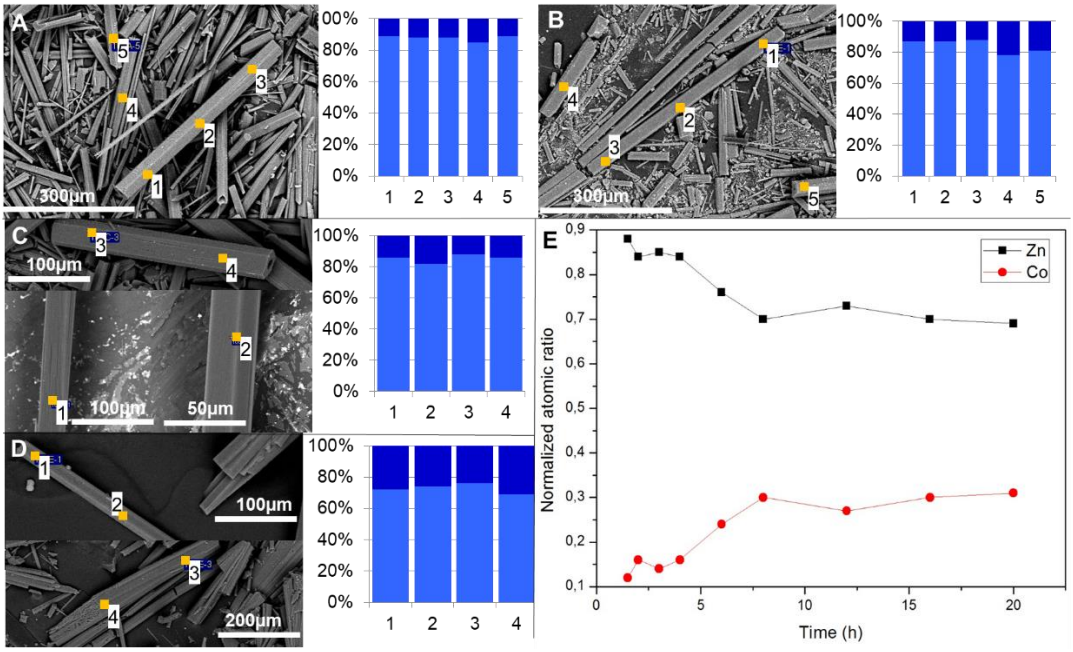

Figure 5. 7. SEM-EDS analyses from MOFs prepared from a Zn:Co 1:2 molar codes with different reaction times: A) 1.5 hours, B) 3 hours, C) 6 hours and D) 12 hours. 20 hours EDS-SEM results are depicted in figure 5.5. Orange spots indicate the areas where EDS were performed. Plot (middle) shows the metal ratios (%Zn in light blue and %Co in dark blue) by EDS analyses, where each column corresponds to the area indicated by a number in the SEM pictures.

A cobalt-rich sample was prepared from a Zn:Co 1:10 initial molar code and the resulting formula was $Zn_{0.21}Co_{0.79}$(hfipbb). SEM-EDS analyses consistently showed that the amount of cobalt is larger in external areas of the crystals. This phenomenon is more pronounced in this

material than in the compounds prepared with Zn:Co 1:1, 1:2 and 1:4, as shown in figure 5.8. Unexpectedly, the X-ray single crystal diffraction study shows a unit cell with a doubled *c* parameter and $P6_522$ space group. This lattice constant change arises from the splitting of the crystallographic metal sites within the SBUs, which are now composed of alternating tetrahedral and octahedral metal sites (figure 5.9). The results of the XRD refinement suggest that the octahedral sites are occupied by cobalt atoms whereas the tetrahedral ones are occupied by both zinc and cobalt. Despite the change in the coordination environment, the transformed SBU remains unaltered in its points of extension, which in turn define the MOF topology.[14]

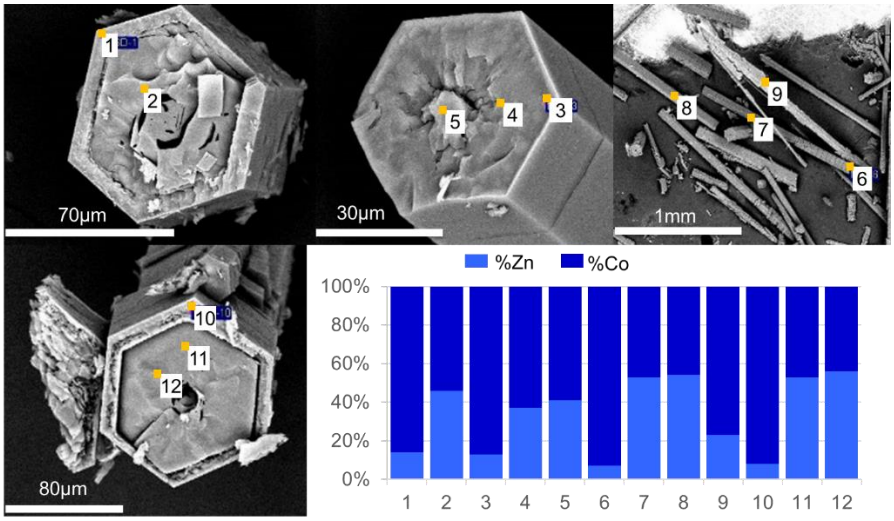

Figure 5. 8. SEM-EDS analyses corresponding to $Zn_{0.21}Co_{0.79}$(hfipbb) crystals (molar code: Zn:Co 1:10). Orange spots indicate the areas where EDS were performed. Plot (middle) shows the metal ratios by EDS analyses, where each column corresponds to the area indicated by a number in the SEM pictures.

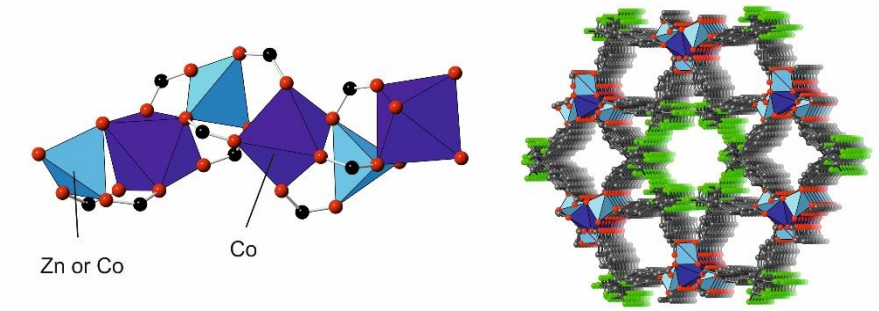

Figure 5. 9. Depiction of the inorganic SBU of $Zn_{0.21}Co_{0.79}$(hfipbb) (left) and its three-dimensional structure. O, C and F atoms are depicted as red, gray, and green balls respectively. Tetrahedral atoms are depicted in pale blue and octahedral ones in dark blue.

To obtain further insight into this phase transformation, a low-temperature single crystal diffraction study was performed for the sample prepared with a Zn:Co 1:2 molar code. As described above the room temperature data showed the presence of just one tetrahedral metal site with mixed Zn/Co occupancy.

We then collected XRD data at 200, 150, 100 and 50 K. No changes were observed for the 200 K measurement as compared to room temperature. A phase transition was first observed at 150 K with the corresponding doubling of the *c* lattice parameter. Consequently, two crystallographic metal positions are now present in the SBU, with a distorted tetrahedral coordination environment denoted as Td1 and Td2 in figure 5.10. Analysis of the difference Fourier maps showed a large residual electron density near the metal atoms which we assign as additional metal sites with partial occupancy (Td1b and Td2b) arising from the ongoing atomic rearrangement. However, the presence of residual electron density indicates that the transformation is not complete yet. This is only achieved at 50 K where the crystal structure is equivalent to the one determined for the Zn:Co 1:10 sample with both an octahedral and a tetrahedral site. The results of this study suggest that the presence of cobalt in the structure has a stabilizing effect on the octahedral site. On the contrary, ZnPF-1 does not undergo any phase transformation, as no changes in the unit cell were observed for a crystal collected at 50 K. Since zinc and cobalt have similar atomic numbers, it is no possible to unambiguously determine the occupancy of the metal sited with just XRD. Therefore, a neutron diffraction experiment was performed for this purpose.

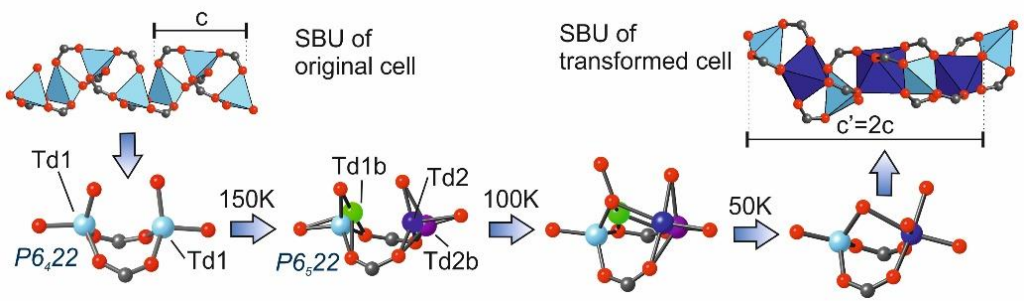

Figure 5. 10. The inorganic SBU might adapt to include octahedrally coordinated cation, which results in a unit cell transformation where the c parameter is doubled.

5.4.1. Unveiling the atomic arrangement

To uncover the atomic arrangement of the metal cations within the MOF crystals a neutron powder diffraction (NPD) study at variable temperatures was completed for zinc and cobalt-rich samples. In particular, MOFs prepared from Zn:Co 1:2 and Zn:Co 1:10 molar codes were selected. NPD is a particularly suitable technique because of the different scattering length of these elements, in contrast to XRD, as discussed in chapter 3.

Themodiffraction experiments evidenced a structural phase transition at 140 and 80 K for the Zn:Co 1:2 and Zn:Co 1:10 samples, respectively (figure 5.11).

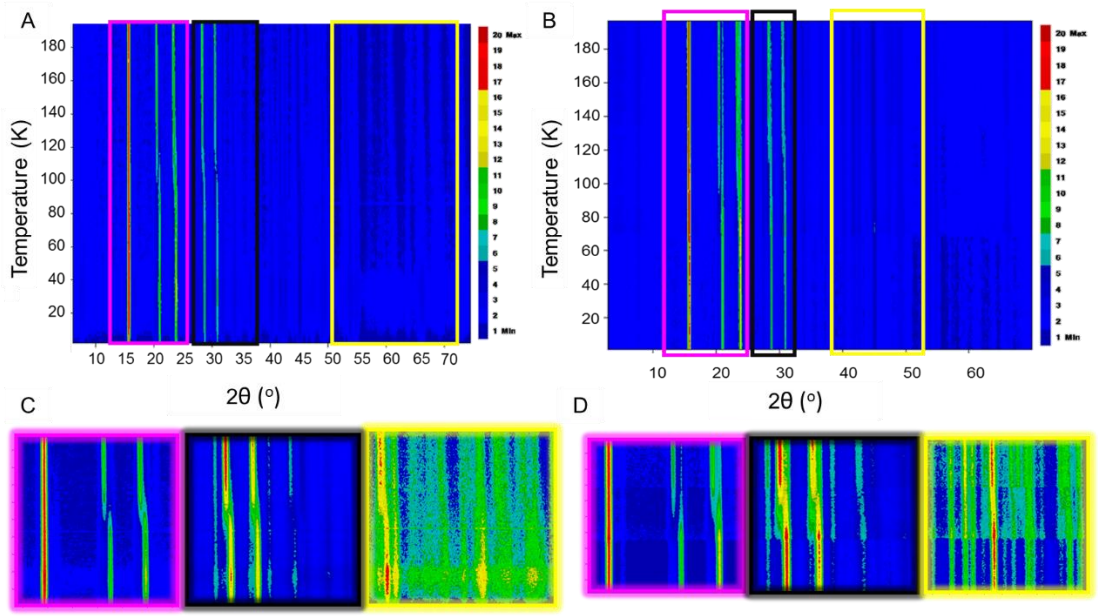

Figure 5. 11. Contour 2D neutron thermodiffraction patterns: $Zn_{0.59}Co_{0.41}$(hfipbb) (molar code: Zn:Co 1:2) and (A), blow up of marked areas (B) and $Zn_{0.21}Co_{0.79}$(hfipbb) (molar code: Zn:Co 1:10) (C), blow up of marked areas from $Zn_{0.59}Co_{0.41}$(hfipbb) compound and (D) blow up of marked areas from $Zn_{0.21}Co_{0.79}$(hfipbb).

The Rietveld refinement for the room temperature NPD pattern of the Zn:Co 1:2 sample indicated the unique presence of the original phase (ZnPF-1 phase) with only one tetrahedral metal site in the SBU, which was refined as being occupied by Zn or Co with ratio coincident with the one determined by ICP analysis (figure 5.12.A). For the low-temperature pattern (50 K) a satisfactory refinement could not be achieved by considering just the transformed crystal cell. A careful analysis showed the presence of a remaining amount of an untransformed

crystal phase. The presence of ZnPF-1 crystals has been ruled out because the SEM and EDS analyses prove the presence of cobalt in all crystals, as a result of the compositional variations. A multiphase Rietveld refinement was thus performed and the percentage of each phase was estimated on the basis of the ratio of the integrated intensities. The best refinement results were obtained for a combination of the original and transformed phases at ratios of 15 and 85%, respectively (figure 5.12.B). The metal sites in the original phase (exclusively tetrahedral) were refined as zinc atoms. whereas for the transformed phase the tetrahedral site was refined as fully occupied by zinc, and the octahedral site as fully occupied by cobalt.

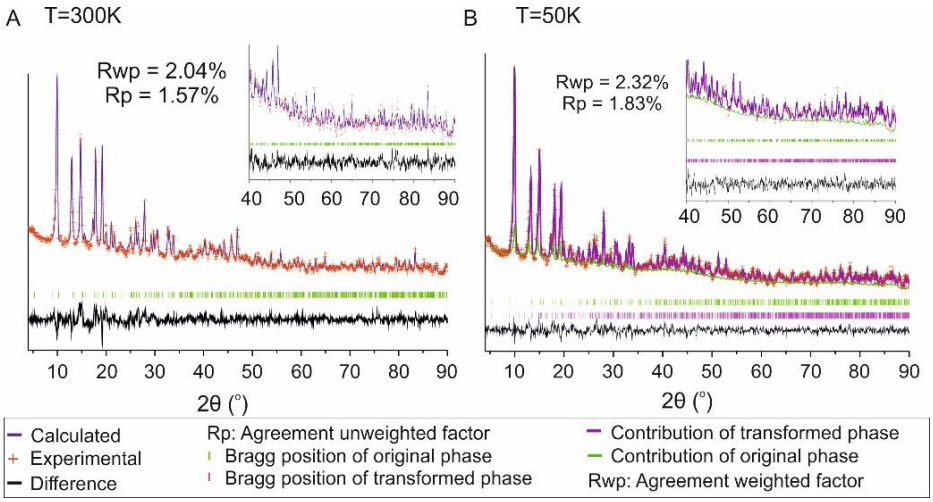

Figure 5. 12. NPD Rietveld refinements of $Zn_{0.59}Co_{0.41}$(hfipbb) (molar code Zn:Co 1:2). A) The refinements indicate the presence of only the original cell at 300 K and B) both original (15%) and transformed (85%) cells at 50 K. In both cases, the composition of the metal sites was refined. For multiphase refinements, the percentage of each unit cell was determined by the ratio of the integrated intensities.

These results, along with the presence of holes and compositional gradient in the crystals, indicate that this MOF is composed of an inner core with SBUs made of zinc atoms and an outer shell with SBUs made of alternating zinc and cobalt atoms. At room temperature, both atoms are in a tetrahedral environment, whereas by lowering the temperature only the cobalt atoms become octahedral, resulting in the unit cell change.

In the case of the sample prepared from a Zn:Co 1:10 molar code, the room temperature NPD pattern already indicates the presence of both phases. These two unit cells at room temperature could not be detected by single crystal X-ray analysis because of the overlapping of reflection

positions (the *hkl* reflections in the original phase appear at virtually the same position of the corresponding *hkl/2* reflections of the transformed phase). Through a multiphase Rietveld refinement, the percentage of both phases at room temperature was estimated to be 67 and 33% for the original and transformed one, respectively (figure 5.13.A). The portion of the crystal corresponding to the transformed phase was refined to be composed exclusively of cobalt having both tetrahedral and octahedral environments. The portion of the crystal corresponding to the original phase was refined to be composed of both zinc (30%) and cobalt (70%) (figure 5.13.B). By lowering the temperature (10 K) most of this portion of the crystal is also transformed. However, the 10 K NPD pattern shows the presence of small shoulders in the (102) and (2-12) diffraction peaks which indicate that there is also a residual portion of the crystal that retains the original phase.

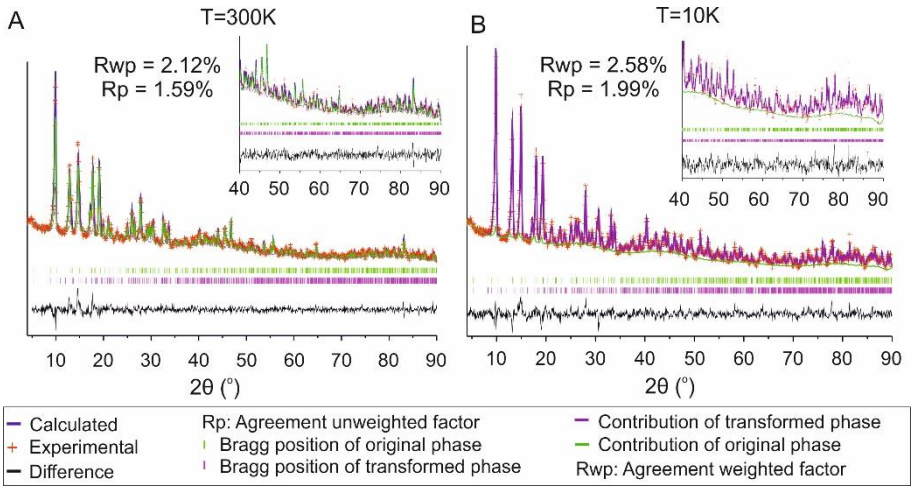

Figure 5. 13. NPD Rietveld refinements of $Zn_{0.21}Co_{0.79}$(hfipbb) (molar code Zn:Co 1:10). A) At 300 K both phases appear: original (66%) and transformed (33%). B) At 10 K the transformation id almost complete (95%). In both cases, the composition of the metal sites was refined. For the multiphase refinements, the percentage of each unit cell was determined by the ratio of the integrated intensities.

Consequently, the MOF $Zn_{0.59}Co_{0.41}$(hfipbb) has two compositional domains: a core composed of zinc tetrahedra (near to 15% according to NPD Rietveld refinement) and an external shell (around 85%) composed of alternated zinc and cobalt tetrahedral. At low temperature Co atoms become octahedral (figure 5.14). Similar results are found for the $Zn_{0.89}Co_{0.11}$(hfipbb) and $Zn_{0.55}Co_{0.45}$(hfipbb) compounds, prepared from initial molar codes Zn:Co 1:1 and 1:4, respectively.

In addition, $Zn_{0.21}Co_{0.79}$(hfipbb) has three compositional domains: i) a small core (no more than 5% according to NPD Rietveld refinement) exclusively made of zinc, ii) a shell where the SBUs are composed of zinc and cobalt cations at a Zn:Co 3:7 ratio, all of them being tetrahedral at room temperature whereas at low temperature part of the cobalt cations become octahedral, iii) an outer shell (around 33%), where the SBUs are exclusively composed of cobalt cations with alternating tetrahedral and octahedral coordination environments (figure 5.14).

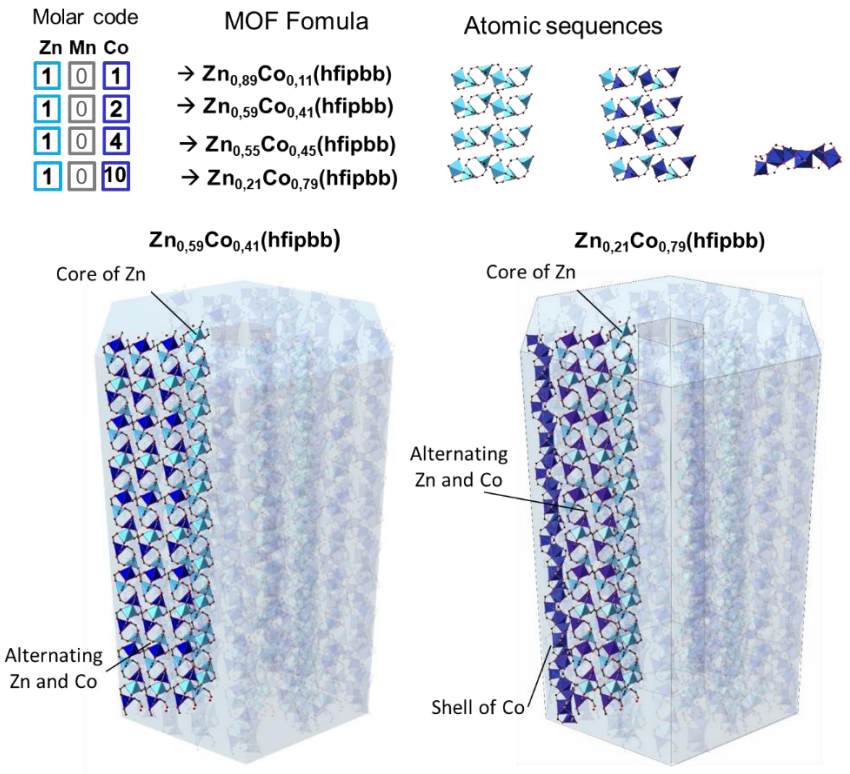

Figure 5. 14. Scheme of different molar codes, formulae and atomic sequences in the Zn:Co system (up). Model of real arrangement of SBUs in the crystal of $Zn_{0.59}Co_{0.41}$(hfipbb) (left) and $Zn_{0.21}Co_{0.79}$(hfipbb) (right).

5.5. Expanding the Use of Molar Codes to Produce MOFs with Controllable Metal Arrangements

The selected inorganic SBU has shown adaptability and dynamism through the possibility of including multiple metal elements with variable coordination environments, such as cobalt, while maintaining the overall MOF topology and connectivity, which is seemingly directed by the use of zinc. By selecting the appropriate molar code, it is possible to control the introduced amount of a second metal cation, as well as its arrangement and coordination environment. On the other hand, if an element with clear propensity for an octahedral coordination environment is chosen, then this should preferentially occupy certain sites in the inorganic SBUs.

5.5.1. Zn:Mn system

A MOF with a $Zn_{0.5}Mn_{0.5}$(hfipbb) composition was prepared by starting from a Zn:Mn 1:1 molar code. The single crystal XRD study shows lattice parameters of a = 21.2897(5) Å and c = 15.1282(5) Å and $P6_522$ space group. Its SBUs are formed by alternating tetrahedral zinc and octahedral manganese metal positions (figure 5.15.A-B). Crystals of this MOF are hexagonal prisms, which are not hollow. In these crystals, EDS analyses reveal that there are no compositional gradients along the crystals (figure 5.16). NPD Rietveld refinement proves that there is only one type of unit cell present at room temperature (figure 5.15.C).

5.5.2. Zn:Mn:Co system

Moreover, the introduction of manganese into the molar code allows for the homogeneous distribution of cobalt. Thus, in contrast to the Zn:Co systems, ternary MOFs with molar codes including Zn:Mn:Co do not exhibit compositional gradients and all three elements are equally distributed in all areas of the crystals, as shown by EDS analysis (figure 5.17). The room temperature single crystal XRD studies demonstrate that these MOFs have unit cells with double c parameter and the presence of both octahedral and tetrahedral metal sites in the SBUs. Zinc and manganese are exclusively occupying tetrahedral and octahedral crystallographic sites, respectively. Conversely, cobalt can occupy both sites, as deduced by the chemical composition of the resulting MOFs. For example, a MOF obtained from a Zn:Mn:Co 1:2:1 molar code has a formula $Zn_{0.37}Mn_{0.50}Co_{0.13}$(hfipbb), which implies that one out of five

tetrahedral sites in the SBUs is occupied by cobalt, resulting in an atomic sequence as shown in Scheme 5.1.

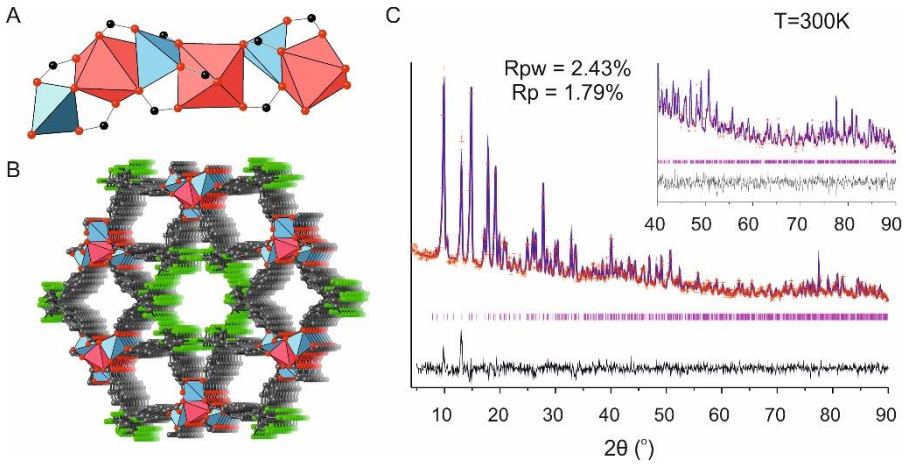

Figure 5. 15. A) Depiction of the inorganic SBU of $Zn_{0.50}Mn_{0.50}$(hfipbb); B) its three-dimensional structure, O, C and F atoms are depicted as red, gray, and green balls respectively. Tetrahedral atoms (Zn) are depicted in pale blue and octahedral ones in pink (Mn). Hydrogen atoms are omitted for clarity; C) NPD Rietveld at 300 K, showing only presence of the transformed phase. The composition of the metal sites was refined.

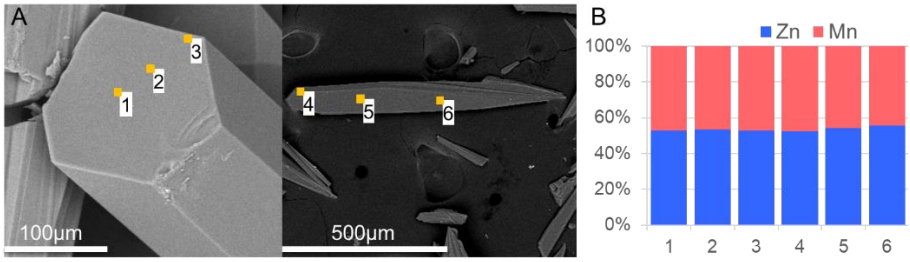

Figure 5. 16. A) SEM-EDS analyses corresponding to $Zn_{0.50}Mn_{0.50}$(hfipbb) crystals (molar code: Zn:Mn 1:1). Orange spots indicate the areas where EDS were performed; B) Plot shows the metal ratios by EDS analyses, where each column corresponds to the area indicated by a number in the SEM pictures.

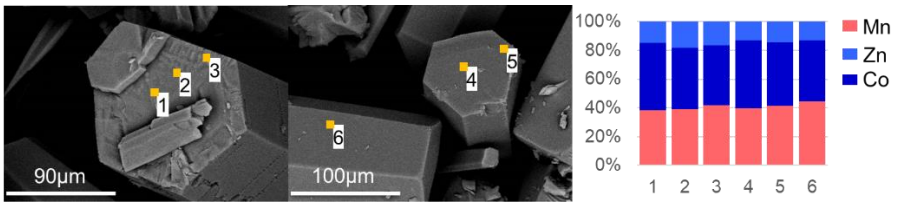

Figure 5. 17. SEM-EDS analyses corresponding to $Zn_{0.12}Mn_{0.42}Co_{0.46}$ (hfipbb) crystals (molar code: Zn:Mn:Co 1:3:9). Orange spots indicate the areas where EDS were performed, plot (left) shows the metal ratios by EDS analyses, where each column corresponds to the area indicated by a number in the SEM pictures.

Correspondingly, a MOF obtained from a Zn:Mn:Co 2:1:1 molar code and formula $Zn_{0.54}Mn_{0.37}Co_{0.09}$(hfipbb) expresses an SBU with an atomic sequence as depicted in scheme 5.1, where one out of five octahedral sites is occupied by cobalt. In both cases, other possible combinations involving the coexistence of several compositional domains are ruled out by the compositional homogeneity demonstrated by the EDS analysis. Single crystal XRD analyses further support the location of the cobalt atoms at the proposed sites.

On the other hand, for MOFs prepared from molar codes which contain the same zinc and manganese number, cobalt is directed to be occupying both the octahedral and tetrahedral sites. In samples prepared from Zn:Mn:Co 1:1:1. 1:1:2 and 1:1:8 molar codes and formulae $Zn_{0.44}Mn_{0.44}Co_{0.12}$(hfipbb). $Zn_{0.32}Mn_{0.39}Co_{0.28}$(hfipbb) and $Zn_{0.22}Mn_{0.32}Co_{0.46}$(hfipbb), the cobalt atoms are inevitably occupying both tetrahedral and octahedral sites. In these cases, as shown in the scheme, there are several possible atomic sequences that fulfill the coordination environment requirement for zinc and manganese and agree with the determined composition (scheme 5.1). In all cases, neutron powder thermodiffraction experiments indicate that only one crystalline phase with double *c* parameter is formed (figure 5.18 and appendices). In this complex system, Co is incorporated in a lower amount than manganese. Thus, based on the previous compositions, with the aim of introducing a higher amount of cobalt and manganese into the system, new Zn:Mn:Co MOFs with different molar codes were prepared: Zn:Mn:Co 1:3:9, 1:4:4, 1:4:6, 1:6:12, 1:10:20 and 1:12:6 with formulae $Zn_{0.12}Mn_{0.42}Co_{0.46}$(hfipbb), $Zn_{0.23}Mn_{0.44}Co_{0.33}$(hfipbb), $Zn_{0.17}Mn_{0.41}Co_{0.42}$(hfipbb), $Zn_{0.12}Mn_{0.39}Co_{0.49}$(hfipbb), $Zn_{0.10}Mn_{0.40}Co_{0.50}$(hfipbb) and $Zn_{0.17}Mn_{0.45}Co_{0.38}$(hfipbb), respectively. The maximum amount of Co is incorporated in the MOF prepared with the molar code 1:10:20. Attempts to incorporate larger amounts of Co resulted in the formation of cobalt oxide.

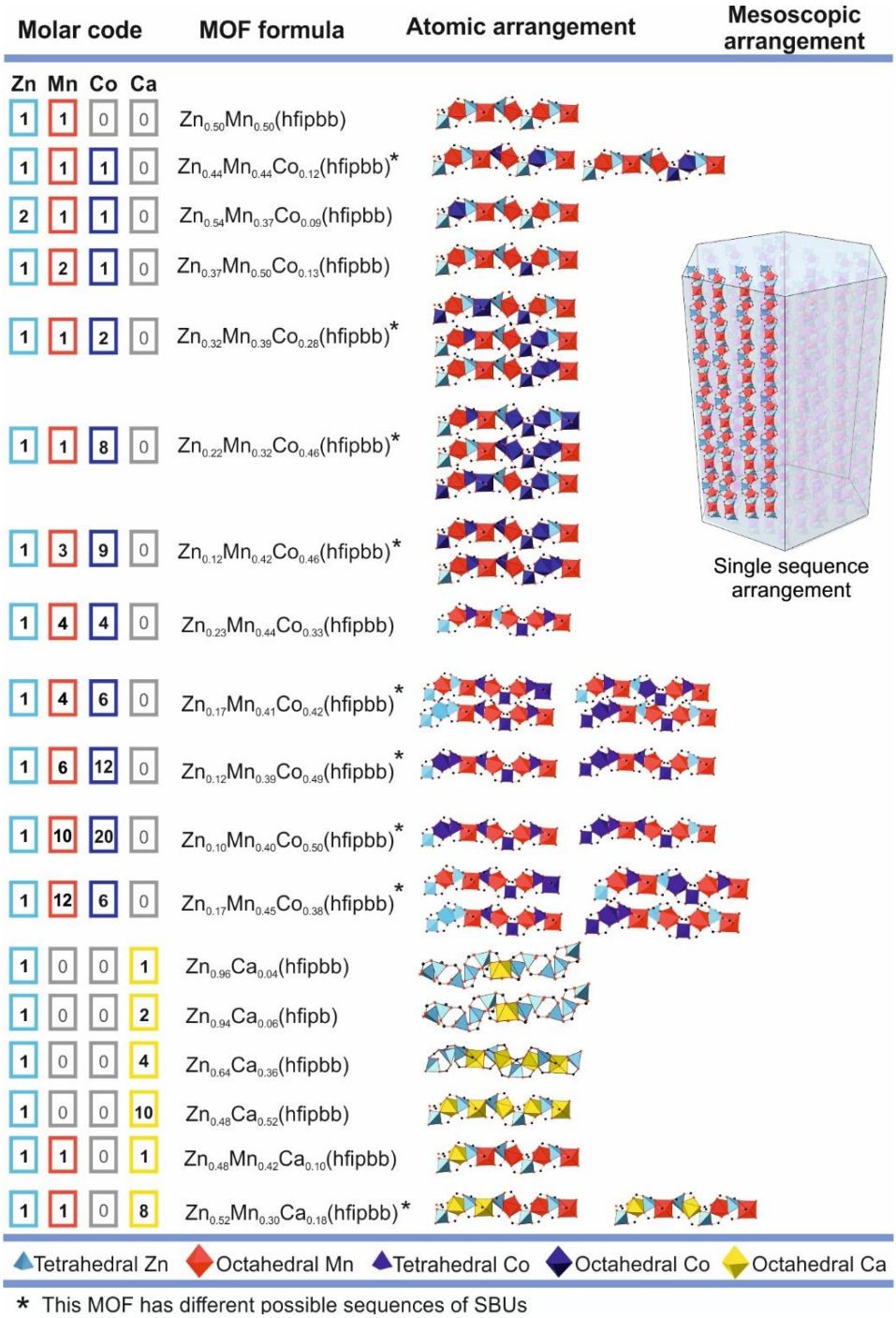

Scheme 5. 1. Selection of appropriate molar codes express the formation of different kinds of atomically sequenced inorganic SBUs.

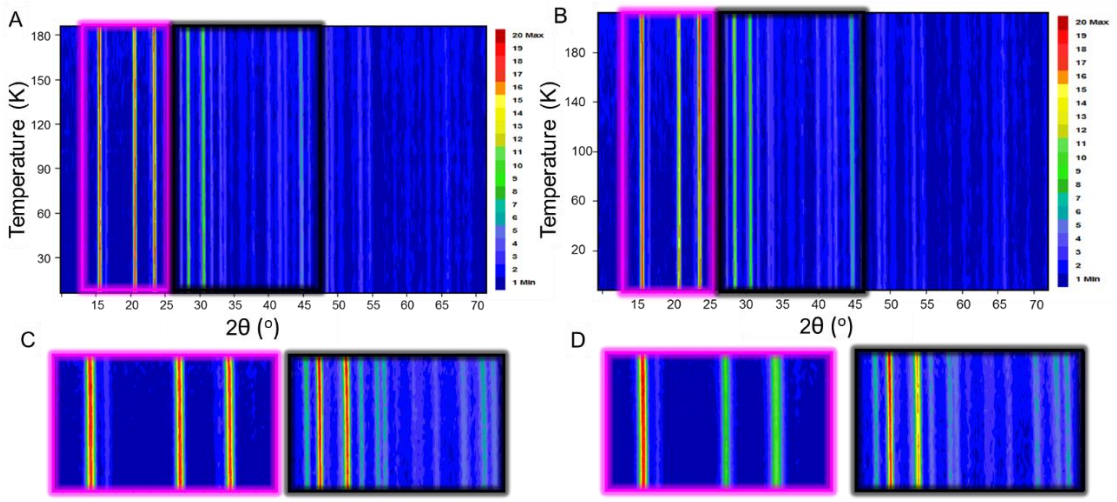

Figure 5. 18. Contour 2D neutron thermodiffraction patterns: $Zn_{0.37}Mn_{0.50}Co_{0.13}$(hfipbb) (molar code: Zn:Mn:Co 1:2:1) and (A), blow up of marked areas (B) and $Zn_{0.32}Mn_{0.39}Co_{0.28}$(hfipbb) (molar code: Zn:Mn:Co 1:1:2) (C), blow up of marked areas from $Zn_{0.37}Mn_{0.50}Co_{0.13}$(hfipbb) compound and (D) blow up of marked areas from $Zn_{0.32}Mn_{0.39}Co_{0.28}$(hfipbb).

Nevertheless, definition of appropriate molar codes allows different degrees of compositional and structural complexities, which are addressable by the selected combination of elements, each one of them with a particular role. Thus, zinc is considered as the structure-directing element, which is necessary to obtain the desired MOF SBU and topology. On the other hand, MOFs prepared from molar codes including manganese demonstrate a homogeneous compositional arrangement, providing atomic control on the SBU sequences. Finally, mesoscopic compositional arrangements might appear through the use of cobalt.

This complexity control is achievable even with the incorporation of other metal elements. Thus, it is also possible to include non-transition metal elements in the molar codes to incorporate them in MOFs with desired complexity.

5.5.3. Zn:Ca system

As proof of concept, we have included calcium into a MOF structure that is not obtainable with the use of only this element. MOFs have thus been prepared with the use of Zn:Ca 1:1 and 1:2 molar codes. These MOFs only contain small amounts of calcium in the structure, their formulae being $Zn_{0.96}Ca_{0.04}$(hfipbb) and $Zn_{0.94}Ca_{0.06}$(hfipbb), and homogeneous

distribution of calcium along the crystals is determined by the EDS analyses. Larger amounts of calcium can be incorporated by using molar codes with larger calcium numbers. Thus, the use of a Zn:Ca 1:4 molar code results in a MOF with the formula $Zn_{0.64}Ca_{0.36}$(hfipbb). Room temperature single crystal XRD shows a double cell with lattice parameters *a* = 21.2239(8) Å and *c* = 15.5784(6) Å and *P6₁22* space group, with two metal sites in the SBUs. One is exclusively occupied by tetrahedral zinc atoms. and the other one is occupied by calcium (72%) or zinc (28%). In this second site, the metal coordination environment is octahedral when is occupied by calcium and tetrahedral when is located the zinc (figure 5.19.A). Thus, the SBUs are composed by alternating zinc and calcium atoms, with 28% of calcium being substituted by zinc, as shown in Scheme 5.1. No compositional gradients are observed in the EDS analysis (figure 5.19.B), which indicates a regular distribution of zinc domains within a zinc-calcium SBU.

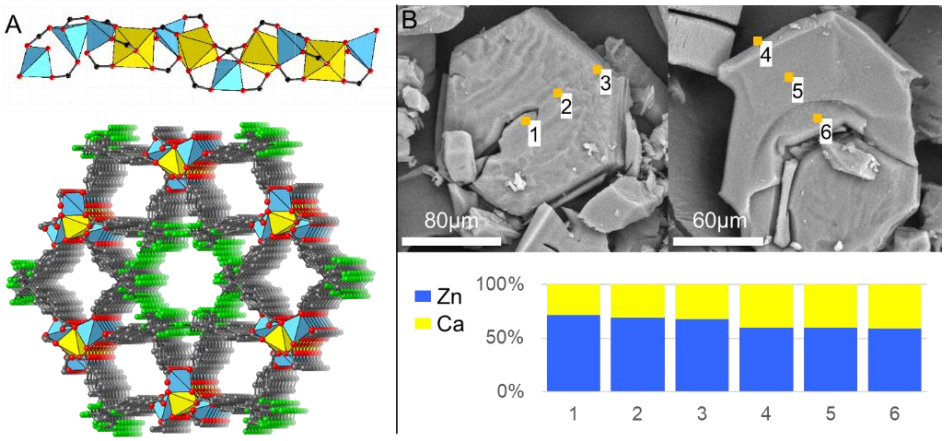

Figure 5. 19. A) Depiction of the inorganic SBU of $Zn_{0.64}Ca_{0.36}$(hfipbb) (up) its three-dimensional structure, O, C and F atoms are depicted as red, gray, and green balls respectively (down). Tetrahedral are depicted in pale blue [15] and octahedral in yellow (Ca). Hydrogen atoms are omitted for clarity; B) SEM-EDS analyses corresponding to $Zn_{0.64}Ca_{0.36}$ (hfipbb) crystals (molar code: Zn:Ca 1:4). Orange spots indicate the areas where EDS were performed, plot (down) shows the metal ratios by EDS analyses, where each column corresponds to the area indicated by a number in the SEM pictures.

The stoichiometric zinc-calcium SBU can be expressed by using a Zn:Ca 1:10 molar code. The corresponding MOF has $Zn_{0.48}Ca_{0.52}$(hfipbb) formula, and EDS indicates compositional homogeneity. Single crystal XRD shows a double cell with an inorganic SBU composed by alternating zinc and calcium in a coordination environment tetrahedral and octahedral,

respectively (appendices). In $Zn_{0.36}Ca_{0.64}$(hfipbb) and $Zn_{0.48}Ca_{0.52}$(hfipbb) compounds, prepared from Zn:Ca 1:4 and 1:10, respectively, thermodiffraction neutron powder diffraction patterns present only one crystalline phase with double *c* parameter (figure 5.20).

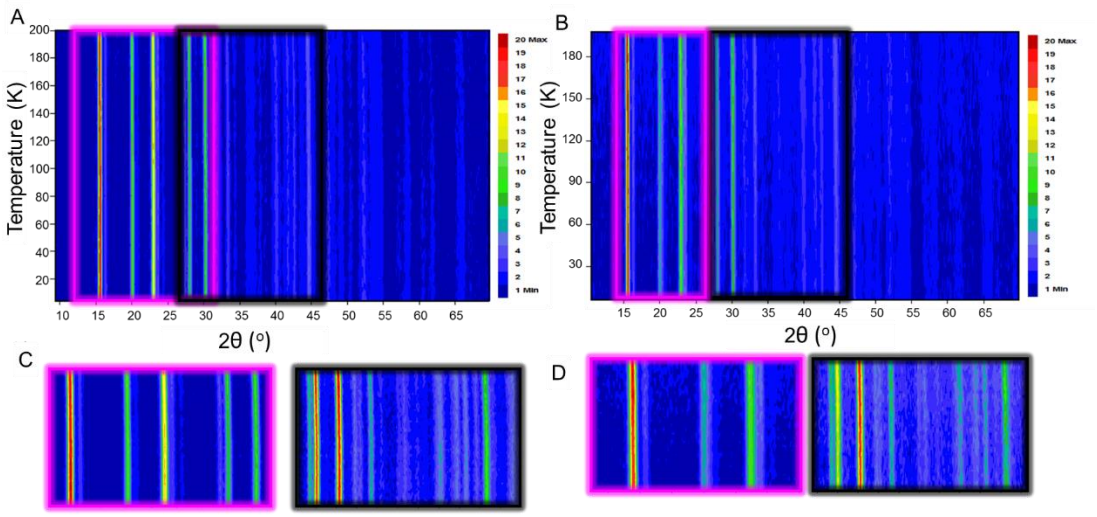

Figure 5. 20. Contour 2D neutron thermodiffraction patterns: $Zn_{0.64}Ca_{0.36}$(hfipbb) (molar code: Zn:Ca 1:4) and (A), blow up of marked areas (B) and $Zn_{0.52}Ca_{0.48}$(hfipbb) (molar code: Zn:Ca 1:10) (C), blow up of marked areas from $Zn_{0.52}Ca_{0.48}$(hfipbb) compound and (D) blow up of marked areas from $Zn_{0.52}Ca_{0.48}$(hfipbb).

5.5.4. Zn:Mn:Ca systems

Molar codes combining zinc, calcium and manganese express SBUs with additional atomic sequences, as proposed in Scheme 5.1, Zn:Mn:Ca 1:1:1 and 1:1:8 molar codes result in MOFs with $Zn_{0.48}Mn_{0.42}Ca_{0.10}$(hfipbb) and $Zn_{0.52}Mn_{0.30}Ca_{0.18}$(hfipbb) formulae, respectively. Single crystal XRD experiments evidence the formation of SBUs with tetrahedral zinc atoms and octahedral calcium and manganese atoms (manganese and calcium are located in the same crystallographic site) (figure 5.21.A). EDS analysis demonstrates homogeneous distribution of the three metal elements along the crystals (figure 5.21.B). In addition, thermodiffraction neutron powder diffraction patterns show that only one crystalline phase with double *c* parameter is formed (appendices).

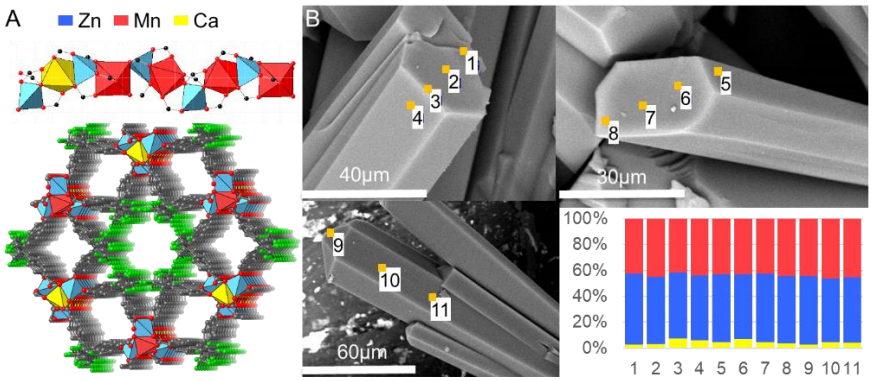

Figure 5. 21. A) Depiction of the inorganic SBU of $Zn_{0.48}Mn_{0.42}Ca_{0.10}$(hfipbb) (molar code: Zn:Mn:Ca 1:1:1) (up) and its three-dimensional structure is depicted (down). Tetrahedral are depicted in pale blue [15], octahedral in pink or yellow (Mn or Ca, respectively); B) SEM-EDS analyses: orange spots indicate the areas where EDS were performed, plot (down) shows the metal ratios by EDS analyses, where each column corresponds to the area indicated by a number in the SEM pictures.

5.5.5. Zn:Co:Ca systems

Mesoscopic control in the incorporation of calcium at preferential crystal faces is possible too by combining this element with cobalt. Thus, the MOF prepared from a Zn:Co:Ca 1:1:1 molar code and formula $Zn_{0.72}Co_{0.17}Ca_{0.11}$(hfipbb) displays a clear compositional gradient, where calcium is preferentially located at the external faces, according to the EDS analyses (figure 5.22). The SEM images show crystals with well-defined core and external shells. The core is mainly composed by zinc and a small amount of cobalt (*ca*. 10%. as determined by EDS), whereas the external shell contains all three elements.

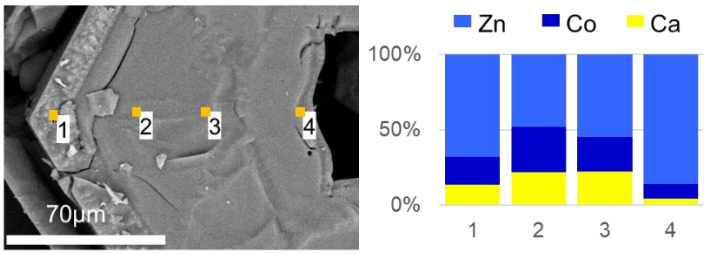

Figure 5. 22. SEM-EDS analyses corresponding to $Zn_{0.72}Co_{0.17}Ca_{0.11}$(hfipbb) crystals (molar code: Zn:Co:Ca 1:1:1). Orange spots indicate the areas where EDS were performed, plot (left) shows the metal ratios by EDS analyses, where each column corresponds to the area indicated by a number in the SEM pictures.

Finally, the use of Zn:Co:Ca 1:4:4 and 1:1:8 molar codes result in MOFs with $Zn_{0.33}Co_{0.37}Ca_{0.30}$(hfipbb) and $Zn_{0.37}Co_{0.14}Ca_{0.49}$(hfipbb) formulae. These MOFs show

mesoscopic compositional gradients of zinc and cobalt, whereas the amount of calcium is homogeneously distributed according to EDS analysis. Single crystal XRD experiments show that, as expected, calcium is occupying the octahedral sites, while zinc is located in tetrahedral sites and cobalt might be at both tetrahedral and octahedral ones (scheme 5.2). NPD only shows a unique transformed phase (figure 5.23 and appendices).

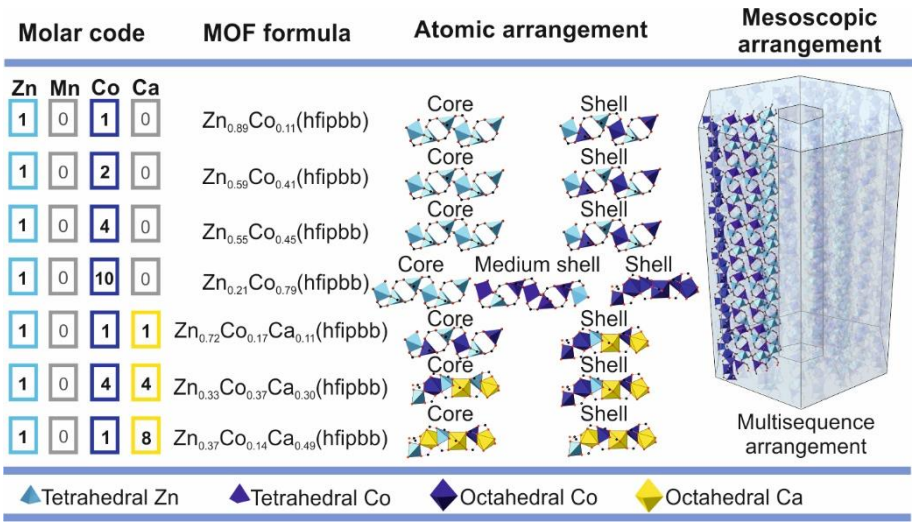

Scheme 5. 2. Selection of appropriate molar codes express the formation of different kinds of atomically sequenced inorganic SBUs. Corresponding MOF crystals might include multiple SBUs mesoscopically arranged.

5.5.6. Zn:Mn:Co:Ca system

In addition, through the combination of zinc, cobalt, manganese and calcium, eleven new quaternary multi-metal MOFs have been synthesized. The employed molar codes and the resulting MOF formulae are given in scheme 5.3. In all cases, the resulting MOF structures exhibit SBUs where the cations are in octahedral and tetrahedral coordination environments, without any compositional gradient, as demonstrated by the neutron powder diffraction (figure 5.24) and SEM-EDS experiments (figure 5.25 and appendices). Consistent with the previously described results, calcium and manganese are accommodated in octahedral coordination, zinc in tetrahedral, and cobalt in both environments.

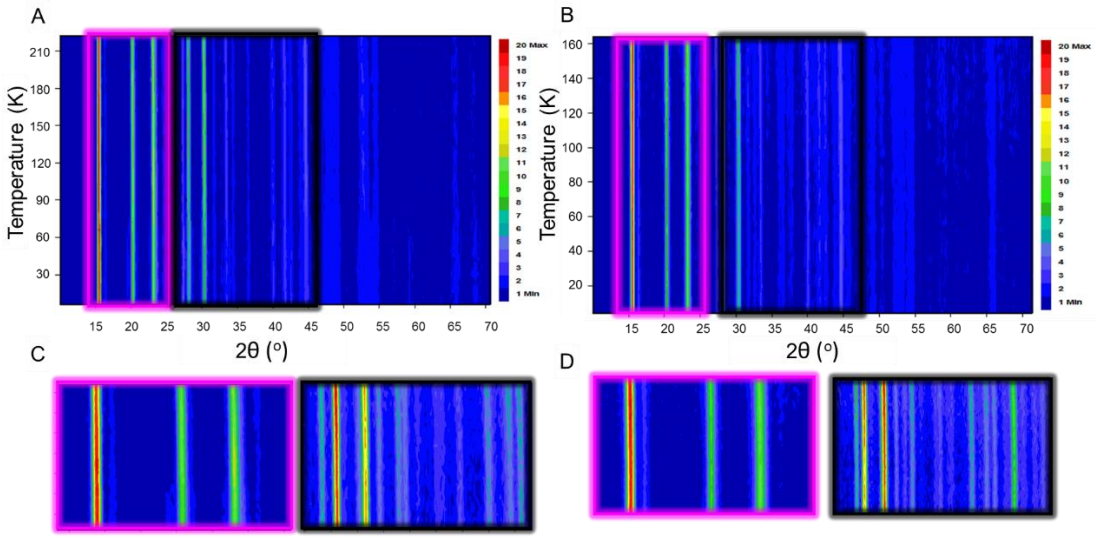

Figure 5. 23 Contour 2D neutron thermodiffraction patterns: $Zn_{0.72}Co_{0.17}Ca_{0.11}$(hfipbb) (molar code: Zn:Co:Ca 1:1:1) and (A), blow up of marked areas (B) and $Zn_{0.37}Co_{0.33}Ca_{0.30}$(hfipbb) (molar code: Zn:Co:Ca 1:4:4) (C), blow up of marked areas from $Zn_{0.72}Co_{0.17}Ca_{0.11}$(hfipbb) compound and (D) blow up of marked areas from $Zn_{0.37}Co_{0.33}Ca_{0.30}$(hfipbb).

The analysis of the obtained metal arrangements shows that the combination of four elements in the initial molar codes results in a complex behavior with and interplay of the four cations, so that a direct relationship between input and output ratios is not evident. Use of an equimolar code (1:1:1:1) results in a low incorporation of calcium into the MOF with composition [$Zn_{0.42}Mn_{0.42}Co_{0.11}Ca_{0.06}$(hfipbb)]. Increasing the initial amount of calcium results in a larger incorporation of this element, although this increment is not linearly related to the starting amount, as demonstrated by the material prepared from a 1:1:1:7 molar code. This can be explained by the fact that calcium atoms will only be occupying sites with octahedral environment in the SBU, which are readily occupied by manganese atoms. However, if the relative amount of calcium and cobalt are simultaneously increased, a higher incorporation of calcium is achieved. Thus, the MOFs prepared from a 1:1:4:4 and 1:1:4:8 molar codes exhibit $Zn_{0.18}Mn_{0.24}Co_{0.41}Ca_{0.16}$(hfipbb) and $Zn_{0.26}Mn_{0.16}Co_{0.37}Ca_{0.21}$(hfipbb) formula, respectively. This observation was consistent with the results previously discussed, where we already found that in ternary Zn:Co:Ca systems the amount of calcium increased when there is larger presence of cobalt. We hypothesized with the fact that presence of cobalt – calcium pairs in the SBU might be favored over zinc – calcium ones.

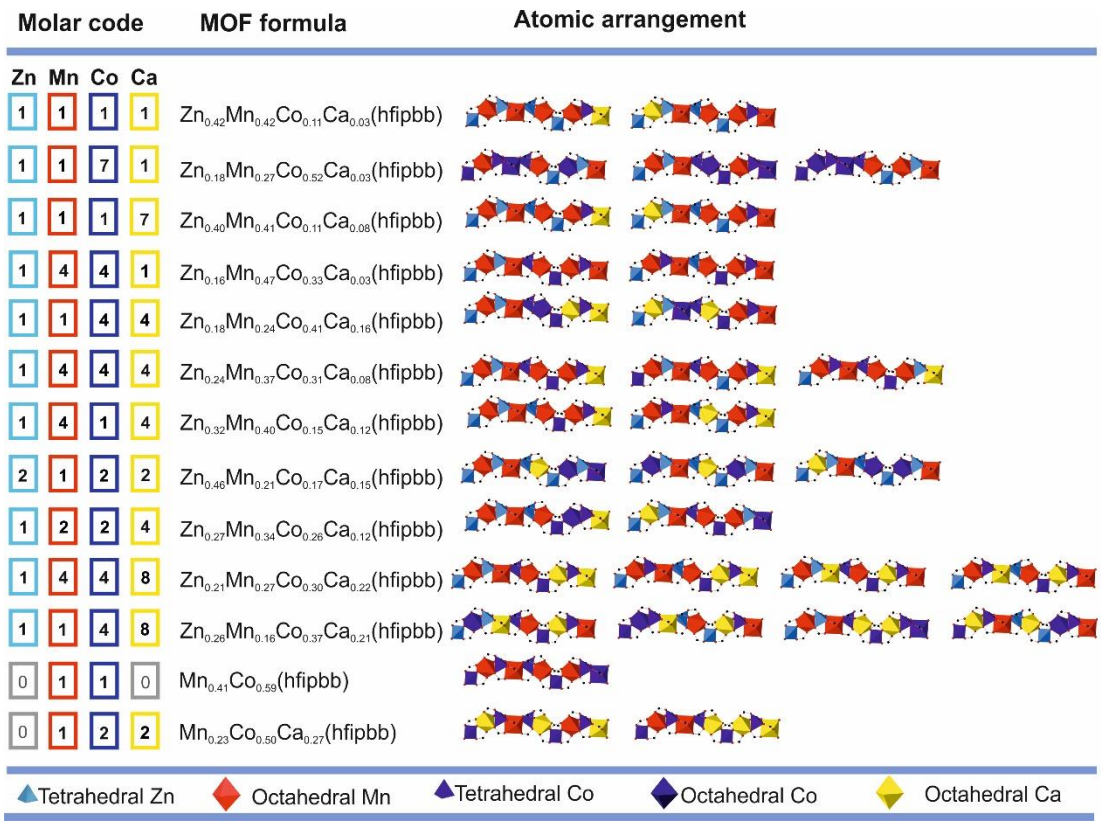

Scheme 5. 3. Selection of appropriate molar codes express the formation of different kinds of atomically sequenced inorganic SBUs.

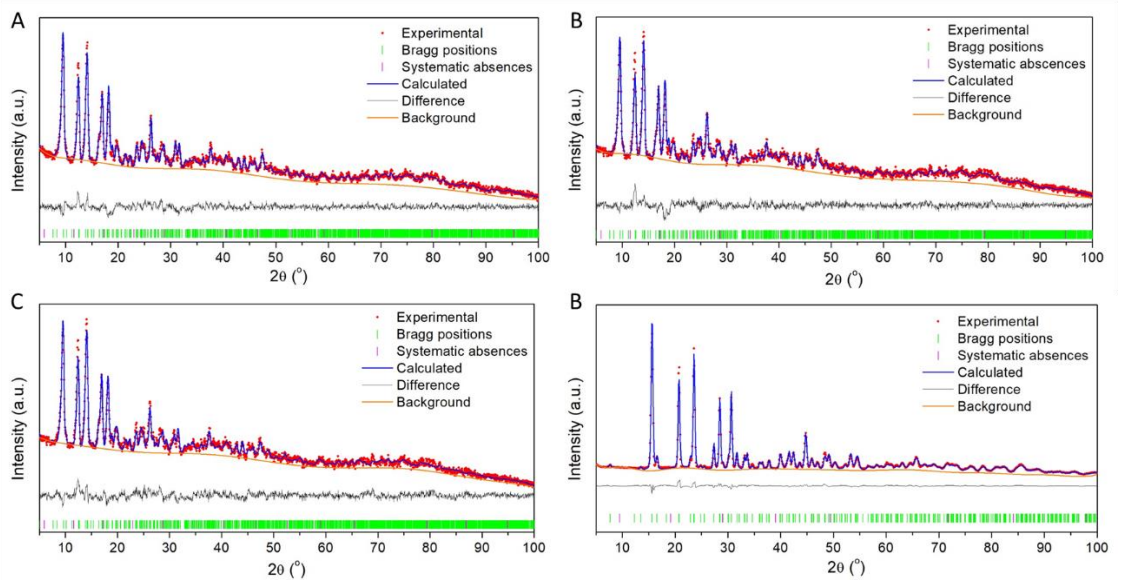

Figure 5. 24. Neutron diffraction pattern Rietveld refinement for: A) $Zn_{0.42}Mn_{0.42}Co_{0.11}Ca_{0.06}$(hfipbb) (molar code: Zn:Mn:Co:Ca 1:1:1:1). Rwp= 2.42%; Rp= 1.71%. This pattern was collected at HRPT instrument; B) $Zn_{0.16}Mn_{0.47}Co_{0.33}Ca_{0.03}$(hfipbb) (molar code: Zn:Mn:Co:Ca 1:4:4:1). Rwp= 2.24%; Rp= 1.59%. This pattern was collected at HRPT instrument; C) $Zn_{0.18}Mn_{0.24}Co_{0.41}Ca_{0.16}$(hfipbb) (molar code: Zn:Mn:Co:Ca 1:1:4:4). Rwp= 2.35%; Rp= 1.72%. This pattern was collected at HRPT instrument; and D) $Zn_{0.13}Mn_{0.27}Co_{0.52}Ca_{0.03}$(hfipbb) (molar code: Zn:Mn:Co:Ca 1:1:7:1). Rwp= 2.09%; Rp= 1.27%. This pattern was collected at D1B instrument.

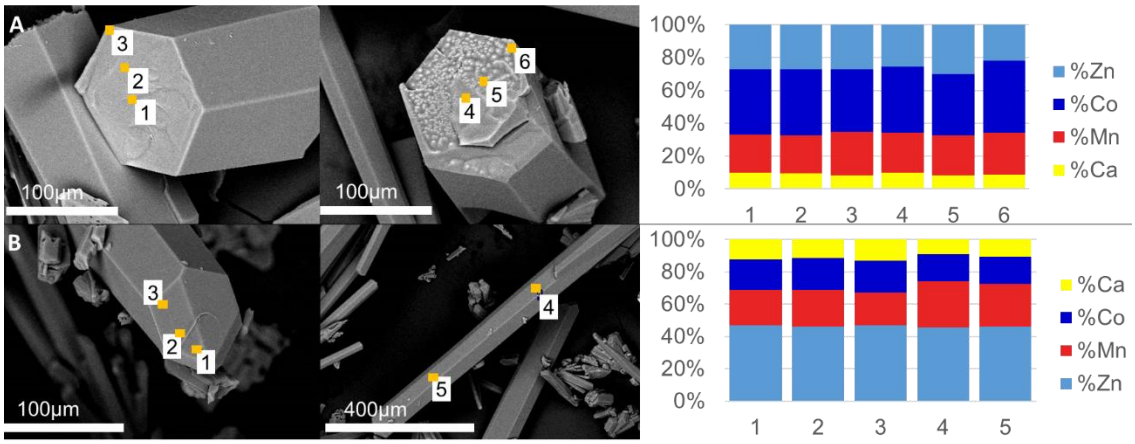

Figure 5. 25. SEM-EDS analyses corresponding to A) $Zn_{0.18}Mn_{0.24}Co_{0.41}Ca_{0.16}$(hfipbb) crystals (molar code: Zn:Mn:Co:Ca 1:1:4:4) and B) $Zn_{0.46}Mn_{0.34}Co_{0.17}Ca_{0.15}$(hfipbb) crystals (molar code: Zn:Mn:Co:Ca 2:1:2:2). Orange spots indicate the areas where EDS were performed, plot (left) shows the metal ratios by EDS analyses, where each column corresponds to the area indicated by a number in the SEM pictures.

At the view of the molar ratios of the materials prepared from molar codes Zn:Mn:Co:Ca 1:4:1:4 with formula $Zn_{0.32}Mn_{0.40}Co_{0.15}Ca_{0.12}$(hfipbb), Zn:Mn:Co:Ca 1:2:2:4 with formula $Zn_{0.27}Mn_{0.34}Co_{0.26}Ca_{0.12}$(hfipbb) and Zn:Mn:Co:Ca 1:4:4:8 with formula $Zn_{0.21}Mn_{0.27}Co_{0.30}Ca_{0.22}$(hfipbb), we can deduce that the sum of the manganese and calcium amount cannot exceed a value of 0.50, because these two cations are exclusively located at octahedral positions. This is also demonstrated in the system Zn:Mn:Ca, previously discussed. The competition between manganese and calcium atoms to occupy these positions observed in the Zn:Mn:Ca systems is also translated to the quaternary ones. As result, in MOFs prepared from Zn:Mn:Co:Ca 1:4:1:4, Zn:Mn:Co:Ca 1:2:2:4 and Zn:Mn:Co:Ca 1:4:4:8 molar codes, the resulting manganese amount is always higher than the calcium one, although initially there is more calcium in the reaction media.

5.5.7. Systems without Zn

Finally, although zinc is crucial for this phase to be generated, different experiments have been carried out in the absence of zinc to try to obtain this same phase without it. Individually, the syntheses made only with manganese or cobalt as the only metals did not give favorable results. Unexpectedly, the combination of both with molar code Mn:Co 1:1 resulted in the obtained of the same MOF with formula $Mn_{0.41}Co_{0.59}$(hfipbb), which crystallizes in the hexagonal space group $P6_122$ with cell parameters a = 21.2619 (13) Å and c = 15.1193 (12) Å. In addition, the molar code Mn:Co:Ca 1:2:2 code, also afforded the sought MOF, with a $Mn_{0.23}Co_{0.50}Ca_{0.27}$(hfipbb) formula, being the material that presents the largest amount of calcium. Single crystal X-ray diffraction analysis shows a SBU with cobalt atoms in tetrahedral environment, and calcium and manganese atoms in octahedral coordination environment (scheme 5.3). This particular result seems to indicate that certain dyads of metal cations might also play a structure directing role analogue to zinc, although further experiments are necessary to confirm to what extend this can be generalized to other metal element combinations. In both cases, Rietveld refinements results show an unique phase with the double cell (figure 5.26) and the SEM-EDS analyses show a homogeneous distribution of metals along a same crystal (figure 5.27).

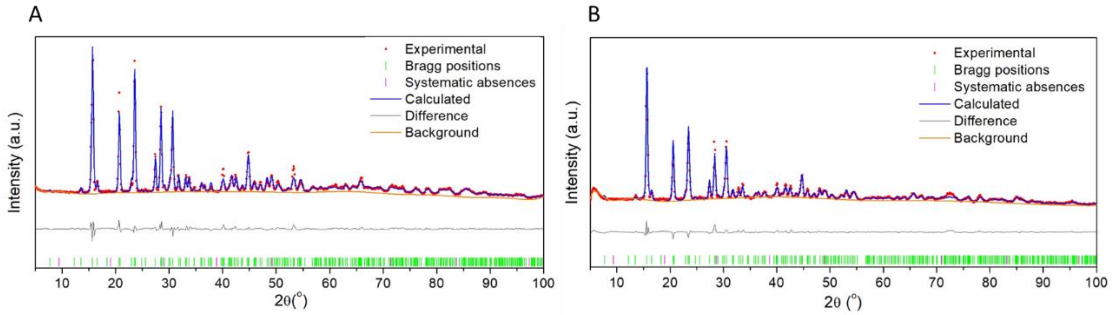

Figure 5. 26. Neutron diffraction pattern Rietveld refinement for: A) $Mn_{0.41}Co_{0.59}$(hfipbb) (molar code: Mn:Co 1:1). Rwp= 2.76%; Rp= 1.89%; and B) $Mn_{0.23}Co_{0.50}Ca_{0.27}$(hfipbb) (molar code: Mn:Co:Ca 1:2:2). Rwp= 2.09%; Rp= 1.27%. These patterns were collected at D1B instrument.

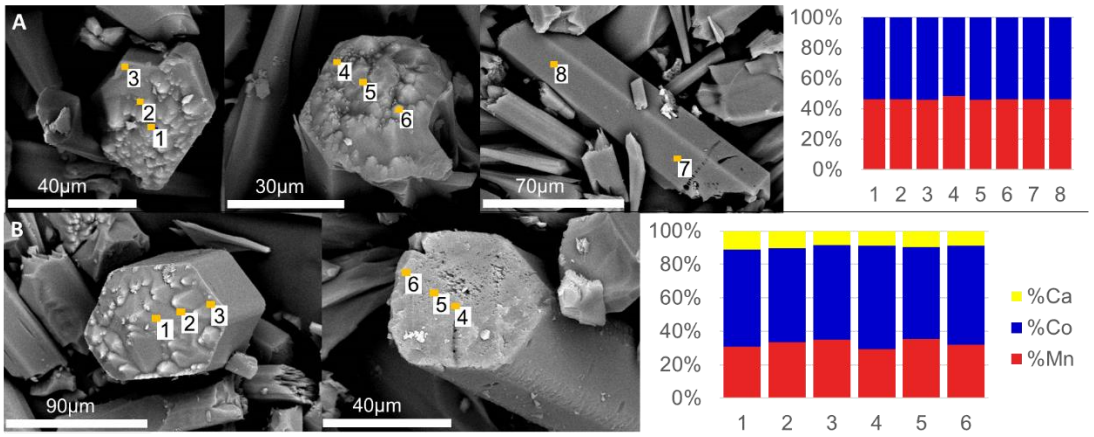

Figure 5. 27. SEM-EDS analyses corresponding to A) $Mn_{0.41}Co_{0.59}$(hfipbb) crystals (molar code: Mn:Co 1:1) and B) $Mn_{0.23}Co_{0.50}Ca_{0.27}$(hfipbb) crystals (molar code: Mn:Co:Ca 1:2:2). Orange spots indicate the areas where EDS were performed, plot (left) shows the metal ratios by EDS analyses, where each column corresponds to the area indicated by a number in the SEM pictures.

5.6. DFT Calculations

Formation energies (ΔE_{Form}) determined by *ab initio* density functional theory (DFT) calculations corroborate the importance of the kinetic control on the first stages of the synthesis.

These theoretical calculations by DFT were carried out using the geometry obtained from single crystal X-ray diffraction data refinements. The DF plane-wave calculations were carried out by means of the VASP package [16-17] considering spin-polarization and dipole corrections explicitly. The total energies corresponding to the optimized geometries of all samples were calculated using the spin polarized version of the exchange and correlation functional of Perdew and Wang.[18-19] The effect of the core electrons on the valence electron density was described by the project or augmented wave (PAW) method.[20-21] The cut-off for the kinetic energy of the plane-waves was set to 415 eV to ensure a total energy convergence better than 10^{-6} eV·K.

Crystal models of MOFs consisting of SBUs formed by alternating tetrahedral zinc atoms and octahedral zinc, cobalt, manganese, or calcium atoms, and another model with alternating tetrahedral and octahedral cobalt atoms were geometrically optimized. In all cases, these models are converged to stable structure with the same topology, although no symmetry constrains were imposed (figure 5.28). The order of stability of the models are in absolute value: Co_{Td}-Co_{Oh} > Zn_{Td}-Mn_{Oh} > Zn_{Td}-Ca_{Oh} > Zn_{Td}-Co_{Oh} > Zn_{Td}-Zn_{Td} > Zn_{Td}-Zn_{Oh}. The hypothetical phase consisting of tetrahedral and octahedral zinc atoms was the only one with a higher formation energy than the original ZnPF-1 phase, which is consistent with impossibility of transformation of the MOF made of only zinc. On the other hand, the calculations also corroborate that the concentration gradient is consistent with an Ostwald ripening process, because the use of cobalt, calcium and manganese leads to a decrease in the formation energy. The pure cobalt phase is the most energetically stable, which is also consistent with the formation of this phase in the outer shells of samples made with longer synthesis time. In addition, density of states reveals that the geometry distortion produced by the introduction of a second metal cation stabilizes the orbitals with higher occupation while destabilizing those with lower occupation, thus breaking the degeneracy of the octahedral geometry.

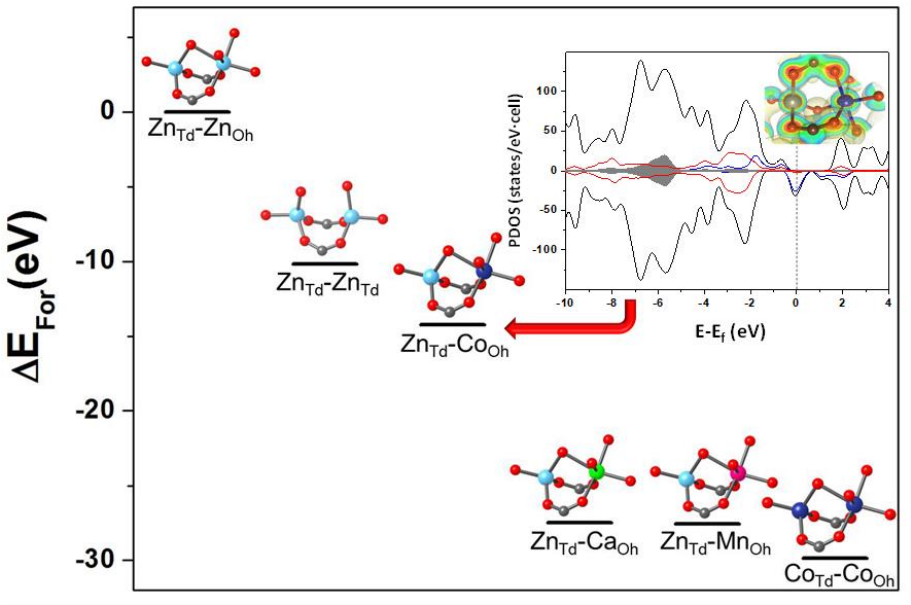

Figure 5. 28. Formation energies (ΔEFor) for the pure and bimetallic structures normalized to the most stable one. These calculations were performed by spin polarized DF plane-waves and GGA exchange correlation functional. Inset: Total DOS (black) and atom-projected (PDOS) for Co (blue), O (red line), Zn (grey shadow) and E_F (black dash) and schematic representation of the isosurfaces of a section of charge density for the Zn_{Td}-Co_{Oh} Atom color: Zn (grey), Co (blue), O (red) and C (gray).

5.7. Magnetic Properties

The inclusion of cobalt on a system which only contains zinc, as metal cation, can induce new properties. Considering that the properties of materials are dictated by their composition and precise atomic and mesoscopic structures, these findings are relevant to various fields. The case of the magnetic properties of MOFs is here illustrated, due to magnetic properties are determined by the combination of these factors, namely, the geometry of the SBUs, the atomic distribution of cations, and the possible mesoscopic interaction among SBUs. Thus, in the case of the MOFs prepared from a Zn:Co 1:2 molar code, ferromagnetism is developed within the SBUs below 15 K, and interchain antiferromagnetic interactions acquire a long-range character below 7 K, although a large-enough applied magnetic field produces a metamagnetic transition, giving rise to a long-range ferromagnetic state. In the MOF prepared from a Zn:Co 1:10 molar code, where the larger incorporation of cobalt in the SBU forces the presence of cobalt neighbor polyhedral, canted antiferromagnetism is developed within the SBUs in such a way that a rather small net magnetization appears below 35.8 K within the SBU composed exclusively of cobalt, and an additional contribution at lower temperatures comes from the SBU with 30% of the tetrahedral sites occupied by cobalt, where the number of consecutive cobalt cations is smaller. The ability to produce MOFs with controllable metal arrangement shown in this chapter opens the possibility to stimulate or block a specific superexchange pathway to develop a specific magnetic interaction within SBUs.

5.7.1. Measurement conditions

Magnetization measurements were carried out on polycrystalline samples using a superconducting quantum interference device magnetometer (Quantum Design, model MPMS-XL). The temperature dependence of the molar magnetic susceptibility (χ) was obtained from the dc magnetization (M) measured with an applied magnetic field (H) during warming the sample from 2 K up to 300 K. Zero-field cooling and field cooling measurement modes were used. In the former, the sample was cooled down from room temperature to 2 K in zero field and in the later the sample was cooled down in the measuring H. The magnetic field dependence of the dc magnetization M(H) was obtained at different temperatures up to

±5 T. The temperature dependence of the real and imaginary part of the ac molar magnetic susceptibility (χ'_{ac} and χ''_{ac}, respectively) was obtained from the ac magnetization measured in the temperature range 2-55 K, with H= 0 and applying an oscillating magnetic field with drive amplitude of 0.35 mT at different frequencies in the range 1-1000 Hz. The diamagnetic contribution was subtracted from the calculated molar susceptibilities χ.

5.7.2. Discussion of magnetic susceptibility measurements

The low temperature magnetism of these compounds is determined by three factors. The first one is the geometric features of the inorganic helical chains where paramagnetic metal cations are present, especially the linkages between the alternating tetrahedral and octahedral metal polyhedrons that set up as building blocks of those SBUs. The second factor, in the same atomic scale, is the distribution of the metal cations between the two metal sites, determining the existence or not of neighboring paramagnetic metal ions. These two factors shape magnetic interactions that will take place in the mentioned SBUs. The third factor, at mesoscopic scale, is the possibility of the SBUs to interact each other through the organic linker and according to the topology of the structure. X-ray single crystal diffraction data at low temperature allow us to carry out a detailed structural analysis at atomic scale concerning the SBUs involved in the magnetic behavior of these samples, i.e., those SBUs with alternating corner-sharing octahedral and tetrahedral units, see Figure 5.29 and Table 5.3. The more effective magnetic superexchange pathway between those two metal sites, M_{Td} and M_{Oh}, involves a bridging oxygen atom coming from a carboxylate group. Goodenough-Kanamori-Anderson[22] rules predict strong antiferromagnetic interaction between two magnetic ions with partially filled d shells for the M-O-M sequence with a bond angle value of 180 °, whereas a weak ferromagnetic one is expected for 90 °. In another magnetic super-exchange pathway, the two metal centers are bridged by a carboxylate group, M_{Oh}-O-C-O-M_{Td}, in a syn-syn mode of connection that promotes weak antiferromagnetic interaction between them. Furthermore, this carboxylate bridging unit could give rise to an orbital counter complementary effect on the magnetic interaction developed through the M_{Oh}-O- M_{Td} pathway. Finally, a third effective magnetic super-exchange pathway must be considered, where a carboxylate group acts as bridging unit between octahedral positions, M_{Oh}-O-C-O-$M_{Oh'}$, in a syn-anti bridging mode that usually promotes weak ferromagnetic interaction. Note that the above mentioned oxygen

atoms acting as sharing vertices are bringing by this later kind of carboxylate ligand. This scenario is rather complex from a magnetic point of view due to the presence of different effective magnetic super-exchange pathways yielding both ferromagnetic and antiferromagnetic interactions within the SBUs.

Sample	**$Zn_{0.59}Co_{0.41}$(hfipbb)**	**$Zn_{0.21}Co_{0.79}$(hfipbb)**
SBU	**Zn_{T_d} and Co_{O_h}**	**Zn_{T_d}/Co_{T_d} and Co_{O_h}**
$d_{intrachain}$ M_{T_d} ···· M_{O_h} (Å)	3.093(8)	3.154(6)
$d_{intrachain}$ M_{O_h} ···· M_{O_h} (Å)	5.605	5.842
α M_{O_h}–O– M_{T_d} (°)	86.6(5)	96.86(6)
***Shortest* $d_{interchain}$ *M* ···· *M* (Å)**	11.640	11.357

Table 5. 3. Selected bond angles and interatomic lengths of the SBUs involved in the low temperature magnetism of the MOFs obtained in the Zn:Co system. The data are obtained from the results of single crystal X-ray diffraction experiments at low temperature.

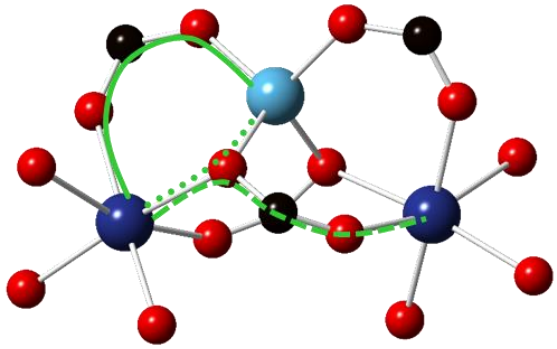

Figure 5. 29. Partial view of the crystal structure of the helical, rod-shaped inorganic chains built up with alternating tetrahedral and octahedral metal polyhedrons. The effective super-exchange magnetic interaction pathways between metal centers are showed: M_{O_h}–O– M_{T_d} (dotted green line), M_{O_h}–O–C–O–M_{T_d} (continuous green line) and M_{O_h}–O–C–O–M'_{O_h} (dashed green line).

However, the competence to produce MOFs with controllable metal arrangements shown in this work opens the possibility to stimulate or to block a specific super-exchange pathway in order to develop a specific magnetic interaction within the SBUs. This is clearly shown by the MOFs obtained in the Zn:Co system, since Zn^{2+} is a diamagnetic cation that exclusively occupies the tetrahedral sites while Co^{2+} is a paramagnetic cation with strong magnetic

anisotropy that might be located at both tetrahedral and octahedral sites. The SBU corresponding to the $Zn_{0.59}Co_{0.41}$(hfipbb) sample is formed by alternating tetrahedral zinc and octahedral cobalt cations initially develops short-range ferromagnetic interactions within the chain below 45 K according to the progressive increasing of the $T\chi ac'$ product as temperature decreases, see Figure 5.26.

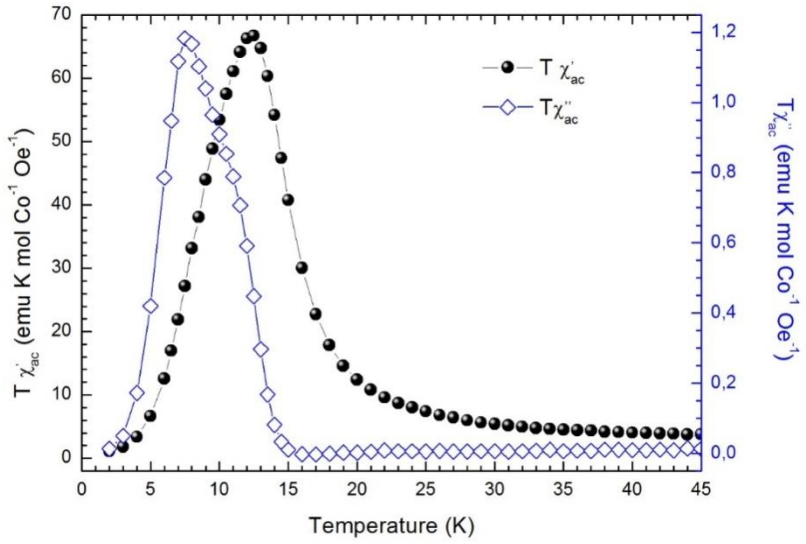

Figure 5. 30. Low temperature dependence of the products temperature by real component (left y-axis) and imaginary component (right y-axis) of the ac magnetic susceptibility obtained for the MOF with formula $Zn_{0.59}Co_{0.41}$(hfipbb).

Such a kind of magnetic interaction is fully confirmed through the absence of absorption of the imaginary part of the ac magnetic susceptibility, $T\chi ac''$ ~0, and the non-linear M(H) obtained at 30 K (see Figure 5.30 and 5.31.a) together with no magnetic hysteresis loop observed at 30 K (see Figure 5.32).

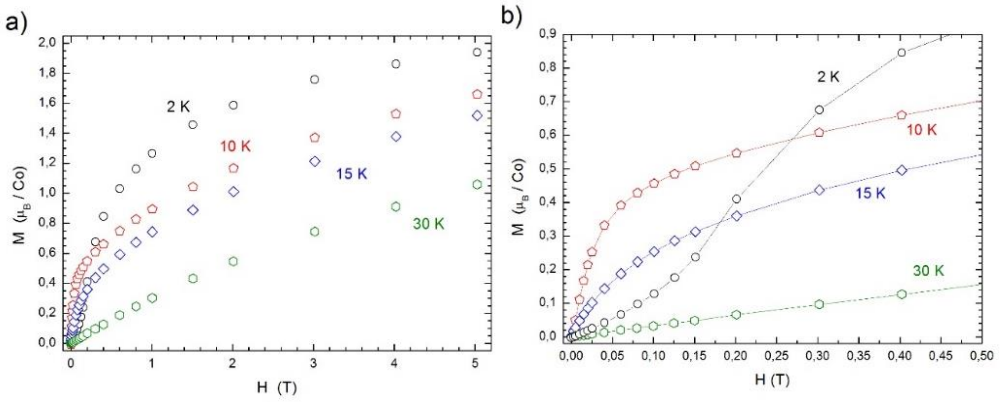

Figure 5. 31. a) Magnetic field dependence of the virgin magnetization curves obtained at 2 K (black circles), 10 K (red pentagons), 15 K (blue diamonds) and 30 K (green hexagons) for the MOF with formula $Zn_{0.59}Co_{0.41}$(hfipbb). b) Low magnetic field region of the same curves. The solid lines are eye guides.

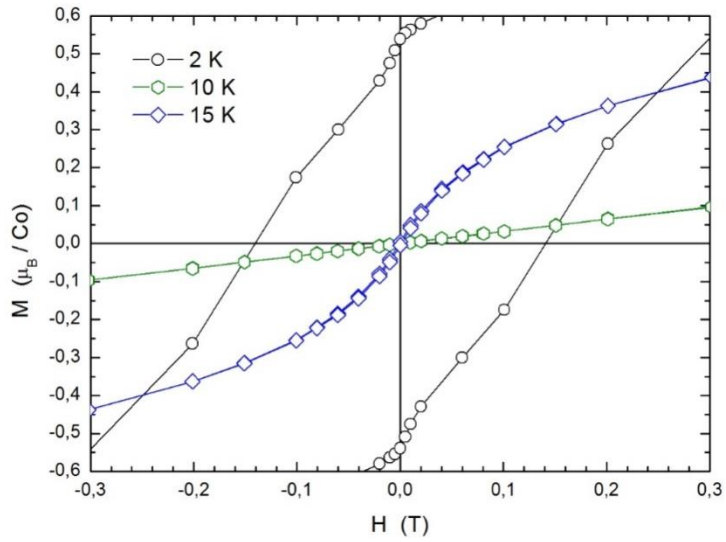

Figure 5. 32. Low magnetic field region of hysteresis loops measured at 2 K (circles), 15 K (diamonds) and 30 K (hexagons) for the MOF with formula $Zn_{0.59}Co_{0.41}$(hfipbb). The solid lines are eye guides.

As temperature decreases the ferromagnetic interaction propagates along the helical chain according to the noticeable increase of the $T\chi_{ac}{}'$ product and at 15 K it is enough extended along the chain to produce a sudden increase of the imaginary component of ac magnetic susceptibility, $T\chi_{ac}{}'' > 0$. This is confirmed through the non-linear M(H) obtained at 15 K (see Figure 5.231.a) and the narrow magnetic hysteresis loop observed at 15 K (see Figure 5.32). At 12.5 K the $T\chi_{ac}{}'$ product reaches a maximum and then it falls down to zero as the

temperature reaches its lowest value of 2 K. This behavior denotes the onset of antiferromagnetic interactions between the ferromagnetic chains at 12.5 K that seem to acquire a long range character below 7 K as indicates the fast fall down of the $T\chi_{ac}{}''$ values. This is supported by the linear M(H) obtained at 2 K, see Figure 5.27.b, even though it becomes non-linear above 60 mT rising the magnetization values up to 1.94 μ_B/Co at 5 T, see Figure 5.31.a; such a value is consistent with the characteristic effective spin S= ½ and isotropic g value of about 4.33 for the low temperature state of octahedral Co^{2+} cations. It is worth mentioning that the cross of the isotherms obtained at 2 and 10 K, see Figure 5.31.b, which takes place between 200 and 300 mT, indicates that the applied magnetic field has an effect on the antiferromagnetic interchain interactions blocking them and giving rise to non-interacting ferromagnetic chains. Finally, the low temperature dependence of the dc magnetic susceptibility obtained at H= 50 Oe under zero-field-cooled (ZFC) and field-cooled (FC) conditions agrees with the magnetic behavior above described, see Figure 5.33 In the other two SBUs which belong to the Zn:Co system, both of them identified in the MOF with chemical formula $Zn_{0.21}Co_{0.79}$(hfipbb), there are neighboring cobalt cations due to the larger incorporation of cobalt than the SBU before. Thus, the magnetic interaction between Co^{2+} in tetrahedral and octahedral sites through an oxygen bridge must be considered in order to explain the low temperature magnetic behavior

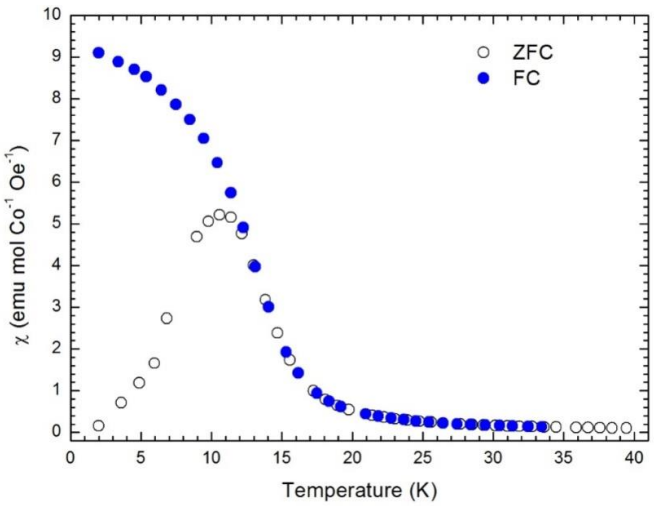

Figure 5. 33. Thermal variation of dc magnetic susceptibility measured in an applied field of 5 mT for the MOF with formula $Zn_{0.59}Co_{0.41}$(hfipbb). The open circles correspond to the zero field cooled (ZFC) measuring protocol and the solid circles correspond to the field cooled (FC) measuring protocol.

observed for that sample. Concerning the Co^{2+}-O-Co^{2+} bond angle α as main factor determining that magnetic coupling, as far as we know it is not clearly stated the existence of a crossover angle value between the strong antiferromagnetic interaction predicted at 180 ° and the weak ferromagnetic one enhanced at 90 °. Despite the α values of nearly 97 ° found in both types of SBUs, antiferromagnetic interactions with uncompensated magnetic moments predominate according to the slight decrease of the $T\chi_{ac}$ product below 55 K and the following small increment to a maximum at 34.8 K, see Figure 5.30. The further small increment of the $T\chi_{ac}$ product to a maximum at 29.4 K reveals an additional contribution to the net magnetization of the sample, which field dependence at 35 and 30 K is typical for a canted antiferromagnetic arrangement of spins, see Figure 5.30. Besides, the increase of the imaginary component of ac magnetic susceptibility ($T\chi_{ac}{}'' > 0$) that

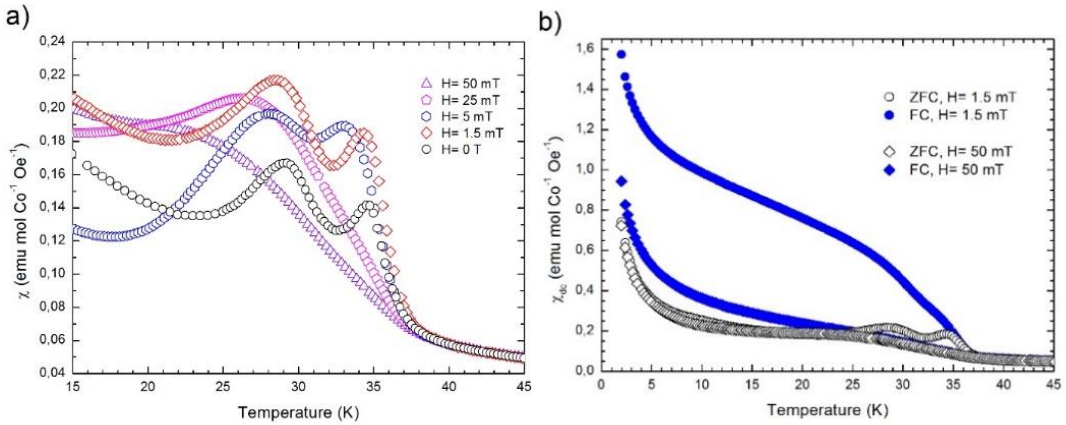

Figure 5. 34. a): Thermal variation of ac magnetic susceptibility measured in absence of an applied magnetic field (black circles), and thermal variation of dc magnetic susceptibilities measured in 1.5 mT (red diamonds), 5 mT (blue hexagons), 25 mT (magenta pentagons) and 50 mT (violet triangles) for the MOF with formula $Zn_{0.21}Co_{0.79}$(hfipbb). b): Thermal variation of dc magnetic susceptibility measured in 1.5 mT (circles) and 50 mT (diamonds) for the MOF with formula $Zn_{0.21}Co_{0.79}$(hfipbb). The open symbols correspond to the zero field cooled (ZFC) measuring protocol and the solid symbols correspond to the field cooled (FC) measuring protocol.

goes with each maximum in $T\chi_{ac}$ product (Figure 5.34) and the very narrow magnetic hysteresis loop observed at 30 and 35 K (Figure 5.35), support the existence of a net magnetization enough extended along the chains. Taking into account all this data we could state the net magnetization of the sample begins within the chains composed exclusively of cobalt, and the additional contribution at lower temperatures comes from the chains with the

40% of the tetrahedral sites occupy by Co,[23] where the length of the chain with consecutive cobalt cations will be shorter. Concerning the two maxima previously mentioned, it is quite improbable they are due to antiferromagnetic interactions between neighboring chains, as such interactions should be operative below 12.5 K because of the rather similar shortest interchain Co⋯Co distance found for the three phases identified in the system Zn:Co, see Table 5.3. ZFC susceptibility of magnetically ordered systems usually shows a maximum and thermomagnetic irreversibility ($\chi_{ZFC} \neq \chi_{FC}$) below its critical temperature when a small measuring dc magnetic fields is used, and

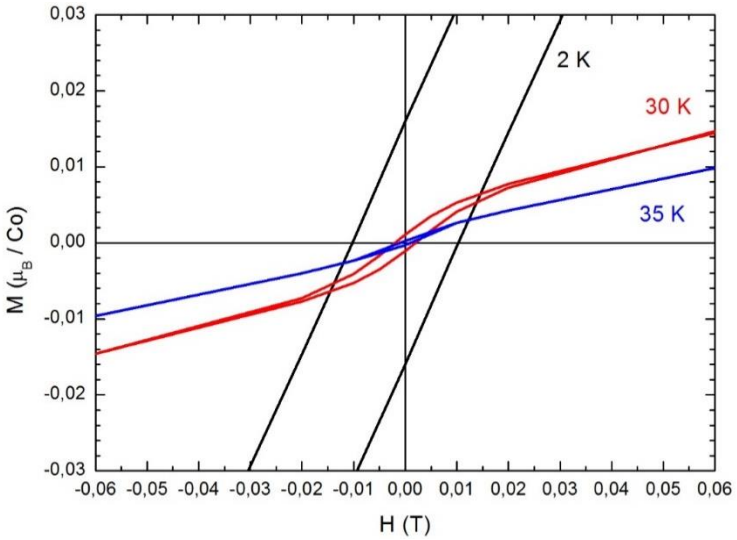

Figure 5. 35. Low magnetic field region of hysteresis loops measured at 2 K (black line), 30 K (red line) and 35 K (blue line) for the MOF with formula $Zn_{0.21}Co_{0.79}$(hfipbb).

therefore, magneto-crystalline anisotropy and domain wall pinning effects become rather important. Such a maximum is broadened and rounded off and moved toward lower temperatures with increasing H. This is the behavior found for the sample $Zn_{0.21}Co_{0.79}$(hfipbb), see Figure 5.34.b. Finally, the different field dependence of the magnetization at 2 K as well as the magnetization value of 2.12 μ_B/Co at 5 T, see Figure 5.34, are indicative of the presence of net magnetization which origin seems to be rather more complex than the canted antiferromagnetism proposed at higher temperature. Both the ground state of octahedral Co^{2+} populated at 2 K and the effectiveness of interchain interactions below 12.5 K, must be

involved in a likely explanation for the value of saturation magnetization higher than 2.2 μ_B/Co that it will be reached at magnetic fields above 5 T.

5.8. Conclusions

The results of this chapter offer a new platform to obtain complex structures where the arrangement of the metal cations can be virtually controlled on demand. Considering that the properties of materials are dictated by their composition and precise atomic and mesoscopic structures, it is reasonable to think that our findings will be relevant to various fields. This is illustrated with the induction of new magnetic properties of these Zn-Co MOFs.

Moreover, in view of the large number of existing MOFs that are constructed from many diverse rod-shaped SBUs,[24] it might be anticipated that this method will be generalized to prepare new materials with topologies and structures fit for specific applications where multiple metal cations can be arranged at desired atomic positions, as well as mesoscopically distributed. The use of the combination of different microscopic and diffractometric techniques such as: SEM-EDS, ICP, Single crystal X-ray diffraction and powder X-ray diffraction, neutron powder diffraction; have been the key to elucidate the arrangement of the SBUs and their mesoscopic distribution.

The results of this chapter have been published in Science Advances in 2017, volume 3, e1700773, with the title '*Addressed realization of multication complex arrangements in metal-organic frameworks*'. And in Journal of American Chemical Society in 2019, 141 (4), 1766, with the title '*Encoding Metal-Cation Arrangements in Metal-Organic Frameworks for Programming the Composition of Electrocatalytically Active Multi-Metal Oxides*'.

5.9. References

1. Monge, A.; Snejko, N.; Gutierrez-Puebla, E.; Medina, M.; Cascales, C.; Ruiz-Valero, C.; Iglesias, M.; Gomez-Lor, B., One teflon®-like channelled nanoporous polymer with a chiral and new uninodal 4-connected net: sorption and catalytic properties. *Chemical Communications* **2005,** (10), 1291-1293.

2. Castillo-Blas, C.; Snejko, N.; de la Pena-O'Shea, V. A.; Gallardo, J.; Gutiérrez-Puebla, E.; Monge, M. A.; Gándara, F., Crystal phase competition by addition of a second metal cation in solid solution metal-organic frameworks. *Dalton Transactions* **2016,** *45* (10), 4327-4337.

3. Zhou, K.; Mousavi, B.; Luo, Z.; Phatanasri, S.; Chaemchuen, S.; Verpoort, F., Characterization and properties of Zn/Co zeolitic imidazolate frameworks vs. ZIF-8 and ZIF-67. *Journal of Materials Chemistry A* **2017,** *5* (3), 952-957.

4. Botas, J. A.; Calleja, G.; Sánchez-Sánchez, M.; Orcajo, M. G., Effect of Zn/Co ratio in MOF-74 type materials containing exposed metal sites on their hydrogen adsorption behaviour and on their band gap energy. *International Journal of Hydrogen Energy* **2011,** *36* (17), 10834-10844.

5. Gu, J.-Z.; Liang, X.-X.; Cui, Y.-H.; Wu, J.; Kirillov, A. M., Exploring 4-(3-carboxyphenyl)picolinic acid as a semirigid building block for the hydrothermal self-assembly of diverse metal-organic and supramolecular networks. *CrystEngComm* **2017,** *19* (1), 117-128.

6. Ma, T.; Li, M.-X.; Wang, Z.-X.; Zhang, J.-C.; Shao, M.; He, X., Structural Diversity, Luminescence, and Magnetic Properties of Eight Co(II)/Zn(II) Coordination Polymers Constructed from Semirigid Ether-Linked Tetracarboxylates and Bend Dipyridyl-Triazole Ligands. *Crystal Growth & Design* **2014,** *14* (8), 4155-4165.

7. Shi, Z.-Q.; Li, Y.-Z.; Guo, Z.-J.; Zheng, H.-G., Six New 2D or 3D Metal-Organic Frameworks Based on Bithiophene-Containing Ligand and Dicarboxylates: Syntheses, Structures, and Properties. *Crystal Growth & Design* **2013,** *13* (7), 3078-3086.

8. Ruano, D.; Díaz-García, M.; Alfayate, A.; Sánchez-Sánchez, M., Nanocrystalline M-MOF-74 as Heterogeneous Catalysts in the Oxidation of Cyclohexene: Correlation of the Activity and Redox Potential. *ChemCatChem* **2015,** *7* (4), 674-681.

9. Liu, Q.; Cong, H.; Deng, H., Deciphering the Spatial Arrangement of Metals and Correlation to Reactivity in Multivariate Metal-Organic Frameworks. *Journal of the American Chemical Society* **2016,** *138* (42), 13822-13825.

10. Bernini, M. C.; de Paz, J. R.; Snejko, N.; Sáez-Puche, R.; Gutierrez-Puebla, E.; Monge, M. Á., Unusual Magnetic Behaviors and Electronic Configurations Driven by Diverse Co(II) or Mn(II) MOF Architectures. *Inorganic Chemistry* **2014,** *53* (24), 12885-12895.

11. Bauer, C. A.; Jones, S. C.; Kinnibrugh, T. L.; Tongwa, P.; Farrell, R. A.; Vakil, A.; Timofeeva, T. V.; Khrustalev, V. N.; Allendorf, M. D., Homo- and heterometallic luminescent 2-D stilbene metal-organic frameworks. *Dalton Transactions* **2014,** *43* (7), 2925-2935.

12. Zhao, F.-H.; Che, Y.-X.; Zheng, J.-M., Two metal-organic frameworks (MOFs) based on binuclear and tetranuclear units: Structures, magnetism and photoluminescence. *Inorganica Chimica Acta* **2012,** *384*, 170-175.

13. Hua Chun, Z., Ostwald Ripening: A Synthetic Approach for Hollow Nanomaterials. *Current Nanoscience* **2007,** *3* (2), 177-181.

14. O'Keeffe, M.; Yaghi, O. M., Deconstructing the Crystal Structures of Metal-Organic Frameworks and Related Materials into Their Underlying Nets. *Chemical Reviews* **2012,** *112* (2), 675-702.

15. Leznoff, D. B.; Xue, B.-Y.; Batchelor, R. J.; Einstein, F. W. B.; Patrick, B. O., Gold−Gold Interactions as Crystal Engineering Design Elements in Heterobimetallic Coordination Polymers. *Inorganic Chemistry* **2001,** *40* (23), 6026-6034.

16. Kresse, G.; Furthmüller, J., Efficiency of ab-initio total energy calculations for metals and semiconductors using a plane-wave basis set. *Computational Materials Science* **1996,** *6* (1), 15-50.

17. Kresse, G.; Hafner, J., Ab initio molecular dynamics for liquid metals. *Physical Review B* **1993,** *47* (1), 558-561.

18. Perdew, J. P.; Wang, Y., Accurate and simple analytic representation of the electron-gas correlation energy. *Physical Review B* **1992,** *45* (23), 13244-13249.

19. Perdew, J. P.; Chevary, J. A.; Vosko, S. H.; Jackson, K. A.; Pederson, M. R.; Singh, D. J.; Fiolhais, C., Atoms, molecules, solids, and surfaces: Applications of the generalized gradient approximation for exchange and correlation. *Physical Review B* **1992,** *46* (11), 6671-6687.

20. Blöchl, P. E., Projector augmented-wave method. *Physical Review B* **1994,** *50* (24), 17953-17979.

21. Kresse, G.; Joubert, D., From ultrasoft pseudopotentials to the projector augmented-wave method. *Physical Review B* **1999,** *59* (3), 1758-1775.

22. Weiss, A., John B. Goodenough: Magnetism and the Chemical Bond. Interscience Publishers. New York, London 1963. 393 Seiten, 89 Abbildungen. Preis: DM 95 s. *Berichte der Bunsengesellschaft für physikalische Chemie* **1964,** *68* (10), 996-996.

23. de la Cruz, C.; Huang, Q.; Lynn, J. W.; Li, J.; Ii, W. R.; Zarestky, J. L.; Mook, H. A.; Chen, G. F.; Luo, J. L.; Wang, N. L.; Dai, P., Magnetic order close to superconductivity in the iron-based layered $LaO_{1-x}F_xFeAs$ systems. *Nature* **2008,** *453*, 899.

24. Schoedel, A.; Li, M.; Li, D.; O'Keeffe, M.; Yaghi, O. M., Structures of Metal-Organic Frameworks with Rod Secondary Building Units. *Chemical Reviews* **2016,** *116* (19), 12466-12535.

CHAPTER 6:

ENCODING METAL-CATION ARRANGEMENTS IN METAL-ORGANIC FRAMEWORKS FOR PROGRAMMING THE COMPOSITION OF ELECTROCATALYTICALLY ACTIVE MULTI-METAL OXIDES

6.1. Introduction

The use of MOFs as precursors to obtain other classes of solids though thermal treatment has emerged as an alternative to traditional synthetic routes, offering the possibility to transfer some of the MOF structural features to the resulting materials.[1-3] In consequence, MOFs have been used to produce different types of metal oxides and metal oxide/carbon materials with unprecedented nanostructures, which find application in renewable energy technologies, such as metal-air batteries, fuel cells, and water electrolyzers through their use as catalysts for efficient and stable oxygen reduction reaction (ORR) and oxygen evolution reaction (OER), as explained previously in the introductory chapter.[4-7]

In this chapter, we show how the compositional complexity emerging from the control on the cation arrangements can be translated from the MOF materials to other classes of active solids. In particular, by using MOFs prepared as described in chapters 5 as precursors,[8] and through a thermal treatment 17 multi-metal oxides with spinel structure and selected compositions have been prepared.

The composition of the resulting spinel type oxides can thus be programmed from the MOF synthesis step, resulting in adjustment of their activity as electrocatalyst in the oxygen reduction reaction (ORR) (figure 6.1). Consequently, a series of oxides with spinel structure, and unprecedent compositions ~~have~~ has been prepared following a simple thermal treatment. Among them, a new oxide that contains zinc, cobalt, manganese and calcium exhibits catalytic activities that are comparable to that of commercial Pt/C catalyst in terms of current density (97.2%), preserving their activity after 20000 seconds, without suffering from poisoning effects due to presence of methanol.

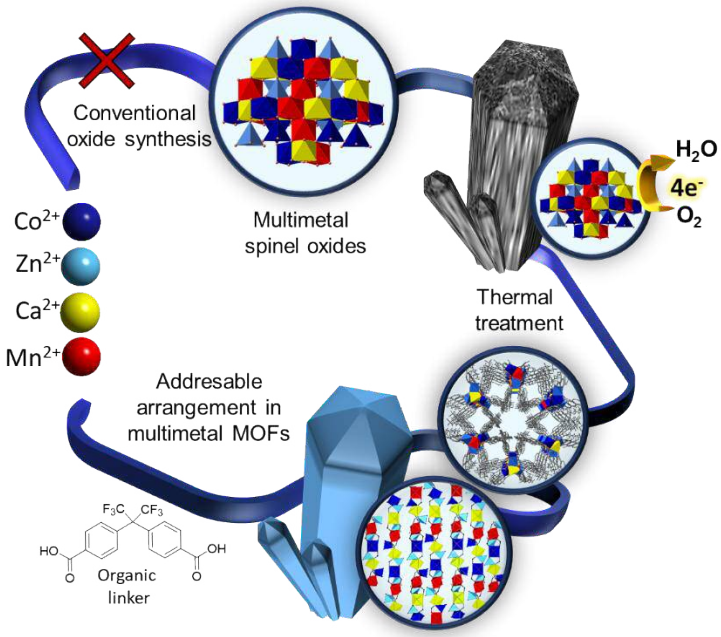

Figure 6. 1. Multi-cation metal-organic frameworks with various arrangements in the SBUs are used as precursors of spinel oxides, with a programmed composition, employed as effective catalysts in oxygen reduction reaction.

6.2. Synthesis and Characterization of Compounds

6.2.1. Thermal treatment

Multi-metal MOFs (100 mg) were subjected to a standard calcination process (1) consisting of a thermal treatment in air, at 800 °C for 24 hours, with a heating rate of 2.5 °C / min in a zirconia crucible, to obtain the corresponding multi-metal oxides preserving the metal ratios. The TG analysis of the multi-cation MOFs presented in chapter 5 confirmed that the transformation occurs between 450-500 °C.

(1) $3[Zn_wMn_xCo_yCa_z(C_{17}H_8O_4F_6)] + 48.5O_2 \rightarrow (Zn_{3w}Mn_{3x}Co_{3y}Ca_{3z}O_4) + 51CO_2 + 3H_2O + 18HF$

6.2.2. Characterization of compounds

After thermal treatment, the resulting products were characterized by CHN elemental analysis to confirm the absence of any organic species in the resulting solids, which were additionally characterized with the use of SEM, TEM, PXRD, and EDS.

Field emission SEM images show that the MOF crystals morphology is maintained in the resulting oxides after the heating process (appendices). This phenomenon has been previously reported.[9] The resulting solids are composed of crystallites of size in the range 30 to 2 μm, which are aggregated preserving the shape of the precursor MOF crystal (Figure 6.2). The SEM-EDS (appendices) and TEM-EDS (appendices) analyses present consistent results and demonstrate a clear correspondence between the metal ratios in the aggregates and the individual particles (figure 6.3).

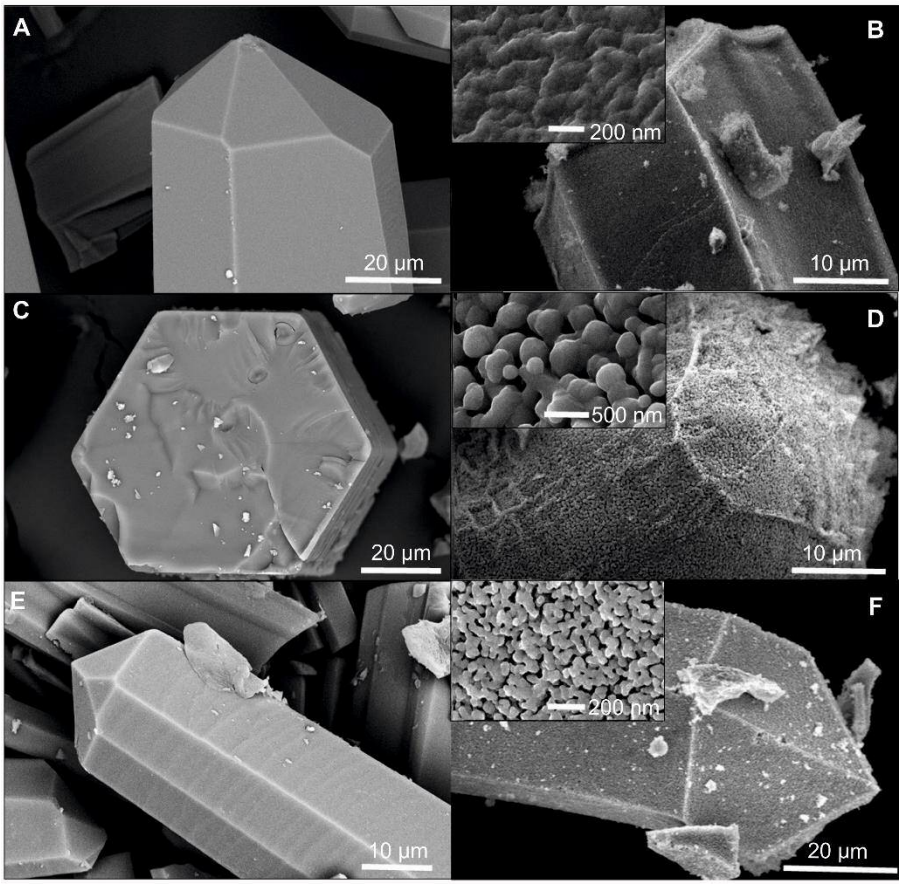

Figure 6. 2. The figure shows MOF-crystal SEM pictures in the left column, and FESEM images of the corresponding calcined product, and its magnification images (x200,000), in the right column. A) $Zn_{0.17}Mn_{0.45}Co_{0.38}$(hfipbb) crystal SEM image; B) FESEM picture of corresponding calcined product with formula $Zn_{0.51}Mn_{1.35}Co_{1.14}O_4$; C) $Mn_{0.23}Co_{0.50}Ca_{0.27}$(hfipbb) crystal SEM image; D) FESEM picture of $Mn_{0.23}Co_{0.50}Ca_{0.27}$(hfipbb) calcined product resulting in a cubic spinel with formula $Mn_{0.69}Co_{1.50}Ca_{0.81}O_4$; E) $Zn_{0.16}Mn_{0.47}Co_{0.33}Ca_{0.03}$(hfipbb) crystal SEM image; F) FESEM picture of calcined product of $Zn_{0.16}Mn_{0.47}Co_{0.33}Ca_{0.03}$(hfipbb) resulting in a cubic spinel with formula $Zn_{0.48}Mn_{1.41}Co_{0.99}Ca_{0.09}O_4$.

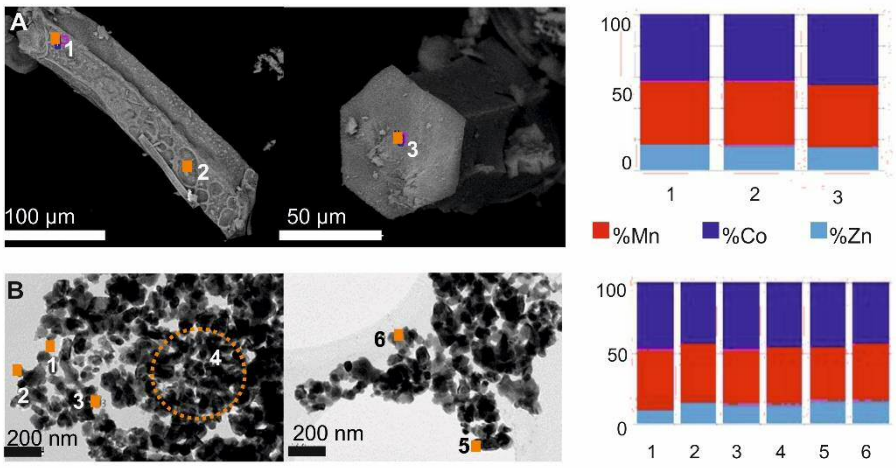

Figure 6. 3. A) SEM-EDS analyses and B) TEM-EDS analyses from $Zn_{0.36}Mn_{1.26}Co_{1.38}O_4$ spinel. Orange spots indicate the areas where EDS were performed. Plot (right) shows the metal ratios by EDS analyses, where each column corresponds to the area indicated by a number in the SEM pictures.

6.3. Discussion of the Thermal Treatment

After exposing the MOFs to a calcination process, the structure type of the resulting oxides was analyzed with the use of PXRD (appendices). Results of the obtained oxides are summarized in table 6.1.

For the sake of comparison, we also studied the MOF prepared with zinc as only metal cation (ZnPF-1).[10] As expected, calcination of ZnPF-1 resulted in the formation of wurtzite type oxide, according to the PXRD pattern (figure 6.4).

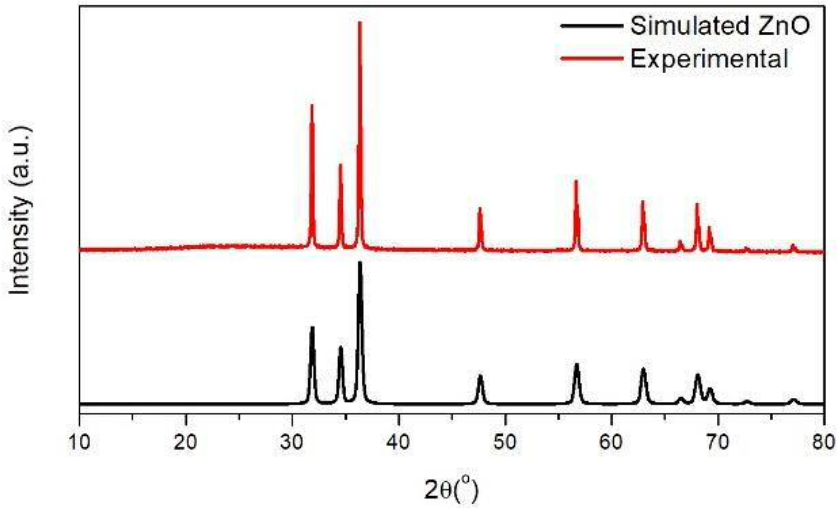

Figure 6. 4. Comparison between the experimental pattern of ZnPF-1 thermal treatment product and the calculated from ZnO (wurtzite).

6.3.1. Binary Zn:Co, Zn:Mn, and Zn:Ca systems

Binary systems consisting of zinc and cobalt resulted in a mixture of crystalline phases. XRPD patterns of $Zn_{0.89}Co_{0.11}$(hfipbb), $Zn_{0.59}Co_{0.51}$(hfipbb) and $Zn_{0.55}Co_{0.45}$(hfipbb) thermal treatment products, with molar codes Zn:Co 1:1, 1:2 and 1:4, respectively, show a mixture of wurtzite, identified as major phase, and spinel type oxide. However, calcination of the MOF formed from Zn:Co 1:10 molar code and formula $Zn_{0.21}Co_{0.79}$(hfipbb), results in the formation of cubic spinel oxide as major phase, although with presence of trazes of wurtzite (figure 6.5).

Entry	Molar Code				MOF formula	Thermal treatment product
	Zn	Mn	Co	Ca		
1	1	0	0	0	Zn(hfipbb)	Wurzite
2	1	0	1	0	$Zn_{0.89}Co_{0.11}$(hfipbb)	Wurzite + Spinel (minor)
3	1	0	2	0	$Zn_{0.59}Co_{0.41}$(hfipbb)	Wurzite + Spinel (minor)
4	1	0	4	0	$Zn_{0.55}Co_{0.45}$(hfipbb)	Wurzite + Spinel (minor)
5	1	0	10	0	$Zn_{0.21}Co_{0.79}$(hfipbb)	Spinel + Wurtzite (minor)
6	1	1	0	0	$Zn_{0.50}Mn_{0.50}$(hfipbb)	Spinel + Hetaerolite
7	1	1	1	0	$Zn_{0.44}Mn_{0.44}Co_{0.12}$(hfipbb)	Spinel + Unknown + Wurtzite
8	2	1	1	0	$Zn_{0.54}Mn_{0.37}Co_{0.09}$(hfipbb)	Wurzite + Spinel
9	1	2	1	0	$Zn_{0.37}Mn_{0.50}Co_{0.13}$(hfipbb)	Spinel + Hydrohetareollite + Unknown
10	1	1	2	0	$Zn_{0.32}Mn_{0.40}Co_{0.28}$(hfipbb)	Wurzite + Spinel
11	1	1	8	0	$Zn_{0.22}Mn_{0.32}Co_{0.46}$(hfipbb)	Multimetallic Spinel
12	1	3	9	0	$Zn_{0.12}Mn_{0.42}Co_{0.46}$(hfipbb)	Multimetallic Spinel
13	1	4	4	0	$Zn_{0.23}Mn_{0.44}Co_{0.33}$(hfipbb)	Multimetallic Spinel
14	1	4	6	0	$Zn_{0.17}Mn_{0.41}Co_{0.42}$(hfipbb)	Multimetallic Spinel
15	1	6	12	0	$Zn_{0.12}Mn_{0.39}Co_{0.49}$(hfipbb)	Multimetallic Spinel
16	1	10	20	0	$Zn_{0.10}Mn_{0.40}Co_{0.50}$(hfipbb)	Multimetallic Spinel
17	1	12	6	0	$Zn_{0.17}Mn_{0.45}Co_{0.38}$(hfipbb)	Multimetallic Spinel
18	1	1	0	1	$Zn_{0.48}Mn_{0.42}Co_{0.10}$(hfipbb)	Spinel + Wurzite + Unknown
19	1	1	0	8	$Zn_{0.52}Mn_{0.30}Co_{0.18}$(hfipbb)	Wurzite + Spinel + Unknown
20	1	1	1	1	$Zn_{0.42}Mn_{0.42}Co_{0.11}Ca_{0.06}$(hfipbb)	Multimetallic Spinel
21	1	1	7	1	$Zn_{0.13}Mn_{0.27}Co_{0.52}Ca_{0.03}$(hfipbb)	Multimetallic Spinel
22	1	1	1	7	$Zn_{0.37}Mn_{0.28}Co_{0.13}Ca_{0.22}$(hfipbb)	Spinel+ Wurzite + Unknown
23	1	4	4	1	$Zn_{0.16}Mn_{0.47}Co_{0.33}Ca_{0.03}$(hfipbb)	Multimetallic Spinel
24	1	1	4	4	$Zn_{0.18}Mn_{0.24}Co_{0.41}Ca_{0.16}$(hfipbb)	Multimetallic Spinel
25	1	4	4	4	$Zn_{0.24}Mn_{0.37}Co_{0.31}Ca_{0.08}$(hfipbb)	Multimetallic Spinel
26	1	4	1	4	$Zn_{0.32}Mn_{0.40}Co_{0.15}Ca_{0.12}$(hfipbb)	Multimetallic Spinel
27	2	1	2	2	$Zn_{0.46}Mn_{0.34}Co_{0.17}Ca_{0.15}$(hfipbb)	Spinel+Wurzite + Unknown
28	1	2	2	4	$Zn_{0.27}Mn_{0.34}Co_{0.26}Ca_{0.12}$(hfipbb)	Multimetallic Spinel
29	1	4	4	8	$Zn_{0.21}Mn_{0.27}Co_{0.30}Ca_{0.22}$(hfipbb)	Multimetallic Spinel
30	1	1	4	8	$Zn_{0.26}Mn_{0.16}Co_{0.37}Ca_{0.21}$(hfipbb)	Spinel + Wurzite
31	0	1	1	0	$Mn_{0.41}Co_{0.59}$(hfipbb)	Multimetallic Spinel
32	0	1	2	2	$Mn_{0.23}Co_{0.50}Ca_{0.27}$(hfipbb)	Multimetallic Spinel
33	1	0	0	4	$Zn_{0.64}Ca_{0.36}$(hfipbb)	Wurzite + Fluorite
34	1	0	0	10	$Zn_{0.48}Ca_{0.52}$(hfipbb)	Wurzite + Fluorite

Table 6. 1. Summary of MOF thermal treatment products with their corresponding initial molar code.

TEM and EDS analyses of this solid indicate that the formed oxide particles do not have a homogeneous composition. This is not surprising, as the parent MOF crystals exhibited a clear compositional gradient, with internal and external areas being rich in zinc or cobalt, respectively (figure 6.6).

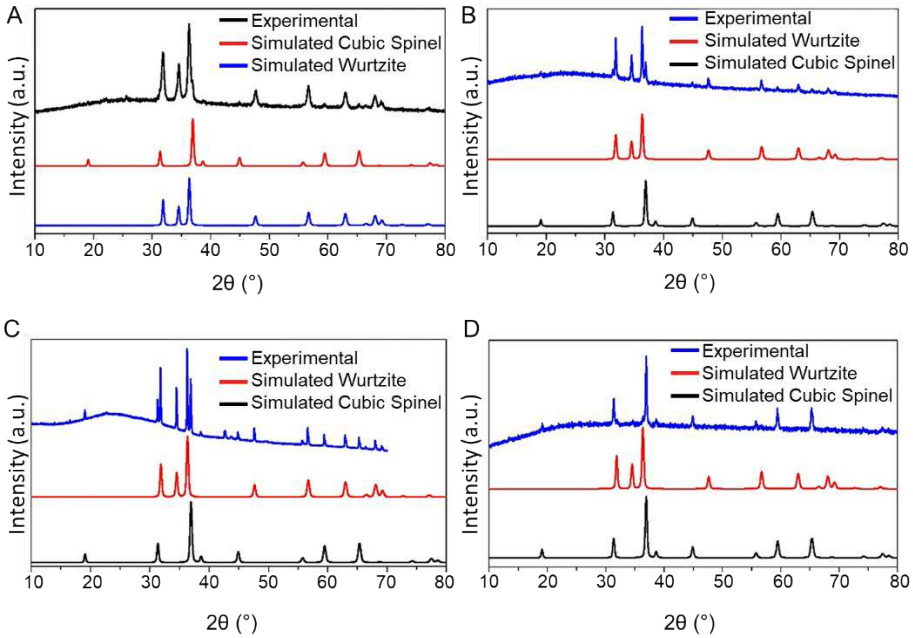

Figure 6. 5. Normalized powder XRD patterns of thermal treatment products from: A) $Zn_{0.89}Co_{0.11}$(hfipbb), B) $Zn_{0.59}Co_{0.41}$(hfipbb), C) $Zn_{0.55}Co_{0.45}$(hfipbb) and D) $Zn_{0.21}Co_{0.79}$(hfipbb) and their comparison with the calculated form the corresponding oxides.

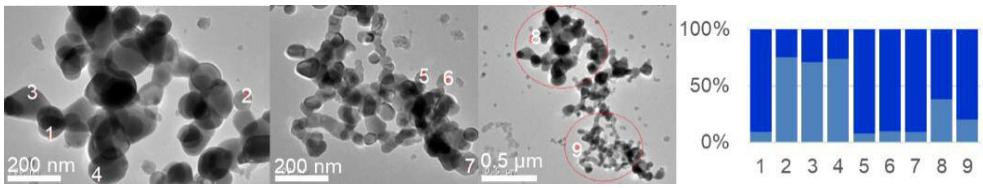

Figure 6. 6. TEM-EDS analyses from thermal treatment product of $Zn_{0.59}Co_{0.41}$(hfipbb). The numbers indicate the areas where EDS were performed. Plot (right) shows the metal ratios by EDS analyses, where each column corresponds to the area indicated by a number in the TEM pictures where %Zn (light blue) and %Co (dark blue).

Similarly, calcination of binary systems composed of zinc and calcium also resulted in formation of wurtzite oxide, and in the cases where there is a larger amount of calcium in the MOF, the presence of fluorite was also detected (figure 6.7). This occurs in samples prepared from Zn:Ca 1:4 and 1:10 molar codes with formulae $Zn_{0.64}Ca_{0.36}$(hfipbb) or $Zn_{0.52}Ca_{0.48}$(hfipbb), respectively.

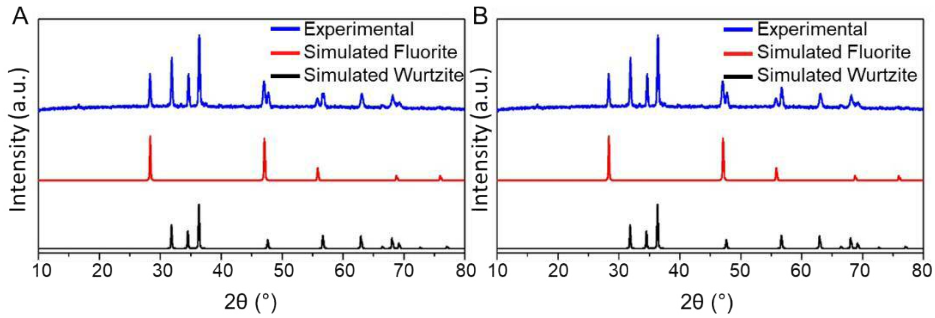

Figure 6. 7. Normalized powder XRD patterns of thermal treatment products from: A) $Zn_{0.64}Ca_{0.36}$(hfipbb) and B) $Zn_{0.52}Ca_{0.48}$(hfipbb) and their comparison with the calculated form the corresponding mixture of oxides.

TEM-EDS analyses show a mixture of particles calcium-rich or zinc-rich, which corroborates the mixture of phases, as can be seen in figure 6.8.

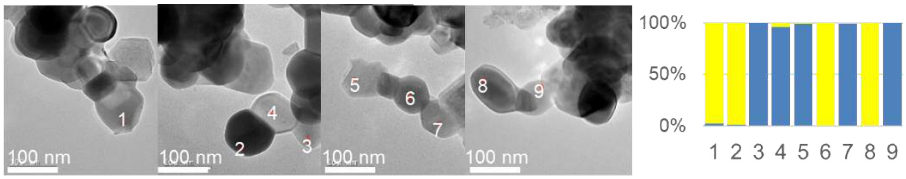

Figure 6. 8. TEM-EDS analyses from thermal treatment product of $Zn_{0.64}Co_{0.36}$(hfipbb). The numbers indicate the areas where EDS were performed. Plot (right) shows the metal ratios by EDS analyses, where each column corresponds to the area indicated by a number in the TEM pictures where %Zn (blue) and %Ca (yellow).

Calcination of the MOF formed from Zn:Mn 1:1 molar code resulted in a mixture of phases containing hetaerolite (tetragonal) and spinel (cubic) type oxides as major phases, as well as traces of other crystalline phases that could not be unambiguously identified (figure 6.9).

Entry	Molar Code				MOF formula	Spinel formula
	Zn	Mn	Co	Ca		
1	1	1	8	0	$Zn_{0.22}Mn_{0.32}Co_{0.46}$(hfipbb)	$Zn_{0.66}Mn_{0.96}Co_{1.38}O_4$
2	1	3	9	0	$Zn_{0.12}Mn_{0.42}Co_{0.46}$(hfipbb)	$Zn_{0.36}Mn_{1.26}Co_{1.38}O_4$
3	1	4	4	0	$Zn_{0.23}Mn_{0.44}Co_{0.33}$(hfipbb)	$Zn_{0.69}Mn_{1.32}Co_{0.99}O_4$
4	1	4	6	0	$Zn_{0.17}Mn_{0.41}Co_{0.42}$(hfipbb)	$Zn_{0.51}Mn_{1.23}Co_{1.26}O_4$
5	1	6	12	0	$Zn_{0.12}Mn_{0.39}Co_{0.49}$(hfipbb)	$Zn_{0.36}Mn_{1.17}Co_{1.47}O_4$
6	1	10	20	0	$Zn_{0.10}Mn_{0.40}Co_{0.50}$(hfipbb)	$Zn_{0.30}Mn_{1.20}Co_{1.50}O_4$
7	1	12	6	0	$Zn_{0.17}Mn_{0.45}Co_{0.38}$(hfipbb)	$Zn_{0.51}Mn_{1.35}Co_{1.14}O_4$
8	1	1	1	1	$Zn_{0.42}Mn_{0.42}Co_{0.11}Ca_{0.06}$(hfipbb)	$Zn_{1.26}Mn_{1.26}Co_{0.33}Ca_{0.18}O_4$
9	1	1	7	1	$Zn_{0.13}Mn_{0.27}Co_{0.52}Ca_{0.03}$(hfipbb)	$Zn_{0.39}Mn_{0.81}Co_{1.56}Ca_{0.09}O_4$
10	1	4	4	1	$Zn_{0.16}Mn_{0.47}Co_{0.33}Ca_{0.03}$(hfipbb)	$Zn_{0.48}Mn_{1.41}Co_{0.99}Ca_{0.09}O_4$
11	1	1	4	4	$Zn_{0.18}Mn_{0.24}Co_{0.41}Ca_{0.16}$(hfipbb)	$Zn_{0.54}Mn_{0.72}Co_{1.23}Ca_{0.48}O_4$
12	1	4	4	4	$Zn_{0.24}Mn_{0.37}Co_{0.31}Ca_{0.08}$(hfipbb)	$Zn_{0.72}Mn_{1.11}Co_{0.93}Ca_{0.24}O_4$
13	1	4	1	4	$Zn_{0.32}Mn_{0.40}Co_{0.15}Ca_{0.12}$(hfipbb)	$Zn_{0.96}Mn_{1.20}Co_{0.45}Ca_{0.36}O_4$
14	1	2	2	4	$Zn_{0.27}Mn_{0.34}Co_{0.26}Ca_{0.12}$(hfipbb)	$Zn_{0.81}Mn_{1.02}Co_{0.78}Ca_{0.36}O_4$
15	1	4	4	8	$Zn_{0.21}Mn_{0.27}Co_{0.30}Ca_{0.22}$(hfipbb)	$Zn_{0.63}Mn_{0.81}Co_{0.90}Ca_{0.66}O_4$
16	0	1	1	0	$Mn_{0.41}Co_{0.59}$(hfipbb)	$Mn_{1.23}Co_{1.77}O_4$
17	0	1	2	2	$Mn_{0.23}Co_{0.50}Ca_{0.27}$(hfipbb)	$Mn_{0.69}Co_{1.50}Ca_{0.81}O_4$

Table 6. 2. The starting molar codes, corresponding MOFs and spinel formula are shown in columns 2, 3 and 4, respectively.

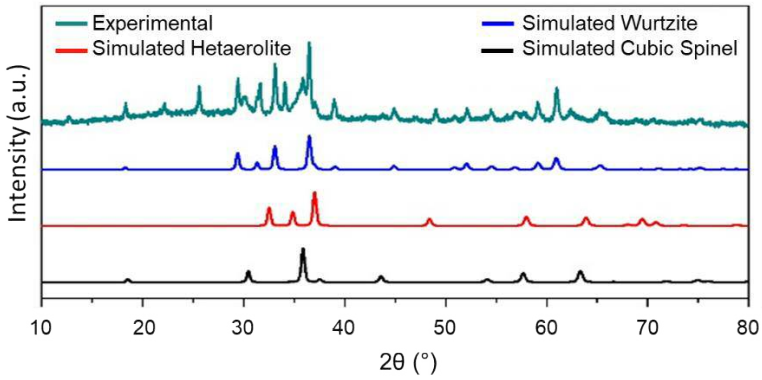

Figure 6. 9. Normalized powder XRD patterns of thermal treatment products from $Zn_{0.50}Mn_{0.50}$(hfipbb) and their comparison with the calculated form the corresponding mixture of oxides.

6.3.2. Ternary Zn:Mn:Co, Zn:Mn:Ca, Mn:Co:Ca systems

On the other hand, the calcination of ternary multi-metal MOFs including zinc, manganese, and cobalt, resulted in the formation of spinel type oxides. When the initial MOF Zn molar

ratio was higher than 30 at%, other crystalline phases were also detected in the PXRD patterns, (mainly wurtzite) (figure 6.10). By decreasing the amount of zinc in ternary multi-metal MOFs, we were able to obtain spinel type oxides as only product of the calcination process, as proved by the PXRD, SEM and TEM analyses. Thus, seven new multi-metal oxides with cubic spinel structure were prepared from the calcination of the corresponding multi-metal MOFs (figure 6.11 and appendices). Their compositions are detailed in table 6.2, entries 1-7. According to TEM-EDS analyses (figure 6.12 and appendices), these new multi-metal spinel oxides are composed of particles with homogeneous composition of metal cations.

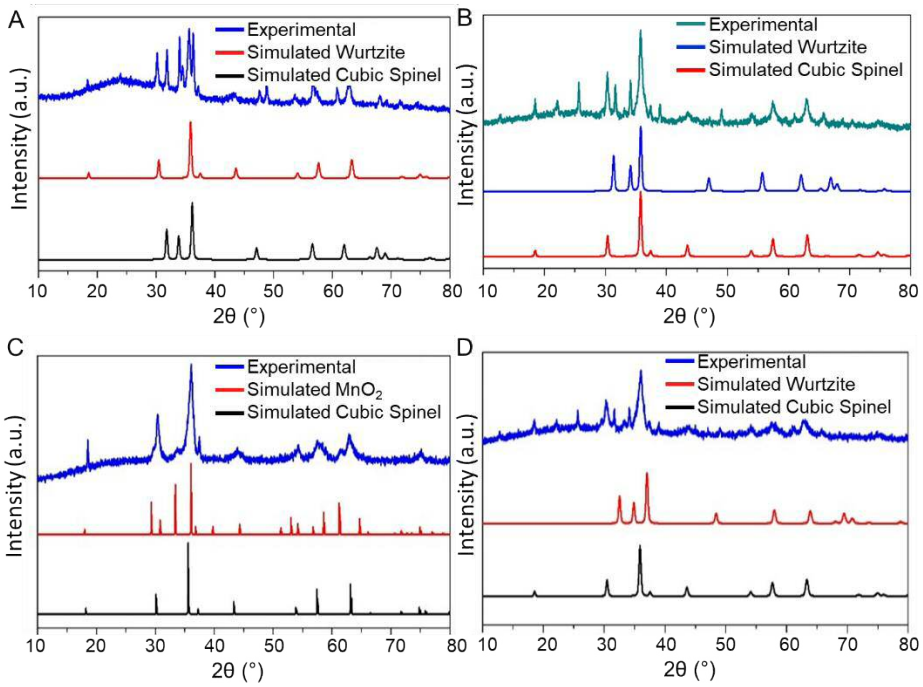

Figure 6. 10. Normalized powder XRD patterns of thermal treatment products from: A) $Zn_{0.44}Mn_{0.44}Co_{0.12}$(hfipbb), B) $Zn_{0.54}Mn_{0.37}Co_{0.09}$(hfipbb), C) $Zn_{0.37}Mn_{0.50}Co_{0.13}$(hfipbb) and D) $Zn_{0.32}Mn_{0.40}Co_{0.28}$(hfipbb) and their comparison with the calculated form the corresponding mixture of oxides.

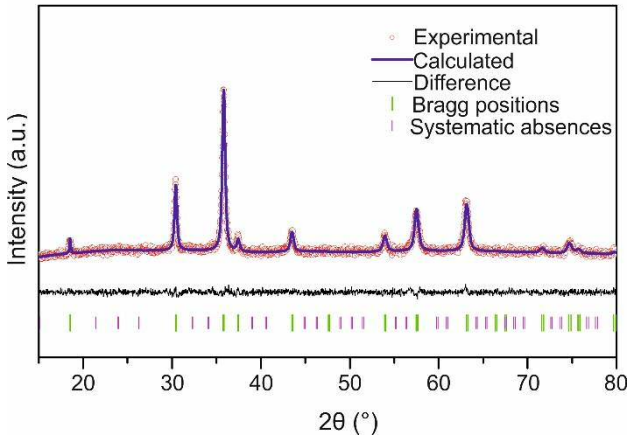

Figure 6. 11. Full pattern profile refinement plot of $Zn_{0.51}Mn_{1.35}Co_{1.14}O_4$ spinel with Fd-3m space group (a = 8.260 Å) obtained from $Zn_{0.17}Mn_{0.45}Co_{0.38}$(hfipbb) MOF.

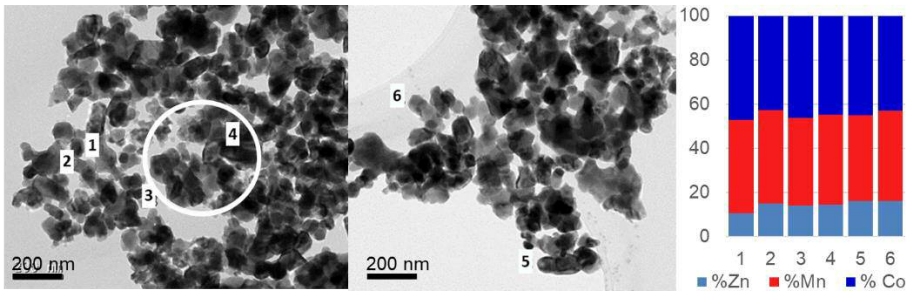

Figure 6. 12. TEM-EDS analyses from thermal treatment product of $Zn_{0.12}Mn_{0.42}Co_{0.46}$(hfipbb) ($Zn_{0.36}Mn_{1.23}Co_{1.38}O_4$ spinel). The numbers indicate the areas where EDS were performed. Plot (right) shows the metal ratios by EDS analyses, where each column corresponds to the area indicated by a number in the TEM pictures

In the case of ternary multi-metal MOFs prepared from molar codes including zinc, manganese, and calcium, spinel oxides were also formed, but mixed with wurtzite and to less extent with other crystalline phases that could not be unambiguously identified. However, calcination of the MOF prepared from a molar code Mn:Co:Ca 1:2:2 also resulted in the obtaining of spinel type oxide as only phase (figure 6.13). In this case, as deduced from the experimentally determined formula of $Mn_{0.69}Co_{1.50}Ca_{0.81}O_4$, an inverse spinel should be formed, with cobalt atoms occupying tetrahedral sites, and manganese and calcium atoms the octahedral sites.

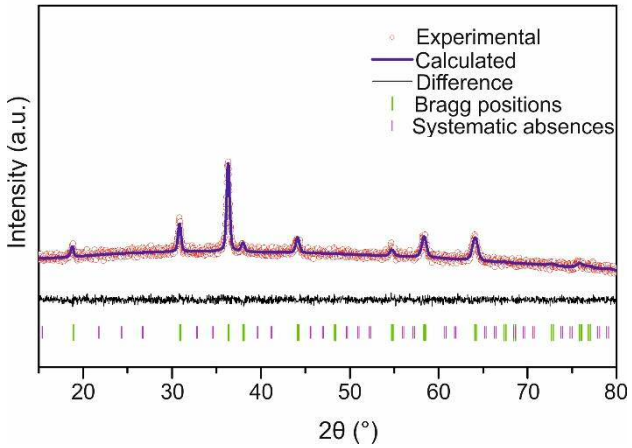

Figure 6. 13. Full pattern profile refinement plot of $Mn_{0.69}Co_{1.50}Ca_{0.81}O_4$ spinel with Fd-3m space group (a = 8.211 Å) obtained from $Mn_{0.23}Co_{0.50}Ca_{0.27}$(hfipbb) MOF.

6.3.3. Quaternary Zn:Mn:Co:Ca systems

Multi-metal spinel oxides containing four elements were readily obtained by calcination of the selected quaternary multi-metal MOFs. Thus, calcination of the MOF with composition $Zn_{0.42}Mn_{0.42}Co_{0.11}Ca_{0.06}$(hfipbb) results in the obtaining of an oxide with cubic spinel structure (figure 6.14) and formula $Zn_{1.26}Mn_{1.26}Co_{0.33}Ca_{0.18}O_4$, as determined by ICP analysis. This is the first time that spinel oxides containing Zn, Mn, Co, and Ca in their structure, as confirmed by the TEM-EDS analyses (figure 6.15), are reported. Most importantly, different metal combinations initially programmed in the selected quaternary multi-metal MOFs could be translated to the spinel oxides (appendices). Thus, a series of eight tetra-cation spinel oxides with variable composition and general formula $\mathbf{Zn_wMn_xCo_yCa_zO_4}$ have been obtained (table 6.2, entries 8-15), where 0.39<w<1.26, 0.72<x<1.26, 0.33<y<1.56, and 0.09<z<0.66.

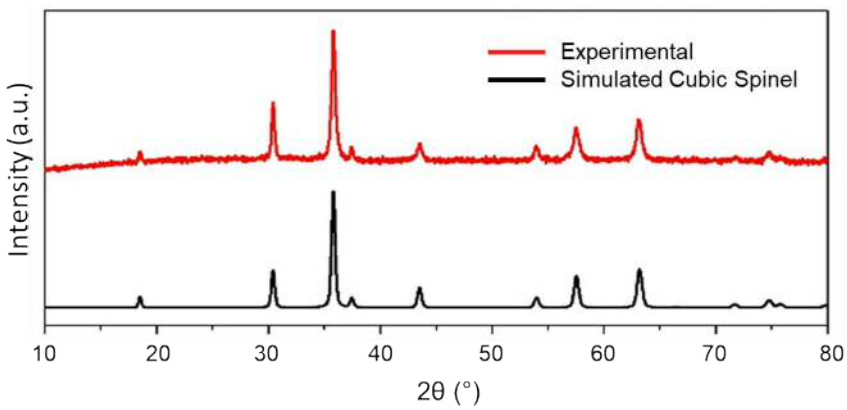

Figure 6. 14. Normalized powder XRD patterns of thermal treatment products from $Zn_{0.42}Mn_{0.42}Co_{0.11}Ca_{0.06}$(hfipbb) and their comparison with the calculated cubic spinel oxide.

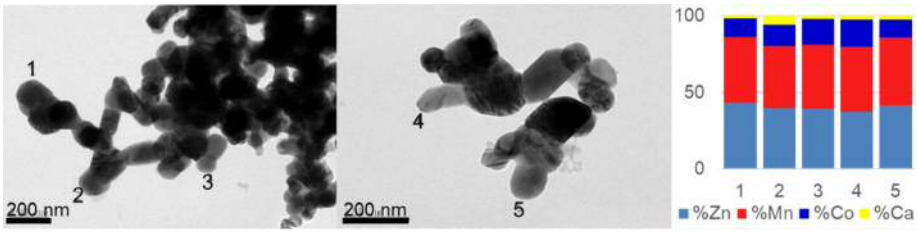

Figure 6. 15. TEM-EDS analyses from thermal treatment product of $Zn_{0.42}Mn_{0.42}Co_{0.11}Ca_{0.06}$(hfipbb) ($Zn_{1.26}Mn_{1.26}Co_{0.33}Ca_{0.18}O_4$ spinel). The numbers indicate the areas where EDS were performed. Plot (right) shows the metal ratios by EDS analyses, where each column corresponds to the area indicated by a number in the TEM pictures.

However, it should be noted that certain limitations for the obtaining of spinel as sole phase where observed regarding the combination of metal elements in the selected MOF. Thus, for MOFs with a low content of manganese, as in the case of the material prepared from molar code Zn:Mn:Co:Ca 1:1:4:8, presence of wurtzite and other crystal phases were detected in the PXRD pattern of the calcined solid, along with the spinel oxide (table 6.1, entry 30 and figure 6.16.A). Conversely, when starting from a MOF with a large amount of zinc in the molar code (Zn:Mn:Co:Ca 2:1:2:2), wurtzite and another unknown phase were formed along with the spinel oxide (table 6.1, entry 27 and figure 6.16.B). Interestingly, the maximum amount of zinc allowed for the obtaining of pure spinel oxides avoiding the appearance of wurtzite is larger in quaternary multi-metal MOFs than in ternary systems, demonstrating the importance of the initial cation arrangement of the MOF precursor on the structure of the obtained oxides. Nevertheless, we emphasize the suitability and wide applicability of this process to prepare a

range of spinel type oxides with novel, desired compositions, easily translated from MOFs with programmable cation arrangements, with a simple calcination process.

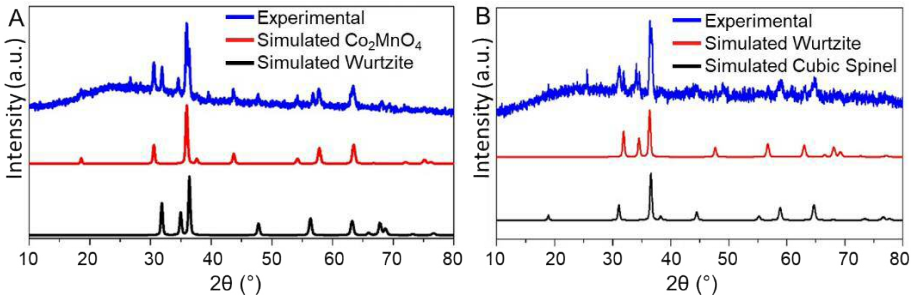

Figure 6. 16. Normalized powder XRD patterns of thermal treatment products from: A) $Zn_{0.46}Mn_{0.34}Co_{0.17}Ca_{0.15}$(hfipbb) and $Zn_{0.26}Mn_{0.16}Co_{0.37}Ca_{0.21}$(hfipbb) and their comparison with the calculated form the corresponding mixture of oxides.

6.4. Evaluation of Multi-Metal Spinel Oxides as ORR Electrocatalysts.

6.4.1. Introduction

The oxygen reduction reaction (ORR) is a series of electrochemical reactions proposed to involve multistep electron transfer processes and oxygen-containing species. This reaction transforms O_2 to H_2O or OH^-. ORR is a vital process of fuel cells and metal-air batteries, determining their work efficiency.

Typically, the reaction occurs via two different ways, in one step known as the 4-electron reaction or in two steps with 2-plus-2 electrons per reactions (see figure 6.17).[11-12]

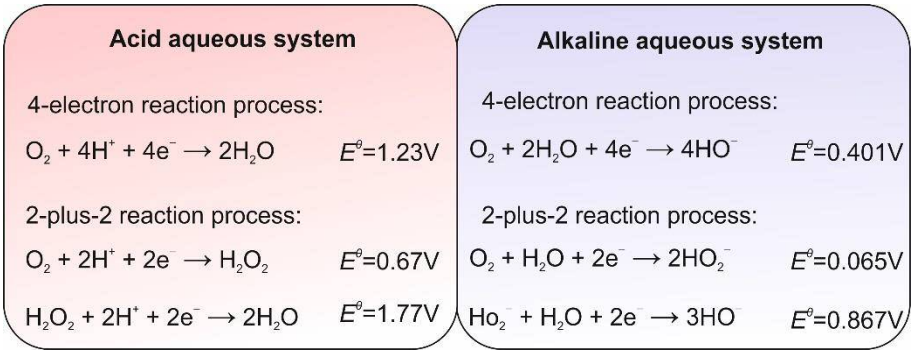

Figure 6. 17. Summary of the reactions involved in the oxygen reduction reaction in different reaction media and by different routes.

Usually, the 4-electron process involves the direct dissociation of an O−O bond, which requires more energy than the dissociation of H_2O_2 or HO_2^- (2-plus-2 electron reaction). This indicates that the 2-plus-2 reaction is more feasible, while the direct 4-electron process is more effective without the generation the byproduct of HO_2^-. In addition, peroxide species are corrosive and can cause premature degradation of the electrochemical cell.[13]

Current benchmark catalysts for the ORR are based on the use of platinum, but metal scarcity, its high cost and inherent deactivation problems have fostered an intensive search for alternatives. As a result, a wide spectrum of materials such as transition metal-/metal oxide nanoparticles,[14] perovskites,[15] spinels and heteroatom doped 3D and 2D carbonaceous materials[16] are being analyzed as substituting candidates. Among them, transition metal spinels

show not only an affordable cost but also the most promising performance as both ORR and OER electrocatalysts.[17] Among the list of transition metals employed, spinel materials based on Mn, Co, Fe and Ni have been widely studied due to their outstanding performance, which is strongly dependent on subtle changes in composition. For example, it has been proposed that in $Mn_xCo_{3-x}O_4$ spinel oxides, the activity improves when $x \leq 2.0$ because Co^{3+} and Mn^{3+} cations present an internal redox reaction that generates Co^{2+} and Mn^{4+} pairs, responsible for an increase in conductivity.[18]

Recently, the use of bimetallic Mn-Co MOFs to obtain multimetal-spinel oxides has been reported. However, other crystal phases might appear during the thermal treatment.[19] In addition, when the spinels have been obtained as pure phases, differences in the structure were found depending on the amount of manganese and cobalt present, finding that mixed $Mn_xCo_{3-x}O_4$ spinels with a high content of manganese have a tetragonal structure (space group *I4-2m*) while spinels rich in Co are cubic (space group *Fd-3m*).[20] Zn-Co multimetal MOFs have been used also to obtain cubic Zn-Co spinel oxides.[21]

6.4.2. ORR results

Following our methodology to translate compositional complexity from multi-metal MOFs to oxides, we have evaluated seventeen tri- and tetra-metallic spinel oxides with unprecedented compositions as electrocatalysts for ORR. First, we investigated the electrochemical activity of the samples towards the ORR by running cyclic voltammetry in both O_2 and N_2 saturated electrolyte solutions. In all cases CV curves in N_2 saturated electrolyte showed a quasi-rectangular shape without any redox peak indicating the good stability of the materials in the studied potential window. Interestingly, voltammograms of all the samples in O_2-saturated electrolyte exhibited a clear cathodic peak centered between 0.3 and 0.42V probing the electrocatalytical activity of the samples (figures 7.19 and appedices). Even though all multi-metal spinel oxides show activity towards the ORR, they present a relatively large overpotential of 200-290 mV, as compared to that of the commercial Pt/C catalyst. One approach to decrease the overpotential of a specific reaction is to load the active material in a more conductive support (e.g., carbon nanotubes, graphene).[22-26] In the present study, samples were evaluated after being mixed with active carbon and Nafion as a binder. However, given

no strong coupling between the carbon and the active material (in this case the MOF derived spinel) no major change in the local electron transfer was expected and thus, the overpotential was still large.[22]

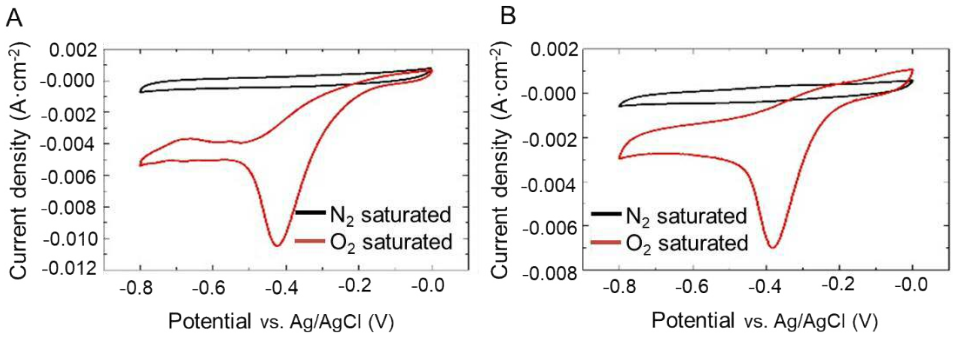

Figure 6. 18. Cyclic voltammetry of multimetal spinels in N_2 saturated 0.1M KOH (black curve) and O_2 saturated 0.1M KOH (red curve). A) $Zn_{0.69}Mn_{1.32}Co_{0.99}O_4$; B) $Zn_{0.39}Mn_{0.81}Co_{1.56}Ca_{0.09}O_4$.

Koutecky-Levich (K-L) plots obtained from the correspondent LSVs at different rotation speeds present a good linearity, indicating that current was mainly kinetically controlled (figures 7.20 and appendices). Table 6.3 summarizes the number of transferred electrons (Ne^-, obtained from the K-L analysis), and the current density of each sample expressed as % of current density measured for commercial Pt/C(20%w).

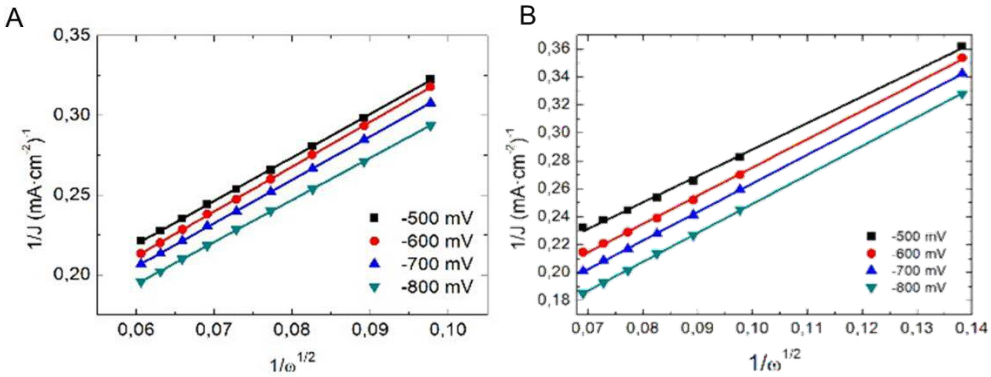

Figure 6. 19. Koutecky-Levich plots of multimetal spinels at different potentials (-500, -600, -700 and -800 mV).A); $Zn_{0.66}Mn_{0.96}Co_{1.38}O_4$ B) $Zn_{0.72}Mn_{1.11}Co_{0.93}Ca_{0.24}O_4$.

Entry	Molar Code				MOF formula	Spinel formula	Ne^-	Current density (%)
	Zn	Mn	Co	Ca				
1	1	1	8	0	$Zn_{0.22}Mn_{0.32}Co_{0.46}$(hfipbb)	$Zn_{0.66}Mn_{0.96}Co_{1.38}O_4$	2.88	67.9
2	1	3	9	0	$Zn_{0.12}Mn_{0.42}Co_{0.46}$(hfipbb)	$Zn_{0.36}Mn_{1.26}Co_{1.38}O_4$	3.81	73.8
3	1	4	4	0	$Zn_{0.23}Mn_{0.44}Co_{0.33}$(hfipbb)	$Zn_{0.69}Mn_{1.32}Co_{0.99}O_4$	3.03	70.6
4	1	4	6	0	$Zn_{0.17}Mn_{0.41}Co_{0.42}$(hfipbb)	$Zn_{0.51}Mn_{1.23}Co_{1.26}O_4$	3.09	71.7
5	1	6	12	0	$Zn_{0.12}Mn_{0.39}Co_{0.49}$(hfipbb)	$Zn_{0.36}Mn_{1.17}Co_{1.47}O_4$	3.06	63.4
6	1	10	20	0	$Zn_{0.10}Mn_{0.40}Co_{0.50}$(hfipbb)	$Zn_{0.30}Mn_{1.20}Co_{1.50}O_4$	3.56	86.6
7	1	12	6	0	$Zn_{0.17}Mn_{0.45}Co_{0.38}$(hfipbb)	$Zn_{0.51}Mn_{1.35}Co_{1.14}O_4$	3.80	91.4
8	1	1	1	1	$Zn_{0.42}Mn_{0.42}Co_{0.11}Ca_{0.06}$(hfipbb)	$Zn_{1.26}Mn_{1.26}Co_{0.33}Ca_{0.18}O_4$	3.10	102.3
9	1	1	7	1	$Zn_{0.13}Mn_{0.27}Co_{0.52}Ca_{0.03}$(hfipbb)	$Zn_{0.39}Mn_{0.81}Co_{1.56}Ca_{0.09}O_4$	3.64	73.4
10	1	4	4	1	$Zn_{0.16}Mn_{0.47}Co_{0.33}Ca_{0.03}$(hfipbb)	$Zn_{0.48}Mn_{1.41}Co_{0.99}Ca_{0.09}O_4$	3.92	97.2
11	1	1	4	4	$Zn_{0.18}Mn_{0.24}Co_{0.41}Ca_{0.16}$(hfipbb)	$Zn_{0.54}Mn_{0.72}Co_{1.23}Ca_{0.48}O_4$	2.76	65.6
12	1	4	4	4	$Zn_{0.24}Mn_{0.37}Co_{0.31}Ca_{0.08}$(hfipbb)	$Zn_{0.72}Mn_{1.11}Co_{0.93}Ca_{0.24}O_4$	3.91	79.9
13	1	4	1	4	$Zn_{0.32}Mn_{0.40}Co_{0.15}Ca_{0.12}$(hfipbb)	$Zn_{0.96}Mn_{1.20}Co_{0.45}Ca_{0.36}O_4$	3.06	80.3
14	1	2	2	4	$Zn_{0.27}Mn_{0.34}Co_{0.26}Ca_{0.12}$(hfipbb)	$Zn_{0.81}Mn_{1.02}Co_{0.78}Ca_{0.36}O_4$	3.41	72.9
15	1	4	4	8	$Zn_{0.21}Mn_{0.27}Co_{0.30}Ca_{0.22}$(hfipbb)	$Zn_{0.63}Mn_{0.81}Co_{0.90}Ca_{0.66}O_4$	2.72	67.9
16	0	1	1	0	$Mn_{0.41}Co_{0.59}$(hfipbb)	$Mn_{1.23}Co_{1.77}O_4$	3.22	75.7
17	0	1	2	2	$Mn_{0.23}Co_{0.50}Ca_{0.27}$(hfipbb)	$Mn_{0.69}Co_{1.50}Ca_{0.81}O_4$	3.82	87.2
18	Pt/C(20%W)						3.67	100

Table 6. 3. The starting molar codes, corresponding MOFs, spinel formula, electron tranfer number (Ne), calculated from the slope of their Koutechy-Levich plot in ORR, and current density are shown in columns 2, 3, 4, 5, and 6, respectively.

The systematic translation of compositional complexity from multi-metal MOFs to oxides allows extracting important information when the elements on the catalytic performance. A simple correlation between composition variation and activity is not evident, and rather a complex behavior is observed. Recently,[23] a correlation between the Mn/Co ratio and electrocatalytic activity due to superexchange effects between the octahedral sites has been reported for Zn:Co:Mn spinels where the tetrahedral sites are occupied by zinc. In our case, the tetrahedral sites are occupied not only by zinc, due to the sample metal ratios, and thus other effects should also influence the catalytic activity. Therefore, analysis of Zn-Co-Mn spinels, including solids with $Zn_{0.36}Mn_{1.26}Co_{1.38}O_4$, $Zn_{0.66}Mn_{0.96}Co_{1.38}O_4$, $Zn_{0.69}Mn_{1.32}Co_{0.99}O_4$, $Zn_{0.51}Mn_{1.23}Co_{1.26}O_4$, $Zn_{0.36}Mn_{1.17}Co_{1.47}O_4$, $Zn_{0.30}Mn_{1.20}Co_{1.50}O_4$ and $Zn_{0.51}Mn_{1.35}Co_{1.14}O_4$ composition (Table 6.3 entries 1 to 7), evidences a strong influence of the ratios of all three different metals: Zn, Mn and Co. Nevertheless, we have found that samples containing the three metal elements (*i.e.*, Zn, Mn and Co) also exhibited a major contribution of the 4 e^-

transfer mechanism and larger current densities (see Figure 6.21). Among the evaluated samples, the oxide with $Zn_{0.51}Mn_{1.35}Co_{1.14}O_4$ composition (table 1, entry 7) demonstrated the best performance, with a high limiting current density value (91.4% of that found for commercial Pt based catalysts) and a number of transferred electrons close to four (3.80). When comparing these results with the performance of the trimetallic sample containing Mn, Co and Ca ($Mn_{0.69}Co_{1.50}Ca_{0.81}O_4$, table 1, entry 17), we realized that this spinel also exhibited an excellent behavior as catalyst in the ORR with a slightly lower current density of 87.2% compared with Pt/C(20%W) and a large contribution of the 4 electron transfer mechanism (n of 3.82) (Figure 6.22.A). Despite calcium as such is not active towards the ORR, its presence in the spinel structure influences the overall activity. For example, it may enhance O_2 adsorption,[22] and moreover, calcium cations should be exclusively occupying octahedral sites (unlike Zn which preferentially occupies tetrahedral sites), therefore inducing the inversion of the spinel structure and altering Mn and Co oxidation states.[27]

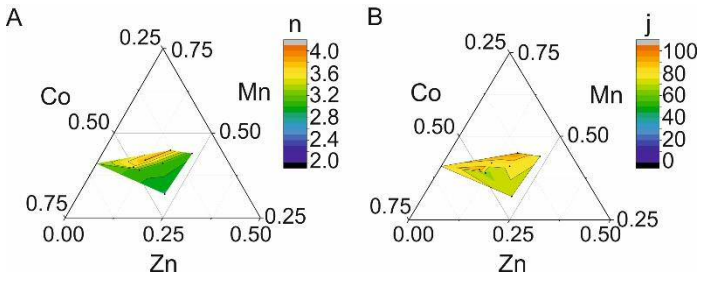

Figure 6. 20. Ternary composition graph of zinc-manganese-cobalt spinels showing A) transferred electron number (n) and B) current density (j).

Furthermore, when comparing with the bimetallic Mn-Co spinel (table 6.3, entry 16), it becomes apparent that in this case the presence of calcium atoms improves the performance in terms of both current density and number of electrons.

Following we sought to study the performance of the newly prepared spinel oxides incorporating four different cations. At the view of the results of the tested materials, we noticed that the solid with the highest content of calcium did not show any improvement compared to the previously evaluated materials. Thus, the spinel with composition $Zn_{0.63}Mn_{0.81}Co_{0.90}Ca_{0.66}O_4$ (table 6.3, entry 15) showed a current density of 67.9% and 2.72 electrons. Similarly, the sample with $Zn_{0.54}Mn_{0.72}Co_{1.23}Ca_{0.48}O_4$ formula exhibited a current

density of 65.6% and 2.76 electrons. These results seem to evidence that a large amount of calcium in the structure is detrimental for the electrocatalytic performance, with a low electron number that indicates that a two-electron process is dominant. However, we found that a fine adjustment of the oxide composition results in a significant improvement in current density. Thus, the oxide with $Zn_{0.48}Mn_{1.41}Co_{0.99}Ca_{0.09}O_4$ formula (table 6.3, entry 10) demonstrated the best behavior among all the seventeen tested materials, with a current density of 97.2% and an electron transfer number of 3.92. This value is among the best obtained for spinel oxides employed as electrocatalyst without additional processing or composite fabrication.

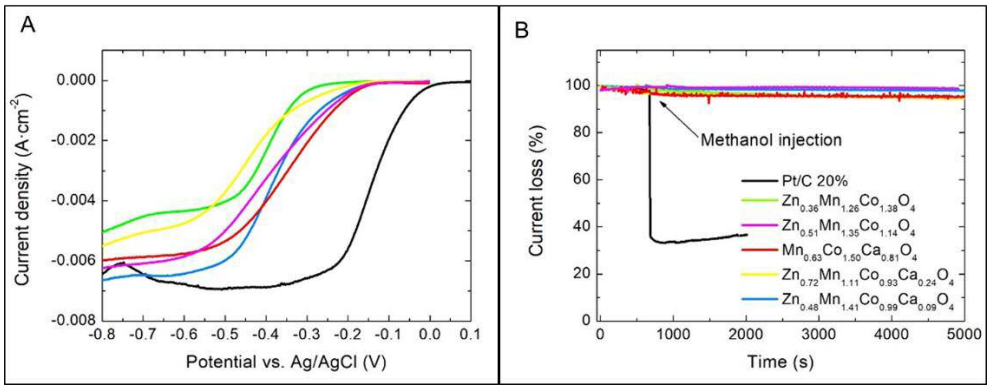

Figure 6. 21. Results of the electrocatalytic ORR study. comparing commercial Pt/C (20%) (black), and spinels with composition $Zn_{0.36}Mn_{1.26}Co_{1.38}O_4$ (green), $Zn_{0.51}Mn_{1.35}Co_{1.14}O_4$ (pink), $Mn_{0.69}Co_{1.50}Ca_{0.81}O_4$, $Zn_{0.72}Mn_{1.11}Co_{0.93}Ca_{0.24}O_4$ (yellow) and $Zn_{0.48}Mn_{1.41}Co_{0.99}Ca_{0.09}O_4$ (blue), A) Comparison of ORR-LSV curves of mixed-metal spinel type oxides prepared from multi-metal MOFs in a O_2-saturated 0.1M KOH solution stirred at 2000 rpm; B) Comparison of methanol crossover in a O_2-saturated in 0.1 M KOH electrolyte stirred at 1600 rpm with methanol injection at 600s.

6.4.3. Stability study

Both long term stability and methanol tolerance are important drawbacks of commercial Pt-based catalysts.[28] Thus, in order to compare our results, we also studied stability as well as tolerance towards methanol crossover of the spinel oxides showing the best catalytic activity. Stability was evaluated by performing a chronoamperometry in saturated O_2 KOH 0.1M electrolyte at 1600 rpm for 20000 s. The results show that all the new materials outperform Pt based catalyst in stability terms showing a slight current attenuation of less than 8% (figure 6.22.B). The methanol crossover test also showed that for all tested spinel oxides, the current is altered in less than a 4% after the addition of methanol at 1600 rpm for 5000 s. In contrast,

methanol addition when using the commercial Pt/C catalyst promoted a sharp drop of the current response of *ca.* 70% (Figure 6.22.B).

6.5. Conclusions

From the obtained results in this chapter different conclusions can be deduced. First, the metal ratios of the MOFs obtained as described in chapter 5 are preserved through the MOF calcination processes, resulting in the ability to program new compositions in spinel type oxides, as proved with the 17 new multi-metal oxides prepared and characterized. Second, this method allows to prepare multi-metal spinel oxides with desired and precise compositions, including four metals: zinc, manganese, cobalt and calcium. To the best of my knowledge, it is the first time that spinels containing these four metal elements are obtained. Third, the incorporation of multiple metal elements results in a complex interplay, where small modifications in metal ratios strongly influence the electrocatalyitical activity in the oxygen reduction reaction, both in terms of current density, and number of transferred electrons. Thus, the material with composition $Zn_{0.48}Mn_{1.41}Co_{0.99}Ca_{0.09}O_4$ that is programmed from a MOF prepared from a Zn:Co:Mn:Ca 1:4:4:1 molar code, achieves a current density that is 97.2% that of commercial Pt/C(20%W) catalyst, with a 3.92 electron process. Finally, these results demonstrate the potential to program and attain new compositions through the selection of adequate molar codes in complex multi-metal MOFs.

This results have been reported in Journal of American Chemical Society in 2019, 141 (4), 1766, with the title '*Encoding Metal-Cation Arrangements in Metal-Organic Frameworks for Programming the Composition of Electrocatalytically Active Multi-Metal Oxides*'.

6.6. References

1. Liu, B.; Shioyama, H.; Jiang, H.; Zhang, X.; Xu, Q., Metal–organic framework (MOF) as a template for syntheses of nanoporous carbons as electrode materials for supercapacitor. *Carbon* **2010,** *48* (2), 456-463.

2. Dang, S.; Zhu, Q.-L.; Xu, Q., Nanomaterials derived from metal–organic frameworks. *Nature Reviews Materials* **2017,** *3*, 17075.

3. Qian, Y.; Khan, I. A.; Zhao, D., Electrocatalysts Derived from Metal–Organic Frameworks for Oxygen Reduction and Evolution Reactions in Aqueous Media. *Small* **2017,** *13* (37), 1701143.

4. Yazdi, A.; Abo Markeb, A.; Garzón-Tovar, L.; Patarroyo, J.; Moral-Vico, J.; Alonso, A.; Sánchez, A.; Bastus, N.; Imaz, I.; Font, X.; Puntes, V.; Maspoch, D., Core–shell Au/CeO_2 nanoparticles supported in UiO-66 beads exhibiting full CO conversion at 100 °C. *Journal of Materials Chemistry A* **2017,** *5* (27), 13966-13970.

5. Yang, H.; Bradley, S. J.; Wu, X.; Chan, A.; Waterhouse, G. I. N.; Nann, T.; Zhang, J.; Kruger, P. E.; Ma, S.; Telfer, S. G., General Synthetic Strategy for Libraries of Supported Multicomponent Metal Nanoparticles. *ACS Nano* **2018,** *12* (5), 4594-4604.

6. Wu, H.; Zhou, W.; Yildirim, T., Hydrogen Storage in a Prototypical Zeolitic Imidazolate Framework-8. *Journal of the American Chemical Society* **2007,** *129* (17), 5314-5315.

7. Choi, K. M.; Jeong, H. M.; Park, J. H.; Zhang, Y.-B.; Kang, J. K.; Yaghi, O. M., Supercapacitors of Nanocrystalline Metal–Organic Frameworks. *ACS Nano* **2014,** *8* (7), 7451-7457.

8. Castillo-Blas, C.; de la Peña-O'Shea, V. A.; Puente-Orench, I.; de Paz, J. R.; Sáez-Puche, R.; Gutiérrez-Puebla, E.; Gándara, F.; Monge, Á., Addressed realization of multication complex arrangements in metal-organic frameworks. *Science Advances* **2017,** *3* (7).

9. Sun, J.-K.; Xu, Q., Functional materials derived from open framework templates/precursors: synthesis and applications. *Energy & Environmental Science* **2014,** *7* (7), 2071-2100.

10. Monge, A.; Snejko, N.; Gutierrez-Puebla, E.; Medina, M.; Cascales, C.; Ruiz-Valero, C.; Iglesias, M.; Gomez-Lor, B., One teflon[registered sign]-like channelled nanoporous polymer with a chiral and new uninodal 4-connected net: sorption and catalytic properties. *Chemical Communications* **2005,** (10), 1291-1293.

11. Ge, X.; Sumboja, A.; Wuu, D.; An, T.; Li, B.; Goh, F. W. T.; Hor, T. S. A.; Zong, Y.; Liu, Z., Oxygen Reduction in Alkaline Media: From Mechanisms to Recent Advances of Catalysts. *ACS Catalysis* **2015,** *5* (8), 4643-4667.

12. Cheng, F.; Chen, J., Metal–air batteries: from oxygen reduction electrochemistry to cathode catalysts. *Chemical Society Reviews* **2012,** *41* (6), 2172-2192.

13. Yuan, C.; Wu, H. B.; Xie, Y.; Lou, X. W., Mixed Transition-Metal Oxides: Design, Synthesis, and Energy-Related Applications. *Angewandte Chemie International Edition* **2014,** *53* (6), 1488-1504.

14. Toh, R. J.; Eng, A. Y. S.; Sofer, Z.; Sedmidubsky, D.; Pumera, M., Ternary Transition Metal Oxide Nanoparticles with Spinel Structure for the Oxygen Reduction Reaction. *ChemElectroChem* **2015,** *2* (7), 982-987.

15. Jiang, S.; Liang, F.; Zhou, W.; Shao, Z., Hierarchical porous cobalt-free perovskite electrode for highly efficient oxygen reduction. *Journal of Materials Chemistry* **2012,** *22* (32), 16214-16218.

16. Odedairo, T.; Yan, X.; Ma, J.; Jiao, Y.; Yao, X.; Du, A.; Zhu, Z., Nanosheets $Co3O_4$ Interleaved with Graphene for Highly Efficient Oxygen Reduction. *ACS Applied Materials & Interfaces* **2015,** *7* (38), 21373-21380.

17. Zhao, Q.; Yan, Z.; Chen, C.; Chen, J., Spinels: Controlled Preparation, Oxygen Reduction/Evolution Reaction Application, and Beyond. *Chemical Reviews* **2017,** *117* (15), 10121-10211.

18. Lee, E.; Jang, J.-H.; Kwon, Y.-U., Composition effects of spinel $Mn_xCo_{3-x}O_4$ nanoparticles on their electrocatalytic properties in oxygen reduction reaction in alkaline media. *Journal of Power Sources* **2015,** *273*, 735-741.

19. Yao, L.; Yang, W.; Liu, H.; Jia, J.; Wu, G.; Liu, D.; Liu, T.; Tan, T.; Wang, C., Synthesis and ORR electrocatalytic activity of mixed Mn–Co oxides derived from divalent metal-based MIL-53 analogues. *Dalton Transactions* **2017,** *46* (44), 15512-15519.

20. Mahata, P.; Sarma, D.; Madhu, C.; Sundaresen, A.; Natarajan, S., $CoMn_2O_4$ spinel from a MOF: synthesis, structure and magnetic studies. *Dalton Transactions* **2011,** *40* (9), 1952-1960.

21. Chen, S.; Xue, M.; Li, Y.; Pan, Y.; Zhu, L.; Zhang, D.; Fang, Q.; Qiu, S., Porous $ZnCo_2O_4$ nanoparticles derived from a new mixed-metal organic framework for supercapacitors. *Inorganic Chemistry Frontiers* **2015,** *2* (2), 177-183.

22. Han, X.; Zhang, T.; Du, J.; Cheng, F.; Chen, J., Porous calcium-manganese oxide microspheres for electrocatalytic oxygen reduction with high activity. *Chemical Science* **2013,** *4* (1), 368-376.

23. Zhou, Y.; Sun, S.; Xi, S.; Duan, Y.; Sritharan, T.; Du, Y.; Xu, Z. J., Superexchange Effects on Oxygen Reduction Activity of Edge-Sharing $[Co_xMn_{1-x}O_6]$ Octahedra in Spinel Oxide. *Advanced Materials* **2018,** *30* (11), 1705407.

24. Li, C.; Han, X.; Cheng, F.; Hu, Y.; Chen, C.; Chen, J., Phase and composition controllable synthesis of cobalt manganese spinel nanoparticles towards efficient oxygen electrocatalysis. *Nature Communications* **2015,** *6*, 7345.

25. Liang, Y.; Li, Y.; Wang, H.; Zhou, J.; Wang, J.; Regier, T.; Dai, H., Co_3O_4 nanocrystals on graphene as a synergistic catalyst for oxygen reduction reaction. *Nature Materials* **2011,** *10*, 780.

26. Wu, Z.-S.; Yang, S.; Sun, Y.; Parvez, K.; Feng, X.; Müllen, K., 3D Nitrogen-Doped Graphene Aerogel-Supported Fe_3O_4 Nanoparticles as Efficient Electrocatalysts for the Oxygen Reduction Reaction. *Journal of the American Chemical Society* **2012,** *134* (22), 9082-9085.

27. Wu, G.; Wang, J.; Ding, W.; Nie, Y.; Li, L.; Qi, X.; Chen, S.; Wei, Z., A Strategy to Promote the Electrocatalytic Activity of Spinels for Oxygen Reduction by Structure Reversal. *Angewandte Chemie International Edition* **2016,** *55* (4), 1340-1344.

28. Sa, Y. J.; Kwon, K.; Cheon, J. Y.; Kleitz, F.; Joo, S. H., Ordered mesoporous Co_3O_4 spinels as stable, bifunctional, noble metal-free oxygen electrocatalysts. *Journal of Materials Chemistry A* **2013,** *1* (34), 9992-10001.

CHAPTER 7:

CONCLUSIONS

In the present work, different conclusions from the obtained analysis results from chapters 4, 5 and 6 have been deduced.

The main conclusions extracted from Chapter 4 are:

- The addition of a second metal element, even at a very low amount, drastically modifies the reaction media, inducing the formation of new phases, as shown by the formation of TMPF-91 with a 10:1 Zn:Co initial ratio using as solvent a mixture of water and ethanol.
- In the mixed-metal, mixed-ligand studied system there is a competition in the MOF formation, where kinetically favored structures (ZnPF-1 and TMPF-90) appear at short reaction times, precluding the formation as a pure phase of other energetically more favorable solid-solution phases (TMPF-88).
- The cobalt amount introduced into the framework is substantially lower than the one initially added to the reaction in the cases of TMPF-91 and TMPF-88, according to EDS and ICP analyses, while in the case of TMPF-90 and TMPF-95, the two elements can be incorporated in comparable amounts. This is related with the kinetic study, where we observed the formation of TMPF-90 as kinetically favored product, which include larger amount of cobalt.
- From all these observations, we deduced that MOFs with a kinetically controlled crystallization might be able to accommodate multiple metal cation with different metal ratios. These results led us to embark in the studies described in Chapter 5, to systematically investigate the outcome of the different combinations of metal elements.

The main conclusions extracted from Chapter 5 are:

- Multiple metal cations can be incorporated into a desired MOF, and directed to be occupying specific positions in the rod-shaped SBU.
- The amount and location of the different cations depends on the selected combination of initial metal elements and their molar ratios. Different elements follow different incorporation kinetics and have different preferential coordination environments, which results in the possibility of exerting control at atomic and mesoscopic scale on their distribution in the MOF crystals.
- These results offer a new platform to obtain complex structures where the arrangement of the metal cations can be virtually controlled on demand.
- Considering that the properties of materials are dictated by their composition and precise atomic and mesoscopic structures, it is reasonable to think that our findings will be relevant to various fields. This is illustrated with the induction of new magnetic properties of these Zn-Co MOFs. As such, different magnetic behaviors have been demonstrated for isoreticular MOFs composed of different atomic sequences in their SBUs.
- The use of the combination of different microscopic and diffractometric techniques such as SEM-EDS, ICP, single crystal X-ray diffraction and powder X-ray diffraction, neutron powder diffraction allow the elucidation of the atomic arrangement in the SBUs and their mesoscopic distribution.
- Moreover, in view of the large number of existing MOFs that are constructed from many diverse rod-shaped SBUs, it might be anticipated that this method will be generalized to prepare new materials with topologies and structures fit for specific applications where multiple metal cations can be arranged at desired atomic positions, as well as mesoscopically distributed.

The main conclusions extracted from Chapter 6 are:

- The metal ratios of the MOFs obtained as described in Chapter 5 are preserved through the MOF calcination processes, resulting in the ability to program new compositions in spinel type oxides, as proved with the 17 new multi-metal oxides prepared and characterized.
- The employed strategy allows to prepare multi-metal spinel oxides with desired and precise compositions, including four metal elements: zinc, manganese, cobalt and calcium. To the best of my knowledge, it is the first time that spinels containing these four metal elements are obtained.
- The incorporation of multiple metal elements results in a complex interplay, where small modifications in metal ratios strongly influence the electrocatalyitical activity in the oxygen reduction reaction, both in terms of current density, and number of transferred electrons.

All these reported results demonstrate the potential to program and attain new compositions through the selection of adequate molar codes in complex multi-metal MOFs.

APPENDICES

A) Appendices from Chapter 5

1. Thermalgravimetric analyses

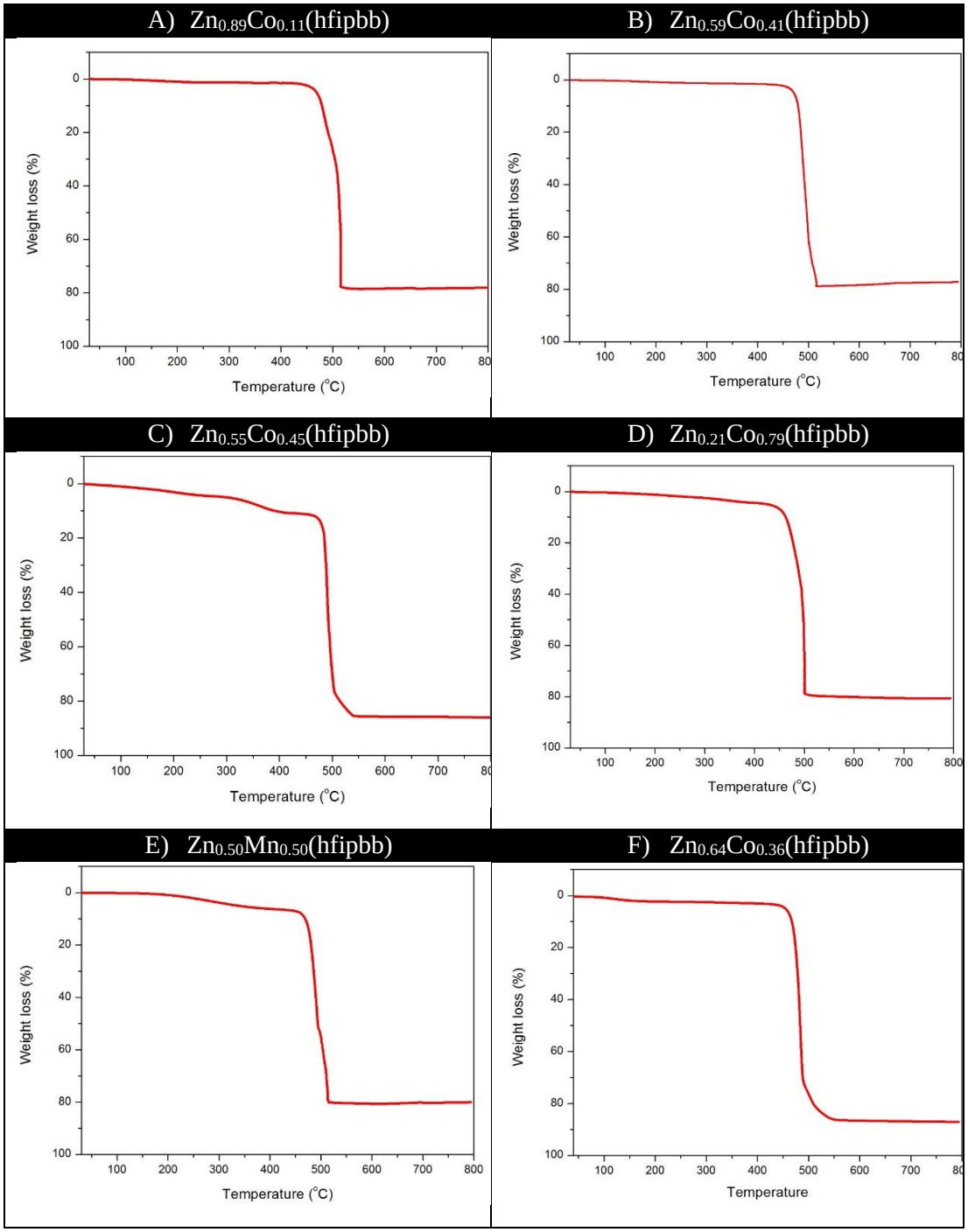

Figure A. 1. TGA curves for dried compounds. A) $Zn_{0.89}Co_{0.11}$(hfipbb) (molar code: Zn:Co 1:1), B) $Zn_{0.59}Co_{0.41}$(hfipbb) (molar code: Zn:Co 1:2, C) $Zn_{0.55}Co_{0.45}$(hfipbb) (molar code: Zn:Co 1:4), D) $Zn_{0.21}Co_{0.79}$(hfipbb) (molar code: Zn:Co 1:10), E) $Zn_{0.50}Mn_{0.50}$(hfipbb) (molar code: Zn:Mn: 1:1), and F) $Zn_{0.64}Ca_{0.36}$(hfipbb) (molar code: Zn:Ca 1:4).

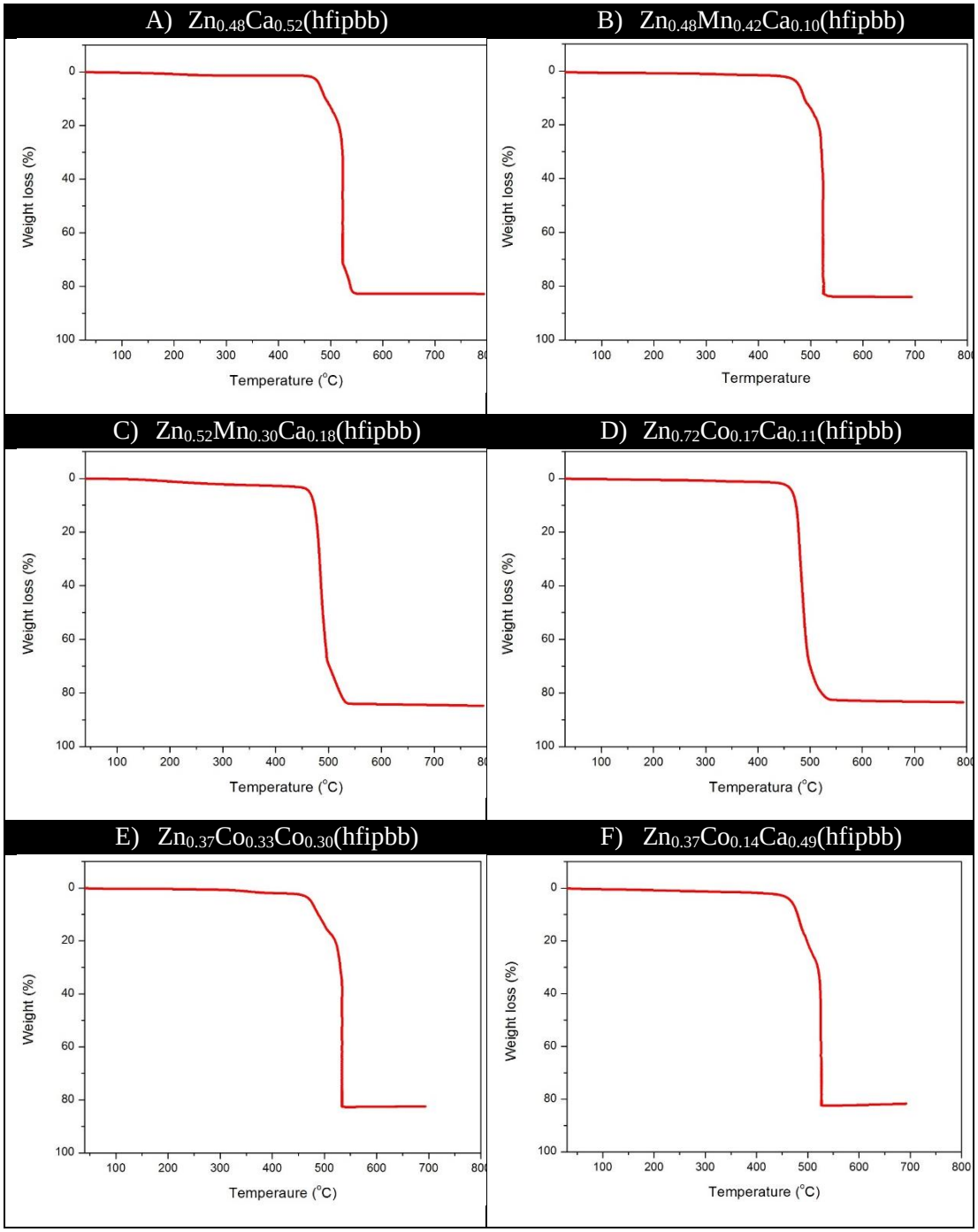

Figure A. 2. TGA curves for dried compounds. A) $Zn_{0.52}Ca_{0.48}$(hfipbb) (molar code: Zn:Ca 1:10), B) $Zn_{0.48}Mn_{0.42}Ca_{0.10}$(hfipbb) (molar code: Zn:Mn:Ca 1:1:1, C) $Zn_{0.52}Mn_{0.30}Ca_{0.18}$(hfipbb) (molar code: Zn:Mn:Ca 1:1:8), D) $Zn_{0.72}Co_{0.17}Ca_{0.11}$(hfipbb) (molar code: Zn:Co:Ca 1:1:1), E) $Zn_{0.37}Co_{0.33}Ca_{0.30}$(hfipbb) (molar code: Zn:Co:Ca: 1:4:4), and F) $Zn_{0.37}Co_{0.14}Ca_{0.49}$(hfipbb) (molar code: Zn:Co:Ca 1:1:8).

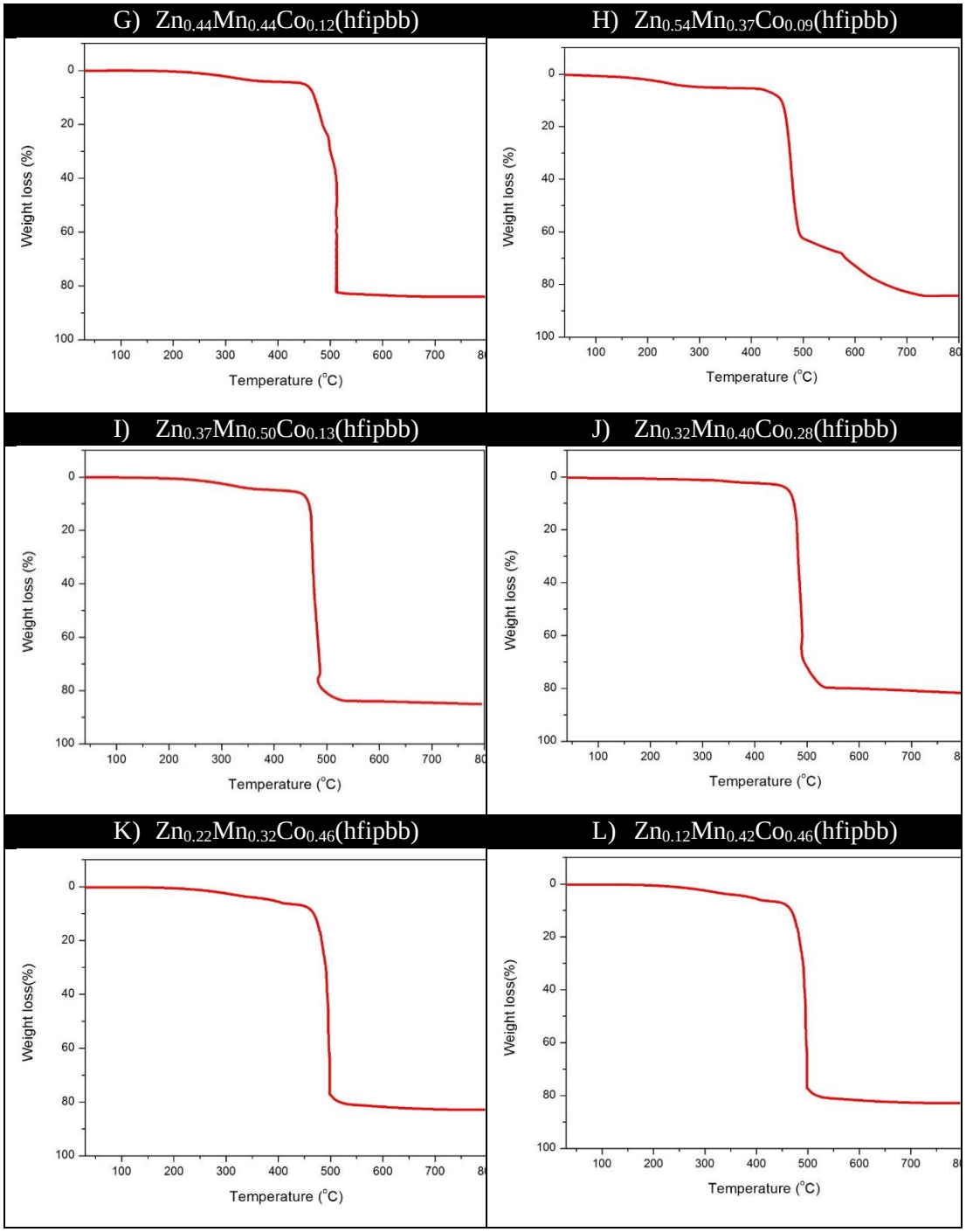

Figure A. 3. TGA curves for dried compounds. A) $Zn_{0.44}Mn_{0.44}Co_{0.12}$(hfipbb) (molar code: Zn:Mn:Co 1:1:1), B) $Zn_{0.52}Mn_{0.37}Co_{0.09}$(hfipbb) (molar code: Zn:Mn:Co 2:1:1, C) $Zn_{0.37}Mn_{0.50}Co_{0.13}$(hfipbb) (molar code: Zn:Mn:Co 1:2:1), D) $Zn_{0.32}Mn_{0.40}Co_{0.28}$(hfipbb) (molar code: Zn:Mn:Co 1:1:2), E) $Zn_{0.22}Mn_{0.32}Co_{0.46}$(hfipbb) (molar code: Zn:Mn:Co: 1:1:8), and F) $Zn_{0.12}Mn_{0.42}Co_{0.46}$(hfipbb) (molar code: Zn:Mn:Co 1:3:9).

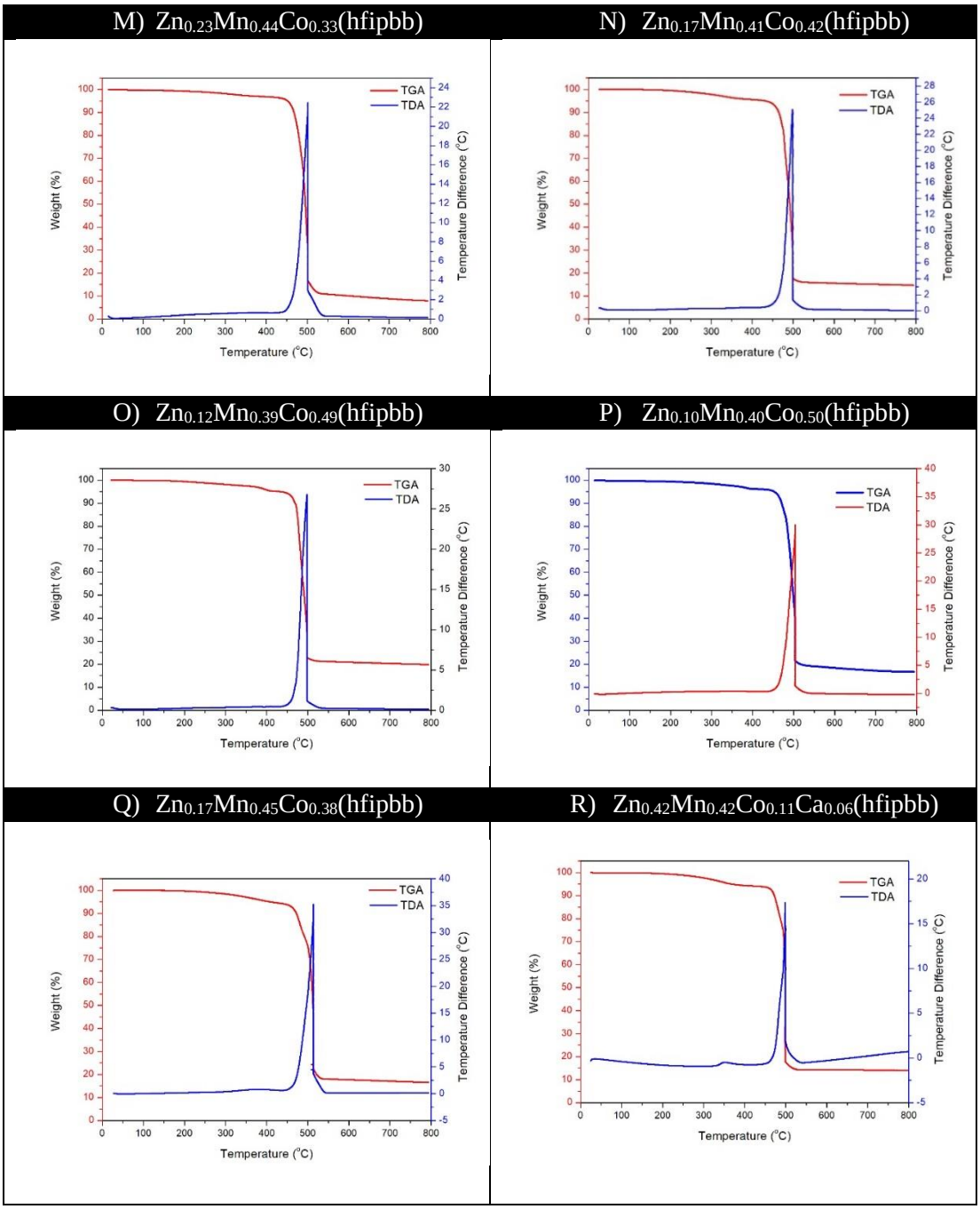

Figure A. 4. TGA-TDA curves for dried compounds. A) $Zn_{0.23}Mn_{0.44}Co_{0.33}$(hfipbb) (molar code: Zn:Mn:Co 1:4:4), B) $Zn_{0.17}Mn_{0.41}Co_{0.42}$(hfipbb) (molar code: Zn:Mn:Co 1:4:6, C) $Zn_{0.12}Mn_{0.39}Co_{0.49}$(hfipbb) (molar code: Zn:Mn:Co 1:6:12), D) $Zn_{0.10}Mn_{0.40}Co_{0.50}$(hfipbb) (molar code: Zn:Mn:Co 1:10:20), E) $Zn_{0.17}Mn_{0.45}Co_{0.38}$(hfipbb) (molar code: Zn:Mn:Co 1:12:6) and F) $Zn_{0.42}Mn_{0.42}Co_{0.11}Ca_{0.06}$(hfipbb) (molar code: Zn:Mn:Co:Ca 1:1:1:1).

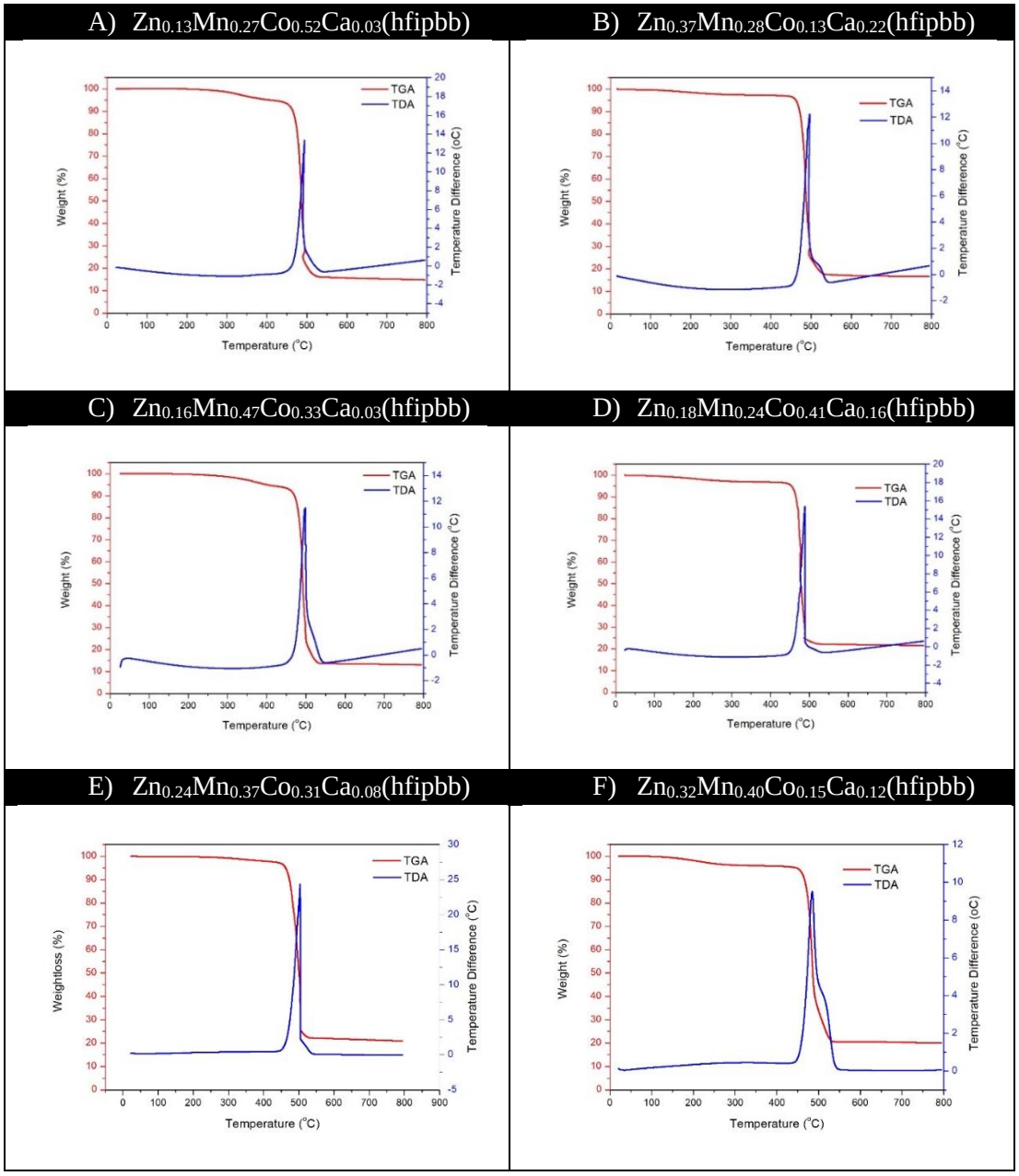

Figure A. 5. TGA-TDA curves for dried compounds. A) $Zn_{0.13}Mn_{0.27}Co_{0.52}Ca_{0.03}$(hfipbb) (molar code: Zn:Mn:Co:Ca 1:1:7:1), B) $Zn_{0.37}Mn_{0.28}Co_{0.13}Ca_{0.22}$(hfipbb) (molar code: Zn:Mn:Co:Ca 1:1:1:7, C) $Zn_{0.16}Mn_{0.47}Co_{0.33}Ca_{0.03}$(hfipbb) (molar code: Zn:Mn:Co:Ca 1:4:4:1), D) $Zn_{0.18}Mn_{0.24}Co_{0.41}Ca_{0.16}$(hfipbb) (molar code: Zn:Mn:Co:Ca 1:1:4:4), E) $Zn_{0.24}Mn_{0.37}Co_{0.31}Ca_{0.08}$(hfipbb) (molar code: Zn:Mn:Co:Ca 1:4:4:4), and F) $Zn_{0.32}Mn_{0.40}Co_{0.15}Ca_{0.12}$(hfipbb)) (molar code: Zn:Mn:Co:Ca 1:4:1:4).

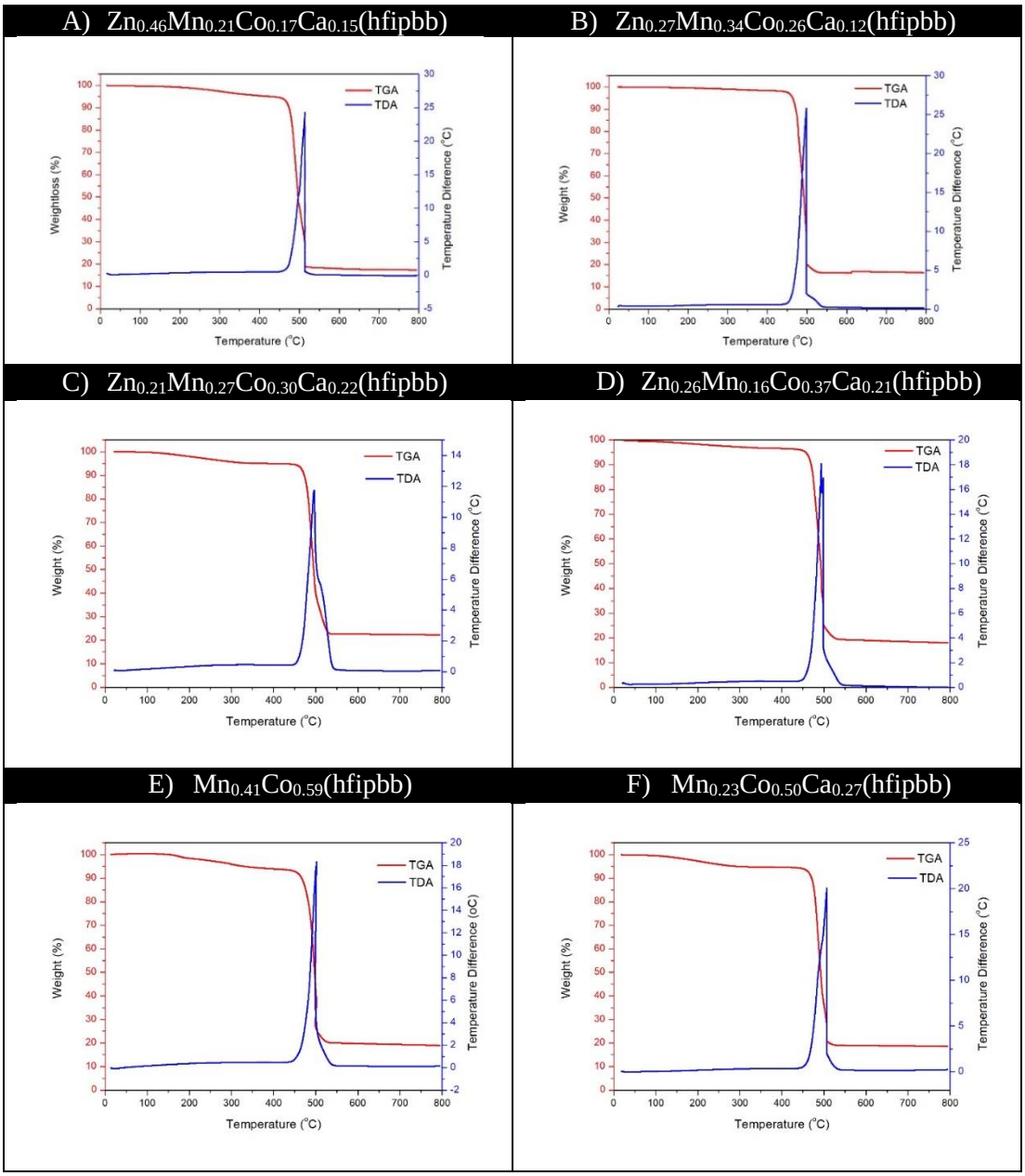

Figure A. 6. TGA-TDA curves for dried compounds. A) $Zn_{0.46}Mn_{0.21}Co_{0.17}Ca_{0.15}$(hfipbb) (molar code: Zn:Mn:Co:Ca 2:1:2:2), B) $Zn_{0.27}Mn_{0.34}Co_{0.26}Ca_{0.12}$(hfipbb) (molar code: ZnMnCoCa-1:2:2:4), C) $Zn_{0.21}Mn_{0.27}Co_{0.30}Ca_{0.22}$(hfipbb) (molar code: Zn:Mn:Co:Ca 1:4:4:8), D) $Zn_{0.26}Mn_{0.16}Co_{0.37}Ca_{0.21}$(hfipbb) (molar code: Zn:Mn:Co:Ca 1:1:4:8, E) $Mn_{0.41}Co_{0.59}$(hfipbb) (molar code: Mn:Co 1:1) and F) $Mn_{0.23}Co_{0.50}Ca_{0.27}$(hfipbb) (molar code: Mn:Co:Ca 1:2:2).

2. X-ray powder diffraction

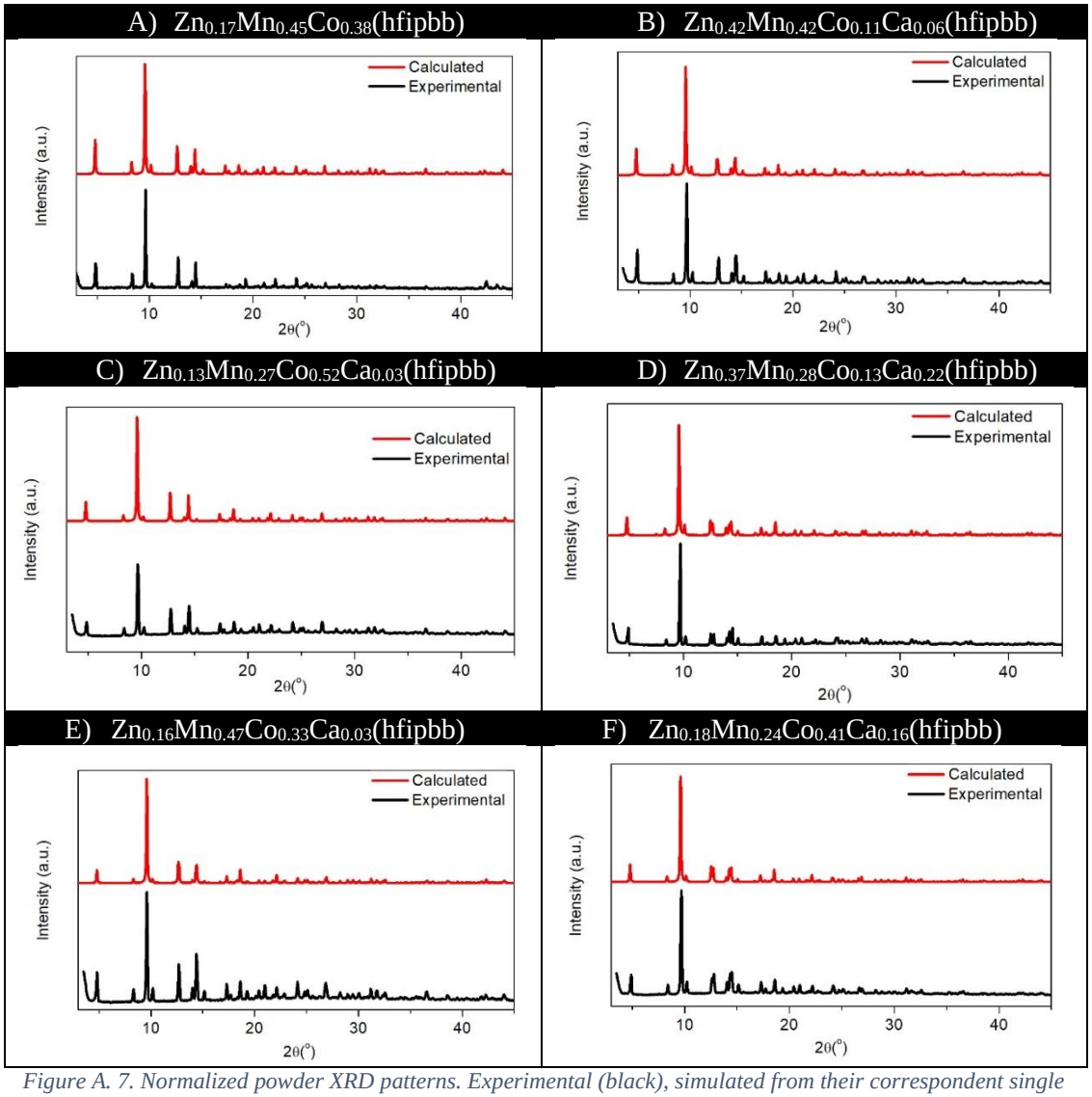

Figure A. 7. Normalized powder XRD patterns. Experimental (black), simulated from their correspondent single crystal X-ray diffraction data (red).

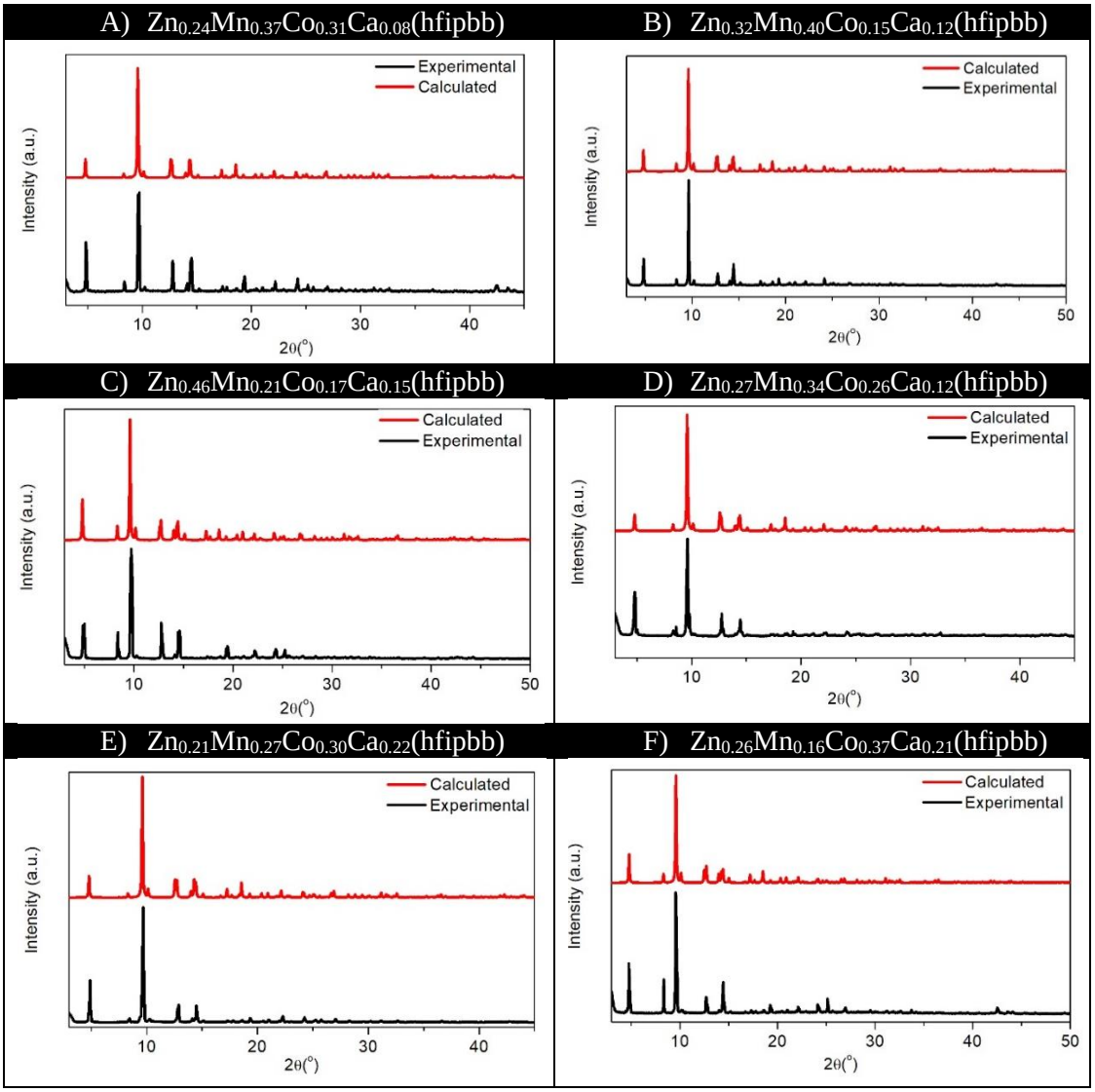

Figure A. 8. Normalized powder XRD patterns. Experimental (black), simulated from their correspondent single crystal X-ray diffraction data (red).

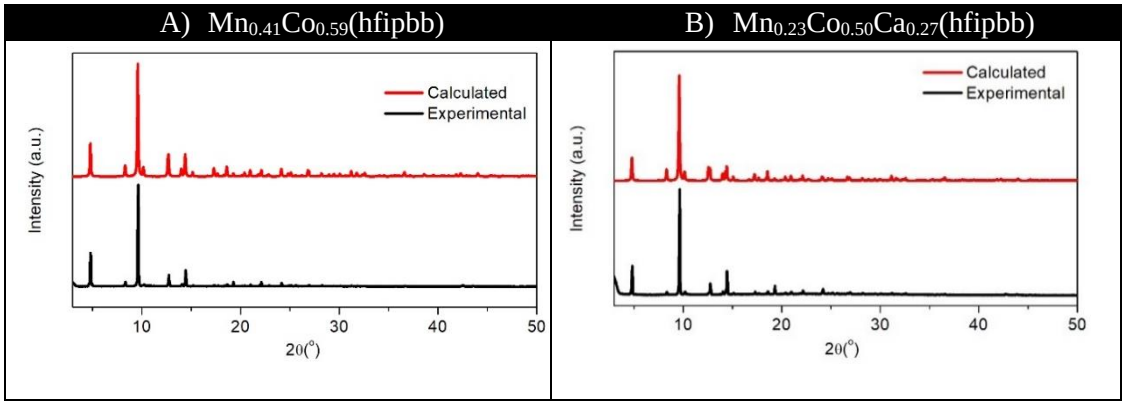

Figure A. 9. Normalized powder XRD patterns. Experimental (black), simulated from their correspondent single crystal X-ray diffraction data (red).

3. Single crystal X-ray diffraction refinement results

Identification code	**$Zn_{0.89}Co_{0.11}$(hfipbb)**	**$Zn_{0.89}Co_{0.11}$(hfipbb)_100K**
CCDC number	1531921	1531920
Empirical formula	$C_{17}H_8Co_{0.21}F_6O_{4.5}Zn_{0.79}$	$C_{2.55}H_{1.2}F_{0.9}O_{0.6}Zn_{0.15}$
Formula weight	462.25	68.34
Temperature/K	300.0	100(2)
Crystal system	hexagonal	hexagonal
Space group	$P6_422$	$P6_422$
a/Å	21.2590(7)	21.123(3)
b/Å	21.2590(7)	21.123(3)
c/Å	7.6841(4)	7.6798(15)
α/°	90	90
β/°	90	90
γ/°	120	120
Volume/$Å^3$	3007.5(3)	2967.4(10)
Z	6	40
$\rho_{calc}g/cm^3$	1.531	1.530
μ/mm^{-1}	3.482	2.432
F(000)	1376.0	1356.0
Crystal size/mm^3	0.16 × 0.06 × 0.04	0.06 × 0.06 × 0.20
Radiation	CuKα (λ = 1.54178)	CuKα (λ = 1.54178)
2Θ range for data collection/°	4.8 to 130.5	4.83 to 133.434
Index ranges	$-24 \leq h \leq 24$, $-24 \leq k \leq 24$, $-8 \leq l \leq 9$	$-24 \leq h \leq 24$, $-24 \leq k \leq 24$, $-8 \leq l \leq 9$
Reflections collected	15853	1730
Independent reflections	1722 [R_{int} = 0.1428, R_{sigma} = 0.0739]	1730 [R_{int} = ?, R_{sigma} = 0.0279]
Data/restraints/parameters	1722/0/135	1730/20/92
Goodness-of-fit on F^2	1.050	1.142
Final R indexes [I>=2σ (I)]	R_1 = 0.0652, wR_2 = 0.1617	R_1 = 0.1301, wR_2 = 0.3263
Final R indexes [all data]	R_1 = 0.0859, wR_2 = 0.1764	R_1 = 0.1314, wR_2 = 0.3272
Largest diff. peak/hole / e $Å^{-3}$	0.60/-0.54	0.84/-1.27
Flack parameter	0.00(3)	0.13(3)

Table A. 1. Crystal data and structure refinement for $Zn_{0.89}Co_{0.11}$(hfipbb) (molar code: Zn:Co 1:1) (CCDC number: 1531921) (second column) and $Zn_{0.89}Co_{0.11}$(hfipbb)_100K (molar code: Zn:Co 1:1) (CCDC number: 1531920) (third column).

Identification code	**$Zn_{0.59}Co_{0.41}$(hfipbb)**	**$Zn_{0.59}Co_{0.41}$(hfipbb)_200K**
CCDC number	1531914	1531918
Empirical formula	$C_{17}H_8Co_{0.28}F_6O_{4.4}Zn_{0.72}$	$C_{17}H_8Co_{0.26}F_6O_{4.2}Zn_{0.73}$
Formula weight	460.21	457.10
Temperature/K	296.15	200
Crystal system	hexagonal	hexagonal
Space group	$P6_422$	$P6_422$
a/Å	21.2286(16)	21.2316(5)
b/Å	21.2286(16)	21.2316(5)
c/Å	7.6921(8)	7.6604(2)
α/°	90	90
β/°	90	90
γ/°	120	120
Volume/$Å^3$	3002.1(5)	2990.52(16)
Z	6	6
$\rho_{calc}g/cm^3$	1.527	1.523
μ/mm^{-1}	3.825	3.760
F(000)	1370.0	1361.0
Crystal size/mm^3	0.4 × 0.4 × 0.22	0.6 × 0.6 × 0.14
Radiation	CuKα (λ = 1.54178)	CuKα (λ = 1.54178)
2Θ range for data collection/°	4.806 to 131.394	4.806 to 130.458
Index ranges	$-25 \leq h \leq 25$, $-24 \leq k \leq 21$, $-8 \leq l \leq 8$	$-25 \leq h \leq 24$, $-21 \leq k \leq 24$, $-8 \leq l \leq 8$
Reflections collected	21258	21087
Independent reflections	1706 [R_{int} = 0.0604, R_{sigma} = 0.0243]	1694 [R_{int} = 0.0606, R_{sigma} = 0.0238]
Data/restraints/parameters	1706/0/139	1694/0/135
Goodness-of-fit on F^2	1.187	1.137
Final R indexes [I>=2σ (I)]	R_1 = 0.0371, wR_2 = 0.1072	R_1 = 0.0396, wR_2 = 0.1227
Final R indexes [all data]	R_1 = 0.0392, wR_2 = 0.1092	R_1 = 0.0409, wR_2 = 0.1242
Largest diff. peak/hole / e $Å^{-3}$	0.52/-0.30	0.78/-0.33
Flack parameter	0.036(8)	0.022(8)

Table A. 2. Crystal data and structure refinement for $Zn_{0.59}Co_{0.41}$(hfipbb) (molar code: Zn:Co 1:2) (CCDC number: 1531914) (second column) and $Zn_{0.59}Co_{0.41}$(hfipbb)_200K (molar code: Zn:Co 1:2) (CCDC number: 1531918) (third column).

Identification code	**$Zn_{0.59}Co_{0.41}$(hfipbb)_150K**	**$Zn_{0.59}Co_{0.41}$(hfipbb)_100K**
CCDC number	1531919	1531923
Empirical formula	$C_{17}H_8Co_{0.28}F_6O_4Zn_{0.8}$	$C_{17}H_8Co_{0.18}F_6O_4Zn_{0.83}$
Formula weight	458.83	454.48
Temperature/K	150	100
Crystal system	hexagonal	hexagonal
Space group	$P6_522$	$P6_522$
a/Å	21.2052(7)	21.1681(8)
b/Å	21.2052(7)	21.1681(8)
c/Å	15.2650(7)	15.0151(9)
α/°	90	90
β/°	90	90
γ/°	120	120
Volume/Å^3	5944.5(5)	5826.7(6)
Z	12	12
ρ_{calc}g/cm^3	1.538	1.554
μ/mm^{-1}	3.928	3.382
F(000)	2730.0	2706.0
Crystal size/mm^3	0.14 × 0.06 × 0.06	0.14 × 0.06 × 0.06
Radiation	CuKα (λ = 1.54178)	CuKα (λ = 1.54178)
2Θ range for data collection/°	4.812 to 131.162	4.82 to 130.508
Index ranges	$-24 \le h \le 21$, $-23 \le k \le 25$, $-16 \le l \le 15$	$-24 \le h \le 24$, $-21 \le k \le 24$, $-15 \le l \le 16$
Reflections collected	39690	41444
Independent reflections	3345 [R_{int} = 0.0760, R_{sigma} = 0.0332]	3270 [R_{int} = 0.1334, R_{sigma} = 0.0466]
Data/restraints/parameters	3345/14/275	3270/102/265
Goodness-of-fit on F^2	1.563	1.526
Final R indexes [I>=2σ (I)]	R_1 = 0.1186, wR_2 = 0.3357	R_1 = 0.1111, wR_2 = 0.3172
Final R indexes [all data]	R_1 = 0.1372, wR_2 = 0.3593	R_1 = 0.1148, wR_2 = 0.3201
Largest diff. peak/hole / e Å^{-3}	0.56/-2.08	2.08/-0.88
Flack parameter	0.213(19)	0.262(13)

Table A. 3. Crystal data and structure refinement for $Zn_{0.59}Co_{0.41}$(hfipbb)_150K (molar code: Zn:Co 1:2) (CCDC number: 1531919) (second column) and $Zn_{0.59}Co_{0.41}$(hfipbb)_100K (molar code: Zn:Co 1:2) (CCDC number: 1531923) (third column).

Identification code	**$Zn_{0.59}Co_{0.41}$(hfipbb)_50K**	**$Zn_{0.55}Co_{0.45}$(hfipbb)_RT**
CCDC number	1531915	1531916
Empirical formula	$C_{17}H_8Co_{0.35}F_6O_4Zn_{0.65}$	$C_{17}H_8Co_{0.26}F_6O_{4.1}Zn_{0.73}$
Formula weight	453.35	454.56
Temperature/K	50	300.0
Crystal system	hexagonal	hexagonal
Space group	$P6_122$	$P6_422$
a/Å	20.50(2)	21.2333(6)
b/Å	20.50(2)	21.2333(6)
c/Å	14.18(2)	7.6981(3)
α/°	90	90
β/°	90	90
γ/°	120	120
Volume/$Å^3$	5159(15)	3005.7(2)
Z	12	6
$\rho_{calc}g/cm^3$	1.751	1.507
μ/mm^{-1}	4.842	3.683
F(000)	2699.0	1353.0
Crystal size/mm^3	0.14 × 0.06 × 0.06	0.2 × 0.06 × 0.06
Radiation	CuKα (λ = 1.54178)	CuKα (λ = 1.54178)
2Θ range for data collection/°	4.978 to 92.126	4.806 to 130.352
Index ranges	$-19 \leq h \leq 18$, $-18 \leq k \leq 19$, $-11 \leq l \leq 9$	$-24 \leq h \leq 24$, $-24 \leq k \leq 24$, $-8 \leq l \leq 9$
Reflections collected	10658	55698
Independent reflections	1414 [R_{int} = 0.1226, R_{sigma} = 0.0772]	1722 [R_{int} = 0.0255, R_{sigma} = 0.0066]
Data/restraints/parameters	1414/90/244	1722/0/135
Goodness-of-fit on F^2	1.265	1.287
Final R indexes [I>=2σ (I)]	R_1 = 0.1098, wR_2 = 0.2665	R_1 = 0.0224, wR_2 = 0.0710
Final R indexes [all data]	R_1 = 0.1371, wR_2 = 0.2965	R_1 = 0.0227, wR_2 = 0.0712
Largest diff. peak/hole / e $Å^{-3}$	1.28/-0.74	0.51/-0.18
Flack parameter	0.30(2)	0.010(3)

Table A. 4. Crystal data and structure refinement for $Zn_{0.59}Co_{0.41}$(hfipbb)_50K (molar code: Zn:Co 1:2) (CCDC number: 1531915) (second column) and $Zn_{0.55}Co_{0.45}$(hfipbb)_RT (molar code: Zn:Co 1:4) (CCDC number: 1531916) (third column).

Identification code	**$Zn_{0.55}Co_{0.45}$(hfipbb)_100K**	**$Zn_{0.21}Co_{0.79}$(hfipbb)_RT**
CCDC number	1531912	1531902
Empirical formula	$C_{17}H_8Co_{0.5}F_6O_{4.15}Zn_{0.5}$	$C_{17}H_8Co_{0.87}F_6O_4Zn_{0.12}$
Formula weight	456.38	449.76
Temperature/K	100 (2)	293
Crystal system	hexagonal	hexagonal
Space group	$P6_522$	$P6_522$
a/Å	21.1760(8)	21.2444(7)
b/Å	21.1760(8)	21.2444(7)
c/Å	14.9203(8)	14.8572(7)
α/°	90	90
β/°	90	90
γ/°	120	120
Volume/$Å^3$	5794.2(5)	5807.1(5)
Z	12	12
$\rho_{calc}g/cm^3$	1.570	1.543
μ/mm^{-1}	5.107	7.013
F(000)	2718.0	2679.0
Crystal size/mm^3	0.2 × 0.06 × 0.06	0.32 × 0.12 × 0.1
Radiation	CuKα (λ = 1.54178)	CuKα (λ = 1.54178)
2Θ range for data collection/°	4.818 to 131.75	4.802 to 131.678
Index ranges	$-24 \leq h \leq 24$, $-24 \leq k \leq 25$, $-17 \leq l \leq 17$	$-25 \leq h \leq 23$, $-25 \leq k \leq 25$, $-17 \leq l \leq 17$
Reflections collected	38686	30328
Independent reflections	3358 [R_{int} = 0.1173, R_{sigma} = 0.0649]	3340 [R_{int} = 0.0898, R_{sigma} = 0.0498]
Data/restraints/parameters	3358/0/258	3340/30/256
Goodness-of-fit on F^2	1.065	1.081
Final R indexes [I>=2σ (I)]	R_1 = 0.0896, wR_2 = 0.2482	R_1 = 0.0660, wR_2 = 0.1702
Final R indexes [all data]	R_1 = 0.1080, wR_2 = 0.2809	R_1 = 0.0760, wR_2 = 0.1779
Largest diff. peak/hole / e $Å^{-3}$	1.48/-0.72	0.41/-0.43
Flack parameter	0.327(10)	0.064(5)

Table A. 5. Crystal data and structure refinement for $Zn_{0.55}Co_{0.45}$(hfipbb)_100K (molar code: Zn:Co 1:4) (CCDC number: 1531912) (second column) and $Zn_{0.21}Co_{0.79}$(hfipbb)_RT (molar code: Zn:Co 1:10) (CCDC number: 1531902) (third column).

Identification code	**$Zn_{0.21}Co_{0.79}$(hfipbb)_100K**	**$Zn_{0.50}Mn_{0.50}$(hfipbb)**
CCDC number	1531903	1531901
Empirical formula	$C_{17}H_8Co_{0.91}F_6O_4Zn_{0.09}$	$C_{34}H_{16}F_{12}MnO_{10.9}Zn$
Formula weight	449.75	947.15
Temperature/K	100	293
Crystal system	hexagonal	hexagonal
Space group	$P6_522$	$P6_522$
a/Å	21.1900(6)	21.2887(5)
b/Å	21.1900(6)	21.2887(5)
c/Å	14.8333(7)	15.1272(5)
α/°	90	90
β/°	90	90
γ/°	120	120
Volume/$Å^3$	5768.1(4)	5937.3(3)
Z	12	6
$\rho_{calc}g/cm^3$	1.554	1.589
μ/mm^{-1}	7.247	4.370
F(000)	2679.0	2821.0
Crystal size/mm^3	0.26 × 0.2 × 0.2	0.3 × 0.08 × 0.06
Radiation	CuKα (λ = 1.54178)	CuKα (λ = 1.54178)
2Θ range for data collection/°	4.816 to 130.672	4.792 to 98.512
Index ranges	$-24 \leq h \leq 23$, $-24 \leq k \leq 24$, $-17 \leq l \leq 17$	$-20 \leq h \leq 20$, $-20 \leq k \leq 20$, $-14 \leq l \leq 14$
Reflections collected	30802	23086
Independent reflections	3292 [R_{int} = 0.0942, R_{sigma} = 0.0437]	1973 [R_{int} = 0.0736, R_{sigma} = 0.0313]
Data/restraints/parameters	3292/0/256	1973/0/268
Goodness-of-fit on F^2	1.126	1.139
Final R indexes [I>=2σ (I)]	R_1 = 0.0507, wR_2 = 0.1357	R_1 = 0.0426, wR_2 = 0.1305
Final R indexes [all data]	R_1 = 0.0562, wR_2 = 0.1404	R_1 = 0.0474, wR_2 = 0.1403
Largest diff. peak/hole / e $Å^{-3}$	0.55/-0.43	0.73/-0.31
Flack parameter	0.086(5)	0.025(7)

Table A. 6. Crystal data and structure refinement for $Zn_{0.21}Co_{0.79}$(hfipbb)_100K (molar code: Zn:Co 1:10) (CCDC number: 1531903) (second column) and $Zn_{0.50}Mn_{0.50}$(hfipbb) (molar code: Zn:Mn 1:1) (CCDC number: 1531901) (third column).

Identification code	**$Zn_{0.96}Ca_{0.04}$(hfipbb)**	**$Zn_{0.94}Ca_{0.06}$(hfipbb)**
CCDC number	1531926	1531924
Empirical formula	$C_{51}H_{24}F_{18}O_{12}Zn_3$	$C_{17}H_8F_6O_4Zn$
Formula weight	1366.81	455.60
Temperature/K	296.15	300.0
Crystal system	hexagonal	hexagonal
Space group	$P6_222$	$P6_422$
a/Å	21.2338(10)	21.2089(5)
b/Å	21.2338(10)	21.2089(5)
c/Å	7.7238(4)	7.7205(2)
α/°	90	90
β/°	90	90
γ/°	120	120
Volume/$Å^3$	3015.9(3)	3007.55(16)
Z	2	6
$\rho_{calc}g/cm^3$	1.505	1.509
μ/mm^{-1}	2.393	2.399
F(000)	1356.0	1356.0
Crystal size/mm^3	0.22 × 0.08 × 0.08	0.16 × 0.08 × 0.08
Radiation	CuKα (λ = 1.54178)	CuKα (λ = 1.54178)
2Θ range for data collection/°	8.328 to 133.044	4.81 to 131.072
Index ranges	$-25 \leq h \leq 25$, $-25 \leq k \leq 25$, $-9 \leq l \leq 8$	$-23 \leq h \leq 24$, $-24 \leq k \leq 24$, $-9 \leq l \leq 9$
Reflections collected	44025	17832
Independent reflections	1762 [R_{int} = 0.0619, R_{sigma} = 0.0341]	1724 [R_{int} = 0.0436, R_{sigma} = 0.0230]
Data/restraints/parameters	1762/0/128	1724/0/128
Goodness-of-fit on F^2	1.792	1.239
Final R indexes [I>=2σ (I)]	R_1 = 0.0630, wR_2 = 0.1933	R_1 = 0.0439, wR_2 = 0.1368
Final R indexes [all data]	R_1 = 0.0811, wR_2 = 0.2059	R_1 = 0.0466, wR_2 = 0.1552
Largest diff. peak/hole / e $Å^{-3}$	1.11/-0.68	0.67/-0.64
Flack parameter	-0.027(11)	0.00(3)

Table A. 7. Crystal data and structure refinement for $Zn_{0.96}Ca_{0.04}$(hfipbb) (molar code: Zn:Ca 1:1) (CCDC number: 1531926) (second column) and $Zn_{0.94}Ca_{0.06}$(hfipbb) (molar code: Zn:Ca 1:2) (CCDC number: 1531924) (third column).

Identification code	**$Zn_{0.64}Ca_{0.36}$(hfipbb)**	**$Zn_{0.48}Ca_{0.52}$(hfipbb)**
CCDC number	1531922	1531909
Empirical formula	$C_{17}H_8Ca_{0.35}F_6O_4Zn_{0.65}$	$C_{17}H_8Ca_{0.45}F_6O_4Zn_{0.55}$
Formula weight	446.75	444.22
Temperature/K	573.15	300.0
Crystal system	hexagonal	hexagonal
Space group	$P6_122$	$P6_122$
a/Å	21.2239(8)	21.2561(4)
b/Å	21.2239(8)	21.2561(4)
c/Å	15.5784(6)	15.6662(3)
α/°	90	90
β/°	90	90
γ/°	120	120
Volume/$Å^3$	6077.2(5)	6130.0(3)
Z	12	12
$\rho_{calc}g/cm^3$	1.465	1.444
μ/mm^{-1}	2.721	2.796
F(000)	2670.0	2658.0
Crystal size/mm^3	0.2 × 0.1 × 0.1	0.4 × 0.2 × 0.2
Radiation	CuKα (λ = 1.54178)	CuKα (λ = 1.54178)
2Θ range for data collection/°	4.808 to 130.3	4.8 to 130.276
Index ranges	$-19 \leq h \leq 24$, $-24 \leq k \leq 24$, $-18 \leq l \leq 18$	$-24 \leq h \leq 25$, $-24 \leq k \leq 25$, $-18 \leq l \leq 18$
Reflections collected	44362	50448
Independent reflections	3462 [R_{int} = 0.0511, R_{sigma} = 0.0247]	3500 [R_{int} = 0.0452, R_{sigma} = 0.0159]
Data/restraints/parameters	3462/0/268	3500/0/259
Goodness-of-fit on F^2	1.124	1.091
Final R indexes [I>=2σ (I)]	R_1 = 0.0281, wR_2 = 0.0681	R_1 = 0.0232, wR_2 = 0.0608
Final R indexes [all data]	R_1 = 0.0292, wR_2 = 0.0690	R_1 = 0.0239, wR_2 = 0.0612
Largest diff. peak/hole / e $Å^{-3}$	0.22/-0.27	0.15/-0.33
Flack parameter	0.024(6)	0.023(4)

Table A. 8. Crystal data and structure refinement for $Zn_{0.64}Ca_{0.36}$(hfipbb) (molar code: Zn:Ca 1:4) (CCDC number: 1531922) (second column) and $Zn_{0.48}Ca_{0.52}$(hfipbb) (molar code: Zn:Ca 1:10) (CCDC number: 1531909) (third column).

Identification code	**$Zn_{0.72}Co_{0.17}Ca_{0.11}$(hfipbb)**	**$Zn_{0.33}Co_{0.37}Ca_{0.30}$(hfipbb)**
CCDC number	1531925	1531907
Empirical formula	$C_{17}H_8Ca_{0.2}Co_{0.16}F_6O_4Zn_{0.64}$	$C_{17}H_8Ca_{0.28}Co_{0.45}F_6O_4Zn_{0.28}$
Formula weight	449.54	445.72
Temperature/K	293	296.15
Crystal system	hexagonal	hexagonal
Space group	$P6_122$	$P6_122$
a/Å	21.2155(6)	21.247(3)
b/Å	21.2155(6)	21.247(3)
c/Å	15.4126(5)	15.347(3)
α/°	90	90
β/°	90	90
γ/°	120	120
Volume/$Å^3$	6007.8(4)	6000(2)
Z	12	12
$\rho_{calc}g/cm^3$	1.491	1.480
μ/mm^{-1}	3.388	4.919
F(000)	2682.0	2663.0
Crystal size/mm^3	0.16 × 0.12 × 0.1	0.16 × 0.06 × 0.06
Radiation	CuKα (λ = 1.54178)	CuKα (λ = 1.54178)
2Θ range for data collection/°	7.486 to 130.304	4.802 to 130.522
Index ranges	$-24 \leq h \leq 23$, $-24 \leq k \leq 24$, $-17 \leq l \leq 14$	$-24 \leq h \leq 23$, $-25 \leq k \leq 25$, $-18 \leq l \leq 16$
Reflections collected	36661	72178
Independent reflections	3419 [R_{int} = 0.0722, R_{sigma} = 0.0330]	3430 [R_{int} = 0.2441, R_{sigma} = 0.0816]
Data/restraints/parameters	3419/0/264	3430/0/257
Goodness-of-fit on F^2	1.993	1.074
Final R indexes [I>=2σ (I)]	R_1 = 0.1514, wR_2 = 0.4056	R_1 = 0.0666, wR_2 = 0.1047
Final R indexes [all data]	R_1 = 0.1606, wR_2 = 0.4184	R_1 = 0.1291, wR_2 = 0.1253
Largest diff. peak/hole / e $Å^{-3}$	0.91/-2.70	0.26/-0.39
Flack parameter	0.420(13)	0.069(6)

Table A. 9. Crystal data and structure refinement for $Zn_{0.72}Co_{0.17}Ca_{0.11}$(hfipbb) (molar code: Zn:Co:Ca 1:1:1) (CCDC number: 1531925) (second column) and $Zn_{0.33}Co_{0.37}Ca_{0.30}$(hfipbb) (molar code: Zn:Co:Ca 1:4:4) (CCDC number: 1531907) (third column).

Identification code	**$Zn_{0.37}Co_{0.14}Ca_{0.49}$(hfipbb)**	**$Zn_{0.48}Mn_{0.42}Ca_{0.10}$(hfipbb)**
CCDC number	1531908	1531917
Empirical formula	$C_{17}H_8Ca_{0.5}Co_{0.12}F_6O_4Zn_{0.38}$	$C_{17}H_8Ca_{0.1}F_6Mn_{0.4}O_4Zn_{0.5}$
Formula weight	442.19	448.90
Temperature/K	300	300
Crystal system	hexagonal	hexagonal
Space group	$P6_122$	$P6_522$
a/Å	21.2593(3)	21.2996(4)
b/Å	21.2593(3)	21.2996(4)
c/Å	15.6553(3)	15.1816(3)
α/°	90	90
β/°	90	90
γ/°	120	120
Volume/$Å^3$	6127.6(2)	5964.7(3)
Z	12	12
$\rho_{calc}g/cm^3$	1.438	1.500
μ/mm^{-1}	3.436	3.994
F(000)	2648.0	2676.0
Crystal size/mm^3	0.4 × 0.2 × 0.2	0.12 × 0.06 × 0.06
Radiation	CuKα (λ = 1.54178)	CuKα (λ = 1.54178)
2Θ range for data collection/°	4.8 to 130.41	7.542 to 130.274
Index ranges	$-24 \leq h \leq 24$, $-24 \leq k \leq 24$, $-16 \leq l \leq 18$	$-25 \leq h \leq 25$, $-24 \leq k \leq 25$, $-17 \leq l \leq 16$
Reflections collected	70665	75667
Independent reflections	3493 [R_{int} = 0.0848, R_{sigma} = 0.0265]	3404 [R_{int} = 0.0982, R_{sigma} = 0.0207]
Data/restraints/parameters	3493/0/254	3404/0/259
Goodness-of-fit on F^2	1.137	1.073
Final R indexes [I>=2σ (I)]	R_1 = 0.0396, wR_2 = 0.0968	R_1 = 0.0296, wR_2 = 0.0794
Final R indexes [all data]	R_1 = 0.0463, wR_2 = 0.1004	R_1 = 0.0297, wR_2 = 0.0795
Largest diff. peak/hole / e $Å^{-3}$	0.39/-0.31	0.18/-0.36
Flack parameter	0.023(7)	-0.001(2)

Table A. 10. Crystal data and structure refinement for $Zn_{0.37}Co_{0.14}Ca_{0.49}$(hfipbb) (molar code: Zn:Co:Ca 1:1:8) (CCDC number: 1531908) (second column) and $Zn_{0.48}Mn_{0.42}Ca_{0.10}$(hfipbb) (molar code: Zn:Mn:Ca 1:1:1) (CCDC number: 1531917) (third column).

Identification code	**$Zn_{0.52}Mn_{0.30}Ca_{0.18}$(hfipbb)**	**$Zn_{0.44}Mn_{0.44}Co_{0.12}$(hfipbb)**
CCDC number	1531911	1531913
Empirical formula	$C_{17}H_8Ca_{0.14}F_6Mn_{0.36}O_4Zn_{0.5}$	$C_{17}H_8Co_{0.06}F_6Mn_{0.47}O_{4.25}Zn_{0.47}$
Formula weight	448.32	455.65
Temperature/K	300.0	573.15
Crystal system	hexagonal	hexagonal
Space group	$P6_122$	$P6_122$
a/Å	21.2727(5)	21.2842(7)
b/Å	21.2727(5)	21.2842(7)
c/Å	15.3429(4)	15.1094(6)
α/°	90	90
β/°	90	90
γ/°	120	120
Volume/$Å^3$	6012.9(3)	5927.8(5)
Z	12	12
$\rho_{calc}g/cm^3$	1.486	1.532
μ/mm^{-1}	3.858	4.502
F(000)	2674.0	2714.0
Crystal size/mm^3	0.18 × 0.1 × 0.1	0.26 × 0.12 × 0.12
Radiation	CuKα (λ = 1.54178)	CuKα (λ = 1.54178)
2Θ range for data collection/°	4.796 to 131.682	4.794 to 130.608
Index ranges	$-25 \leq h \leq 25$, $-22 \leq k \leq 25$, $-18 \leq l \leq 18$	$-25 \leq h \leq 25$, $-25 \leq k \leq 25$, $-17 \leq l \leq 15$
Reflections collected	40514	89840
Independent reflections	3477 [R_{int} = 0.0568, R_{sigma} = 0.0256]	3399 [R_{int} = 0.0884, R_{sigma} = 0.0244]
Data/restraints/parameters	3477/0/260	3399/0/265
Goodness-of-fit on F^2	1.104	1.149
Final R indexes [I>=2σ (I)]	R_1 = 0.0396, wR_2 = 0.1172	R_1 = 0.0396, wR_2 = 0.1073
Final R indexes [all data]	R_1 = 0.0422, wR_2 = 0.1243	R_1 = 0.0452, wR_2 = 0.1100
Largest diff. peak/hole / e $Å^{-3}$	0.90/-0.64	0.84/-0.38
Flack parameter	0.002(5)	0.016(3)

Table A. 11. Crystal data and structure refinement for $Zn_{0.52}Mn_{0.30}Ca_{0.18}$(hfipbb) (molar code: Zn:Mn:Ca 1:1:8) (CCDC number: 1531911) (second column) and $Zn_{0.44}Mn_{0.44}Co_{0.12}$(hfipbb) (molar code: Zn:Mn:Co 1:1:1) (CCDC number: 1531913) (third column).

Identification code	**$Zn_{0.54}Mn_{0.37}Co_{0.09}$(hfipbb)**	**$Zn_{0.37}Mn_{0.50}Co_{0.13}$(hfipbb)**
CCDC number	1531910	1531905
Empirical formula	$C_{8.5}H_4Co_{0.04}F_3Mn_{0.21}O_{2.25}Zn_{0.25}$	$C_{17}H_8Co_{0.13}F_6Mn_{0.5}O_4Zn_{0.37}$
Formula weight	229.35	449.57
Temperature/K	273.15	300
Crystal system	hexagonal	hexagonal
Space group	$P6_522$	$P6_122$
a/Å	21.2838(11)	21.2989(4)
b/Å	21.2838(11)	21.2989(4)
c/Å	15.0974(12)	15.1248(3)
α/°	90	90
β/°	90	90
γ/°	120	120
Volume/$Å^3$	5922.9(8)	5942.0(3)
Z	24	12
$\rho_{calc}g/cm^3$	1.543	1.508
μ/mm^{-1}	4.433	4.920
F(000)	2732.0	2677.0
Crystal size/mm^3	0.12 × 0.08 × 0.08	0.1 × 0.04 × 0.04
Radiation	CuKα (λ = 1.54178)	CuKα (λ = 1.54178)
2Θ range for data collection/°	7.568 to 130.368	4.79 to 130.316
Index ranges	$-16 \le h \le 24$, $-24 \le k \le 24$, $-17 \le l \le 17$	$-22 \le h \le 25$, $-24 \le k \le 22$, $-16 \le l \le 17$
Reflections collected	22355	64057
Independent reflections	3384 [R_{int} = 0.0976, R_{sigma} = 0.0556]	3394 [R_{int} = 0.0355, R_{sigma} = 0.0117]
Data/restraints/parameters	3384/0/267	3394/0/260
Goodness-of-fit on F^2	1.033	1.073
Final R indexes [I>=2σ (I)]	R_1 = 0.0529, wR_2 = 0.1370	R_1 = 0.0279, wR_2 = 0.0731
Final R indexes [all data]	R_1 = 0.0684, wR_2 = 0.1491	R_1 = 0.0293, wR_2 = 0.0743
Largest diff. peak/hole / e $Å^{-3}$	0.54/-0.39	0.21/-0.18
Flack parameter	0.054(7)	-0.006(2)

Table A. 12. Crystal data and structure refinement for $Zn_{0.54}Mn_{0.37}Co_{0.09}$(hfipbb) (molar code: Zn:Mn:Co 2:1:1) (CCDC number: 1531910) (second column) and $Zn_{0.37}Mn_{0.50}Co_{0.13}$(hfipbb) (molar code: Zn:Mn:Co 1:2:1) (CCDC number: 1531905) (third column).

Identification code	**$Zn_{0.32}Mn_{0.39}Co_{0.28}$(hfipbb)**	**$Zn_{0.22}Mn_{0.32}Co_{0.46}$(hfipbb)**
CCDC number	1531904	1531900
Empirical formula	$C_{17}H_8Co_{0.25}F_6Mn_{0.4}O_{4.2}Zn_{0.35}$	$C_{17}H_8Co_{0.53}F_6Mn_{0.26}O_{4.5}Zn_{0.21}$
Formula weight	453.02	457.42
Temperature/K	296.15	296.15
Crystal system	hexagonal	hexagonal
Space group	$P6_522$	$P6_522$
a/Å	21.2813(5)	21.2551(7)
b/Å	21.2813(5)	21.2551(7)
c/Å	15.0807(4)	15.0041(7)
α/°	90	90
β/°	90	90
γ/°	120	120
Volume/$Å^3$	5914.9(3)	5870.4(5)
Z	12	12
$\rho_{calc}g/cm^3$	1.526	1.553
μ/mm^{-1}	5.212	6.169
F(000)	2698.0	2725.0
Crystal size/mm^3	0.12 × 0.06 × 0.06	0.1 × 0.04 × 0.04
Radiation	CuKα (λ = 1.54178)	CuKα (λ = 1.54178)
2Θ range for data collection/°	4.794 to 131.184	4.8 to 130.99
Index ranges	$-24 \le h \le 25$, $-25 \le k \le 25$, $-17 \le l \le 17$	$-24 \le h \le 25$, $-25 \le k \le 25$, $-17 \le l \le 17$
Reflections collected	46276	46565
Independent reflections	3405 [R_{int} = 0.1307, R_{sigma} = 0.0486]	3379 [R_{int} = 0.1124, R_{sigma} = 0.0428]
Data/restraints/parameters	3405/0/260	3379/0/266
Goodness-of-fit on F^2	1.092	1.035
Final R indexes [I>=2σ (I)]	R_1 = 0.0525, wR_2 = 0.1392	R_1 = 0.0487, wR_2 = 0.1309
Final R indexes [all data]	R_1 = 0.0613, wR_2 = 0.1462	R_1 = 0.0581, wR_2 = 0.1387
Largest diff. peak/hole / e $Å^{-3}$	0.82/-0.41	0.72/-0.34
Flack parameter	0.064(7)	-0.003(4)

Table A. 13. Crystal data and structure refinement for (second column) $Zn_{0.32}Mn_{0.38}Co_{0.28}$(hfipbb) (molar code: Zn:Mn:Co 1:1:2) (CCDC number: 1531904) and $Zn_{0.22}Mn_{0.32}Co_{0.46}$(hfipbb) (molar code: Zn:Mn:Co 1:1:8) (CCDC number: 1531900) (third column).

Identification code	**$Zn_{0.12}Mn_{0.42}Co_{0.46}$(hfipbb)**	**$Zn_{0.23}Mn_{0.44}Co_{0.33}$(hfipbb)**
CCDC number	1531906	1853404
Empirical formula	$C_{17}H_8Co_{0.52}F_6Mn_{0.38}O_{4.4}Zn_{0.11}$	$C_{17}Co_{0.48}F_6Mn_{0.35}O_4Zn_{0.17}H_8$
Formula weight	456.29	440.83
Temperature/K	300	250
Crystal system	hexagonal	hexagonal
Space group	$P6_122$	$P6_522$
a/Å	21.2847(4)	21.2639(12)
b/Å	21.2847(4)	21.2639(12)
c/Å	15.1009(3)	15.1083(12)
α/°	90	90
β/°	90	90
γ/°	120	120
Volume/$Å^3$	5924.7(3)	5916.1(8)
Z	12	12
$\rho_{calc}g/cm^3$	1.535	1.485
μ/mm^{-1}	6.508	6.202
F(000)	2718.0	2578.0
Crystal size/mm^3	0.12 × 0.06 × 0.06	0.08 × 0.02 × 0.02
Radiation	CuKα (λ = 1.54178)	CuKα (λ = 1.54178)
2Θ range for data collection/°	4.794 to 130.358	4.798 to 131.17
Index ranges	$-25 \leq h \leq 25$, $-25 \leq k \leq 24$, $-17 \leq l \leq 15$	$-25 \leq h \leq 25$, $-25 \leq k \leq 24$, $-17 \leq l \leq 17$
Reflections collected	92627	34738
Independent reflections	3384 [R_{int} = 0.0472, R_{sigma} = 0.0131]	3406 [R_{int} = 0.1470, R_{sigma} = 0.0739]
Data/restraints/parameters	3384/0/266	3406/0/266
Goodness-of-fit on F^2	1.104	1.053
Final R indexes [I>=2σ (I)]	R_1 = 0.0313, wR_2 = 0.1137	R_1 = 0.0615, wR_2 = 0.1574
Final R indexes [all data]	R_1 = 0.0326, wR_2 = 0.1156	R_1 = 0.0791, wR_2 = 0.1661
Largest diff. peak/hole / e $Å^{-3}$	0.38/-0.34	0.71/-0.54
Flack parameter	-0.0026(14)	0.001(9)

Table A. 14. Crystal data and structure refinement details for $Zn_{0.12}Mn_{0.42}Co_{0.46}$(hfipbb) (molar code: Zn:Mn:Co 1:3:9) (CCDC number: 1531906) (second column) and $Zn_{0.23}Mn_{0.44}Co_{0.33}$(hfipbb) (molar code: Zn:Mn:Co 1:4:4) (CCDC number: 1853404) (third column).

Identification code	**$Zn_{0.17}Mn_{0.41}Co_{0.42}$(hfipbb)**	**$Zn_{0.12}Mn_{0.39}Co_{0.49}$(hfipbb)**
CCDC number	1853405	1853407
Empirical formula	$C_{17}H_8Co_{0.3}F_6Mn_{0.49}O_{4.25}Zn_{0.21}$	$C_{17}Co_{0.49}F_6Mn_{0.41}O_4Zn_{0.1}H_8$
Formula weight	452.58	440.24
Temperature/K	250	250
Crystal system	hexagonal	hexagonal
Space group	$P6_122$	$P6_122$
a/Å	21.2528(9)	21.286(3)
b/Å	21.2528(9)	21.286(3)
c/Å	15.0710(7)	15.082(2)
α/°	90	90
β/°	90	90
γ/°	120	120
Volume/$Å^3$	5895.3(6)	5918.0(17)
Z	12	12
$\rho_{calc}g/cm^3$	1.530	1.482
μ/mm^{-1}	5.813	6.441
F(000)	2696.0	2575.0
Crystal size/mm^3	0.1 × 0.02 × 0.02	0.1 × 0.03 × 0.03
Radiation	CuKα (λ = 1.54178)	CuKα (λ = 1.54178)
2Θ range for data collection/°	4.8 to 131.212	4.794 to 131.13
Index ranges	$-25 \le h \le 25$, $-20 \le k \le 25$, $-17 \le l \le 17$	$-25 \le h \le 25$, $-25 \le k \le 24$, $-17 \le l \le 16$
Reflections collected	26342	32046
Independent reflections	3330 [R_{int} = 0.0583, R_{sigma} = 0.0369]	3407 [R_{int} = 0.1023, R_{sigma} = 0.0533]
Data/restraints/parameters	3330/0/247	3407/0/262
Goodness-of-fit on F^2	2.611	1.321
Final R indexes [I>=2σ (I)]	R_1 = 0.0949, wR_2 = 0.2446	R_1 = 0.0678, wR_2 = 0.1753
Final R indexes [all data]	R_1 = 0.1172, wR_2 = 0.3139	R_1 = 0.0815, wR_2 = 0.1856
Largest diff. peak/hole / e $Å^{-3}$	1.48/-1.25	0.92/-0.83
Flack parameter	-0.022(7)	-0.012(6)

Table A. 15. Crystal data and structure refinement details for $Zn_{0.17}Mn_{0.41}Co_{0.42}$(hfipbb) (molar code: Zn:Mn:Co 1:4:6) (CCDC number: 1853405) (second column) and $Zn_{0.12}Mn_{0.39}Co_{0.49}$(hfipbb) (molar code: Zn:Mn:Co 1:6:12) (CCDC number: 1853407) (third column).

Identification code	**$Zn_{0.10}Mn_{0.40}Co_{0.50}$(hfipbb)**	**$Zn_{0.17}Mn_{0.45}Co_{0.38}$(hfipbb)**
CCDC number	1853408	1853406
Empirical formula	$C_{17}H_8Co_{0.38}F_6Mn_{0.52}O_{4.5}Zn_{0.12}$	$C_{17}Co_{0.44}F_6Mn_{0.43}O_4Zn_{0.13}H_8$
Formula weight	457.26	440.30
Temperature/K	250	250
Crystal system	hexagonal	hexagonal
Space group	$P6_122$	$P6_522$
a/Å	21.2553(10)	21.2819(9)
b/Å	21.2553(10)	21.2819(9)
c/Å	15.0696(11)	15.1237(8)
α/°	90	90
β/°	90	90
γ/°	120	120
Volume/$Å^3$	5896.1(7)	5932.1(6)
Z	12	12
$\rho_{calc}g/cm^3$	1.545	1.479
μ/mm^{-1}	6.409	6.275
F(000)	2724.0	2575.0
Crystal size/mm^3	0.1 × 0.03 × 0.03	0.08 × 0.02 × 0.02
Radiation	CuKα (λ = 1.54178)	CuKα (λ = 1.54178)
2Θ range for data collection/°	4.8 to 130.164	4.794 to 130.782
Index ranges	$-24 \leq h \leq 24$, $-24 \leq k \leq 24$, $-16 \leq l \leq 17$	$-25 \leq h \leq 24$, $-25 \leq k \leq 24$, $-17 \leq l \leq 17$
Reflections collected	34740	34454
Independent reflections	3360 [R_{int} = 0.2062, R_{sigma} = 0.1189]	3396 [R_{int} = 0.0999, R_{sigma} = 0.0515]
Data/restraints/parameters	3360/0/264	3396/0/260
Goodness-of-fit on F^2	1.129	1.056
Final R indexes [I>=2σ (I)]	R_1 = 0.0892, wR_2 = 0.1983	R_1 = 0.0535, wR_2 = 0.1399
Final R indexes [all data]	R_1 = 0.1053, wR_2 = 0.2095	R_1 = 0.0647, wR_2 = 0.1488
Largest diff. peak/hole / e $Å^{-3}$	0.65/-0.59	0.68/-0.54
Flack parameter	-0.001(10)	0.002(6)

Table A. 16. Crystal data and structure refinement details for $Zn_{0.10}Mn_{0.40}Co_{0.50}$(hfipbb) (molar code: Zn:Mn:Co 1:10:20) (CCDC number: 1853408) (second column) and $Zn_{0.17}Mn_{0.45}Co_{0.38}$(hfipbb) (molar code: Zn:Mn:Co 1:12:6) (CCDC number: 1853406) (third column).

Identification code	**$Zn_{0.42}Mn_{0.42}Co_{0.11}Ca_{0.06}$(hfipbb)**	**$Zn_{0.13}Mn_{0.27}Co_{0.52}Ca_{0.03}$(hfipbb)**
CCDC number	1853391	1853395
Empirical formula	$C_{17}H_8Co_{0.1}F_6Mn_{0.5}O_{4.15}Zn_{0.4}$	$C_{17}H_8Co_{0.47}F_6Mn_{0.33}O_{4.33}Zn_{0.2}$
Formula weight	452.29	454.41
Temperature/K	273.15	250
Crystal system	hexagonal	hexagonal
Space group	$P6_522$	$P6_122$
a/Å	21.2761(12)	21.2398(5)
b/Å	21.2761(12)	21.2398(5)
c/Å	15.1699(10)	15.0528(5)
α/°	90	90
β/°	90	90
γ/°	120	120
Volume/$Å^3$	5947.0(8)	5881.0(3)
Z	12	12
$\rho_{calc}g/cm^3$	1.515	1.540
μ/mm^{-1}	4.794	6.103
F(000)	2694.0	2707.0
Crystal size/mm^3	0.4 × 0.14 × 0.14	0.14 × 0.06 × 0.06
Radiation	CuKα (λ = 1.54178)	CuKα (λ = 1.54178)
2Θ range for data collection/°	4.796 to 130.458	4.804 to 131.694
Index ranges	$-25 \leq h \leq 25$, $-25 \leq k \leq 25$, $-17 \leq l \leq 17$	$-21 \leq h \leq 25$, $-25 \leq k \leq 24$, $-17 \leq l \leq 16$
Reflections collected	56557	46450
Independent reflections	3404 [R_{int} = 0.0664, R_{sigma} = 0.0240]	3413 [R_{int} = 0.0880, R_{sigma} = 0.0339]
Data/restraints/parameters	3404/0/264	3413/0/266
Goodness-of-fit on F^2	1.168	1.115
Final R indexes [I>=2σ (I)]	R_1 = 0.0307, wR_2 = 0.0918	R_1 = 0.0413, wR_2 = 0.1134
Final R indexes [all data]	R_1 = 0.0322, wR_2 = 0.0928	R_1 = 0.0467, wR_2 = 0.1173
Largest diff. peak/hole / e $Å^{-3}$	0.73/-0.26	0.66/-0.33
Flack parameter	0.006(2)	-0.005(4)

Table A. 17. Crystal data and structure refinement for $Zn_{0.42}Mn_{0.42}Co_{0.11}Ca_{0.06}$(hfipbb) (molar code: Zn:Mn:Co:Ca 1:1:1:1) (CCDC number: 1853391) (second column) and $Zn_{0.13}Mn_{0.27}Co_{0.52}Ca_{0.03}$(hfipbb) (molar code: Zn:Mn:Co:Ca 1:1:7:1) (CCDC number: 1853395) (third column).

Identification code	**$Zn_{0.37}Mn_{0.28}Co_{0.13}Ca_{0.22}$(hfipbb)**	**$Zn_{0.16}Mn_{0.47}Co_{0.33}Ca_{0.03}$(hfipbb)**
CCDC number	1853392	1853397
Empirical formula	$C_{17}H_8Ca_{0.21}Co_{0.12}F_6Mn_{0.29}O_4Zn_{0.38}$	$C_{17}H_8Co_{0.36}F_6Mn_{0.49}O_{4.17}Zn_{0.14}$
Formula weight	446.47	450.40
Temperature/K	296.15	296.15
Crystal system	hexagonal	hexagonal
Space group	$P6_522$	$P6_522$
a/Å	21.2824(18)	21.2423(6)
b/Å	21.2824(18)	21.2423(6)
c/Å	15.3210(14)	15.1282(6)
α/°	90	90
β/°	90	90
γ/°	120	120
Volume/$Å^3$	6009.8(12)	5911.8(4)
Z	12	12
$\rho_{calc}g/cm^3$	1.480	1.518
μ/mm^{-1}	4.248	6.128
F(000)	2665.0	2683.0
Crystal size/mm^3	0.1 × 0.04 × 0.04	0.12 × 0.04 × 0.04
Radiation	CuKα (λ = 1.54178)	CuKα (λ = 1.54178)
2Θ range for data collection/°	7.504 to 131.078	4.804 to 131.38
Index ranges	$-25 \le h \le 15$, $-19 \le k \le 25$, $-18 \le l \le 18$	$-24 \le h \le 25$, $-25 \le k \le 24$, $-17 \le l \le 17$
Reflections collected	30147	46154
Independent reflections	3351 [R_{int} = 0.0663, R_{sigma} = 0.0336]	3427 [R_{int} = 0.0847, R_{sigma} = 0.0347]
Data/restraints/parameters	3351/0/258	3427/0/263
Goodness-of-fit on F^2	1.655	0.956
Final R indexes [I>=2σ (I)]	R_1 = 0.1315, wR_2 = 0.3060	R_1 = 0.0398, wR_2 = 0.1156
Final R indexes [all data]	R_1 = 0.1396, wR_2 = 0.3335	R_1 = 0.0441, wR_2 = 0.1190
Largest diff. peak/hole / e $Å^{-3}$	1.91/-2.00	0.78/-0.28
Flack parameter	-0.044(12)	-0.001(4)

Table A. 18. Crystal data and structure refinement for $Zn_{0.37}Mn_{0.28}Co_{0.13}Ca_{0.22}$(hfipbb) (molar code: Zn:Mn:Co:Ca 1:1:1:7) (CCDC number: 1853392) (second column) and $Zn_{0.16}Mn_{0.47}Co_{0.33}Ca_{0.03}$(hfipbb) (molar code: Zn:Mn:Co:Ca 1:4:4:1) (CCDC number: 1853397) (third column).

Identification code	**$Zn_{0.18}Mn_{0.24}Co_{0.41}Ca_{0.16}$(hfipbb)**	**$Zn_{0.24}Mn_{0.37}Co_{0.31}Ca_{0.08}$(hfipbb)**
CCDC number	1853393	1853399
Empirical formula	$C_{17}H_8Ca_{0.13}Co_{0.28}F_6Mn_{0.37}O_{4.5}Zn_{0.22}$	$C_{17}H_8Ca_{0.07}Co_{0.27}F_6Mn_{0.43}O_{4.38}Zn_{0.23}$
Formula weight	454.73	453.68
Temperature/K	296.15	250
Crystal system	hexagonal	hexagonal
Space group	$P6_122$	$P6_522$
a/Å	21.2251(7)	21.2716(12)
b/Å	21.2251(7)	21.2716(12)
c/Å	15.2830(7)	15.1756(11)
α/°	90	90
β/°	90	90
γ/°	120	120
Volume/$Å^3$	5962.6(5)	5946.7(8)
Z	12	12
$\rho_{calc}g/cm^3$	1.520	1.520
μ/mm^{-1}	5.349	5.474
F(000)	2712.0	2704.0
Crystal size/mm^3	0.12 × 0.06 × 0.06	0.14 × 0.06 × 0.06
Radiation	CuKα (λ = 1.54178)	CuKα (λ = 1.54178)
2Θ range for data collection/°	4.808 to 133.55	4.796 to 131.722
Index ranges	$-25 \leq h \leq 25$, $-24 \leq k \leq 24$, $-18 \leq l \leq 17$	$-25 \leq h \leq 25$, $-24 \leq k \leq 25$, $-17 \leq l \leq 17$
Reflections collected	39066	27460
Independent reflections	3461 [R_{int} = 0.0847, R_{sigma} = 0.0428]	3440 [R_{int} = 0.0798, R_{sigma} = 0.0425]
Data/restraints/parameters	3461/0/264	3440/0/263
Goodness-of-fit on F^2	1.162	1.618
Final R indexes [I>=2σ (I)]	R_1 = 0.0770, wR_2 = 0.1891	R_1 = 0.0774, wR_2 = 0.2006
Final R indexes [all data]	R_1 = 0.0955, wR_2 = 0.2050	R_1 = 0.0850, wR_2 = 0.2064
Largest diff. peak/hole / e $Å^{-3}$	0.74/-0.50	0.89/-0.77
Flack parameter	0.000(7)	-0.026(9)

Table A. 19. Crystal data and structure refinement for $Zn_{0.18}Mn_{0.24}Co_{0.41}Ca_{0.16}$(hfipbb) (molar code: Zn:Mn:Co:Ca 1:1:4:4) (CCDC number: 1853393) (second column) and $Zn_{0.24}Mn_{0.37}Co_{0.31}Ca_{0.08}$(hfipbb) (molar code: Zn:Mn:Co:Ca 1:4:4:4) (CCDC number: 1853399) (third column).

Identification code	**$Zn_{0.32}Mn_{0.40}Co_{0.15}Ca_{0.12}$(hfipbb)**	**$Zn_{0.46}Mn_{0.21}Co_{0.17}Ca_{0.15}$(hfipbb)**
CCDC number	1853396	1853401
Empirical formula	$C_{17}H_8Co_{0.14}F_6Mn_{0.51}O_{4.25}Zn_{0.36}Ca_{0.08}$	$C_{17}H_8Ca_{0.04}Co_{0.06}F_6Mn_{0.46}O_{4.5}Zn_{0.44}$
Formula weight	457.10	457.40
Temperature/K	250	250
Crystal system	hexagonal	hexagonal
Space group	$P6_522$	$P6_522$
a/Å	21.2398(7)	21.2232(6)
b/Å	21.2398(7)	21.2232(6)
c/Å	15.1793(9)	15.1771(6)
α/°	90	90
β/°	90	90
γ/°	120	120
Volume/$Å^3$	5930.4(5)	5920.3(4)
Z	12	12
$\rho_{calc}g/cm^3$	1.536	1.540
μ/mm^{-1}	5.228	4.530
F(000)	2722.0	2725.0
Crystal size/mm^3	0.08 × 0.03 × 0.03	0.14 × 0.06 × 0.06
Radiation	CuKα (λ = 1.54178)	CuKα (λ = 1.54178)
2Θ range for data collection/°	4.804 to 132.44	4.808 to 131.474
Index ranges	$-25 \leq h \leq 24$, $-23 \leq k \leq 25$, $-17 \leq l \leq 18$	$-24 \leq h \leq 21$, $-24 \leq k \leq 25$, $-17 \leq l \leq 17$
Reflections collected	34671	33724
Independent reflections	3451 [R_{int} = 0.1178, R_{sigma} = 0.0630]	3391 [R_{int} = 0.0776, R_{sigma} = 0.0374]
Data/restraints/parameters	3451/0/269	3391/0/266
Goodness-of-fit on F^2	1.185	1.064
Final R indexes [I>=2σ (I)]	R_1 = 0.0676, wR_2 = 0.1733	R_1 = 0.0589, wR_2 = 0.1717
Final R indexes [all data]	R_1 = 0.0807, wR_2 = 0.1841	R_1 = 0.0706, wR_2 = 0.1950
Largest diff. peak/hole / e $Å^{-3}$	0.76/-0.49	0.83/-0.59
Flack parameter	-0.012(10)	0.033(6)

Table A. 20. Crystal data and structure refinement for $Zn_{0.32}Mn_{0.40}Co_{0.15}Ca_{0.12}$(hfipbb) (molar code: Zn:Mn:Co:Ca 1:4:1:4) (CCDC number: 1853396) (second column) and $Zn_{0.46}Mn_{0.21}Co_{0.17}Ca_{0.15}$(hfipbb) (molar code: Zn:Mn:Co:Ca 2:1:2:2) (CCDC number: 1853401) (third column).

Identification code	**$Zn_{0.27}Mn_{0.34}Co_{0.26}Ca_{0.12}$(hfipbb)**	**$Zn_{0.21}Mn_{0.27}Co_{0.30}Ca_{0.22}$(hfipbb)**
CCDC number	1853398	1853400
Empirical formula	$C_{17}Ca_{0.08}F_6Mn_{0.42}O_{4.08}Zn_{0.5}Co_{0.08}H_8$	$C_{17}H_8Ca_{0.11}Co_{0.3}F_6Mn_{0.4}O_{4.5}Zn_{0.2}$
Formula weight	447.33	455.24
Temperature/K	250	250
Crystal system	hexagonal	hexagonal
Space group	$P6_122$	$P6_122$
a/Å	21.2746(11)	21.2258(6)
b/Å	21.2746(11)	21.2258(6)
c/Å	15.2223(9)	15.2542(5)
α/°	90	90
β/°	90	90
γ/°	120	120
Volume/Å^3	5966.7(7)	5951.8(4)
Z	12	12
ρ_{calc}g/cm^3	1.494	1.524
μ/mm^{-1}	4.576	5.563
F(000)	2616.0	2715.0
Crystal size/mm^3	0.12 × 0.08 × 0.08	0.12 × 0.04 × 0.04
Radiation	CuKα (λ = 1.54178)	CuKα (λ = 1.54178)
2Θ range for data collection/°	4.796 to 131.842	4.808 to 131.438
Index ranges	-24 ≤ h ≤ 25, -25 ≤ k ≤ 25, -17 ≤ l ≤ 17	-24 ≤ h ≤ 24, -25 ≤ k ≤ 24, -17 ≤ l ≤ 17
Reflections collected	33414	31965
Independent reflections	3458 [R_{int} = 0.0672, R_{sigma} = 0.0331]	3385 [R_{int} = 0.0802, R_{sigma} = 0.0395]
Data/restraints/parameters	3458/0/267	3385/0/270
Goodness-of-fit on F^2	1.192	1.376
Final R indexes [I>=2σ (I)]	R_1 = 0.0491, wR_2 = 0.1395	R_1 = 0.0574, wR_2 = 0.1632
Final R indexes [all data]	R_1 = 0.0539, wR_2 = 0.1453	R_1 = 0.0653, wR_2 = 0.1724
Largest diff. peak/hole / e Å^{-3}	0.78/-0.51	0.54/-0.52
Flack parameter	-0.008(5)	-0.003(8)

Table A. 21. Crystal data and structure refinement for $Zn_{0.27}Mn_{0.34}Co_{0.26}Ca_{0.12}$(hfipbb) (molar code: Zn:Mn:Co:Ca 1:2:2:4) (CCDC number: 1853398) (second column) and $Zn_{0.21}Mn_{0.27}Co_{0.30}Ca_{0.22}$(hfipbb) (molar code: Zn:Mn:Co:Ca 1:4:4:8) (CCDC number: 1853400)(third column).

Identification code	**$Zn_{0.26}Mn_{0.16}Co_{0.37}Ca_{0.21}$(hfipbb)**	**$Mn_{0.41}Co_{0.59}$(hfipbb)**
CCDC number	1853394	1853402
Empirical formula	$C_{17}H_8Ca_{0.21}Co_{0.27}F_6Mn_{0.29}O_{4.33}Zn_{0.23}$	$C_{17}H_8Co_{0.5}F_6Mn_{0.5}O_4$
Formula weight	450.88	447.17
Temperature/K	250	250
Crystal system	hexagonal	hexagonal
Space group	$P6_522$	$P6_122$
a/Å	21.250(2)	21.2619(13)
b/Å	21.250(2)	21.2619(13)
c/Å	15.3379(18)	15.1193(12)
α/°	90	90
β/°	90	90
γ/°	120	120
Volume/$Å^3$	5998.4(14)	5919.2(9)
Z	12	12
$\rho_{calc}g/cm^3$	1.498	1.505
μ/mm^{-1}	5.075	6.840
F(000)	2692.0	2664.0
Crystal size/mm^3	0.1 × 0.04 × 0.04	0.12 × 0.04 × 0.04
Radiation	CuKα (λ = 1.54178)	CuKα (λ = 1.54178)
2Θ range for data collection/°	4.802 to 132.522	4.798 to 131.778
Index ranges	$-21 \le h \le 25$, $-25 \le k \le 23$, $-18 \le l \le 15$	$-25 \le h \le 22$, $-25 \le k \le 25$, $-17 \le l \le 16$
Reflections collected	27144	32725
Independent reflections	3504 [R_{int} = 0.1203, R_{sigma} = 0.0933]	3414 [R_{int} = 0.1328, R_{sigma} = 0.0708]
Data/restraints/parameters	3504/0/270	3414/0/262
Goodness-of-fit on F^2	0.975	1.481
Final R indexes [I>=2σ (I)]	R_1 = 0.0635, wR_2 = 0.1555	R_1 = 0.0653, wR_2 = 0.1764
Final R indexes [all data]	R_1 = 0.1067, wR_2 = 0.1818	R_1 = 0.0953, wR_2 = 0.2175
Largest diff. peak/hole / e $Å^{-3}$	0.33/-0.40	0.84/-0.66
Flack parameter	-0.014(11)	-0.092(9)

Table A. 22. Crystal data and structure refinement for $Zn_{0.26}Mn_{0.16}Co_{0.37}Ca_{0.21}$(hfipbb) (molar code: Zn:Mn:Co:Ca 1:1:4:8) (CCDC number: 1853394) (second column) and $Mn_{0.41}Co_{0.59}$ (hfipbb) (molar code: Mn:Co 1:1) (CCDC number: 1853402) (third column).

Identification code	**$Mn_{0.23}Co_{0.50}Ca_{0.27}$(hfipbb)**
CCDC number	1853403
Empirical formula	$C_{17}H_8Ca_{0.07}Co_{0.5}F_6Mn_{0.43}O_4$
Formula weight	446.18
Temperature/K	250
Crystal system	hexagonal
Space group	$P6_522$
a/Å	21.2499(7)
b/Å	21.2499(7)
c/Å	15.2397(6)
α/°	90
β/°	90
γ/°	120
Volume/$Å^3$	5959.6(5)
Z	12
$\rho_{calc}g/cm^3$	1.492
μ/mm^{-1}	6.615
F(000)	2660.0
Crystal size/mm^3	0.08 × 0.02 × 0.02
Radiation	CuKα (λ = 1.54178)
2Θ range for data collection/°	4.802 to 131.684
Index ranges	$-24 \leq h \leq 24$, $-25 \leq k \leq 24$, $-17 \leq l \leq 16$
Reflections collected	35814
Independent reflections	3435 [R_{int} = 0.1257, R_{sigma} = 0.0642]
Data/restraints/parameters	3435/0/256
Goodness-of-fit on F^2	1.003
Final R indexes [I>=2σ (I)]	R_1 = 0.0605, wR_2 = 0.1502
Final R indexes [all data]	R_1 = 0.0795, wR_2 = 0.1618
Largest diff. peak/hole / e $Å^{-3}$	0.42/-0.52
Flack parameter	-0.017(7)

Table A. 23. Crystal data and structure refinement for $Mn_{0.23}Co_{0.50}Ca_{0.27}$(hfipbb) (molar code: Mn:Co:Ca 1:2:2) (CCDC number: 1853403).

4. SEM-EDS analyses

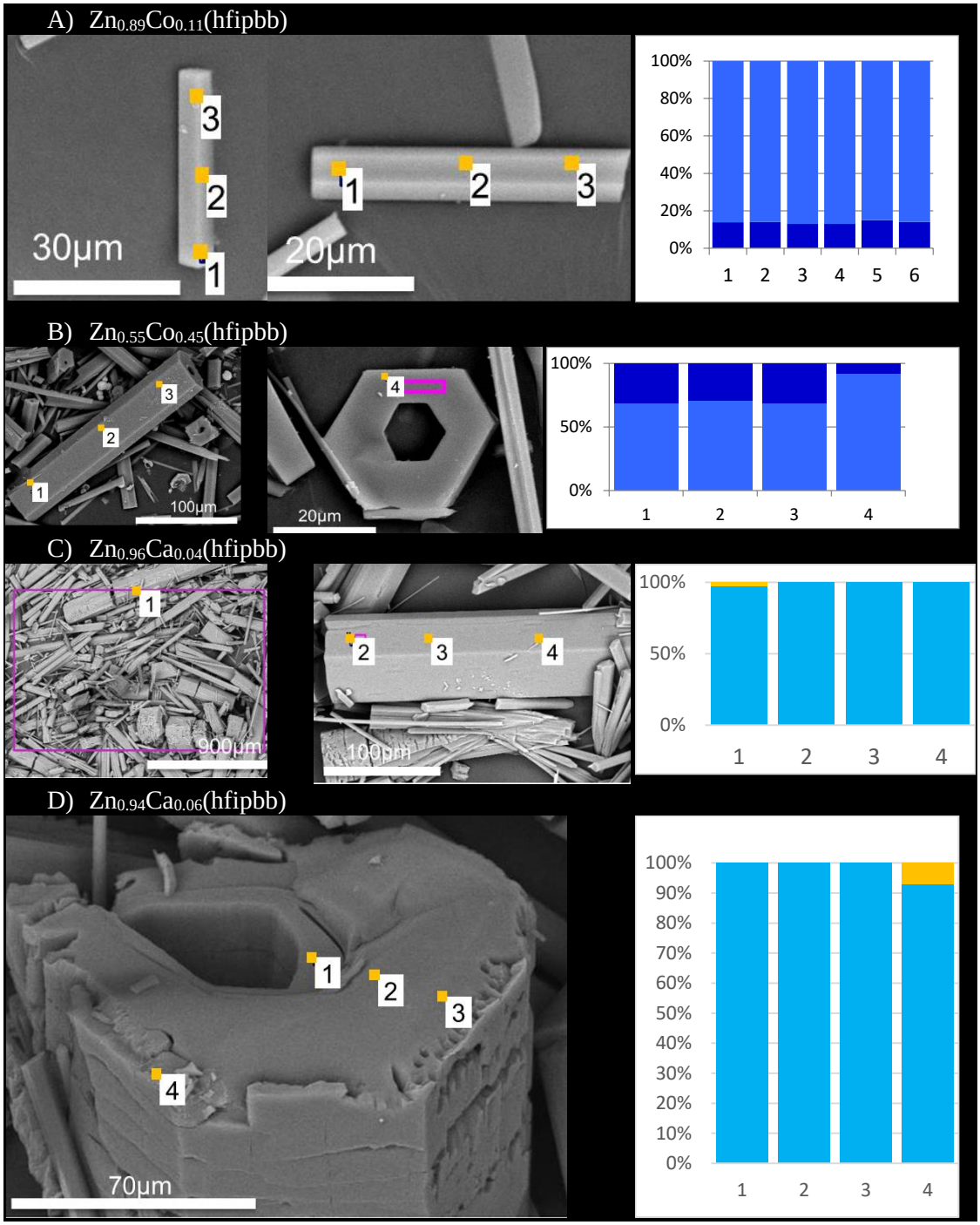

Figure A. 10. Orange spots indicate the areas where EDS were performed. Plot (right) shows the ratio of metals by EDS analyses, where each column corresponds to the area indicated by a number in the SEM pictures.%Zn (light blue), %Co(dark blue) and %Ca (yellow).

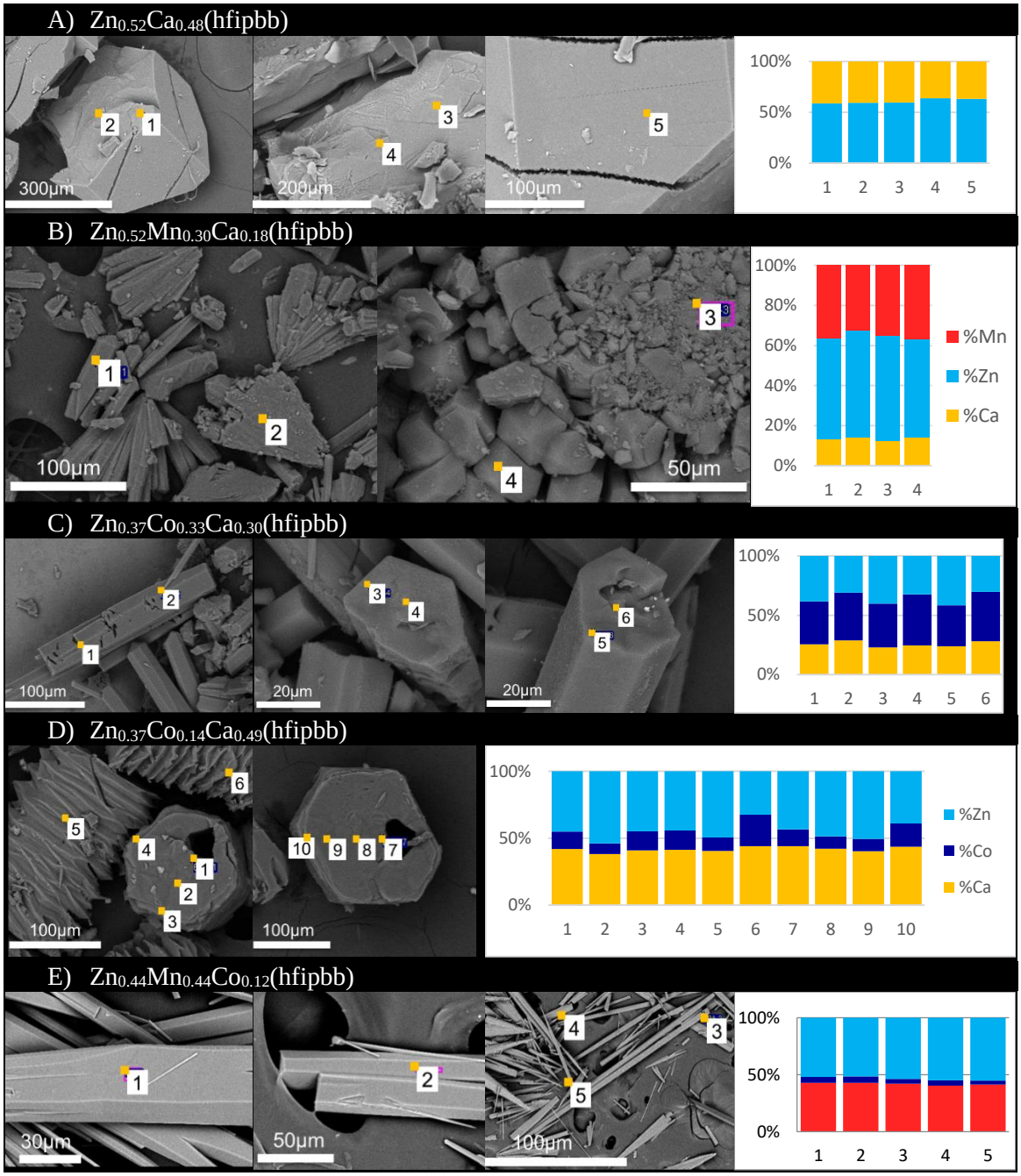

Figure A. 11. Orange spots indicate the areas where EDS were performed. Plot (right) shows the ratio of metals by EDS analyses, where each column corresponds to the area indicated by a number in the SEM pictures.

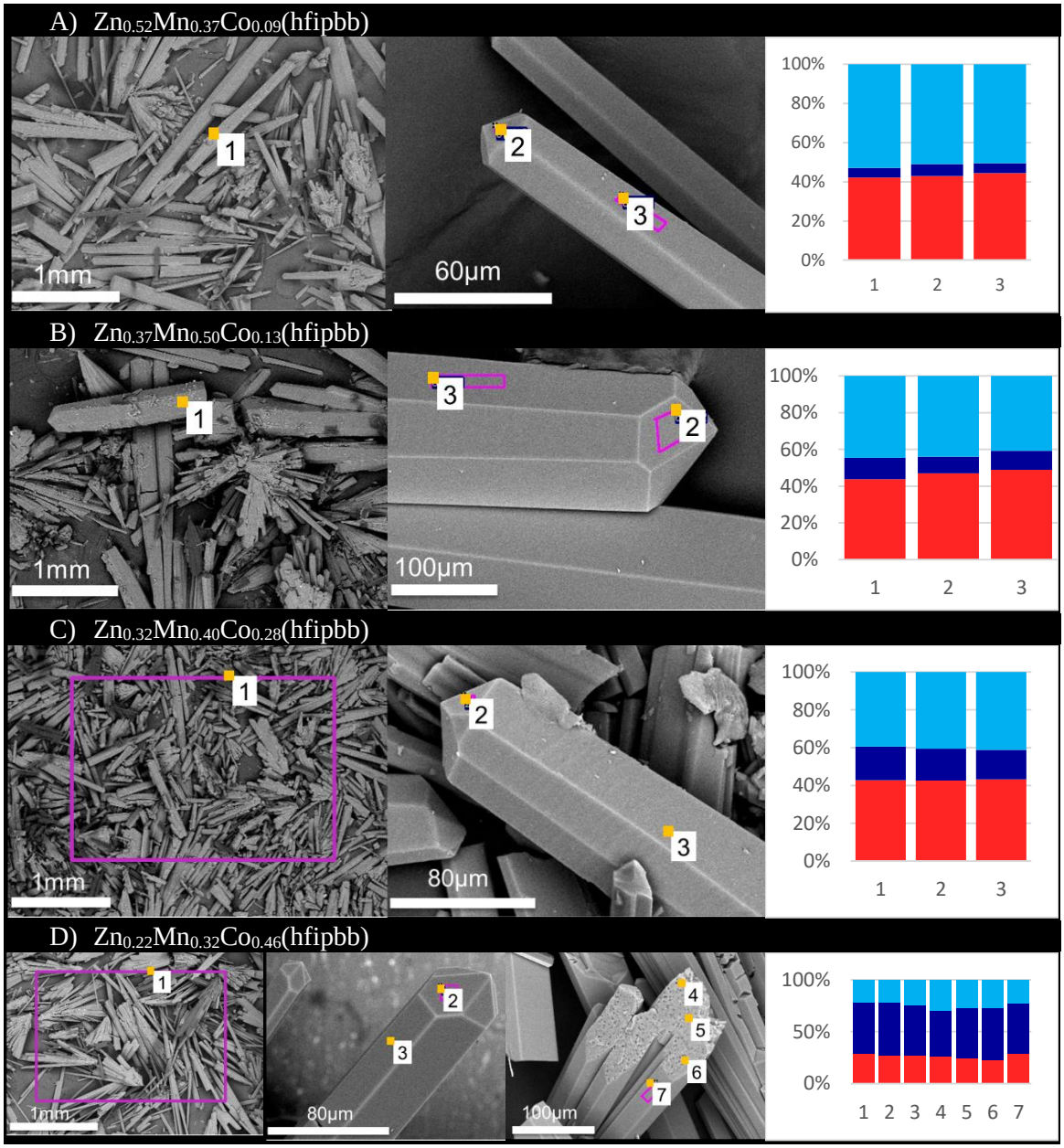

Figure A. 12. Orange spots indicate the areas where EDS were performed. Plot (right) shows the ratio of metals by EDS analyses, where each column corresponds to the area indicated by a number in the SEM pictures. %Zn (light blue), %Co(dark blue) and %Mn (red).

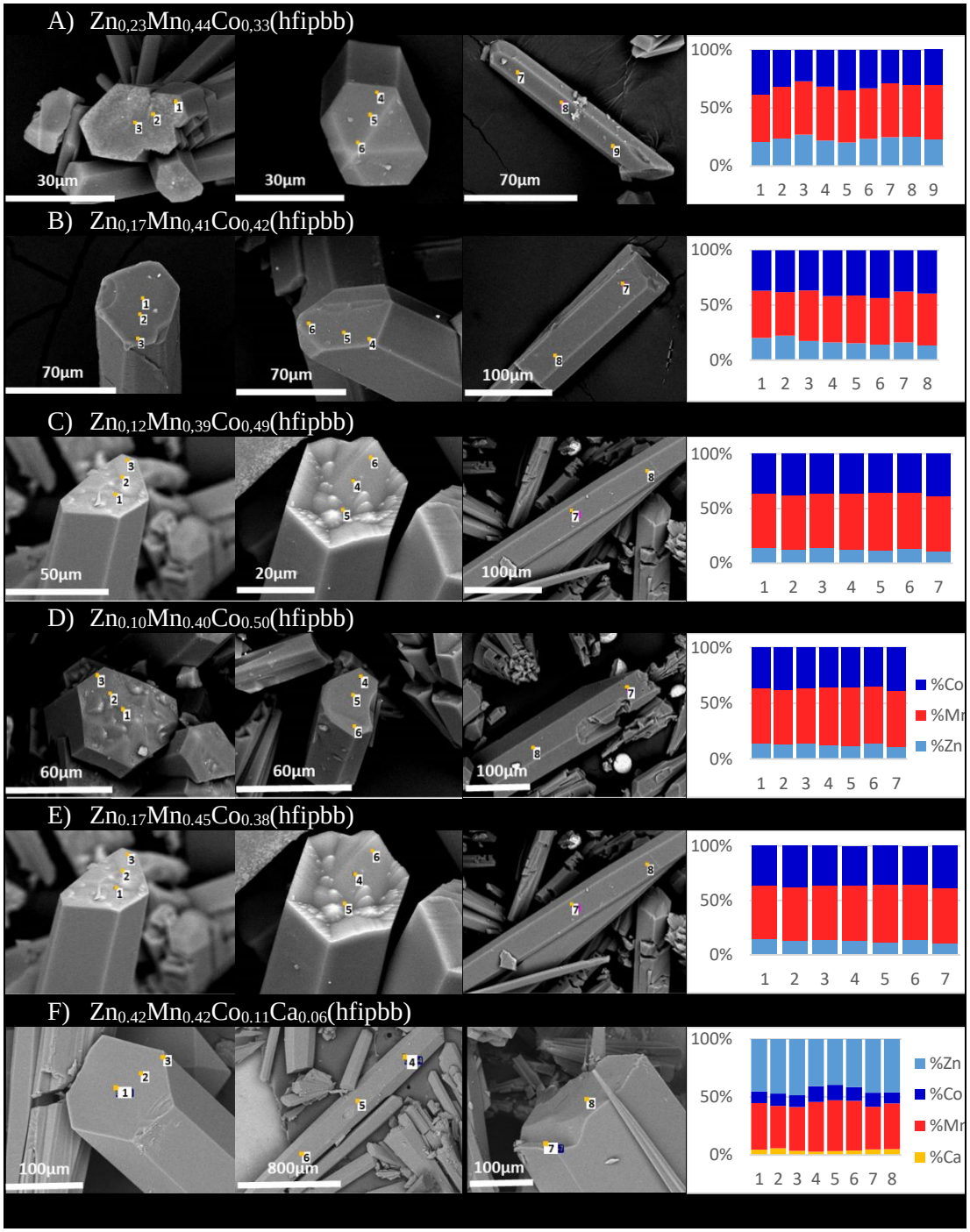

Figure A. 13. Orange spots indicate the areas where EDS were performed. Plot (right) shows the ratio of metals by EDS analyses, where each column corresponds to the area indicated by a number in the SEM pictures.

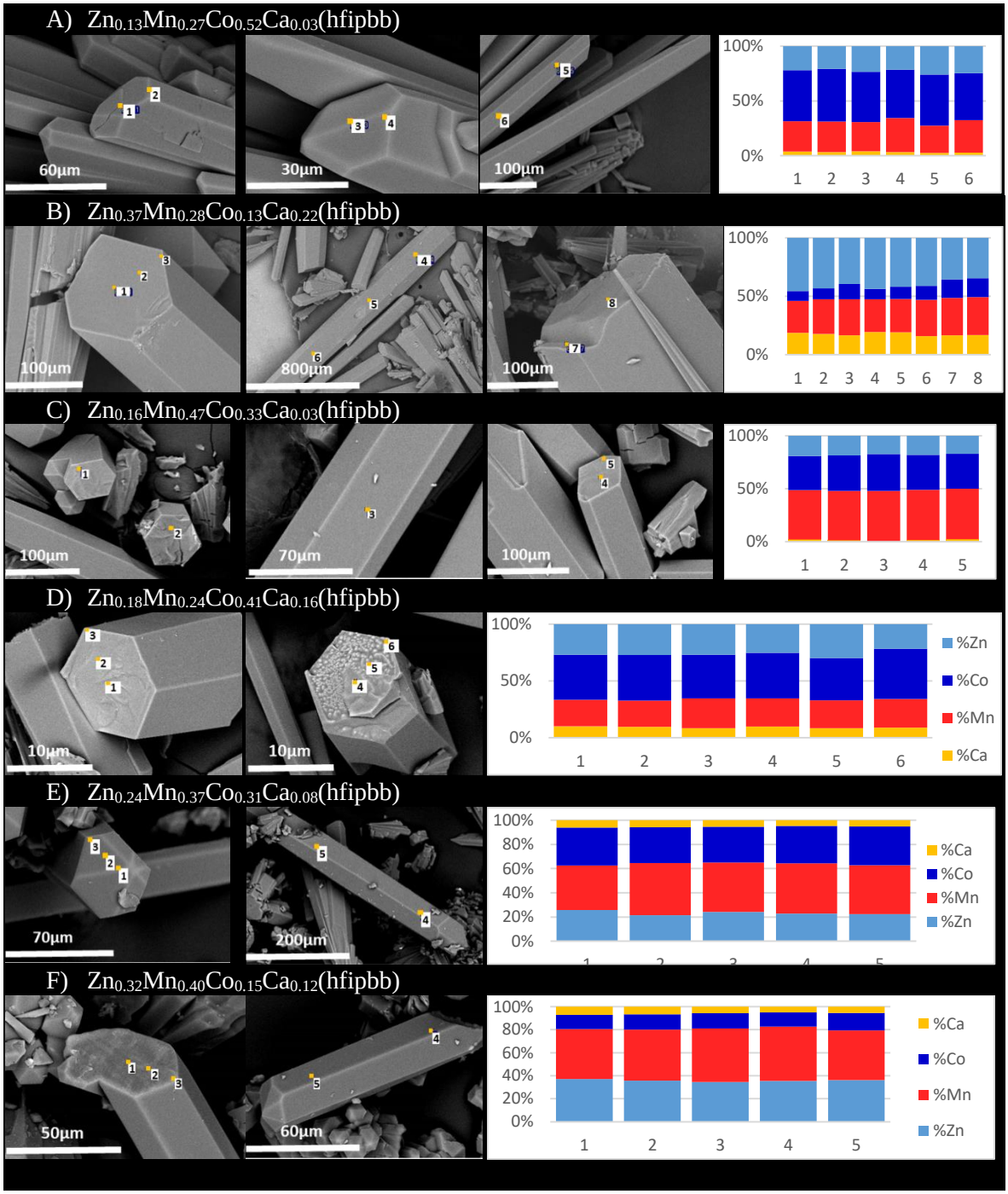

Figure A. 14. Orange spots indicate the areas where EDS were performed. Plot (right) shows the ratio of metals by EDS analyses, where each column corresponds to the area indicated by a number in the SEM pictures.

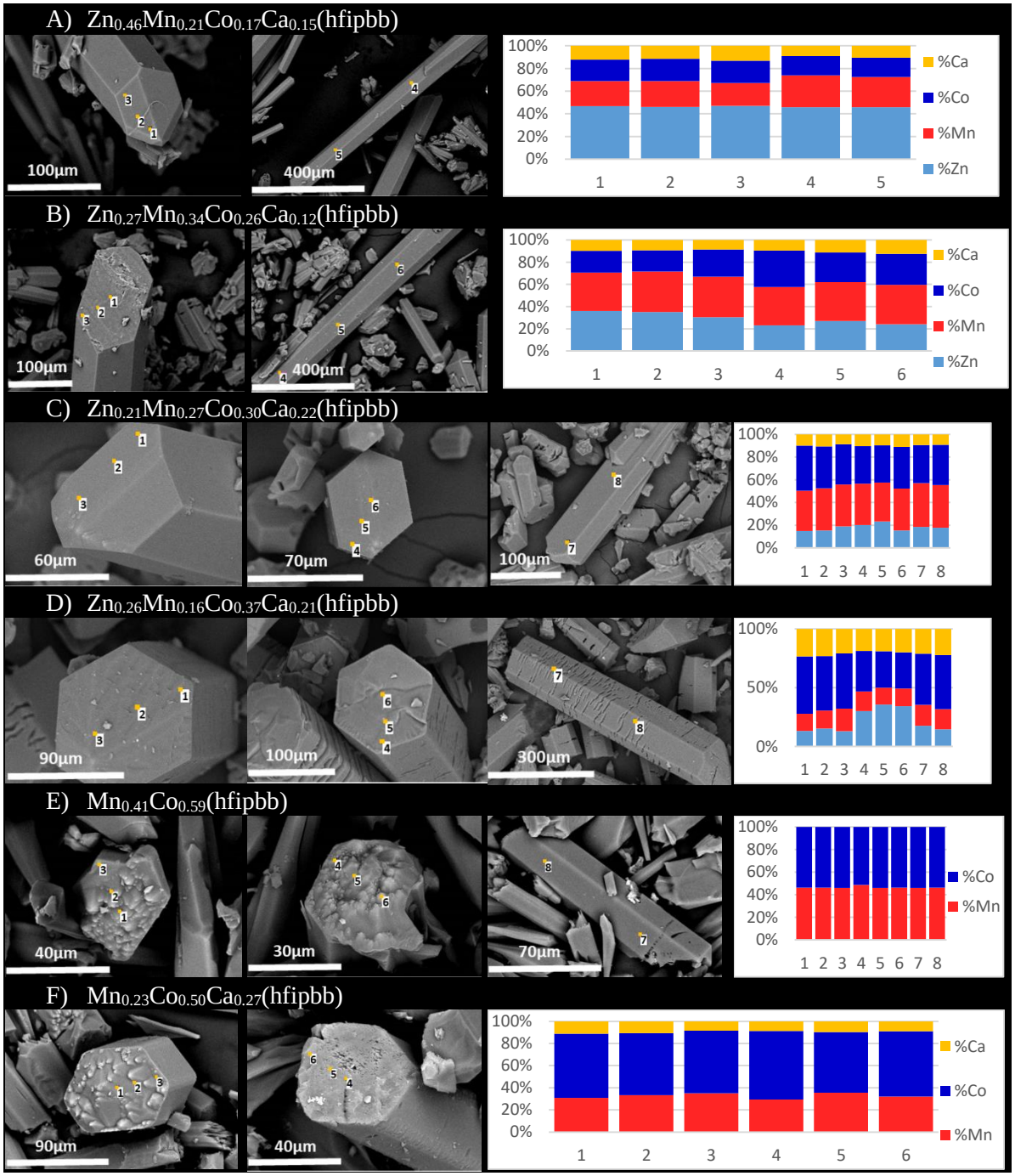

Figure A. 15. Orange spots indicate the areas where EDS were performed. Plot (right) shows the ratio of metals by EDS analyses, where each column corresponds to the area indicated by a number in the SEM pictures.

5. Neutron powder thermo-diffraction patterns

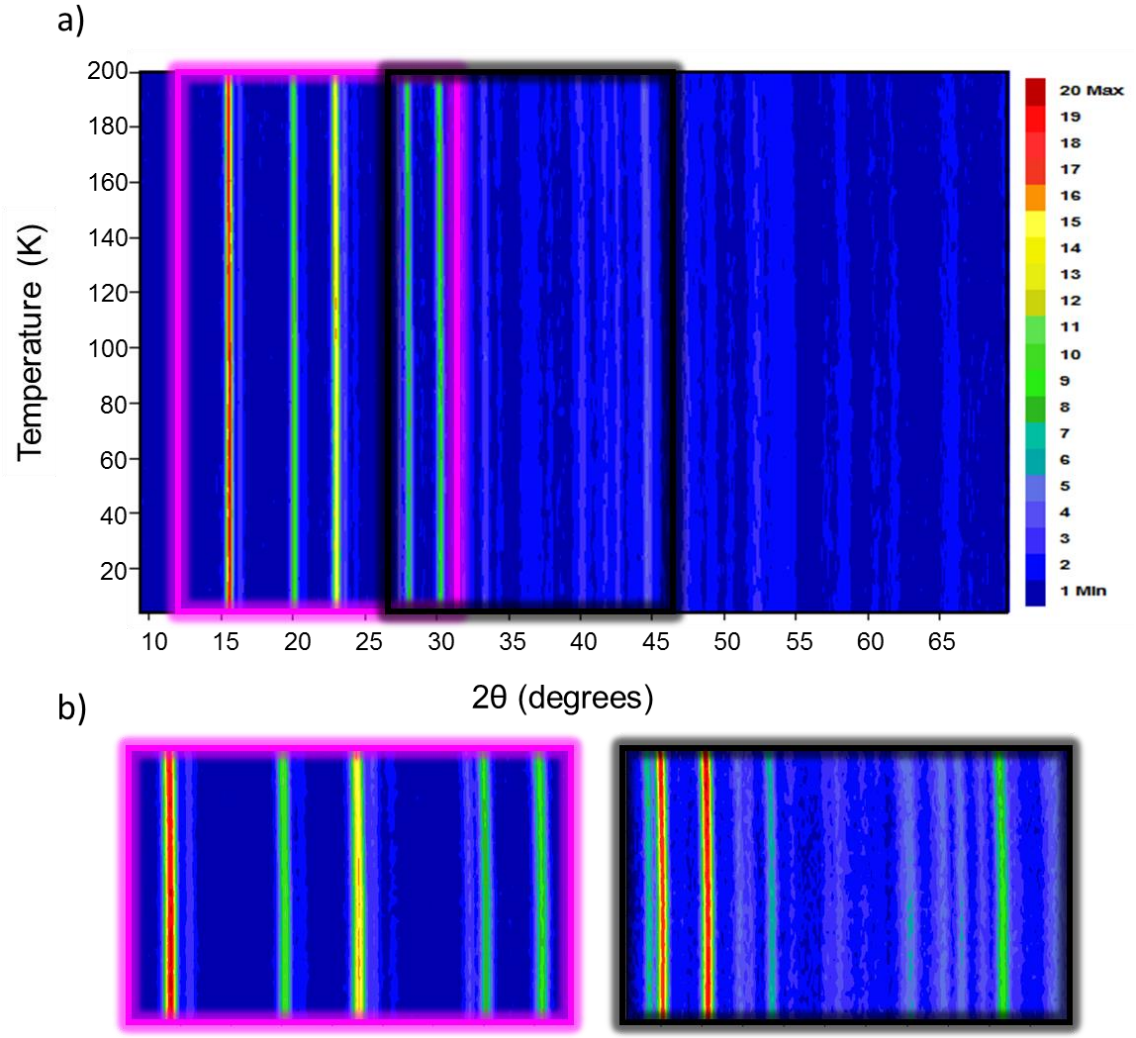

Figure A. 16. a) $Zn_{0.64}Ca_{0.36}$(hfipbb) (molar code: Zn:Ca 1:4) contour 2D neutron diffraction pattern. b) Blow up of marked areas.

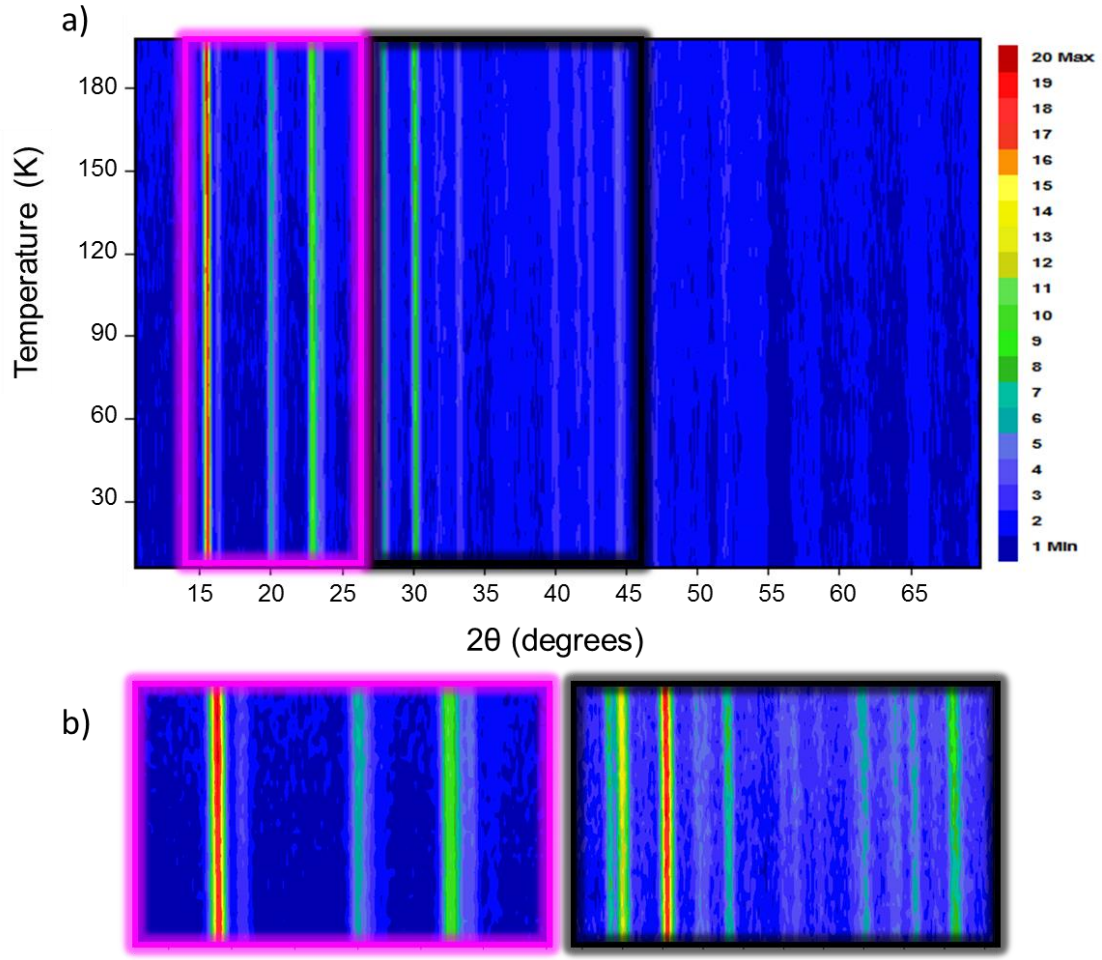

Figure A. 17. a) $Zn_{0.52}Ca_{0.48}$(hfipbb) (molar code: Zn:Ca 1:10) contour 2D neutron diffraction pattern. b) Blow up of marked areas.

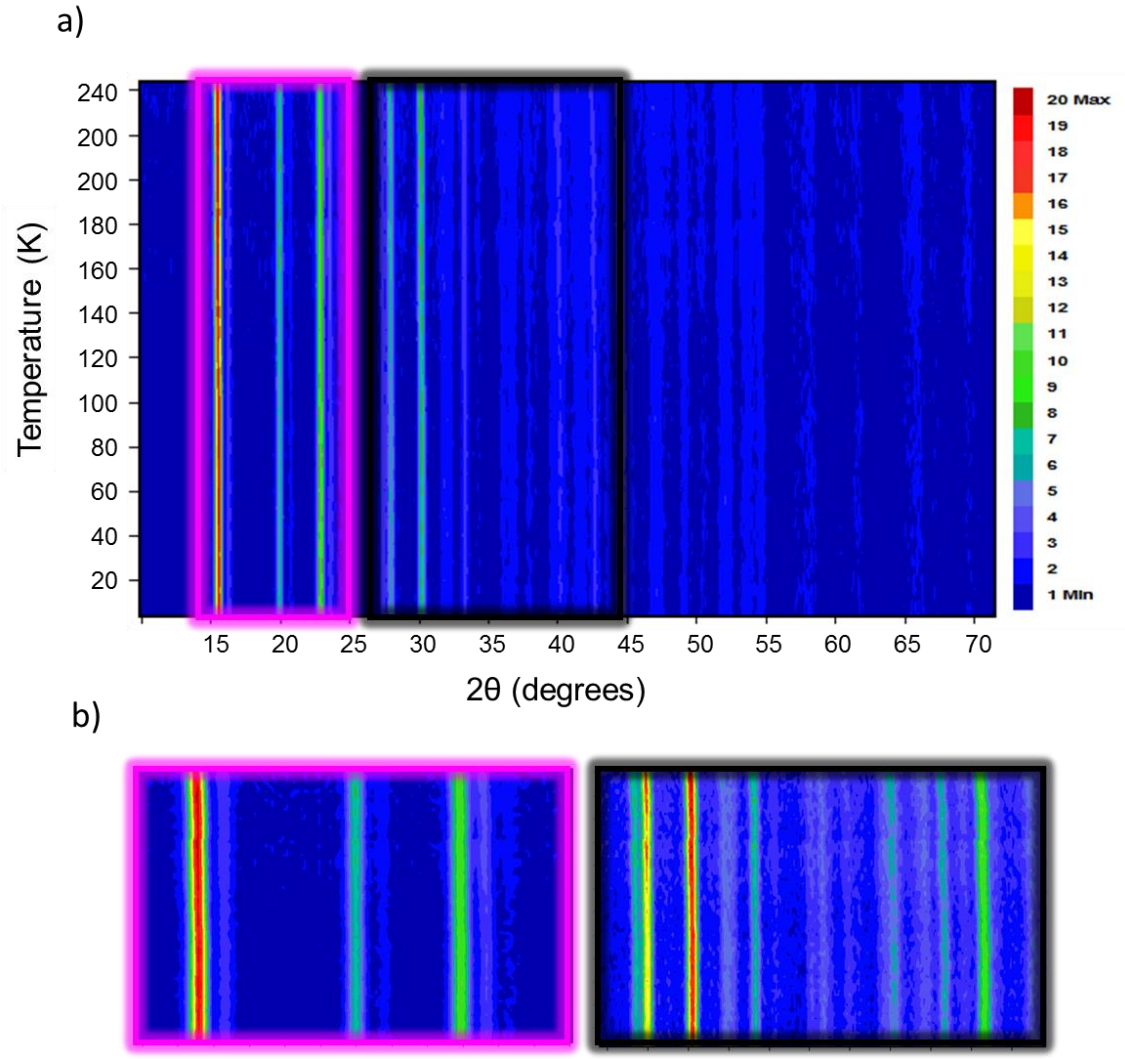

Figure A. 18. a) $Zn_{0.37}Co_{0.14}Ca_{0.49}$(hfipbb) (molar code: Zn:Co:Ca 1:1:8) contour 2D neutron diffraction pattern. b) Blow up of marked areas.

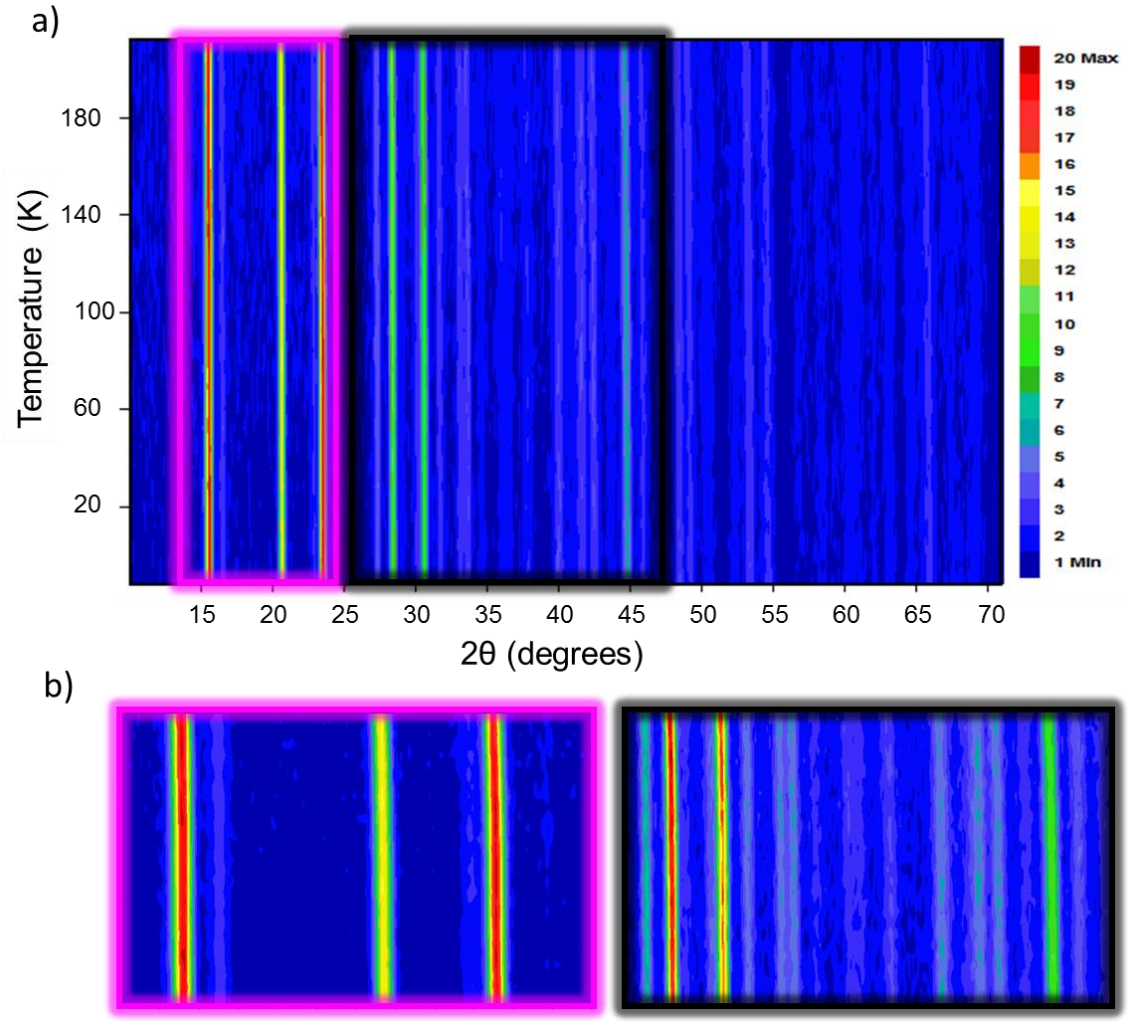

Figure A. 19. a) $Zn_{0.54}Mn_{0.37}Co_{0.09}$(hfipbb) (molar code: Zn:Mn:Co 2:1:1) contour 2D neutron diffraction pattern. b) Blow up of marked areas.

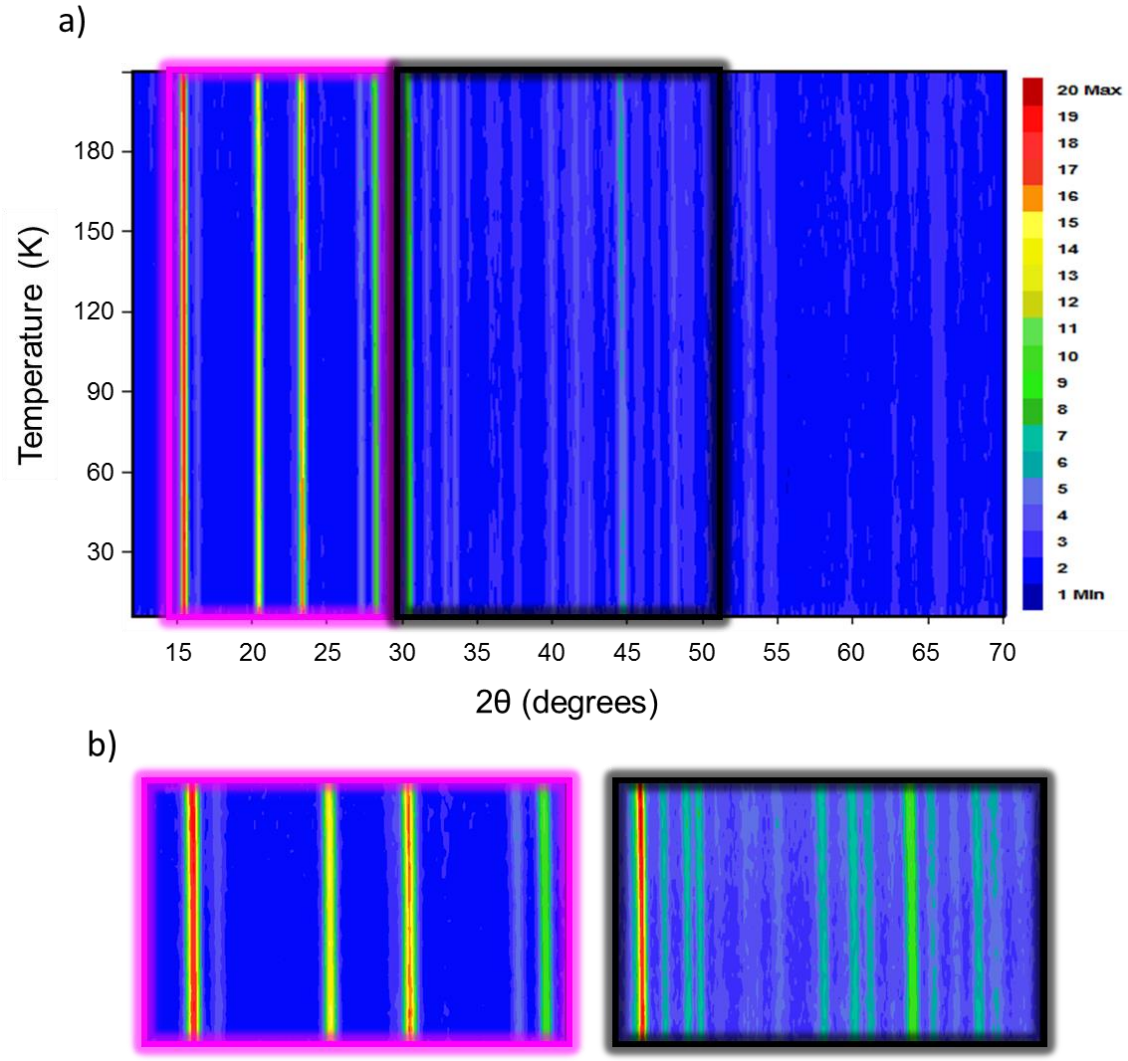

Figure A. 20. a) $Zn_{0.48}Mn_{0.42}Ca_{0.10}$(hfipbb) (molar code: Zn:Mn:Ca 1:1:1)contour 2D neutron diffraction pattern. b) Blow up of marked areas.

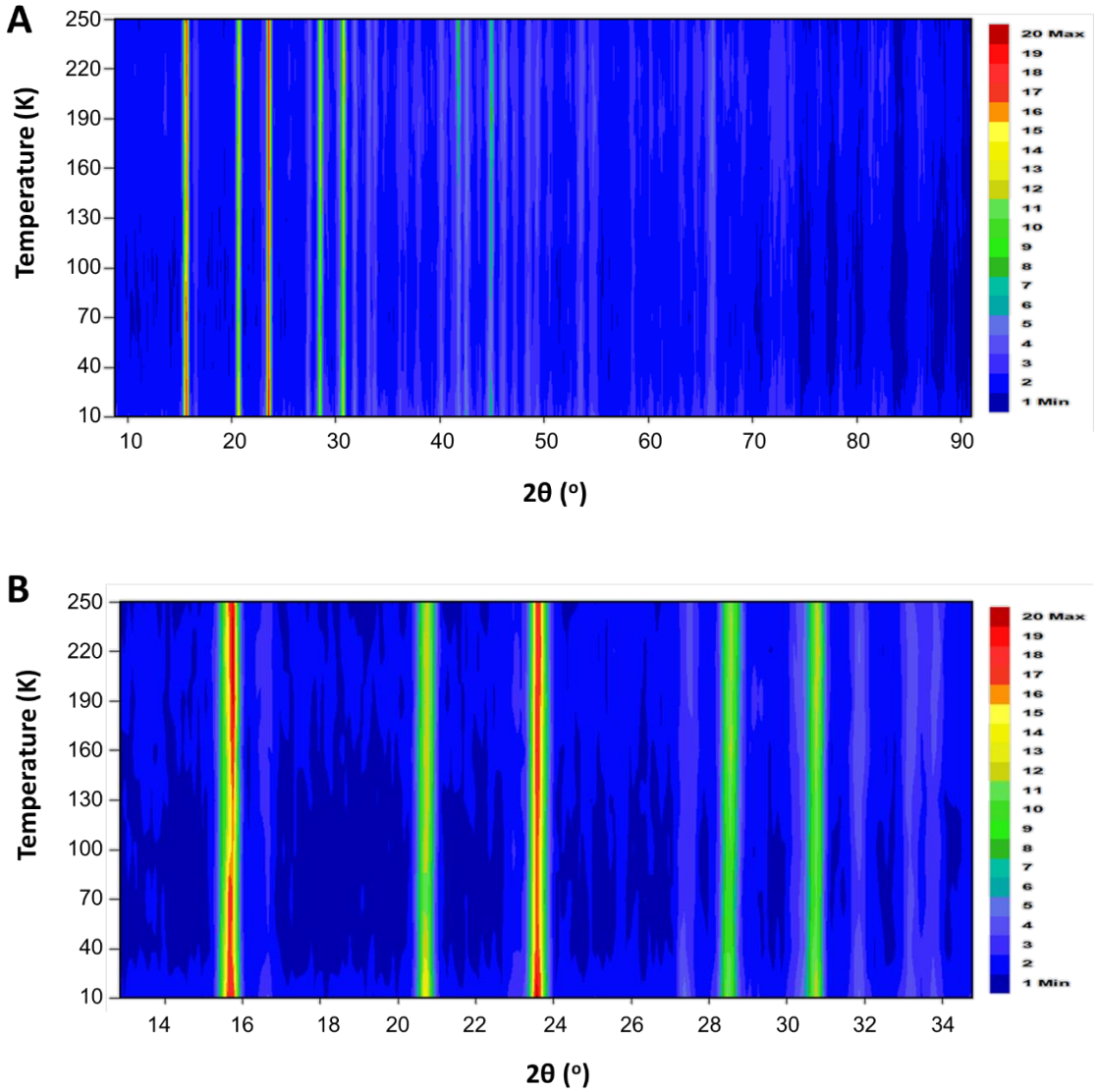

Figure A. 21. Variable temperature neutron diffraction pattern for $Mn_{0.41}Co_{0.59}$(hfipbb) (molar code: Mn:Co 1:1). A) Contour 2D diffraction pattern. B) Zoom up of 13-35 degree area.

6. Neutron powder Rietveld refinements

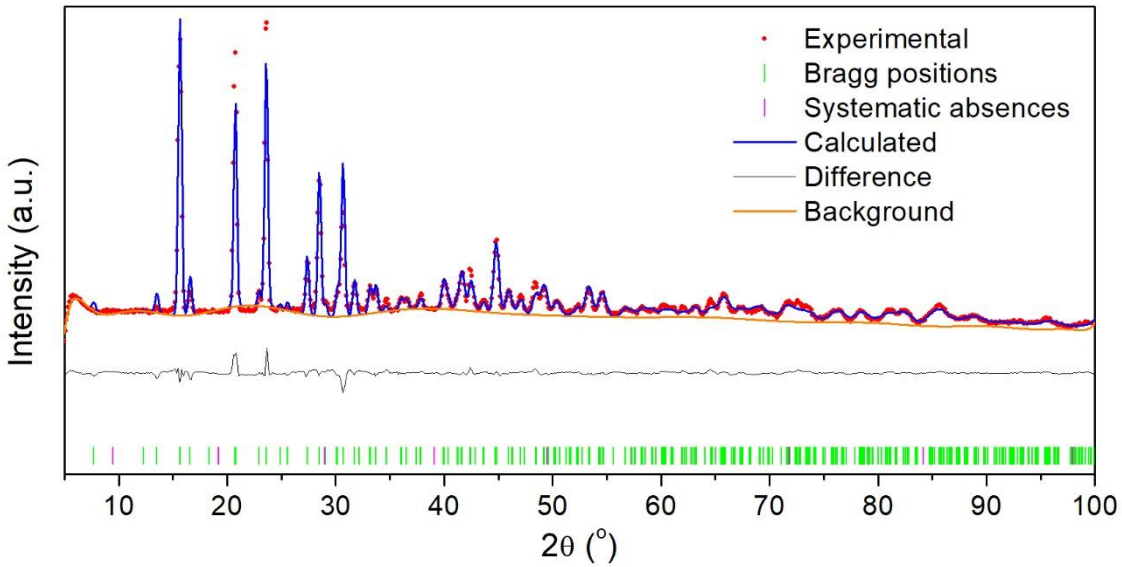

Figure A. 22. Neutron diffraction pattern Rietveld refinement for $Zn_{0.17}Mn_{0.45}Co_{0.38}$(hfipbb) (molar code: Zn:Mn:Co 1:12:6). Rwp= 3.09%; Rp= 1.67%. This pattern was collected at D1B instrument.

B) Appendices from Chapter 6

1. Powder X-ray diffraction

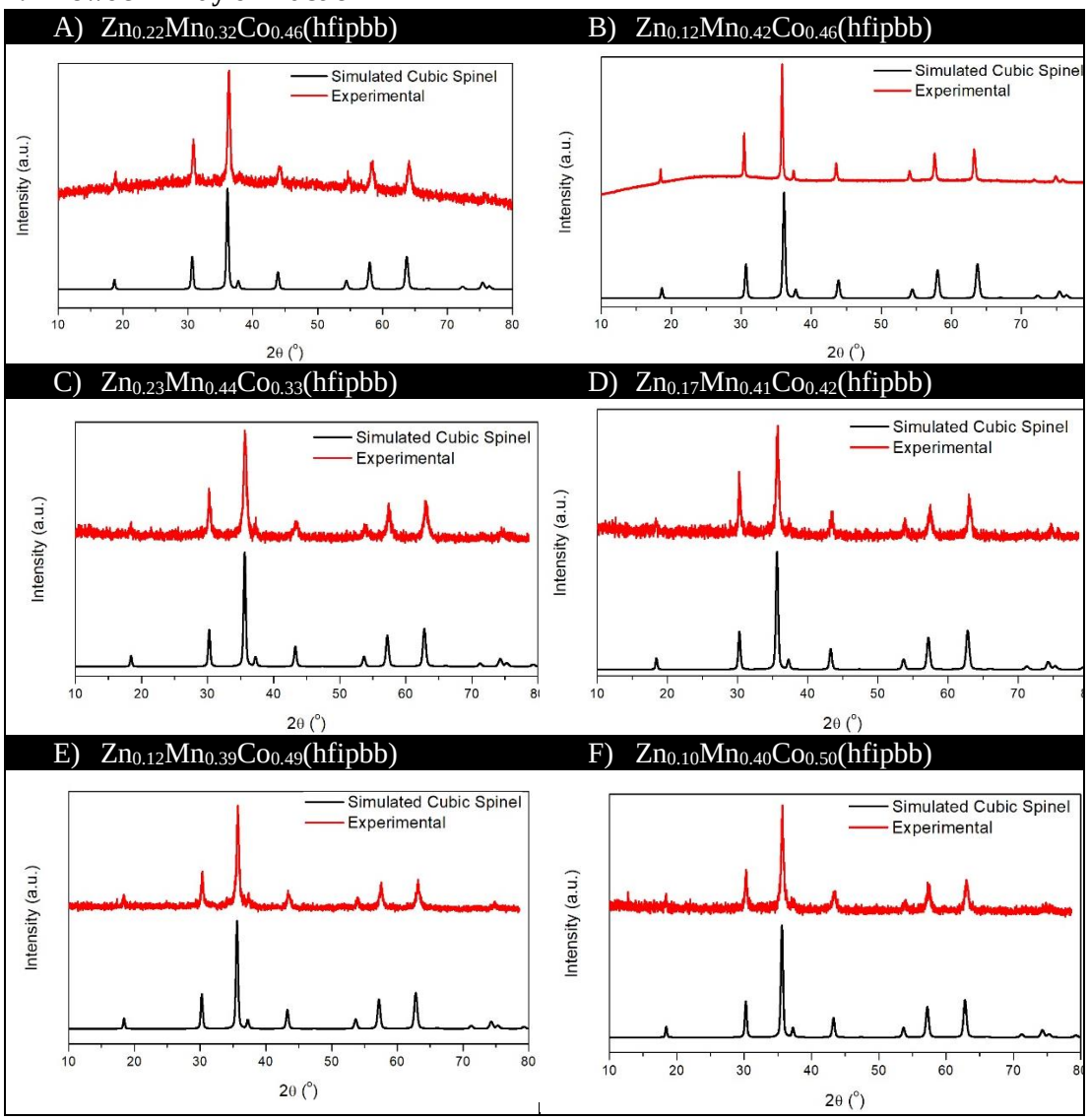

Figure B. 1. Normalized powder XRD patterns and their comparison with the calculated for the corresponding oxides.

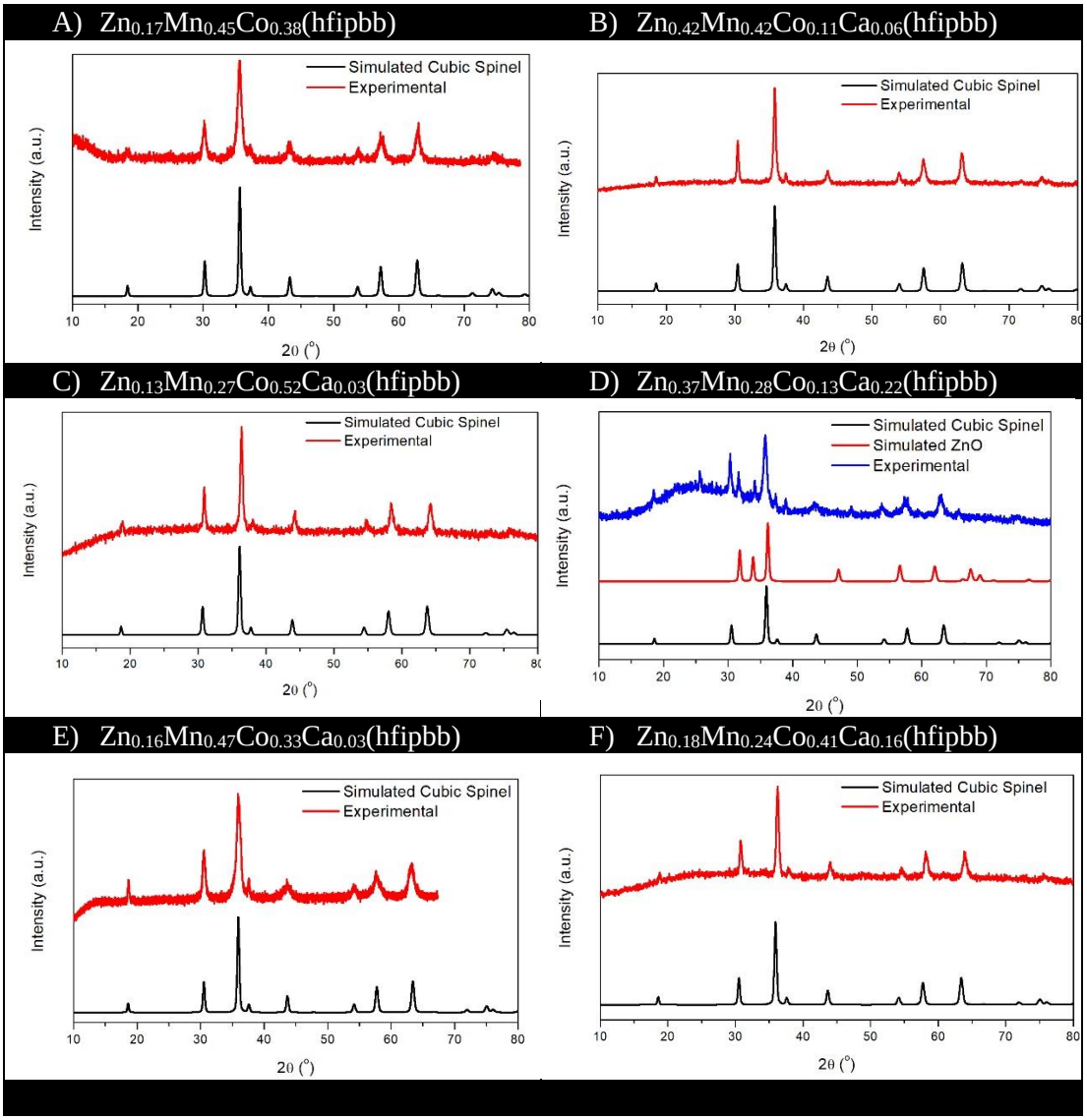

Figure B. 2. Normalized powder XRD patterns and their comparison with the calculated for the corresponding oxides.

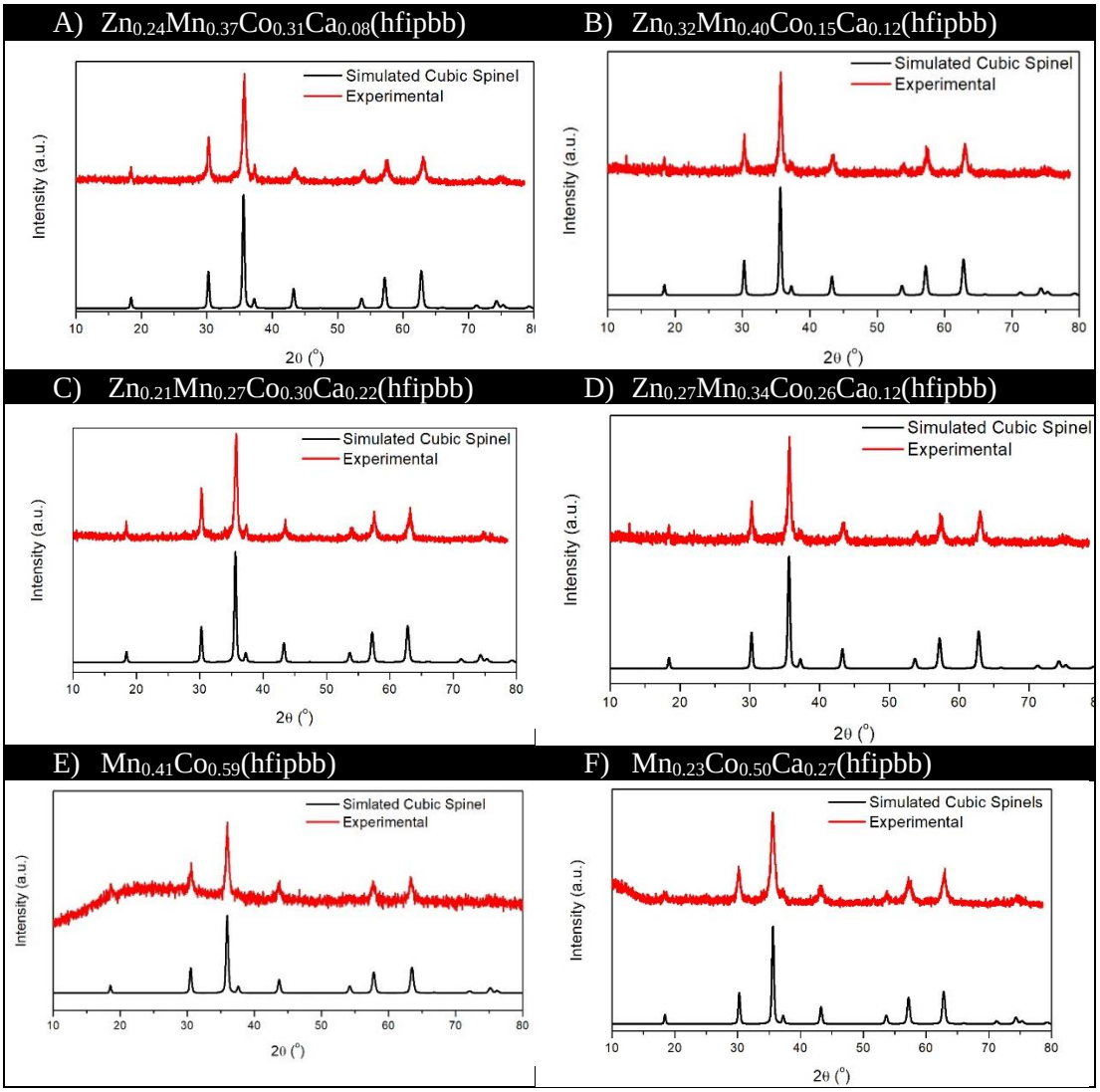

Figure B. 3. Normalized powder XRD patterns and their comparison with the calculated for the corresponding oxides.

2. FE-SEM of spinel oxides

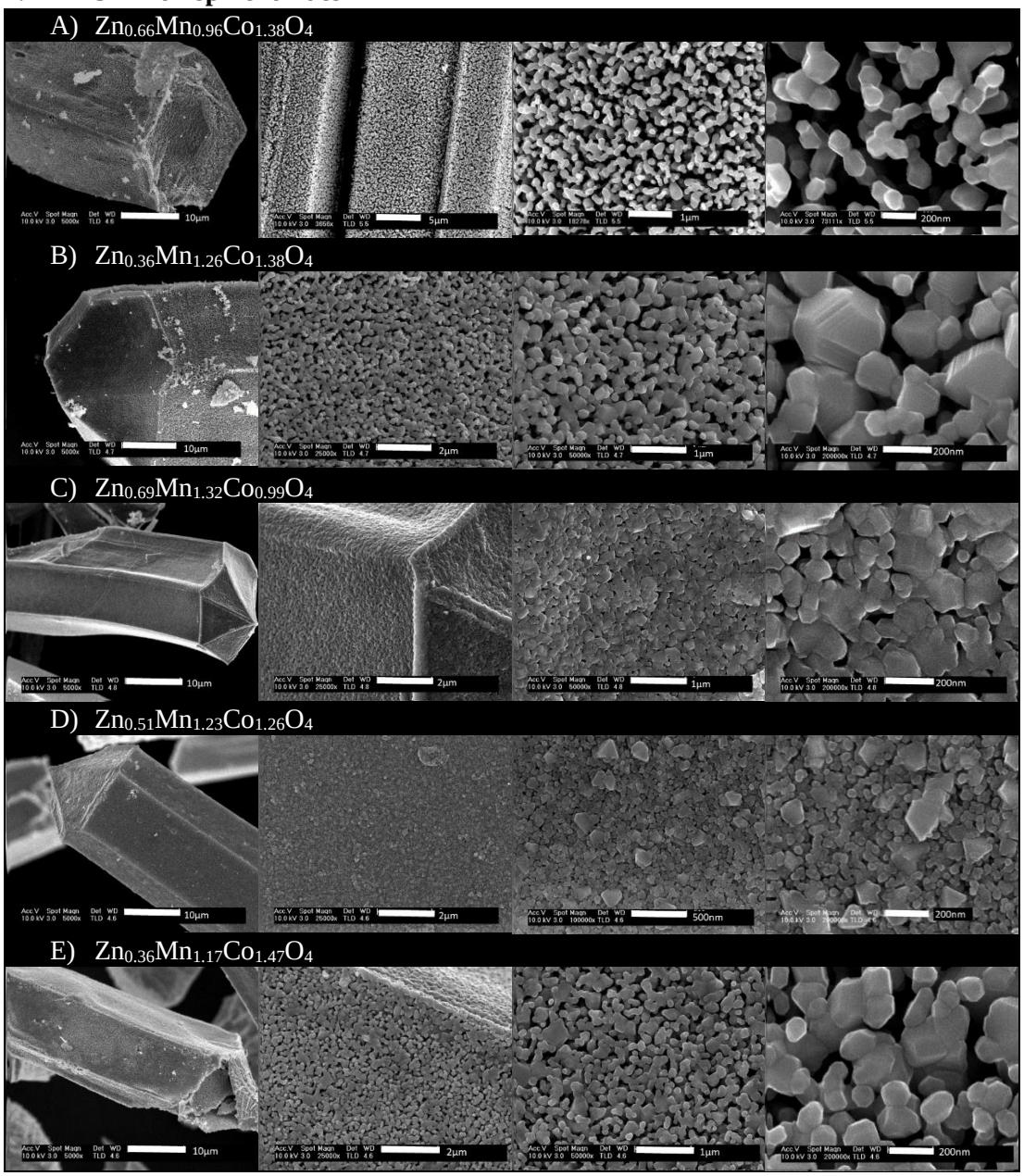

Figure B. 4. FE-SEM images with different magnification (from left to right: x1000, x10000, x50000, x200000).

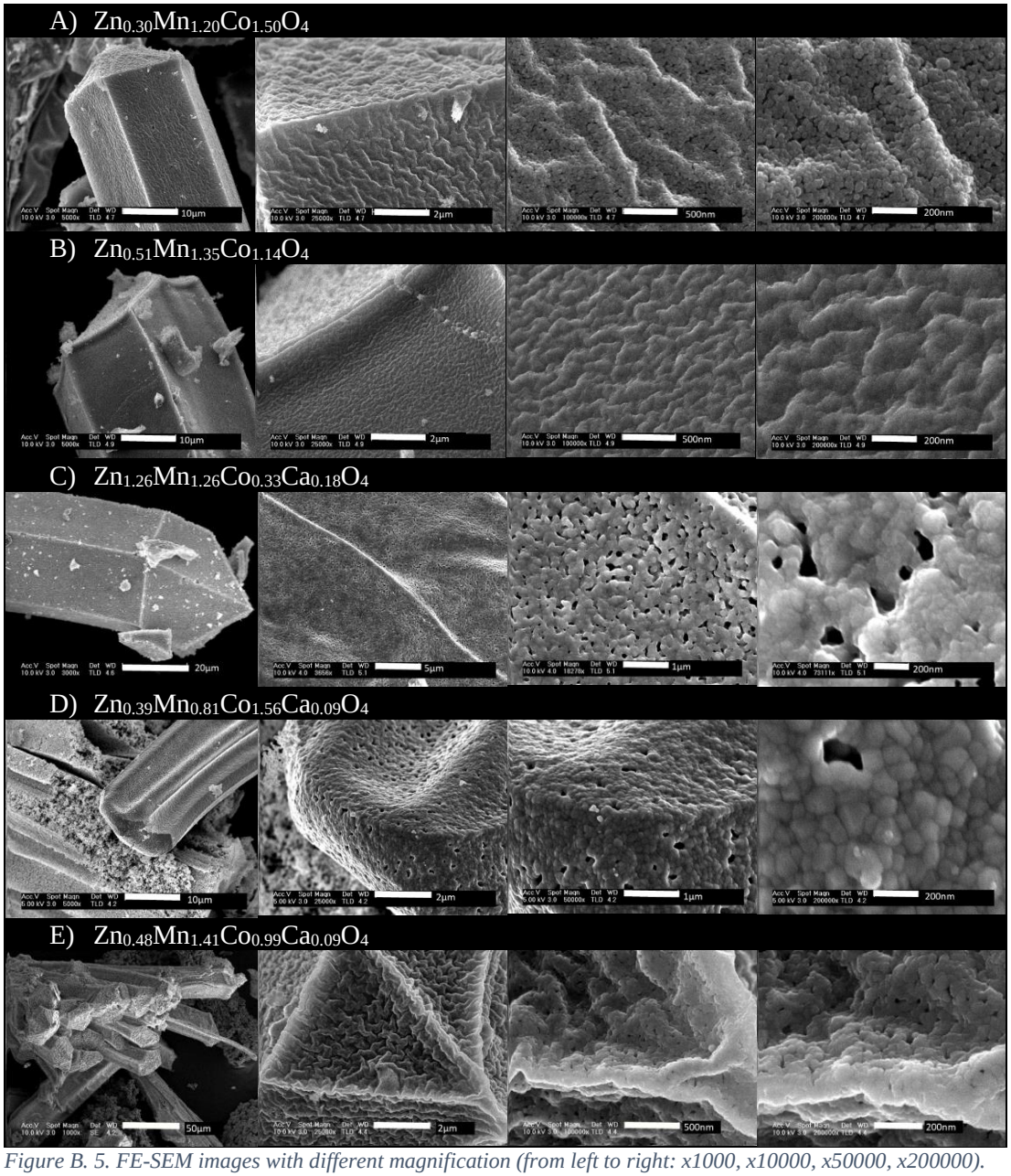

Figure B. 5. FE-SEM images with different magnification (from left to right: x1000, x10000, x50000, x200000).

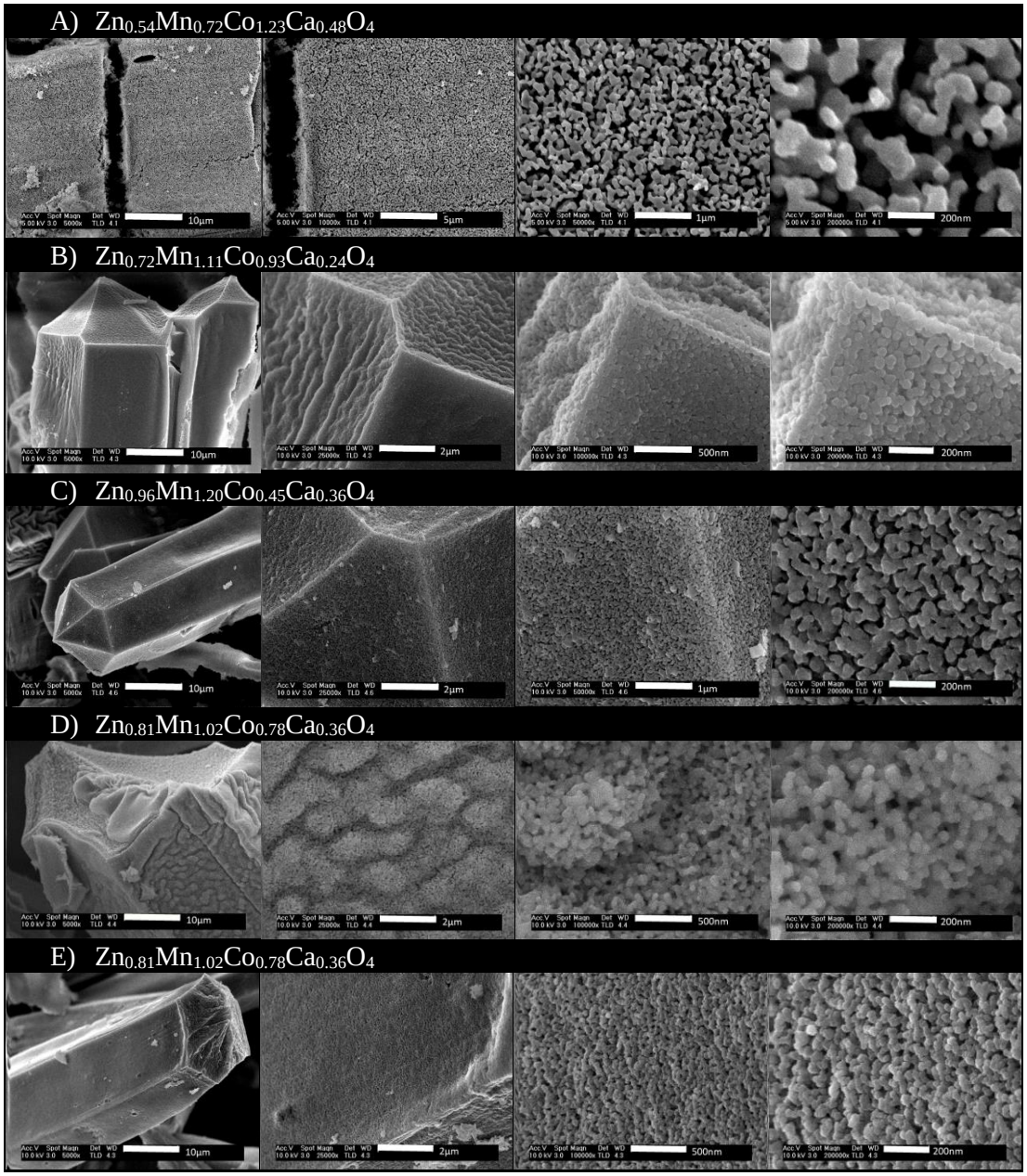

Figure B. 6. FE-SEM images with different magnification (from left to right: x1000, x10000, x50000, x200000).

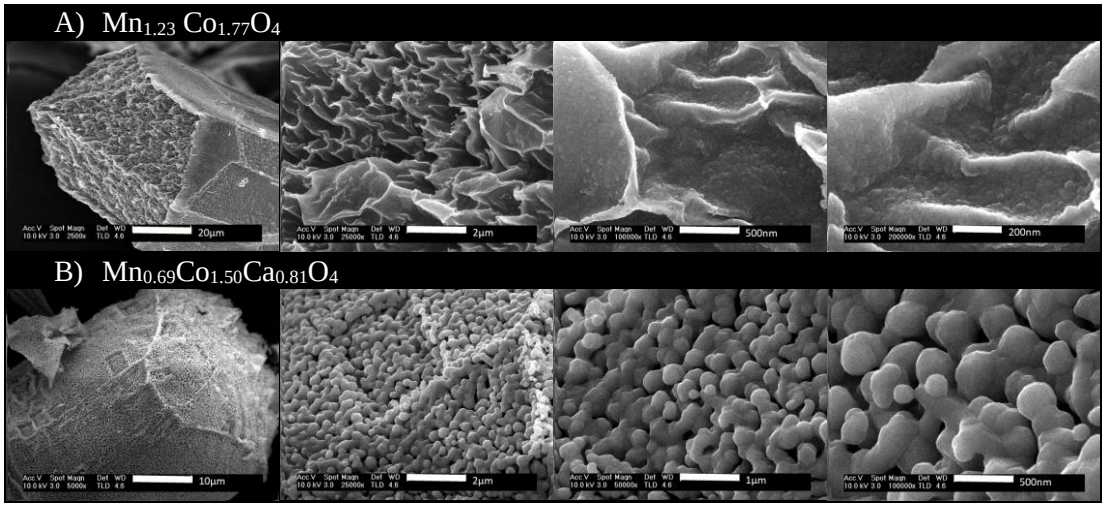

Figure B. 7. FE-SEM images with different magnification (from left to right: x1000, x10000, x50000, x200000).

3. SEM-EDS of spinel oxides

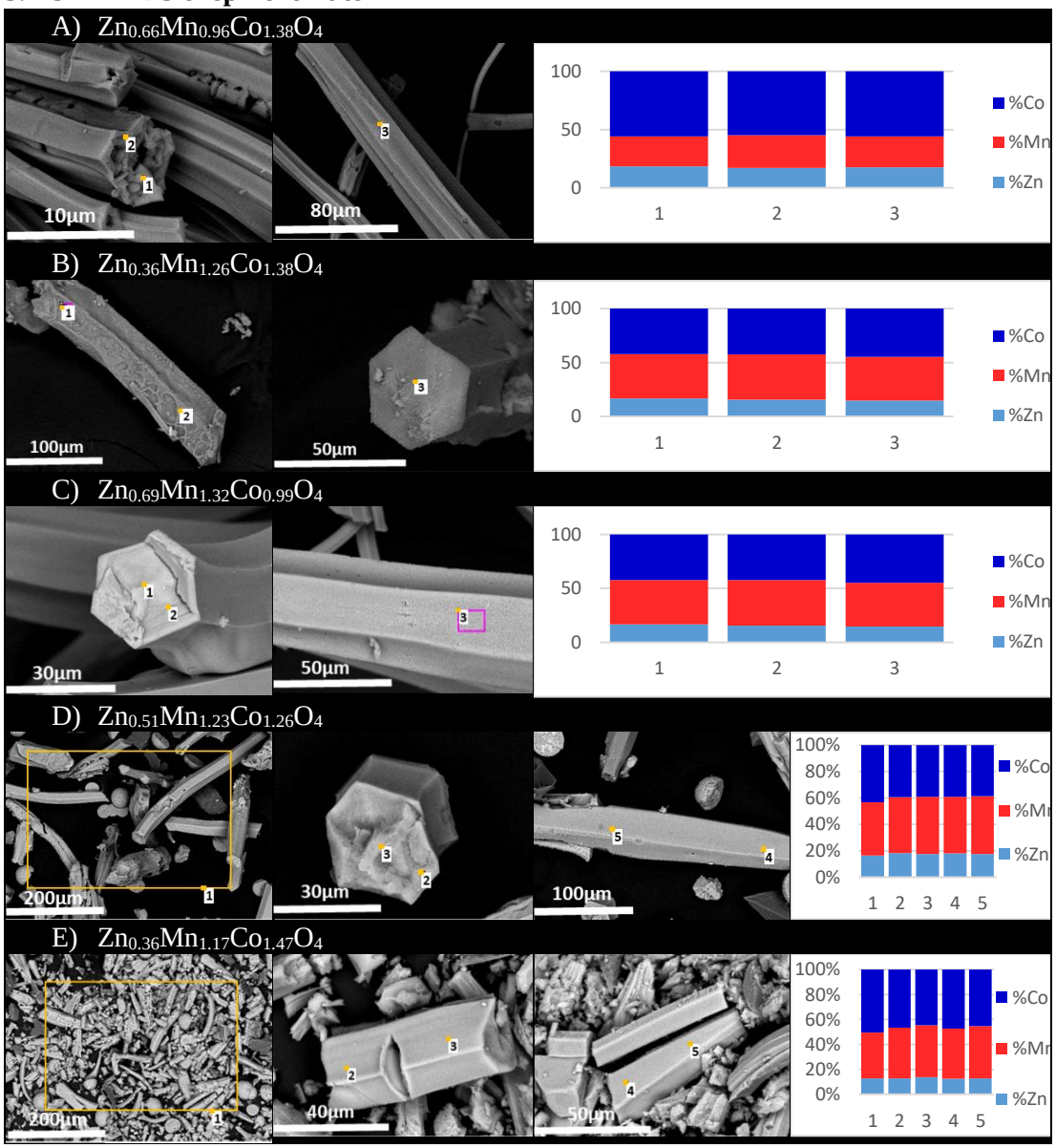

Figure B. 8. SEM-EDS analyses. Orange spots indicate the areas where EDS were performed. Plot (right) shows the metal ratios by EDS analyses, where each column corresponds to the area indicated by a number in the SEM pictures.

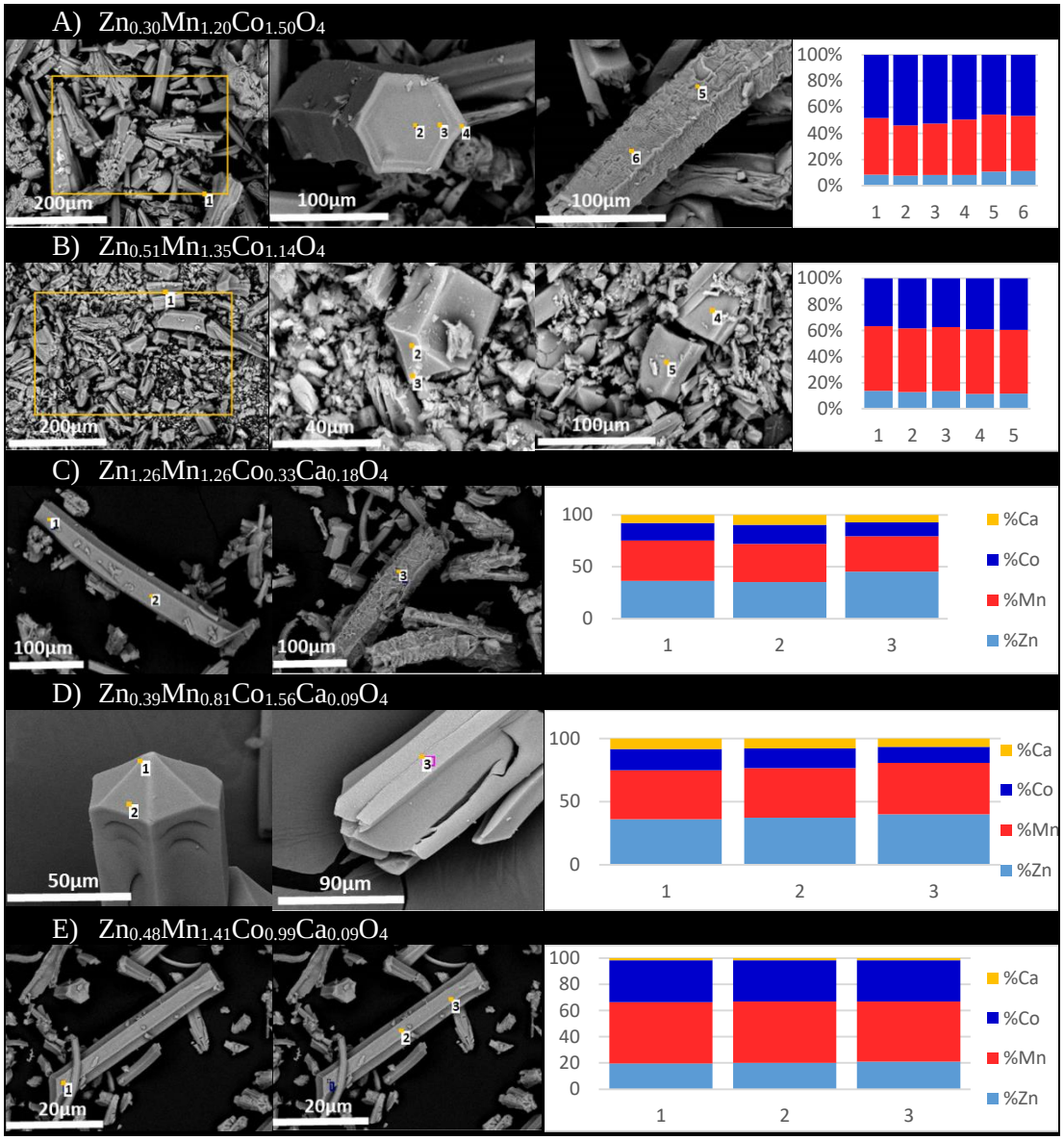

Figure B. 9. SEM-EDS analyses. Orange spots indicate the areas where EDS were performed. Plot (right) shows the metal ratios by EDS analyses, where each column corresponds to the area indicated by a number in the SEM pictures.

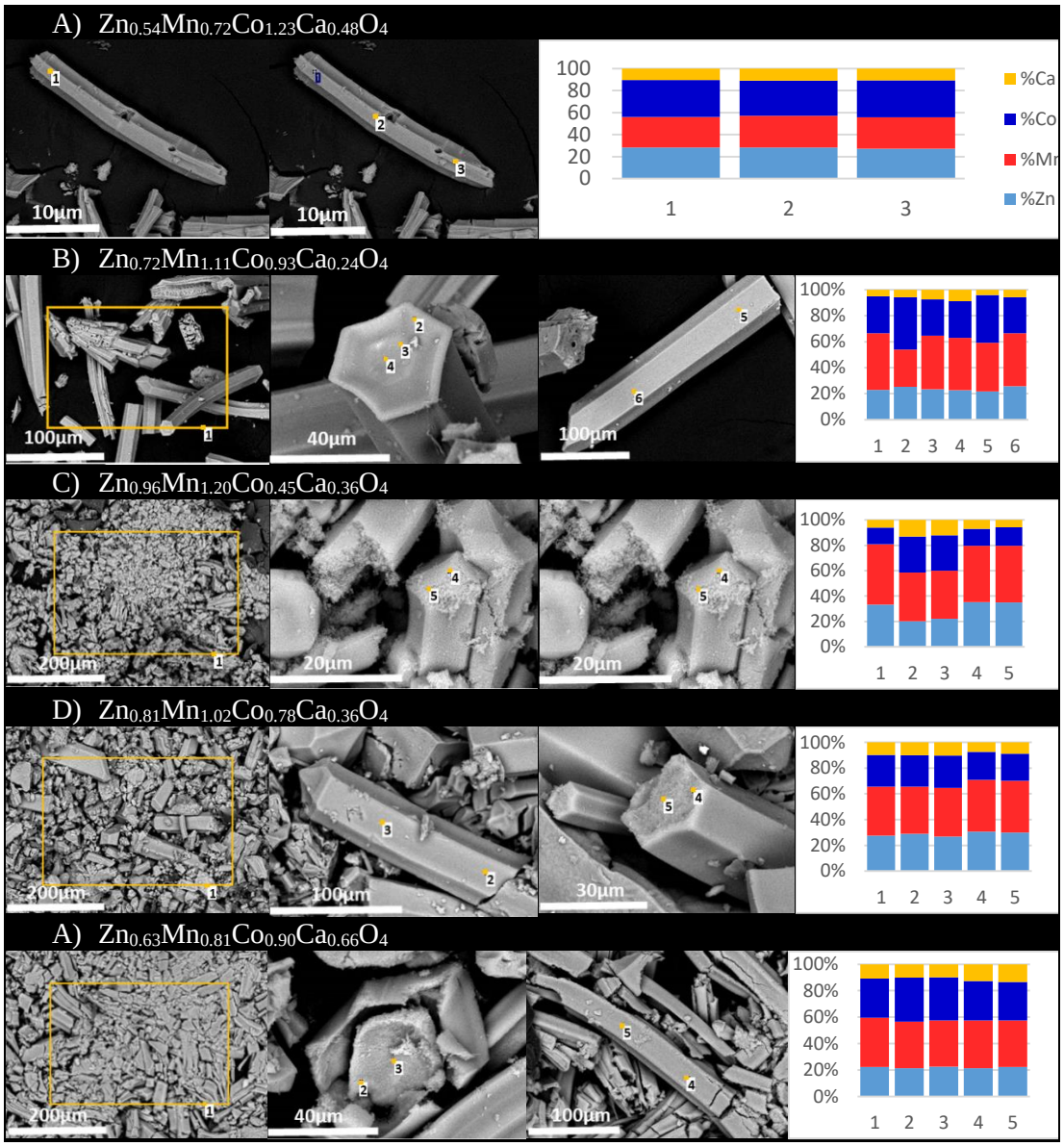

Figure B. 10. SEM-EDS analyses. Orange spots indicate the areas where EDS were performed. Plot (right) shows the metal ratios by EDS analyses, where each column corresponds to the area indicated by a number in the SEM pictures.

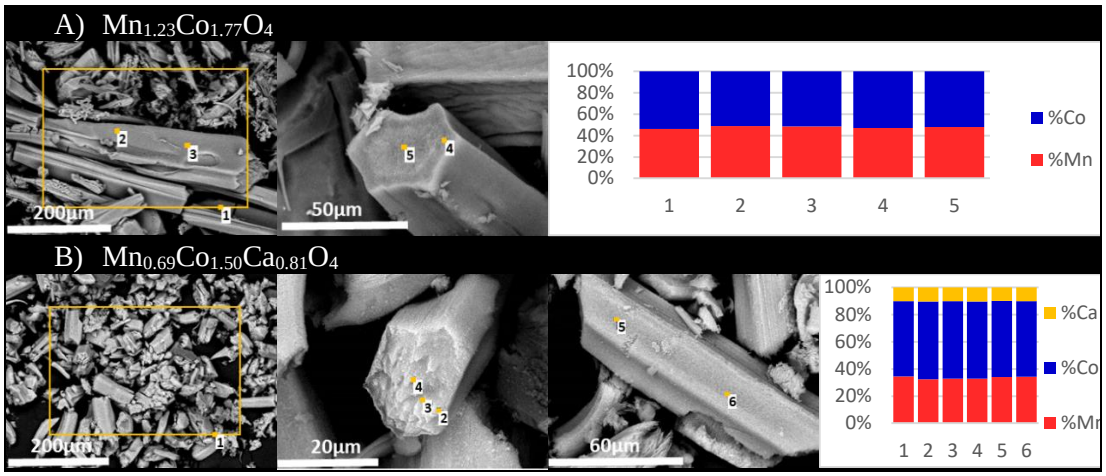

Figure B. 11. SEM-EDS analyses. Orange spots indicate the areas where EDS were performed. Plot (right) shows the metal ratios by EDS analyses, where each column corresponds to the area indicated by a number in the SEM pictures.

4. TEM-EDS of spinel oxides

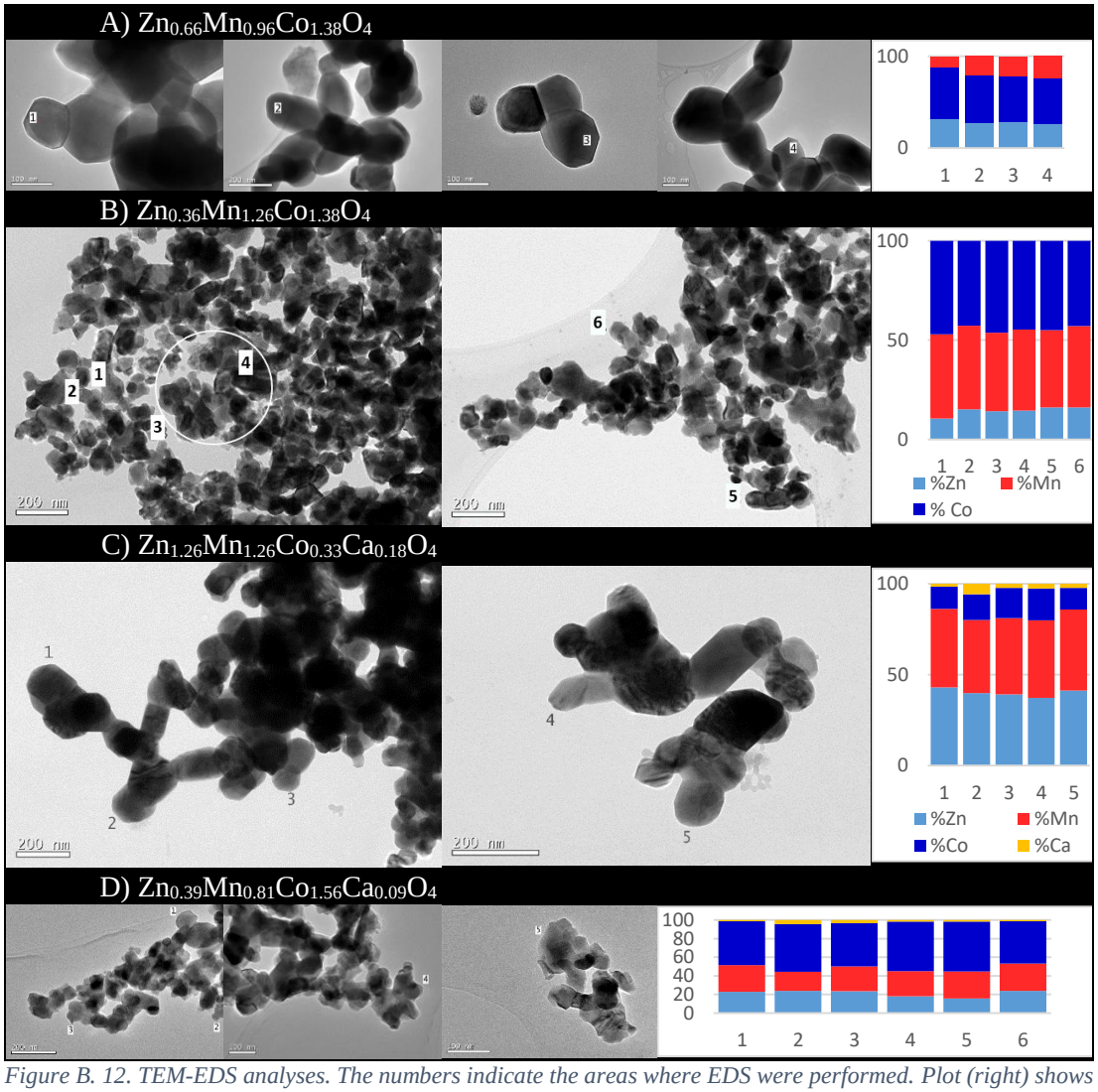

Figure B. 12. TEM-EDS analyses. The numbers indicate the areas where EDS were performed. Plot (right) shows the metal ratios by EDS analyses, where each column corresponds to the area indicated by a number in the TEM pictures.

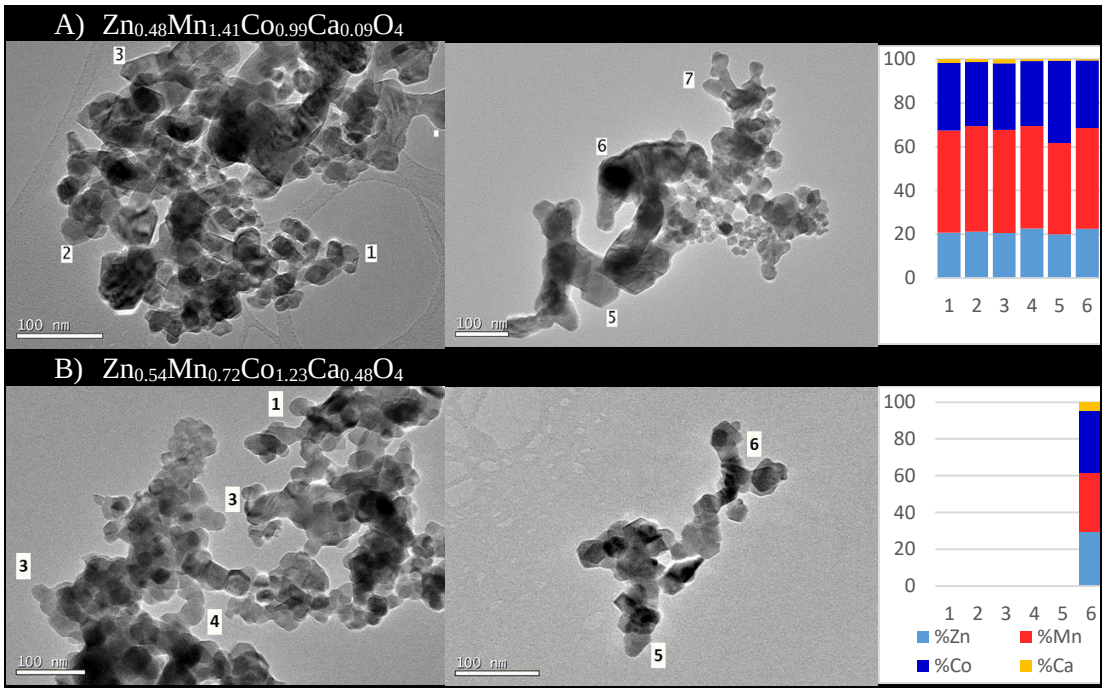

Figure B. 13. TEM-EDS analyses. The numbers indicate the areas where EDS were performed. Plot (right) shows the metal ratios by EDS analyses, where each column corresponds to the area indicated by a number in the TEM pictures.

5. Cyclic voltammetry of spinel oxides

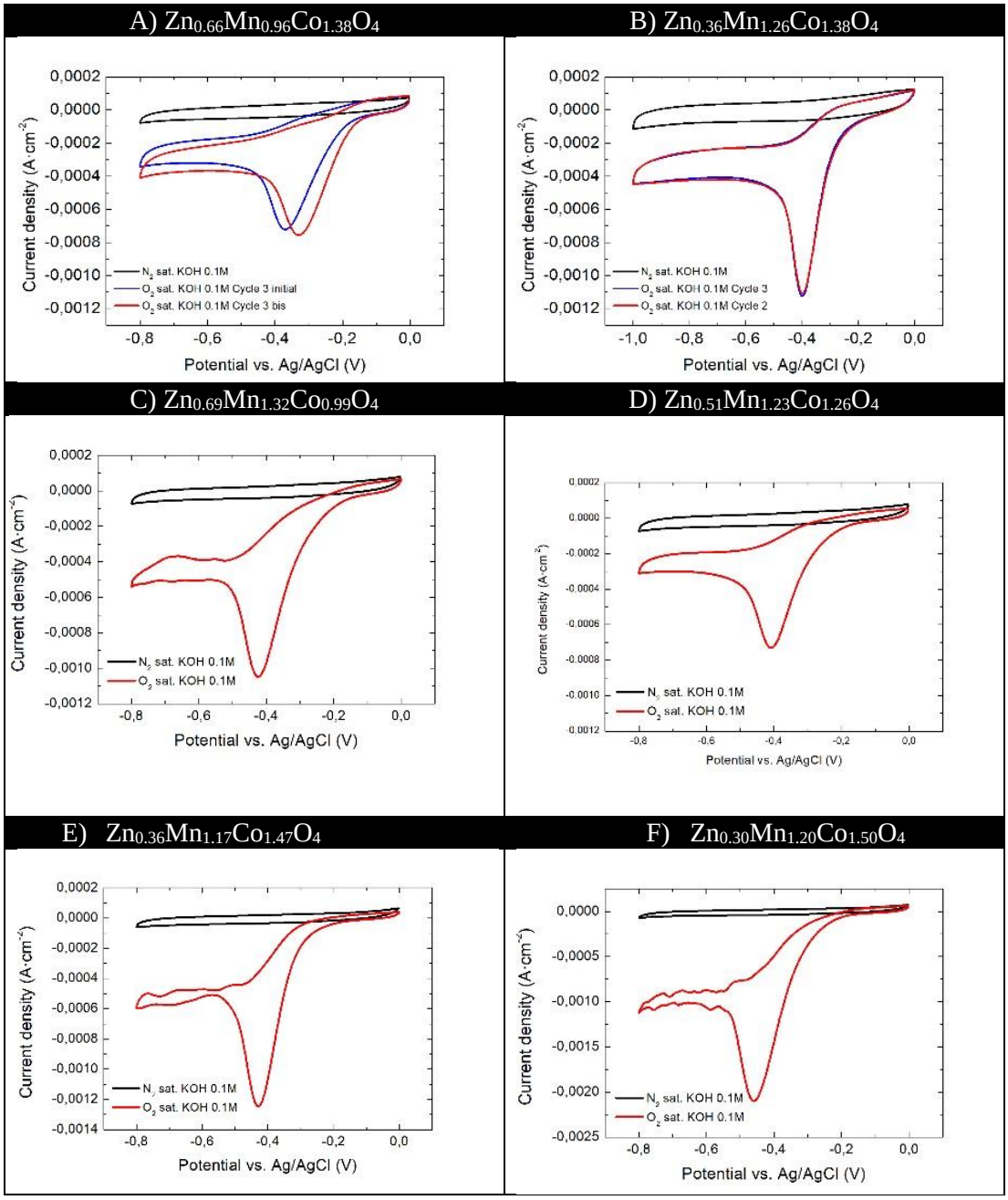

Figure B. 14. Cyclic voltammetry of multimetal spinels in N_2 saturated 0.1M KOH (black curve) and O_2 saturated 0.1M KOH (red curve).

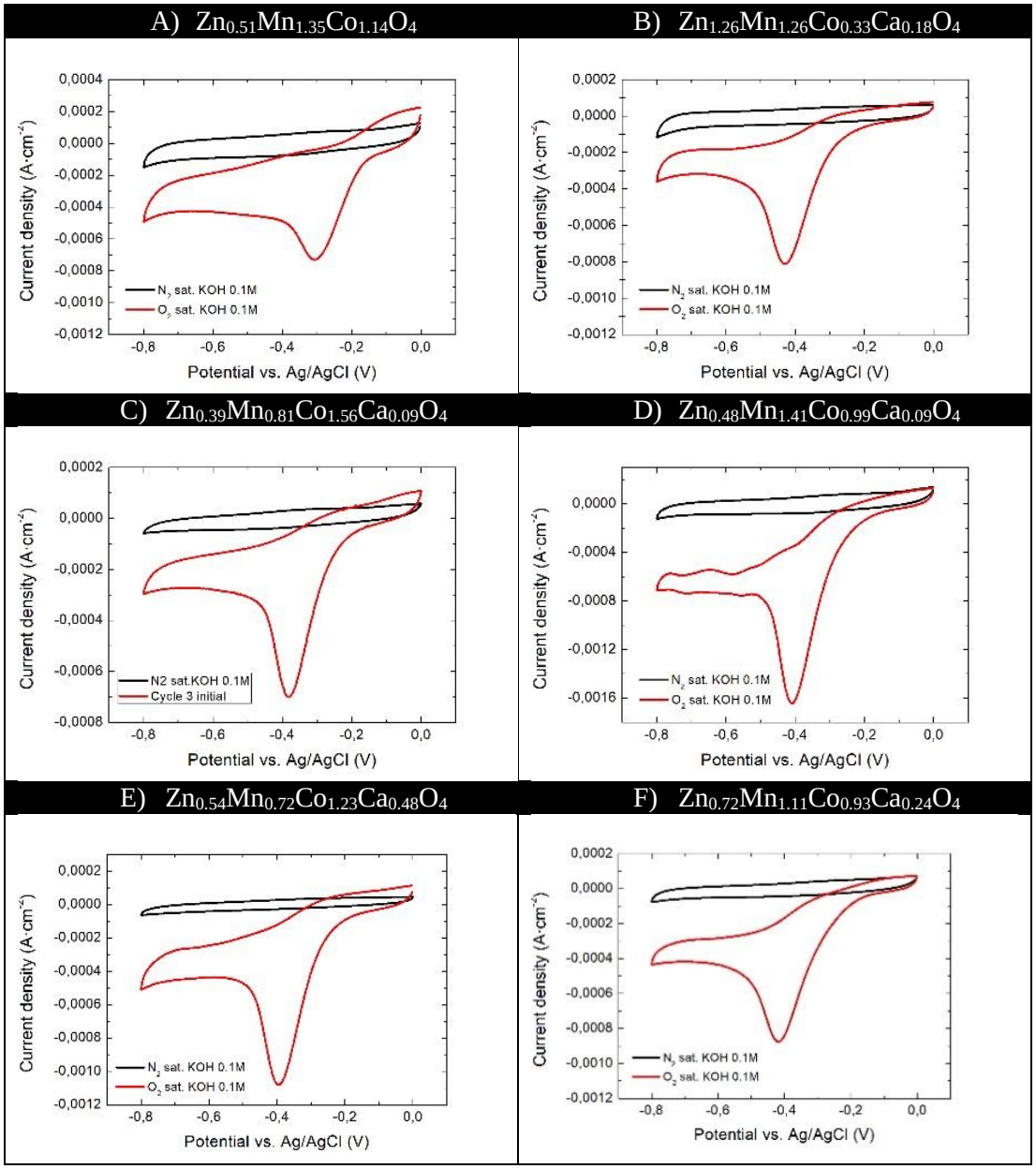

Figure B. 15. Cyclic voltammetry of multimetal spinels in N_2 saturated 0.1M KOH (black curve) and O_2 saturated 0.1M KOH (red curve).

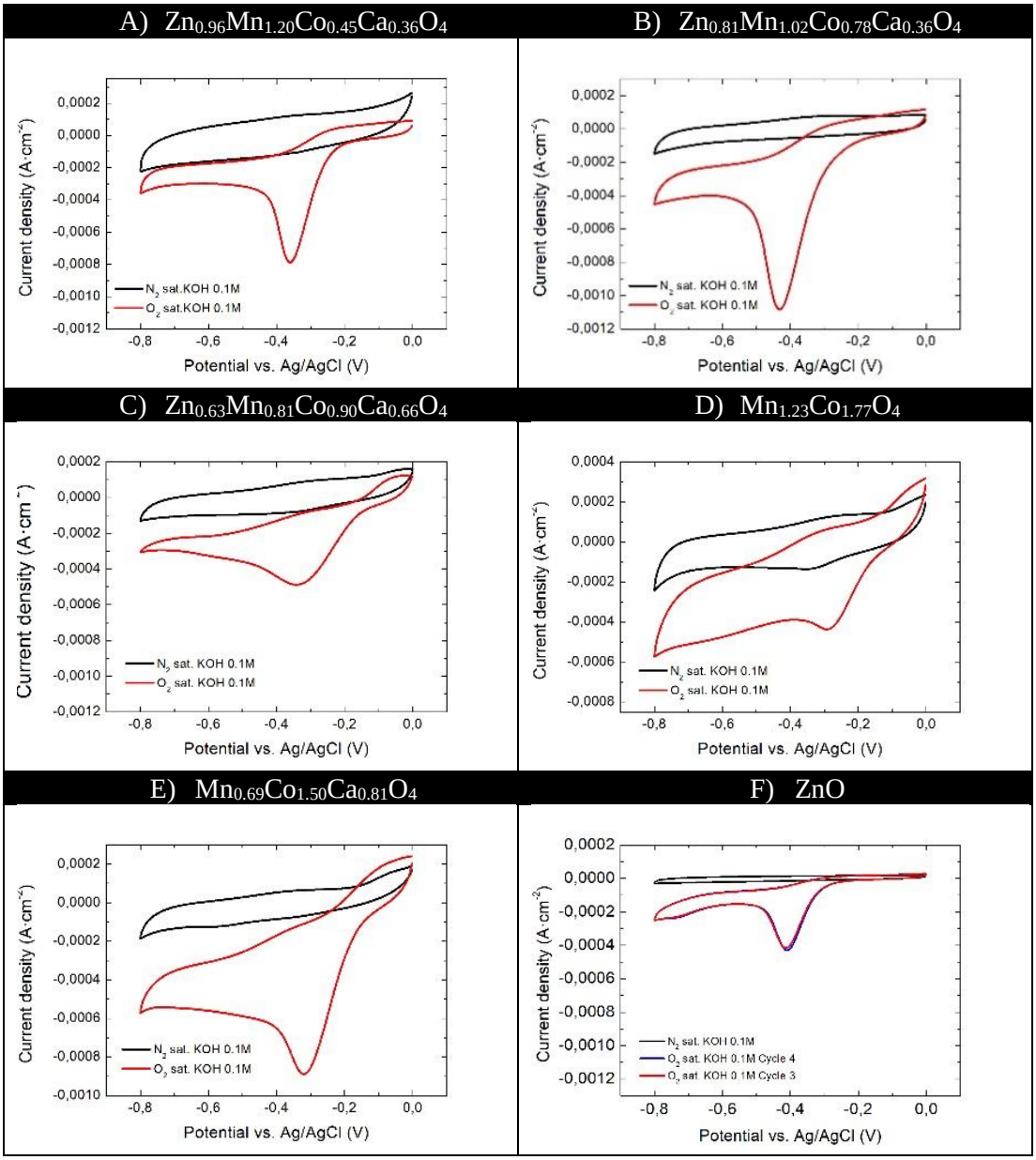

Figure B. 16. Cyclic voltammetry of multimetal spinels in N_2 saturated 0.1M KOH (black curve) and O_2 saturated 0.1M KOH (red curve).

6. ORR equations

For reactions that are controlled by both diffusion and kinetics at (rotating disk electrodes) RDEs, the total current density (j) of the reacting electroactive species is related to the speed of rotation of the electrode (ω) by what is commonly known as Koutecky-Levich equation:

$$\frac{1}{J} = \frac{1}{J_K} + \frac{1}{J_L} = \frac{1}{nFkC_0} + \frac{1}{0.62nFC_0(D_0)^{2/3}\upsilon^{-1/6}\omega^{1/2}}$$

Where J_K is the kinetic current density, J_L is the diffusion-limiting current density, n is the overall number of electrons transferred, F is the Faraday constant, k is the electron transfer rate constant, C_0 is the O_2 concentration in the electrolyte, D_0 is the diffusion coefficient of O_2 in the electrolyte, υ is the viscosity of the electrolyte, and ω is the angular velocity in units of $rad \cdot s^{-1}$.

The number of electrons transferred (n)and the electron transfer rate constant (k) can be obtained from the slope and intercept of Koutecky-Levich plots (J^{-1} vs $\omega^{-1/2}$) at various rotation speeds, respectively. It is important to note that Koutecky-Levich equation is based on smooth electrode surfaces under laminar flow hydrodynamics. Therefore, the quality of a given catalyst film can greatly impact the accuracy of the kinetic current calculation in the RDE measurements. A good catalyst film is thin, uniform, and smooth. Thick films lead to increased mass-transport resistance through the film and incomplete utilization of the catalyst. It is clear that irregularly built-up films (no uniform coverage, very rough surface, etc.) must be avoided in RDE measurements because the K-L equation if not valid under those conditions.

7. Koutecky-Levich plots

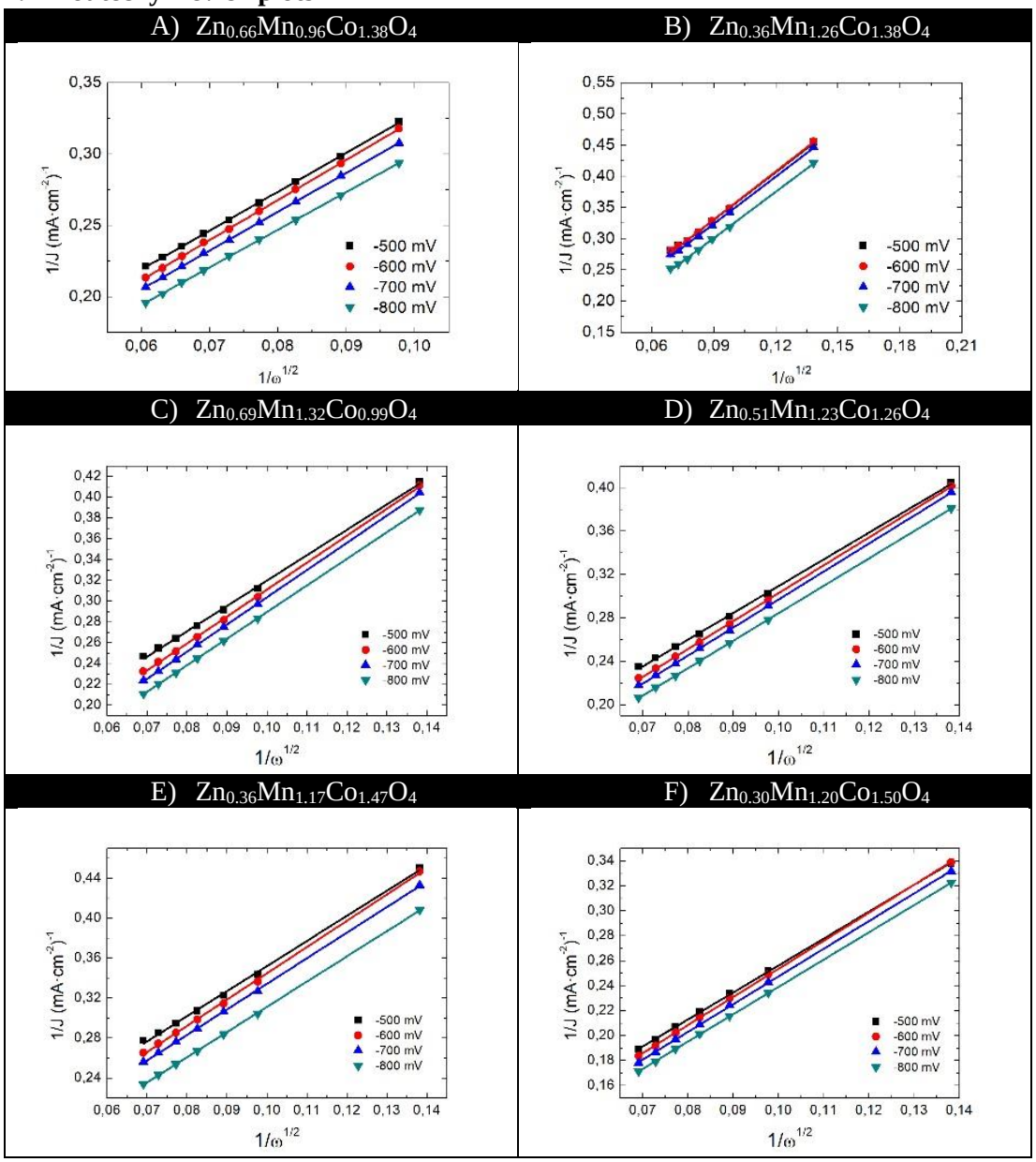

Figure B. 17. Koutecky-Levich plots of multimetal spinels at different potentials (-500, -600, -700 and -800 mV).

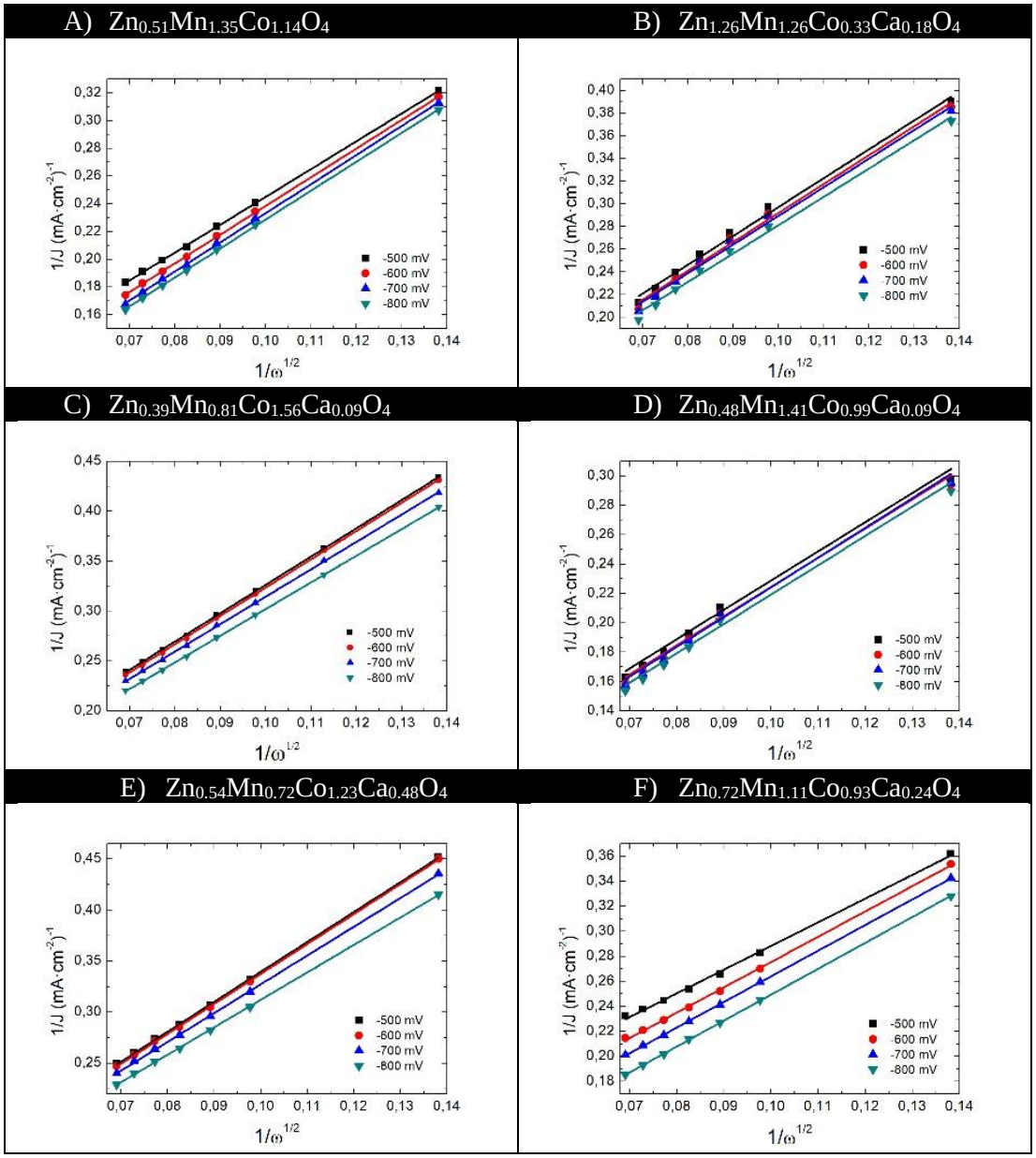

Figure B. 18. Koutecky-Levich plots of multimetal spinels at different potentials (-500, -600, -700 and -800 mV).

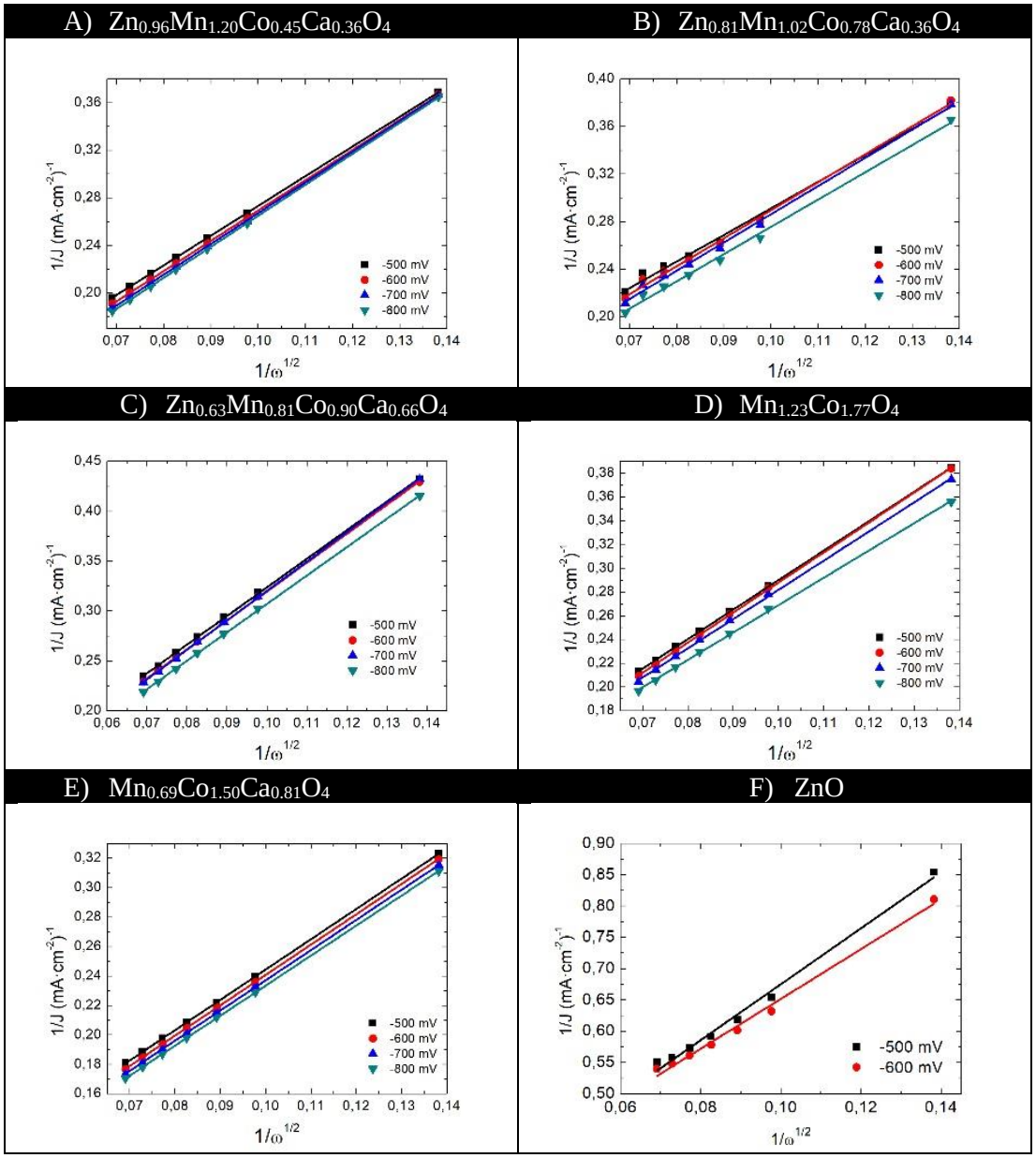

Figure B. 19. Koutecky-Levich plots of multimetal spinels at different potentials (-500, -600, -700 and -800 mV). ZnO K-L plot is also included for comparison.

8. Linear sweep voltammetry

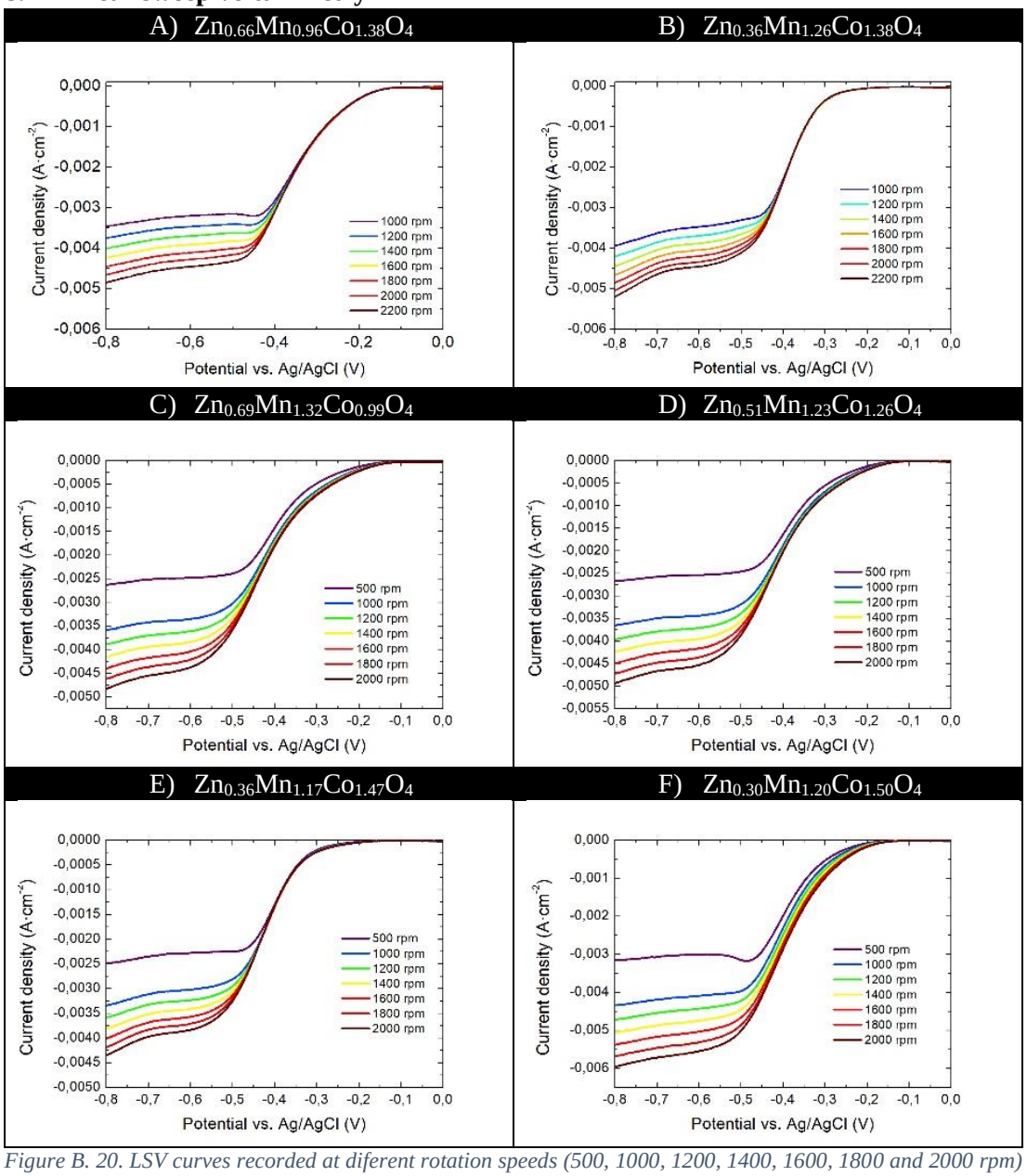

Figure B. 20. LSV curves recorded at diferent rotation speeds (500, 1000, 1200, 1400, 1600, 1800 and 2000 rpm) of $Mn_{0.69}Co_{1.50}Ca_{0.81}O_4$ multimetal spinel in O_2 saturated 0.1M KOH.

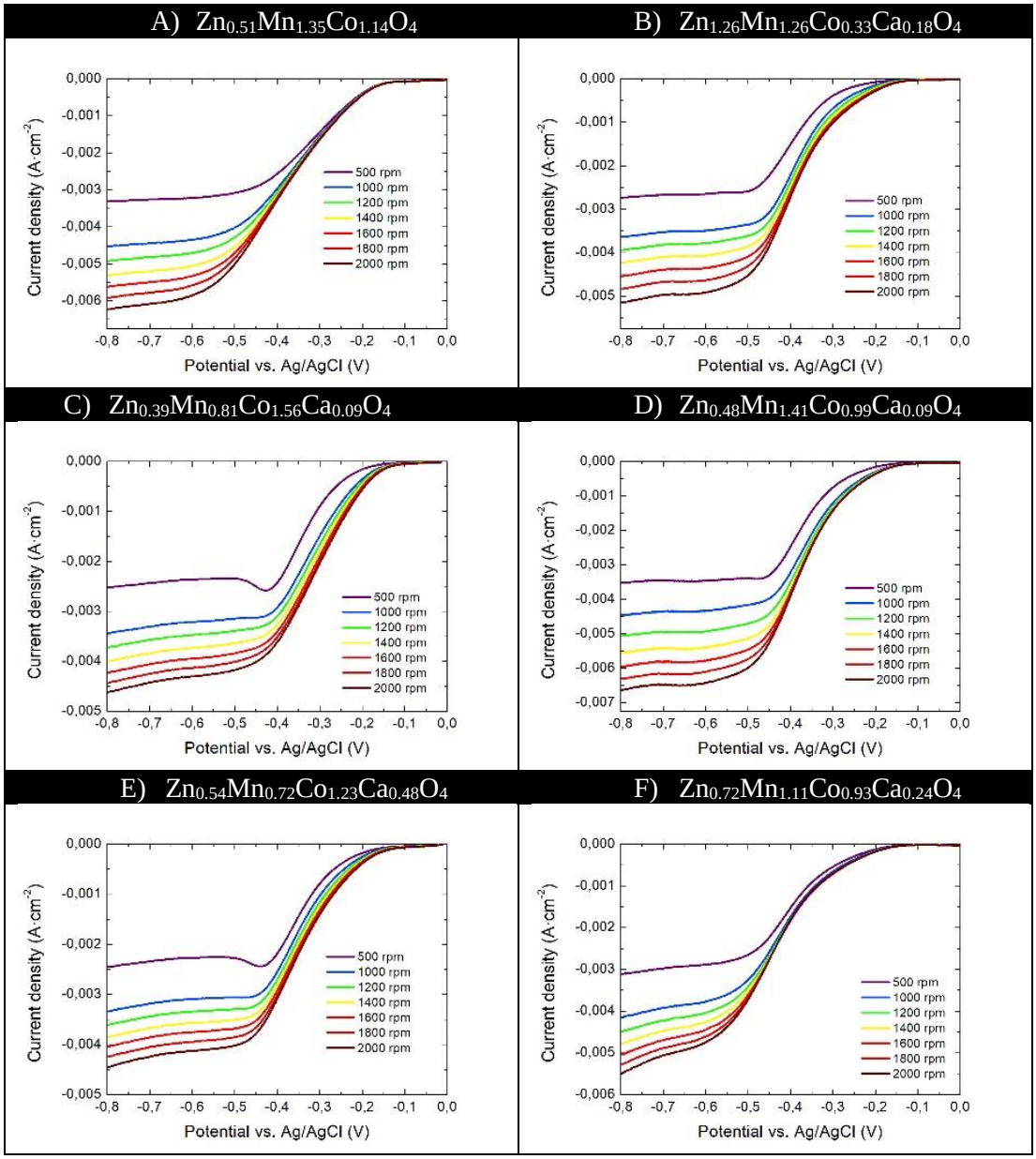

Figure B. 21. LSV curves recorded at diferent rotation speeds (500, 1000, 1200, 1400, 1600, 1800 and 2000 rpm) of $Mn_{0.69}Co_{1.50}Ca_{0.81}O_4$ multimetal spinel in O_2 saturated 0.1M KOH.

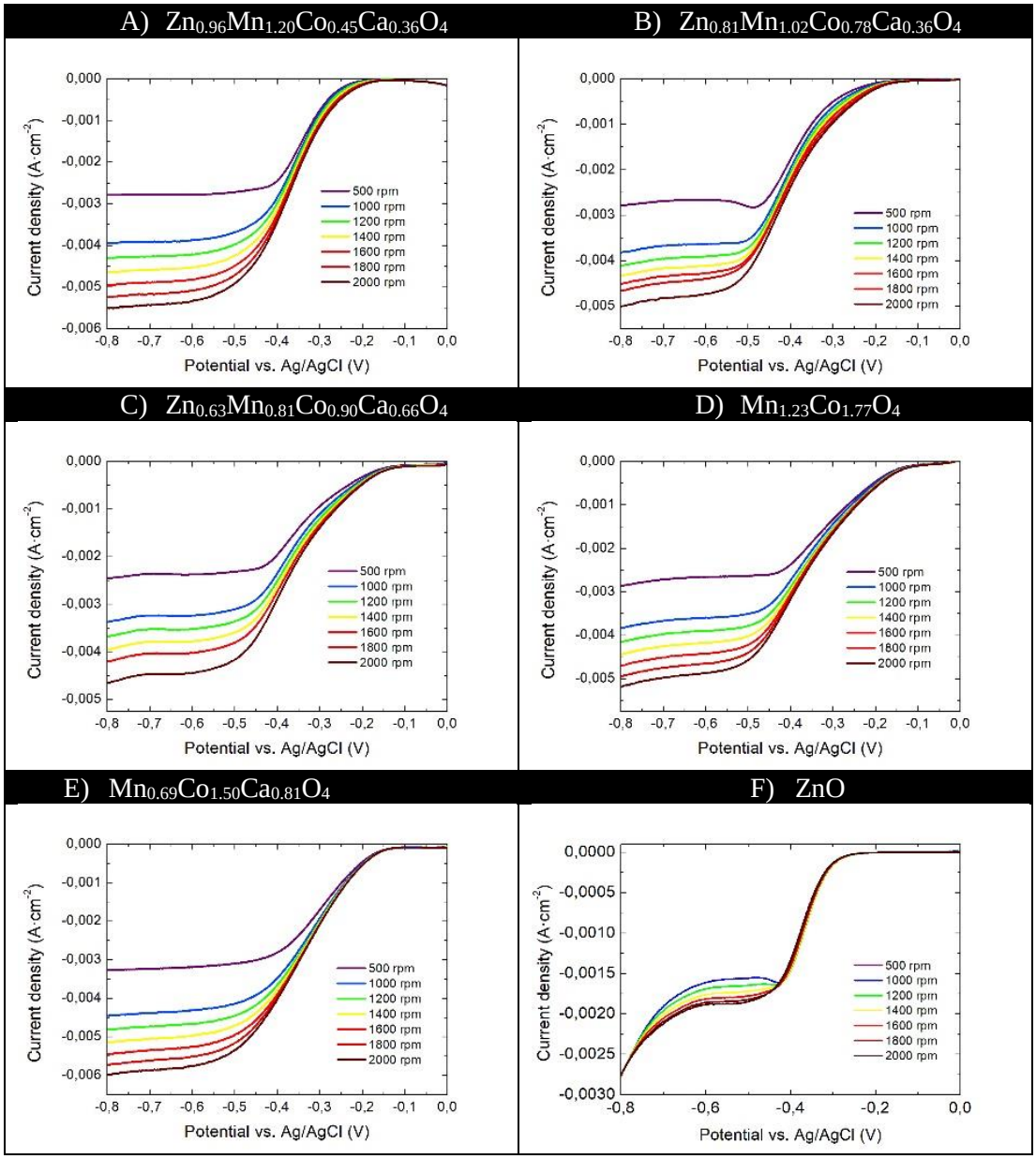

Figure B. 22. LSV curves recorded at diferent rotation speeds (500, 1000, 1200, 1400, 1600, 1800 and 2000 rpm) of multimetal spinels in O_2 saturated 0.1M KOH. ZnO LSV lines are also included for comparison.

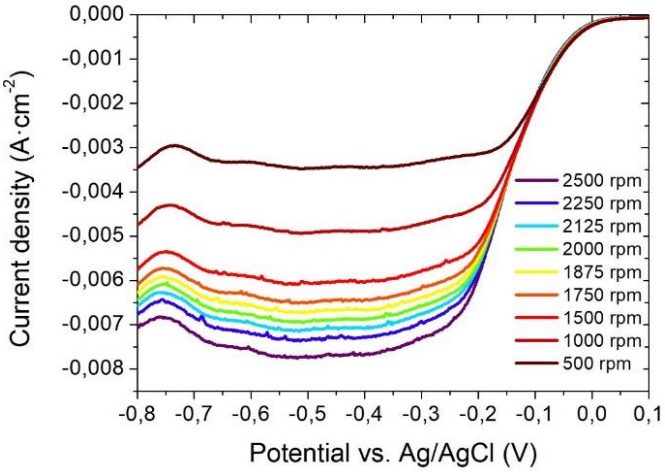

Figure B. 23. LSV lines of Pt/C (20% wt) at different speeds in O_2 saturated 0.1M KOH.

C) Abbreviations

4-pyrdpm: 5-(4pyridyl)-4,6-dipyrrinato

acac: acetylacetonate

Bdc: 1,4-benzenedicarboxilic acid

BET: Brunauer-Emmett-Teller

Btc: 1,3,5-benzenetricarboxilic acid

Btt: 1,3,5-benzenetristetrazolate

CVD: Chemical vapor deposition

DFT: Density function theory

DMSO: dimethylsulfoxide

EA: Elemental analyses

EDS: Energy dispersive X-ray spectroscopy

EtOH: Ethanol

H_2bpydc: 2,2′-bipyridine-5,5′-dicarboxylic acid

H_2hfipbb: 4,4'-(hexafluoroisopropylidene)bis(benzoic) acid

H_4mesox: dihydroxymalonic acid

HCPP: 5,15-bis(4´-carbomethoxyphenyl)-10,20-bis(3,5-biscarboethoxyphenyl)porphyrin)

ICP: Inductively coupled plasma

id_a: iminodiacetic acid

ILL: Institut Laue Langevin

Ina: isonicotinate

IRMOF: Isoreticular metal-organic framework

LSV: Linear sweep voltammetry

MIL: Materiaux de l'Institut Lavoisier/Materials from the Lavoisier Institute

MO: Metal oxide

NP: Nanoparticle

NPD: Neutron powder diffraction

OCCP: tetrakis-(3,5dicarboxyphenyl)porphyrin

OES: optical emission spectroscopy

ORR: Oxygen reduction reaction

ox: oxalate

PSI: Paul Scherrer Institute

PVP: polyvinylpyrrolidone

PXRD: Powder X-ray diffraction

SBU: Secondary building unit

SEM: Scanning electron microscopy

TCCP: tetrakis(4-carboxyphenyl)porphyrin

TEM: Transmission electron microscopy

TGA: Thermalgravimetric analysis

TMPF: Transition metal polymeric framework

TPPCOOMe: 5,10,15,20-Tetrakis(4-methoxycarbonylphenyl)porphyrin

XRD: X-ray diffraction

ZFC: Zero field cooling

ZIF: Zeolitic imidazolate framework

D) List of publications

1. C. Castillo-Blas, N. Snejko, V.A. de la Peña-O'Shea, J. Gallardo, E. Gutiérrez-Puebla, M.A. Monge and F. Gándara. *'Crystal phase competition by addition of a second metal cation in sold solution metal-organic frameworks'*. ***Dalton Transactions***, **2016**, 45 (13), 4327. DOI: 10.1039/C5DT03856A

2. C. Castillo-Blas, V.A. de la Peña-O'Shea, I. Puente-Orench, J. Romero de Paz, R. Sáez-Puche, E. Gutiérrez-Puebla, F. Gándara and Á. Monge. *'Addessed realization of multication complex arrangements in metal-organic frameworks'*. ***Science Advances.***, **2017**, 3 (7), e1700773. DOI: 10.1126/sciadv.1700773

3. C. Castillo-Blas and F. Gándara., *'Metal-organic frameworks incorporating multiple metal elements'*. ***Israel Journal of Chemistry***, **2018**, 58 (9), 1036-1043. DOI: 10.1002/ijch.201800085

4. C. Castillo-Blas, N. López-Salas, M.C. Gutiérrez, I. Puente-Orench, E. Gutiérrez-Puebla, M.L. Ferrer, M. Á. Monge and F. Gándara. *'Enconding metal-cation arrangements in metal-organic frameworks for programming the composition of electrocatalytically active multimetal oxides'*. ***Journal of American Chemical Society***, **2019**. DOI: 10.1021/jacs.8b12860

Dalton Transactions

PAPER

View Article Online
View Journal

Cite this: DOI: 10.1039/c5dt03856a

Crystal phase competition by addition of a second metal cation in solid solution metal–organic frameworks†

C. Castillo-Blas,[a] N. Snejko,[a] V. A. de la Peña-O'Shea,[b] J. Gallardo,[a] E. Gutiérrez-Puebla,[a] M. A. Monge*[a] and F. Gándara*[a]

Received 2nd October 2015,
Accepted 2nd December 2015

DOI: 10.1039/c5dt03856a

www.rsc.org/dalton

Herein we report a synthetic study focused on the preparation of solid-solution metal–organic frameworks, MOFs, with the use of two kinds of linkers. In particular, we have explored the system composed by zinc, cobalt, 1,2,4-triazole and 4,4′-hexafluoroisopropylidenebisbenzoic acid (H_2hfipbb). During this study, four new MOFs have been isolated, denoted **TMPF-88** [M_3(hfipbb)$_2$(triazole)$_2$(H_2O)], **TMPF-90** [M_2(triazole)$_3$(OCH_2CH_3)], **TMPF-91** [M_2(hfipbb)(triazole)$_2$(H_2O)] and **TMPF-95** [M_5(hfipbb)$_4$(triazole)$_2$-(H_2O)] (TMPF = transition metal polymeric framework, M = Zn, Co, or mixture of them). The study demonstrates that the addition of a second metal element during the MOF synthesis has a major effect in the formation of new phases, even at very high Zn/Co metal ratios. Furthermore, we show that during the MOF formation reaction, there is a competition among different crystal phases, where kinetically favoured phases of various compositions crystallize in short reaction times, precluding the formation of the pure solid-solution phases of other energetically more stable MOFs.

Introduction

Metal–organic frameworks, MOFs, are a class of materials constructed by the assembly of metal cations and organic linkers into extended, ordered structures.[1] Traditionally, MOFs are built by the combination of one kind of inorganic secondary building unit, SBU, and one kind of organic linker to form well-defined networks; it is also possible to build MOFs with multiple linkers or building units of different geometries or connectivities, which are occupying specific positions in the framework.[2] Currently, there is great interest in the development of MOFs that are able to display heterogeneity and disorder along with the order inherent to their crystalline nature. MOFs with these features are able to show new emerging properties, or enhancement of known ones.[3] The combination of heterogeneity and order can be afforded following different strategies, such as combination of different SBUs and/or linkers, combination of multiple functional groups,[4] introduction of defects,[5–9] pore modification, *etc*.

On the other hand, many properties exhibited by MOFs, such as gas adsorption selectivity,[10,11] catalytic activity,[12] or electrical conductivity[13,14] largely depend on the metal element that is incorporated in the SBUs. In many cases, a MOF structure type can be prepared with just a metal element or a very limited number of them. Thus, in these cases the introduction of a desired element into a targeted MOF structure is only achievable by following a post-synthetic metal exchange, allowing the total or partial replacement of the metal cations. The cation exchange process in MOFs has been recently reviewed,[15] and some SBUs and metal coordination environments that are more suitable to undergo this process have been identified. Recently, it has also been demonstrated that it is possible to selectively remove part of the metal cations and linkers of a MOF to produce vacancies at defined sites,[16] which can be subsequently occupied by a different metal cation. Alternative to metal-exchange, it is also possible to incorporate a mixture of different metal cations into a desired MOF in a one pot synthesis. With this strategy, it is possible to prepare multi-metal or solid-solution MOFs where different cations are occupying the same crystallographic position. MM-MOF-74 appears as a notable example of solid solution MOFs, which can be prepared with a mixture of 2, 4, 6, 8 and 10 different metal elements, including some elements that cannot afford MOF-74 by themselves (Ba, Ca, Sr).[17]

[a]*Department of New Architectures in Materials Chemistry – Instituto de Ciencia de Materiales de Madrid, CSIC, Sor Juana Inés de la Cruz 3, Cantoblanco, Madrid 28049, Spain. E-mail: gandara@icmm.csic.es, amonge@icmm.csic.es*
[b]*IMDEA Energy Institute, Móstoles Technology Park, Av. Ramón de la Sagra 3, 28935 Móstoles, Madrid, Spain*

†Electronic supplementary information (ESI) available: Additional characterization including PXRD patterns, ICP-CHN-EDX analyses, sorption isotherm, FT-IR and TG analyses. CCDC 1429138–1429141. For ESI and crystallographic data in CIF or other electronic format see DOI: 10.1039/c5dt03856a

Rare-earth based MOFs are also known to be susceptible of being prepared as solid solution MOFs, since lanthanide elements can easily replace one another. Here, the introduction of different rare-earth elements into the same framework results in the modification of the luminescence properties of the MOFs.[18] It is also expected that the introduction of multiple cations within the same SBU might result in modification of the materials' properties such as catalytic activity.[19] Recently, we have shown that it is possible to prepare a series of isostructural MOFs with group 13 elements, Al, Ga and In, as well as solid solution mixtures containing Ga and In in different ratios.[20] Remarkably, modification of the Ga/In ratio in the resulting solid-solution MOFs provides control on the catalytic activity of the materials in complex multicomponent reactions carried out in one-pot. However, it is still unclear which are the most important factors that drive the introduction of different metal cations into a single crystalline phase, rather than producing phase segregation, and thus, to what extent it is possible to prepare solid-solution MOFs of a given structure. In the work presented here, we have carried out a synthetic study that involves the combination of zinc and cobalt with two different linkers, with the aim of understanding how the synthesis conditions led to the formation of a desired phase with a mixture of metal elements randomly distributed in the inorganic SBUs.

In particular, we have combined dicarboxylic 4,4′-hexafluoroisopropyliden-bis-benzoic acid and 1,2,4-triazole along with zinc and cobalt, two metal elements that typically exhibit a similar coordination environment. As a result, we have obtained four new MOFs (Scheme 1), denoted **TMPF-88**, **TMPF-90**, **TMPF-91** and **TMPF-95** (TMPF = transition metal polymeric framework). The introduction of two kinds of linkers results in a complex system with multiple possible combinations of reactants. Thus, our study demonstrates that the introduction of a second cation in the synthesis media significantly modifies the reaction system, resulting in the appearance of competing crystalline phases, which might even undergo phase transformation. Our results illustrate the importance of synthesis variables such as pH and solvents in the formation of the desired solid solution MOFs, where a mixture of metal cations can be disorderly incorporated into the SBUs. Furthermore, we show that the value of the metal cation ratio added in the synthesis drastically influences the appearance of new phases, and that under certain conditions the incorporation of a second cation can only be achieved at a trace level.

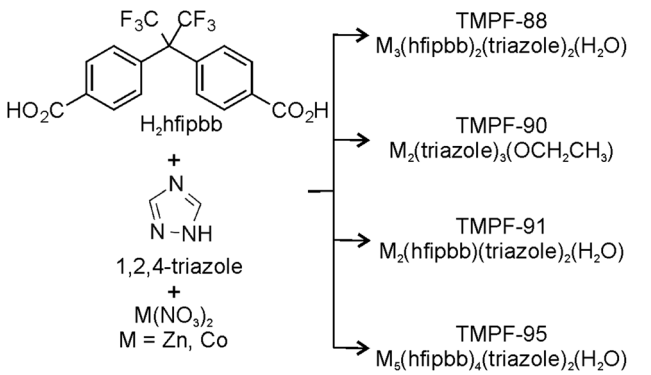

Scheme 1 Combination of 4,4′-hexafluoroisopropylidenebisbenzoic acid (H_2hfipbb), 1,2,4-triazole and zinc and cobalt nitrate salts results in the formation of four new MOFs. In the MOF formulae, M might stand for Zn, or a mixture of Zn and Co in various ratios, as explained in the text.

Experimental

General information

All reagents and solvents employed were commercially available and used as received without further purification: 4,4′-hexafluoroisopropylidene-bis-(benzoic acid), H_2hfipbb (98% ABCR GmbH & Co); 1,2,4-triazole (≥99% Fluka); zinc nitrate, $Zn(NO_3)_2{\cdot}6H_2O$ (≥99% Scharlab) and cobalt nitrate, $Co(NO_3)_2{\cdot}6H_2O$ (≥99% Sigma Aldrich).

Powder X-ray diffraction (PXRD) patterns were collected with a Bruker D8 diffractometer, equipped with a copper source operated at 1600 W, and a position sensitive detector. The patterns were collected with a step size of 0.02° and an exposure time of 0.5 s per step.

Single crystal X-ray data were obtained in a Bruker four circle kappa-diffractometer equipped with a Cu INCOATEC microfocused source, operated at 30 W power (45 kV, 0.60 mA) to generate Cu Kα radiation (λ = 1.54178 Å), and a Bruker VANTEC 500 area detector (microgap technology). The diffraction data were collected exploring over a hemisphere or a quadrant of the reciprocal space in a combination of φ and ω scans to reach a resolution of 0.85 Å, using a Bruker APEX2 software suite. Unit cell dimensions were determined for least-squares fit of reflections with $I > 5\sigma$. Space group determination was carried out using XPREP. The structures were solved by direct methods. The final cycles of refinement were carried out by full-matrix least-squares analyses with anisotropic thermal parameters of all non-hydrogen atoms. The hydrogen atoms were fixed at their calculated positions using distances and angle constraints. All calculations were performed using APEX2 software for data collection and SHELXTL[21] and OLEX2-1.2[22] to resolve and refine the structure.

Elemental analyses were performed in an ECO CHNS-932 analyzer.

Scanning electron microscopy (SEM) images and energy dispersive X-ray spectra (EDS) were collected with an S-3000N microscope, equipped with an ESED and an INCAx-sight of Oxford Instruments, respectively. All samples were prepared for SEM and EDS by dispersing the material onto a double sided adhesive conductive carbon tape that was attached to a flat aluminum sample holder and were metallized with a gold layer of 12 nm with a Quórum Q150T-S sputter.

N_2 sorption isotherms were measured with an AUTOSORB-1 from Quantachrome Instruments at 77 K in the relative pressure range of 10^{-6} to 1 atm. Before adsorption measure-

ments, the samples were activated by solvent exchange with methanol (15 mL, 3 times exchanged over a 2 day period) and outgassed at 408 K overnight.

The thermogravimetric and differential thermal analyses were performed with a SDT Q600 from TA Instruments equipment in a temperature range between 45 and 700 °C in air (100 mL min^{-1} flow) and at a heating rate of 10 °C min^{-1}.

IR spectra were recorded from KBr pellets in the range of 4000–350 cm^{-1} on a Nicolet FT-IR 20SXC spectrometer.

Computational details

Plane-wave density functional (PW-DF) calculations were done using the VASP package.[23,24] The energy was calculated employing the generalized gradient approximation, in particular, the exchange and correlation functional of Perdew and Wang (PW91).[25,26] The effect of the core electrons on the valence electron density was described by the projector augmented wave (PAW) method.[27,28] The cutoff for the kinetic energy of the plane waves was set to 415 eV throughout, which after extensive tests proved to ensure a total energy convergence better than 10^{-6} eV. Geometry optimization was carried out using a gradient-conjugate method. The formation energy (ΔE_{Form}) was calculated as the difference between the corresponding energies of the reagents and MOF structures.

General synthetic conditions

Preparation of TMPF-88, $M_3(hfipbb)_2(triazole)_2(H_2O)$. General procedure for Zn-**TMPF-88**: a mixture of H_2hfipbb (130 mg, 0.33 mmol), 1,2,4-triazole (75 mg, 1.09 mmol), $Zn(NO_3)_2{\cdot}6H_2O$ (100 mg, 0.34 mmol) in 5 ml of distilled water and 5 ml of absolute ethanol was stirred at room temperature for 5 minutes. The resulting mixture was placed in a Teflon-lined steel autoclave and heated at 170 °C overnight. After cooling to room temperature, colourless crystals were filtered off and washed with distilled water, ethanol and acetone. Yield 61% (79 mg). Elemental analysis, %weight found (calculated): C, 40.95 (39.51); H, 2.20 (2.01); N, 6.78 (7.27). **TMPF-88** was also obtained as a pure phase with a mixture of Zn and Co for synthesis carried out with the amounts shown in Table 1, entries 3–6.

Preparation of TMPF-91, $M_2(hfipbb)(triazole)_2(H_2O)$. General procedure with an initial 10 : 1 Zn : Co molar ratio: a mixture of H_2hfipbb (130 mg, 0.33 mmol), 1,2,4-triazole (75 mg, 1.09 mmol), $Zn(NO_3)_2{\cdot}6H_2O$ (91 mg, 0.31 mmol), $Co(NO_3)_2{\cdot}6H_2O$ (9 mg, 0.03 mmol) and a mixture of ethanol : water (5 ml/5 ml) was stirred at room temperature for 10 minutes. To the resulting mixture 300 μL of an aqueous 1 M solution of HNO_3 was added to adjust the pH to ~2.5 and the reaction mixture was placed in a Teflon-lined steel autoclave and heated at 170 °C overnight. After cooling to room temperature colourless crystals were filtered off and washed with distilled water, ethanol and acetone. Yield 36% (41 mg). Elemental analysis, %weight found (calculated): C, 38.11 (37.42); H, 2.37 (1.94); N, 12.25 (12.47). **TMPF-91** was also obtained as a pure phase for synthesis reactions carried out with the amounts shown in Table 1, entries 1 and 2.

Preparation of TMPF-95, $M_5(hfipbb)_4(triazole)_2(H_2O)$. A mixture of H_2hfipbb (130 mg, 0.33 mmol), 1,2,4-triazole (60 mg, 0.87 mmol), $Zn(NO_3)_2{\cdot}6H_2O$ (33 mg, 0.11 mmol), $Co(NO_3)_2{\cdot}6H_2O$ (65 mg, 0.22 mmol) and 10 ml of distilled water was stirred at room temperature for 5 minutes. The resulting mixture was placed in a Teflon-lined steel autoclave and heated at 170 °C for 3 days. After cooling to room temperature, purple crystals were filtered off and washed with distilled water, ethanol and acetone. Yield 61% (102 mg). Elemental analysis, weight% found (calculated): C, 42.87 (42.87); H, 1.94 (1.90); N, 4.51 (4.57).

Preparation of TMPF-90, $M_2(triazole)_3(OCH_2CH_3)$. General procedure with an initial 4 : 1 Zn : Co molar ratio: a mixture of 1,2,4-triazole (69 mg, 1 mmol), $Zn(NO_3)_2{\cdot}6H_2O$ (24 mg, 0.08 mmol), $Co(NO_3)_2{\cdot}6H_2O$ (6 mg, 0.02 mmol) and a mixture of ethanol: water (3 ml/3 ml) was stirred at room temperature for 10 minutes. The resulting mixture was heated at 90 °C overnight. After cooling to room temperature, yellow powder was filtered off and washed with distilled water, ethanol and acetone. Yield 73% (9 mg). Elemental analysis, weight% found

Table 1 Optimized synthetic conditions for obtaining pure samples. Temperature = 170 °C, and reaction time = 18 h

	Initial amounts					Experimental	
Entry	H_2hfipbb/mg, mmol	1,2,4-Triazole/mg, mmol	$Zn(NO_3)_2$/mg, mmol	$Co(NO_3)_2$/mg, mmol	H_2O : EtOH	Phase	Formula[a]
1	130, 0.33	75, 1.09	100, 0.34	—	5 ml : 5 ml	**TMPF-91**	$Zn_2(hfipbb)(triazole)_2(H_2O)$
2	130, 0.33	75, 1.09	91, 0.31	9, 0.03	5 ml : 5 ml	**TMPF-91**	$Zn_{1.90}Co_{0.10}(hfipbb)(triazole)_2(H_2O)$
3	130, 0.33	75, 1.09	100, 0.34	—	5 ml : 5 ml	**TMPF-88**	$Zn_3(hfipbb)_2(triazole)_2(H_2O)$
4	130, 0.33	60, 0.87	91, 0.31	9, 0.03	10 ml : 0 ml	**TMPF-88**	$Zn_{2.98}Co_{0.02}(hfipbb)_2(triazole)_2(H_2O)$
5	130, 0.33	60, 0.87	80, 0.27	19, 0.07	10 ml : 0 ml	**TMPF-88**	$Zn_{2.96}Co_{0.04}(hfipbb)_2(triazole)_2(H_2O)$
6	130, 0.33	60, 0.87	67, 0.23	33, 0.11	10 ml : 0 ml	**TMPF-88**	$Zn_{2.96}Co_{0.04}(hfipbb)_2(triazole)_2(H_2O)$
7	—	69, 1.00	6, 0.02	24, 0.08	3 ml : 3 ml	**TMPF-90**	$Zn_{0.86}Co_{1.14}(triazole)_3(CH_3CH_2O)$
8	—	69, 1.00	17, 0.05	17, 0.05	3 ml : 3 ml	**TMPF-90**	$Zn_{1.10}Co_{0.90}(triazole)_3(CH_3CH_2O)$
9	—	69, 1.00	24, 0.08	6, 0.02	3 ml : 3 ml	**TMPF-90**	$Zn_{1.21}Co_{0.79}(triazole)_3(CH_3CH_2O)$
10	—	69, 1.00	—	34, 0.10	3 ml : 3 ml	**TMPF-90**	$Co_2(triazole)_3(CH_3CH_2O)$
11[b]	130, 0.33	60, 0.87	33, 0.11	65, 0.22	10 ml : 0 ml	**TMPF-95**	$Zn_{1.84}Co_{3.16}(hfipbb)_4(triazole)_2(H_2O)$

[a] Formula determined by elemental and ICP analyses. [b] Reaction time = 3 days.

(calculated): C, 24.09 (23.29); H, 1.81 (1.67); N, 35.91 (38.80). **TMPF-91** was also obtained as a pure phase for synthesis reactions carried out with the amounts shown in Table 1, entries 7–10.

Crystal structure descriptions

A summary of the crystal and refinement data for the new MOFs is given in Table 2.

TMPF-88, Zn_3(hfipbb)$_2$(triazole)$_2$(H_2O). The compound crystallizes in the monoclinic *C*2/*c* space group. There are three crystallographically independent zinc atoms in the asymmetric unit, all of them in a tetrahedral coordination environment. The Zn atoms are coordinated to three triazolate anions and six carboxylate groups from the hfipbb linkers. A water ligand completes the coordination sphere of Zn2. Additionally another water ligand with partial occupancy was located at 2.67 Å from Zn3. The position of Zn3 could actually be split into two positions, so that this atom is partially found in a tetrahedral environment and in a trigonal bypiramidal environment when there is the presence of this additional water ligand. The occupancy for the two positions of Zn3 was refined to a 51 : 49 ratio.

The inorganic SBUs consist of three metal cations (Fig. 1A). They have a linear shape and are disposed along the *c* axis. Triazolate and hfipbb linkers connect the SBUs to form a three dimensional framework, with channels running along the *c* axis (Fig. 1B). The channels are of 8.8 by 8.4 Å dimensions. N_2 sorption isotherm shows that **TMPF-88** is permanently porous, with a BET surface area of 120 $m^2\ g^{-1}$ (190 $m^2\ g^{-1}$ Langmuir).

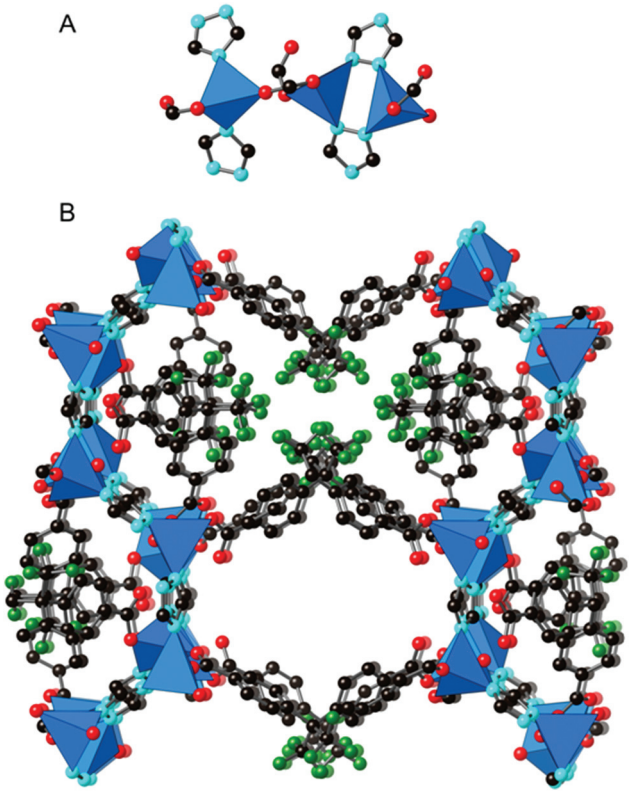

Fig. 1 (A) The inorganic SBU in **TMPF-88** is composed of three linearly disposed tetrahedral metal cations. (B) Depiction of **TMPF-88**, viewed along the *c* axis. Carbon is black, oxygen is red, fluorine is green and nitrogen is cyan. Blue polyhedra represent metal (Zn, Co) cations. Hydrogen atoms are omitted for clarity.

Table 2 Crystal and refinement data for **TMPF-88**, **TMPF-90**, **TMPF-91** and **TMPF-95**

	Compound **TMPF-88**	Compound **TMPF-90**[a]	Compound **TMPF-91**	Compound **TMPF-95**
Formula	$C_{38}H_{23}F_{12}N_6O_{10.46}Zn_3$	$C_8H_6N_9OZn_2$	$C_{21}H_{13}F_6N_6O_5Zn_2$	$C_{72}H_{38}Co_5F_{24}N_6O_{17.48}$
Molecular Weight/g mol^{-1}	1155.12	374.97	674.11	2017.37
Temperature/K	296 (2)	296	296 (2)	233 (2)
Wavelenght/Å	1.54178	1.54056, 1.54439	1.54178	1.54178
Crystal system	Monoclinic	Orthorhombic	Monoclinic	Monoclinic
Space group	*C*2/*c*	*Pnma*	*Cc*	$P2_1/n$
a/Å	36.4551(9)	7.598(7)	10.0888(4)	14.8692(5)
b/Å	18.1156(4)	10.016(6)	33.8241(11)	24.8713(8)
c/Å	14.1588(4)	17.457(8)	7.0903(2)	22.1361(7)
α/°	90	90	90	90
β/°	93.8165(13)	90	96.002(2)	91.621(2)
γ/°	90	90	90	90
V/$Å^3$	9329.8(4)	1328.7(5)	2406.26(14)	8183.0(5)
Z	8	4	4	4
D_x/g cm^{-3}	1.645	1.809	1.861	1.638
μ/mm^{-1}	2.789		3.328	83 887
F(000)	4597.0		1340.0	4011.0
GOF F^2	1.082		1.182	1.013
Final *R* índices	R_1 = 0.0410	R_p = 2.34%	R_1 = 0.0410	R_1 = 0.0776
[$I > 2\sigma(I)$]	wR_2 = 0.1307	R_{wp} = 3.43%	wR_2 = 0.1137	wR_2 = 0.1994
R índices (all data)	R_1 = 0.0521		R_1 = 0.0518	R_1 = 0.1298
	wR_2 = 0.1613		wR_2 = 0.1451	wR_2 = 0.2400

[a] Rietveld refinement against PXRD data.

TMPF-91, Zn_2(hfipbb)(triazole)$_2$. The compound crystallizes in the monoclinic *Cc* space group. There are two crystallographically independent Zn atoms in the asymmetric unit. One of them is in a tetrahedral coordination environment, coordinated to two nitrogen atoms from the triazolate linkers, and to two oxygen atoms, one from a carboxylic group of hfipbb and the other one is a water ligand. The second Zn atom is pentacoordinated, with a square pyramidal environment. The coordination sphere is made of four nitrogen atoms from triazolate anions, and one oxygen atom from a carboxylic group of a hfipbb linker. The Zn atoms are connected along the *a* and *c* axes by triazolate anions (Fig. 2A), while the hfibpp^{2-} anions connect the metal cations along the *b* axis. The resulting three-dimensional structure is densely packed, with no open space (Fig. 2B).

TMPF-95, $Co_{5-x}Zn_x$(hfipbb)$_4$(triazole)$_2$(H_2O). The compound crystallizes in the monoclinic $P2_1/n$ space group, in the form of prismatic crystals with intense pink color. There are five crystallographically independent metal atoms, three of them in a tetrahedral coordination environment, and the other two ones in an octahedral environment. The inorganic SBUs are U-shaped, consisting of five metal cations, which are coordinated to eight carboxylic groups and to four triazolates, with a total coordination number of twelve (Fig. 3A). As we explain below, the metal cations were assigned as cobalt during the crystal structure refinement, although elemental analysis indicates the presence of zinc. The positions of these two elements were indistinguishable in the structure, indicating that they must be disorderly occupying the five metal positions of the framework. The coordination of the SBUs through the organic linkers results in a three dimensional structure with a calculated 10.5% of accessible void space (Fig. 3B).

TMPF-90, Zn_2(triazole)$_3$(CH_3CH_2O) only appears as a microcrystalline powder. A small single crystal was obtained in a synthesis carried out with a mixture of Zn(acetate)$_2$, 1,2,4-triazole

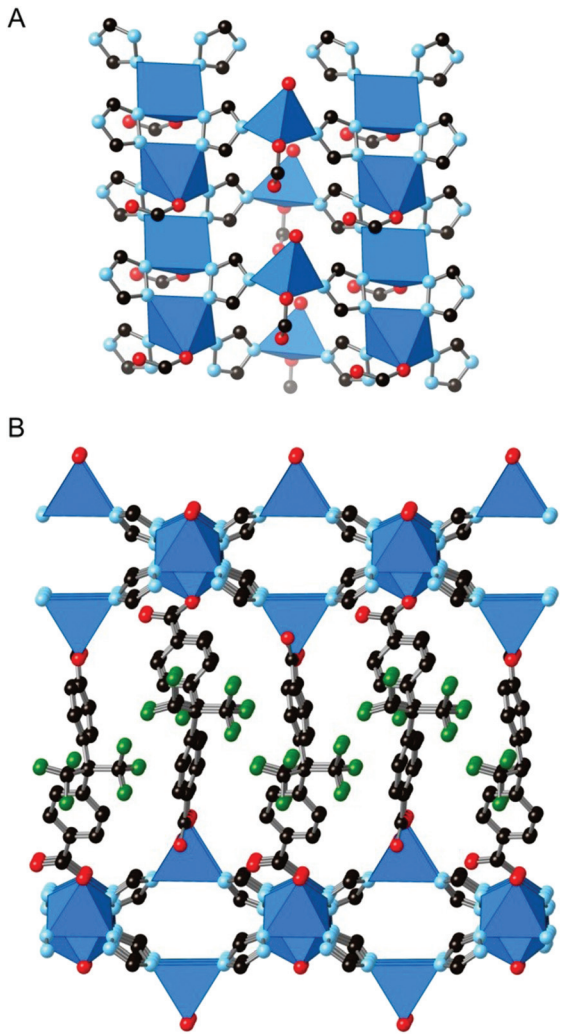

Fig. 2 (A) The inorganic SBU in **TMPF-91** can be depicted as rods of metal cations, which are linked by triazolate anions. (B) Representation of the three dimensional structure of the **TMPF-91** along the *c* axis. Layers depicted in (A) are perpendicular to the figure, and are connected by hfipbb^{2-} linkers. Carbon is black, oxygen is red, fluorine is green and nitrogen is cyan. Blue polyhedra represent metal (Zn, Co) cations. Hydrogen atoms are omitted for clarity.

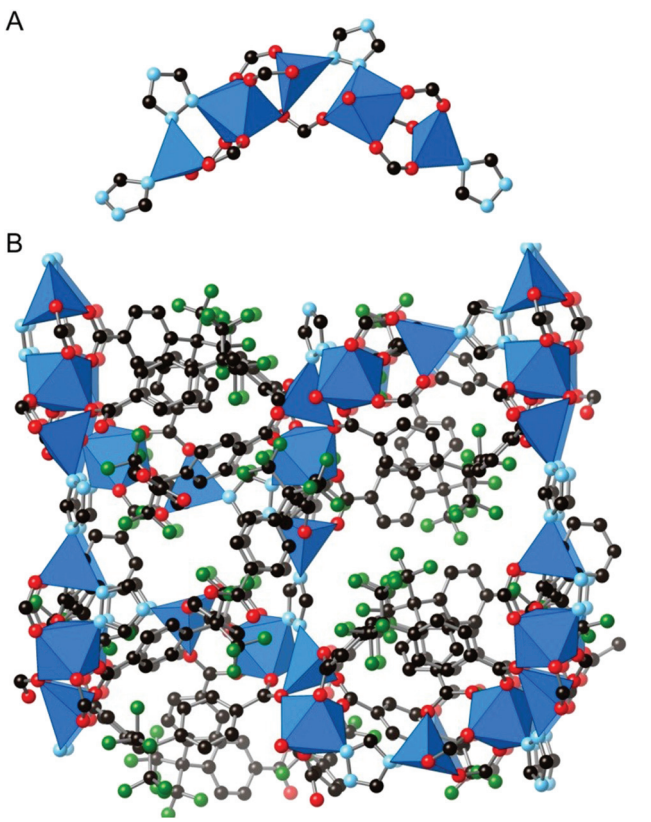

Fig. 3 (A) The inorganic SBUs in **TMPF-95** are composed of five V-shaped disposed polyhedral metal cations. (B) Representation of the three dimensional structure of **TMPF-95**. Carbon is black, oxygen is red, fluorine is green and nitrogen is cyan. Blue polyhedra represent metal (Zn, Co) cations. Hydrogen atoms are omitted for clarity.

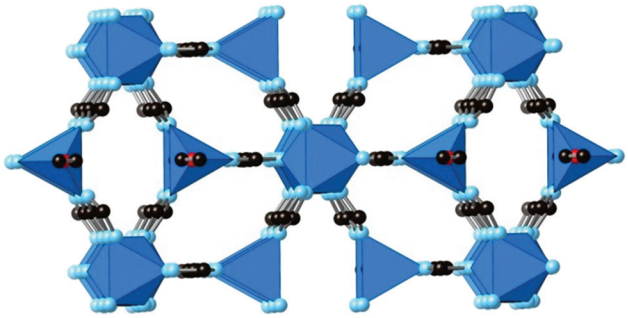

Fig. 4 Structural representation of **TMPF-90** viewed along the *a* axis. Carbon is black, oxygen is red and nitrogen is cyan. Blue polyhedra represent metal (Zn, Co) cations. Hydrogen atoms are omitted for clarity.

and H_2hfipbb in a 1 : 3 : 1 molar ratio, heated at 150 °C for 18 h.

However, the small size of the crystal and its poor diffracting quality precluded from completing a full diffraction data collection. Nevertheless, with data collected up to 1.1 Å and 49.3% completeness, it was possible to obtain the unit cell parameters and an initial set of atomic coordinates. The experimental PXRD patterns and the one calculated with this data set are in good agreement, and a Rietveld refinement was then carried out to confirm the correctness of the crystal structure, with final refinement indicators being R_{wp} = 3.71%, R_p = 2.55% (Fig. S4†). The compound crystallizes in the orthorhombic *Pnma* space group. There are two crystallographically independent metal atoms, one in tetrahedral and the other in an octahedral coordination environment. The octahedral centers are exclusively coordinated to N atoms from the triazolate anions, while in the tetrahedral centers, there are only three N atoms. The fourth coordination site is occupied by an O atom coming from the ethanol solvent molecules, which should be deprotonated to account for the charge balance. The metal centers are linked through the 1,2,4-triazolate anions, such as the nitrogen atoms in position 4 of the triazole ring coordinate to the tetrahedral cations, while nitrogen atoms in positions 1 and 2 coordinate to the octahedral cations. Each tetrahedral cation is thus linked to six octahedral cations, which are disposed forming rods along the *a* axis (Fig. 4).

Results and discussion

The combination of zinc nitrate with 1,2,4-triazole and H_2hfipbb in a 1 : 3 : 1 ratio resulted in obtaining Zn-**TMPF-88**. Initially, we carried out the synthesis using water as the only solvent. Zn-**TMPF-88** was isolated as a pure phase as shown by PXRD, although in a low yield, a fact that we attributed to the low solubility of H_2hfipbb in water, since a large amount of unreacted linkers remained in the reaction media. The use of a water : ethanol solvent mixture in a 1 : 1 ratio greatly improved the yield. With these optimized conditions, we then attempted to introduce cobalt in the structure by adding cobalt nitrate in the reaction media at the various Zn : Co ratios of 10 : 1, 8 : 1, 4 : 1, 2 : 1, 1 : 1, 1 : 2 and 0 : 1. The measured pH of the synthesis initial mixtures was fixed with 1 M NaOH to a value of 3.5. This is the same pH value measured in the reaction carried out exclusively with zinc nitrate as the only metal salt. The phase diagram for the obtained products under these conditions is shown in Fig. 5. It should be noted that the conditions for obtaining pure phases were further optimized and are listed in Table 1.

Surprisingly, the addition of cobalt even at the lowest 10 : 1 and 8 : 1 Zn : Co ratios precludes the formation of **TMPF-88**, resulting in the appearance of a different phase, **TMPF-91**. Pale pink microcrystalline powder was obtained in both the cases, whose PXRD patterns are in agreement with the calculated one for **TMPF-91** (Fig. S5†). SEM images show plate like crystals as a major phase, although the presence of a small amount of smaller particles without well-defined shape is also observed (Fig. 6A). EDS analyses were performed on different areas of the crystals to determine whether cobalt was actually incorporated into the structure. The results indicate that cobalt is indeed present in the structure, although the quantified amount of cobalt is much lower than the one initially added. Furthermore, the Zn : Co ratio is not constant along the crystals. For the sample prepared with an initial 10 : 1 ratio, the Zn/Co ratios observed in three different areas of the same crystal are 34.0, 26.7 and 26.6. In the case of the sample prepared with an initial 8 : 1 Zn : Co ratio the differences are even larger, with the observed Zn/Co ratios of 21.9, 20.9 and 45.7 (Fig. 6). Although the experimental error associated with the variations in beam penetration in a tilted sample cannot be completely ruled out, these results seem to indicate that the incorporation of cobalt into the structure is not homogeneous, and therefore the MOF composition varies along the crystals. This is also in agreement with the differences in the composition previously observed for multi-metal MOF-74.[17]

When we increase the amount of cobalt in the reaction to 4 : 1, 2 : 1, and 1 : 1, **TMPF-88** is obtained in the form of large crystals with pale pink colour (crystal size largest dimension around 500 μm). However, the MOF now appears mixed with a yellow microcrystalline powder, which is actually formed by needle-like microcrystals (5 μm), as observed in the SEM images (Fig. 7A). This powder was identified as **TMPF-90**, according to the PXRD pattern (Fig. S9†). EDS analysis carried out for the crystals of **TMPF-88** prepared with an initial 2 : 1 Zn : Co ratio demonstrates that cobalt is included in the MOF. Similar to the previous observation, the amount of cobalt incorporated is substantially lower than the amount initially added. Besides, the distribution of cobalt also varies along the same crystal, as shown by the measurements performed in different areas of the same crystal. The Zn/Co ratios are in the range between 24 and 15, measured in three areas from three different crystals (Fig. 7B). Since **TMPF-90** only contains 1,2,4-triazole as the organic linker, we attempted to obtain **TMPF-88** as a pure phase by decreasing the amount of triazole in the reaction media, which otherwise is added in excess (1.09 mmol). However, in all reactions with an amount of

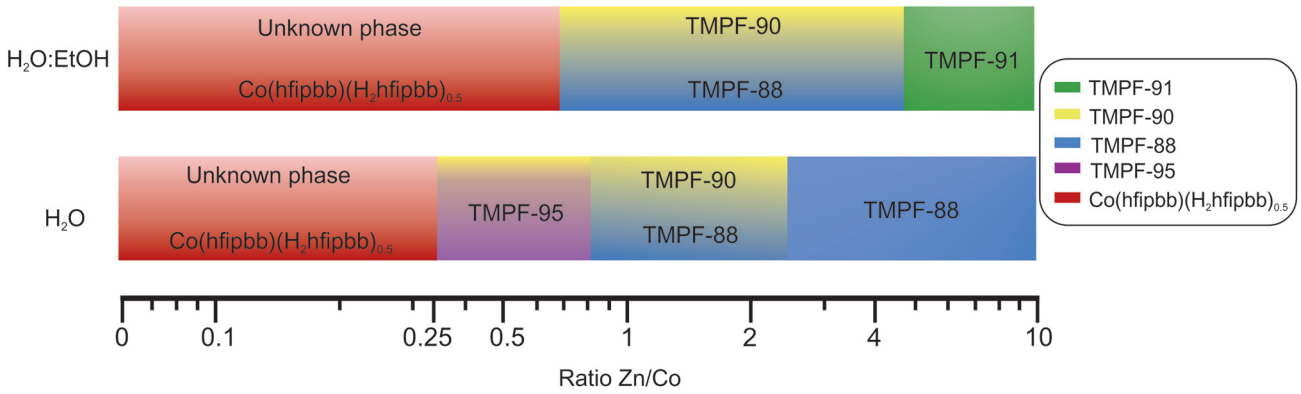

Fig. 5 The phase diagram for the obtained products with varying Zn/Co ratios, in two different conditions: water : ethanol (up) and water (down). For all experiments, temperature was 170 °C, and heating time 18 h. The Zn/Co ratio is shown in the logarithmic scale, indicating the values that were investigated.

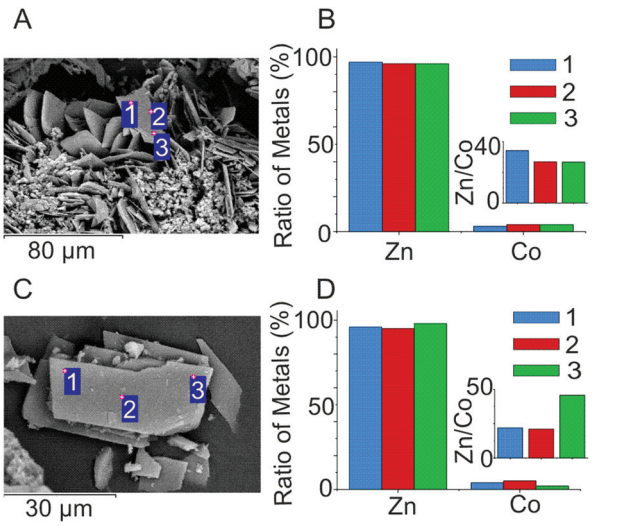

Fig. 6 SEM images corresponding to **TMPF-91** crystals, indicating the areas where the EDS analyses were performed. (A) Sample prepared with an initial 10 : 1 Zn : Co ratio. (B) Plot of the ratio of metals (%) and the Zn/Co ratio (inset) determined by EDS analysis, where each column corresponds to the area indicated by a number in panel A. (C) Sample prepared with an initial 8 : 1 Zn : Co ratio. (D) Plot of the ratio of metals (%) and the Zn/Co ratio determined by EDS analysis, where each column corresponds to the area indicated by a number in panel C.

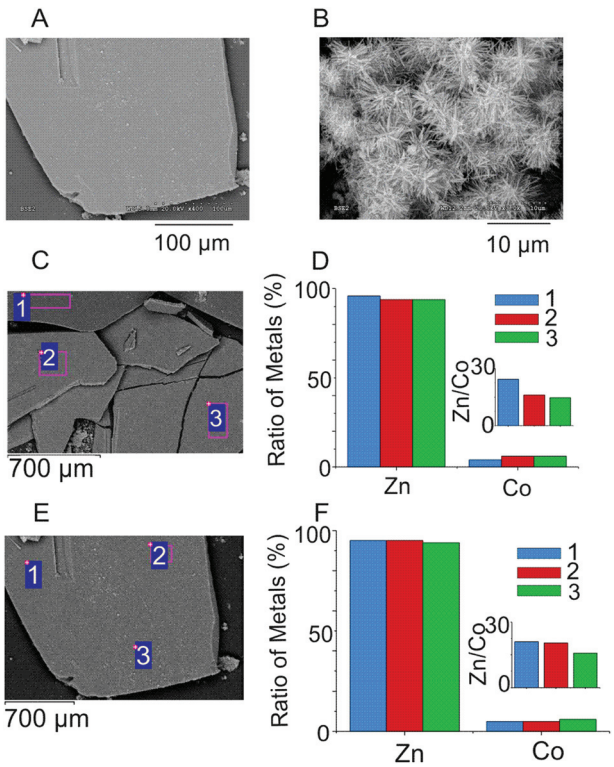

Fig. 7 SEM images corresponding to **TMPF-88** crystals, indicating the areas where the EDS analyses were performed (A) SEM images of two areas corresponding to the sample prepared with an initial 2 : 1 Zn : Co ratio showing a crystal of **TMPF-88** and (B) microcrystals of **TMPF-90**. (C) SEM image showing **TMPF-88** crystals corresponding to a sample prepared with an initial 2 : 1 Zn : Co ratio, indicating the points where the EDS analyses were performed. (D) Plot of the ratio of metals (%) and the Zn/Co ratio determined by EDS analysis, where each column corresponds to the area indicated by a number in panel C. (E) Sample prepared with an initial 2 : 1 Zn : Co ratio and shows the points of the same crystal. (F) Plot of the ratio of metals (%) and the Zn/Co ratio determined by EDS analysis, where each column corresponds to the area indicated by a number in panel E.

1,2,4-triazole between 1.09 and 0.80 mmol, **TMPF-90** is always present. Furthermore, if the amount of 1,2,4-triazole is lower than 0.80 mmol, **TMPF-88** is no longer formed.

In another effort to separate both the phases, we then studied the kinetics of this reaction system, by collecting the PXRD patterns of the products obtained after reaction times of 1 h, 2 h, 3 h, 4 h, 6 h, 8 h and 18 h (Fig. 8). After 1 hour of heating, only the unreacted H_2hfipbb linker was present in the PXRD pattern.

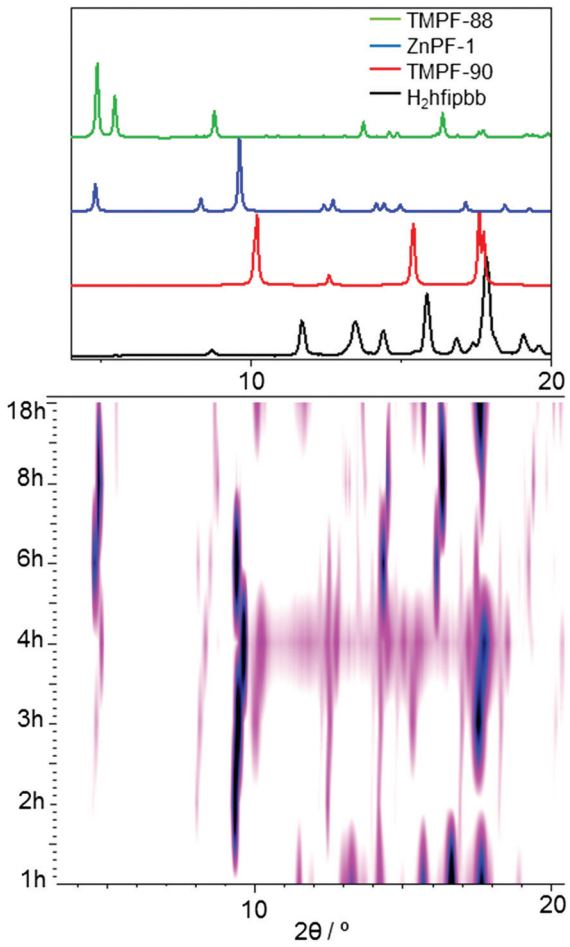

Fig. 8 Two-dimensional plot of the PXRD patterns corresponding to the samples obtained at different reaction times. The composition of the initial synthesis mixture is 130 mg, 0.33 mmol of H_2hfipbb; 75 mg, 1.09 mmol of triazole; 67 mg, 0.23 mmol of $Zn(NO_3)_2$ and 33 mg, 0.11 mmol of $Co(NO_3)_2$ in all cases. The simulated PXRD patterns of the phases involved in the kinetic study are shown in the top of the figure, as a guide to the eye.

Interestingly, after 2 hours the PXRD pattern indicates the formation of an additional crystalline phase, which was identified as a MOF with a composition Zn(hfipbb), which was previously reported by us, and hereon we denote it as ZnPF-1.[29] **TMPF-90** appears after 3 hours of heating, mixed with ZnPF-1. It seems reasonable to think that the formation of ZnPF-1 results in a higher relative concentration of triazole in the reaction solution, therefore favouring the formation of **TMPF-90**. After 4 hours of heating, the presence of **TMPF-88** is already identified in the PXRD pattern, although still mixed with **TMPF-90** and ZnPF-1. After 8 hours of heating, the intensities of the diffraction peaks corresponding to both ZnPF-1 and **TMPF-90** drastically decrease. Visual inspection of the product under an optical microscope still shows the presence of a yellowish microcrystalline powder typical of **TMPF-90**, along with large plate-like crystals of **TMPF-88**, suggesting that **TMPF-90** is only partially re-dissolved. At this point, ZnPF-1 seems to be completely re-dissolved, as it is no longer observed in the PXRD pattern or visually under an microscope. Interestingly, after longer reaction times (18 h), the intensities corresponding to **TMPF-90** peaks increase again, being the final product a mixture of **TMPF-88** and **TMPF-90**. To gain more insight on the formation of the different phases involved in the reaction, we estimated the structural stability of crystal phases and their synthesis mechanism during the MOF crystallization by means of theoretical calculations.[30–34] In this work, formation energies were calculated (ΔE_{Form}) using the VASP package. The geometry optimization was determined using the experimental structures obtained by X-ray diffraction and always converged to a stable structure even though no symmetry constraints were imposed. The results of these calculations show that **TMPF-90** and ZnPF-1 have very similar formation energies, much lower than that of **TMPF-88**, which is energetically more stable (Fig. 9).

In the case of ZnPF-1 and **TMPF-90**, the calculations were performed assuming that zinc is the only metal present. However, taking into account that **TMPF-90** can be obtained independently with both zinc and cobalt (*vide infra*), we performed two calculations for this phase, one considering zinc as the only metal element present (Zn-**TMPF-90**), and the other one with cobalt as the only metal element (Co-**TMPF-90**). This study shows that the Co-based structure presents a higher stability than the Zn one. These results suggest that the inclusion of Co in the bimetallic TMPF compounds might lead to a stabilization of their structures. Thus, small differences were observed in the case of **TMPF-90** depending on the metal element included, although it is likely that the actual product is composed of both zinc and cobalt, being the formation energy order Zn**TMPF-90** > ZnPF-1 > Co**TMPF-90**. Nevertheless, these calculations support the experimental observations of the kinetic study, demonstrating that in the mixed-metal

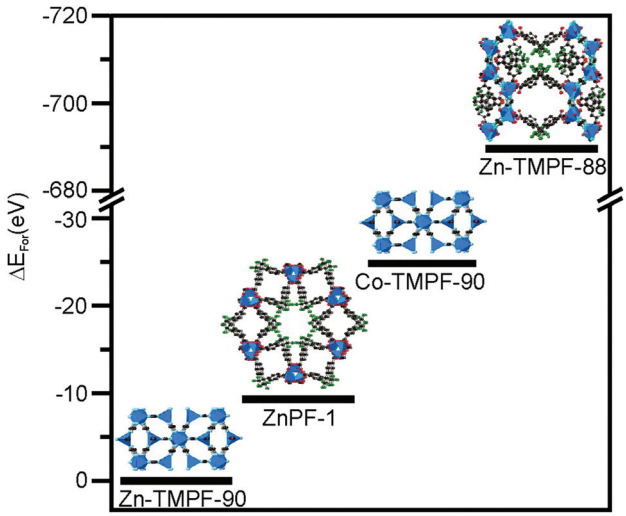

Fig. 9 Relative formation energies for the phases involved in the kinetic study. ΔE_{Form} values have been normalized to the most stable phase.

system with multiple kinds of linkers, kinetically favoured phases are readily formed, and consequently the composition and concentration of the synthesis media is not homogeneous during the MOF formation reaction.

TMPF-90 can be readily obtained with various Zn : Co ratios (4 : 1, 1 : 1, 1 : 4 and 0 : 1) as a pure phase when H_2hfipbb is not added during the synthesis and the reaction is carried out at 90 °C. EDS analyses indicate that in this phase the Zn : Co ratio is homogeneous along the sample. For the sample prepared with a 1 : 1 ratio, the Zn/Co ratio obtained in three different areas of sample is 0.55 : 0.45. In the case of the sample prepared with a 4 : 1 ratio, a similar Zn/Co ratio is found in three areas of the sample (0.6 : 0.4), suggesting a preference for the introduction of cobalt over zinc in this structure (Fig. 10).

If the Zn/Co ratio lies below 1 and the amount of cobalt is larger than that of zinc, **TMPF-88** is no longer formed. For syntheses with Zn : Co ratios 1 : 2, 1 : 4, 1 : 10 and 0 : 1, crystals corresponding to a previously reported MOF[35] with the formula Co(hfipbb)(H_2hfipbb)$_{0.5}$ are formed, along with a yellowish powder, whose crystal phase could not be identified. EDS analysis indicates a large percentage of nitrogen and the absence of fluorine in this solid, suggesting that it might correspond to a different crystalline form of cobalt-triazolate.

Initial synthesis experiments had showed that Zn-**TMPF-88** could be obtained with the use of water as the only solvent, although in a low yield. We therefore also decided to perform synthesis reactions with the mixture of zinc and cobalt in the absence of ethanol. Syntheses carried out with water as the only solvent result in a different phase diagram, shown in the bottom part of Fig. 5. Thus, in the absence of ethanol, **TMPF-91** is no longer observed for any of the Zn : Co explored ratios. **TMPF-88** can be obtained as a pure phase, according to PXRD and SEM analysis, for various Zn : Co ratios of 10 : 1, 4 : 1 and 2 : 1. However, ICP analyses of the samples indicate that cobalt is present only in trace amounts (0.10% Co, 16.86% Zn for 149 ratio Zn/Co; 0.18%Co, 16.81%Zn with 99 ratio Zn/Co and 0.20%Co, 16.76%Zn with 74 ratio Zn/Co). These values are not even detected by the EDS analyses. With equimolar amounts of zinc and cobalt, **TMPF-90** is again observed in the PXRD pattern, mixed with **TMPF-88** (Fig. S10†). A further increase in the amount of cobalt (Zn : Co 1 : 2) results in the appearance of a new phase, **TMPF-95**. **TMPF-90** is still present according to the PXRD patterns, although as a minor phase. The Zn : Co ratio for **TMPF-95** crystals according to EDS analysis is 1 : 2 (Fig. 11), which is coincident with the initial ratio of the reactants. Yield and purity of this phase increase when the reaction is carried out for a 3 day period. A single crystal X-ray diffraction analysis was carried out for a Zn–Co-**TMPF-95**. In this crystal structure there are five crystallographically independent metal atoms, three of them in a tetrahedral coordination environment, and two of them octahedrally coordinated. Despite the similar electron density of cobalt and zinc, we attempted to assign the different metal positions to both elements, to ascertain whether there is an ordered metal distribution. The results of the structural refinements indicate that this is not the scenario, but on the contrary, the two metal cations should be randomly distributed in the SBUs along the crystals. Indeed, the best refinement indicators were obtained when all five metal positions were assigned as cobalt, as expected this is the element in a larger amount according to the spectroscopic analysis.

With a further increase in the amount of cobalt in the synthesis mixture, and for Zn : Co ratios of 1 : 4, 1 : 10 and 0 : 1, crystals of the Co(hfipbb)(H_2hfipbb)$_{0.5}$ phase area again formed along with a yellowish powder, similar to what we observed in the water : ethanol system.

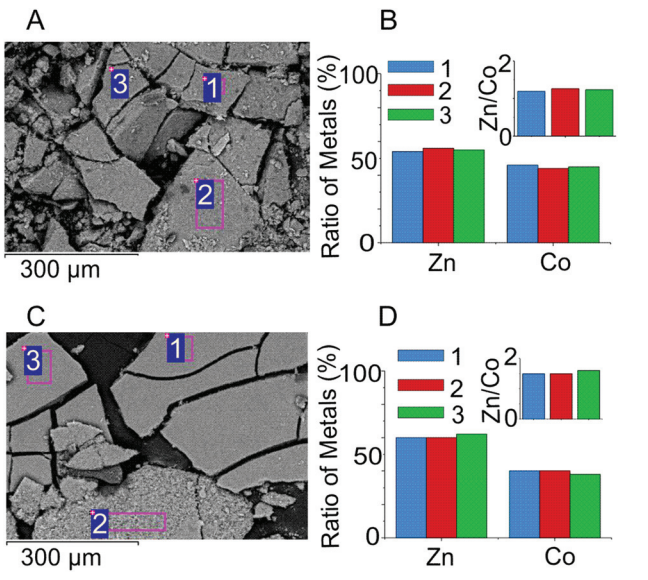

Fig. 10 SEM images corresponding to **TMPF-90** crystals, indicating the areas where the EDS analyses were performed. (A) Sample prepared with an initial 1 : 1 Zn : Co ratio. (B) Plot of the ratio of metals (%) and the Zn/Co ratio determined by EDS analysis, where each column corresponds to the area indicated by a number in panel A. (C) Sample prepared with an initial 4 : 1 Zn : Co ratio. (D) Plot of the ratio of metals (%) and the Zn/Co ratio determined by EDS analysis, where each column corresponds to the area indicated by a number in panel C.

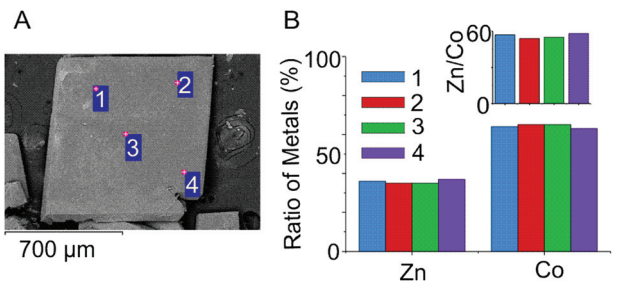

Fig. 11 SEM images corresponding to **TMPF-95** crystals, indicating the areas where the EDS analyses were performed. (A) Sample prepared with an initial 1 : 2 Zn : Co ratio. (B) Plot of the ratio of metals (%) and the Zn/Co ratio determined by EDS analysis, where each column corresponds to the area indicated by a number in panel A.

Conclusions

In summary, in this work we have shown that the addition of a second metal element, even at a very low amount, drastically modifies the reaction media, inducing the formation of new phases, as shown by the formation of **TMPF-91** with a 10 : 1 Zn : Co intial ratio. Furthermore, in the mixed-metal, mixed-ligand system studied here, there is a competition in MOF formation, where kinetically favoured structures (ZnPF-1 and **TMPF-90**) appear at short reaction times, precluding the formation as a pure phase of other energetically more favourable solid-solution phases (**TMPF-88**). In addition, another MOF was isolated (**TMPF-95**), which could be prepared only with a very specific Zn : Co ratio (1 : 2). Despite the restricted amount required for preparing this phase, the single crystal X-ray diffraction analysis indicates that the two metal cations are disorderly disposed occupying different crystallographic sites. EDS and ICP analyses demonstrate that solid-solution phases can be obtained, although the amount of cobalt incorporated into the framework is substantially lower than the one initially added to the reaction in the cases of **TMPF-91** and **TMPF-88**, while in the case of **TMPF-90** and **TMPF-95**, the two elements can be incorporated in comparable amounts.

Acknowledgements

This work has been supported by the Spanish Ministry of Economy and Competitiveness, project MAT2013-45460-R. Financial support by Fundación General CSIC (Programa ComFuturo) is acknowledged (F.G.). Computational time has been provided by the Centre de Supercomputació de Catalunya (CESCA). We thank E. Rodríguez-Cañas from the Servicio Interdepartamental de Investigación (SIdI) at Universidad Autónoma de Madrid for valuable support with SEM images and EDS analyses acquisition.

Notes and references

1 H. Furukawa, K. E. Cordova, M. O'Keeffe and O. M. Yaghi, *Science*, 2013, **341**, 974–986.
2 M. Li, D. Li, M. O'Keeffe and O. M. Yaghi, *Chem. Rev.*, 2014, **114**, 1343–1370.
3 H. Furukawa, U. Müller and O. M. Yaghi, *Angew. Chem., Int. Ed.*, 2015, **54**, 3417–3430.
4 H. Deng, C. J. Doonan, H. Furukawa, R. B. Ferreira, J. Towne, C. B. Knobler, B. Wang and O. M. Yaghi, *Science*, 2010, **327**, 846–850.
5 J. M. Taylor, S. Dekura, R. Ikeda and H. Kitagawa, *Chem. Mater.*, 2015, **27**, 2286–2289.
6 O. Karagiaridi, N. A. Vermeulen, R. C. Klet, T. C. Wang, P. Z. Moghadam, S. S. Al-Juaid, J. F. Stoddart, J. T. Hupp and O. K. Farha, *Inorg. Chem.*, 2015, **54**, 1785–1790.
7 Z. Fang, J. P. Dürholt, M. Kauer, W. Zhang, C. Lochenie, B. Jee, B. Albada, N. Metzler-Nolte, A. Pöppl, B. Weber, M. Muhler, Y. Wang, R. Schmid and R. A. Fischer, *J. Am. Chem. Soc.*, 2014, **136**, 9627–9636.
8 M. J. Cliffe, W. Wan, X. Zou, P. A. Chater, A. K. Kleppe, M. G. Tucker, H. Wilhelm, N. P. Funnell, F. X. Coudert and A. L. Goodwin, *Nat. Commun.*, 2014, **5**, 4176.
9 H. Wu, Y. S. Chua, V. Krungleviciute, M. Tyagi, P. Chen, T. Yildirim and W. Zhou, *J. Am. Chem. Soc.*, 2013, **135**, 10525–10532.
10 D. Britt, H. Furukawa, B. Wang, T. G. Glover and O. M. Yaghi, *Proc. Natl. Acad. Sci. U. S. A.*, 2009, **106**, 20637–20640.
11 T. M. McDonald, J. A. Mason, X. Kong, E. D. Bloch, D. Gygi, A. Dani, V. Crocellà, F. Giordanino, S. O. Odoh, W. S. Drisdell, B. Vlaisavljevich, A. L. Dzubak, R. Poloni, S. K. Schnell, N. Planas, K. Lee, T. Pascal, L. F. Wan, D. Prendergast, J. B. Neaton, B. Smit, J. B. Kortright, L. Gagliardi, S. Bordiga, J. A. Reimer and J. R. Long, *Nature*, 2015, **519**, 303–308.
12 J. Y. Lee, O. K. Farha, J. Roberts, K. A. Scheidt, S. T. Nguyen and J. T. Hupp, *Chem. Soc. Rev.*, 2009, **38**, 1450–1459.
13 F. Gándara, F. J. Uribe-Romo, D. K. Britt, H. Furukawa, L. Lei, R. Cheng, X. Duan, M. O'Keeffe and O. M. Yaghi, *Chem. – Eur. J.*, 2012, **18**, 10595–10601.
14 L. Sun, C. H. Hendon, M. A. Minier, A. Walsh and M. Dincă, *J. Am. Chem. Soc.*, 2015, **137**, 6164–6167.
15 C. K. Brozek and M. Dincă, *Chem. Soc. Rev.*, 2014, **43**, 5456–5467.
16 B. Tu, Q. Pang, D. Wu, Y. Song, L. Weng and Q. Li, *J. Am. Chem. Soc.*, 2014, **136**, 14465–14471.
17 L. J. Wang, H. Deng, H. Furukawa, F. Gándara, K. E. Cordova, D. Peri and O. M. Yaghi, *Inorg. Chem.*, 2014, **53**, 5881–5883.
18 R. F. D'Vries, S. Álvarez-García, N. Snejko, L. E. Bausá, E. Gutiérrez-Puebla, A. de Andrés and M. Á. Monge, *J. Mater. Chem. C*, 2013, **1**, 6316–6324.
19 L. Mitchell, P. Williamson, B. Ehrlichová, A. E. Anderson, V. R. Seymour, S. E. Ashbrook, N. Acerbi, L. M. Daniels, R. I. Walton, M. L. Clarke and P. A. Wright, *Chem. – Eur. J.*, 2014, **20**, 17185–17197.
20 L. M. Aguirre-Díaz, F. Gándara, M. Iglesias, N. Snejko, E. Gutiérrez-Puebla and M. Á. Monge, *J. Am. Chem. Soc.*, 2015, **137**, 6132–6135.
21 G. M. Sheldrick, *Acta Crystallogr., Sect. A: Found. Crystallogr.*, 2008, **64**, 112–122.
22 O. V. Dolomanov, L. J. Bourhis, R. J. Gildea, J. A. K. Howard and H. Puschmann, *J. Appl. Crystallogr.*, 2009, **42**, 339–341.
23 G. Kresse and J. Furthmüller, *Comput. Mater. Sci.*, 1996, **6**, 15–50.
24 G. Kresse and J. Hafner, *Phys. Rev. B: Condens. Matter*, 1993, **47**, 558–561.
25 J. P. Perdew and Y. Wang, *Phys. Rev. B: Condens. Matter*, 1992, **45**, 13244–13249.
26 J. P. Perdew, J. A. Chevary, S. H. Vosko, K. A. Jackson, M. R. Pederson, D. J. Singh and C. Fiolhais, *Phys. Rev. B: Condens. Matter*, 1992, **46**, 6671–6687.

27 G. Kresse and D. Joubert, *Phys. Rev. B: Condens. Matter Mater. Phys.*, 1999, **59**, 1758–1775.
28 P. E. Blöchl, *Phys. Rev. B: Condens. Matter*, 1994, **50**, 17953–17979.
29 A. Monge, N. Snejko, E. Gutiérrez-Puebla, M. Medina, C. Cascales, C. Ruiz-Valero, M. Iglesias and B. Gómez-Lor, *Chem. Commun.*, 2005, 1291–1293.
30 F. Gándara, V. A. de la Peña-O'Shea, F. Illas, N. Snejko, D. M. Proserpio, E. Gutiérrez-Puebla and M. A. Monge, *Inorg. Chem.*, 2009, **48**, 4707–4713.
31 M. C. Bernini, V. A. de la Peña-O'Shea, M. Iglesias, N. Snejko, E. Gutiérrez-Puebla, E. V. Brusau, G. E. Narda, F. Illas and M. Á. Monge, *Inorg. Chem.*, 2010, **49**, 5063–5071.
32 A. E. Platero-Prats, V. A. de la Peña-O'Shea, D. M. Proserpio, N. Snejko, E. Gutiérrez-Puebla and Á. Monge, *J. Am. Chem. Soc.*, 2012, **134**, 4762–4771.
33 R. F. D'Vries, V. A. de la Peña-O'Shea, N. Snejko, M. Iglesias, E. Gutiérrez-Puebla and M. Angeles Monge, *J. Am. Chem. Soc.*, 2013, **135**, 5782–5792.
34 R. F. D'Vries, V. A. de la Peña-O'Shea, Á. Benito Hernández, N. Snejko, E. Gutiérrez-Puebla and M. A. Monge, *Cryst. Growth Des.*, 2014, **14**, 5227–5233.
35 H.-L. Jiang and Q. Xu, *CrystEngComm*, 2010, **12**, 3815–3819.

CHEMISTRY

Addressed realization of multication complex arrangements in metal-organic frameworks

Celia Castillo-Blas,[1] Víctor A. de la Peña-O'Shea,[2] Inés Puente-Orench,[3,4] Julio Romero de Paz,[5] Regino Sáez-Puche,[6] Enrique Gutiérrez-Puebla,[1] Felipe Gándara,[1]* Ángeles Monge[1]*

The preparation of materials with structures composed of multiple metal cations that occupy specific sites is challenging owing to the difficulty of simultaneously addressing the incorporation of different elements at desired precise positions. We report how it is possible to use a metal-organic framework (MOF) built with a rod-shaped inorganic secondary building unit (SBU) to combine multiple metal elements at specific positions in a manner that is controllable at atomic and mesoscopic scales. Through the combination of four different metal elements at judiciously selected molar ratios, 20 MOFs of different compositions and the same topology have been prepared and characterized. The use of diffraction techniques, supported by density functional theory calculations, has led us to determine various possible atomic arrangements of the metal cations within the SBUs. In addition, seven of the compounds combine multiple types of atomic arrangements, which are mesoscopically distributed along the crystals. Given the large diversity and importance of rod-based MOFs, we believe that these findings offer a new general strategy to produce complex materials with required compositions and controllable arrangements of the metal cations for desired applications.

INTRODUCTION

Materials with structures comprising the presence of multiple metal elements are important in many fields because the combination of different metal cations typically offers new or enhanced properties that are not attainable with the use of just one metal. Thus, mixed-metal oxides and salts are extensively used as anode materials in batteries (*1*); superconductivity has been demonstrated in several families of multimetal materials, such as oxides or pnictides, whose structures are made of the combination of several cations (*2*–*5*). Doped metal oxides are frequently used in optical devices, and diluted magnets are prepared by the introduction of a paramagnetic element, such as cobalt, into the structure of zinc or titanium oxide, with these materials exhibiting magnetoresistance properties (*4*, *6*–*8*). Mixed-metal oxides are also good catalysts in key chemical transformations (*9*). However, it still remains a challenge to synthesize new materials with structures where the disposition of the metal elements is highly controllable. Up to now, control over the arrangement of the different elements in most of the existing materials has been limited or inexistent. Limitations regarding the amount and nature of the elements that can be combined within a same structure also exist. Metal-organic frameworks (MOFs) are a class of crystalline materials, composed by the combination of metal clusters [secondary building units (SBUs)] and organic linkers (*10*). Although MOFs have been traditionally constructed with just one metal cation, they have recently shown the potential to incorporate multiple metal elements within the same crystal structure by either a postsynthetic transmetalation process (*11*) or the combination of multiple metal salts during the MOF synthesis (*12*), in some cases resulting in the formation of cation domains (*13*). However, thus far, most of the reported systems lack fundamental control on the disposition of the used metal elements, neither at the atomic, nano-, or mesoscopic scale.

Here, we report a platform MOF that allows the directed incorporation of multiple metal elements into the same structure at precise locations, resulting in materials where the arrangement of the metal cations is controllable at various length scales through the use of an appropriate SBU and framework topology. The judicious selection of a molar code defined by the initial molar ratio of the used metal elements drives the incorporation and arrangement of the MOF metal components (i) at the atomic and nanoscales, by producing sequences of elements within the same SBU, and (ii) at the mesoscopic scale, by producing crystals where SBUs of different compositions are preferentially located at different shells of the crystals.

Synthesis of MOFs with multiple metal cations from an adaptable SBU

Our strategy to prepare new multimetal systems of addressable complexity involves the selection of a MOF whose crystallization process has been proven to be kinetically driven. A MOF structure whose formation is thermodynamically highly favorable for a given cation will not allow the corresponding solid-solution systems to be obtained, whereas a MOF structure whose formation is kinetically governed may be in an equilibrium that will allow the incorporation of additional elements into the framework during the synthesis reaction (*14*). This is the case of ZnPF-1, a MOF built with 4,4′-(hexafluoroisopropylidene) bis(benzoic acid) (H_2hfipbb) as organic linker. This MOF has a helical, rod-shaped inorganic SBU formed by tetrahedral zinc atoms and a three-dimensional structure with square and hexagonal channels running parallel to the *c* axis (Fig. 1). It crystallizes in the hexagonal $P6_422$ space group [a = 21.22(1) Å and c = 7.710(5) Å] (*15*). Despite the extensive use of this organic linker to prepare different MOFs with various metal elements, thus far this MOF topology has only been reported with the use of zinc. By maintaining a constant metal-to-linker molar ratio of 1.65 (section S1 and table S1), the addition of cobalt nitrate in the initial mixture results in the formation of needle-like crystals with intense blue color. We coined the term "molar code" to indicate the

[1]Departamento de Nuevas Arquitecturas en Química de Materiales, Materials Science Factory, Instituto de Ciencia de Materiales de Madrid–Consejo Superior de Investigaciones Científicas, Sor Juana Inés de la Cruz 3, Madrid 28049, Spain. [2]IMDEA Energy Institute, Móstoles Technology Park, Avenida Ramón de la Sagra 3, 28935 Móstoles, Madrid, Spain. [3]Instituto de Ciencia de Materiales de Aragón, Pedro Cerbuna 12, 50009 Zaragoza, Spain. [4]Institut Laue Langevin, 71 Avenue des Martyrs, 38042 Grenoble, France. [5]Centros de Apoyo a la Investigación Técnicas Físicas, Facultad de Ciencias Físicas, Universidad Complutense de Madrid, Avenida Complutense s/n, 28040 Madrid, Spain. [6]Departamento de Química Inorgánica, Facultad de Ciencias Químicas, Universidad Complutense de Madrid, 28040 Madrid, Spain.
*Corresponding author. Email: gandara@icmm.csic.es (F.G.); amonge@icmm.csic.es (Á.M.)

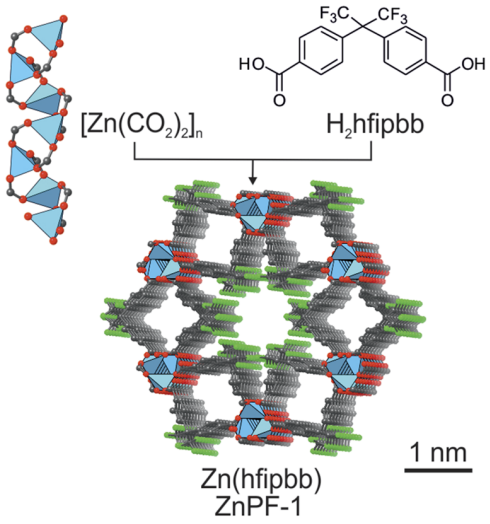

Fig. 1. ZnPF-1 is formed by the combination of H_2hfipbb with a helical inorganic SBU where the zinc atoms are tetrahedrally coordinated. O, C, and F atoms are depicted as red, gray, and green balls, respectively, and pale blue tetrahedra represent zinc cations.

selected molar relationship between metal elements. Thus, Zn:Co molar codes of 1:1, 1:2, 1:4, and 1:10 were selected to prepare the corresponding MOFs of variable composition (Scheme 1). The chemical composition of the bulk samples was determined by means of inductively coupled plasma (ICP) and elemental analysis (table S2). A room temperature x-ray diffraction (XRD) study of a single crystal prepared from a Zn:Co 1:2 molar code proved that the sample was isostructural to the original ZnPF-1, with the crystallographic metal position occupied by both zinc and cobalt (section S2).

Through scanning electron microscopy (SEM) and energy-dispersive x-ray spectroscopy (EDS) analyses of MOFs, it was consistently found that the amount of cobalt is larger in the external areas of the crystals (Fig. 2 and section S3). In addition, the crystals were found to be hollow, with a central hole running along the longest crystal axis. This hollow morphology and the concentration gradient are consistent with an Ostwald ripening process (*16*), where zinc-rich crystals are initially formed, followed by partial redissolution of the inner parts and crystal growing of the external faces through the incorporation of cobalt in larger proportion. A synthesis and kinetic study carried out for the MOF prepared from a Zn:Co 1:2 molar code further validated this point, as evidenced by the increase in cobalt incorporation with longer heating times up to 20 hours (section S4).

A cobalt-rich sample was produced by introducing a sufficiently large amount of cobalt in the molar code. Thus, the sample prepared from a Zn:Co 1:10 molar code has a chemical formula of $Zn_{0.21}Co_{0.79}$(hfibpbb). Unexpectedly, the x-ray single-crystal study shows a unit cell with a doubled *c* parameter and $P6_522$ space group. This lattice constant change arises from the splitting of the crystallographic metal sites within the SBUs, which are now composed of alternating tetrahedral and octahedral metal sites (Fig. 3, bottom). The results of the XRD refinement suggest that the octahedral sites are occupied by cobalt atoms, whereas the tetrahedral ones are occupied by both zinc and cobalt. Despite the change in the coordination environment, the transformed SBU remains unaltered in its points of extension, which, in turn, define the MOF topology (*17*).

To obtain further insight into this phase transformation, we performed a low-temperature single-crystal diffraction study for the sample prepared from a Zn:Co 1:2 molar code. As described above, the room temperature data showed the presence of just one tetrahedral metal site, with mixed Zn/Co occupancy. We then collected XRD data at 200, 150, 100, and 50 K. No changes were observed for the 200 K data, as compared to room temperature. A phase transition was first observed at 150 K, with the corresponding doubling of the *c* lattice parameter. Consequently, two crystallographic metal positions are present in the SBU, with a distorted tetrahedral coordination environment, denoted as Td1 and Td2 in Fig. 3. Analysis of the difference Fourier maps showed a large residual electron density near the metal atoms, which we assign as additional metal sites with partial occupancy (Td1b and Td2b), arising from the ongoing atomic rearrangement. However, the presence of residual electron density indicates that the transformation is not complete yet. This is only achieved at 50 K, where the crystal structure is equivalent to the one determined for the Zn:Co 1:10 sample, with both an octahedral and a tetrahedral site. The results of this study suggest that the presence of cobalt in the structure has a stabilizing effect on the octahedral site. On the contrary, ZnPF-1 does not undergo any phase transformation, because no change in the unit cell was observed for a crystal collected at 50 K. Because zinc and cobalt have similar atomic numbers, it is not possible to unambiguously determine the occupancy of the metal sites with just XRD. We therefore performed a neutron diffraction experiment for this purpose.

Unveiling atomic arrangement

To uncover the atomic arrangement of the metal cations within the solid-solution MOF crystals, we completed a neutron powder diffraction (NPD) study at variable temperatures for zinc- and cobalt-rich samples. In particular, we selected MOFs prepared from Zn:Co 1:2 and Zn:Co 1:10 molar codes. NPD is a particularly suitable technique because of the different scattering length of these elements, in contrast to XRD.

Thermodiffraction experiments evidenced a structural phase transition at 140 and 80 K for the Zn:Co 1:2 and Zn:Co 1:10 samples, respectively (section S5). The Rietveld refinement for the room temperature NPD pattern of the Zn/Co 1:2 sample indicates the sole presence of the original phase with only one tetrahedral metal site in the SBU, which was refined as being occupied by Co or Zn, with ratio coincident with the one determined by ICP analysis (Fig. 4A). For the low-temperature pattern (50 K), a satisfactory refinement could not be achieved by considering just the transformed crystal cell. A careful analysis shows the presence of a remaining amount of untransformed crystal phase. The presence of ZnPF-1 crystals has been ruled out because the SEM and EDS analyses prove the presence of cobalt in all crystals. We can therefore conclude that both phases are coexisting within the MOF crystals, as a result of the compositional variations.

A multiphase Rietveld refinement was carried out, and the percentage of each phase was estimated on the basis of the ratio of the integrated intensities. The best refinement results were obtained for a combination of the original and transformed phases at ratios of 15 and 85%, respectively (Fig. 4B). The metal sites in the original phase (exclusively tetrahedral) were refined as zinc atoms, whereas for the transformed phase, the tetrahedral site was refined as fully occupied by zinc, and the octahedral site as fully occupied by cobalt. These results, along with the presence of holes and compositional gradient in the crystals, indicate that this MOF is composed of an inner core with SBUs made of zinc atoms and an outer shell with SBUs made of alternating zinc and cobalt atoms. At room temperature, both atoms are in a tetrahedral environment, whereas by lowering the temperature, only the cobalt atoms become octahedral, resulting in the unit cell change.

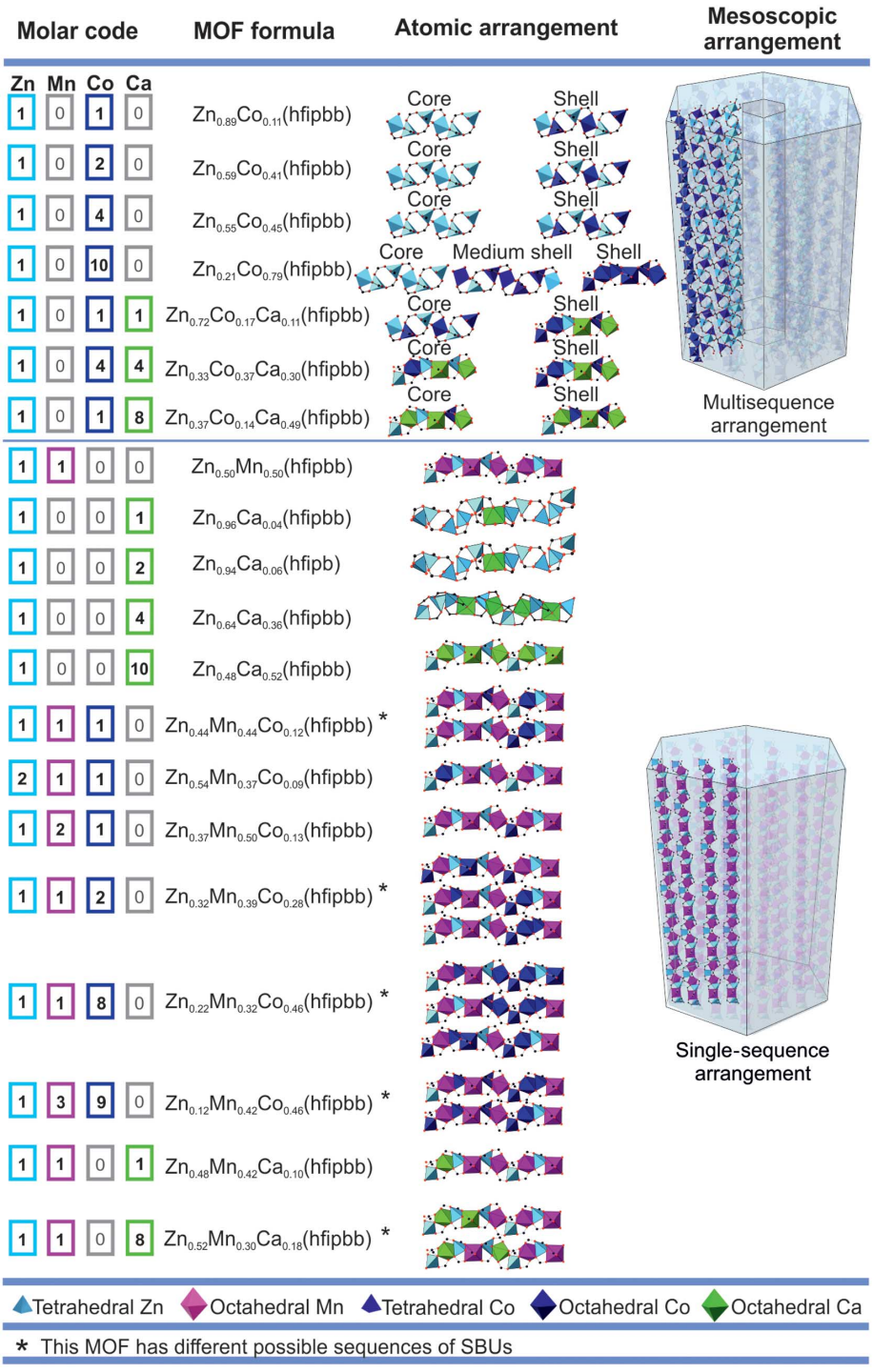

Scheme 1. Selection of appropriate molar codes express the formation of different kinds of atomically sequenced inorganic SBUs. Corresponding MOF crystals might include multiple SBUs mesoscopically arranged, or just one.

In the case of the sample prepared from a Zn:Co 1:10 molar code, the room temperature NPD pattern indicates the presence of both phases. These two unit cells at room temperature could not be detected by single-crystal x-ray analysis because of the overlapping of reflection positions (the *hkl* reflections in the original phase appear at virtually the same position of the corresponding *hkl*/2 reflections of the transformed phase). Through a multiphase Rietveld refinement, the percentage of both phases at room temperature was estimated to be 67 and 33% for the original and transformed one, respectively (Fig. 4C). The portion of the crystal corresponding to the transformed phase was refined to be composed exclusively of cobalt, having both tetrahedral and octahedral environments. The portion of the crystal corresponding to the

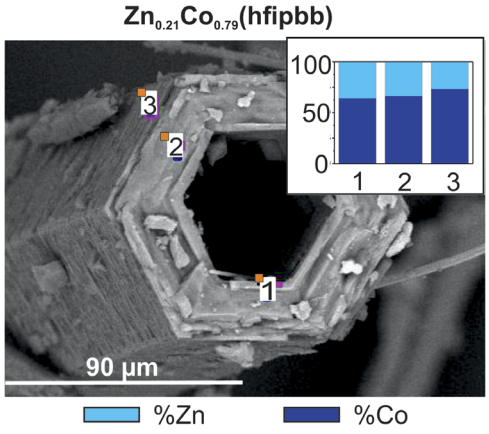

Fig. 2. SEM image and EDS analysis of $Zn_{0.21}Co_{0.79}$(hfipbb). Metal atomic percent was determined with the spectra recorded at the various points of the crystal indicated in the image.

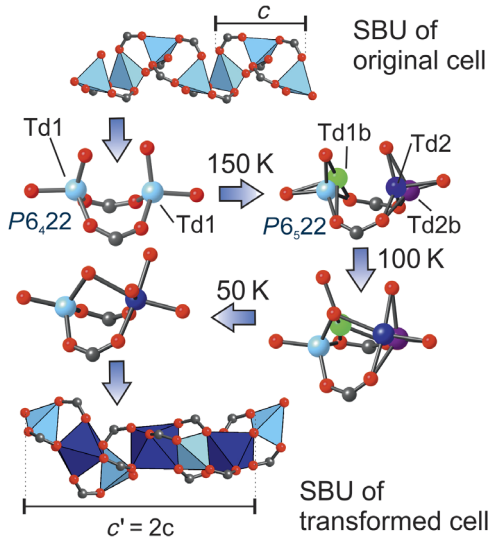

Fig. 3. The inorganic SBU might adapt to include octahedrally coordinated cations, which results in a unit cell transformation where the *c* parameter is doubled. This transformation was monitored by temperature-variable single-crystal XRD and NPD. O, C, and F atoms are depicted as red, gray, and green balls, respectively. Pale blue tetrahedra and dark blue octahedra might represent different metal elements (see text). For the phase transformation depiction, the color of the balls representing the metal elements corresponds to independent crystallographic sites.

original phase was refined to be composed of both zinc (30%) and cobalt (70%) (Fig. 4D). By lowering the temperature (10 K), most of this portion of the crystal is also transformed. However, the 10 K NPD pattern shows the presence of small shoulders in the (102) and ($2\bar{1}2$) diffraction peaks, which indicate that there is also a residual portion of the crystal that retains the original phase [the shoulders corresponding to the (101) and ($2\bar{1}1$) reflections of the untransformed phase]. Consequently, this MOF has three compositional domains: a small core (no more than 5% according to NPD Rietveld refinement) exclusively made of zinc, followed by a shell where the SBUs are composed of zinc and cobalt cations at a Zn/Co 3:7 ratio, all of them being tetrahedral at room temperature, whereas at low temperature, part of the cobalt cations become octahedral. In the third outer shell (around 33%), the SBUs are exclusively composed of cobalt cations with alternating tetrahedral and octahedral coordination environments.

Expanding the use of molar codes to produce MOFs with controllable metal arrangements

The selected inorganic SBU has shown adaptability and dynamism through the possibility of including multiple elements with variable coordination environments, such as cobalt, while maintaining the overall MOF topology and connectivity, which is seemingly directed by the use of zinc. By selecting the appropriate molar code, it is possible to control the introduced amount of a second element, as well as its arrangement and coordination environment. On the other hand, if an element with clear propensity for an octahedral coordination environment is chosen, then this should preferentially occupy certain sites in the inorganic SBUs. A MOF with a $Zn_{0.5}Mn_{0.5}$(hfipbb) composition was prepared by starting from a Zn:Mn 1:1 molar code. The single-crystal XRD study shows lattice parameters of a = 21.2897(5) Å and c = 15.1282(5) Å and $P6_522$ space group, with the SBUs being formed by alternating tetrahedral zinc and octahedral manganese atoms. Crystals of this MOF are not hollow, and the EDS study shows that there are no compositional gradients along the crystals (Fig. 5A). NPD Rietveld refinement proves that there is only one type of unit cell present at room temperature (Fig. 5B).

Moreover, the introduction of manganese into the molar code allows for the homogeneous distribution of cobalt. Thus, in contrast to the Zn/Co systems, ternary MOFs with molar codes including Zn/Mn/Co, do not exhibit compositional gradients, and all three elements are equally distributed in all areas of the crystals, as shown by the EDS analysis.

The room temperature single-crystal XRD studies demonstrate that these MOFs have unit cells with double *c* parameter and the presence of both octahedral and tetrahedral metal sites in the SBUs. Because zinc and manganese exclusively occupy the tetrahedral or octahedral sites, respectively, by adjusting the molar codes, it is possible to address the incorporation of cobalt at either tetrahedral, octahedral, or both sites, as deduced by the chemical composition of the resulting MOFs. For example, a MOF obtained from a Zn:Mn:Co 1:2:1 molar code has a formula $Zn_{0.37}Mn_{0.5}Co_{0.13}$(hfipbb), which implies that one of five tetrahedral sites in the SBUs is occupied by cobalt, resulting in an atomic sequence, as shown in Scheme 1. Correspondingly, a MOF obtained from a Zn:Mn:Co 2:1:1 molar code and formula $Zn_{0.54}Mn_{0.37}Co_{0.09}$(hfipbb) expresses an SBU with an atomic sequence, as depicted in Scheme 1, where one of five octahedral sites is occupied by cobalt. In both cases, other possible combinations involving the coexistence of several compositional domains are ruled out by the compositional homogeneity demonstrated by the EDS analysis. Single-crystal XRD analyses further support the location of the cobalt atoms at the proposed sites.

On the other hand, for MOFs prepared from molar codes that contain the same zinc and manganese number, cobalt is directed to be occupying both the octahedral and tetrahedral sites. In samples prepared from Zn:Mn:Co 1:1:1, 1:1:2, and 1:1:8 molar codes and formulae $Zn_{0.44}Mn_{0.44}Co_{0.12}$(hfipbb), $Zn_{0.32}Mn_{0.39}Co_{0.28}$(hfipbb), and $Zn_{0.22}Mn_{0.32}Co_{0.46}$(hfipbb), the cobalt atoms are inevitably occupying both tetrahedral and octahedral sites. In these cases, as shown in the scheme, there are several possible atomic sequences that fulfill the coordination environment requirement for zinc and manganese and agree with the determined composition (Fig. 6A). In all cases, neutron powder thermodiffraction experiments indicate that only one crystalline phase with double *c* parameter is formed (section S5).

Definition of appropriate molar codes allows different degrees of compositional and structural complexities, which are addressable by

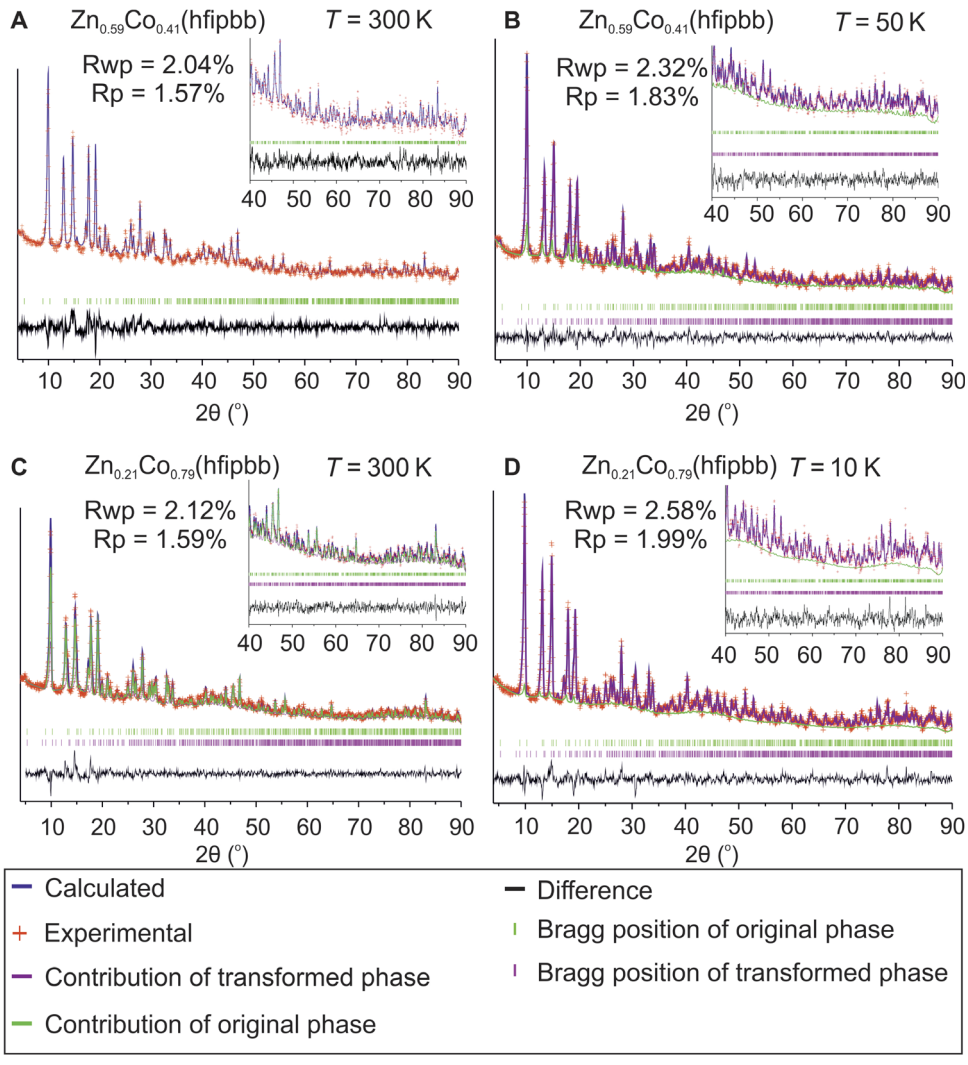

Fig. 4. NDP Rietveld refinements. In the case of the $Zn_{0.59}Co_{0.41}$(hfipbb) MOF, the refinements indicate the presence of only the original cell at 300 K (**A**) and both original (15%) and transformed (85%) cells at 50 K (**B**). In the case of the $Zn_{0.21}Co_{0.79}$(hfipbb) MOF, both original (66%) and transformed (33%) unit cells are present at 300 K (**C**), whereas the transformation is almost complete (95%) at 10 K (**D**). In all cases, the composition of the metal sites was refined. For the multiphase refinements (B to D), the percentage of each unit cell was determined by the ratio of the integrated intensities. Rp and Rwp are unweighted and weighted agreement profile factors, respectively.

the selected combination of elements, each one of them with a particular role. Thus, zinc is the structure-directing element which is necessary to obtain the desired MOF SBU and topology. On the other hand, MOFs prepared from molar codes including manganese, demonstrate a homogeneous compositional arrangement, providing atomic control on the SBU sequences. Finally, mesoscopic compositional arrangements might appear through the use of cobalt.

This complexity control is achievable even with the incorporation of other metal elements. Thus, it is also possible to include nontransition metal elements in the molar codes to incorporate them in MOFs with desired complexity.

As proof of concept, we have included calcium into a MOF structure that is not obtainable with the use of only this element. We have prepared MOFs from Zn:Ca 1:1 and 1:2 molar codes. These MOFs only contain small amounts of calcium in the structure, their formulae being $Zn_{0.96}Ca_{0.04}$(hfipbb) and $Zn_{0.94}Ca_{0.06}$(hfipbb), and homogeneous distribution of calcium along the crystals. Larger amounts of calcium can be incorporated by using molar codes with larger calcium numbers. Thus, the use of a Zn:Ca 1:4 molar code results in a MOF with the formula $Zn_{0.64}Ca_{0.36}$(hfipbb). Room temperature single-crystal XRD shows lattice parameters a = 21.2239(8) Å and c = 15.5784(6) Å and $P6_122$ space groups, with two metal sites in the SBUs. One is exclusively occupied by tetrahedral zinc atoms, and the other one is occupied by calcium (72%) or zinc (28%). In this second site, the metal coordination environment is octahedral when occupied by calcium and tetrahedral when occupied by zinc. Thus, the SBUs comprise alternating zinc and calcium atoms, with 28% of calcium being substituted by zinc. No compositional gradients are observed in the EDS analysis (Fig. 6B), which indicates a regular distribution of zinc domains within a zinc-calcium SBU.

The pure zinc-calcium SBU can be expressed by using a Zn:Ca 1:10 molar code. The corresponding MOF has $Zn_{0.48}Ca_{0.52}$(hfipbb) formula, and EDS indicates compositional homogeneity.

Molar codes combining zinc, calcium, and manganese express SBUs with additional atomic sequences, as proposed in Scheme 1. Zn:Mn:Ca 1:1:1 and 1:1:8 molar codes result in MOFs with $Zn_{0.48}Mn_{0.42}Ca_{0.10}$(hfipbb)

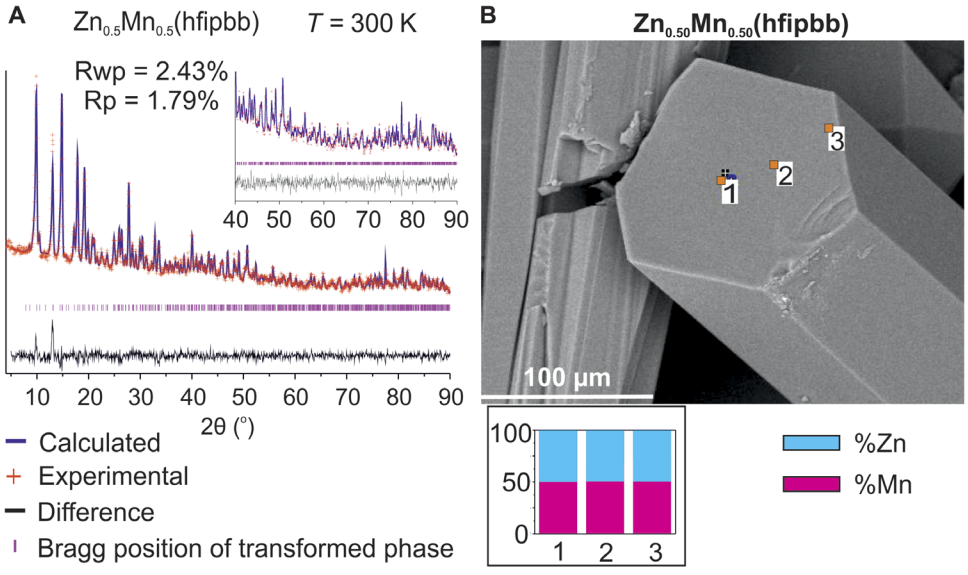

Fig. 5. NPD and EDS analysis of $Zn_{0.50}Mn_{0.50}$(hfipbb) MOF. (**A**) For the $Zn_{0.50}Mn_{0.50}$(hfipbb) MOF, the Rietveld refinement is consistent with presence of only a cell with alternating tetrahedral zinc–octahedral manganese SBUs at 300 K. (**B**) SEM and EDS analyses show homogeneous distribution of metal elements in $Zn_{0.50}Mn_{0.50}$(hfipbb).

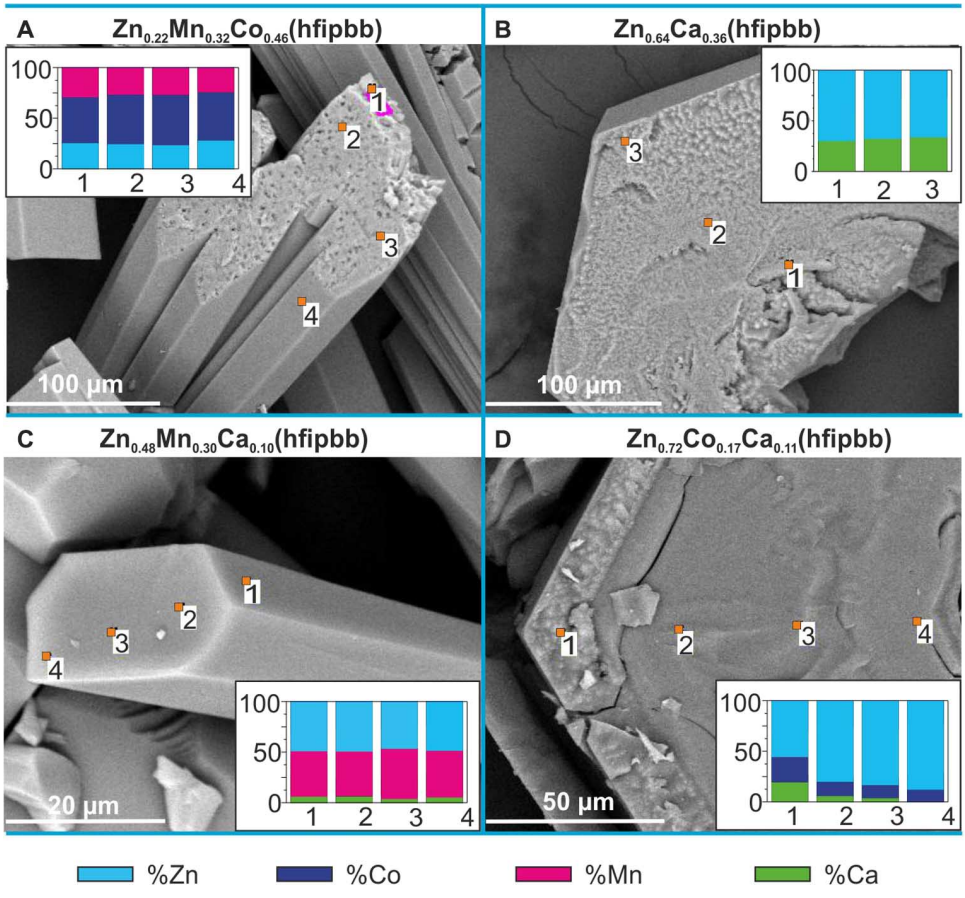

Fig. 6. SEM images and EDS analysis of selected MOFs. Representative examples of different MOFs prepared from various molar codes are shown in (**A**) to (**D**), demonstrating both homogeneous arrangements (A to C) and compositional gradients (D). Metal atomic percent was determined with the spectra recorded at multiple points or areas of each crystal, as indicated in the images.

and $Zn_{0.52}Mn_{0.30}Ca_{0.18}$(hfipbb) formulae, respectively. Single-crystal XRD experiments show SBUs with tetrahedral zinc atoms, and octahedral calcium and manganese atoms, which are occupying the same crystallographic site. EDS demonstrates homogeneous distribution (Fig. 6C).

Mesoscopic control in the incorporation of calcium at preferential crystal faces is possible by combining it with cobalt. Thus, the MOF prepared from a Zn:Co:Ca 1:1:1 molar code displays a clear compositional gradient, where calcium is preferentially located at the external faces, according to the EDS analysis (Fig. 6D). The SEM images show crystals with well-differentiated core and external shells. The core is mainly composed of zinc and a small amount of cobalt (ca. 10%, as determined by EDS), whereas the external shell contains all three elements. Finally, the use of Zn:Co:Ca 1:4:4 and 1:1:8 molar codes result in MOFs with the formulae $Zn_{0.33}Co_{0.37}Ca_{0.30}$(hfipbb) and $Zn_{0.37}Co_{0.14}Ca_{0.49}$(hfipbb). These MOFs show mesoscopic compositional gradients of zinc and cobalt, whereas the amount of calcium is homogeneously distributed, according to EDS analysis. Single-crystal XRD experiments show that, as expected, calcium is occupying the octahedral sites, whereas cobalt might be at both tetrahedral and octahedral ones.

Formation energies (ΔE_{Form}) determined by ab initio density functional theory (DFT) calculations corroborate the importance of the kinetic control on the first stages of the synthesis (section S6). Crystal models of MOFs consisting of SBUs formed by alternating tetrahedral zinc atoms and octahedral zinc, cobalt, manganese, or calcium atoms, and another model with alternating tetrahedral and octahedral cobalt atoms were geometrically optimized, in all cases converging to stable structures with the same topology, although no symmetry constraints were imposed. The hypothetical phase consisting of tetrahedral and octahedral zinc atoms was the only one with a higher formation energy than the original ZnPF-1 phase, which is consistent with the impossibility of transformation of the MOF made of only zinc. On the other hand, the calculations also corroborate that the concentration gradient is consistent with an Ostwald ripening process, because the use of cobalt, calcium, and manganese leads to a decrease in the formation energy. The pure cobalt phase is the most energetically stable, which is also consistent with the formation of this phase in the outer shells of samples made with longer synthesis time. In addition, density of states reveals that the geometry distortion produced by the introduction of a second cation stabilizes the orbitals with higher occupation while destabilizing those with lower occupation, thus breaking the degeneracy of the octahedral geometry.

Compositional and structural complexities define physical properties of MOFs

The results of this work offer a new platform to obtain complex structures where the arrangement of the metal cations can be virtually controlled on demand. Considering that the properties of materials are dictated by their composition and precise atomic and mesoscopic structures, we believe that our findings will be relevant to various fields. The case of the magnetic properties of MOFs is illustrated; magnetic properties are determined by the combination of these factors, namely, the geometry of the SBUs, the atomic distribution of cations, and the possible mesoscopic interaction among SBUs. Thus, in the case of the MOF prepared from a Zn:Co 1:2 molar code, ferromagnetism is developed within the SBUs below 15 K, and interchain antiferromagnetic interactions acquire a long-range character below 7 K, although a large-enough applied magnetic field produces a metamagnetic transition, giving rise to a long-range ferromagnetic state. In the MOF prepared from a Zn:Co 1:10 molar code, where the larger incorporation of cobalt in the SBU forces the presence of cobalt neighbor polyhedra, canted antiferromagnetism is developed within the SBUs in such a way that a rather small net magnetization appears below 35.8 K within the SBU composed exclusively of cobalt, and an additional contribution at lower temperatures comes from the SBU with 30% of the tetrahedral sites occupied by cobalt, where the number of consecutive cobalt cations is smaller (section S7). The ability to produce MOFs with controllable metal arrangements shown in this work opens the possibility to stimulate or block a specific superexchange pathway to develop a specific magnetic interaction within SBUs.

In view of the large number of existing MOFs that are constructed from many diverse rod-shaped SBUs (*18*), it might be anticipated that this method will be generalized to prepare new materials with topologies and structures fit for specific applications where multiple metal cations can be arranged at desired atomic positions, as well as mesoscopically distributed. During the revision of this work, Kim and Coskun (*19*) reported the preparation of bimetallic MOF-74 through a heterogeneous phase synthetic method, where the resulting materials have nearly 1:1 metal ratios regardless of the initially used ratios.

MATERIALS AND METHODS

Synthetic procedure

All reagents and solvents used were commercially available and used as received without further purification: H_2hfipbb (98%; ABCR GmbH and Co.); zinc nitrate, $Zn(NO_3)_2{\cdot}6H_2O$ (≥99%; Scharlab); calcium nitrate, $Ca(NO_3)_2{\cdot}4H_2O$ (≥99%; Sigma-Aldrich); manganese chloride, $MnCl_2{\cdot}4H_2O$ (≥98%; Sigma-Aldrich); and cobalt nitrate, $Co(NO_3)_2{\cdot}6H_2O$ (≥99%; Sigma-Aldrich). General synthetic procedure for all the MOFs involved the dissolution of the selected metal salts and the organic linker in a water/ethanol/nitric acid solvent mixture, followed by heating at 170°C for an overnight period. An illustrative example of the synthesis procedure is given here for the $Zn_{0.59}Co_{0.41}$(hfipbb) compound: H_2hfipbb (78 mg, 0.2 mmol), $Zn(NO_3)_2{\cdot}6H_2O$ (33 mg, 0.11 mmol), and $Co(NO_3)_2{\cdot}6H_2O$ (66 mg, 0.22 mmol) were dissolved in 5 ml of distilled water, 5 ml of absolute ethanol, and 300 µl of a 1 M HNO_3 solution. The mixture was stirred at room temperature for 5 min, placed in a Teflon-lined steel autoclave, and heated at 170°C overnight. After cooling to room temperature, blue needle-shaped crystals were filtered off, washed with water and acetone, and dried under vacuum (61 mg of solid recovered). The rest of the materials were similarly prepared using the amounts of metal salt specified in table S1 and keeping the same amounts of linker and solvents.

Single-crystal XRD

Crystals were selected using a polarized optical microscope for a single-crystal XRD experiment. Single-crystal x-ray data were collected in Bruker four-circle kappa diffractometers equipped with a Cu INCOATED microsource, operated at 30-W power (45 kV, 0.60 mA) to generate Cu Kα radiation (λ = 1.54178 Å), and a Bruker VANTEC-500 area detector (microgap technology) or a Bruker PHOTON II area detector (CPAD Technology). Diffraction data were collected, exploring over the reciprocal space in a combination of ϕ and ω scans to reach a resolution of 0.85 Å, with a completeness >95% and a redundancy >3. For this, either a generic hemisphere collection strategy or a specific one determined using Bruker APEX3 (*20*) software suite was used. The exposure time was adjusted on the basis of size and diffracting quality of the

specimens, each exposure covering 1° in ω or ϕ. Unit cell dimensions were determined for least-squares fit of reflections with $I > 4\sigma$. The structures were solved by direct methods implemented in the SHELX package. The hydrogen atoms were fixed at their calculated positions using distances and angle constraints. All calculations were performed using APEX3 software for data collection and OLEX2-1.2 (*21*) and SHELXTL (*22*) to resolve and refine the structure. All nonhydrogen atoms were anisotropically refined.

Powder XRD

Powder XRD (PXRD) patterns were measured using a Bruker D8 diffractometer with a copper source operated at 1600 W, with step size = 0.02° and exposure time = 0.5 s per step. PXRD measurements were used to check the purity of the obtained microcrystalline products by a comparison of the experimental results with the calculated patterns obtained from single-crystal XRD data.

SEM and EDS analyses

SEM images and EDS were collected using an S-3000N microscope, equipped with an ESED and an INCAx-sight from Oxford Instruments, respectively. All samples were prepared for SEM and EDS analyses by dispersing the material onto a double-sided adhesive conductive carbon tape that was attached to a flat aluminum sample holder and were metalized using a 12-nm gold layer with a Quorum Q150T-S sputter.

Neutron powder diffraction

NPD experiments were performed on the high-resolution multidetector and on the high-intensity powder diffractometers D2B and D1B, respectively, at the Institut Laue-Langevin in Grenoble (France). The samples were contained in a 6-mm cylindrical vanadium can and placed on a cryostat (vanadium-tailed 69ILHV25 and Orange Cryostat for D1B and D2B, respectively). The data sets were collected with calibrated neutrons of wavelengths 2.5260 and 1.5923 Å for D1B and D2B, respectively. Neutron thermodiffractograms were collected using the high-flux D1B diffractometer, between 10 and 300 K, with a heating rate of 0.5 K/min, covering a 2θ range of 0.2° to 128°. The high-resolution neutron diffraction profiles were collected at 300 K for $Zn_{0.59}Co_{0.41}$(hfipbb), $Zn_{0.21}Co_{0.79}$(hfipbb), and $Zn_{0.50}Mn_{0.50}$(hfipbb); at 50 K for $Zn_{0.59}Co_{0.41}$(hfipbb); and at 10 K for $Zn_{0.21}Co_{0.79}$(hfipbb) in the D2B diffractometer, covering a 2θ range of 0.2° to 150°, every 0.05°. The data reduction (including the application of some basic operations as those related with the addition of several patterns or detector efficiency corrections) was carried out with the LAMP software. Rietveld refinements were performed using the Reflex module of Materials Studio 8.0 (*23*). Initial atomic coordinates were taken from the single crystal–determined structures.

DFT calculations

Theoretical calculations by periodic DFT were carried out using the geometry obtained in single-crystal resolution. The density functional plane-wave calculations were carried out by means of the VASP package (*24*, *25*), considering spin polarization and dipole corrections explicitly. The total energies corresponding to the optimized geometries of all samples were calculated using the spin-polarized version of the exchange and correlation functional of Perdew and Wang (*26*, *27*). The effect of the core electrons on the valence electron density was described by the projector augmented wave method (*28*, *29*). The cutoff for the kinetic energy of the plane waves was set to 415 eV to ensure a total energy convergence better than 10^{-6} eV/K.

Magnetic susceptibility measurements

Magnetization measurements were carried out on polycrystalline samples using a superconducting quantum interference device magnetometer (Quantum Design, model MPMS-XL). The temperature dependence of the molar magnetic susceptibility (χ) was obtained from the dc magnetization (*M*) measured with an applied magnetic field (*H*) during warming of the sample from 2 up to 300 K. Zero-field cooling and field-cooling measurement modes were used. In the former, the sample was cooled down from room temperature to 2 K in zero field, and in the latter, the sample was cooled down in the measuring *H*. The magnetic field dependence of the dc magnetization *M*(*H*) was obtained at different temperatures up to ±5 T. The temperature dependence of the real and imaginary parts of the ac molar magnetic susceptibility (χ'_{ac} and χ''_{ac}, respectively) was obtained from the ac magnetization measured in the temperature range 2 to 55 K, with $H = 0$, and by applying an oscillating magnetic field with a drive amplitude of 0.35 mT at different frequencies in the range 1 to 1000 Hz. The diamagnetic contribution was subtracted from the calculated molar susceptibilities χ.

SUPPLEMENTARY MATERIALS

Supplementary material for this article is available at http://advances.sciencemag.org/cgi/content/full/3/7/e1700773/DC1

Supplementary Text

section S1. Synthesis and characterization

section S2. X-ray diffraction

section S3. SEM and EDS analyses

section S4. Kinetic study of $Zn_{0.59}Co_{0.41}$(hfipbb)

section S5. Neutron powder diffraction

section S6. DFT calculations

section S7. Magnetic susceptibility measurements

table S1. Chemical formula and corresponding molar codes and amount of metal salts used for MOF preparation.

table S2. Results of carbon, hydrogen, and nitrogen analyses and ICP analyses in %weight for all MOFs.

table S3. Crystal and refinement details for $Zn_{0.89}Co_{0.11}$(hfipbb) (molar code: Zn:Co 1:1) [Cambridge Crystallographic Data Centre (CCDC) number: 1531921].

table S4. Crystal data and structure refinement for $Zn_{0.89}Co_{0.11}$(hfipbb) at 100 K (molar code: Zn:Co 1:1) (CCDC number: 1531920).

table S5. Crystal and refinement details for $Zn_{0.59}Co_{0.41}$(hfipbb) (molar code: Zn:Co 1:2) (CCDC number: 1531914).

table S6. Crystal data and structure refinement for $Zn_{0.59}Co_{0.41}$(hfipbb) at 200 K (molar code: Zn:Co 1:2) (CCDC number: 1531918).

table S7. Crystal data and structure refinement for $Zn_{0.59}Co_{0.41}$(hfipbb) at 150 K (molar code: Zn:Co 1:2) (CCDC number: 1531919).

table S8. Crystal data and structure refinement for $Zn_{0.59}Co_{0.41}$(hfipbb) at 100 K (molar code: Zn:Co 1:2) (CCDC number: 1531923).

table S9. Crystal data and structure refinement for $Zn_{0.59}Co_{0.41}$(hfipbb) at 50 K (molar code: Zn:Co 1:2) (CCDC number: 1531915).

table S10. Crystal data and structure refinement for $Zn_{0.55}Co_{0.45}$(hfipbb) at room temperature (molar code: Zn:Co 1:4) (CCDC number: 1531916).

table S11. Crystal data and structure refinement for $Zn_{0.55}Co_{0.45}$(hfipbb) at 100 K (molar code: Zn:Co 1:4) (CCDC number: 1531912).

table S12. Crystal data and structure refinement for $Zn_{0.21}Co_{0.79}$(hfipbb) at room temperature (molar code: Zn:Co 1:10) (CCDC number: 1531902).

table S13. Crystal data and structure refinement for $Zn_{0.21}Co_{0.79}$(hfipbb) at 100 K (molar code: Zn:Co 1:10) (CCDC number: 1531903).

table S14. Crystal data and structure refinement for $Zn_{0.50}Mn_{0.5}$(hfipbb) (molar code: Zn:Mn 1:1) (CCDC number: 1531901).

table S15. Crystal data and structure refinement for $Zn_{0.96}Ca_{0.04}$(hfipbb) (molar code: Zn:Ca 1:1) (CCDC number: 1531926).

table S16. Crystal data and structure refinement for $Zn_{0.94}Ca_{0.06}$(hfipbb) (molar code: Zn:Ca 1:2) (CCDC number: 1531924).

table S17. Crystal data and structure refinement for $Zn_{0.64}Ca_{0.36}$(hfipbb) (molar code: Zn:Ca 1:4) (CCDC number: 1531922).

table S18. Crystal data and structure refinement for $Zn_{0.48}Ca_{0.52}$(hfipbb) (molar code: Zn:Ca 1:10) (CCDC number: 1531909).

fig. S90. Variable temperature NPD for $Zn_{0.54}Mn_{0.37}Co_{0.09}$(hfipbb) (molar code: Zn:Mn:Co 2:1:1).
fig. S91. Variable temperature NPD for $Zn_{0.37}Mn_{0.50}Co_{0.13}$(hfipbb) (molar code: Zn:Mn:Co 1:2:1).
fig. S92. Variable temperature NPD for $Zn_{0.32}Mn_{0.39}Co_{0.28}$(hfipbb) (molar code: Zn:Mn:Co 1:1:2).
fig. S93. Variable temperature NPD for $Zn_{0.48}Mn_{0.42}Ca_{0.10}$(hfipbb) (molar code: Zn:Mn:Ca 1:1:1).
fig. S94. ΔE_{Form} for the pure and bimetallic structures normalized to the most stable one.
fig. S95. Partial view of the crystal structure of the helical, rod-shaped inorganic chains built up with alternating tetrahedral and octahedral metal polyhedrons.
fig. S96. Low-temperature dependence of the product temperature by real component (left *y* axis) and imaginary component (right *y* axis) of the ac magnetic susceptibility obtained for the MOF with formula $Zn_{0.59}Co_{0.41}$(hfipbb).
fig. S97. Magnetic field dependence of the virgin magnetization curves for $Zn_{0.59}Co_{0.41}$(hfipbb).
fig. S98. Low–magnetic field region of hysteresis loops measured at 2 K (circles), 15 K (diamonds), and 30 K (hexagons) for the MOF with formula $Zn_{0.59}Co_{0.41}$(hfipbb).
fig. S99. Thermal variation of dc magnetic susceptibility measured in an applied field of 5 mT for the MOF with formula $Zn_{0.59}Co_{0.41}$(hfipbb).
fig. S100. Low-temperature dependence of the product temperature by ac magnetic susceptibility (left *y* axis) and temperature by the imaginary component (right *y* axis) of the ac magnetic susceptibility obtained for the MOF with formula $Zn_{0.21}Co_{0.79}$(hfipbb).
fig. S101. Magnetic field dependence of the virgin magnetization curves for $Zn_{0.21}Co_{0.79}$(hfipbb).
fig. S102. Low–magnetic field region of hysteresis loops measured at 2 K (black line), 30 K (red line), and 35 K (blue line) for the MOF with formula $Zn_{0.21}Co_{0.79}$(hfipbb).
fig. S103. Thermal variation of magnetic susceptibility for $Zn_{0.21}Co_{0.79}$(hfipbb).

REFERENCES AND NOTES

1. J. B. Goodenough, K.-S. Park, The Li-ion rechargeable battery: A perspective. *J. Am. Chem. Soc.* **135**, 1167–1176 (2013).
2. D. E. Farrell, B. S. Chandrasekhar, M. R. DeGuire, M. M. Fang, V. G. Kogan, J. R. Clem, D. K. Finnemore, Superconducting properties of aligned crystalline grains of $Y_1Ba_2Cu_3O_{7-\delta}$. *Phys. Rev. B* **36**, 4025–4027 (1987).
3. X. H. Chen, T. Wu, G. Wu, R. H. Liu, H. Chen, D. F. Fang, Superconductivity at 43K in $SmFeAsO_{1-x}F_x$. *Nature* **453**, 761–762 (2008).
4. Z. Jin, T. Fukumura, M. Kawasaki, K. Ando, H. Saito, T. Sekiguchi, Y. Z. Yoo, M. Murakami, Y. Matsumoto, T. Hasegawa, H. Koinuma, High throughput fabrication of transition-metal-doped epitaxial ZnO thin films: A series of oxide-diluted magnetic semiconductors and their properties. *Appl. Phys. Lett.* **78**, 3824–3826 (2001).
5. C. Yuan, H. B. Wu, Y. Xie, X. W. Lou, Mixed transition-metal oxides: Design, synthesis, and energy-related applications. *Angew. Chem. Int. Ed.* **53**, 1488–1504 (2014).
6. T. Fukumura, Z. Jin, M. Kawasaki, T. Shono, T. Hasegawa, S. Koshihara, H. Koinuma, Magnetic properties of Mn-doped ZnO. *Appl. Phys. Lett.* **78**, 958–960 (2001).
7. C. de la Cruz, Q. Huang, J. W. Lynn, J. Li, W. Ratcliff II, J. L. Zarestky, H. A. Mook, G. F. Chen, J. L. Luo, N. L. Wang, P. Dai, Magnetic order close to superconductivity in the iron-based layered $LaO_{1-x}F_xFeAs$ systems. *Nature* **453**, 899–902 (2008).
8. L. Lin, Y. Yang, L. Men, X. Wang, D. He, Y. Chai, B. Zhao, S. Ghoshroy, Q. Tang, A highly efficient TiO_2@ZnO n–p–n heterojunction nanorod photocatalyst. *Nanoscale* **5**, 588–593 (2013).
9. B. Donkova, D. Dimitrov, M. Kostadinov, E. Mitkova, D. Mehandjiev, Catalytic and photocatalytic activity of lightly doped catalysts M:ZnO (M = Cu, Mn). *Mater. Chem. Phys.* **123**, 563–568 (2010).
10. H. Furukawa, K. E. Cordova, M. O'Keeffe, O. M. Yaghi, The chemistry and applications of metal-organic frameworks. *Science* **341**, 1230444 (2013).
11. C. K. Brozek, M. Dincă, Cation exchange at the secondary building units of metal–organic frameworks. *Chem. Soc. Rev.* **43**, 5456–5467 (2014).
12. L. M. Aguirre-Díaz, F. Gándara, M. Iglesias, N. Snejko, E. Gutiérrez-Puebla, M. Monge, Tunable catalytic activity of solid solution metal–organic frameworks in one-pot multicomponent reactions. *J. Am. Chem. Soc.* **137**, 6132–6135 (2015).
13. Q. Liu, H. Cong, H. Deng, Deciphering the spatial arrangement of metals and correlation to reactivity in multivariate metal–organic frameworks. *J. Am. Chem. Soc.* **138**, 13822–13825 (2016).
14. C. Castillo-Blas, N. Snejko, V. A. de la Peña-O'Shea, J. Gallardo, E. Gutiérrez-Puebla, M. A. Monge, F. Gándara, Crystal phase competition by addition of a second metal cation in solid solution metal-organic frameworks. *Dalton Trans.* **45**, 4327–4337 (2016).
15. A. Monge, N. Snejko, E. Gutiérrez-Puebla, M. Medina, C. Cascales, C. Ruiz-Valero, M. Iglesias, B. Gómez-Lor, One teflon®-like channelled nanoporous polymer with a chiral and new uninodal 4-connected net: Sorption and catalytic properties. *Chem. Commun.* **2005**, 1291–1293 (2005).
16. H. C. Zeng, Ostwald ripening: A synthetic approach for hollow nanomaterials. *Curr. Nanosci.* **3**, 177–181 (2007).
17. M. O'Keeffe, O. M. Yaghi, Deconstructing the crystal structures of metal–organic frameworks and related materials into their underlying nets. *Chem. Rev.* **112**, 675–702 (2012).
18. A. Schoedel, M. Li, D. Li, M. O'Keeffe, O. M. Yaghi, Structures of metal–organic frameworks with rod secondary building units. *Chem. Rev.* **116**, 12466–12535 (2016).
19. D. Kim, A. Coskun, Template-directed approach towards the realization of ordered heterogeneity in bimetallic metal–organic frameworks. *Angew. Chem. Int. Ed.* **56**, 5071–5076 (2017).
20. B. A. Inc. (Bruker AXS Inc., Madison, Wisconsin, 2015).
21. O. V. Dolomanov, L. J. Bourhis, R. J. Gildea, J. A. K. Howard, H. Puschmann, OLEX2: A complete structure solution, refinement and analysis program. *J. Appl. Cryst.* **42**, 339–341 (2009).
22. G. M. Sheldrick, A short history of SHELX. *Acta Crystallogr. A* **64**, 112–122 (2008).
23. Biovia, Materials Studio 8.0 (2016).
24. G. Kresse, J. Furthmüller, Efficiency of ab-initio total energy calculations for metals and semiconductors using a plane-wave basis set. *Comput. Mater. Sci.* **6**, 15–50 (1996).
25. G. Kresse, J. Hafner, Ab initio molecular dynamics for liquid metals. *Phys. Rev. B* **47**, 558–561 (1993).
26. J. P. Perdew, Y. Wang, Accurate and simple analytic representation of the electron-gas correlation energy. *Phys. Rev. B* **45**, 13244–13249 (1992).
27. J. P. Perdew, J. A. Chevary, S. H. Vosko, K. A. Jackson, M. R. Pederson, D. J. Singh, C. Fiolhais, Atoms, molecules, solids, and surfaces: Applications of the generalized gradient approximation for exchange and correlation. *Phys. Rev. B* **46**, 6671–6687 (1992).
28. P. E. Blöchl, Projector augmented-wave method. *Phys. Rev. B* **50**, 17953–17979 (1994).
29. G. Kresse, D. Joubert, From ultrasoft pseudopotentials to the projector augmented-wave method. *Phys. Rev. B* **59**, 1758–1775 (1999).

Acknowledgments: We acknowledge Institut Laue-Langevin and Spanish Initiatives on Neutron Scattering (SpINS-ILL) for beamtime at instruments D2B and D1B, respectively. We thank E. Rodríguez-Cañas from the Servicio Interdepartamental de Investigación at Universidad Autónoma de Madrid for valuable support with SEM images and EDS analyses acquisition. **Funding:** Work at Instituto de Ciencia de Materiales de Madrid–Consejo Superior de Investigaciones Científicas (CSIC) has been supported by the Spanish Ministry of Economy and Competitiveness (MINECO) Projects MAT2013-45460-R, CTQ2014-61748-EXP, and MAT2016-78465-R. F.G. acknowledges financial support from Fundación General CSIC (Programa ComFuturo) and MINECO (Ramón y Cajal program). Computational time has been provided by the Centre de Supercomputació de Catalunya. This work, developed under the HyMAP project, has received funding from the European Research Council under the European Union's Horizon 2020 research and innovation program (grant 648319). **Author contributions:** F.G. and Á.M. conceived and coordinated the work. C.C.-B. synthesized and analytically characterized all compounds. C.C.-B., E.G.-P., Á.M., and F.G. collected and analyzed the single-crystal XRD data. C.C.-B. collected the SEM and EDS data. I.P.-O., C.C.-B., and F.G. collected and processed the NPD data. R.S.-P. and J.R.d.P. collected the magnetic susceptibility data and analyzed and interpreted the data. V.A.d.l.P.-O. carried out and analyzed DFT calculations. All authors discussed the data, commented on the discussion, and contributed to the manuscript preparation. **Competing interests:** The authors declare that they have no competing interests. **Data and materials availability:** All data needed to evaluate the conclusions in the paper are present in the paper and/or the Supplementary Materials. Additional data related to this paper may be requested from the authors.

Submitted 6 March 2017
Accepted 12 June 2017
Published 21 July 2017
10.1126/sciadv.1700773

Citation: C. Castillo-Blas, V. A. de la Peña-O'Shea, I. Puente-Orench, J. R. de Paz, R. Sáez-Puche, E. Gutiérrez-Puebla, F. Gándara, Á. Monge, Addressed realization of multication complex arrangements in metal-organic frameworks. *Sci. Adv.* **3**, e1700773 (2017).

Science Advances

Addressed realization of multication complex arrangements in metal-organic frameworks

Celia Castillo-Blas, Víctor A. de la Peña-O'Shea, Inés Puente-Orench, Julio Romero de Paz, Regino Sáez-Puche, Enrique Gutiérrez-Puebla, Felipe Gándara and Ángeles Monge

Sci Adv **3** (7), e1700773.
DOI: 10.1126/sciadv.1700773

Review

Israel Journal of Chemistry

DOI: 10.1002/ijch.201800085

Metal-organic Frameworks Incorporating Multiple Metal Elements

Celia Castillo-Blas[a] and Felipe Gándara*[a]

Dedicated to Prof. Omar M. Yaghi in celebration of the 2018 Wolf Prize

Abstract: The obtaining of materials incorporating multiple metal elements is of interest because the combination of various metal cations results in the achievement of new and enhanced properties. Metal-organic frameworks (MOFs) offer a suitable platform to combine multiple metal elements due to their modular nature and highly controllable structure. The incorporation of various metal elements into MOFs might be accomplished by following different synthetic approaches, which in turn determine the way in which the various metal elements are arranged in the framework. In this contribution, we will overview the formation of multi-metal MOFs by the introduction of new metal sites in the organic linkers, or in the inorganic secondary building units through cation exchange process, or one-pot synthesis.

Keywords: Reticular Chemistry · MOFs · multi-metals · advanced materials

1. Introduction

Recent years have witnessed the rise of reticular chemistry as a new field in chemistry and materials science, whose significance is being recognized with the 2018 Wolf Prize being awarded to Omar Yaghi, a pioneer of the field. The development of reticular chemistry has provided the chemists with the tools for the rational construction of new crystalline, porous materials such as metal-organic frameworks, MOFs,[1] which can nowadays be virtually designed to incorporate desired structural, compositional, and topological features for specific applications, such as gas storage,[2,3] gas separation,[4] catalysis,[5] luminesce applications,[6] bio-imaging,[7] or drug delivery,[8] among other applications in energy and life technologies.[9]

The versatility of MOFs arguably emerges from their modular nature based on the assembly of metal-based inorganic secondary building units (SBUs) and organic linkers, and the structural and topological features of MOFs arise from the geometry and points of extension of both building components.[10] Thus, the selection of metal element governs the type of SBU to be formed, which in turns dictates the framework topology. Importantly, it also influences most of the properties of the resulting MOF, from chemical stability to sorption selectivity or catalytic activity. Thus, while typically MOFs have been formed with the use of only one metal element, the introduction of multiple metal atoms within a given framework expands the range of properties that can be displayed by a desired MOF family.

Consequently, a number of different approaches have been developed in order to incorporate multiple metal elements within a certain MOF. Three are the main approaches to achieve MOFs with structures bearing more than one metal cation: use of organic ligands with additional metal binding sites (metalloligands), post-synthetic metal exchange, or the one-pot synthesis of multi-metal MOFs (Figure 1). The degree of control on the incorporation of the additional metal sites into the MOFs, as well as the number of elements that can be introduced strongly depend on the selected methodology. In this contribution, we discuss some of these approaches, highlighting selected relevant examples from the literature and with special focus on the one-pot synthesis of multi-metal MOFs.

2. MOFs with Linkers Containing Metal-binding Sites

MOFs basic constituents are metal cations and organic linkers. Metal cations form inorganic clusters through the formation of coordination bonds with the linkers to build up the MOF extended structures. As a way of incorporating additional metal cations different to those forming the inorganic SBUs, it is possible to use organic linkers that possess additional metal binding sites. These additional metal binding sites are not playing any structural role in the construction of the MOF, but they are incorporated as additional chemical decoration of the framework, to provide the MOF with extra functionalities. Organic linkers bearing additional metal binding sites can be referred to as metalloligands. The metalloligand approach

[a] C. Castillo-Blas, Dr. F. Gándara
Department of New Architectures in Materials Chemistry, Instituto de Ciencia de Materiales de Madrid – Consejo Superior de Investigaciones Científicas
Sor Juana Inés de la Cruz, 3, Madrid, 28049, Spain
E-mail: gandara@icmm.csic.es

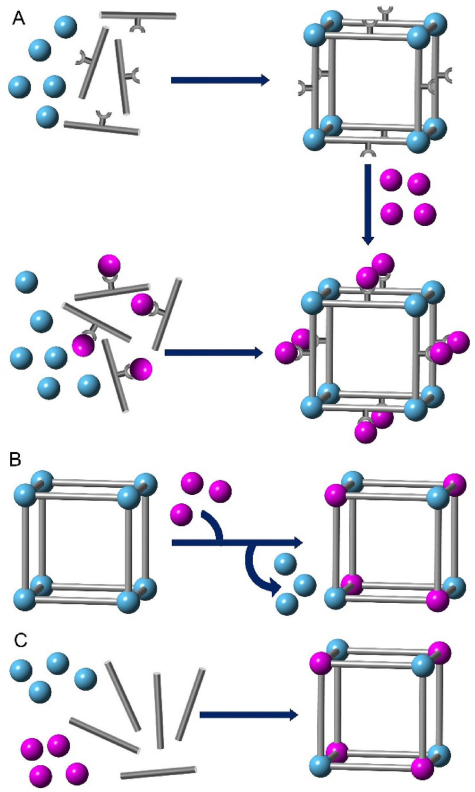

Figure 1. Illustration of possible pathways for the incorporation of various metal elements in MOFs. (A) MOFs formation with linkers containing additional metal binding sites; (B) Post-synthetic cation exchange; (C) One-pot synthesis with multiple metal elements. Metal elements are represented as colored spheres, and organic linkers as grey cylinders.

offers as main advantage the control over the position of the additional metal-cation, as result of the pre-defined location of the metal binding site in the MOF organic linker. As such, it allows the tuning of the MOF pore environment. Several types of metallo-ligands have been reported in the construction of multi-metal MOFs, including β-diketones,[11] acetylacetonates,[12] Schiff bases,[13] oxamates,[14] pyridines,[15] dipyrrinates, and most notably, metallo-porphyrin based linkers, among others.

In 2005 Halper and Cohen reported one of the first examples of heterometallic MOFs with the use of dipyrrinates metalloligands.[16] The authors employed [Co(4-pyrdpm)$_3$] and [Fe(4-pyrdpm)$_3$] ((4-pyrdpm) = 5-(4-pyridyl)-4,6-dipyrrinato)) as metalloligands in combination with a solution of Ag(I), resulting in two isostructural bimetallic MOFs, MOF–Co/Ag-1 and MOF–Fe/Ag-1. Later, in 2006 they studied the influence of the Ag counterion employed in the synthesis on the resulting topology,[17] and continued with the study of new examples of heterobimetallic MOFs by combination of [M(4-pyrdpm)$_3$] (M = Ga or In) and different Ag-salts.[18]

Bipirydin based ligands have been extensively employed for the incorporation of additional metal sites in MOFs, thanks to its ability to easily chelate metal cations. MOF-253 [Al(OH)(bpydc)] (H_2bpydc = 2,2′-bipyridine-5,5′-dicarboxylic acid) was reported in 2010, by Long, Yaghi, and co-workers.[19] This MOF, with a highly porous structure and surface area exciding 2100 $m^2 g^{-1}$, allows the incorporation of metal cations into the bipyridine sites of the organic linkers. Thus, palladium or copper complexes were formed in nearly quantitative yield following a post-synthetic metalation process, resulting in an enhancement of the gas sorption selectivity properties of the MOFs (Figure 2). There are many other examples of other MOFs where metal complexes have been incorporated by using bipyridine based organic linkers. Among them, several members of the zirconium-MOFs family have been prepared with the use of these linkers,[20] exploiting the high chemical stability of zirconium MOFs and adding new properties arising from the introduction of active complexes in the linkers, such as incorporation of iridium complexes for water oxidation,[21a] or rhenium complexes for carbon dioxide reduction.[21b]

Metalloporphyrins are a family of metalloligands extensively employed as MOF linkers. Due to their electronic properties, the use of porphyrins as linkers in MOFs is of interest, for example to introduce active redox sites. Thus, metalloporphyrin-based MOFs are excellent candidates for the preparation of heterogeneous catalysts for oxidation reactions.[22–25] In addition, the geometry of the porphyrin molecules might be advantageous in the design of MOFs with particular topologies. In 2012 Yaghi *et al.* reported the synthesis of new zirconium MOFs with the use of porphyrin linkers, as well as the corresponding multimetallic materials

Celia Castillo-Blas was born in 1990. She received her BS degree in Chemistry in 2013 and her MSc in Chemical Science and Technology in 2014 from Complutense University of Madrid. She is currently completing her PhD program at the Materials Science Institute of Madrid (ICMM–CSIC), and her research focuses on the synthesis and characterization of metal–organic frameworks with multiple metal elements.

Felipe Gándara is currently a "Ramón y Cajal" researcher at the Materials Science Institute of Madrid – CSIC. He obtained his PhD in 2009, under the supervision of Prof. A. Monge, and then joined the group of Prof. O. M. Yaghi where he was a post-doctoral fellow from 2009 to 2014, first at University of California Los Angeles, and then at UC Berkeley and Lawrence Berkeley National Laboratory. His research interest is on the development of reticular materials for energy and environmental applications.

Israel Journal of Chemistry

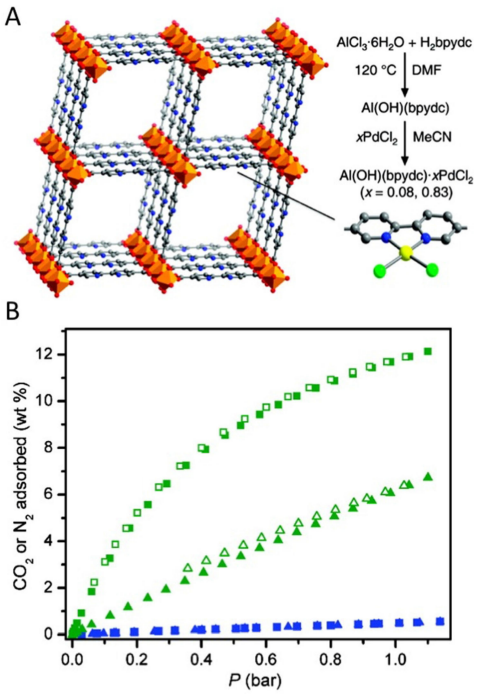

Figure 2. (A) The structure of MOF-253 includes metal binding sites in the bipyridine based linkers, which can be used to create palladium complexes. (B) The 298 K carbon dioxide isotherm of MOF-253 (green triangles) and MOF-253·0.97Cu$(BF_4)_2$, (green squares) evidence the differences in gas sorption properties. Reprinted with permission from reference 19, Copyright 2010 American Chemical Society.

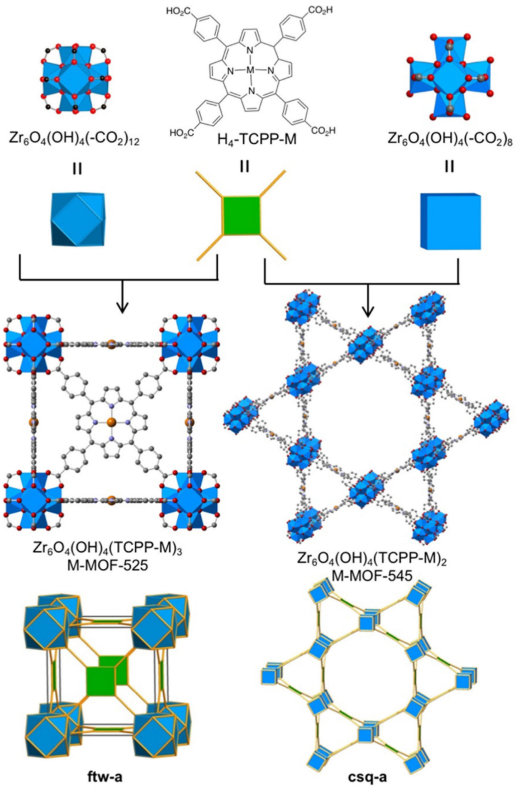

Figure 3. MOF-525 and -545 were prepared by combining Zr_6 SBUs and the porphyrin linker TCCP (reference 26). In MOF-525, the zirconium SBU has 12 points extension, and the framework belongs to the **ftw** topology, whereas in MOF-525 the SBU has a cubic shape, and the framework is of the **csq** type. In both cases, additional metal cations can be introduced in the porphyrin linkers.

with the use of the metalated analogues or with a post-synthetic metalation.[26] Thus, MOF-525 and MOF-545 were the first examples of MOFs prepared with the combination of zirconium SBUs and the porphyrin based linker TCCP (tetrakis(4-carboxyphenyl)porphyrin), resulting in materials with **ftw** and **csq** topologies (Figure 3). MOF-525 and -545 were metalated with iron(III) and copper(II) without losing their high surface area (above 2000 $m^2 g^{-1}$). Several metalated versions of MOF-545 were shortly after reported by Zhou's group, who proved that they exhibit highly effective biomimetic oxidation activity with different substrates in aqueous media.[27] Other examples of zirconium MOFs have been subsequently reported with the use of related porphyrin based linkers, such as M-TPPCOOMe (M = Ni, Co or Fe; TPPCOOMe = 5,10,15,20-Tetrakis(4-methoxycarbonylphenyl) porphyrin),[28] or M-TCBPP (M = Zn, Fe, Co; TCBPP = tetrakis(4-carboxybiphenyl)porphyrin).[29]

In addition to zirconium, metalloporphyrins have also been employed to construct MOFs based on other metal elements. For example, Johnson *et al.* prepared a zwiterionic MOF composed of a cationic Fe(III) or Mn(III)-porphyrin with a $[In(CO_2)_4]^-$ cluster, and they tested it in electrocyclization reactions.[30] Tripuramallu *et al.*[31] used a hexatopic porphyrin linker denoted HCPP (5,15-bis(4′-carbomethoxyphenyl)-10,20-bis(3,5-biscarboethoxyphenyl)porphyrin) in combination with SBUs formed by 3d (Mn or Co), 4f (Pr, Gd or Yb), or 4d (Pb or In) metal elements. In this line, there are other examples with the Zr_6 cluster and other metalloligands such as $[Cu_4I_4(Ina)_4]^{4-}$ (Ina = isonicotinate) employed as catalyst in the styrene oxide ring-opening reaction with mono alcohols.[32]

The combination of transition and rare earth metals has a great interest for obtaining heterometallic MOFs with luminescent properties. Different structural types of Ln–Ni(IDA) (IDA = iminodiacetic acid) have been studied by Kong *et al.*[33] Authors proposed new heterometallic MOFs with formula $\{[Ln_4(ox)_3(Ni(IDA)_2)_3(H_2O)_6]\}_n \cdot xH_2O$ (ox = oxalate; Ln = Dy, La, Nd, Eu, Gd or Pr) where the Ln-oxalate tetramers (type I), dimers (type II) or one dimensional polymers (type III) are bridged by the metalloligand$[Ni(IDA)_2]^{2-}$. Ln–Cu (metalloligands) with magnetic properties have also been reported, such as the $\{[Dy_2Cu_3(IDA)_6] \cdot 1.5H_2O\}_n$ material, which presents a weak ferromagnetic interaction between the metal ions.[34] $[Ln(H_2O)_2Cu_3(Hmesox)_3DMSO] \cdot xH_2O \cdot yDMSO$ materials (Ln(III) = La, Ce, Pr, Nd and Eu; H_4mesox = dihydroxymalonic acid; and DMSO = dimethylsulfoxide) have been prepared by crystal growth in agarose gel in a mixed solvent

(DMSO/water) medium. The magnetic susceptibility study performed for $LaCu_3$ revealed the occurrence of antiferromagnetically coupled Cu(II) equilateral triangles whose apical positions can also be occupied by water molecules.[35] Tripuramallu *et al.* reported in 2016 five new crystalline lanthanoid–metalloporphyrin porous frameworks composed of the octatopic Zn-OCPP linker (tetrakis-(3,5-dicarboxyphenyl) porphyrin = OCPP) and a rod-shaped SBU with formula $\{NaGd(H_2O)_2(COO^-)_4\}_n$.[36]

2. Post-synthetic Metal Exchange

Transmetalation, cation exchange process, or ion methatesis, is a post-synthetic method used to substitute the metal cations employed in the MOF SBU formation by other metal elements, while maintaining the original MOF structure. The synthetic method typically consists of immersing the selected MOF into a solution saturated with the metal cations to be introduced in the structure.[38] With some exceptions where the transmetalation process is quantitative, typically the cation exchange is only partly completed, so that the resulting MOF contains a mixture of metal elements. Nonetheless, this method has been proven to be effective is cases where a desired MOF SBU is only obtained with certain cations, and the formation of isoreticular materials with other metal elements is sought. This is, for instance, the case of metal substitution in MOF-5, where the introduction of metal cations with redox activity in the prototypical zinc acetate SBU was accomplished following this methodology.[38] The metal exchange process has also been proved to be effective in order to increase the gas sorption capacity of MOFs by means of introducing elements with higher affinity towards the selected gas. Thus, Dinca and Long demonstrated the increase in the H_2 storage capacity of MOFs derived from the exchange of Mn^{2+} centers in the family of $\{Mn_3[(Mn_4Cl)_3(btt)_8(CH_3OH)_{10}]_2\}$ (btt = 1,3,5-benzenetristetrazolate) materials, by other metal elements.[39]

The formation of titanium MOFs through partial cation exchange of parent zirconium MOFs has been reported. However, despite the incorporation of titanium into the materials is accomplished, there is controversy regarding the actual location of the titanium cations, and recent studies indicate that the addition of titanium cations takes place through a grafting process into the SBU[40] or in the form of nanoscale surface deposited titanium oxide,[41] rather than an actual cation exchange in the SBU. This is in line with computational studies that correlates the energetic stability of bimetallic MOFs, showing that the titanium/zirconium metal exchange is not energetically favourable.[42]

An exquisite control in the cation exchange process was recently achieved, such as the controlled formation of metal cation vacancies and their subsequent occupation with other metal elements has been accomplished, and characterized with the use of single crystal X-ray diffraction.[43] In particular, Li and co-workers employed a cubic MOF based on zinc and a pyrazole carboxylic acid linker, which was subjected to an acid treatment to remove a quarter of the metal ions and half of the linkers (Figure 4). New metal cations were further incorporated into the MOF structure at the vacancy positions.

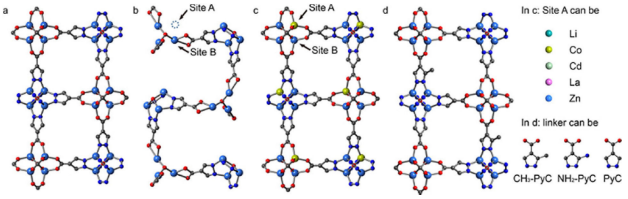

Figure 4. Ordered vacancies and cation exchange in MOF single-crystals: a) Parent MOF without vacancies; b) with vacancies and c) and d) with metal cations in the vacancies: cobalt replaced and 4-CH_3 substitution in the linker in c) and d), respectively. Zinc (light blue), nitrogen (dark blue), oxygen[2] and carbon (gray).Reprinted with permission from reference 43. Copyright (2014) American Chemical Society.

In some occasions, transmetalation occurs in a specific and easily detectable way and it can be used for sensing metal cations. For instance this is the case of the detection of Fe^{3+} in aqueous solution by fluorescence changes in metal exchanged MIL-53(Al).[44] The cation exchange between Fe^{3+} and Al^{3+} in MIL-53(Al) metallic centers generates the quenching of the emission of MIL-53(Al) due to the transformation of strong-fluorescent MIL-53(Al) to weak-fluorescent MIL-53(Fe), allowing highly selective and sensitive detection of Fe^{3+} ions in a 3–200 μM concentration range.

In addition to the exchange of framework cations, it is also possible to incorporate a second metal element in the form of extra-framework cations. Navarro *et al.* introduced potassium ions into the $[Ni_8(OH)_4(H_2O)_2(BDP\_X)_6]$ MOF (H_2BDP_X = 1,4-bis(pyrazol-4-yl)benzene-4-X with X=H, OH, NH_2) by generating defect sites after immersing the MOF in KOH ethanolic solutions.[45] Furthermore, they showed that the extra-framework K^+ ions might be replaced by Ba^{2+} ions, resulting in a material with improved affinity for the capture of SO_2.[46] Other examples of extra-framework metal cation incorporation include the exchange of the dimethylammonium ions present in the pores of bio-MOF-1[47] by lanthanide ions.[48] As result of the incorporation of the lanthanide cations, the luminescence properties of these materials were fine tuned for fluorescence and sensing.

3. One-pot Synthesis of Multi-metal MOFs

The most direct approach for the incorporation of multiple metal elements into a MOF is the combination of different metal precursors during the MOF synthesis. As opposed to the previously discussed approaches where the resulting materials are generally bimetallic, following this strategy it is possible to incorporate a larger number of different metal cations in the same SBU.

Lanthanide based MOFs are a particularly favourable case for the preparation of multi-metal MOFs, as rare-earth elements are easily found forming solid solutions. The controlled introduction of multiple lanthanide cations within a MOF structure allows the modification of the luminescence properties of the solids. A series of multi-metallic lanthanide based MOFs was prepared by Rosi, Petoud, *et al.* in 2009, and their emission properties could be finely tuned through the control of the initial metal ratios.[49] Similarly, through the combination of lanthanide cation with the 3,5-disulfobenzoic acid linker, a series of MOFs was prepared with an heptanuclear SBU by Monge *et al.*[50] The emission of the triplet state of the linker in the gadolinium material is highly efficient, and the external efficiency is dramatically enhanced with the incorporation of small amounts of europium and/or terbium in the multi-metal analogues. This series of MOFs were evaluated as materials for lighting and thermometry.

The ability to combine multiple metal cations allows the modification of the catalytic properties of a certain MOF type. Thus, the catalytic activity of a series of solid solution MIL-100 (Sc, M, with M = Al, Cr, Fe) materials in Lewis acid catalysed Friedel-Craft reactions was found to be related to the amount of scandium.[51] In another example of multi-metal MOFs based on the same trimeric SBU, Deng *et al.*[52] reported a series of porphyrin based materials prepared with a single metal element (Mg, Mn, Co, Ni, and Fe) as well as the corresponding multimetal materials (Mn_xFe_{3-x}, Ni_xFe_{3-x}, Co_xNi_{3-x}, Mn_xCo_{3-x}, Mn_xMg_{3-x}, and Mn_xNi_{3-x}). Spectroscopic analyses of this family of materials showed that the multi-metal MOFs might appear forming domains of cations, as well as in the form of well-mixed systems, with different performance in the photo-oxidation of 1,5-dihydroxynaphthalene. Gascon *et al.* have shown how the incorporation of iron cations within the MIL-53(Al) MOF endows this material with catalytic activity in the conversion of methane to methanol. The enzyme-like catalytic activity of this material arises from the ability to isolate oxo-bridged iron units within the multi-metal MOF SBU.[53] Recently, Martí-Gastaldo *et al.*[54] have reported the modification of the electronic structure of a new titanium MOF by adding a second metal cation, resulting in a tuning of the material band-gap, and consequently its photo-catalytic activity.

Moreover, the catalytic activity of solid-solution MOFs can actually be tuned by virtue of the combination of multiple metal cations, so that solid-solution MOFs exhibit different activity than their single metal counterparts. Thus, in 2015 we synthesized a series of solid solution MOFs based on the combination of group 13 elements, and general formula [$In_xGa_{1-x}(O_2C_2H_4)_{0.5}$(hfipbb)] [$H_2$hfipbb = 4,4′-(hexafluoroisopropylidene) *bis*(benzoic acid)].[55] These MOFs are isostructural with their single metal analogues, synthesized with Al, Ga, or In. The catalytic activity of this series of MOFs in the one-pot multicomponent Strecker reaction was evaluated, and differences in the behaviour of the materials were correlated with their metal ratios. Thus, by using the Ga or In MOF as catalyst, only reaction intermediates or by-products were yielded. However, the combination of both elements in the form of solid solution MOFs resulted in the obtaining of the desired α-aminonitrile Strecker product (Figure 5). The differences in activity are rationalized based on the ability of the solid solution material to address the different stages involved in the reaction mechanism by virtue of the presence of multiple metal cations.

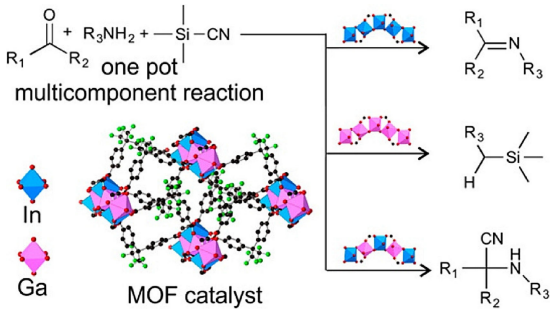

Figure 5. Solid solution [$In_xGa_{1-x}(O_2C_2H_4)_{0.5}$(hfipbb)] MOF as heterogeneous catalyst. The MOF composition has a direct influence in the obtained product of the multi-component Strecker reaction. Indium (light blue), galium (pink), carbon (black), fluorine (green). Reprinted with permission from reference 51. Copyright (2015) American Chemical Society.

Regarding transition metal solid-solution MOFs, it is worth pointing out the case of MOF-74. This MOF was reported by Yaghi *et al.* in 2005[56] with the use of zinc as metal cation, followed by other reports where the same MOF structure type was obtained with the use of Co,[57] Mg,[58] Ni,[59] Mn,[60] Cu,[61] and Fe.[62] In all cases, the metal cations appear in octahedral coordination environment in the rod-shaped SBU used to build up this structure. Influence of the selected metal element on the sorption properties of this MOF type have been extensively evaluated, including the case of mixed metal Zn/Co MOF-74.[63] Combination of 2, 4, 6, 8, and 10 different metal elements in MOF-74 was demonstrated in 2014 by Yaghi *et al.*[64] In addition to the elements that were previously used to produce single metal MOF-74, it was demonstrated the feasibility of the one pot synthesis to incorporate other cations that would not afford this MOF type if used alone, such as barium, strontium, or calcium. The incorporation of the employed metal elements was demonstrated with ICP and EDS mapping analysis of the samples. The results of the analyses showed that while all the metal elements were effectively incorporated into MOF-74 crystals, different metal distributions were found for individual crystals. In a more recent report, Kim and Coskun employed a different approach to obtain bimetallic MOF-74, based on the use of a one-dimensional coordination polymer as starting material to produce Zn/M–MOF-74 (M = Ni, Mg) with 1 : 1 metal ratios.[65]

On the other hand, the combination of multiple metal elements during the one-pot synthesis might result in the

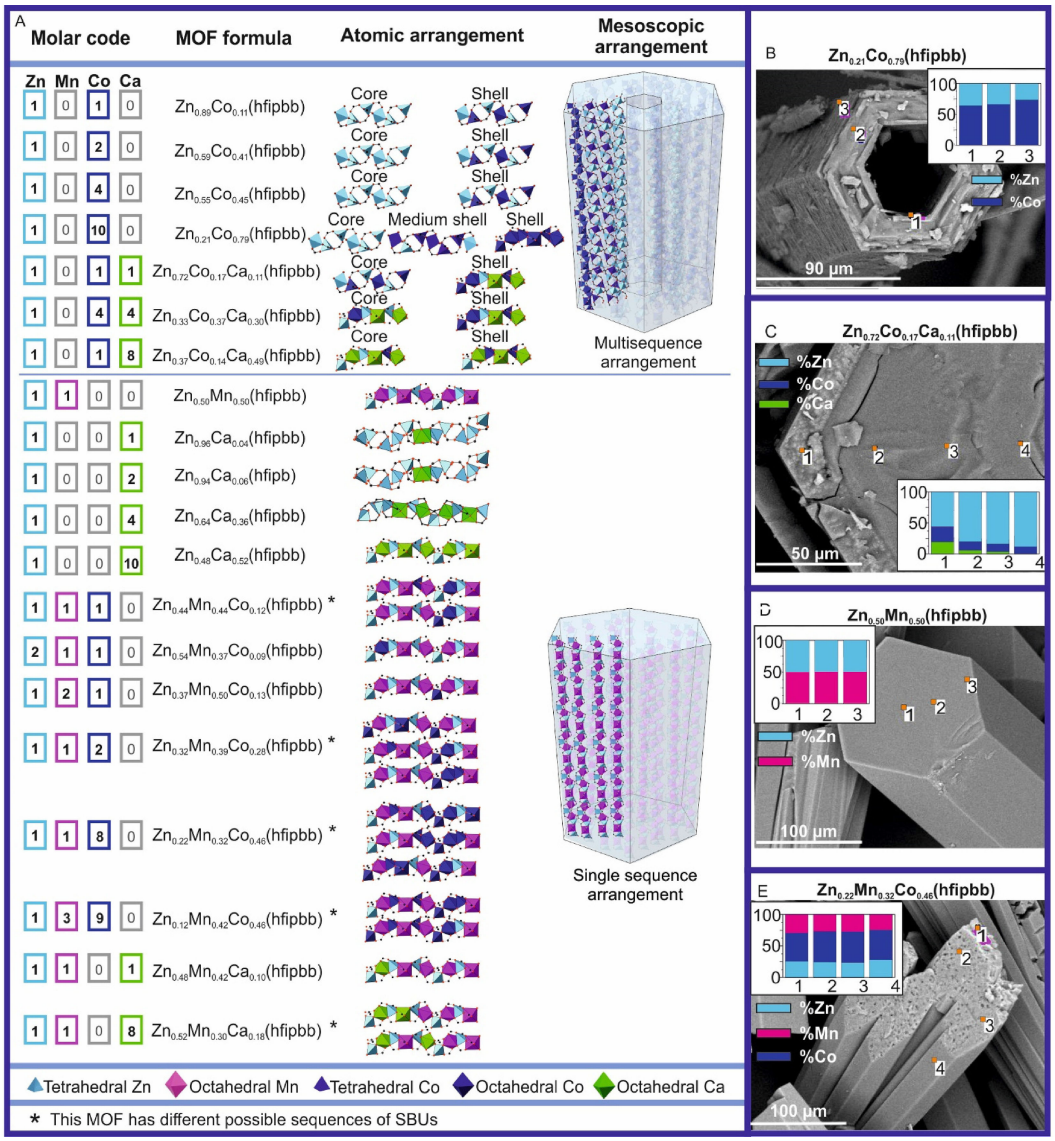

Figure 6. One-pot synthesis of mult-metal MOFs with addressable arrangements of metal cations (A) Selection of appropriate molar codes allows the formation of different kinds of atomically sequenced inorganic SBUs. Corresponding MOF crystals might include multiple SBUs mesoscopically arranged, or just one. (B)–(E) SEM-EDS analyses were used to evaluate the distribution of metal elements within MOF crystals. Representative examples of different MOFs prepared from various molar codes are shown in panels B to E, demonstrating both compositional gradients (B and C), as well as homogeneous arrangements (D and E). Metal atomic percent was determined with the spectra recorded at multiple points or areas of each crystal, as indicated in the images. From *Sci. Adv.* 2017, 3, e1700773 (reference 63). Reprinted with permission from AAAS.

appearance of competitive crystallization processes, rather than in the formation of the multi-metal MOF. Indeed, in 2016 we found that the addition of small amounts of cobalt during the synthesis of a MOF based on the combination of zinc and 1,2,4-triazole and H_2hfipbb resulted in the formation of various MOF phases.[66] The study of the influence of the initial Zn/Co molar ratio resulted in the isolation of up to five different structure types. Interestingly, a kinetic study combined with the results of formation energy calculations indicated that those crystal phases that are thermodynamically more stable when prepared with zinc will not allow the formation of the solid solution Zn/Co analogue, so that cobalt was found only in trace amounts in these cases. Otherwise, MOFs whose crystallization is kinetically driven can be obtained in the mixed metal form. In principle, during the synthesis reaction these MOFs will be in an equilibrium that allows the incorporation of additional elements into the framework. Based on these findings, we recently demonstrated that it is possible to address the location of various metal cations in the SBU of MOFs by taking advantage of differ-

ences in the metal incorporation rates, and changes in the coordination environment.[67] In particular, we focused on a MOF that was initially prepared with zinc as metal cation.[68] This structure type, consisting of helical SBUs with the zinc cations tetrahedrally coordinated had not been synthesized with any other metal element. Combination of zinc and cobalt at different ratios resulted in the formation of the corresponding mixed-metal systems. Single crystal X-ray diffraction studies showed that cobalt atoms might adopt octahedral coordination environment depending on the initial Zn/Co molar ratio, resulting in a crystal symmetry change. A combination of SEM, EDS, X-ray and neutron diffraction, and DFT studies demonstrated that compositional gradients are produced in this multi-metal system, where MOF crystals are formed by an inner core with SBUs composed exclusively of zinc, and an outer shell where the SBUs are made of alternating zinc and cobalt cations. If the initially used amount of cobalt is sufficiently large, another external shell is also formed, where the SBUs are exclusively made of cobalt. In this structure type, the zinc cations are always in tetrahedral coordination environment, while cobalt cations appear in tetrahedral or octahedral environment. On the other hand, when zinc is combined with manganese, the SBUs will be formed by alternating tetrahedral zinc and octahedral manganese cations. These differences in preferential coordination environments results in the ability to address the location of the metal cations in the inorganic SBUs of tri-metallic systems composed of zinc, cobalt and manganese, by adjusting the initial molar ratios, and a series of materials with addressed arrangements of metal cations were produced (Figure 6).

3. Summary (or Outlook)

Multi-metal MOFs offer new possibilities in reticular chemistry. Along with the addition of new functionalities by placing different metal cations in the skeleton of MOFs, the ability to create new chemical environment by placing together multiple metal elements opens up new opportunities to finely modulate the properties of these materials, and to yield new ones. In this sense, the control over the arrangement of multiple metal elements appears as a powerful tool to create new advanced reticulated materials. To achieve this, a fundamental understanding of the multi-metal MOF formation processes will be crucial to develop new methodologies that allows the desired atomic level structural control already available in single metal MOFs.

Acknowledgements

We acknowledge the Spanish Ministry for Science, Innovation and Universities, for funding through the “Ramón y Cajal” program, and grant CTQ2017-87262-R.

References

[1] H. Furukawa, K. Cordova, M. O'Keeffe, O. Yaghi, *Sci.* **2013**, *341*, 974–986.
[2] A. R. Millward, O. M. Yaghi, *J. Am. Chem. Soc.* **2005**, *127*, 17998–17999.
[3] H. Furukawa, N. Ko, Y. B. Go, N. Aratani, S. B. Choi, E. Choi, A. Ö. Yazaydin, R. Q. Snurr, M. O'Keeffe, J. Kim, O. M. Yaghi, *Sci.* **2010**, *329*, 424–428.
[4] J.-R. Li, R. J. Kuppler, H.-C. Zhou, *Chem. Soc. Rev.* **2009**, *38*, 1477–1504.
[5] A. Corma, H. Garcia, F. X. L. I. Llabres i Xamena, *Chem. Rev.* **2010**, *110*, 4606–4655.
[6] Y. Cui, Y. Yue, G. Qian, B. Chen, *Chem. Rev.* **2012**, *112*, 1126–1162.
[7] J. Della Rocca, D. Liu, W. Lin, *Acc. Chem. Res.* **2011**, *44*, 957–968.
[8] P. Horcajada, R. Gref, T. Baati, P. K. Allan, G. Maurin, P. Couvreur, G. Férey, R. E. Morris, C. Serre, *Chem. Rev.* **2012**, *112*, 1232–1268.
[9] S.-L. Li, Q. Xu, *Energy Environ. Sci.* **2013**, *6*, 1656–1683.
[10] M. O'Keeffe, O. M. Yaghi, *Chem. Rev.* **2012**, *112*, 675–702.
[11] L. Carlucci, G. Ciani, S. Maggini, M. Proserpio Davide, M. Visconti, *Chem. Eur. J.* **2010**, *16*, 12328–12341.
[12] B. Chen, F. R. Fronczek, A. W. Maverick, *Inorg. Chem.* **2004**, *43*, 8209–8211.
[13] S.-H. Cho, B. Ma, S. T. Nguyen, J. T. Hupp, T. E. Albrecht-Schmitt, *Chem. Commun.* **2006**, 2563–2565.
[14] D. Cangussu, E. Pardo, M.-C. Dul, R. Lescouëzec, P. Herson, Y. Journaux, E. F. Pedroso, C. L. M. Pereira, H. O. Stumpf, M. Carmen Muñoz, R. Ruiz-García, J. Cano, M. Julve, F. Lloret, *Inorg. Chim. Acta* **2008**, *361*, 3394–3402.
[15] S.-i. Noro, S. Kitagawa, M. Yamashita, T. Wada, *CrystEngComm* **2002**, *4*, 162–164.
[16] S. R. Halper, S. M. Cohen, *Inorg. Chem.* **2005**, *44*, 486–488.
[17] S. R. Halper, L. Do, J. R. Stork, S. M. Cohen, *J. Am. Chem. Soc.* **2006**, *128*, 15255–15268.
[18] J. R. Stork, V. S. Thoi, S. M. Cohen, *Inorg. Chem.* **2007**, *46*, 11213–11223.
[19] E. D. Bloch, D. Britt, C. Lee, C. J. Doonan, F. J. Uribe-Romo, H. Furukawa, J. R. Long, O. M. Yaghi, *J. Am. Chem. Soc.* **2010**, *132*, 14382–14384.
[20] T. N. Tu, M. V. Nguyen, H. L. Nguyen, B. Yuliarto, K. E. Cordova, S. Demir, *Coord. Chem. Rev.* **2018**, *364*, 33–50.
[21] a) C. Wang, J.-L. Wang, W. Lin, *J. Am. Chem. Soc.* **2012**, *134*, 19895–19908. b) K. M. Choi, D. Kim, B. Rungtaweevoranit, C. A. Trickett, J. T. D. Barmanbek, A. S. Alshammari, P. Yang, O. M. Yaghi, *J. Am. Chem. Soc.* **2017**, *139*, 356–362.
[22] M. Zhao, S. Ou, C.-D. Wu, *Acc. Chem. Res.* **2014**, *47*, 1199–1207.
[23] O. K. Farha, A. M. Shultz, A. A. Sarjeant, S. T. Nguyen, J. T. Hupp, *J. Am. Chem. Soc.* **2011**, *133*, 5652–5655.
[24] L. Meng, Q. Cheng, C. Kim, W. Y. Gao, L. Wojtas, Y. S. Chen, J. Zaworotko Michael, X. P. Zhang, S. Ma, *Angew. Chem. Int. Ed.* **2012**, *51*, 10082–10085; *Angew. Chem.* **2012**, *124*, 10229–10232.
[25] K. Wang, D. Feng, T.-F. Liu, J. Su, S. Yuan, Y.-P. Chen, M. Bosch, X. Zou, H.-C. Zhou, *J. Am. Chem. Soc.* **2014**, *136*, 13983–13986.
[26] W. Morris, B. Volosskiy, S. Demir, F. Gándara, P. L. McGrier, H. Furukawa, D. Cascio, J. F. Stoddart, O. M. Yaghi, *Inorg. Chem.* **2012**, *51*, 6443–6445.

[27] D. Feng, Z. Y. Gu, J. R. Li, H. L. Jiang, Z. Wei, H. C. Zhou, *Angew. Chem. Int. Ed.* **2012**, *51*, 10307–10310; *Angew. Chem.* **2012**, *124*, 10453–10456.
[28] D. Feng, W.-C. Chung, Z. Wei, Z.-Y. Gu, H.-L. Jiang, Y.-P. Chen, D. J. Darensbourg, H.-C. Zhou, *J. Am. Chem. Soc.* **2013**, *135*, 17105–17110.
[29] Q. Lin, X. Bu, A. Kong, C. Mao, X. Zhao, F. Bu, P. Feng, *J. Am. Chem. Soc.* **2015**, *137*, 2235–2238.
[30] J. A. Johnson, B. M. Petersen, A. Kormos, E. Echeverría, Y.-S. Chen, J. Zhang, *J. Am. Chem. Soc.* **2016**, *138*, 10293–10298.
[31] B. K. Tripuramallu, S. Goswami, I. Goldberg, *Cryst. Growth Des.* **2018**, *18*, 230–241.
[32] Y.-X. Tan, X. Yang, B.-B. Li, D. Yuan, *Chem. Commun.* **2016**, *52*, 13671–13674.
[33] X.-J. Kong, Y.-P. Ren, L.-S. Long, R.-B. Huang, L.-S. Zheng, M. Kurmoo, *CrystEngComm* **2008**, *10*, 1309–1314.
[34] J.-x. Ma, X.-f. Huang, X.-q. Song, L.-q. Zhou, W.-s. Liu, *Inorg. Chim. Acta* **2009**, *362*, 3274–3278.
[35] B. Gil-Hernandez, P. Gili, M. Quiros, J. Sanchiz, *CrystEngComm* **2015**, *17*, 6555–6565.
[36] B. K. Tripuramallu, H. M. Titi, S. Roy, R. Verma, I. Goldberg, *CrystEngComm* **2016**, *18*, 515–520.
[37] C. K. Brozek, M. Dincă, *Chem. Soc. Rev.* **2014**, *43*, 5456–5467.
[38] C. K. Brozek, M. Dincă, *J. Am. Chem. Soc.* **2013**, *135*, 12886–12891.
[39] M. Dincă, J. R. Long, *J. Am. Chem. Soc.* **2007**, 129, 11172–11176.
[40] J. G. Santaclara, A. I. Olivos-Suarez, A. Gonzalez-Nelson, D. Osadchii, M. A. Nasalevich, M. A. Van Der Veen, F. Kapteijn, A. M. Sheveleva, S. L. Veber, M. V. Fedin, A. T. Murray, C. H. Hendon, A. Walsh, J. Gascon, *Chem. Mater.* **2017**, *29*, 8963–8967.
[41] M. S. Denny, L. R. Parent, J. P. Patterson, S. K. Meena, H. Pham, P. Abellan, Q. M. Ramasse, F. Paesani, N. C. Gianneschi, S. M. Cohen, *J. Am. Chem. Soc.* **2018**, *140*, 1348–1357.
[42] F. Trousselet, A. Archereau, A. Boutin, F.-X. Coudert, *J. Phys. Chem. C* **2016**, *120*, 24885–24894.
[43] B. Tu, Q. Pang, D. Wu, Y. Song, L. Weng, Q. Li, *J. Am. Chem. Soc.* **2014**, *136*, 14465–14471.
[44] C.-X. Yang, H.-B. Ren, X.-P. Yan, *Anal. Chem.* **2013**, *85*, 7441–7446.
[45] E. López-Maya, C. Montoro, V. Colombo, E. Barea, J. A. R. Navarro, *Adv. Funct. Mater.* **2014**, *24*, 6130–6135.
[46] L. M. Rodríguez-Albelo, E. López-Maya, S. Hamad, A. R. Rioz-Salvador, S. Calero, J. A. R. Navarro, *Nat. Commun.* **2017**, *8*, 14457.
[47] J. An, C. M. Shade, D. A. Chengelis-Czegant, S. Peoud, N. Rosi. *J. Am. Chem. Soc.* **2011**, *133*, 1220–1223.
[48] X. Shen, B. Yan, *J. Colloid Interface Sci.* **2015**, *415*, 63–68
[49] K. A. White, D. A. Chengelis, K. A. Gogick, J. Stehman, N. L. Rosi, S. Petoud, *J. Am. Chem. Soc.* **2009**, *131*, 18069–18071.
[50] R. F. D'Vries, S. Alvarez-García, N. Snejko, L. E. Bausá, E. Gutiérrez-Puebla, A. de Andrés, M. Á. Monge, *J. Mater. Chem. C* **2013**, *1*, 6316–6324.
[51] L. Mitchell, P. Williamson, B. Ehrlichov, A. E. Anderson, V. R. Seymour, S. E. Ashbrook, N. Acerbi, L. M. Daniels, R. I. Walton, M. L. Clarke, P. A. Wright, *Chem. Eur. J.* **2014**, *20*, 17185–17197.
[52] Q. Liu, H. Cong, H. Deng, *J. Am. Chem. Soc.* **2016**, *138*, 13822–13825.
[53] D. Y. Osadchii, A. I Olivos-Suarez, A. Szécsényi, G. Li, M. A. Nasalevich, I. A. Dugulan, P. Serra Crespo, E. J. M. Hensen, M.V Fedin, G. Sankar, E. A. Pidko, J. Gascon, *ACS Catal.* **2018**, *8*, 5542–5548.
[54] J. Castells-Gil, N. M. Padial, N. Almora-Barrios, J. Albero, A. R. Ruiz-Salvador, J. González-Platas, H. García, C. Martí-Gastaldo, *Angew. Chem. Int. Ed.* **2018**, *57*, 8453–8457
[55] L. M. Aguirre-Díaz, F. Gándara, M. Iglesias, N. Snejko, E. Gutiérrez-Puebla, M. Á. Monge, *J. Am. Chem. Soc.* **2015**, *137*, 6132–6135.
[56] N. L. Rosi, J. Kim, M. Eddaoudi, B. Chen, M. O'Keeffe, O. M. Yaghi, *J. Am. Chem. Soc.* **2005**, *127*, 1504–1518.
[57] P. D. C. Dietzel, Y. Morita, R. Blom, H. Fjellvag, *Angew. Chem. Int. Ed.* **2005**, *44*, 6354–6358; *Angew. Chem.* **2005**, *117*, 6512–6516.
[58] P. D. C. Dietzel, R. Blom, H. Fjellvag, *Eur. J. Inorg. Chem.* **2008**, 3624–3632.
[59] P. D. C. Dietzel, B. Panella, M. Hirscher, R. Blom, H. Fjellvag, *Chem. Commun.* **2006**, 959–961.
[60] W. Zhou, H. Wu, T. Yildirim, *J. Am. Chem. Soc.* **2008**, *130*, 15268–15269.
[61] R. Sanz, F. Martínez, G. Orcajo, L. Wojtas, D. Briones, *Dalton Trans.* **2013**, *42*, 2392–2398.
[62] S. Bhattacharjee, J. S. Choi, S. T. Yang, S. B. Choi, J. Kim, W. S. Ahn, *J. Nanosci. Nanotechnol.* **2010**, *10*, 135–141.
[63] J. A. Botas, G. Calleja, M. Sánchez-Sánchez, M. G. Orcajo, *Int. J. Hydrogen Energy* **2011**, *36*, 10834–10844.
[64] L. J. Wang, H. Deng, H. Furukawa, F. Gándara, K. E. Cordova, D. Peri, O. M. Yaghi, *Inorg. Chem.* **2014**, *53*, 5881–5883.
[65] D. Kim, A. Coskun, *Angew. Chem. Int. Ed.* **2017**, *56*, 5071–5076; *Angew. Chem.* **2017**, *129*, 5153–5158.
[66] C. Castillo-Blas, N. Snejko, V. A. de la Peña-O'Shea, J. Gallardo, E. Gutiérrez-Puebla, M. A. Monge, F. Gándara, *Dalton Trans.* **2016**, *45*, 4327–4337.
[67] C. Castillo-Blas, V. A. de la Peña-O'Shea, I. Puente-Orench, J. Romero de Paz, R. Saez-Puche, E. Gutiérrez-Puebla, F. Gándara, Á. Monge, *Sci. Adv.* **2017**, *3*, e1700773.
[68] A. Monge, N. Snejko, E. Gutiérrez-Puebla, M. Medina, C. Cascales, C. Ruiz-Valero, M. Iglesias, B. Gomez-Lor, *Chem. Commun.* **2005**, 1291–1293.

Received: July 3, 2018
Accepted: July 26, 2018
Published online on August 17, 2018

JACS
JOURNAL OF THE AMERICAN CHEMICAL SOCIETY

Article

Encoding Metal-Cation Arrangements in Metal-Organic Frameworks for Programming the Composition of Electrocatalytically Active Multi-Metal Oxides

Celia Castillo-Blas, Nieves López-Salas, Maria C. Gutiérrez, Inés Puente Orench, Enrique Gutiérrez-Puebla, María Luisa Ferrer, M. Ángeles Monge, and Felipe Gándara

J. Am. Chem. Soc., **Just Accepted Manuscript** • DOI: 10.1021/jacs.8b12860 • Publication Date (Web): 09 Jan 2019

Just Accepted

ACS Publications

is published by the American Chemical Society. 1155 Sixteenth Street N.W., Washington, DC 20036

Encoding metal-cation arrangements in metal-organic frameworks for programming the composition of electrocatalytically active multi-metal oxides.

Celia Castillo-Blas†, Nieves López-Salas†, María C. Gutiérrez†, Inés Puente-Orench‡§, Enrique Gutiérrez-Puebla†, M. Luisa Ferrer†, M. Ángeles Monge†*, Felipe Gándara†*.

†Materials Science Factory, Instituto de Ciencia de Materiales de Madrid (ICMM) - Consejo Superior de Investigaciones Científicas (CSIC), C/ Sor Juana Inés de la Cruz, 3, Madrid, Spain.

‡Univ. Grenoble Alpes, CNRS, Grenoble INP, Institut Néel, 38000 Grenoble, France

§Institut Laue Langevin, 71 avenue des Martyrs, CS 20156, 38042 Grenoble Cedex 9, France

KEYWORDS. Multication metal-organic frameworks, Oxygen reduction, spinel oxides.

ABSTRACT: In the present contribution, we report how through the use of metal-organic frameworks (MOFs) composed of addressable combinations of up to four different metal elements it is possible to program the composition of multi-metal oxides, which are not attainable by other synthetic methodologies. Thus, due to the ability to distribute multiple metal cations at specific locations in the MOF secondary building units it is possible to code and transfer selected metal ratios to multi-metal oxides with novel, desired compositions through a simple calcination process. The demonstration of an enhancement in the electrocatalytic activity of new oxides by pre-adjusting the metal ratios is here reported for the oxygen reduction reaction, for which activity values comparable to commercial Pt/C catalysts are reached, while showing long stability and methanol tolerance.

INTRODUCTION

Materials that are able to modulate their chemical composition through the combination of various elements while preserving their overall structure are scarce. Thus, the introduction of various metal elements in a same compound is synthetically challenging because typically a mixture of phases is obtained.[1] In this context, metal-organic frameworks, MOFs, are demonstrating to be a suitable class of materials to combine multiple metal elements within a same structure type.[2] MOFs are reticular materials formed by the joining of metal cations through organic linkers, giving rise to solids with extended, porous frameworks.[3] In MOF chemistry, it is possible to introduce more than one metal cation within a given framework by following different synthetic approaches, ranging from post-synthetic transmetalation[4-5] to one-pot synthesis with multiple cations.[6-7] MOFs prepared with multiple metal cations exhibit properties that differ from their single-metal counterparts, such as enhancement in gas sorption selectivity,[8] luminescent properties,[9] mechanical properties,[10]or catalytic activity.[11-12] Recently, we have showed that MOFs offer a suitable platform to incorporate various combinations of metal cations in a controllable way within a same crystal structure.[13] Judicious selection of inorganic secondary building unit (SBU), network topology, and initial molar ratios resulted in the formation of a series of isoreticular materials incorporating various metal-cation sequences formed by two or three elements. On the other hand, the use of MOFs as precursors to obtain other classes of solids though thermal treatment has emerged as an alternative to traditional synthetic routes, offering the possibility to transfer some of the MOF structural features to the resulting materials.[14-16] In consequence, MOFs have been used to produce different types of metal oxides and metal oxide/carbon materials with unprecedented nanostructures, which find application in renewable energy technologies, such as metal-air batteries, fuel cells, and water electrolyzers through their use as catalysts for efficient and stable oxygen reduction reaction (ORR) and oxygen evolution reaction (OER).[17-20]

Following this line, in the present contribution we demonstrate that i) it is possible to produce MOFs incorporating complex metal arrangements composed of four different metal cations; ii) this compositional complexity emerging from the control on the cation arrangements can be translated to other classes of active solids by using MOFs as precursors. In particular, we show that thermal treatment of multi-metal MOFs with selected metal arrangements is an effective way to prepare multi-metal oxides with spinel structure and selected compositions; iii) the composition of the resulting spinel type oxides can be programmed from the MOF synthesis step, resulting in adjustment of their activity as electrocatalyst in the ORR. Consequently, we have prepared a series of oxides with spinel structure, some of them with compositions that have not been reported previously, including zinc, cobalt, manganese and calcium in the same material. Our results show that spinel type oxides with unprecedented compositions can be prepared from multi-

metal MOFs following a simple thermal treatment, exhibiting catalytic activity that is comparable to that of commercial Pt/C catalyst in terms of current density (97.2%), preserving the activity after 5000 seconds, and without suffering from poisoning effects due to presence of methanol.

EXPERIMENTAL SECTION

MOF synthesis

General synthetic procedure for all the MOFs involve the dissolution of the selected metal salts and the organic linker in a water:ethanol:nitric acid solvent mixture, followed by heating at 170 °C overnight. An illustrative example of the synthesis procedure is given here for the compound with formula $Zn_{0.23}Mn_{0.44}Co_{0.33}$(hfipbb): 4,4'-(hexafluoroisopropylidene)bis(benzoic acid) ($C_{17}H_{10}O_4F_6$, H_2hfipbb) (78 mg, 0.2 mmol), $Zn(NO_3)_2{\cdot}6H_2O$ (11 mg, 0.047 mmol), $MnCl_2{\cdot}6H_2O$ (29 mg, 0.147 mmol) and $Co(NO_3)_2{\cdot}6H_2O$ (43 mg, 0.147 mmol) were dissolved in 5 mL of distilled water and 5 mL of absolute ethanol and 300 µL of a 1 M HNO_3 solution. The mixture was stirred at room temperature for 5 minutes, placed in a Teflon-lined steel autoclave, and heated at 170 °C overnight. After cooling to room temperature, blue needle shaped crystals were filtered off, washed with water and acetone, and dry under vacuum. Yield: 32 mg, 24% (based on linker). All other MOFs were similarly prepared using the amounts of metal salt specified in table S1, and keeping the same amounts of linker and solvents. The CHN and ICP analyses are contained in table S2.

Multi-metal oxide synthesis.

Multi-metal MOFs (100 mg) were subjected to a standard calcination process consisting of a thermal treatment in air, at 800 °C for 24 hours, with a heating rate of 2.5 °C / min in a zirconia crucible.

Single crystal X-ray diffraction

Crystals were selected with a polarized optical microscope for a single crystal X-ray diffraction experiment. Single crystal X-ray data were collected in Bruker four circle kappa-diffractometers equipped with a Cu INCOATED microsource, operated at 30 W power (45 kV, 0.60 mA) to generate Cu Kα radiation (λ = 1.54178 Å), and a Bruker VANTEC 500 area detector (microgap technology). Diffraction data were collected exploring over the reciprocal space in a combination of φ and ω scans to reach a resolution of 0.85 Å, with a completeness > 95%, and redundancy >3. For this, either a generic quadrant collection strategy or a specific one determined using Bruker APEX3 software suite was used. The exposure time was adjusted based on the size and diffracting quality of the specimens, each exposure covering 1° in ω or φ. Unit cell dimensions were determined for least-squares fit of reflections with I>4σ. The structures were solved by intrinsic phasing or direct methods, implemented in SHELX package. The hydrogen atoms were fixed at their calculated positions using distances and angle constraints. All calculations were performed using APEX3 software for data collection and OLEX2-1.2[21] and SHELXTL[22] to resolve and refine the structure. All non-hydrogen atoms were anisotropically refined. It should be noted that the chemical composition deduced from the X-ray diffraction data do not necessarily correspond with that of the bulk analytically determined, due to the close atomic number of the employed elements. Therefore, ID codes are given based on the CHN/ICP analyses for all samples. Tables S3-S20 summarize the crystal and refinement data of all MOFs compositions.

X-ray powder diffraction

Powder X-ray diffraction (PXRD) patterns (figures S1-S3 and S15-S18) were measured with a Bruker D8 diffractometer with a copper source operated at 1600 W, with step size = 0.02 ° and exposure time = 0.5 s/step for MOFs measurements and step size = 0.016 ° and exposure time = 1.5 s/step for calcination products.

Neutron powder diffraction

Neutron powder diffraction experiments were performed on the high-intensity powder diffractometer D1B and high resolution HRPT powder diffractometer at the Institut Laue-Langevin in Grenoble (France) and Paul Scherrer Institut (Switzerland), respectively. The samples were contained in 5 mm cylindrical vanadium cans and placed inside a cryostat. The data sets were collected with calibrated neutrons of wavelengths 2.5260 Å and 1.4939 Å for D1B and HRPT, respectively.

ORR activity

The ORR activity was investigated using an Autolab PGSTAT302N with a three-electrode setup. A platinum mesh and an Ag/AgCl/KCl (0.1 M) were used as counter and reference electrodes, respectively. The active material was prepared mixing 3.5 mg of super P carbon black and 1.5 mg of the corresponding catalytic oxide with 47.5 µL of Nafion 177 and 117 µL of absolute ethanol. The mixture was sonicated for 15 minutes. The glassy carbon rotating-disk-working electrode (RDE, 4 mm in diameter) was polished and coated twice, by drop casting, with 3.5 µL of slurry. All electrochemical measurements, including cyclic voltammograms (CV), linear sweep voltammograms (LSV) on a RDE at a rotation rate of up to 2000 rpm and chronoamperometry, were performed at room temperature in 0.1 M KOH solutions, previously purged with high purity either nitrogen or oxygen for at least 1 hour. Both CV and LSV were recorded at 10 mVs^{-1} scan rate and the potential window ranged from 0.0 to -0.8 V. The stability and tolerance of the materials to methanol (CH_3OH) crossover was studied by chronoamperometry measurements, which were performed at 1600 rpm over 5000s and upon the addition of CH_3OH (0.3 M final concentration) to the O_2-saturated 0.1 M KOH electrolyte.

RESULTS AND DISCUSSION

The role of zinc as structure directing element in multi-metal complex MOFs

In our previous work, we demonstrated that the incorporation of multiple metal elements within a same MOF crystal can be accomplished with control over the disposition of the metal cations.[13] In particular, we showed that zinc, cobalt, manganese, and/or calcium can be combined in a SBU and their atomic arrangements in the SBUs addressed through the right combination of the initial molar codes (*i.e.*, molar ratios), as consequence of the differences in the coordination environment of the selected metal elements. A series of

isoreticular materials were prepared, with a structure based on the MOF known as ZnPF-1 (Zn-hfipbb),[23] which consists of helical shaped inorganic SBUs composed of zinc atoms in tetrahedral coordination environment. Cobalt, manganese, or calcium atoms with octahedral coordination environment were introduced in the SBU, resulting in a change in the crystal symmetry, while preserving the original network topology (Figure 1). Furthermore, we found that cobalt atoms might be found in both tetrahedral and/or octahedral environment depending on the selected initial molar ratios, while manganese and zinc cations are exclusively in octahedral or tetrahedral coordination, respectively. These differences in the preferential environments for the metal cations allowed us to produce different metal cation arrangements in the inorganic SBUs. By adjusting the initial three-element molar code it is possible to address the location of cobalt cations in the SBUs. Following these findings, we decided to evaluate whether it would be possible to introduce different combinations of metal cations, with the ultimate goal of demonstrating that the metal arrangements and ratios might be translated to metal oxides after MOF calcination, as described below.

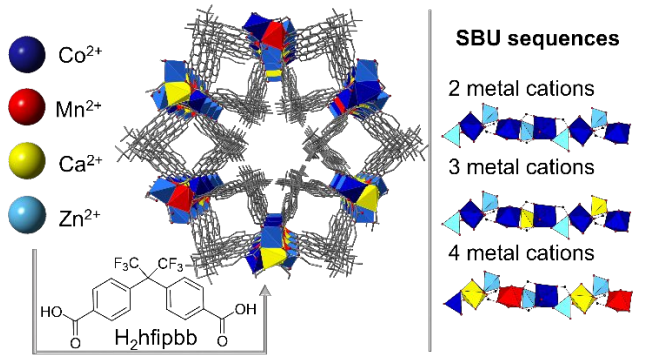

FIGURE 1. The multi-metal MOF is formed by the combination of different cations (Zn^{2+}, Co^{2+}, Mn^{2+} and Ca^{2+}) forming a helical inorganic SBU, and the organic linker H_2hfipbb (left). The helical shaped inorganic SBUs are formed by alternating tetrahedral and octahedral coordination polyhedra. The SBUs contain 2, 3 or 4 different metal elements (right).

All the previously reported members of this family of materials include zinc in their composition, as the addition of this element was found to be necessary to yield the desired MOF type, suggesting a structure directing role of this element. To study to what extend this is accurate, we first decreased the relative amount of zinc to produce MOFs with higher content of manganese and cobalt. Generally, when synthesis experiments were carried out with the use of either cobalt or manganese, and low amount or absence of zinc, other crystalline phases were obtained.[12] However, we found that it is possible to obtain the same MOF topology in absence of zinc provided that cobalt and manganese are combined at appropriate ratios, although the product was obtained only with low yield (9 mg, 7% based on ligand). A MOF was thus prepared from a Mn:Co 1:1 ratio with the resulting composition of $Mn_{0.41}Co_{0.59}$(hfipbb). Single crystal X-ray diffraction analysis shows a unit cell in which the *c* parameter is twice that of the ZnPF-1 MOF, and a SBU with alternating octahedral and tetrahedral sites (as it happens in previously reported Zn:Mn and Zn:Co members of the series). Manganese atoms are in octahedral environment, while cobalt cations are mostly in tetrahedral one, with some of them in octahedral environment, partly replacing the manganese positions. Neutron powder diffraction analysis further supports this metal cation arrangement, also showing that there is no temperature dependent structural change in the 298 K to 10 K range (Figure S4).

Despite this experiment shows that it is possible to obtain the same MOF topology in absence of zinc, the resulting yield is very low (7%). Moreover, all other explored combinations of Co:Mn molar codes were not successful in obtaining this MOF type. Therefore, the role of zinc as structure directing element in the achieving of this MOF topology come out evident, being required to afford an inorganic SBU that otherwise has shown adaptability and dynamism for including multiple elements with variable coordination environments.

Obtaining new ternary and quaternary multi-metal MOFs with programmed composition

Based on the previous success preparing Zn-Mn-Co MOFs with various cation arrangements, we prepared five new ternary multi-metal MOFs combining Zn, Co, and Mn with new metal-cation ratios (table S1, entries 1-5). In line with our previous observations, and due to the different incorporation kinetic of the metal cations, it was necessary to start with a high amount of cobalt in order to obtain MOFs with a large content of this element in their composition. This is in contrast to the case of manganese, which is more homogeneously incorporated in all the cases.

In addition to ternary systems, we have now expanded the number of different cations that can be incorporated up to four elements. Previously, we already showed that calcium can be introduced in this MOF structure when combined with zinc and either cobalt or manganese.[12] Now, we have synthesized eleven new quaternary multi-metal MOFs combining zinc, cobalt, manganese and calcium. Ultimately, we have prepared these materials to demonstrate that metal oxides with new compositions including these four elements can be produced from MOFs, and that their electrocatalyitc activity is subsequently enhanced. The employed molar codes and the resulting MOF formulae are given in table S1, entries 6-16. In all cases, the resulting MOF structures exhibit SBUs where the cations are in octahedral and tetrahedral coordination environments, without any compositional gradient, as demonstrated by the neutron powder diffraction and SEM-EDS experiments (figures S6-S9 and S12-S14).

The analysis of the obtained metal arrangements shows that the combination of four elements in the initial molar codes results in a complex behavior with and interplay of the four cations, so that a direct relationship between input and output ratios is not evident. Use of an equimolar code (1:1:1:1) results in a low incorporation of calcium into the MOF with composition [$Zn_{0.42}Mn_{0.42}Co_{0.11}Ca_{0.06}$(hfipbb)]. Increasing the initial amount of calcium results in a larger incorporation of this element, although this increment is not linearly related to the starting amount, as demonstrated by the material prepared from a 1:1:1:7 molar code (table S1, entry 8). This can be explained by the fact that calcium atoms will only be occupying sites with octahedral environment in the SBU, which are readily occupied by manganese atoms. However, if the relative amount of calcium and cobalt are simultaneously increased, a higher incorporation of calcium is achieved. Thus,

the MOF prepared from a 1:1:4:4 molar code exhibits a $Zn_{0.18}Mn_{0.24}Co_{0.41}Ca_{0.16}$(hfipbb) formula. This observation was consistent with our previous work, where we already found that in ternary Zn:Co:Ca systems the amount of calcium increased when there is larger presence of cobalt.[13] We hypothesized with the fact that presence of cobalt – calcium pairs in the SBU might be favored over zinc – calcium ones. Indeed, the MOF with the largest amount of calcium was obtained in absence of zinc, and the material prepared from a Mn:Co:Ca 1:2:2 molar code has a $Mn_{0.23}Co_{0.50}Ca_{0.27}$(hfipbb) formula. Single crystal X-ray diffraction analysis shows a SBU with cobalt atoms in tetrahedral environment, and calcium and manganese atoms in octahedral coordination environment. This particular result seems to indicate that certain dyads of metal cations might also play a structure directing role analogue to zinc, although further experiments are necessary to confirm to what extend this can be generalized to other metal element combinations.

Obtaining of multi-metal oxides with programmed composition through multi-metal MOF calcination

Through our developed method to produce complex multi-metal MOFs, we have in hand an array of materials with precise control of the metal cation distribution, which in principle could be advantageous to obtain oxides with compositions that are not attainable following other synthetic routes (Figure 2). In principle, the ability to pre-organize various cations at desired ratios in the helix-shaped SBU of this MOF provides a platform to adjust the composition of MOF derived materials. Thus, we proceeded to expose the MOFs to a calcination process, and the structure type of the resulting oxide was analyzed with the use of PXRD (Figures S15-S18). Results of the obtained oxides are summarized in table S21.

Multi-metal MOFs were subjected to a standard calcination process (1), consisting of a thermal treatment in air, at 800 °C for 24 h, with a heating rate of 2.5 °C / min, to obtain the corresponding multi-metal oxides preserving the metal ratios.

(1) $3[Zn_wMn_xCo_yCa_z\ (C_{17}H_8O_4F_6)] + 48.5O_2 \rightarrow (Zn_{3w}Mn_{3x}Co_{3y}Ca_{3z}O_4) + 51CO_2 + 3H_2O + 18HF$

Thermal gravimetric analysis of the corresponding MOFs indicate that the decomposition of the materials occurs at 500 °C, with no additional weight loss at higher temperature (figures S19-S21). Therefore, the organic linker is fully combusted at the employed calcination temperature. A CHN elemental analysis for calcined samples further confirmed the absence of any organic species in the resulting solids, which were additionally characterized with the use of SEM, TEM, PXRD, and EDS. Field emission SEM images show that the MOF crystals morphology is maintained in the resulting oxides after the heating process (figures S22-S24).[24] The resulting solids are composed of crystallites of size in the range 30 to 2 µm, which are aggregated preserving the shape of the precursor MOF crystal (Figure 3). The SEM-EDS (figures S25-S27) and TEM-EDS (figures S28-S29) analyses present consistent results and demonstrate a clear correspondence between the metal ratios in the aggregates and the individual particles (figure 4). For the sake of comparison, we also studied the MOF prepared with zinc as only metal cation (ZnPF-1).[23] As expected, calcination of ZnPF-1 resulted in the formation of wurtzite type oxide, according to the PXRD pattern (figure S15A).

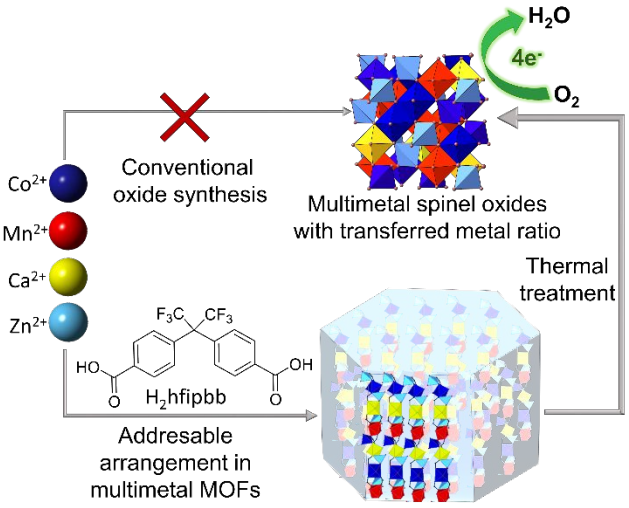

FIGURE 2. Thermal decomposition of multi-metal MOFs allow the obtaining of multi-cation oxides with compositions not attainable with conventional oxide synthetic routes. The metal ratios in the resulting oxides are transferred from their correspondent parent MOFs.

Binary Zn:Co, Zn:Mn, and Zn:Ca systems

Binary systems consisting of zinc and cobalt resulted in a mixture of crystalline phases, which were identified as wurtzite as major phase, mixed with spinel type oxide. Calcination of the MOF formed from Zn:Co 1:10 molar code and formula $Zn_{0.21}Co_{0.79}$(hfipbb), results in the formation of cubic spinel oxide as major phase, although with presence of a small amount of wurtzite (figures S15E). TEM and EDS analyses of this solid indicate that the formed oxide particles do not have a homogeneous composition. This is not surprising, as the parent MOF crystals exhibited a clear compositional gradient, with internal and external areas being rich in zinc or cobalt, respectively (figures S28A-C). Similarly, calcination of binary systems composed of zinc and calcium also resulted in formation of wurtzite oxide, and in the cases where there is a larger amount of calcium in the MOF, the presence of fluorite was also detected (figures S18G-H and S28D-E). Calcination of the MOF formed from Zn:Mn 1:1 molar code resulted in a mixture of phases containing hetaerolite (tetragonal) and spinel (cubic) type oxides as major phases, as well as traces of other crystalline phases that could not be unambiguously identified (figure S15F).

Ternary Zn:Mn:Co, Zn:Mn:Ca, Mn:Co:Ca systems

On the other hand, the calcination of ternary multi-metal MOFs including zinc, manganese, and cobalt, resulted in the formation of spinel type oxides. When the initial Zn molar ratio was higher than 30 at%, other crystalline phases were also detected in the PXRD patterns, (mainly wurtzite). By decreasing the amount of zinc in ternary multi-metal MOFs, we were able to obtain spinel type oxides as only product of the calcination process, as proved by the PXRD, SEM and TEM analyses. Thus, seven new multi-metal oxides with cubic spinel structure were prepared from the calcination of the corresponding multi-metal MOFs (figure 5A and S16-17A). Their compositions are detailed in table 1, entries 1-7.

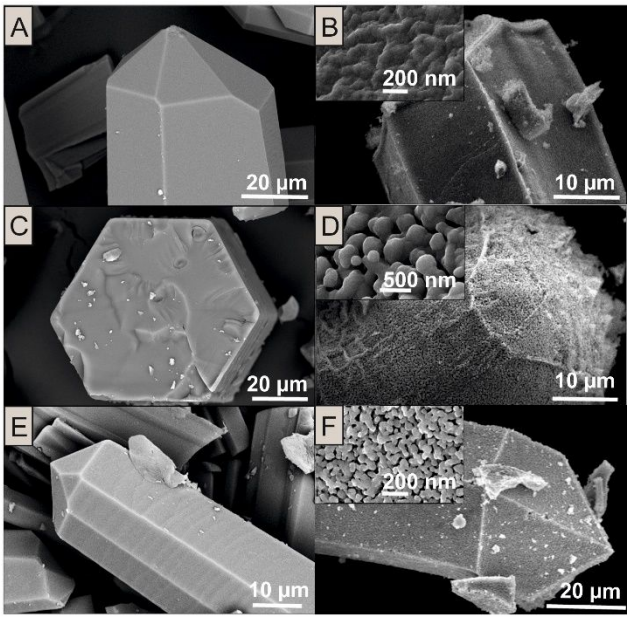

FIGURE 3. The figure shows MOF-crystal SEM pictures in the left column, and FESEM images of the corresponding calcined product, and its magnification images (x200,000), in the right column. A) $Zn_{0.17}Mn_{0.45}Co_{0.48}$(hfipbb) crystal SEM image; B) FESEM picture of corresponding calcined product with formula $Zn_{0.51}Mn_{1.35}Co_{1.14}O_4$; C) $Mn_{0.23}Co_{0.50}Ca_{0.24}$(hfipbb) crystal SEM image; D) FESEM picture of $Mn_{0.23}Co_{0.50}Ca_{0.24}$(hfipbb) calcined product resulting in a cubic spinel with formula $Mn_{0.69}Co_{1.50}Ca_{0.81}O_4$; E) $Zn_{0.16}Mn_{0.47}Co_{0.33}Ca_{0.03}$(hfipbb) crystal SEM image; F) FESEM picture of calcined product of $Zn_{0.16}Mn_{0.47}Co_{0.33}Ca_{0.03}$(hfipbb) resulting in a cubic spinel with formula $Zn_{0.48}Mn_{1.41}Co_{0.99}Ca_{0.09}O_4$.

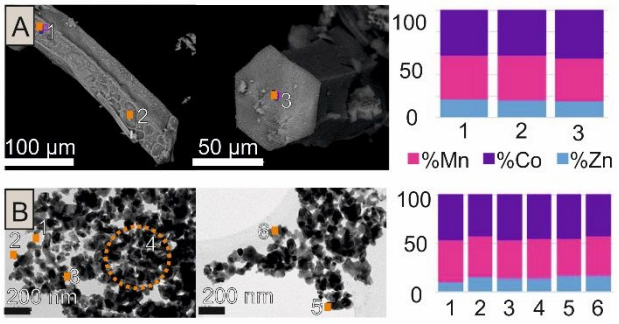

FIGURE 4. A) SEM-EDS analyses and B) TEM-EDS analyses from $Zn_{0.36}Mn_{1.26}Co_{1.38}O_4$ spinel. Orange spots indicate the areas where EDS were performed. Plot (right) shows the metal ratios by EDS analyses, where each column corresponds to the area indicated by a number in the SEM pictures.

In the case of ternary multi-metal MOFs prepared from molar codes including zinc, manganese, and calcium, spinel oxides were also formed, but mixed with wurtzite and to less extent with other crystalline phases that could not be unambiguously identified (figure S15-18). However, calcination of the MOF prepared from a molar code Mn:Co:Ca 1:2:2 also resulted in the obtaining of spinel type oxide as only phase (figure 5B and S18F). In this case, as deduced from the experimentally determined formula of $Mn_{0.69}Co_{1.50}Ca_{0.81}O_4$, an inverse spinel should be formed, with cobalt atoms occupying tetrahedral sites, and manganese and calcium atoms at the octahedral sites.

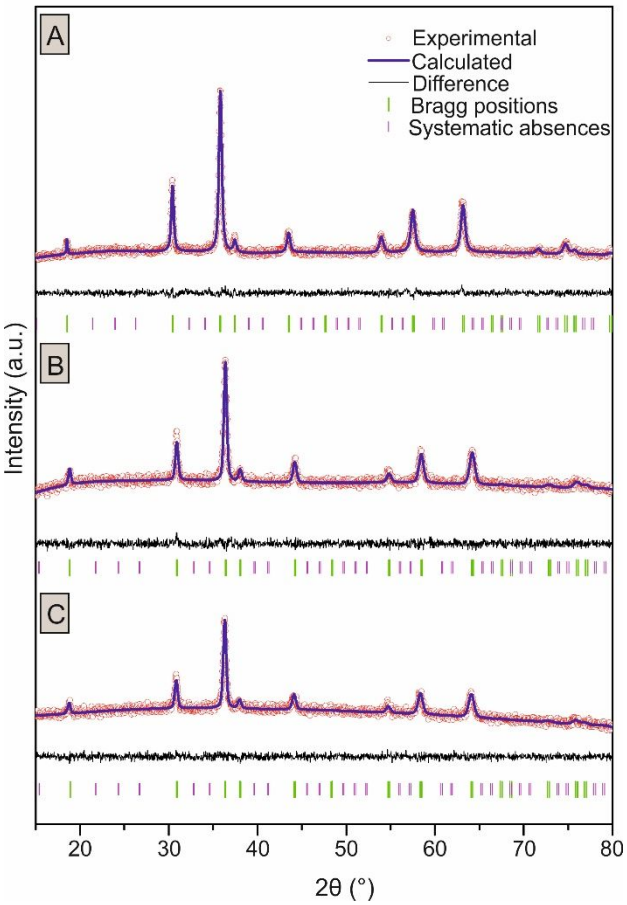

FIGURE 5. Full pattern profile refinement plot of A) $Zn_{0.51}Mn_{1.35}Co_{1.14}O_4$ spinel with *Fd-3m* space group (a = 8.260 Å); B) $Mn_{0.69}Co1.50Ca_{0.81}O_4$ spinel with *Fd-3m* space group (a = 8.211 Å); C) $Zn_{0.48}Mn_{1.41}Co_{0.99}Ca_{0.09}O_4$ spinel with *Fd-3m* space group (a = 8.306 Å).

Quaternary Zn:Mn:Co:Ca systems

Multi-metal spinel oxides containing four elements were readily obtained by calcination of the selected quaternary multi-metal MOFs. Thus, calcination of the MOF with composition $Zn_{0.42}Mn_{0.42}Co_{0.11}Ca_{0.06}$(hfipbb) results in the obtaining of an oxide with cubic spinel structure (figure S17) and formula $Zn_{1.26}Mn_{1.26}Co_{0.33}Ca_{0.18}O_4$, as determined by ICP analysis (figure S16). To the best of our knowledge, this is the first time that spinel oxides are obtained incorporating Zn, Mn, Co, and Ca in their structure. Most importantly, different metal combinations initially programmed in the selected quaternary multi-metal MOFs could be translated to the spinel oxides (figures 5C and S17-18). Thus, a series of eight tetra-cation spinel oxides with variable composition and general formula $\mathbf{Zn_wMn_xCo_yCa_zO_4}$ have been obtained (table 1, entries 8-15), where 0.39<w<1.26, 0.72<x<1.26, 0.33<y<1.56, and 0.09<z<0.66.

However, it should be noted that certain limitations for the obtaining of spinel as sole phase where observed regarding the combination of metal elements in the selected MOF. Thus, for MOFs with a low content of manganese, as in the case of the material prepared from molar code Zn:Mn:Co:Ca 1:1:4:8, presence of wurtzite and other crystal phases were detected in

the PXRD pattern of the calcined solid, along with the spinel oxide (table S21, entry 30 and figure S18D). Conversely, when starting from a MOF with a large amount of zinc in the molar code (Zn:Mn:Co:Ca 2:1:2:2), wurtzite and another unknown phase were formed along with the spinel oxide (table S21, entry 27 and figure S18A). Interestingly, the maximum amount of zinc allowed for the obtaining of pure spinel oxides avoiding the appearance of wurtzite is larger in quaternary multi-metal MOFs than in ternary systems, demonstrating the importance of the initial cation arrangement of the MOF precursor on the structure of the obtained oxides. Nevertheless, we emphasize the suitability and wide applicability of this process to prepare a range of spinel type oxides with novel, desired compositions, easily translated from MOFs with programmable cation arrangements, with a simple calcination process. Furthermore, at the view of these initial results, we anticipate that other types of mixed-metal oxides can be obtained through the judicious selection of MOF topology, SBU type, and cation arrangement. Synthetic studies are currently ongoing in this direction.

Evaluation of multi-metal spinel oxides as ORR electrocatalysts.

Current benchmark catalysts for the ORR are based on the use of platinum, but metal scarcity, its high cost and inherent deactivation problems have fostered an intensive search for alternatives. As a result, a wide spectrum of materials such as transition metal-/metal oxide nanoparticles,[25] perovskites,[26] spinels and heteroatom doped 3D and 2D carbonaceous materials[27] are being analyzed as substituting candidates. Among them, transition metal spinels show not only an affordable cost but also the most promising performance as both ORR and OER electrocatalysts.[28] Among the list of transition metals employed, spinel materials based on Mn, Co, Fe and Ni have been widely studied due to their outstanding performance, which is strongly dependent on subtle changes in composition. For example, it has been proposed that in $Mn_xCo_{3-x}O_4$ spinel oxides, the activity improves when $x \leq 2.0$ because Co^{3+} and Mn^{3+} cations present an internal redox reaction that generates Co^{2+} and Mn^{4+} pairs, responsible for an increase in conductivity.[29]

Recently, the use of bimetallic Mn-Co MOFs to obtain multimetal-spinel oxides has been reported. However, other crystal phases might appear during the thermal treatment.[30] In addition, when the spinels have been obtained as pure phases, differences in the structure were found depending on the amount of manganese and cobalt present, finding that mixed $Mn_xCo_{3-x}O_4$ spinels with a high content of manganese have a tetragonal structure (space group *I4-2m*) while spinels rich in Co are cubic (space group *Fd-3m*).[31] Zn-Co multimetal MOFs have been used also to obtain cubic Zn-Co spinel oxides.[32]

Following our methodology to translate compositional complexity from multi-metal MOFs to oxides, we have evaluated seventeen tri- and tetra-metallic spinel oxides with unprecedented compositions as electrocatalysts for ORR. First, we investigated the electrochemical activity of the samples towards the ORR by running cyclic voltammetry (CV) in both O_2 and N_2 saturated electrolyte solutions. In all cases CV curves in N_2 saturated electrolyte showed a quasi-rectangular shape without any redox peak (figures S30-S32) indicating the good stability of the materials in the studied potential window. Interestingly, voltammograms of all the samples in O_2-saturated electrolyte exhibited a clear cathodic peak centered between 0.3 and 0.42 V probing the electrocatalytical activity of the samples (figures S30-S32). Even though all multi-metal spinel oxides show activity towards the ORR, they present a relatively large overpotential of 200-290 mV, as compared to that of the commercial Pt/C catalyst. One approach to decrease the overpotential of a specific reaction is to load the active material in a more conductive support (e.g., carbon nanotubes, graphene).[33-37] In the present study, samples were evaluated after being mixed with active carbon and Nafion as a binder. However, given no strong coupling between the carbon and the active material (in this case the MOF derived spinel) no major change in the local electron transfer was expected and thus, the overpotential was still large.[37]

The Koutecky-Levich (K-L) plots obtained from the correspondent LSVs at different rotation speeds present a good linearity, indicating that current was mainly kinetically controlled (figures S33-S38). Table 1 summarizes the number of transferred electrons (Ne, obtained from the K-L analysis), and the current density of each sample expressed as % of current density measured for commercial Pt/C(20%w). The systematic translation of compositional complexity from multi-metal MOFs to oxides allows extracting important information when the evaluation of the sample compositions is done. Thus, analysis of Zn-Co-Mn spinels, including solids with $Zn_{0.36}Mn_{1.26}Co_{1.38}O_4$, $Zn_{0.66}Mn_{0.96}Co_{1.38}O_4$, $Zn_{0.69}Mn_{1.32}Co_{0.99}O_4$, $Zn_{0.51}Mn_{1.23}Co_{1.26}O_4$, $Zn_{0.36}Mn_{1.17}Co_{1.47}O_4$, $Zn_{0.30}Mn_{1.20}Co_{1.50}O_4$ and $Zn_{0.51}Mn_{1.35}Co_{1.14}O_4$ composition (Table 1 entries 1 to 7), evidences a strong influence of the ratios of all three different elements on the catalytic performance. A simple correlation between composition variation and activity is not evident, and rather a complex behavior is observed. Recently,[36] a correlation between the Mn/Co ratio and electrocatalytic activity due to superexchange effects between the octahedral sites has been reported for Zn:Co:Mn spinels where the tetrahedral sites are occupied by zinc. In our case, the tetrahedral sites are occupied not only by zinc, due to the sample metal ratios, and thus other effects should also influence the catalytic activity. We are currently investigating the distribution of the metal cations in the spinel structure to determine the occupancy of each site. Nevertheless, we have found that samples containing the three metal elements (*i.e.*, Zn, Mn and Co) also exhibited a major contribution of the 4 e^- transfer mechanism and larger current densities (see Figure 6). Among the evaluated samples, the oxide with $Zn_{0.51}Mn_{1.35}Co_{1.14}O_4$ composition (table 1, entry 7) demonstrated the best performance, with a high limiting current density value (91.4% of that found for commercial Pt based catalysts) and a number of transferred electrons close to four (3.80).

When comparing these results with the performance of the trimetallic sample containing Mn, Co and Ca ($Mn_{0.69}Co_{1.50}Ca_{0.81}O_4$, table 1, entry 17), we realized that this spinel also exhibited an excellent behavior as catalyst in the ORR with a slightly lower current density of 87.2% compared with Pt/C(20 wt %) and a large contribution of the 4 electron transfer mechanism (Ne of 3.82) (Figure 7a). Despite calcium as such is not active towards the ORR, its presence in the spinel structure influences the overall activity. For example, it

may enhance O_2 adsorption,[37] and moreover, calcium cations should be exclusively occupying octahedral sites (unlike Zn which preferentially occupies tetrahedral sites), therefore inducing the inversion of the spinel structure and altering Mn and Co oxidation states.[38] Furthermore, when comparing with

Entry	Molar Code				MOF formula	Spinel formula	Ne	Current density (%)
	Zn	Mn	Co	Ca				
1	1	1	8	0	$Zn_{0.22}Mn_{0.32}Co_{0.46}$(hfipbb)	$Zn_{0.66}Mn_{0.96}Co_{1.38}O_4$	2.88	67.9
2	1	3	9	0	$Zn_{0.12}Mn_{0.42}Co_{0.46}$(hfipbb)	$Zn_{0.36}Mn_{1.26}Co_{1.38}O_4$	3.81	73.8
3	1	4	4	0	$Zn_{0.23}Mn_{0.44}Co_{0.33}$(hfipbb)	$Zn_{0.69}Mn_{1.32}Co_{0.99}O_4$	3.03	70.6
4	1	4	6	0	$Zn_{0.17}Mn_{0.41}Co_{0.42}$(hfipbb)	$Zn_{0.51}Mn_{1.23}Co_{1.26}O_4$	3.09	71.7
5	1	6	12	0	$Zn_{0.12}Mn_{0.39}Co_{0.49}$(hfipbb)	$Zn_{0.36}Mn_{1.17}Co_{1.47}O_4$	3.06	63.4
6	1	10	20	0	$Zn_{0.10}Mn_{0.40}Co_{0.50}$(hfipbb)	$Zn_{0.30}Mn_{1.20}Co_{1.50}O_4$	3.56	86.6
7	1	12	6	0	$Zn_{0.17}Mn_{0.45}Co_{0.38}$(hfipbb)	$Zn_{0.51}Mn_{1.35}Co_{1.14}O_4$	3.80	91.4
8	1	1	1	1	$Zn_{0.42}Mn_{0.42}Co_{0.11}Ca_{0.06}$(hfipbb)	$Zn_{1.26}Mn_{1.26}Co_{0.33}Ca_{0.18}O_4$	3.10	102.3
9	1	1	7	1	$Zn_{0.13}Mn_{0.27}Co_{0.52}Ca_{0.03}$(hfipbb)	$Zn_{0.39}Mn_{0.81}Co_{1.56}Ca_{0.09}O_4$	3.64	73.4
10	1	4	4	1	$Zn_{0.16}Mn_{0.47}Co_{0.33}Ca_{0.03}$(hfipbb)	$Zn_{0.48}Mn_{1.41}Co_{0.99}Ca_{0.09}O_4$	3.92	97.2
11	1	1	4	4	$Zn_{0.18}Mn_{0.24}Co_{0.41}Ca_{0.16}$(hfipbb)	$Zn_{0.54}Mn_{0.72}Co_{1.23}Ca_{0.48}O_4$	2.76	65.6
12	1	4	4	4	$Zn_{0.24}Mn_{0.37}Co_{0.31}Ca_{0.08}$(hfipbb)	$Zn_{0.72}Mn_{1.11}Co_{0.93}Ca_{0.24}O_4$	3.91	79.9
13	1	4	1	4	$Zn_{0.32}Mn_{0.40}Co_{0.15}Ca_{0.12}$(hfipbb)	$Zn_{0.96}Mn_{1.20}Co_{0.45}Ca_{0.36}O_4$	3.06	80.3
14	1	2	2	4	$Zn_{0.27}Mn_{0.34}Co_{0.26}Ca_{0.12}$(hfipbb)	$Zn_{0.81}Mn_{1.02}Co_{0.78}Ca_{0.36}O_4$	3.41	72.9
15	1	4	4	8	$Zn_{0.21}Mn_{0.27}Co_{0.30}Ca_{0.22}$(hfipbb)	$Zn_{0.63}Mn_{0.81}Co_{0.90}Ca_{0.66}O_4$	2.72	67.9
16	0	1	1	0	$Mn_{0.41}Co_{0.59}$(hfipbb)	$Mn_{1.23}Co_{1.77}O_4$	3.22	75.7
17	0	1	2	2	$Mn_{0.23}Co_{0.50}Ca_{0.27}$(hfipbb)	$Mn_{0.69}Co_{1.50}Ca_{0.81}O_4$	3.82	87.2
18	Pt/C(20%W)						3.67	100

Table 1. The starting molar codes, corresponding MOFs, spinel formula, electron tranfer number (Ne), calculated from the slope of their Koutechy-Levich plot in ORR, and current density are shown in columns 2, 3, 4, 5, and 6, respectively. Entries 1-2 MOFs were prepared according to reference [12].

the bimetallic Mn-Co spinel (table 1, entry 16), it becomes apparent that in this case the presence of calcium atoms improves the performance in terms of both current density and number of electrons.

Following we sought to study the performance of the newly prepared spinel oxides incorporating four different cations. At the view of the results of the tested materials, we noticed that the solid with the highest content of calcium did not show any improvement compared to the previously evaluated materials. Thus, the spinel with composition $Zn_{0.63}Mn_{0.81}Co_{0.90}Ca_{0.66}O_4$ (table 1, entry 15) showed a current density of 67.9% and 2.72 electrons. Similarly, the sample with $Zn_{0.54}Mn_{0.72}Co_{1.23}Ca_{0.48}O_4$ formula exhibited a current density of 65.6% and 2.76 electrons. These results seem to evidence that a large amount of calcium in the structure is detrimental for the electrocatalytic performance, with a low electron number that indicates that a two-electron process is dominant. However, we found that a fine adjustment of the oxide composition results in a significant improvement in current density. Thus, the oxide with $Zn_{0.48}Mn_{1.41}Co_{0.99}Ca_{0.09}O_4$ formula (table 1,

entry 10) demonstrated the best behavior among all the seventeen tested materials, with a current density of 97.2% and an electron transfer number of 3.92. This value is among the best obtained for spinel oxides employed as ORR electrocatalysts without additional processing or composite fabrication.

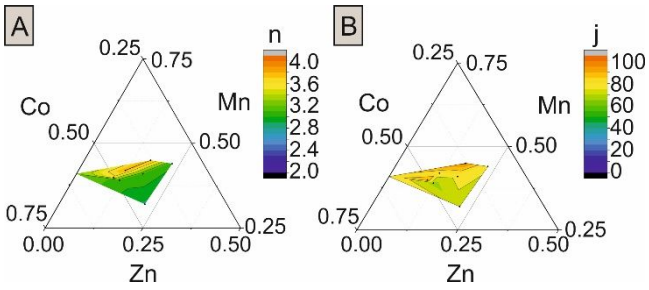

FIGURE 6. Ternary composition graph of zinc-manganese-cobalt spinels showing A) transferred electron number (n) and B) current density (j).

Both long term stability and methanol tolerance are important drawbacks of commercial Pt-based catalysts.[39] Thus, in order to compare our results, we also studied stability as well as tolerance towards methanol crossover of the spinel oxides showing the best catalytic activity. Stability was evaluated by performing a chronoamperometry in saturated O_2 KOH 0.1 M electrolyte at 1600 rpm for 5000 s. The results show that all the new materials outperform Pt based catalyst in stability terms showing a slight current attenuation of less than 8% (figure 7b). The methanol crossover test also showed that for all tested spinel oxides, the current is altered in less than a 4% after the addition of methanol. In contrast, methanol addition when using the commercial Pt/C catalyst promoted a sharp drop of the current response of *ca.* 70% (Figure 7b).

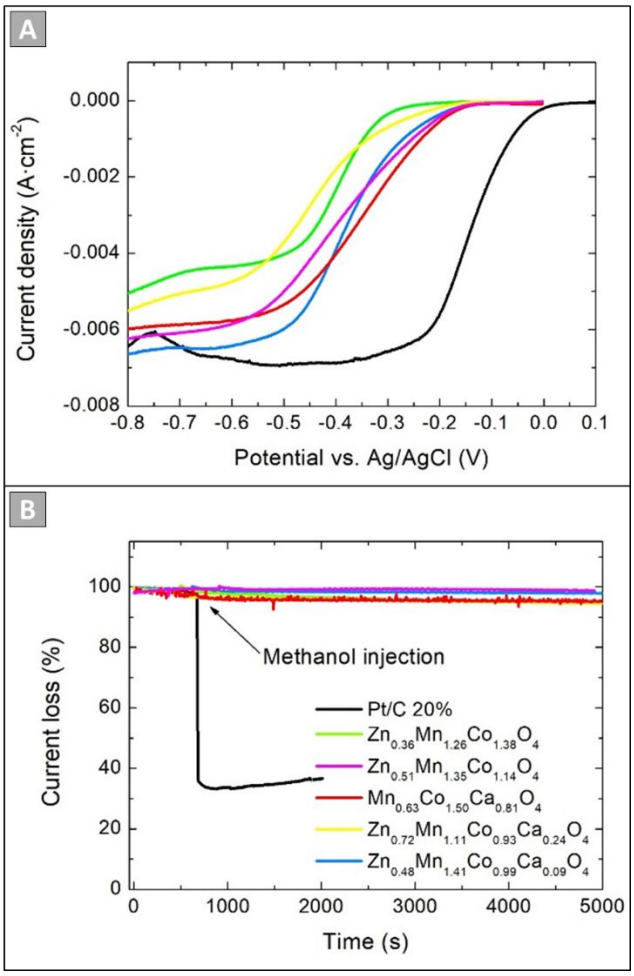

FIGURE 7. Results of the electrocatalytic ORR study. comparing commercial Pt/C (20%) (black), and spinels with composition $Zn_{0.36}Mn_{1.26}Co_{1.38}O_4$ (green), $Zn_{0.51}Mn_{1.35}Co_{1.14}O_4$ (pink), $Mn_{0.69}Co_{1.50}Ca_{0.81}O_4$, $Zn_{0.72}Mn_{1.11}Co_{0.93}Ca_{0.24}O_4$ (yellow) and $Zn_{0.48}Mn_{1.41}Co_{0.99}Ca_{0.09}O_4$ (blue), A) Comparison of ORR-LSV curves of mixed-metal spinel type oxides prepared from multi-metal MOFs in a O_2-saturated 0.1 M KOH solution stirred at 2000 rpm; B) Comparison of methanol crossover in a O_2-saturated in 0.1 M KOH electrolyte stirred at 1600 rpm with methanol injection at 600s.

SUMMARY

In summary, new isoreticular MOFs with different arrangements of up to four metal-cations have been realized through the adjustment of the selected molar codes. The resulting metal ratios are preserved through the MOF calcination processes, resulting in the ability to program new compositions in spinel type oxides, as proved with the 17 new multi-metal oxides prepared and characterized. We show that the incorporation of multiple metal elements results in a complex interplay, where small modifications in metal ratios strongly influence the electrocatalytical activity in the oxygen reduction reaction, both in terms of current density, and number of transferred electrons. Thus, the material with composition $Zn_{0.48}Mn_{1.41}Co_{0.99}Ca_{0.09}O_4$ that is programmed from a MOF prepared from a Zn:Co:Mn:Ca 1:4:4:1 molar code, achieves a current density that is 97.2% that of commercial

Pt/C(20%W) catalyst, with a 3.92 electron process. These results demonstrate the potential to program and attain new compositions through the selection of adequate molar codes in complex multi-metal MOFs.

ASSOCIATED CONTENT

SUPPORTING INFORMATION.

Supporting figures and tables, single crystal X-ray results, SEM-EDS, TEM-EDS, FE-SEM images, powder X-ray diffraction patterns, powder neutron diffraction patterns and Rietveld refinements, TGA plots, CV curves, K-L plots and LSV curves. This material is available free of charge via the Internet at http://pubs.acs.org.

AUTHOR INFORMATION

Corresponding Author

* gandara@icmm.csic.es
* amonge@icmm.csic.es

Author Contributions

The manuscript was written through contributions of all authors.

Funding Sources

MAT2016-78465-R, MAT2015-68639-R and CTQ2017-87262-R

ACKNOWLEDGMENT

We acknowledge Institut Laue-Langevin and Spanish Initiatives on Neutron Scattering (ILL- SpINS) for beamtime at instrument D1B and G. Cuello for assistance during data acquisition. Paul Scherrer Institute is also acknowledged for beamtime at instrument HRPT, V. Pomjakhusin for assistance during data acquisition. We thank E. Rodríguez-Cañas and Isidoro Poveda from the Servicio Interdepartamental de Investigación at Universidad Autónoma de Madrid for valuable support with SEM images and EDS analyses and FE-SEM images acquisition, respectively. We acknowledge E. Urones for the TEM images and TEM-EDS analyses acquisition at Centro Nacional de Microscopía Electrónica. Funding: Work at Instituto de Ciencia de Materiales de Madrid–Consejo Superior de Investigaciones Científicas (CSIC) has been supported by the Spanish Ministry for Science, Innovation and Universities (MINECO) and FEDER funds: Projects MAT2016-78465-R, MAT2015-68639-R and CTQ2017-87262-R. F.G. and N.L.-S. acknowledge financial support from MINECO (Ramón y Cajal program and FPI research contract, respectively).

REFERENCES

1. Castillo-Blas, C.; Snejko, N.; de la Peña-O'Shea, V. A.; Gallardo, J.; Gutiérrez-Puebla, E.; Monge, M. A.; Gándara, F., Crystal phase competition by addition of a second metal cation in solid solution metal-organic frameworks. *Dalton Transactions* **2016**, *45 (10)*, 4327-4337.
2. D'Vries, R. F.; Alvarez-García, S.; Snejko, N.; Bausá, L. E.; Gutiérrez-Puebla, E.; de Andrés, A.; Monge, M. A., Multimetal rare earth MOFs for lighting and thermometry: tailoring color and optimal temperature range through enhanced disulfobenzoic triplet phosphorescence. *Journal of Materials Chemistry C* **2013**, *1 (39)*, 6316-6324.
3. Furukawa, H.; Cordova, K. E.; O'Keeffe, M.; Yaghi, O. M., The Chemistry and Applications of Metal-Organic Frameworks. *Science* **2013**, *341* (6149).
4. Yuan, S.; Chen, Y. P.; Qin, J.; Lu, W.; Wang, X.; Zhang, Q.; Bosch, M.; Liu, T. F.; Lian, X.; Zhou, H. C., Cooperative Cluster Metalation and Ligand Migration in Zirconium Metal–Organic Frameworks. *Angewandte Chemie International Edition* **2015**, *54 (49)*, 14696-14700.
5. Brozek, C. K.; Dincă, M., Cation exchange at the secondary building units of metal–organic frameworks. *Chemical Society Reviews* **2014**, *43 (16)*, 5456-5467.
6. Castells-Gil, J.; Padial, N. M.; Almora-Barrios, N.; Albero, J.; Ruiz-Salvador, A. R.; González-Platas, J.; García, H.; Martí-Gastaldo, C., Chemical Engineering of Photoactivity in Heterometallic Titanium–Organic Frameworks by Metal Doping. *Angewandte Chemie International Edition* **2018**, *57 (28)*, 8453-8457.
7. Wang, L. J.; Deng, H.; Furukawa, H.; Gándara, F.; Cordova, K. E.; Peri, D.; Yaghi, O. M., Synthesis and Characterization of Metal–Organic Framework-74 Containing 2, 4, 6, 8, and 10 Different Metals. *Inorganic Chemistry* **2014**, *53 (12)*, 5881-5883.
8. Zhai, Q.-G.; Bu, X.; Mao, C.; Zhao, X.; Feng, P., Systematic and Dramatic Tuning on Gas Sorption Performance in Heterometallic Metal–Organic Frameworks. *Journal of the American Chemical Society* **2016**, *138 (8)*, 2524-2527.
9. Liu, Z.-F.; Wu, M.-F.; Wang, S.-H.; Zheng, F.-K.; Wang, G.-E.; Chen, J.; Xiao, Y.; Wu, A. Q.; Guo, G.-C.; Huang, J.-S., Eu^{3+}-doped Tb^{3+} metal-organic frameworks emitting tunable three primary colors towards white light. *Journal of Materials Chemistry C* **2013**, *1 (31)*, 4634-4639.
10. Sapnik, A.F.; Gedes, H.S.; Reynolds, E.M.; Yeung, H.H.-M; Goodwin, A.L., Compositional inhomogeneity and tuneable thermal expansion in mixed-metal ZIF-8 analogues. *Chemical Communications* **2018**, *54*, 9651-9654.
11. Aguirre-Díaz, L. M.; Gándara, F.; Iglesias, M.; Snejko, N.; Gutiérrez-Puebla, E.; Monge, M. Á., Tunable Catalytic Activity of Solid Solution Metal–Organic Frameworks in One-Pot Multicomponent Reactions. *Journal of the American Chemical Society* **2015**, *137 (19)*, 6132-6135.
12. Liu, Q.; Cong, H.; Deng, H., Deciphering the Spatial Arrangement of Metals and Correlation to Reactivity in Multivariate Metal–Organic Frameworks. *Journal of the American Chemical Society* **2016**, *138*, 13822-13825.
13. Castillo-Blas, C.; de la Peña-O'Shea, V. A.; Puente-Orench, I.; de Paz, J. R.; Sáez-Puche, R.; Gutiérrez-Puebla, E.; Gándara, F.; Monge, Á., Addressed realization of multication complex arrangements in metal-organic frameworks. *Science Advances* **2017**, *3 (7)*, 1700773.
14. Qian, Y.; Khan Inayat, A.; Zhao, D., Electrocatalysts Derived from Metal–Organic Frameworks for Oxygen Reduction and Evolution Reactions in Aqueous Media. *Small* **2017**, *13 (37)*, 1701143.
15. Liu, B.; Shioyama, H.; Jiang, H.; Zhang, X.; Xu, Q., Metal–organic framework (MOF) as a template for syntheses of nanoporous carbons as electrode materials for supercapacitor. *Carbon* **2010**, *48* (2), 456-463.
16. Dang, S.; Zhu, Q.-L.; Xu, Q., Nanomaterials derived from metal–organic frameworks. *Nature Reviews Materials* **2017**, *3*, 17075.
17. Wu, H.; Zhou, W.; Yildirim, T., Hydrogen Storage in a Prototypical Zeolitic Imidazolate Framework-8. *Journal of the American Chemical Society* **2007**, *129 (17)*, 5314-5315.
18. Choi, K. M.; Jeong, H. M.; Park, J. H.; Zhang, Y.-B.; Kang, J. K.; Yaghi, O. M., Supercapacitors of Nanocrystalline Metal–Organic Frameworks. *ACS Nano* **2014**, *8 (7)*, 7451-7457.

19. Yang, H.; Bradley, S. J.; Wu, X.; Chan, A.; Waterhouse, G. I. N.; Nann, T.; Zhang, J.; Kruger, P. E.; Ma, S.; Telfer, S. G., General Synthetic Strategy for Libraries of Supported Multicomponent Metal Nanoparticles. *ACS Nano* **2018**, *12 (5)*, 4594-4604.
20. Yazdi, A.; Abo Markeb, A.; Garzón-Tovar, L.; Patarroyo, J.; Moral-Vico, J.; Alonso, A.; Sánchez, A.; Bastus, N.; Imaz, I.; Font, X.; Puntes, V.; Maspoch, D., Core–shell Au/CeO_2 nanoparticles supported in UiO-66 beads exhibiting full CO conversion at 100 °C. *Journal of Materials Chemistry A* **2017**, *5 (27)*, 13966-13970.
21. Dolomanov, O.V.; Bourhis, L.J.; Gildea, R.J.; Howard, J.A.K.; Puschmann, H., OLEX2: A complete structure solution, refinement and analysis program. *Journal of Applied Crystallography* **2009**, *42*, 339-341.
22. Sheldrick, G.M., A short history of SHELX. *Acta Crystallographica A* **2008**, *64*, 112-122.
23. Monge, A.; Snejko, N.; Gutierrez-Puebla, E.; Medina, M.; Cascales, C.; Ruiz-Valero, C.; Iglesias, M.; Gomez-Lor, B., One teflon-like channelled nanoporous polymer with a chiral and new uninodal 4-connected net: sorption and catalytic properties. *Chemical Communications* **2005**, *(10)*, 1291-1293.
24. Sun, J.-K.; Xu, Q., Functional materials derived from open framework templates/precursors: synthesis and applications. *Energy & Environmental Science* **2014**, *7 (7)*, 2071-2100.
25. Toh, R.J.; Eng, A.Y.S.; Safer, Z.; Sedmidubsky, S; Pumera, D., Ternary Transition Metal Oxide nanoparticles with Spinel Structure for the Oxygen Reduction Reaction. *ChemElectroChem* **2015**, *2*,982-987.
26. Jiang, S.; Liang, F.; Zhou, W.; Shao, Z, Hierarchical porous cobalt-free perovskite electrode for highly efficient oxygen reduction. *Journal of Materials Chemistry* **2012**, *22*, 16214-16218.
27. Oderairo, T.; Yan, X.; Ma, J.; Jiao, Y.; Yao, X.; Du, A.; Zhu, Z., Nanosheets Co_3O_4 Interleaved with Graphene for Highly Efficient Oxygen Reduction. *Applied Materials & Interfaces* **2015**, *7*, 21373-21380.
28. Zhao, Q.; Yan, Z.; Chen, C.; Chen, J., Spinels: Controlled Preparation, Oxygen Reduction/Evolution Reaction Application, and Beyond. *Chemical Reviews* **2017**, *117 (15)*, 10121-10211.
29. Lee, E.; Jang, J.-H.; Kwon, Y.-U., Composition effects of spinel $Mn_xCo_{3-x}O_4$ nanoparticles on their electrocatalytic properties in oxygen reduction reaction in alkaline media. *Journal of Power Sources* **2015**, *273*, p 735–741.
30. Yao, L.; Yang, W.; Liu, H.; Jia, J.; Wu, G.; Liu, D.; Liu, T.; Tan, T.; Wang, C., Synthesis and ORR electrocatalytic activity of mixed Mn-Co oxides derived from divalent metal-based MIL-53 analogues. *Dalton Transactions* **2017**, *46 (44)*, 15512-15519.
31. Mahata, P.; Sarma, D.; Madhu, C.; Sundaresen, A.; Natarajan, S., $CoMn_2O_4$ spinel from a MOF: synthesis, structure and magnetic studies. *Dalton Transactions* **2011**, *40 (9)*, 1952-1960.
32. Chen, S.; Xue, M.; Li, Y.; Pan, Y.; Zhu, L.; Zhang, D.; Fang, Q.; Qiu, S., Porous $ZnCo_2O_4$ nanoparticles derived from a new mixed-metal organic framework for supercapacitors. *Inorganic Chemistry Frontiers* **2015**, *2 (2)*, 177-183.
33. Wu, Z.-S.; Yang, S.; Sun, Y.; Parvez, K.; Feng, X.; Müllen, K., 3D Nitrogen-Doped Graphene Aerogel-Supported Fe_3O_4 Nanoparticles as Efficient Electrocatalysts for the Oxygen Reduction Reaction. *Journal of the American Chemical Society* **2012**, *134 (22)*, 9082-9085.
34. Liang, Y.; Li, Y.; Wang, H.; Zhou, J.; Wang, J.; Regier, T.; Dai, H., Co_3O_4 nanocrystals on graphene as a synergistic catalyst for oxygen reduction reaction. *Nature Materials* **2011**, *10*, 780.
35. Li, C.; Han, X.; Cheng, F.; Hu, Y.; Chen, C.; Chen, J., Phase and composition controllable synthesis of cobalt manganese spinel nanoparticles towards efficient oxygen electrocatalysis. *Nature Communications* **2015**, *6*, 7345.
36. Zhou, Y.; Sun, S.; Xi, S.; Duan, Y.; Sritharan, T.; Du, Y.; Xu, Z.J., Superexchange Effects on Oxygen Reduction Activity of Edge-Sharing [$Co_xMn_{1-x}O_6$] Octahedra in Spinel Oxide. *Advanced Materials* **2018**, *30*, 1705407.
37. Han, X.; Zhang, T.; Du, J.; Cheng, F.; Chen, J., Porous calcium-manganese oxide microspheres for electrocatalytic oxygen reduction with high activity. *Chemical Science* **2013**, *4 (1)*, 368-376.
38. Wu, G.; Wang, J.; Ding, W.; Nie, Y.; Li, L.; Qi, X.; Chen, S.; Wei, Z., A strategy to promote the electrocatalytic activity of spinels dor oxygen reduction by structure reversal. *Angewandte Chemie International Edition* **2016**, 55, 1340-1344.
39. Sa, Y. J.; Kwon, K.; Cheon, J. Y.; Kleitz, F.; Joo, S. H., Ordered mesoporous Co_3O_4 spinels as stable, bifunctional, noble metal-free oxygen electrocatalysts. *Journal of Materials Chemistry A* **2013**, *1 (34)*, 9992-10001.

SYNOPSIS TOC: Multi-cation metal-organic frameworks with various arrangements in the SBUs are used as precursors of spinel oxides, with a programmed composition, employed as effective catalysts in oxygen reduction reaction.